*Physics of Atomic Nuclei, Vol. 67, No. 4, 2004, pp. 653–661. Translated from Yadernaya Fizika, Vol. 67, No. 4, 2004, pp. 675–683.*
*Original Russian Text Copyright © 2004 by Elkin, Ishkhanov, Kapitonov, Lileeva, Shirokov.*

NUCLEI
Experiment

# Isotopic Effect in the Width of a Giant Dipole Resonance in Light Nuclei

**M. A. Elkin, B. S. Ishkhanov, I. M. Kapitonov, E. I. Lileeva, and E. V. Shirokov**

*Institute of Nuclear Physics, Moscow State University, Vorob'evy gory, Moscow, 119899 Russia*

Received December 26, 2002; in final form, July 1, 2003

**Abstract**—An isotopic effect in the widths of giant dipole resonances is established on the basis of an analysis of the latest systematics of photoabsorption cross sections for nuclei containing 12 to 65 nucleons. This effect arises owing to isospin splitting of a giant resonance and is enhanced by its configuration splitting. © *2004 MAIK "Nauka/Interperiodica"*.

## 1. INTRODUCTION

The giant dipole resonance in nuclei has been investigated for more than 50 years, and many aspects of this important phenomenon in nuclear physics have received quite a comprehensive study. Despite this, there is still no definitive understanding of some of its features, including the shape and width of a giant dipole resonance in light nuclei ($A \leq 60$). In nuclei from this mass region, a giant dipole resonance is scattered over a rather wide energy region, and its shape changes pronouncedly from one nucleus to another. For example, a change of one to two in the number of nucleons in a light nucleus can lead to a change in the width of a giant dipole resonance by a factor of 2 to 3. Concurrently, the overall shape of the resonance changes drastically, so that one cannot trace any regular dependence of the features being discussed on the mass number $A$. Such behavior of a giant dipole resonance in light nuclei is associated with the fact that its properties are affected by a number of factors, including, above all, configuration and isospin resonance splitting [1–3]. The contributions of these factors are highly sensitive not only to the total number of intranuclear nucleons but also to the relationship between the numbers of intranuclear protons and neutrons. In order to clarify the factors affecting the shape and width of a giant dipole resonance in light nuclei, it is necessary to have reliable data on the cross sections for nuclear photoabsorption in the photon-energy region extending up to about 40 MeV. The results reported in [4], where the systematics of the cross sections for photon absorption by $A = 12$–$65$ nuclei at photon energies up to 40 MeV was compiled on the basis of a thorough analysis of the entire body of available relevant information, opened a possibility for revealing the most important factors affecting the width of a giant dipole resonance in light nuclei. In the present study, the photoabsorption cross sections quoted in [4] are used to analyze the general features of a giant dipole resonance in light nuclei, including its shape and width.

## 2. SYSTEMATICS OF PHOTOABSORPTION CROSS SECTIONS AND GENERAL FEATURES OF GIANT DIPOLE RESONANCES IN LIGHT NUCLEI

The systematics of photon-absorption cross sections [4] was compiled on the basis of an analysis of 40 photonuclear experiments that are the most precise ones. It includes the photon-absorption cross sections for 31 nuclides containing 12 to 65 nucleons ($^{12,13,14}$C, $^{14,15}$N, $^{16,17,18}$O, $^{19}$F, $^{23}$Na, $^{24,25,26}$Mg, $^{27}$Al, $^{28,29,30}$Si, $^{32,34}$S, $^{40}$Ar, $^{40,42,44,48}$Ca, $^{46,48}$Ti, $^{52}$Cr, $^{58,60}$Ni, $^{63,65}$Cu) and covers the photon-energy region that extends up to 40 MeV and which is dominated by a giant dipole resonance. For the majority of nuclides, the photon-absorption cross sections were obtained by summing the photonucleon cross sections $\sigma(\gamma,p)$, $\sigma(\gamma,n)$, $\sigma(\gamma,2n)$, and $\sigma(\gamma,\mathrm{p}n)$. For $^{12}$C, $^{14}$N, $^{16}$O, $^{19}$F, $^{27}$Al, $^{28}$Si, and $^{40}$Ca, these were directly measured photon-absorption cross sections. By way of example, the photon-absorption cross sections for carbon, oxygen, and calcium isotopes are presented in Figs. 1–3.

This systematics of photon-absorption cross sections makes it possible to trace the variations in the basic features of a giant dipole resonance over a broad mass-number range (from 12 to 65), including light $1p$-, $1d2s$-, and $1f2p$-shell nuclei. We will analyze the following features of giant dipole resonances: (i) the integrated photoabsorption cross section, (ii) the position of a giant dipole resonance on the energy scale, and (iii) the width of a giant dipole resonance.

Let us consider these features successively.

1063-7788/04/6704-0653$26.00 © 2004 MAIK "Nauka/Interperiodica"

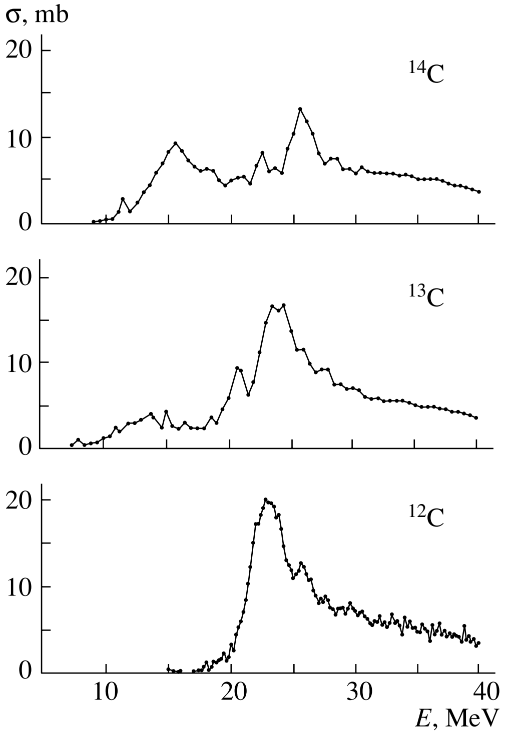

**Fig. 1.** Cross sections for photon absorption by carbon isotopes. Here and in Figs. 2 and 3 below, the photon energy is plotted along the abscissa.

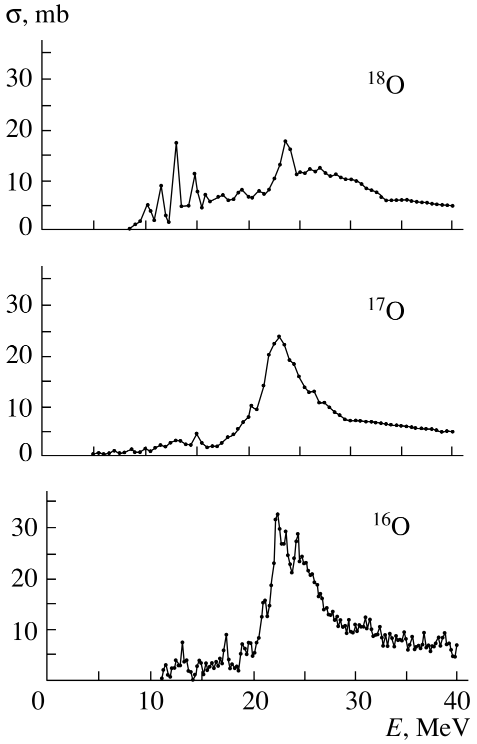

**Fig. 2.** Cross sections for photon absorption by oxygen isotopes.

The integrated photoabsorption cross section is given by

$$\sigma^{\text{int}} = \int\limits_{0}^{40\ \text{MeV}} \sigma(E)dE. \qquad (1)$$

The systematics of integrated cross sections over the photon-energy region extending up to 40 MeV is presented in Fig. 4. For the mass-number dependence of $\sigma^{\text{int}}$, a linear approximation of the data in question yields

$$\sigma^{\text{int}} = (-75 + 21A)\ \text{MeV mb}, \qquad (2)$$

with the correlation factor being 0.993. The mean deviation of the experimental points from this dependence is 16 MeV mb, the actual relative deviation nowhere exceeding 20%. The dependence in (2) corresponds to the following formula for the electric-dipole sum rule:

$$\int\limits_{0}^{\infty} \sigma(E)dE = 60\frac{NZ}{A}(1 + \Delta). \qquad (3)$$

Here, $\Delta = 0.33$ is the correction to the classical dipole sum rule ($60NZ/A$ MeV mb) due to exchange forces.

The position of a giant dipole resonance on the energy scale is traditionally characterized by its mean energy (centroid). However, the energy $E^{\max}$ corresponding to the maximum of the photoabsorption cross section is more appropriate for the purposes of our investigation, since it is much more sensitive to the mechanism of giant-dipole-resonance formation. The energy $E^{\max}$ can be determined by different methods—for example, as the position of an individual experimental point at which the cross section is maximal. In this case, however, statistical fluctuations of experiments will have the strongest effect on the value of $E^{\max}$.

In the region of a giant-dipole-resonance maximum, a number of cross sections (those for $^{28}$Si, $^{30}$Si, $^{52}$Cr, $^{60}$Ni) develop a few rather narrow peaks of commensurate magnitude. Other cross sections (those for $^{14}$C, $^{19}$F, $^{23}$Na, $^{40}$Ar) are scattered over a rather broad energy interval, exhibiting no distinct peak.

We used the following method to assess the position of the giant-dipole-resonance maximum. For a maximum, we took the midpoint of the energy interval 5 MeV in width that made the greatest contribution to the integrated cross section. In this case, a rather large number of neighboring points (up to 25) were involved in assessing the position of the giant-dipole-resonance maximum, whereby the effect of statistical

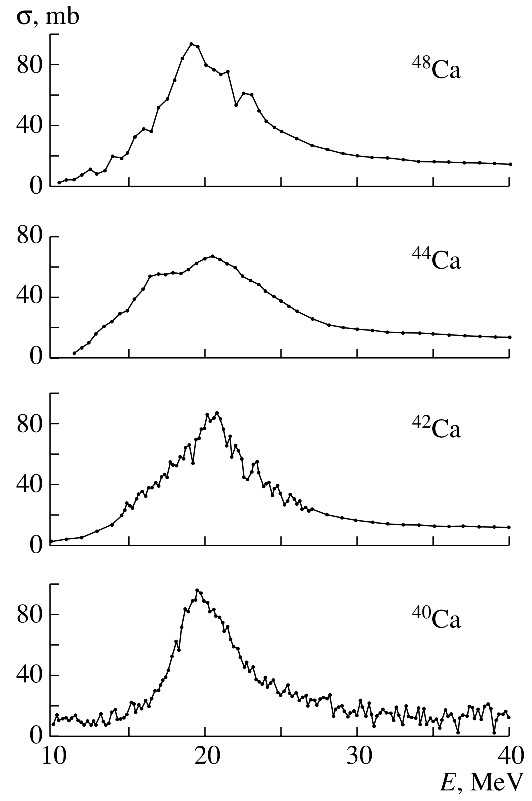

**Fig. 3.** Cross sections for photon absorption by calcium isotopes.

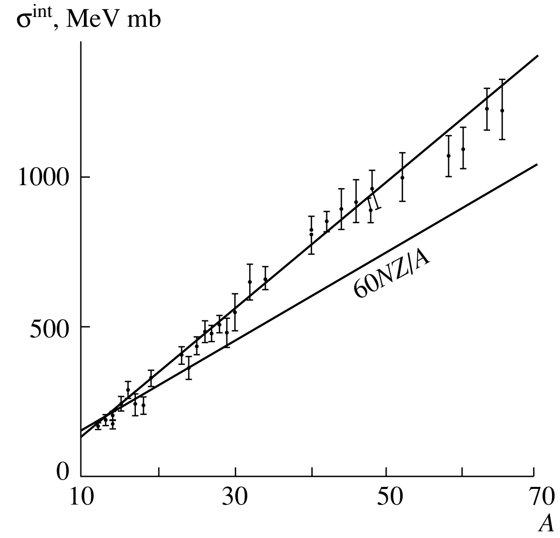

**Fig. 4.** Photon-absorption cross sections integrated up to 40 MeV.

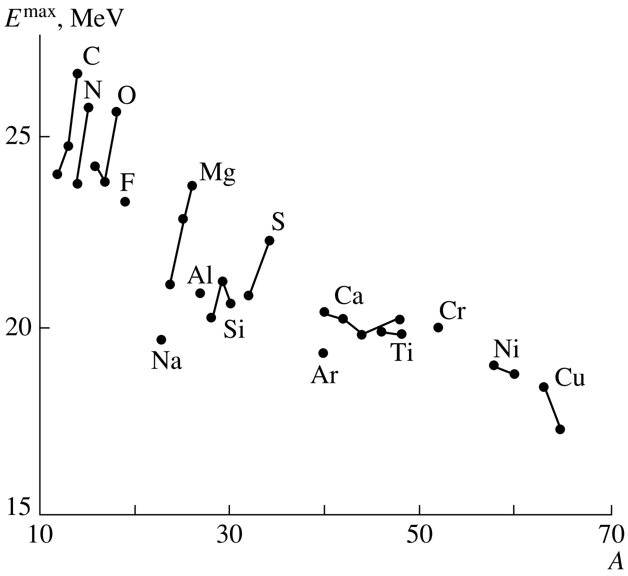

**Fig. 5.** Energies corresponding to the maxima of photon-absorption cross sections.

fluctuations of individual points was leveled out almost completely. The choice of energy-interval width is quite arbitrary in this procedure. For this width, we took the value of 5 MeV, which corresponds to the FWHM of the cross sections for photon absorption by nuclei involving filled shells or subshells—that is, the magic and semimagic nuclei of $^{12}$C, $^{16}$O, $^{28}$Si, and $^{40}$Ca. In experiments having a not very high energy resolution, the giant dipole resonance in such nuclei assumes the form of a single resonance having a rather regular form, its FWHM being minimal. In the following, we will refer to the width of 5 MeV as a magic width and to the corresponding energy interval as the magic interval.

For all 31 nuclei, the data on $E^{\max}$ are given in Fig. 5. With increasing mass number $A$, $E^{\max}$ decreases, on average, from 24–27 MeV for carbon isotopes to 17 or 18 MeV for copper isotopes. Against the background of a rather smooth decrease in $E^{\max}$ with increasing mass number, there are local deviations caused by different numbers of neutrons in the nucleus of one element or another. This "isotopic effect" is especially pronounced in the case of carbon, nitrogen, oxygen, magnesium, and sulfur isotopes. The isotopic effect in question will be discussed below in connection with the problem of the giant-dipole-resonance width.

## 3. DATA ON GIANT-DIPOLE-RESONANCE WIDTH

Let us now consider data on the width of a giant dipole resonance. For an individual resonance of regular Breit–Wigner shape, the width is usually defined as its FWHM (it is denoted by Γ). In the case of a giant dipole resonance, however, we are dealing with a complicated photoabsorption-cross-section curve

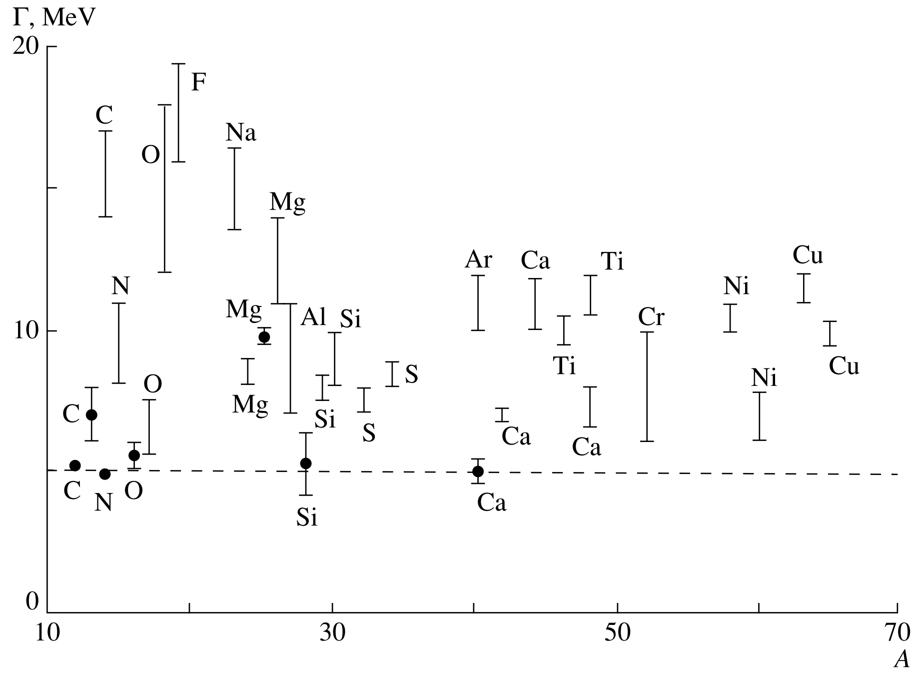

**Fig. 6.** FWHM Γ for photon-absorption cross sections. Intervals of possible values are indicated for the majority of nuclei. The most probable values (points) are given for five nuclei along with the respective errors.

formed by a set of overlapping narrower resonances scattered over a broad energy region, so that a giant dipole resonance has a shape that is highly dissimilar to the shape of an individual resonance, even the determination of the position of the giant-dipole-resonance maximum being sometimes ambiguous. A good illustration of the aforesaid is provided by the photoabsorption cross sections for about half of the nuclei subjected to analysis ($^{14}$C, $^{18}$O, $^{19}$F, $^{23}$Na, $^{24}$Mg, $^{26}$Mg, $^{30}$Si, $^{32}$S, $^{34}$S, $^{40}$Ar, $^{48}$Ti, $^{52}$Cr, $^{58}$Ni, $^{60}$Ni, $^{63}$Cu). Only for some magic and semimagic nuclei does the photoabsorption cross section have, in the case of a not very high energy resolution, the "correct" shape of an individual resonance ($^{12}$C, $^{16}$O, $^{28}$Si, $^{40}$Ca). The traditional concept of a giant-dipole-resonance width is applicable to such nuclei—that is, it can be defined as the FWHM Γ of the respective photoabsorption cross section.

We also used the concept of the width Γ for the other nuclei, which are characterized by a complicated form of a giant dipole resonance. By the width Γ, we meant, in those cases, the width of that energy range of a giant dipole resonance within which the photoabsorption cross section decreased by a factor of 2 in relation to its maximum value. All data on the giant-dipole-resonance width determined in this way are given in Fig. 6. It can be seen that the giant-dipole-resonance width is minimal for the magic and semimagic nuclei of $^{12}$C, $^{16}$O, $^{28}$Si, and $^{40}$Ca (as well as for $^{14}$N). This width, $\Gamma \approx 5$ MeV, is referred to as a magic width. For the remaining nuclei, the width Γ is greater, by a factor of about 2 for the majority of them and by a factor of 3 or greater for some other nuclei ($^{14}$C, $^{18}$O, $^{19}$F, $^{23}$Na).

Despite a considerable uncertainty in Γ for some nuclei, the data in Fig. 6 display a distinct isotopic effect (dependence on the number of neutrons in the isotopes of the same element), and one of the purposes that we pursue in this study is to explain this effect.

Since the notion of a width in the rigorous sense that it has for an individual resonance is inapplicable to giant dipole resonances in many (especially light) nuclei, we attempted to specify a different quantity that would have a clear mathematical meaning and which would characterize the energy region of giant-dipole-resonance spreading.

Having considered various versions, we found such a quantity. It is physically adequate to the giant-dipole-resonance width and reflects the most important features of the variations that this width suffers in response to the variation in the mass number. This is the contribution to the integrated photoabsorption cross section from a magic interval of width 5 MeV in the region of the giant-dipole-resonance maximum (the position of this 5-MeV interval on the energy scale is chosen in such a way that this contribution is maximal). Obviously, the quantity introduced in this way, which is hereafter

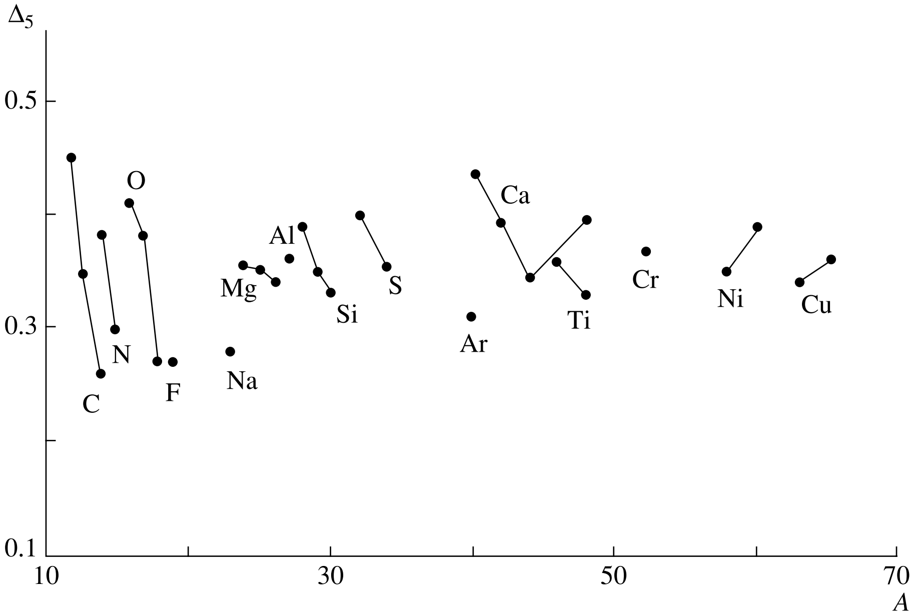

**Fig. 7.** Integrated-cross-section fractions $\Delta_5$ within an energy range of width 5 MeV in the region of the giant-dipole-resonance maximum.

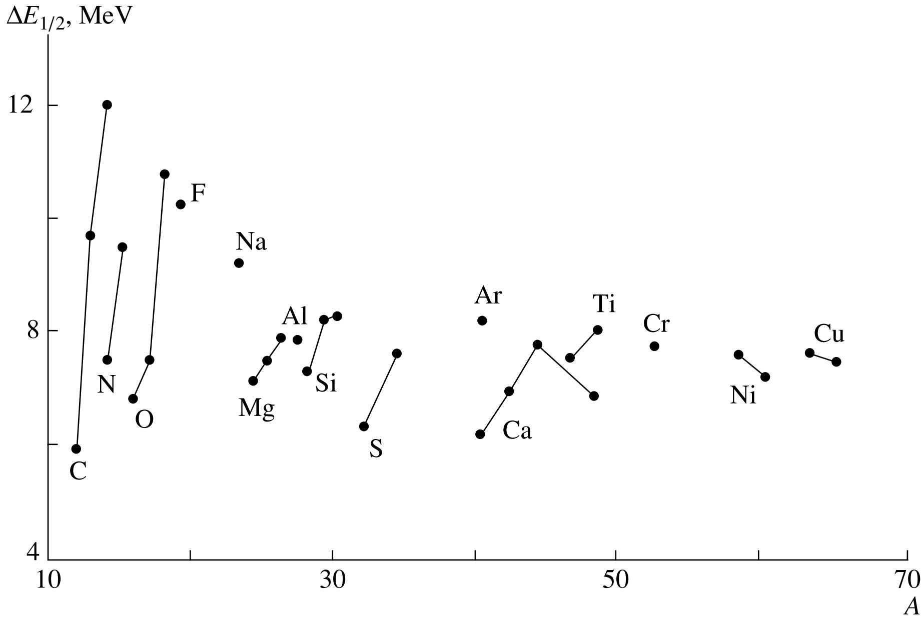

**Fig. 8.** Minimum energy interval $\Delta E_{1/2}$ lying in the region of the giant-dipole-resonance maximum and contributing one-half to the integrated cross section for photoabsorption.

denoted by $\Delta_5$, is directly related to the energy $E^{\max}$, which was used above as the energy corresponding to the giant-dipole-resonance maximum. In order to clarify this point, we recall that $E^{\max}$ is the midpoint of the energy range having a width of 5 MeV and making a dominant contribution to the respective integrated cross section. Obviously, $\Delta_5$ and $E^{\max}$ are related by the equation

$$\Delta_5 = \int\limits_{E^{\max}-2.5\text{ MeV}}^{E^{\max}+2.5\text{ MeV}} \sigma(E)dE \Bigg/ \int\limits_{0}^{40\text{ MeV}} \sigma(E)dE. \quad (4)$$

The quantity $\Delta_5$ characterizes the width of the energy region of giant-dipole-resonance spreading. Indeed, the larger this width, the smaller the contribution that

**Table 1.** Isotopic families

| Number of protons $Z$ | Number of neutrons | | | | | | |
|---|---|---|---|---|---|---|---|
| | $Z$ | $Z+1$ | $Z+2$ | $Z+4$ | $Z+5$ | $Z+7$ | $Z+8$ |
| 6 | $^{12}$C | $^{13}$C | $^{14}$C | | | | |
| 7 | $^{14}$N | $^{15}$N | | | | | |
| 8 | $^{16}$O | $^{17}$O | $^{18}$O | | | | |
| 12 | $^{24}$Mg | $^{25}$Mg | $^{26}$Mg | | | | |
| 14 | $^{28}$Si | $^{29}$Si | $^{30}$Si | | | | |
| 16 | $^{32}$S | | $^{34}$S | | | | |
| 20 | $^{40}$Ca | | $^{42}$Ca | $^{44}$Ca | | | $^{48}$Ca |
| 22 | | | $^{46}$Ti | $^{48}$Ti | | | |
| 28 | | | $^{58}$Ni | $^{60}$Ni | | | |
| 29 | | | | | $^{63}$Cu | $^{65}$Cu | |

the integrated photoabsorption cross section receives from the region around the giant-dipole-resonance maximum. On the contrary, the smaller the quantity $\Gamma$, the greater the integrated-cross-section fraction that is grouped immediately around the giant-dipole-resonance maximum. Thus, the quantities $\Delta_5$ and $\Gamma$ can be interpreted as measures of the mirror reflections of the same phenomenon.

All data on $\Delta_5$ are given in Fig. 7, which shows that, for the magic (semimagic) nuclei of $^{12}$C, $^{16}$O, and $^{40}$Ca, $\Delta_5 = 0.41$–$0.45$, which means that, for these nuclei, the region of width $\Gamma \approx 5$ MeV (where the cross section decreases by a factor of 2 in relation to the maximum value) contributes somewhat more than 40% to the integrated photoabsorption cross section. For the remaining nuclei, $\Delta_5$ is smaller, lying in the range 0.26–0.40. It is of importance that isotopic effects clearly manifest themselves in $\Delta_5$.

The use of the quantity $\Delta_5$ in the analysis instead of $\Gamma$ is advantageous in that the former has a clear mathematical meaning [see Eq. (4)], the uncertainties in it being much less than those in $\Gamma$. Ultimately, this makes it possible to reveal and study subtler effects associated with the giant-dipole-resonance width in going from one nucleus to another, even if the giant dipole resonance in these nuclei has a complicated shape strongly dissimilar to that of an individual resonance.

In order to prove that the isotopic effect steadily manifests itself in the giant-dipole-resonance width for different definitions of this width, we also considered, for a width, the minimum (for each nucleus) energy interval $\Delta E_{1/2}$ saturating half the photoabsorption cross section (integration region within 40 MeV). In just the same way as $\Delta_5$ and $E^{\max}$, this quantity has but a slight uncertainty. Figure 8 shows data on $\Delta E_{1/2}$, which compellingly demonstrate all basis features of the isotopic effect in the giant-dipole-resonance width that were manifested both in $\Gamma$ and in $\Delta_5$ (see Figs. 6 and 7, respectively).

## 4. ISOTOPIC EFFECT

Owing to the systematics presented in [4], we have at our disposal photoabsorption cross sections for ten chains of isotopes. These chains are listed in Table 1.

The chains in question include five isotopic doublets ($^{14,15}$N, $^{32,34}$S, $^{46,48}$Ti, $^{58,60}$Ni, $^{63,65}$Cu), four isotopic triplets ($^{12,13,14}$C, $^{16,17,18}$O, $^{24,25,26}$Mg, $^{28,29,30}$Si), and one isotopic quartet ($^{40,42,44,48}$Ca). So vast a systematics of data on isotopes makes it possible to observe the isotopic effect in the giant-dipole-resonance width clearly (Figs. 1–3, 6–8) and to obtain deeper insight into this phenomenon. As can be seen from these figures, the isotopic effect itself in the giant-dipole-resonance width amounts to the following features in the behavior of these widths:

(i) In the isotopic triplets where $N = Z$, $Z+1$, and $Z+2$ (carbon, oxygen, magnesium, and silicon), the giant dipole resonance becomes broader with increasing number of neutrons, this broadening in the heaviest isotope of the lightest isotopic triplets ($^{14}$C in the chain of carbon isotopes and $^{18}$O in the chain of oxygen isotopes) going over to the splitting of the respective giant dipole resonances into two groups of transitions, a low-energy (10–20 MeV) and a high-energy (20–40 MeV) group. A trend toward the broadening of a giant dipole resonance with increasing number of neutrons can also be traced in the isotopic doublets of nitrogen ($^{14,15}$N), sulfur ($^{32,34}$S), and titanium ($^{46,48}$Ti).

(ii) In the longest chain of calcium isotopes ($^{40,42,44,48}$Ca), the broadening of the giant dipole resonance with increasing number of neutrons is observed from the magic nucleus of $^{40}$Ca (where the width is the smallest) to $^{44}$Ca (where the width becomes the largest). As the number of neutrons increases further ($^{48}$Ca), the giant-dipole-resonance width decreases to values characteristic of $^{42}$Ca.

(iii) An inverse trend toward a decrease in the giant-dipole-resonance width with increasing number of neutrons is observed for the heaviest isotopic doublets ($^{58,60}$Ni, $^{63,65}$Cu).

(iv) By and large, the scale of the isotopic effect decreases with increasing mass number $A$. This effect is seen most clearly in carbon, nitrogen, and oxygen isotopes, where the width of the giant dipole resonance in the heaviest isotope is larger than that in the lightest isotope ($N = Z$) by a factor of 1.5 to 3. In the heaviest nuclei (titanium, nickel, copper), relative isotopic changes decrease to 10–20%.

All of the aforementioned special features of the isotopic effect in the width of a giant dipole resonance can be explained in the most natural way by invoking the concept of the isospin splitting of giant dipole resonances [5, 6].

## 5. EXPLANATION OF THE ISOTOPIC EFFECT

We recall that, in self-conjugate nuclei ($N = Z$), there exists only one isospin branch of a giant dipole resonance, that of isospin $T_> = 1$. In $N \neq Z$ nuclei, the giant dipole resonance is split in isospin. If $T_0 = (N - Z)/2$ is the ground-state isospin of the nucleus being considered, then, upon the absorption of an $E1$ photon by this nucleus, two group of states (two giant-dipole-resonance branches) are excited in it, that of isospin $T_< = T_0$ and that of isospin $T_> = T_0 + 1$. The centroid $E_>$ of the $T_>$ branch lies higher than the centroid $E_<$ of the $T_<$ branch; that is, there arises the splitting of a giant dipole resonance in isospin, the magnitude of this splitting being given by [6]

$$\Delta E = E_> - E_< = \frac{U}{A}(T_0 + 1), \tag{5}$$

where $U$ is a constant that is related to the symmetry energy. According to a major part of available data, $U \approx 60$ MeV.

The cross sections $\sigma_<(E)$ and $\sigma_>(E)$ for the excitation of the giant-dipole-resonance branches characterized by the different isospin values satisfy the relation [5]

$$\int \frac{\sigma_>(E)}{E} dE \Big/ \int \frac{\sigma_<(E)}{E} dE = \frac{1}{T_0} \frac{1 - \frac{3}{2} T_0 A^{-2/3}}{1 + \frac{3}{2} A^{-2/3}}. \tag{6}$$

We will now show that the isospin splitting of a giant dipole resonance may explain all those facets of the isotopic effect in the widths of photoabsorption cross sections that were listed in Section 4.

We begin by illustrating this statement for the example of isotopic triplets. Special features of the behavior of giant dipole resonances in the isotopes entering into the composition of these triplets are the most pronounced in the lightest nuclei—that is, carbon and oxygen isotopes (see Figs. 1, 2). In self-conjugate nuclei ($N = Z$), where $T_0 = 0$, there is only one isospin branch of a giant dipole resonance, that of isospin $T_> = T_0 + 1 = 1$; it is formed by nucleon transitions from the closed-shell (closed-subshell) core—this is the $B$ branch, according to the terminology associated with the concept of the configuration splitting of giant dipole resonances [1–3]. Its FWHM value is $\Gamma = 5$ to 6 MeV. In such nuclei ($^{12}$C, $^{16}$O, $^{28}$Si, $^{40}$Ca), a giant dipole resonance is completely determined by this single isospin branch; therefore, it has the form of a resonance having a minimum width of 5 to 6 MeV (see Fig. 9*a*).

Upon the addition of one neutron (whereby one naturally arrives at an $N = Z + 1$ isotope), the $T_< = T_0 = 1/2$ branch, formed by transitions from a neutron-rich shell (this is the $A$ branch, according to the terminology associated with the concept of the configuration splitting of giant dipole resonances), is added to (see Fig. 9*b*) the main $T_> = T_0 + 1 = 3/2$ isospin branch, formed by $B$ transitions from the closed-shell (closed-subshell) core. This excess is insignificant for $N = Z + 1$ nuclei (one neutron), with the result that the relative contribution of the $T_<$ branch is small in such nuclei [the factor $1/T_0$ in (6)]. The $T_<$ branch forms a so-called pygmy resonance, which is strongly spread in energy and is shifted toward lower energy with respect to the $T_>$ branch by a value given by (5)—that is, by a few megaelectronvolts. As a result, the total width of the photoabsorption cross section increases (Fig. 9*b*).

Upon the addition of yet another neutron (that is, upon a transition to an $N = Z + 2$ isotope), the intensity of the $T_<$ branch of a giant dipole resonance ($T_< = T_0 = 1$) increases sharply, with the result that this branch saturates about half of the integrated photoabsorption cross sections [the factor $1/T_0$ in Eq. (6)]. The $T_<$ branch remains broad (it is widely spread in energy). It is shifted still farther toward lower energies with respect to the $T_>$ branch (see Fig. 9*c*). The respective giant dipole resonance then assumes the shape of a very broad two-humped curve (this effect is the most pronounced in the cross section for photoabsorption on a $^{14}$C nucleus).

It can easily be seen that all of the aforementioned effects manifest themselves in the triplets of carbon and oxygen isotopes. We emphasize once again that the $T_<$ branch is formed by nucleon transitions from unfilled outer shells but that the $T_>$ branch is formed predominantly by transitions from closed inner shells. Therefore, the broadening of a giant dipole resonance in non-self-conjugate nuclei belonging to isotopic triplets is due to the concerted effect of the isospin and configuration splitting of a giant dipole resonance.

The above explanation of the isotopic effect in the width of a giant dipole resonance in the isotopic triplets of carbon and oxygen is also applicable to the isotopic triplets of the heavier nuclei of $^{24,25,26}$Mg and $^{28,29,30}$Si (Figs. 6–8), although the scale of the effect there is much smaller (see below).

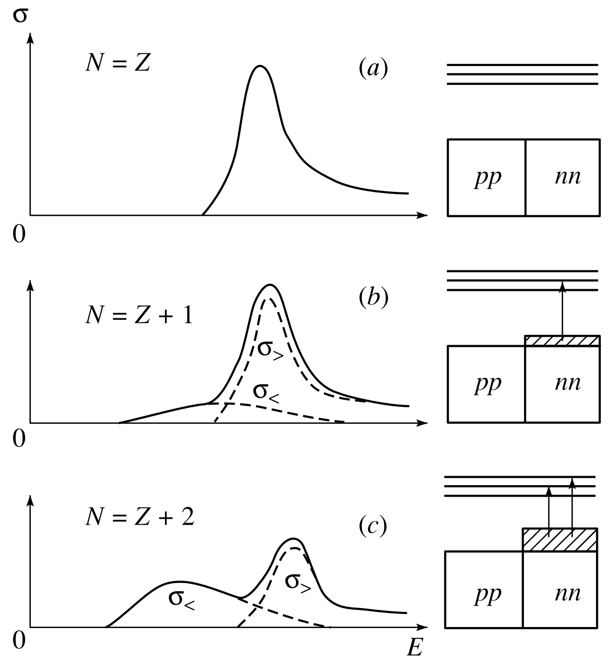

**Fig. 9.** Qualitative illustration of the neutron-excess effect on the shape of the photoabsorption cross section.

The broadening of the photoabsorption cross section for the heavier isotope in the nuclide pairs $^{14,15}$N and $^{32,34}$S and, possibly, in $^{46,48}$Ti is also associated with the isospin splitting of a giant dipole resonance.

It was indicated above that, in the longest chain of calcium isotopes ($^{40,42,44,48}$Ca), the width of a giant dipole resonance first grows with increasing neutron excess up to $^{44}$Ca, then decreasing in the heaviest isotope of $^{48}$Ca. This trend also fits well in the concept of the isospin splitting of a giant dipole resonance. Indeed, a high neutron excess (such as that in $^{48}$Ca) leads, owing to the factor $1/T_0$ in Eq. (6), to a strong decrease in the fraction of the $T_>$ component in the giant dipole resonance, this component being well offset in energy from the $T_<$ component [see Eq. (5)]. Under such conditions, the width of a giant dipole resonance is formed owing predominantly to the width of one isospin component and is close to the width of the giant dipole resonance in a self-conjugate nucleus (although it remains larger than that by a factor of 1.5).

**Table 2.** Experimental and model widths of giant dipole resonances in carbon and calcium isotopes (in MeV)

| Isotopes | $^{12}$C | $^{13}$C | $^{14}$C | $^{40}$Ca | $^{42}$Ca | $^{44}$Ca | $^{48}$Ca |
|---|---|---|---|---|---|---|---|
| Experiment | 6.0 | 9.7 | 12.0 | 6.2 | 6.9 | 7.8 | 6.8 |
| Model | 6.0 | 9.0 | 12.1 | 6.0 | 6.8 | 7.4 | 6.5 |

In the pairs of the heaviest nuclides, $^{58,60}$Ni and $^{63,65}$Cu, the decrease in the width of a giant dipole resonance upon going over to the heavy isotope may also be associated with this circumstance.

The entire body of experimental information about the widths of giant dipole resonances in the isotopic chains being considered (see Figs. 6–8) suggests that the scale of the isotopic effect decreases with increasing mass number $A$. Obviously, this is because the splitting $\Delta E$ of isospin components of a giant dipole resonance is in inverse proportion to the mass number $A$ [see Eq. (5)]. As a result, the isotopic effect in the widths of giant dipole resonances is expected to disappear for $A > 70$–80.

By employing Eqs. (5) and (6), which follow from the concept of the isospin splitting of a giant dipole resonance, one can easily verify that this concept makes it possible to reproduce the isotopic effect in the widths of giant dipole resonances quantitatively. Approximating the isospin components of a giant dipole resonance by two Gaussian distributions and choosing the positions of these distributions, $E_<$ and $E_>$, and their amplitudes in such a way as to ensure fulfillment of relations (5) and (6), we can obtain, for each isotope, a model expression for the photoabsorption cross section and determine its width. We have implemented this procedure for the majority of non-self-conjugate ($N \neq Z$) nuclei studied here. In doing this, we set the widths (FWHM) of individual Gaussian distributions to 6 MeV. It is this value that characterizes the widths $\Delta \mathrm{E}_{1/2}$ for the $^{12}$C and $^{40}$Ca nuclei, whose photoabsorption cross sections, which are formed by a single isospin component, are the most narrow. For carbon and calcium isotopes, the results obtained from the model calculations of the giant-dipole-resonance widths are given in Table 2, along with respective experimental values (Fig. 8). It is obvious that our model calculation, which is based on the concept of the isospin splitting of a giant dipole resonance, reproduces quantitatively all of the observed trends in the change in the widths of giant dipole resonances in isotopic chains.

Thus, the concept of the isospin splitting of a giant dipole resonance makes it possible to explain all basic features in the widths of giant dipole resonances in the isotopic chains of light nuclei. It should be emphasized that examples of a more detailed investigation into the role of the isospin splitting of a giant dipole resonance for individual nuclei or groups of nuclei in the mass-number region being considered [7–17] confirm our conclusions completely.

## 6. CONCLUSION

On the basis of an analysis of the latest data on the shape of photoabsorption cross sections for ten isotopic chains, we have established the existence of a distinct isotopic effect in the widths of giant dipole resonances. This effect has been traced from carbon to copper isotopes. The scale of the isotopic effect has been found to decrease with increasing mass number $A$. The effect itself is expected to disappear in nuclei of mass number in the region $A > 70$–80. The isotopic effect in the widths of giant dipole resonances is due to the isospin splitting of a giant dipole resonance and is enhanced by its configuration splitting.

## REFERENCES

1. R. A. Eramzhyan, B. S. Ishkhanov, I. M. Kapitonov, and V. G. Neudatchin, Phys. Rep. **136** (4–6) (1986).
2. B. S. Ishkhanov, I. M. Kapitonov, V. G. Neudatchin, *et al.,* Usp. Fiz. Nauk **160** (3), 57 (1990) [Sov. Phys. Usp. **33**, 204 (1990)].
3. B. S. Ishkhanov, I. M. Kapitonov, V. G. Neudatchin, and N. P. Yudin, Fiz. Élem. Chastits At. Yadra **31**, 1343 (2000).
4. B. S. Ishkhanov, I. M. Kapitonov, E. I. Lileeva, *et al.*, Preprint No. 2002/711, NIIYaF MGU (Institute of Nuclear Physics, Moscow State University, Moscow, 2002).
5. B. Goulard and S. Fallieros, Can. J. Phys. **45**, 3221 (1967).
6. R. Ö. Akyüz and S. Fallieros, Phys. Rev. Lett. **27**, 1016 (1971).
7. K. G. McNeill, M. N. Thompson, A. D. Bates, *et al.*, Phys. Rev. C **47,** 1108 (1993).
8. N. G. Goncharova, H. R. Kissener, and R. A. Éramzhyan, Fiz. Élem. Chastits At. Yadra **16**, 773 (1985) [Sov. J. Part. Nucl. **16**, 337 (1985)].
9. N. G. Goncharova, A. N. Golzov, and H. R. Kissener, Nucl. Phys. A **462**, 367 (1987).
10. Y. I. Assafiri and I. Morrison, Nucl. Phys. A **427,** 460 (1984).
11. Y. I. Assafiri and M. N. Thompson, Preprint No. UM-P-86/48 (University of Melbourne 1986).
12. R. A. Sutton, P. D. Allen, M. N. Thompson, and E. G. Muirhead, Nucl. Phys. A **398**, 415 (1983).
13. Y. I. Assafiri and M. N. Thompson, Nucl. Phys. A **357**, 429 (1981).
14. P. D. Harty and M. N. Thompson, Aust. J. Phys. **34**, 505 (1981).
15. R. A. Sutton, M. N. Thompson, M. Hirooka, *et al.*, Preprint No. UM-P-84/68 (University of Melbourne 1984).
16. G. J. O'Keefe, M. N. Thompson, Y. I. Assafiri, *et al.*, Preprint No. UM-P-86/54 (University of Melbourne 1986).
17. R. Sutton, M. N. Thompson, M. Sugawara, *et al.*, Nucl. Phys. A **339**, 125 (1980).

*Translated by A. Isaakyan*

Physics of Atomic Nuclei, Vol. 67, No. 4, 2004, pp. 662–671. Translated from Yadernaya Fizika, Vol. 67, No. 4, 2004, pp. 684–693.
Original Russian Text Copyright © 2004 by Sukhovoj, Khitrov.

# Potential of Present-Day Experiments for Determining the Parameters of the Gamma Decay of Compound States of Heavy Nuclei in a Model-Independent Way

**A. M. Sukhovoj*** **and V. A. Khitrov****

*Joint Institute for Nuclear Research, Dubna, Moscow oblast, 141980 Russia*

Received December 26, 2002; in final form, March 13, 2003

**Abstract**—Experimental data on two-step cascades initiated by thermal-neutron capture in $^{184,186}$W and $^{190,192}$Os nuclei are analyzed from the point of view of prospects for improving the reliability of a model-independent determination of the density of levels in a given interval of $J^\pi$ and the radiative strength functions for $E1$ and $M1$ transitions exciting these levels in the region $E_{\text{exc}} \leq B_n$. *© 2004 MAIK "Nauka/Interperiodica".*

## 1. INTRODUCTION

Until recently, the level density $\rho = D^{-1}$ and the radiative strength function

$$k = \Gamma_{\lambda i}/(E_\gamma^3 A^{2/3} D_\lambda) \tag{1}$$

for an $E1$ or an $M1$ transition that is characterized by the energy $E_\gamma$ and the mean width $\Gamma_{\lambda i}$ and which connects the states $\lambda$ and $i$ were determined in the range of the excitation energy $E_{\text{exc}}$ between about 1 to 2 MeV and the neutron binding energy $B_n$ in a nucleus of mass number $A$ only from the evaporation spectra for respective $(p, n)$ reactions and from the spectrum of primary gamma transitions. The main flaw in these procedures is that they require employing model-dependent concepts of the penetrability of the nuclear surface for evaporated nucleons [1] or a model-dependent level density in determining radiative strength functions [2].

The situation changed when it was shown in [3] that the total radiative width $\Gamma_\lambda = \langle\Gamma_{\lambda i}\rangle m_{\lambda i}$ and the intensity of two-step cascades, $I_{\gamma\gamma}$,

$$I_{\gamma\gamma} = \sum_{J,\pi} (\Gamma_{\lambda i}/\langle\Gamma_{\lambda i}\rangle m_{\lambda i}) \cdot n_{\lambda i} \cdot (\Gamma_{if}/\langle\Gamma_{if}\rangle m_{if}), \tag{2}$$

connecting a compound state $\lambda$ with specific low-lying nuclear levels $f$ and exciting simultaneously $n_{\lambda i} = \rho_i \Delta E$ intermediate states $i$ from any interval of width $\Delta E$ can be reproduced in a calculation to a precision on the same order of magnitude as the experimental accuracy. This is possible only in the case where an infinite number of variations in the level density and the radiative strength function such that each of these makes it possible to reproduce $\Gamma_\lambda$ and $I_{\gamma\gamma}$ faithfully lie in a very narrow interval for any photon energy and for any nuclear excitation energy in the region $E_{\text{exc}} < B_n$.

In expression (2), summation is performed over all possible values of $J^\pi$ of the intermediate and final levels of relevant cascades and, if necessary, over both values of the spin of the compound state that is excited by a thermal neutron. The known values of $J^\pi$ for the initial and final levels of the cascades and the multipolarity selection rules determine unambiguously the interval of the spins and the parity of levels that must be taken into account in the analysis.

In (2), the total radiative widths of the decaying states $\lambda$ and $i$ are represented as the product of the spectrum-averaged partial width $\langle\Gamma_{\lambda i}\rangle$ or $\langle\Gamma_{if}\rangle$ and the number $m = \rho\Delta E$ of levels excited in their decay. Here, averaging is performed over the spectrum of all possible values of the partial widths with respect to primary and secondary transitions participating in the cascades and exciting $m_{\lambda i}$ and $m_{if}$ levels, respectively. This substitution is performed on the basis of the theorem of mean with the aim of obtaining a clear representation of the form of the experimentally measured dependences of $\Gamma_\lambda$ and $I_{\gamma\gamma}$ on the parameters $\rho$ and $k$ of the process being considered.

Unfortunately, the procedure proposed in [3] involves, in addition to ordinary errors of any experiment, two errors peculiar to this procedure:

(a) First, there is an error in breaking down [4] the experimental spectrum of two-step cascades into two mirror-symmetric parts that depend only on the

---

[*] e-mail: `suchovoj@nf.jinr.ru`
[**] e-mail: `khitrov@nf.jinr.ru`

energy of the primary ($E_1$) and only on the energy of the secondary ($E_2$) gamma transition of a cascade.

(b) Second, there is an uncertainty that is associated with the need for introducing some assumption concerning the relationship between the radiative strength functions for primary and secondary gamma transitions of a cascade for photons of the same energy and multipolarity in the decay of the states $\lambda$ and $i$, respectively.

It should be considered that the degree to which these uncertainties affect the level densities and radiative strength functions determined in [3] obviously becomes smaller with increasing statistics of useful $\gamma\gamma$ coincidences.

## 2. ON THE DEGREE OF RELIABILITY IN ASSESSING LEVEL DENSITIES AND RADIATIVE STRENGTH FUNCTIONS

### *2.1. Contribution of the Error in Determining the Cascade Intensity*

All of the experimentally measured distributions of cascade intensities are superpositions of some numbers of pairs of peaks having various intensities and a "noise" band having zero mean (result of background subtraction) [5]. In the case of rather vast statistics, it is therefore possible in practice to single out, even in any deformed nucleus, a few hundred pairs of resolved intense peaks from any spectrum of two-photon cascades connecting a compound state with a specific low-lying level, this corresponding to 90 or more percent of the intensity of cascades for which the energy of the intermediate level is not greater than $0.5B_n$. With the aid of the maximum-likelihood method, the order in which gamma transitions follow each other can be determined for these cascades [6], the energies of the nuclear levels involved and the arrangement of relevant transitions in the gamma-decay diagram being reliably established in doing this [7]. However, the arrangement of the transitions can be determined only in the case where the intermediate level of the cascade is deexcited by at least two gamma transitions of relatively high intensity; otherwise, it is impossible to pinpoint, without resort to additional information, the order in which the cascade photons follow each other.

After that, the intensities of the cascades arranged in the decay diagram according to [6] that involve transitions of energy in the region $E_1 > 0.5B_n$ are subtracted from experimental spectra [4]. The remaining part of the spectrum is predominantly a superposition of the intensities of a large number of cascades where the energy of a primary transition is below $0.5B_n$ and a "noise" distribution having zero mean value. An example of such a decomposition is given in Fig. 1.

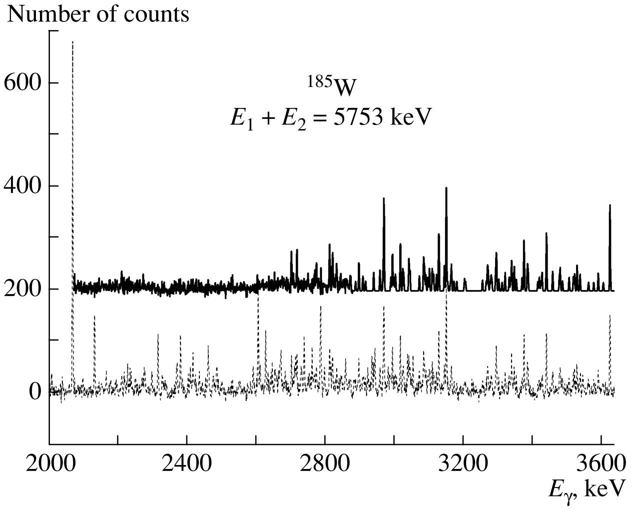

**Fig. 1.** Section of the experimentally measured distribution of the intensities of two-step cascades to the $^{185}$W ground state versus the photon energy $E_\gamma$ and that component of this distribution which corresponds to detecting only the primary transition of energy $E_1 = E_\gamma$ (the oscillogram is shifted upward). In order to improve the resolution, use is made of the numerical method proposed in [8].

Since, for two-step cascades whose primary transitions are of energy in the region $E_1 > 0.5B_n$ and whose intensities and photon energies can be determined from the respective spectrum, the detection threshold in the intensity $I_{\gamma\gamma}$ is nonzero, the procedure developed in [4] may somewhat overestimate the total intensity of cascades where $E_1 < 0.5B_n$ and, accordingly, underestimate the cascade intensity for symmetric energies of cascade photons by the same value. Also, the situation is possible where the order in which the photons involved follow each other is determined incorrectly in some number of resolved cascades. Such an error reduces the uncertainty being considered and may even change its sign (if the total intensity of cascades for which the order of transitions was determined erroneously is quite large).

An estimate of the maximum relative error being considered does not exceed 25% for the bulk of experimental data obtained at the Joint Institute for Nuclear Research (JINR, Dubna) and is much less in the latest experiments performed with a coincidence spectrometer of higher efficiency at Řež [9]. This can be seen from Fig. 2, which shows, for four nuclei considered here ($^{185,187}$W, $^{191,193}$Os), an example of the approximation [10] of the cumulative sums of the intensities of all cascades populating the same intermediate level in a fixed excitation-energy interval around $0.5B_n$.

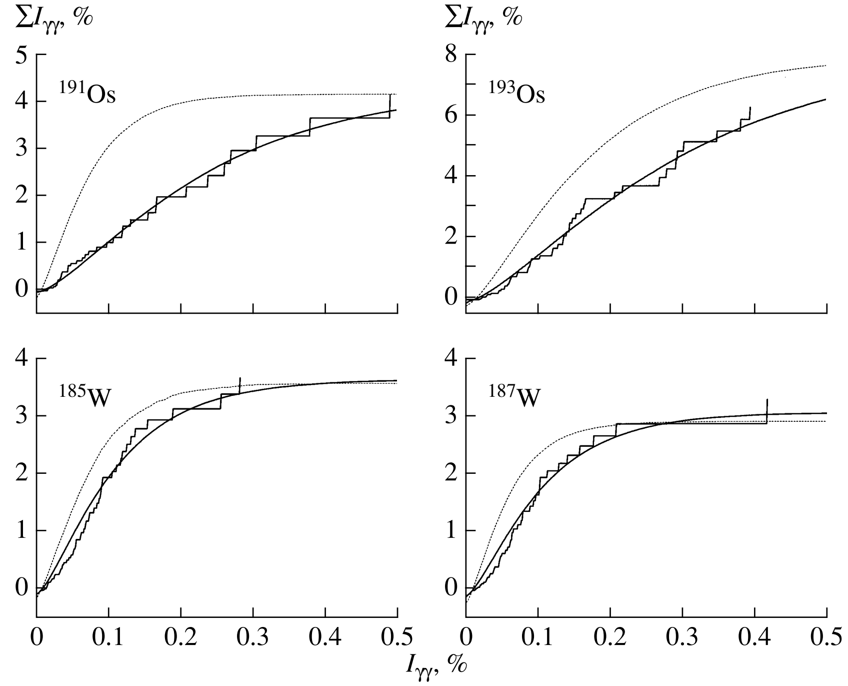

**Fig. 2.** Cumulative sums $I_{\gamma\gamma}$ of the intensities of cascades observed experimentally in $^{185,187}$W and $^{191,193}$Os (histograms) for the energies of their intermediate levels between 2.5 and 2.75 MeV (percentage of the number of compound-state decays), along with an approximated dependence (solid curves) and the dependence expected for the number of levels predicted by the Fermi gas model [12] (dashed curves) for the same sum of cascade intensities.

The absolute value of the extrapolated dependence for $I_{\gamma\gamma} = 0$ determines the expected absolute value of the intensity of unresolved weak cascades for which the energy of their intermediate level lies in the interval indicated above.

From an analysis of similar data obtained for other intervals up to an excitation energy of about 2.8 MeV, it follows that, in present-day experiments, the fraction of the intensity of weak cascades where $E_1 > 0.5B_n$ that were not singled out in the spectrum and which are therefore not arranged in the decay diagram does not exceed a value of about 1% if the deviations of the intensities of primary transitions from the mean value are described by the Porter–Thomas distribution [11] (or by any other distribution characterized by a smaller variance).

From the analysis presented in [10], it can also be deduced that, in the excitation-energy range of width 1.5 MeV (or even in a broader range), the density of intermediate levels of the cascades involved is much lower than that which is predicted by the Fermi gas model [12]. This is suggested, in particular, by a much faster growth of the cumulative sums of cascade intensities calculated within this model with allowance for a normalization to the total experimental intensity. A still greater discrepancy between these dependences is observed for the case where the total intensity of cascades for the expected cumulative sum is equal to the computed value, which is much smaller.

If, for the group of the strongest primary transitions of cascades, the intensity $I_1$ known to date, reported in the literature (see [13]), and used to normalize $I_{\gamma\gamma}$ does not involve sizable systematic errors (for example, greater than 5 to 10%), the total intensity obtained in accordance with [4] for two-step cascades in $^{185,187}$W and $^{191,193}$Os and presented in Fig. 3 features an error not greater than 10% in each interval of the excitation energy of their intermediate levels. To some extent, this conclusion follows from the data in the table, where, among other things, we list the intensities measured for cascades in the $^{183,187}$W isotopes under different experimental conditions (geometry of an experiment, spectrum of captured neutrons, etc.) at JINR [19], in Riga [21], and at Řež.

In order to verify whether the above conclusions are unambiguous, the total intensities of cascades to final levels that are members of the rotational band built on the [510]↑ single-quasiparticle neutron state are also presented in the table for all those even–odd nuclei for which relevant experimental information is available. In such a comparison, the possible effect of the structure of the final levels of the cascades being considered on the partial cascade-transition widths must lead to a correlated change in $I_{\gamma\gamma}$ in neighboring

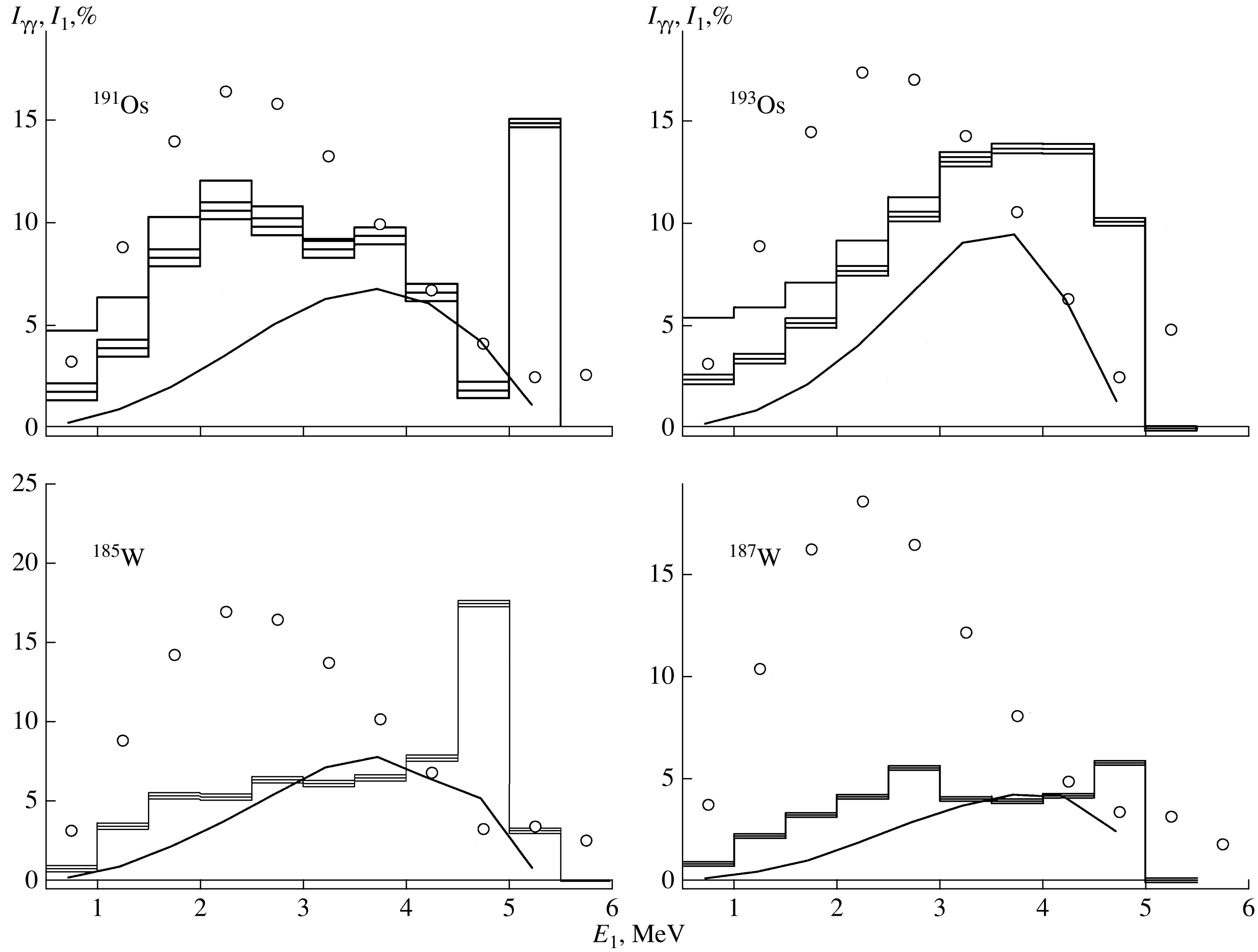

**Fig. 3.** Intensity of two-step cascades as a function of the energy $E_1$ of their primary transition (percentage of the number of decays) along with the statistical errors (histograms). The solid lines represent the results of the calculations performed with the aid of the models used in [12, 14, 15], while the points correspond to the spectrum of primary gamma transitions that is expected for the same models of the level density and radiative strength functions.

nuclei. Not only is the fact that the total intensity of cascades quoted in the table is not constant due to the possible errors in experimental data, but it also reflects the individual features of the nuclei being studied. These features may be caused by a change in the position of the [510]↑ state with respect to the Fermi level and by the related variation in the coefficients $u$ and $v$ in the Bogolyubov canonical transformation, these coefficients appearing in the matrix element of the partial widths with respect to cascade transitions. By way of example, we indicate that, from the degree of the discrepancy between the approximating dependence and the level density expected within the Fermi gas model (Fig. 2), it immediately follows that the level density is greater in tungsten isotopes than in osmium isotopes, at least for $E_{\text{exc}} < 3$ MeV. Accordingly, the intensity of the cascades is lower in tungsten isotopes than in osmium isotopes [this also follows from expression (2)].

Local deviations from a general trend may also be considered as the maximum possible estimate of the systematic error in determining the cascade intensity in a specific nucleus. From the data presented in the table, it follows that, even in the worst case, the possible systematic error in determining $I_{\gamma\gamma}$ will not exceed 25–50% (unless the data presented in [13] involve a systematic methodological error similar for all nuclei).

A somewhat smaller estimate (about 20%) of the error in part of the gamma-transition intensities $I_1$ reported in [13] is obtained from their comparison with the analogous data from measurements performed in Budapest [24].

A simulation revealed that an error on this order of magnitude does not introduce radical changes in the results obtained according to [3] for the shape of the excitation-energy dependence of the level density

Intensities of two-photon cascades to levels of the [510]$\uparrow$ band (percentage of the number of decays) according to measurements in various experiments along with the results of respective calculations

| Nucleus | $E_f$, keV | $I_{\gamma\gamma}^{\mathrm{expt}}$ | $I_{\gamma\gamma}^{\mathrm{calc}}$ | Nucleus | $E_f$, keV | $I_{\gamma\gamma}^{\mathrm{expt}}$ | $I_{\gamma\gamma}^{\mathrm{calc}}$ |
|---|---|---|---|---|---|---|---|
| $^{175}$Yb [16] | 515 | 17.2(40) | 7.4 | $^{179}$Hf [17] | 375 | 15.5(16) | 5.8 |
| | 556 | 18.1(47) | 6.7 | | 421 | 16.5(21) | 5.4 |
| | 602 | 9.0(16) | 3.1 | | 476 | 7.6(6) | 3.0 |
| Sum | | 44(6) | 17.2 | Sum | | 40(3) | 14.2 |
| $^{181}$Hf [18] | 0 | 15.2(20) | 10.5 | $^{183}$W [19] | 0 | 13.3(11) | 8.7 |
| | 46 | 15.6(20) | 11.0 | | 46 | 10.2(7) | 8.7 |
| | 99 | 8.9(20) | 5.2 | | 99 | 1.4(2) | 3.9 |
| Sum | | 40(4) | 26.7 | Sum | | 24.9(24) | 21.3 |
| $^{183}$W | 0 | 11.1(7) | 8.7 | $^{185}$W [20] | 23 | 11.0(6) | 6.5 |
| | 46 | 9.7(4) | 8.7 | | 93 | 12.0(7) | 6.6 |
| | 99 | [1.3] | 3.9 | | 188 | 3.8(2) | 2.3 |
| Sum | | 22.1(8) | 21.3 | Sum | | 26.8(9) | 15.4 |
| $^{187}$W [21] | 146 | 8.0(9) | 6.3 | $^{187}$W | 146 | 7.8(2) | 6.3 |
| | 205 | 8.3(12) | 6.0 | | 205 | 9.9(2) | 6.0 |
| | 305 | 4.9(15) | 2.5 | | 305 | 4.8(5) | 2.5 |
| Sum | | 21.2(21) | 14.8 | Sum | | 22.5(6) | 14.8 |
| $^{191}$Os [22] | 84 | 19.1(5) | 3.8 | $^{193}$Os [23] | 41 | 12.2(2) | 5.6 |
| | 142 | 7.5(3) | 3.1 | | 102 | 19.0(2) | 5.1 |
| | [272] | 3.5(3) | 1.3 | | [296] | 3.9(2) | 2.0 |
| Sum | | 30.1(7) | 8.2 | Sum | | 35.1(4) | 12.7 |

Note: The quoted errors are purely statistical. There is no exact identification of the 5/2 level of the rotational band built on the 1/2[510]$\uparrow$ state in osmium isotopes; presented in the table are the lowest levels of this spin, their structure not being determined experimentally.

(Fig. 4) and for the shape of the dependence of the radiative strength functions on the energy of the primary gamma transition in the respective cascade (Fig. 5). These statements were verified under the assumption that the intensities of the cascades in the nuclei under analysis were overestimated by 50%. For the sake of comparison, the results of the simulation are also given in Figs. 4 and 5.

The experimental intensity of the cascades is determined by specific level-density and radiative-strength-function values in the range of excitation energies and gamma transitions under consideration. The calculated intensity is determined by their mean values. This circumstance calls for optimizing the calculation with respect to the degree of possible random local variations in the level density and radiative strength functions.

Basically, it is the need for including in the analysis [3] a sizable local enhancement of radiative strength functions in excitation-energy intervals narrower than the summation interval $\Delta E$ that is of prime practical interest. By using the procedure developed in [3], this situation can be readily implemented either for a group of closely spaced levels associated with the cascades in question or even for one primary transition that is the most intense (for example, for the very intense cascade involving the primary gamma transition of energy 5147 keV and occurring in $^{191}$Os). This correction improves considerably the convergence of the iterative process constructed according to [3], but it leads to the appearance of local variations in the radiative strength functions (Fig. 5). In principle, such variations may be due to a strong effect of the structure of the levels that are connected by the gamma transition in question on its width (and on the radiative strength functions) rather than to random deviations of $I_1$. This possibility is suggested by Malov's calculation of the population of isomeric states [27]. From that calculation, it follows that this process receives a dominant contribution only from some of the excited states, those whose wave functions involve sizable phonon components. In principle, a similar mechanism can also control the parameters of the cascade gamma decay. The possibly equidistant character of the excitation spectra that was found in all nuclei studied to date [28] is indicative of the presence of sizable phonon components in the wave function for intermediate levels (at least in the most intense cascades).

By and large, the experience gained from the analysis performed in [3] reveals that the possible nonmonotonic character of radiative strength functions must be taken into account above all in even–odd deformed nuclei and in near-magic nuclei where the numbers of nucleons are of an arbitrary parity. The data given in Figs. 4 and 5 were obtained with allowance for the above refinement of the procedure developed in [3]. The basic result of the analysis—that is, the statement that the actual level density is much lower than that which is predicted by the Fermi gas model [12]—remains unchanged irrespective of whether one employs the procedure from [3] with a smoothed radiative strength function or with a radiative strength function similar to that which is displayed in Fig. 5.

The conclusion that the actual level density does not comply with the predictions of the Fermi gas model [12] also follows from a comparison of the experimentally observed cascade intensities with the results of model calculations—in particular, from a comparison of the distributions of $I_{\gamma\gamma}$ with the calculated spectra of primary transitions. The intensity observed for $^{185}$W and $^{191,193}$Os in the form of two-step cascades is 60 to 82% of the total intensity of their primary transitions of energy in the region $E_\gamma > 0.52$ MeV. Taking into account the intensities of primary transitions to the ground state and the intensities of cascades where one of the photons has a low energy (such cascades were not included in the data given in Fig. 3), we can find that the experimentally unobservable intensity of primary transitions in $^{191,193}$Os constitutes approximately 10% of decays. This experimentally unobservable intensity must be distributed over a rather wide interval of energies of the primary transitions in the cascades being considered. For $E_1 < 3$–$4$ MeV, the actual spectrum of primary transitions in the two nuclei under study therefore occurs between the cascade intensity and the result of the model calculation for the dependence in Fig. 3; moreover, it is rather close to $I_{\gamma\gamma}$. By way of example, we present in Fig. 3 a version of the distribution of the unobserved intensity of primary transitions in the energy range of width 3 MeV, the intensity added to $I_{\gamma\gamma}^{\text{expt}}$ increasing linearly. On the basis of the best currently available experimental information, this example provides an independent argument in favor of the statement that, in describing the properties of heavy nuclei, the accuracy of model concepts like those in [12, 14, 15, 25, 26] is insufficient at excitation energies in excess of $E_{\text{exc}} \sim 1$–$2$ MeV.

### 2.2. Role of Model Assumptions

The level-density values that are extracted from experimental data with the aid of the procedures proposed in [3] and [10] must comply with each other, and this is indeed observed for many nuclei. The maximum disagreement is observed predominantly in the region $A > 180$, this being so not only for the even–odd nuclei considered here but also for even–even and odd–odd nuclei. In this mass region, the procedure used in [10] yields a level-density value somewhat greater than that produced by the procedure from [3]. This is because, in some of the cascades not arranged in the decay diagram according to [6], the energy of the primary transition is less than the energy of the secondary transition. In this case, the approximation of the distribution of random cascade intensities on the basis of the recipe from [10] accordingly leads to an exaggerated estimate of the level density. However, alternative explanations are also possible:

(i) There is a set of level-density and radiative-strength-function values that make it possible to reproduce $I_{\gamma\gamma}$ and the level-density value from [10] simultaneously, but which are not revealed by the analysis based on the procedure from [3].

(ii) The assumptions adopted in [3] for the relation between the radiative strength functions for primary and secondary transitions of the cascade being considered call for a significant correction.

For tungsten and osmium isotopes, data on $I_{\gamma\gamma}$ were analyzed by using the procedure developed in [3] and modified in such a way as to take into account a constraint on the minimum value of the level density at excitation energies below 2 to 3 MeV. In any case, the functional dependence of the level density on the excitation energy—we use this dependence to reproduce $I_{\gamma\gamma}$—then develops a step at $E_{\text{exc}} \simeq 5$ MeV, this step being more pronounced than that in Fig. 4. The level density at this excitation-energy value proves to be commensurate with that at the neutron-binding energy $B_n$ or even exceeds it. But even in this case, we were unable to reproduce the cascade intensities in $^{191}$Os faithfully. On the basis of the aforesaid, it is

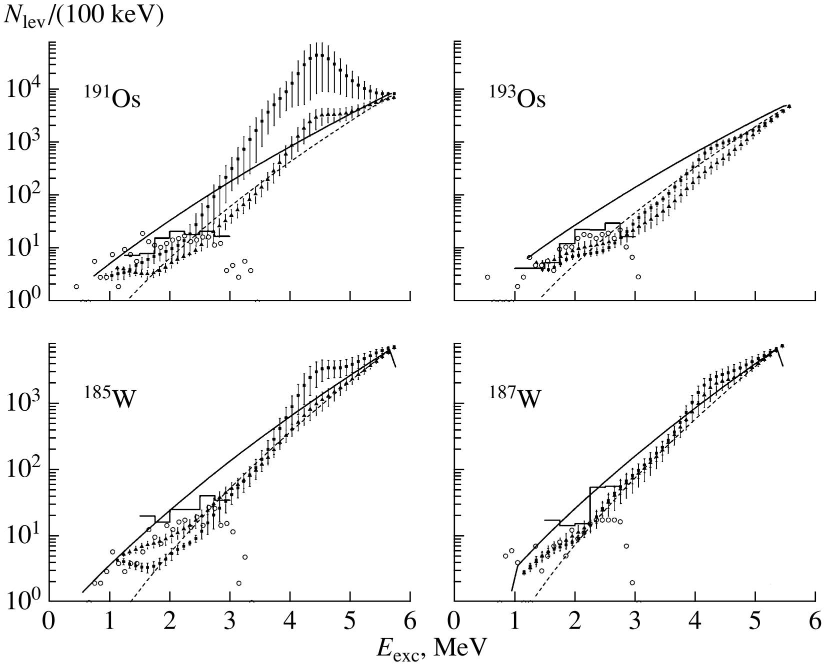

**Fig. 4.** Number $N_{\rm lev}$ of levels of both parities excited by primary dipole transitions in the interval of width 100 keV versus the excitation energy $E_{\rm exc}$. The open circles represent the number of the experimentally observed intermediate levels of the two-step cascades under study, while the histograms show their most probable values expected at zero cascade-detection threshold [10]. The closed circles with error bars correspond to the most probable values satisfying relations (2) and complying with the experimental value of the total radiative width of the respective compound state. The solid and dashed curves represent the results of the calculations performed on the basis of the models proposed in [12] and [25], respectively, their parameters being determined individually by fitting the experimental spacings between the respective neutron resonances. The closed triangles correspond to the level density reproducing the values of $I_{\gamma\gamma}$ from Fig. 3 that were reduced by a factor of 1.5.

natural to expect that a still more reliable determination of level densities and radiative strength functions would require taking into account distinctions between the energy dependences of radiative strength functions for the primary and secondary transitions in the respective cascades.

## 3. POSSIBLE EFFECT OF THE STRUCTURE OF LEVELS INVOLVED IN A CASCADE ON THE PARAMETERS OF THE GAMMA-DECAY PROCESS TO BE DETERMINED

From theoretical concepts, it follows that the structure of a decaying level has the strongest effect on the gamma-decay probability at the lowest excitation energies. As applied to the problem being considered, this means that the partial-width ratio

$$R = \Gamma_{\lambda i}/\Gamma_{if} \qquad (3)$$

and, accordingly, the ratio of the radiative strength functions for primary and secondary transitions of the same multipolarity and energy may depend on $E_\gamma$. In this case, the unavoidable systematic error in parameter values extracted from an analysis based on the procedure proposed in [3] will depend on the degree of the deviation of $R$ from a constant value. The possible inclusion of new variables in such an analysis would sharply increase the uncertainty in the values found for the level density and radiative strength functions. Therefore, we do not see at present a real possibility for separately determining radiative strength functions for primary and secondary transitions in the cascades being considered (yet, it is possible in principle to obtain information about two-step cascades to their final levels for $E_f > 1$ MeV).

It should be noted that, if the width ratio $R$ depends only on the energy of the intermediate level $i$, being independent of the photon energy, the parameters determined in accordance with the method proposed in [3] do not involve the systematic error considered here.

But if $R$ depends on $E_\gamma$ strongly, the systematic error in the constructed level density (Fig. 4) can be compensated by the systematic error in the resulting radiative strength functions (Fig. 5).

Two versions are possible here:

(a) With increasing $E_\gamma$, the radiative strength function for secondary transitions increases much faster than that for primary transitions.

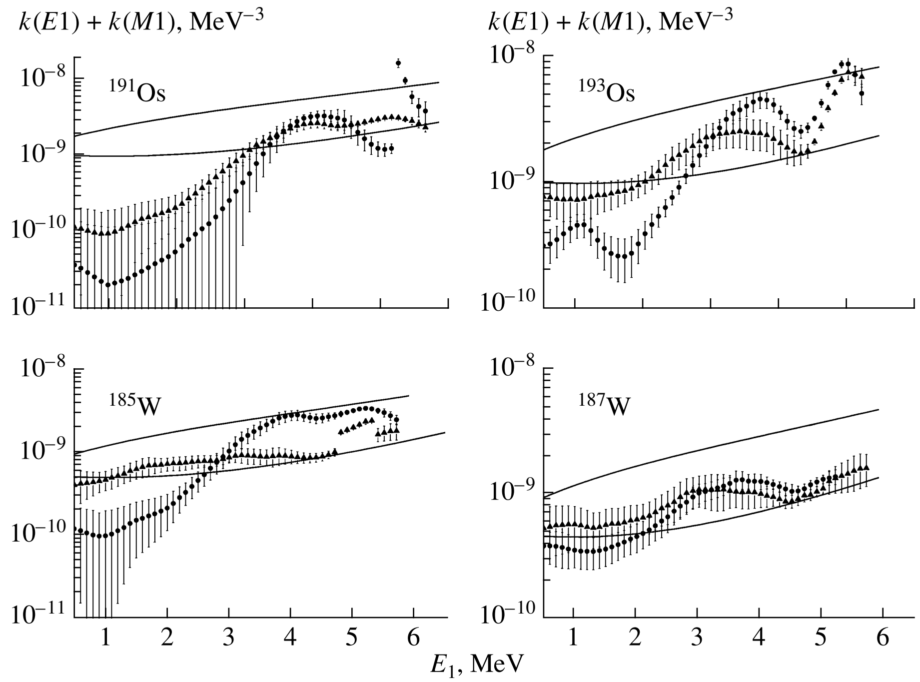

**Fig. 5.** Most probable sum $k(E1) + k(M1)$ of the strength functions for $E1$ and $M1$ transitions in radiative thermal-neutron capture along with its uncertainty versus the energy $E_1$ of the primary gamma transition in the cascade (closed circles). The upper and lower curves correspond to the data based on the model concepts proposed in [14] and [26], respectively, in the sum featuring the $k(M1) =$ const values normalized to the experimental result from [15]. The closed triangles represent the radiative strength function reproducing the values of $I_{\gamma\gamma}$ from Fig. 3 that were reduced by a factor of 1.5.

(b) With increasing $E_\gamma$, the radiative strength function for primary transitions increases much faster than that for secondary transitions.

In the first case, the actual level density may prove to be higher than that which is obtained on the basis of an analysis performed by the method proposed in [3], while, in the second case, the situation may be inverse.

The total spectra of photons from the radiative capture of thermal and fast neutrons were calculated in [29] under various assumptions about the shape of the $E_\gamma$ dependence of the radiative strength functions for primary and secondary transitions. This calculation revealed that, for almost all of the nuclei from the mass region $114 \leq A \leq 200$, version (b) provides better agreement with experimental data than the version that employs only the data from the analysis in [3] for primary and secondary gamma transitions. It follows that the level density given in Fig. 4 reflects the most general features of its dependence on the excitation energy.

Nevertheless, an independent verification of this statement is necessary. It can be accomplished in the following way: the deviation of the energy dependence of the radiative strength functions for primary and secondary transitions in the cascades being considered from that obtained in [3] under the condition $\Gamma_{\lambda i}/\Gamma_{if} =$ const leads to a discrepancy between the calculated and experimental intensities of the cascades for various energies of their final levels. It is necessary to consider here that, even for neighboring final levels (their energies being denoted by $E_f$), the intensities of the cascades may depend on the structure of their wave function or even only on their spin (as can be seen from the table, this is indeed observed in the $^{183}$W and $^{191,193}$Os isotopes).

With allowance for this circumstance, the ratios of the experimental and calculated intensities of two-step cascades in the $^{185}$W and $^{191,193}$Os nuclei versus the energy $E_f$ are given in Fig. 6 for the cases where different level densities and radiative strength functions are used in calculating the respective intensities. (According to the experimental conditions, the energy $E_f$ for $^{187}$W was not greater than 305 keV.)

The growth of the ratio $I_{\gamma\gamma}^{\rm expt}/I_{\gamma\gamma}^{\rm calc}$ with increasing $E_f$ in the calculations with the level densities and radiative strength functions from [3] means that the photon-energy ($E_\gamma$) dependence of the radiative strength functions for secondary transitions in the respective cascades can have a shape that is closer to that prescribed by the model concepts in [14, 15, 26] than the shape arising upon the application of the procedure proposed in [3] (Fig. 5). But even in this

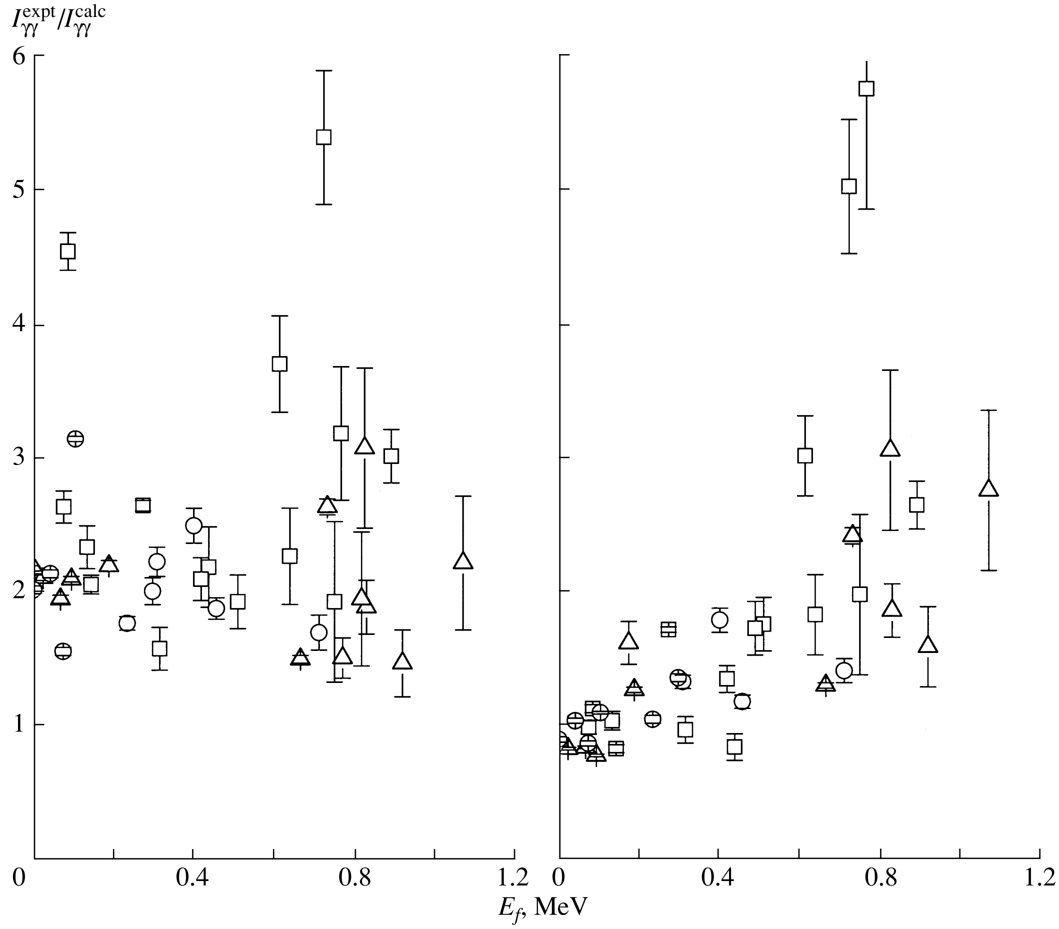

**Fig. 6.** Ratio $I_{\gamma\gamma}^{\rm expt}/I_{\gamma\gamma}^{\rm calc}$ as a function of $E_f$ for (open triangles) $^{185}$W, (open boxes) $^{191}$Os, and (open circles) $^{193}$Os according to the calculations employing (left panel) the models from [12, 14, 15] and (right panel) the parameters given in Figs. 4 and 5.

case, its deviation averaged over the energy of the intermediate level of the cascade can hardly exceed two for final-level energies around $E_f \sim 1$ MeV. Although the data in Fig. 6 cannot be directly extrapolated to the region of higher values of $E_f$, not only would the extension of the interval of $E_f$ make it possible to fix the discrepancy between the theoretical and experimental results, but this would also contribute to solving the problem of more reliably determining level densities and radiative strength functions by including additional information in the respective analysis.

## 4. CONCLUSION

In dealing with processes involved in the cascade gamma decay of compound states, the level densities and radiative strength functions for respective gamma transitions are basic quantities that control such processes. A radically new procedure for simultaneously determining these quantities was implemented at the Laboratory for Neutron Physics (JINR, Dubna) [3]. In contrast to other existing procedures, it enables one to determine the level density within a fixed interval of spins and has the highest sensitivity in the region of its lowest values.

The results obtained previously in [3] may involve a significant systematic error because of an insufficient accuracy of data accumulated to date on the intensities of two-step cascades. New data [20, 23] obtained with a high-efficiency spectrometer at Řež made it possible to improve considerably the accuracy in determining the dependence of $I_{\gamma\gamma}^{\rm expt}$ on the energy of the primary transition in the respective cascade, whereby the errors in the resulting level densities and radiative strength functions were reduced.

In the case of $^{185,187}$W and $^{191,193}$Os, the values obtained in accordance with [3] for these basic parameters of cascade gamma decay fully confirm the discrepancies revealed previously between experimental data and generally accepted model concepts, this concerning both level densities and radiative strength functions:

(i) The observation of a steplike structure in the energy dependence of the level density corroborates the conclusion drawn previously that the idea of a smooth variation of the properties of a nucleus as it goes over from an "ordered" state to a state of "chaos" is inapplicable.

(ii) The radiative strength functions for electric and magnetic dipole transitions are also strongly affected by the structure of the wave functions for the levels excited by them. At primary-transition energies in the region $E_1 < 2$ MeV, their most probable values can even be less than those prescribed by the model used in [26]. A considerable increase in the radiative strength functions for cascade transitions exciting nuclear levels in the region of the steplike structure in the level density, along with data from [29] on the possible large phonon components in their wave functions, makes it possible to confirm, at a new level, the main physical conclusion drawn previously: at excitation energies below 3 to 4 MeV, nuclear properties that manifest themselves experimentally in thermal-neutron capture are determined primarily by nuclear vibrations. At higher excitation energies, the structure of the levels is likely to be controlled by the quasiparticle components of their wave functions.

## ACKNOWLEDGMENTS

We are grateful to J. Honzátko and I. Tomandl, who performed the experiment at Řež, and to V. Bondarenko, who placed at our disposal his data on the absolute intensities of primary gamma rays from radiative thermal-neutron capture by the $^{184,186}$W isotopes.

This work was supported by the Russian Foundation for Basic Research (project no. 99-02-17863).

## REFERENCES

1. E. M. Rastopchin, M. I. Svirin, and G. N. Smirenkin, Yad. Fiz. **52**, 1258 (1990) [Sov. J. Nucl. Phys. **52**, 799 (1990)].
2. G. E. Bartholomew *et al.*, Adv. Nucl. Phys. **7**, 229 (1973).
3. E. V. Vasilieva, A. M. Sukhovoj, and V. A. Khitrov, Yad. Fiz. **64**, 195 (2001) [Phys. At. Nucl. **64**, 153 (2001)].
4. S. T. Boneva *et al.*, Z. Phys. A **338**, 319 (1991); Nucl. Phys. A **589**, 293 (1995).
5. S. T. Boneva, É. V. Vasil'eva, Yu. P. Popov, *et al.,* Fiz. Élem. Chastits At. Yadra **22**, 479 (1991).
6. Yu. P. Popov *et al.,* Izv. Akad. Nauk SSSR, Ser. Fiz. **48**, 891 (1984).
7. S. T. Boneva, É. V. Vasil'eva, and A. M. Sukhovoĭ, Izv. Akad. Nauk SSSR Ser. Fiz. **51**, 2023 (1987).
8. A. M. Sukhovoĭ and V. A. Khitrov, Prib. Tekh. Éksp., No. 5, 27 (1984).
9. J. Honzátko *et al.*, Nucl. Instrum. Methods Phys. Res. A **376**, 434 (1996).
10. A. M. Sukhovoj and V. A. Khitrov, Yad. Fiz. **62**, 24 (1999) [Phys. At. Nucl. **62**, 19 (1999)].
11. C. F. Porter and R. G. Thomas, Phys. Rev. **104**, 483 (1956).
12. W. Dilg *et al.*, Nucl. Phys. A **217**, 269 (1973).
13. M. A. Lone, R. A. Leavitt, and D. A. Harrison, Nucl. Data Tables **26**, 511 (1971).
14. P. Axel, Phys. Rev. **126**, 671 (1962).
15. J. M. Blatt and V. F. Weisskopf, *Theoretical Nuclear Physics* (Wiley, New York, 1952; IL, Moscow, 1953).
16. É. V. Vasil'eva, Yu. P. Popov, A. M. Sukhovoĭ, *et al.,* Izv. Akad. Nauk SSSR, Ser. Fiz. **48**, 1907 (1984).
17. S. T. Boneva, É. V. Vasil'eva, Yu. P. Popov, *et al.*, Report No. R6-86-493, OIYaI (Joint Institute for Nuclear Research, Dubna, 1986).
18. V. A. Bondarenko, I. L. Kuvaga, Le Hong Kh"em, *et al.,* Izv. Akad. Nauk SSSR, Ser. Fiz. **55**, 2091 (1991).
19. S. T. Boneva, É. V. Vasil'eva, Yu. P. Popov, *et al.,* Izv. Akad. Nauk SSSR, Ser. Fiz. **53**, 7 (1989).
20. V. A. Bondarenko, J. Honzátko, V. A. Khitrov, *et al.,* Fizika B (Zagreb) **11**, 201 (2002).
21. M. P. Beitins, S. T. Boneva, V. A. Khitrov, *et al.*, Z. Phys. A **341**, 155 (1992).
22. V. A. Bondarenko, V. A. Khitrov, A. M. Sukhovoj, *et al.*, Preprint No. E3-99-343, OIYaI (Joint Institute for Nuclear Research, Dubna, 1999).
23. V. A. Bondarenko, J. Honzátko, V. A. Khitrov, *et al.*, Fizika B (Zagreb) **11**, 83 (2002).
24. G. L. Molnar *et al.*, Appl. Rad. Isotop. **53**, 527 (2000).
25. A. V. Ignatyuk, in *Proceedings of the IAEA Consultants Meeting on the Use of Nuclear Theory, Neutron Nuclear Data Evaluation, Trieste, Italy, 1975,* IAEA-190 (1976), Vol. 1, p. 211.
26. S. G. Kadmenskiĭ, V. P. Markushev, and W. I. Furman, Yad. Fiz. **37**, 277 (1983) [Sov. J. Nucl. Phys. **37**, 165 (1983)].
27. L. A. Malov, in *LI Meeting on Nuclear Spectroscopy and Atomic Nuclear Structure, Abstracts of Papers* (VNIIF, Sarov, 2001), p. 107.
28. A. M. Sukhovoĭ and V. A. Khitrov, Izv. Akad. Nauk, Ser. Fiz. **61**, 2068 (1997).
29. V. A. Khitrov, A. M. Sukhovoj, and E. P. Grigoriev, in *Proceedings of the IX International Seminar on Interaction of Neutrons with Nuclei, Dubna, 2001*, E3-2001-192, JINR (Dubna, 2001), p. 173; A. M. Sukhovoj, V. A. Khitrov, and E. P. Grigor'ev, Vopr. At. Nauki Tekh., Ser. Yad. Konstanty, No. 1, 94 (2001).

*Translated by A. Isaakyan*

*Physics of Atomic Nuclei, Vol. 67, No. 4, 2004, pp. 672–681. Translated from Yadernaya Fizika, Vol. 67, No. 4, 2004, pp. 694–703.*
*Original Russian Text Copyright © 2004 by Kornoukhov, Starostin.*

**ELEMENTARY PARTICLES AND FIELDS**
**Experiment**

# Employing Low-Power Reactors in Studying the Mixing Parameter $\sin^2(2\theta_{13})$

**V. N. Kornoukhov and A. S. Starostin***

*Institute of Theoretical and Experimental Physics,*
*Bol'shaya Cheremushkinskaya ul. 25, Moscow, 117259 Russia*

Received September 18, 2003

**Abstract**—Measurement of the mixing parameter $\sin^2(2\theta_{13})$ is one of the pressing problems in neutrino physics. Projects of reactor experiments characterized by a sensitivity of $\sin^2(2\theta_{13}) \approx 0.01$ are being presently discussed. Almost all of them are based on the *one reactor—two detectors* scheme. Within this methodological approach, one employs an NPP reactor of power about a few GW for an antineutrino source and two detectors of identical configurations that are arranged at different distances from the reactor. In such experiments, the systematic error may be about 1%, which ensures a precision of about 0.01. In the present study, it is proposed to use, in a measurement of $\sin^2(2\theta_{13})$, the existing SuperKamiokande (SK) detector combined with its own antineutrino source, a nuclear reactor of low thermal power, about 300 MW (low-power reactor, or LPR). Such an experiment can be performed within a rather short time. An analysis that studied various detection mechanisms revealed that the LPR—SK combination would make it possible to attain a sensitivity of $\sin^2(2\theta_{13}) \approx 0.002$. *© 2004 MAIK "Nauka/Interperiodica".*

## INTRODUCTION

Investigation of the mass structure of neutrinos is one of the most important problems in neutrino physics. Experiments devoted to searches for neutrino oscillations provide an efficient tool for solving this problem. In observing neutrino oscillations, one can measure the parameters of the Pontecorvo—Maki—Nakagawa—Sakata (PMNS) matrix [1, 2]—that is, the mixing angles $\theta_{12}$, $\theta_{23}$, and $\theta_{13}$ and the mass parameters $\Delta m^2_{21} = m^2_2 - m^2_1$, $\Delta m^2_{32} = m^2_3 - m^2_2$, and $\Delta m^2_{31} = \Delta m^2_{21} + \Delta m^2_{32}$. Full information about the parameters of this matrix would make it possible to determine the structure of active neutrinos. In particular, the electron neutrino can be represented in the form of a superposition of neutrino mass eigenstates $(\nu_1, \nu_2, \nu_3)$ that involves specific weight factors:

$$\nu_e = \cos\theta_{12}\cos\theta_{13}\nu_1 + \sin\theta_{12}\cos\theta_{13}\nu_2 + \sin\theta_{13}\nu_3. \quad (1)$$

In recent years, some positive results were obtained in experiments aimed at searches for the oscillations of atmospheric, solar, and reactor neutrinos. A global analysis of experimental data from SuperKamiokande [3], K2K [4] (atmospheric neutrinos), CHOOZ [5], Palo Verde [6], and KamLAND [7] (reactor neutrinos) and all data on solar neutrinos [8], including SNO results [9], made it possible to draw some conclusions concerning the mechanism of the oscillations and to determine some of the parameters of the PMNS matrix. Under the assumption of a natural hierarchy of the neutrino masses ($m_1 < m_2 < m_3$), the results of this global analysis [10, 11] of the aforementioned experiments are the following:

$$\Delta m^2_{\text{sol}} \equiv \Delta m^2_{12} = 7.1^{+1.2}_{-0.6} \times 10^{-5}\ \text{eV}^2, \quad (2)$$
$$\sin^2(2\theta_{12}) = 0.821^{+0.0647}_{-0.062};$$
$$\Delta m^2_{\text{atm}} \equiv \Delta m^2_{23} \approx \Delta m^2_{13} = 3^{+3}_{-2} \times 10^{-3}\ \text{eV}^2,$$
$$\sin^2(2\theta_{23}) = 1^{+0.0}_{-0.2}.$$

These data contain no information about a very important element, the mixing angle $\theta_{13}$. To date, only a constraint on this parameter has been obtained from the analysis of the CHOOZ data [5]:

$$\sin^2(2\theta_{13}) \le 0.14 \quad (3)$$
$$(90\%\ \text{C.L. at}\ \Delta m^2 = 2.5 \times 10^{-3}\ \text{eV}^2).$$

However, this is insufficient for obtaining answers to a number of important questions in fundamental physics. Apart from what is concerned with solving the problem of reconstructing the structure of active neutrinos [see Eq. (1)], the presence of a nonzero mixing angle $\theta_{13}$ is a necessary condition for the manifestation of $CP$ violation in the lepton sector. Therefore, it is of paramount importance to establish a nonzero value of $\sin^2(2\theta_{13})$ or to strengthen constraints on it at least by an order of magnitude.

---

[*] e-mail: `starostin@vitep1.itep.ru`

1063-7788/04/6704-0672$26.00 © 2004 MAIK "Nauka/Interperiodica"

Accelerator experiments employing either standard neutrino beams (K2K [4], MINOS [12]) or superbeams (JHF–SuperKamiokande [13], NuMI [14]) and requiring much work and large expenditures were proposed for solving this problem. However, a thorough analysis revealed [15–17] that reactor experiments provide better opportunities for achieving the highest sensitivity to the parameter $\sin^2(2\theta_{13})$. In addition to a higher sensitivity, reactor experiments are advantageous in that they are much cheaper and make it possible to obtain a significant gain in the time of measurements.

## 1. REACTOR EXPERIMENTS

In searches for reactor-antineutrino oscillations, use is made of the inverse-beta-decay reaction

$$\bar{\nu}_e + p \to e^+ + n. \qquad (4)$$

In this process, almost the entire neutrino energy, with the exception of the energy threshold (1.804 MeV), is transferred to the product positron. After the absorption of annihilation photons, the total energy transfer increases by $2 \cdot 511$ keV. Therefore, the energy spectrum of reaction (4) in a scintillation detector, where intrinsic energy thresholds do not exceed a value of about 100 to 200 keV, begins at about 1 MeV. In a Cherenkov detector, the intrinsic threshold is determined by the kinetic energy of the positron. We will return to the discussion of this issue below.

The problem of separating the reaction in (4) from the background is significantly simplified if use is made of the method of delayed coincidences between the signals from the detection of the product positron and the product neutron. The time interval between these events depends on the absorber used. If the neutron is captured in water, the time of expectation of the second event is about 1 ms, the deposited energy being 2.2 MeV. But if gadolinium is employed for the neutron absorber, the interval in question reduces to 100 $\mu$s, the total energy from the cascade of gamma rays originating from neutron capture amounting to about 8 MeV.

In reactor experiments, oscillations are sought by using the principle of departure: if an electron neutrino changes the flavor state ($\nu_e \to \nu_{\mu,\tau}$), it does not manifest itself in the inverse-beta-decay reaction, this leading to a change in the counting rate and, hence, to the oscillation-induced distortion of the positron spectrum of the reaction in (4). In the case where mixing occurs between the mass eigenstates $\nu_1$ and $\nu_3$, the probability of the $\nu_e \to \nu_\tau$ transition is given by

$$\sim \sin^2(2\theta_{13}) \sin^2(\varphi), \qquad (5)$$

where $\sin^2(2\theta_{13})$ is the mixing parameter, $\varphi = 1.27 \times \Delta m^2_{31} L E^{-1}$, $\Delta m^2_{31}$ is the mass parameter, $E$ is the antineutrino energy, and $L$ is the distance from the reactor to the detector used. The value of the mass parameter is known from the results of the analysis performed in [10, 11]: $\Delta m^2_{31} = 3^{+3}_{-2} \times 10^{-3}$ eV$^2$. The optimum distance $L$ for the observation of the $\nu_e \to \nu_\tau$ transition is determined from the condition requiring that the first maximum in expression (5) ($\varphi \approx \pi/2$) be reachable. With allowance for the known parameters, it is $L \approx 2$ km.

One cannot rule out the possibility that $\sin^2(2\theta_{13})$ is much less than the experimental limit in (3). It follows that, even in the first new-generation reactor experiments, a precision of about 1% would be required for measuring the mixing angle $\theta_{13}$. The required statistical accuracy may be ensured by increasing the detector mass. In the CHOOZ experiment, the target for neutrinos had a mass of 5 t, while the statistical error was 2.8%. For an accuracy of about 1% to be achieved, the detector mass must therefore not be less than 50 t. The reduction of the systematic error of measurements presents a more serious problem. This error receives contributions from the uncertainty in determining the cross section for the reaction in (4), the effect of the physical deterioration of the fuel material and the corresponding change in the neutrino flux, and the uncertainty in the detection efficiency for neutrino events and in the number of protons in the target. In the CHOOZ experiment, the systematic error caused by these factors was 2.7%. In order to reduce it, the authors of the Kr2Det project [15] proposed the *one reactor–two detectors* method, which is based on simultaneously using, in an experiment, two detectors identical in size and configuration. One of these, a "near" one, is positioned at a distance of 100 to 150 m from the reactor used—that is, in the region where the effect of neutrino oscillations is negligible. It serves for measuring the undistorted spectrum of positrons. The second, "far," detector is placed in the region that is the most efficient for observing the oscillations in question (1000 to 2000 m from the reactor). A signal suggesting the presence of the oscillation effect and information about the respective parameters can be obtained by comparing the positron spectra from the near and the far detector. For the case of identical detectors, the results of such an analysis are independent of a precise knowledge of the reactor parameters, the antineutrino spectrum, and the concentration of hydrogen atoms in the target used, the distinctions between the detection efficiencies and between the effective volumes of the detectors being readily taken into account. In this way, one removes the main systematic effects. The calculations performed in [15, 16] revealed that, in an

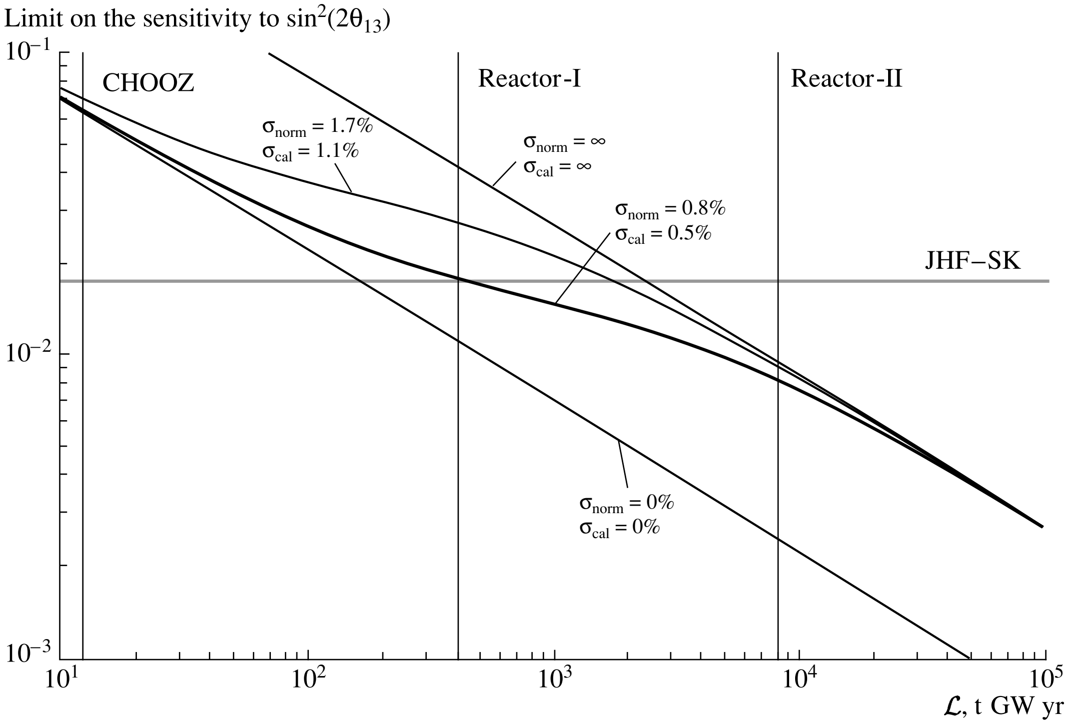

**Fig. 1.** Limit on the sensitivity to the parameter $\sin^2(2\theta_{13})$ as a function of the integrated luminosity for various values of the error in normalization, $\sigma_{\rm norm}$, and of $\sigma_{\rm cal}$ [17].

experiment performed according to the *one reactor—two detectors* scheme, the systematic error would not exceed 0.5%.

A comprehensive analysis of various approaches aimed at reaching a sensitivity of $\sin^2(2\theta_{13}) < 0.01$ was performed by Huber *et al.* [17], who also gave preference to an experimental scheme involving a near and a far detector simultaneously that differ only in size. For the main characteristic of the experiment, they took the integrated luminosity defined as $\mathcal{L} =$ detector mass [t] × thermal power of the reactor [GW] × duration of the measurements [yr]. This made it possible to perform an analysis for two classes of facilities: Reactor-I at the integrated luminosity of $\mathcal{L}_I = 400$ t GW yr and Reactor-II at the integrated luminosity that is 20 times as great as that, $\mathcal{L}_{II} = 8000$ t GW yr. Two types of systematic error were introduced: $\sigma_{\rm norm}$, which is the total error including uncertainties in the parameters of the neutrino flux and in the parameters of the near and the far detector, and $\sigma_{\rm cal}$, which is the error in the energy calibration of the detectors. In addition, fulfillment of some conditions concerning the properties of the detectors was required:

(i) In order to reduce the systematic error, the near and the far detector must be identical, with the exception of their volumes.

(ii) The near detector is one-tenth as large as the far one and is placed at a distance of about 100 to 170 m from the reactor, where the effect of oscillations is negligible. The distance between the reactor and the far detector is ten times as long as the distance between the reactor and the near detector. In turn, the counting rate in the near detector must be an order of magnitude higher than that in the far detector.

An analysis made it possible to establish the integrated-luminosity dependence of the limit on the sensitivity in measuring $\sin^2(2\theta_{13})$. It can be seen from Fig. 1 [17] that, for $\mathcal{L} > 10^4$ t GW yr, the sensitivity of the experiment in the measurements of $\sin^2(2\theta_{13})$ varies in proportion to $\mathcal{L}^{-1/2}$ and is weakly dependent on the systematic errors. Huber *et al.* [17] attribute the reduction of the systematic effect to the possibility of performing, in the case of vast statistics ($\mathcal{L} > 10^4$ t GW yr), high-precision measurements of not only the oscillation-induced distortion of the positron spectrum but also experimental parameters that affect the systematic error.

As a more general result, it is indicated in [17] that the limiting sensitivity of about $10^{-3}$ to $\sin^2(2\theta_{13})$ can be obtained in experiments characterized by an integrated luminosity of about $10^5$ t GW yr. In order to reach an integrated luminosity on this order of magnitude, it would be necessary to have a near and a far detector of weight $10^3$ t and about

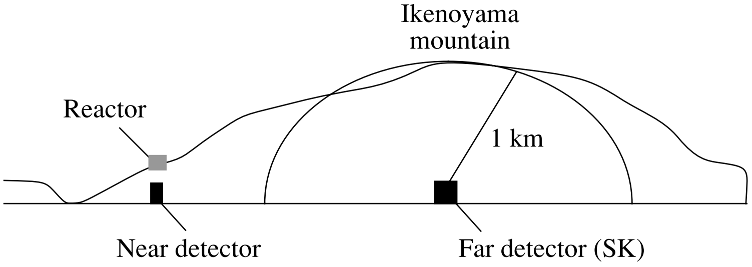

**Fig. 2.** Profile of Ikenoyama mountain and the schematic arrangement of the reactor and the near and far detectors.

$10^4$ t, respectively, and to conduct measurements for five years at a reactor of thermal power about 3 GW. It should be emphasized that even the near detector must have the dimensions and weight of the KamLAND facility. Nevertheless, problems arising in the creation of such detectors seem solvable from the engineering and technological points of view. However, the deployment of an experimental facility of such large dimensions under an operating reactor would generate problems associated with the engineering and civil safety of the reactor, so that solving these problems (if this is possible in principle) would require additional expenditures and additional time.

In order to reach a sensitivity of $\sin^2(2\theta_{13}) < 0.01$, we propose here a different approach that would employ a facility of weight about or somewhat greater than $10^4$ t combined with its "own" antineutrino source, for which one can take a nuclear reactor of relatively low thermal power, about 300 MW (low-power reactor, or LPR). The respective measurement could be performed within a rather short time if use was made of an LPR together with the existing SuperKamiokande (SK) facility. As will be shown below, the LPR–SK combination would make it possible to obtain an integrated luminosity of about $10^5$ t GW yr, which corresponds to a sensitivity of $\sin^2(2\theta_{13}) \approx 0.002$.

The ensuing exposition is organized as follows. In Section 2, we will describe the general scheme of the LPR–SK experiment, touching upon the geometry of this experiment and upon the general features of an LPR and of a near and a far detector. In Section 3, we will discuss various methods for recording reactor antineutrinos in the SK detector. In Section 4, we will present estimates of the sensitivity of the LPR–SK experiment to $\sin^2(2\theta_{13})$ for various modes of the SK detector.

## 2. SCHEME OF THE EXPERIMENT

We will adhere to the *one reactor–two detectors* scheme [15]. A near and a far detector must be identical, with the exception of their volumes. The near detector is arranged in the region where the effect of neutrino oscillations is negligible. Specifically, we consider the case where it is placed at distance of about 150 m from the reactor at a depth of about 250 mwe. The far detector (SK [3, 18]) is situated in the underground laboratory under Ikenoyama mountain at an altitude of 370 m above sea level (Fig. 2). The underground laboratory lies under 1000 m of rock, which corresponds to the effective absorbing-layer thickness of 2700 mwe. The shortest distances from the underground laboratory to the surface are 2 to 3 km along the horizontal direction and less than 1 km to a point at an altitude of 1400 m above sea level. This profile makes it possible to choose an optimum distance between the reactor situated at the slope of the mountain and the far detector. As follows from (5), the distance $L$ necessary for observing the oscillations in question depends on the averaged neutrino energy and, hence, on the energy threshold of the detector. Below, we will consider various methods for reducing thresholds at the SK. For the time being, we will set the threshold to 3.8 MeV for the sake of definiteness, this corresponding to $L \sim 2$ km. In order to be within the conditions under which the sensitivity in measuring $\sin^2(2\theta_{13})$ varies in proportion to $\mathcal{L}^{-1/2}$, the counting rate in the near detector must be an order of magnitude higher than that in the far detector. With allowance for the reactor–detector distances, the mass of the near detector may be less than the mass of the SK detector by a factor of about 20.

### *2.1. Low-Power Reactors*

As an antineutrino source, we propose employing a KLT-40S reactor facility involving two reactor blocks of total thermal power 300 MW ($2 \cdot 150$ MW) that are equipped with a cooling system, an emergency protection, and a spent-nuclear-fuel storage [19]. Facilities of this type have been exploited in the Soviet Union (presently the Russian Federation) since 1959 as power stations for icebreakers. At the present time, a project of floating atomic power plants that are intended for use in the northern and eastern regions of the Russian Federation [20] and on the seaboard of continental China [21] has been developed on the basis of the KLT-40S.

Reactors of the PWR type are placed in a metal–water shield tank and are equipped with an emergency-protection system satisfying all IAEA safeguards. The equipment and control systems are enclosed by an air tight casing. The duration of the reactor operating period (to a new loading of the fuel material) is 3 yr. The rate of water consumption is $2 \cdot 250 = 500$ m$^3$/h. The KLT-40S facility satisfies the most stringent seismic requirements (the admissible acceleration is $12g$).

The minimum volume of the room for the deployment of the reactor facility alone is $25 \times 25(\mathrm{H}) \times 30$ m$^3$. The full atomic-power-plant assembly, including two steam-turbine setups and two steam generators, is placed in a hall of volume $25 \times 25 \times 70$ m$^3$. At a weight of 62 t, the dimensions of the reactor vessel are $\varnothing 2.93 \times 5.35$ m$^3$. An atomic power plant based on a KLT-40S can produce 520 GW h of electric power per year. At a price of US \$0.1/kW h, the total cost of electric power per year will be about \$50 million [22].

Yet another advantage of operation with one's "own" reactor is worthy of special note. Reactors of the KLT-40S type admit easy control and possess a low inertia. Within a scientific experiment, one can preset an optimum relationship between the time of measurements with an operating reactor ("on" mode) and the time of measurements with a shut-down reactor ("off" mode), this making it possible to perform high-precision measurements of the background.

### *2.2. SuperKamiokande Far Detector*

The SK detector is intended for studying solar and atmospheric neutrinos and the proton-decay process. Its operation is based on recording Cherenkov radiation arising upon the propagation of a high-energy charged particle through water. The SK detector is a cylinder 39.3 m in diameter and 41.4 m in height filled with water. Within the cylinder, metallic structures to which multiplier phototubes and an optically nontransparent partition are fastened are arranged at a distance of 2.5 m from its walls. The partition divides the detector into an external (external detector) and an internal (internal detector) part. The external detector is viewed by 1885 multiplier phototubes of diameter 20 cm. It serves as an active shield. The internal detector is viewed by 11 146 multiplier phototubes of diameter 50 cm. The total area covered by the multiplier phototubes amounts to 40% of the internal-detector surface. The active part of the internal detector serves as a target, its mass being 22 500 t. Neutrino events in the internal detector are determined by the number of actuated multiplier phototubes (in the absence of a signal in the external detector). The resolution of the SK detector is 20.9% for electrons of energy 4.89 MeV. The threshold for analysis of events is 4.5 MeV. These data concern the operation of the detector before the accident in the fall of 2001, the so-called SKI phase.

The energy threshold of the detector used, $E_{\mathrm{thr}}$, is one of the main parameters in a reactor experiment. Its magnitude determines the spectrum of antineutrinos and their mean energy $\bar{E}_\nu$. In turn, the spectrum affects useful statistics, while $\bar{E}_\nu$ affects the optimum reactor–detector distance ($L$), which also exerts influence on experimental statistics. In the operation of the SK in the mode of a solar-neutrino detector, the energy threshold for recording scattered electrons exceeded 4.5 MeV. The magnitude of the threshold was determined by a sharp growth of the background with decreasing energy and by the sensitivity of the multiplier phototubes.

The preservation of the threshold $E_{\mathrm{thr}}$ for positrons at a level of about 5 MeV in a reactor experiment would lead to considerable losses of useful events since, upon going over from the positron spectrum to the antineutrino spectrum, the threshold will increase further by 1.8 MeV, which is the threshold for the inverse-beta-decay reaction (4). Moreover, neutron capture in water with the emission of a 2.2-MeV photon will not be recorded for $E_{\mathrm{thr}} \geq 4.5$ MeV. As a result, the problem of separating the reaction in (4) from the background becomes much more involved. A high threshold is an intrinsic drawback constraining the SK potential in almost all experiments. In the course of the restoration of the SK, the upgrade of the instrumental equipment and of the respective software is being performed with the aim of improving the functioning of the trigger. Upon the completion of this work, the detector will record scattered electrons of kinetic energy above 2 MeV [23]. In the reactor experiment, this will correspond to antineutrino energies in the region $E_\nu \geq 3.8$ MeV. The positron-detection efficiency will be 60% of the highest possible efficiency in reaction (4). In order to reduce the radiation background, all multiplier phototubes will be covered with a protecting film preventing the penetration of radon to the sensitive volume of the detector [24].

### *2.3. Near Detector*

According to the general scheme of the proposed experiment, the near detector must be identical in configuration to the far detector, the SK in the present case. The near detector will be placed in the region where the effect of oscillations is negligible—specifically, at a distance of about 100 to 170 m from the reactor at a depth of 250 mwe. Its counting rate must be an order of magnitude higher than that in the far detector. With allowance for this and for the reactor—detector distances, the sensitive mass of the near detector must be less than the SK mass by a factor of about 20, which corresponds approximately to 1000 t. At a depth of 250 mwe, the counting rate in the active-shield system of the near detector due to the charged component of cosmic rays will be about 300 events per second. At an anticoincidence-gate duration of about 100 $\mu$s, this counting rate in the active shield will have no effect on the efficiency of useful-event counting.

## 3. POSSIBLE METHODS FOR DETECTING REACTOR ANTINEUTRINOS

In the proposed experiment based on the *LPR—two detectors* scheme, a few methods can be used for separating neutrino events:

(i) There is the standard mode of a water Cherenkov detector, in which case only positrons are detected.

(ii) An aqueous solution of gadolinium salts is used in the intrinsic volumes of the detectors. The Cherenkov counter mode is not changed, but delayed signals from neutron absorption are recorded in addition to positrons.

(iii) A scintillator is employed for a working medium. The detectors operate as scintillation counters. Both positrons and neutrons are recorded.

For each of the aforementioned detection methods, we will now consider in detail the parameters of the experiment and the sensitivity that can be achieved in measuring $\sin^2(2\theta_{13})$.

**Standard mode of a water Cherenkov counter.** In the experiment that studied solar neutrinos with the aid of the SK detector, use was made of elastic electron—neutrino scattering. Neutrinos were recorded by Cherenkov radiation from scattered electrons. The energy threshold in the kinetic energy of scattered electrons was about 4.5 MeV. This made it possible to record only B-cycle solar neutrinos, whose mean energy was about 8 MeV. Events associated with solar neutrinos had an anisotropic distribution—they were concentrated in a cone having an angle of about 60° at the apex with respect to the axis directed from the Sun. This angular asymmetry was used to separate useful events from the background.

In going over to an experiment aimed at measuring the parameter $\sin^2(2\theta_{13})$, one must consider, first of all, that, after the upgrade of the SK, the reduction of the threshold for positrons will correspond to $T_{\text{kin}} \geq 2$ MeV, which, for antineutrino energies, rescales to $E_\nu \geq 3.8$ MeV. The reduction of the threshold, along with an increase in useful statistics, will lead to a sharp growth of the background. Relying on the measurements of the SK background that were performed before the termination of the experiment at the threshold values of 4.5, 5.0, 5.5, and 6.0 MeV [25] and assuming that the increase in the background will follow the same law at lower threshold values, we find that the background will increase by three orders of magnitude in response to the reduction of the threshold from 5 to 2 MeV. According to our estimates, the SK background may become about $6 \times 10^4$ events per day. It cannot be suppressed either by choosing a specific direction in the distribution of positrons or by using the method of delayed coincidences between the signals from the product positron and the product neutron. The former is inefficient because the spectrum of reactor antineutrinos is much softer than the spectrum of solar neutrinos originating from the boron cycle. Therefore, positrons that are produced by reactor antineutrinos in the inverse-beta-decay process (4) will have a nearly isotropic distribution. In order to make use of the method of delayed coincidences, it is necessary to record both the positron and the neutron from the reaction in (4). The capture of a neutron in water leads to the production of a 2.2-MeV photon, which, in the the subsequent Compton scattering, transfers only part of its energy to the electron involved. Since the threshold of the Cherenkov counter is such that $T_{\text{kin}} \geq 2$ MeV, the overwhelming majority of Compton electrons will not be recorded.

In view of the aforesaid, the method of on—off measurements seems the only way to separate product positrons in the standard mode of a water Cherenkov counter. Within this method, useful and background events are collected in the on-mode, whereupon the background is measured in the off-mode. The effect is determined from the difference $N_{\text{eff}} = N_{\text{on}} - N_{\text{off}}$, the accuracy of the measurements being determined by the statistical error ($\Delta N_{\text{eff}} = (N_{\text{on}}^2 + N_{\text{off}}^2)^{0.5}/N_{\text{eff}}$). The total experimental time may reach five years, two and a half years in the on-mode and two and a half years in the off-mode. In the absence of oscillations, the number of recorded positrons, $N_{e^+}$, is determined by the reactor power (0.3 GW), the distance between the reactor and the far detector (2 km), the cross section for the inverse-beta-decay reaction, the sensitive volume of the detector (about 20 kt), and its energy threshold (3.8 MeV). With allowance for the aforementioned basic parameters of the experiment, we have $N_{e^+} \approx 800$ events per day, which is almost two orders of magnitude smaller than the expected background. At this effect-to-background ratio, our estimation of the statistical error of the experiment yields a value of about 1.4%, which is much poorer than that in [15–17]. Within the method being discussed, there are two possibilities for improving the statistical accuracy to a value of about 0.1%:

The first is to reduce the background by two orders of magnitude. As was indicated above, work along these lines is under way.

The second is to reduce the energy threshold for positrons to $T_{\rm kin} \geq 1.5$ MeV. This will make it possible to use the method of delayed coincidences and, as a consequence, lead to a suppression of the background by three orders of magnitude.

**Cherenkov detector employing an aqueous solution of gadolinium salts.** The possibility of employing the SK detector to record neutrinos from far reactors is being presently discussed [24]. An acqueous solution of gadolinium salts is proposed for use as a neutron absorber. As was indicated above, the mean delay time between the signals from the product positron and the product neutron is about 100 $\mu$s in this case, the total energy of the photon cascade arising upon neutron absorption being about 8 MeV. According to the calculations presented in [26], the photon-cascade energy visible to the Cherenkov detector is approximately equal to $5 \pm 2$ MeV. For neutrons originating from the inverse-beta-decay reaction (4) to be almost completely absorbed (more than 90% of them), one would need an aqueous solution of gadolinium concentration about 0.1% or 100 t of gadolinium chloride ($\mathrm{GdCl_3}$) for the whole internal volume of the SK. The detection of two events occurring in the same spatial region ($R < 3$ m) within an interval of about 100 $\mu$s, the first and the second stemming, respectively, from a positron of kinetic energy in the region $T_{\rm kin} \geq 2$ MeV and from a photon cascade of mean visible energy $5 \pm 2$ MeV, must be a criterion for separating reactor antineutrinos. Simple estimations reveal that the above selection criteria are sufficient for suppressing all forms of the radiation background by eight orders of magnitude. Antineutrinos from far nuclear reactors provide the only source of background that may affect the accuracy of the experiment. The mean distance from the SK detector to the surrounding atomic power plants is about 175 km, their total thermal power being about 70 GW [7]. For the SK detector, the antineutrino-counting rate from far reactors is about 17 events per day, which is about 2% of the total antineutrino counting rate. The experience gained from the experiments performed at Rovno [27], CHOOZ [5], and KamLAND [7] revealed that the antineutrino flux from far atomic power plants can be monitored to within 2% by using data on the thermal power of these plants. Therefore, the measurement error associated with antineutrinos from far atomic power plants will be negligible. Nonetheless, measurements at the SK for antineutrinos from far atomic power plants are of value in themselves. In particular, they can be used to refine the mass parameter $\Delta m^2_{12}$. In the Cherenkov detector mode, the overall statistical accuracy in measuring the parameter $\sin^2(2\theta_{13})$ is about 0.1% for the case of filling with an aqueous solution of gadolinium salts.

**Scintillation-detector mode.** The use of a scintillator for a working medium—that is, a transition to the scintillation-detector mode in the SK—may be the most radical solution to the problem of improving the sensitivity of measurements. This will lead to some positive changes in relation to the mode of a water Cherenkov counter and the mode of a Cherenkov counter featuring gadolinium. The energy threshold of a scintillation detector will make it possible to measure the spectrum of positrons from the reaction in (4) from about 0.8 MeV and, accordingly, the spectrum of reactor antineutrinos from 1.8 MeV. The reduction of the threshold will entail, first, an increase in the number of recorded antineutrinos by a factor of 1.7 and, second, a corresponding decrease in the mean antineutrino energy and a change in the optimum distance between the reactor and the far detector from $L \sim 2$ km to $L \sim 1.7$ km. In turn, this will lead to an additional increase in the antineutrino flux by a factor of 1.4.

The background will be determined by the purity of a scintillator. In view of the expected rate of useful-event counting (about 1900 events per day), the requirements on the level of radioactive admixtures in the scintillator employed may not be as stringent as those in the KamLAND experiment. The use of a scintillator combined with gadolinium may be an alternative means for reducing the background. The time of delay between the signals from the product positron and the product neutron will become shorter by a factor of 10, which will lead to the respective reduction of the background from random coincidences. It is therefore likely that the use of gadolinium will make it possible to suppress the background to a level at which it does not have an adverse effect on the statistical error of the measurements.

## 4. ATTAINABLE SENSITIVITY IN MEASURING $\sin^2(2\theta_{13})$

In considering various methods for detecting reactor antineutrinos, we did not go beyond the main requirements for experiments of the *one reactor—two detectors* type. This makes it possible to employ the results of the analysis performed in [17] and to determine the attainable limit in measurements of $\sin^2(2\theta_{13})$ with respect to the integrated luminosity $\mathcal{L}$ of an experiment. There are, however, two distinctions between the parameters of the experiment in the present study and those in [17], and it is necessary to take these distinctions into account in evaluating the integrated luminosity. These are the distance between the reactor and the far detector and the range of reactor-antineutrino energies. We recall that, in determining $\mathcal{L}$, Huber *et al.* [17] set this distance and this energy range to about 1.7 km and $1.8 \le E_\nu \le 8$ MeV, respectively.

For various antineutrino-detection methods, the table presents basic parameters of the experiment proposed here for measuring $\sin^2(2\theta_{13})$ with the aid of an LPR. On the basis of these data, we have calculated the integrated luminosity, the number $N_{e^+}$ of recorded positrons, and the sensitivity of the experiment. For the mode of a water Cherenkov counter (WCC), we have considered only those cases (I, II) that ensure statistical accuracy at the level of 0.1%. Mode I corresponds to an on–off experiment at a background level two orders of magnitude lower than the present-day level of the background in the SK detector. Mode II implies the positron-energy threshold corresponding to $T_{\rm kin} \ge 1.5$ MeV, which makes it possible to employ the method of delayed coincidences, whereby one can reduce the background by three orders of magnitude. In calculating the integrated luminosity, we originally set $\mathcal{L} = 22\,500 \cdot 0.3 \cdot 5 = 33\,750$ t GW yr, whereupon we introduced corrections for the reactor–detector distances, the time of measurements in the on-mode, the energy threshold for the $\bar{\nu}_e$ spectrum, and the neutron-detection efficiency. After that, the integrated luminosities in the present study and in [17] corresponded to the same number of recorded positrons and, accordingly, the same statistical accuracy. The distance between the reactor and the facility used was determined from relation (5). As a rule, the antineutrino energy is set to an averaged value that depends on the energy threshold in the detector. This approach is justified for experiments characterized by relatively low statistics ($\mathcal{L} \approx 10^3$ t GW yr), in which case the separation of the effect of oscillations requires employing a wide section of the antineutrino spectrum. At integrated luminosities of $\mathcal{L} \ge 10^4$ t GW yr, there arises the possibility of observing, in a narrow region near the energy threshold, oscillation-induced distortions of the spectrum (see Fig. 1 [17]). In this case, the reactor–detector distance is determined by nearly threshold values of the antineutrino energy. In estimating the sensitivity for all detector modes, with the exception of the Scintillation* mode, we have used the mean antineutrino energy. Although this method of estimation is quite straightforward and clear, it underestimates the results of experiments significantly at $\mathcal{L} \approx 10^4$ t GW yr. In the Scintillation* mode, where the statistical accuracy makes it possible to single out distortions of the antineutrino spectrum in the region around 2 MeV quite reliably, the distance in question can therefore be reduced from 1700 to 800 m.

As can be seen from the table, the total number $N_{e^+}$ of recorded positrons exceeds $10^6$ in all cases, with the exception of that of the WCC I mode. This corresponds to a statistical error not exceeding 0.1%. In experiments performed according to the *one reactor–two detectors* scheme, the total systematic error ($\sigma_{\rm syst}$) in the measured parameter is not expected to exceed a value of about 1%. Moreover, the sensitivity in measuring the parameter $\sin^2(2\theta_{13})$ at integrated luminosities of $\mathcal{L} \ge 10^4$ t GW yr is only slightly dependent on $\sigma_{\rm syst}$ (see Fig. 1). Our analysis revealed that, in an LPR–SK experiment, the sensitivity in measuring $\sin^2(2\theta_{13})$ varies within the range $(2\text{–}8) \times 10^{-3}$, its specific value being dependent on the detection method.

## CONCLUSION

The CHOOZ experiment, which resulted in obtaining the constraint $\sin^2(2\theta_{13}) \le 0.14(3)$, may be considered as a starting point in determining the order of magnitude of the parameter $\sin^2(2\theta_{13})$. The systematic error in that experiment, $\sigma_{\rm syst}$, was 2.7%, and its magnitude was the main factor that hindered the improvement of the accuracy in similar reactor experiments. In order to reduce the systematic error $\sigma_{\rm syst}$, the authors of the Kr2Det project [15] proposed the *one reactor–two detectors* method, which makes it possible to remove the main sources of errors and to reduce the total systematic error to a value of about 0.8%. This ensured the respective improvement of the sensitivity in measuring $\sin^2(2\theta_{13})$. The study of Huber *et al.* [17], who performed a comprehensive analysis of various approaches aimed at reaching sensitivities of $\sin^2(2\theta_{13}) < 0.01$, may be considered as a next step along these lines. They showed that, in the case of vast statistics, the effect of systematic errors on the sensitivity of such experiments becomes weaker and that, at a luminosity of about $10^5$, it is possible in principle to reach a sensitivity of about $10^{-3}$ to $\sin^2(2\theta_{13})$. In order to implement an experiment at this luminosity value in practice, it is necessary, however, to deploy a huge underground detector facility within the territory of an operating atomic power plant. Apart from purely engineering difficulties, this can cause serious problems associated with the radiation safety and security of the respective atomic power plant.

In view of this, we have proposed here an alternative approach to measuring $\sin^2(2\theta_{13})$. This approach, which can provide substantially easier and faster ways to solving the problem of reaching a sensitivity in the region $\sin^2(2\theta_{13}) < 0.01$, consists in the following: without going beyond the *one reactor–two detectors* scheme, one arranges, instead of

Sensitivity of the LPR—SK experiment for various methods of reactor-antineutrino detection

| Detector mode | Distance, m | Time in the on-mode, day/yr | Threshold, MeV | $\mathcal{L}$, kt GW yr | $N_{e^+}$ event/(5 yr) | $\sin^2(2\theta_{13})$ |
|---|---|---|---|---|---|---|
| WCC I | 2000 | 180 | 3.8 | 7.3 | $6.8 \times 10^5$ | $\leq 8.0 \times 10^{-3}$ |
| WCC II | 2000 | 300 | 3.3 | 14.8 | $1.4 \times 10^6$ | $\leq 6.5 \times 10^{-3}$ |
| WCC + Gd | 2000 | 300 | 3.8 | 12.0 | $1.1 \times 10^6$ | $\leq 7.0 \times 10^{-3}$ |
| Scintill. | 1700 | 300 | 1.8 | 27.7 | $2.6 \times 10^6$ | $\leq 5.0 \times 10^{-3}$ |
| Scintill.* | 800 | 300 | 1.8 | 125.0 | $11.7 \times 10^6$ | $\leq 1.8 \times 10^{-3}$ |

creating an experimental facility near an operating atomic power plant, a small-size nuclear reactor of thermal power about 300 MW at an optimum distance from a facility of weight about $10^4$ t (far detector). For such a facility, already an operating one, we can take the SK water Cherenkov detector. Since the SK detector was originally intended for recording solar neutrinos and since it has a rather high energy threshold, we have analyzed a few approaches ensuring the required sensitivity. As a result, it has been shown that the use of an LPR together with the SK detector in an experiment aimed at measuring $\sin^2(2\theta_{13})$ will make it possible to attain a sensitivity in the range $(2–8) \times 10^{-3}$.

For the sake of convenience, we have discussed an experiment that would employ a specific reactor type (KLT-40S) and a specific detector (SK). In fact, the proposed approach implies a rather free choice of reactor facilities and neutrino detectors. For example, the KamLAND facility, where sensitivities of $\sin^2(2\theta_{13}) \leq 0.01$ are reachable without introducing significant changes, can be used for a far detector. The present study was devoted to solving only one of the pressing experimental problems—the discussion of questions concerning the use of small-size reactors as sources of antineutrinos for other problems of neutrino physics remained beyond its scope.[1]

## ACKNOWLEDGMENTS

We are indebted to V.I. Kopeikin, L.A. Mikaelyan, and V.V. Sinev, whose articles have taught us much and have stimulated our interest in studies devoted to measuring the parameter $\sin^2(2\theta_{13})$. We are also indebted to Mark Vagins (University of California at Irvine, USA) for numerous consultations on the status of the SK detector. Special thanks are due to Y. Kishimoto (Tohoku University, Japan) and Yu. Kamyshkov (University of Tennessee, USA) for information about the Kamioka underground laboratory.

This work was supported by the Russian Foundation for Basic Research (project no. 02-02-16111).

## REFERENCES

1. B. M. Pontekorvo, Zh. Éksp. Teor. Fiz. **34**, 247 (1958) [Sov. Phys. JETP **7**, 172 (1958)]; **53**, 1717 (1967) [**26**, 984 (1967)].
2. Z. Maki, M. Nakagawa, and S. Sakata, Prog. Theor. Phys. **28**, 870 (1962).
3. Kamiokande Collab. (Y. Fukuda *et al.*), Phys. Lett. B **335**, 237 (1994); Phys. Rev. Lett. **81**, 1562 (1998); hep-ex/9807003; Phys. Rev. Lett. **85**, 3999 (2000); hep-ex/0009001.
4. K2K Collab. (M. H. Ahn *et al.*), Phys. Rev. Lett. **90**, 041801 (2003); hep-ex/0212007.
5. CHOOZ Collab. (M. Apollonio *et al.*), Phys. Lett. B **466**, 415 (1999); hep-ex/9907037; M. Apollonio *et al.*, hep-ex/0301017.
6. F. Boehm, J. Busenitz, *et al.*, Phys. Rev. Lett. **84**, 3764 (2000); Phys. Rev. D **62**, 072002 (2000).
7. KamLAND Collab. (K. Eguchi *et al.*), Phys. Rev. Lett. **90**, 0211802 (2003).
8. B. T. Cleveland *et al.*, Astrophys. J. **496**, 505 (1998); SAGE Collab. (J. N. Abdurashitov *et al.*), Phys. Rev. C **60**, 055801 (1999); astro-ph/9907113; GALLEX Collab. (W. Hampel *et al.*), Phys. Lett. B **447**, 127 (1999); Super-Kamiokande Collab. (S. Fukuda *et al.*), Phys. Rev. Lett. **86**, 5656 (2001); hep-ex/0103033; SNO Collab. (Q. R. Ahmad *et al.*), Phys. Rev. Lett. **87**, 071301 (2001); nucl-ex/0106015; SNO Collab. (Q. R. Ahmad *et al.*), Phys. Rev. Lett. **89**, 011301 (2002); nucl-ex/0204008.
9. SNO Collab. (Q. R. Ahmad *et al.*), Phys. Rev. Lett. **89**, 011302 (2002); nucl-ex/0204009.

---

[1] About fifteen years ago, L.A. Popeko proposed seeking neutrino oscillations under water in experiments that would employ the power plant of a submarine as a source of antineutrinos. Before the start of the KamLAND experiment, L.A. Mikaelyan proposed employing an LPR of power about 50 MW for the calibration of the neutrino detector (private communication). In the article of J. Detwiler, G. Gratta, *et al.*, Phys. Rev. Lett. **89**, 191802 (2002), the attention of researchers is called to the effect of moving submarines on the results of long-base-line experiments.

10. M. Maltoni, T. Schwetz, M. A. Tortola, and J. W. F. Valle, Phys. Rev. D **67**, 013011 (2003); hep-ph/0207227; G. L. Fogli, E. Lisi, A. Marrone, and D. Montanino, hep-ph/0303064.
11. P. C. de Holanda and A. Y. Smirnov, hep-ph/0212270; A. Bandyopadhyay, S. Choubey, R. Gandhi, *et al.*, hep-ph/0212146.
12. V. Paolone, Nucl. Phys. B (Proc. Suppl.) **100**, 197 (2001).
13. Y. Itow *et al.*, Nucl. Phys. B (Proc. Suppl.) **111**, 146 (2001); hep-ex/0106019.
14. D. Ayres *et al.*, hep-ex/0210005.
15. L. Mikaelyan *et al.*, Nucl. Phys. B (Proc. Suppl.) **91**, 120 (2001); V. Martemyanov, L. Mikaelyan, V. Sinev, *et al.*, hep-ex/0211070.
16. H. Minakata, H. Sugiyama, O. Yasuda, *et al.*, hep-ph/0211111.
17. P. Huber, M. Lindner, T. Schwetz, and W. Winter, hep-ph/0303232.
18. S. Fukuda *et al.*, Preprint of Super-Kamiokande Collab., submitted to Elsevier Preprint, 6 Dec. 2002.
19. G. N. Alekseev, *Formation and Development of Nuclear Energy* (Nauka, Moscow, 1990) [in Russian].
20. Experimental Design Office for Machine Building, Nizhni Novgorod, http://www.okbm.nnov.ru; JSC "Malaya Energetica," Moscow, http://www.energetica.ru.
21. *Project of Small Size Power Plant for China*, http://www.nuclear.ru.
22. E. A. Kuzin, private communication.
23. M. Vagins, private communication.
24. J. F. Beacom and M. R. Vagins, hep-ph/0309300.
25. SuperKamiokande Collab. (M. Nakahata *et al.*), in *LowNu2003, College de France, Paris, 2003,* http://cdfinfo.in2p3.fr/LowNu2003.
26. C. K. Hargrove *et al.*, Nucl. Instrum. Methods Phys. Res. A **357**, 157 (1995).
27. A. I. Afonin, S. N. Ketov, V. I. Kopeĭkin, *et al.,* Zh. Éksp. Teor. Fiz. **94**, 1 (1988) [Sov. Phys. JETP **67**, 213 (1988)].

*Translated by A. Isaakyan*

*Physics of Atomic Nuclei, Vol. 67, No. 4, 2004, pp. 682–687. From Yadernaya Fizika, Vol. 67, No. 4, 2004, pp. 704–709.*
*Original English Text Copyright © 2004 by Asratyan, Dolgolenko, Kubantsev.*

**ELEMENTARY PARTICLES AND FIELDS**
**Experiment**

# Evidence for Formation of a Narrow $K^0_S p$ Resonance with Mass near 1533 MeV in Neutrino Interactions*

**A. E. Asratyan**, A. G. Dolgolenko, and M. A. Kubantsev[1]**

*Institute of Theoretical and Experimental Physics,*
*Bol'shaya Cheremushkinskaya ul. 25, Moscow, 117259 Russia*

Received September 18, 2003

**Abstract**—A narrow baryon resonance is observed in the invariant mass of the $K^0_S p$ system formed in neutrino and antineutrino collisions with nuclei. The mass of the resonance is estimated at $1533 \pm 5$ MeV. The observed width is less than 20 MeV and is compatible with being entirely due to experimental resolution. The statistical significance of the signal is near 6.7 standard deviations. Since the position of the observed resonance does not match the mass of any known $\Sigma^{*+}$ states, we believe that it arises from the neutrino production of the $\Theta^+$ pentaquark baryon. The analysis is based on the data obtained in past neutrino experiments with big bubble chambers: WA21, WA25, WA59, E180, and E632. *© 2004 MAIK "Nauka/Interperiodica".*

A narrow baryon resonance with mass near 1540 MeV and unnatural (positive) strangeness has been recently detected in the $K^+n$ system formed in the reaction $\gamma n \to K^+K^-n$ on carbon [1] and in the $K^0p$ system from the charge-exchange reaction $K^+n \to K^0p$ in low-energy $K^+$Xe collisions [2]. Similar observations have since been reported by two other photoproduction experiments [3, 4]. This object, referred to as $\Theta^+(1540)$, is tentatively interpreted as the lightest member of an antidecuplet of pentaquark baryons, as predicted some time ago in the framework of the chiral soliton model [5]. This paper reports on a search for formation of the $\Theta^+$ baryon in neutrino and antineutrino collisions with protons, deuterons, and neon nuclei.

We analyze the data collected by several neutrino experiments with big bubble chambers—BEBC at CERN and the 15-ft chamber at Fermilab. These two bubble chambers were close to each other in geometry, fiducial volume, and operating conditions, and their data were collected and processed using very similar techniques and algorithms. In the past, this already allowed one to combine the neutrino data collected with BEBC and the 15-ft bubble chamber for a number of physics analyses [6]. A database compiled by one of us (A.A.) comprises some 120 000 $\nu_\mu$- and $\bar{\nu}_\mu$-induced charged-current (CC) events and embraces the bulk of neutrino data collected with BEBC (experiments WA21, WA25, and WA59) and a significant fraction of data collected with the 15-ft bubble chamber[2] (experiments E180 and E632). Though obtained several decades ago, the neutrino data from big bubble chambers are still unrivaled in quality and completeness of physics information.

In the BEBC experiments WA21 (hydrogen fill), WA25 (deuterium fill), and WA59 (neon–hydrogen mix), the data were collected using essentially the same wideband horn-focused beam, with mean energies of $\nu_\mu$CC and $\bar{\nu}_\mu$CC events near 50 and 40 GeV, respectively. The experiment E180 used the 15-ft bubble chamber filled with a Ne–$H_2$ mix and exposed to a wideband antineutrino beam under conditions very similar to WA59. In the last bubble-chamber experiment, E632 at Fermilab, the 15-ft chamber was filled with a (lighter) Ne–$H_2$ mix and exposed to a neutrino beam with quadrupole-triplet focusing from the Tevatron. In E632, mean energies of neutrino and antineutrino events reached some 140 and 110 GeV, respectively. Neutral-current (NC) interactions are not systematically included in the database,[3] and therefore our analysis is restricted to CC events with $p_\mu > 4$ GeV. Total numbers and mean energies of $\nu_\mu$CC and $\bar{\nu}_\mu$CC events collected by the aforementioned experiments are summarized in the table. Fur-

---

*This article was submitted by the authors in English.

[1] Now at Department of Physics and Astronomy, Northwestern University, Evanston, USA.

**e-mail: `asratyan@vitep1.itep.ru`

[2] Unfortunately, our database does not include the biggest neutrino sample from the 15-ft bubble chamber—that collected by the $\nu$Ne experiment E53 [7].

[3] In WA59, the bulk of NC events were rejected at scanning stage.

Mean energies of $\nu_\mu$- and $\bar{\nu}_\mu$-induced CC events, mean momenta of $K_S^0$ mesons reconstructed by $K_S^0 \to \pi^+\pi^-$ decays, and the numbers of all measured CC events, of those with detected $K_S^0$ mesons, and of those featuring $K_S^0$ mesons and identified protons with momentum $p_p < 900$ MeV

| Experiment (chamber, fill) | WA21 (BEBC, hydrogen) | WA25 (BEBC, deuterium) | WA59 (BEBC, Ne–$H_2$) | E180 (15-ft chamber, Ne–$H_2$) | E632 (15-ft chamber, Ne–$H_2$) |
|---|---|---|---|---|---|
| Neutrinos: | | | | | |
| Mean $E_\nu$ [GeV] | 48.8 | 51.8 | 56.8 | 52.2 | 136.8 |
| Mean momentum of detected $K_S^0$ [GeV] | 5.7 | 5.7 | 4.5 | 3.4 | 7.7 |
| All measured CC events | 18 746 | 26 323 | 9753 | 882 | 5621 |
| CC events with $K_S^0$ | 1050 | 1279 | 561 | 21 | 587 |
| CC events with $K_S^0$ and identified protons | 82 (78) | 307 (128) | 193 (193) | 9 (8) | 229 (157) |
| Antineutrinos: | | | | | |
| Mean $E_\nu$ [GeV] | 37.5 | 37.9 | 39.5 | 33.8 | 110.0 |
| Mean momentum of detected $K_S^0$ [GeV] | 4.2 | 4.2 | 3.5 | 3.4 | 7.6 |
| All measured CC events | 13 155 | 16 314 | 15 693 | 5927 | 1190 |
| CC events with $K_S^0$ | 702 | 761 | 631 | 231 | 123 |
| CC events with $K_S^0$ and identified protons | 45 (43) | 116 (57) | 185 (185) | 56 (54) | 49 (28) |

Note: The numbers in parentheses are for the additional selection of $p_p > 300$ MeV. In the experiment E632, all neutrino events were measured on part of the exposed film, and only those that showed $K_S^0 \to \pi^+\pi^-$ and $\Lambda^0 \to p\pi^+$ candidates were measured on another part of the film.

ther details on these neutrino experiments can be found in [8].

Unlike charged kaons that are virtually indistinguishable from pions, neutral kaons are identified in a bubble chamber by reconstructing the decays $K_S^0 \to \pi^+\pi^-$. On average, the $K^0(\bar{K^0})$ detection efficiency is near 25%. At the same time, protons with momenta below $\sim 1$ GeV can be identified by the stopping signature, bubble density, and variation of track curvature in the magnetic field. Therefore, the $K^0p$ channel seems mandatory when searching for formation of $\Theta^+$ in a bubble chamber. The numbers of events featuring reconstructed $K_S^0 \to \pi^+\pi^-$ decays and identified protons with $p_p < 900$ MeV, which are used in this analysis, are quoted in the table for each (anti)neutrino sample considered. The momenta of protons identified in hydrogen, deuterium, and neon are plotted in Fig. 1. In deuterium, the enhancement at proton momenta below some 200 MeV is due to spectator protons. For neon events with reconstructed $K_S^0$ mesons and identified protons, mean proton multiplicity is $\simeq 1.4$.

For either fill, the $m(K_S^0p)$ distributions of $\nu_\mu$CC and $\bar{\nu}_\mu$CC events are plotted separately in Fig. 2 and combined in Fig. 3. Protons are selected in the momentum interval of $300 < p_p < 900$ MeV. The combined $\nu + \bar{\nu}$ distribution for neon shows a distinct enhancement at $m(K_S^0p) \simeq 1530$ MeV. No neutrino events contribute twice or more to the peak region. The peak survives the dropping of events that feature two or more identified protons with $300 < p_p < 900$ MeV [see the lower (open) histogram in the bottom panel of Fig. 3]. The combined $\nu + \bar{\nu}$ distribution for deuterium is also slightly enhanced in the same mass region. The background in the peak region is estimated by pairing a $K_S^0$ from one event and a proton from another event randomly selected in the same $\nu/\bar{\nu}$ subsample. The thus obtained "random-star" distribution is then normalized to the $K_S^0p$ mass spectrum by the number of entries in the nonres-

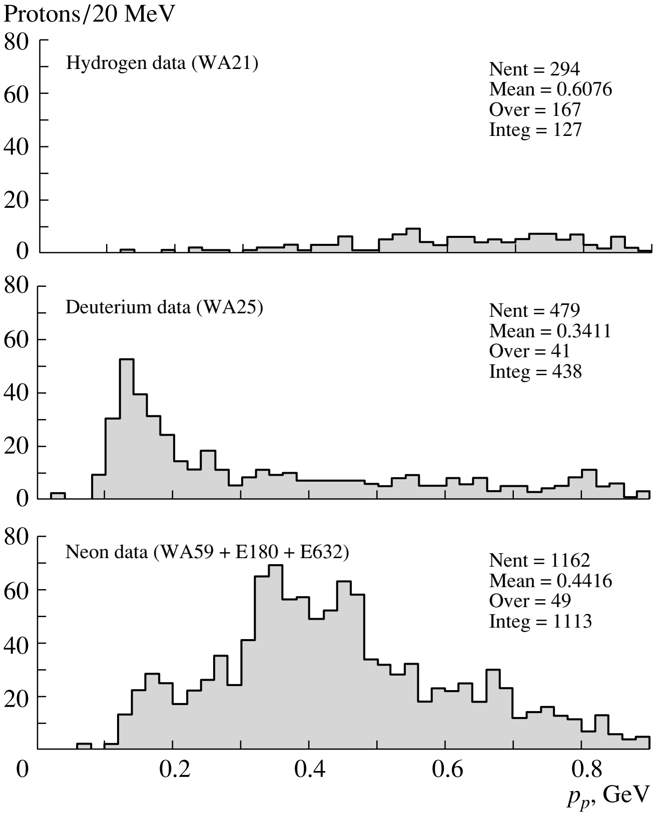

**Fig. 1.** Momenta of identified protons emitted in association with $K_S^0$ mesons in $\nu_\mu$CC and $\bar{\nu}_\mu$CC collisions with hydrogen, deuterium, and neon.

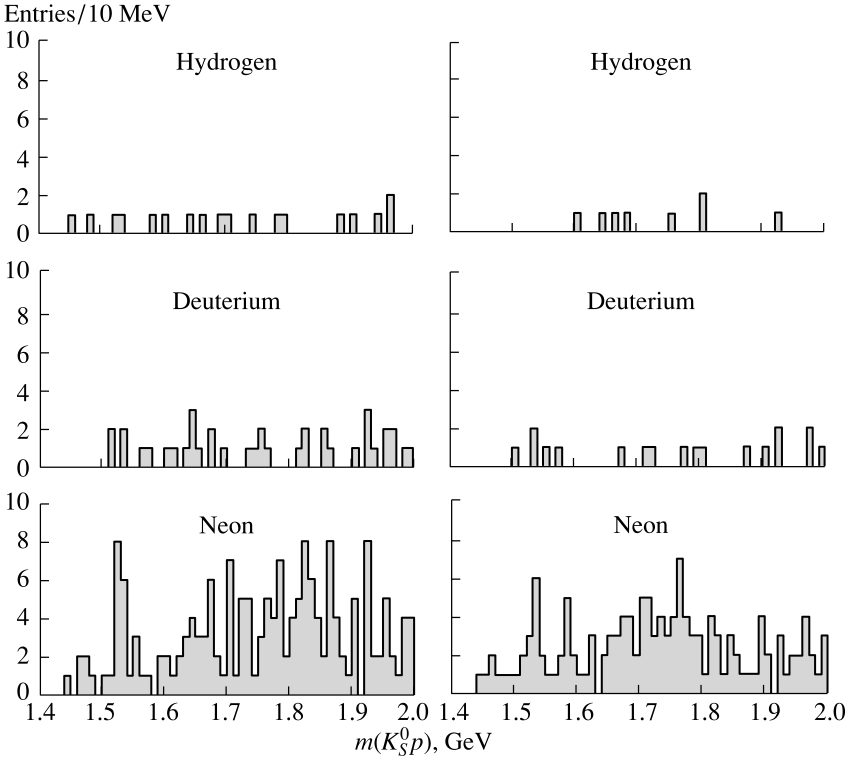

**Fig. 2.** Invariant mass of the $K_S^0p$ system formed in $\nu_\mu$CC (on the left) and $\bar{\nu}_\mu$CC (on the right) collisions with hydrogen, deuterium, and neon.

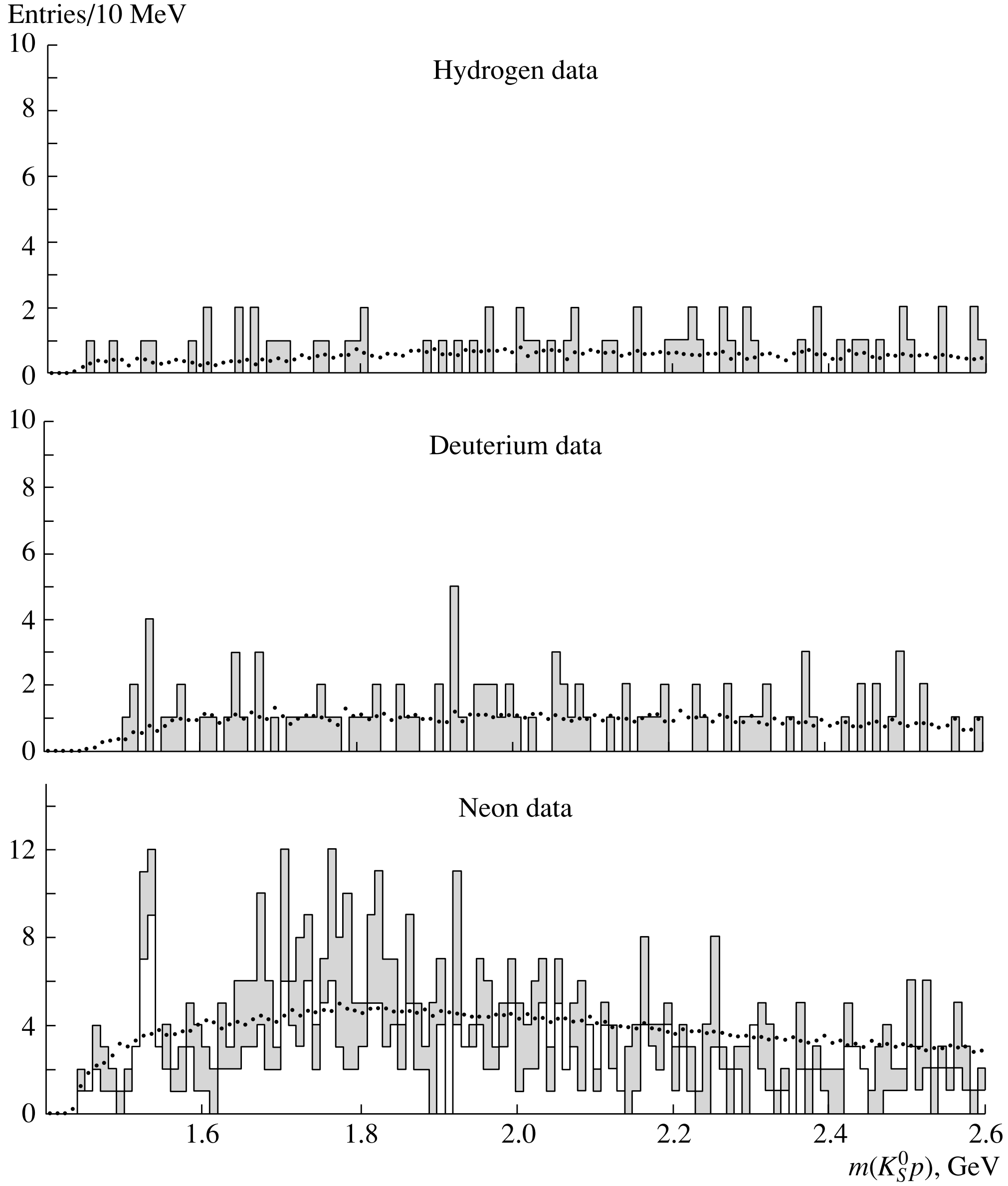

**Fig. 3.** Invariant mass of the $K^0_Sp$ system for the $\nu_\mu$CC and $\bar{\nu}_\mu$CC events combined. The "random-star" background obtained by pairing a $K^0_S$ from one event and a proton from another event is depicted by dots. Dropping the events in neon that feature two or more identified protons with $300 < p_p < 900$ MeV results in the lower (open) histogram in the bottom panel.

onant region of $m(K^0_Sp) > 2$ GeV (see the dotted histograms in Fig. 3). It is noteworthy that, apart from the peak near 1530 MeV in the $m(K^0_Sp)$ distribution for neon, the random-star background fails to reproduce a broad enhancement in the mass region $1650 < m(K^0_Sp) < 1850$ MeV of the same spectrum. The latter enhancement may be due to $\bar{K}^0p$ decays of a number of excited $\Sigma^{*+}$ states that populate this mass region [9].

Figure 4 shows the $m(K^0_Sp)$ distribution for the neon and deuterium data combined. In two 10-MeV bins between 1520 and 1540 MeV, we have 27 events with a background of $\sim 8$ events as estimated from random $K^0_Sp$ pairs (see the dotted histogram). The statistical significance of the peak is thus near 6.7 standard deviations. It makes no sense to fit a signal restricted to just two bins as in the top panel of Fig. 4, so in the bottom panel we plot the same $m(K^0_Sp)$ distribution with bins shifted by 5 MeV. A fit of the latter histogram to a Gaussian on top of the linear background returns $M = 1533 \pm 5$ MeV and $\sigma = 8.4 \pm 2.0$ MeV for the position and rms width of the resonance, respectively. The rms width is found to be

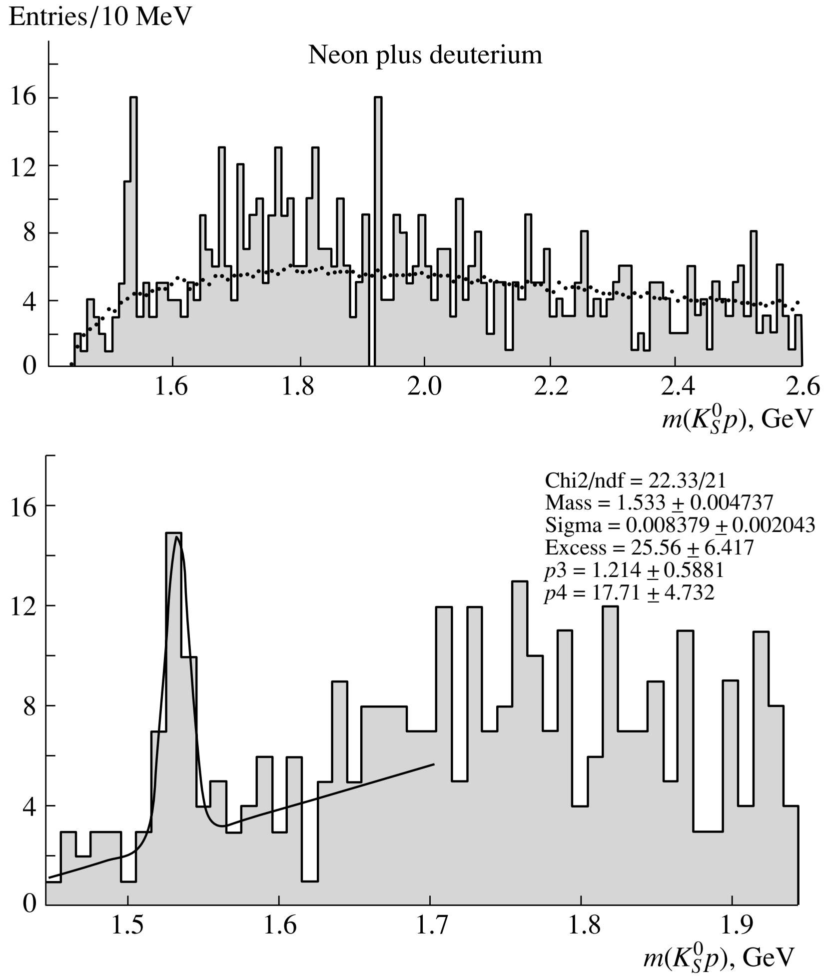

**Fig. 4.** Invariant mass of the $K^0_Sp$ system for the neon and deuterium data combined. The dots depict the "random-star" background. A fit of the same $m(K^0_Sp)$ distribution but plotted with shifted bins is shown in the bottom panel.

consistent with experimental resolution on $m(K^0_Sp)$ estimated from live events in the peak ($\simeq 8.5$ MeV).

For neutrino and antineutrino events that contribute to the peak region of $1510 < m(K^0_Sp) < 1550$ MeV, mean values of $E_\nu$ ($57 \pm 10$ GeV) and $Q^2$ ($12.5 \pm 3.3$ GeV$^2$) are consistent with those for all CC events with detected $K^0_S$ mesons. Mean momentum of the $K^0_Sp$ system for peak events, $\langle p(K^0_Sp)\rangle = 1.08 \pm 0.06$ GeV, is much less than that of all detected $K^0_S$ mesons (see table).

Unfortunately, neutrino data do not allow one to determine the strangeness of the observed resonant state with mass near 1533 MeV, as was done in [1–4]. On the other hand, there are no known $\Sigma^{*+}$ states in this mass region. Therefore, we interpret the enhancement near 1533 MeV observed in the $m(K^0_Sp)$ distribution as a signal from formation of the $\Theta^+$ baryon in neutrino and antineutrino collisions with nuclei. The mass and width of this state are estimated as $M = 1533 \pm 5$ MeV and $\Gamma < 20$ MeV, respectively. The cross section of $\Theta^+$ production by neutrinos appears to increase with atomic number of the target nucleus.

## ACKNOWLEDGMENTS

The excellent neutrino data analyzed in this paper are a result of painstaking and ingenious work of the WA21, WA25, WA59, E180, and E638 experimental teams over many years, and their efforts are gratefully acknowledged.

We wish to thank Prof. M.V. Danilov, Prof. L.B. Okun, Dr. V.S. Borisov, and Dr. V.S. Verebryusov for useful comments and suggestions.

## REFERENCES

1. LEPS Collab. (T. Nakano *et al.*), Phys. Rev. Lett. **91**, 012002 (2003); hep-ex/0301020.

2. DIANA Collab. (V. V. Barmin *et al.*), Yad. Fiz. **66**, 1763 (2003) [Phys. At. Nucl. **66**, 1715 (2003)]; hep-ex/0304040.
3. CLAS Collab. (S. Stepanyan *et al.*), hep-ex/0307018.
4. SAPHIR Collab. (J. Barth *et al.*), hep-ex/0307083.
5. D. Diakonov, V. Petrov, and M. Polyakov, Z. Phys. A **359**, 305 (1997).
6. A. E. Asratyan *et al.*, Phys. Lett. B **257**, 525 (1991); Big Bubble Chamber Neutrino Collab. (A. E. Asratyan *et al.*), Z. Phys. C **58**, 55 (1993); Big Bubble Chamber Neutrino Collab. (V. A. Korotkov *et al.*), Z. Phys. C **60**, 37 (1993); Big Bubble Chamber Neutrino Collab. (V. G. Zaetz *et al.*), Z. Phys. C **66**, 583 (1995).
7. E53 Collab. (N. J. Baker *et al.*), Phys. Rev. D **34**, 1251 (1986).
8. WA21 Collab. (G. T. Jones *et al.*), Z. Phys. C **51**, 11 (1991); WA25 Collab. (D. Allasia *et al.*), Z. Phys. C **37**, 527 (1988); WA59 Collab. (S. Willocq *et al.*), Z. Phys. C **53**, 207 (1992); E180 Collab. (V. V. Ammosov *et al.*), Nucl. Phys. B **177**, 365 (1981); E632 Collab. (D. DeProspo *et al.*), Phys. Rev. D **50**, 6691 (1994).
9. Particle Data Group (K. Hagiwara *et al.*), Phys. Rev. D **66**, 010001 (2002).

Physics of Atomic Nuclei, Vol. 67, No. 4, 2004, pp. 688–692. Translated from Yadernaya Fizika, Vol. 67, No. 4, 2004, pp. 710–714.

# Estimating the Rate of *Photon* + *Jet* Events to Determine the Gluon Distribution in the Tevatron Run II

**D. V. Bandurin*[*] and N. B. Skachkov**[**]**

*Joint Institute for Nuclear Research, Dubna, Moscow oblast, 141980 Russia*

Received May 20, 2003

**Abstract**—It is shown that experiments at an integrated luminosity of $L_{\rm int} = 3$ fb$^{-1}$ in the Tevatron Run II will make it possible to collect about one million *photon + jet* events selected according to the criteria proposed previously. Such statistics would allow one to cover the kinematical region that is specified by the inequalities $2 \times 10^{-3} < x < 1.0$ and $1.6 \times 10^3 \leq Q^2 \leq 2 \times 10^4$ (GeV/$c$)$^2$ and which was not studied in previous experiments devoted to measuring proton structure functions. This region contains values of $Q^2$ that are on average an order of magnitude higher than any ever attained in experiments at the HERA collider. *© 2004 MAIK "Nauka/Interperiodica"*.

## 1. INTRODUCTION

Various parametrizations of the gluon distribution in the proton at small values of $x$ and large values of the momentum transfer squared $Q^2$ are often employed to obtain theoretical predictions for the production of new particles (Higgs boson, supersymmetric particles) at the Tevatron. It is obvious that, by supplementing a correct estimate of the expected number of events necessary for this aim with measurements of gluon distributions in the same experiment at the Tevatron, one could obtain a self consistent picture of the processes under study [1, 2].

In addition, we note that the approach that we develop here makes it possible to determine the gluon distribution in an as-yet-unexplored kinematical region.

The ensuing exposition is organized as follows. In Section 2, the efficiency of suppression of background events and the efficiency of selection of *photon + jet* events are estimated on the basis of the selection criteria proposed in [1, 2]. The values presented in this article were obtained by using the PYTHIA 5.7 event generator [3]. The results of a full simulation on the basis of the GEANT package with a subsequent reconstruction of D0 events can be found in [4].1)

An estimate of the number of signal events needed for measuring, in the Run II, the gluon distribution in the proton2) over various ranges of $x$ and $Q^2$ is given in Section 3.

## 2. SELECTION CRITERIA AND BACKGROUND SUPPRESSION

To estimate the contribution of background processes, we generated three samples of 40 million events each with allowance for all QCD and Standard Model $2 \to 2$ partonic subprocesses incorporated in the PYTHIA package, these samples also including signal *direct photon + jet* events caused by the "Compton" scattering subprocess $qg \to q + \gamma$ and the "annihilation" subprocess $q\overline{q} \to g + \gamma$.3) Each sample was obtained at a fixed value of the minimum transverse momentum of partons,4) $\hat{p}_\perp^{\rm min}$ ($\hat{p}_\perp^{\rm min} = 40$, 70, 100 GeV/$c$), in the $2 \to 2$ hard fundamental subprocess.

We selected events involving one candidate for a direct photon (denoted below as $\tilde{\gamma}$) and one jet whose transverse momentum satisfied the condition $P_t^{\rm jet} > 30$ GeV/$c$.5) By a photon candidate, we hereafter mean not only a direct photon ($\gamma^{\rm dir}$) but also

---

[*] e-mail: `dmv@nusun.jinr.ru`
[**] e-mail: `skachkov@cv.jinr.ru`

1) For example, the use of information from a preshower detector, a tracker, and a calorimeter may substantially improve the signal-to-background ratio obtained in Section 2.

2) The expected number of events that was estimated on the basis of similar selection criteria for *photon + jet* events and which is needed for extracting the gluon distribution from data on $pp$ collisions at the LHC energies is given in [2, 5].

3) It was found that the contribution of the channel $gg \to g\gamma$, which is also possible, is negligible even at the Tevatron energies.

4) See the CKIN(3) parameter in the PYTHIA package [3].

5) Jets were singled out by means of the LUCELL jet finder from the PYTHIA package.

1063-7788/04/6704-0688$26.00 © 2004 MAIK "Nauka/Interperiodica"

**Table 1.** List of the selection criteria used (see also Tables 2 and 3)

**1.** (a) $P_t^{\tilde{\gamma}} \geq 40$ GeV/$c$, (b) $P_t^{\text{jet}} \geq 30$ GeV/$c$, (c) $|\eta^{\tilde{\gamma}}| \leq 2.5$, (d) $P_t^{\text{hadr}} < 7$ GeV/$c^*$;
**2.** $P_t^{\tilde{\gamma}} \geq \hat{p}_{\perp}^{\min}$;
**3.** $P_{t\,\text{ring}}^{\text{isol}} \leq 1$ GeV/$c^{**}$;
**4.** $P_t^{\text{isol}} \leq 2$ GeV/$c$, $\epsilon^{\tilde{\gamma}} < 5\%$;
**5.** $N_{\text{jet}} = 1$;
**6.** $\Delta\phi < 17°$;
**7.** $P_t^{\text{miss}}/P_t^{\tilde{\gamma}} \leq 0.10$;
**8.** $P_t^{\text{clust}} < 10$ GeV/$c$;
**9.** $P_t^{\text{out}} < 10$ GeV/$c$.

* Maximum value of the transverse momentum $P_t$ of a hadron in an electromagnetic-calorimeter cell containing a $\gamma^{\text{dir}}$ candidate.
** Sum of the absolute values of $P_t$ in a ring: $P_t^{\text{sum}}(R = 0.4) - P_t^{\text{sum}}(R = 0.2)$.

many other particles capable of generating a similar signal in the electromagnetic calorimeter.[6] For such particles, we considered electrons/positrons, bremsstrahlung photons, and photons from meson decays [1, 2].

The selection criteria employed in our study are listed in Table 1.[7] The first selection criterion in Table 1 makes the preselection and involves four cuts. These are the transverse-momentum cuts for (a) $\gamma^{\text{dir}}$ candidates and (b) jets, (c) a cut determined by the geometry of the D0 electromagnetic calorimeter,[8] and (d) a cut that excludes $\gamma^{\text{dir}}$ candidates accompanied by energetic hadrons that fall within the cone of radius $R = ((\Delta\eta)^2 + (\Delta\phi)^2)^{1/2} = 0.2$ around the $\gamma^{\text{dir}}$ candidate.

The second criterion selects events involving $\gamma^{\text{dir}}$ candidates whose transverse momentum $P_t$ is greater than the threshold value $\hat{p}_{\perp}^{\min}$ used in the simulation of these events. The third criterion imposes a restriction on $P_{t\,\text{ring}}^{\text{isol}} = P_{t\,R=0.4}^{\text{isol}} - P_{t\,R=0.2}^{\text{isol}}$, where $P_{t\,R}^{\text{isol}}$ is the sum of $P_t$ over all cells of the electromagnetic calorimeter that are within the cone of radius $R$ around the cell involving the $\gamma^{\text{dir}}$ candidate being considered [6]. The fourth criterion makes more stringent the condition requiring that a photon candidate be isolated within the cone of radius $R = 0.7$.

Criteria 1–4 (with the exception of the preselection criterion $P_t^{\text{jet}} \geq 30$ GeV/$c$) are associated with photon selection and may be referred to as photon criteria.

The fifth criterion selects only one-jet events, while the sixth criterion leaves only those events in which the photon and jet transverse momenta (with respect to the beam axis) are opposite to each other—to be more precise, the azimuthal angle between them is required to be within the range $\phi(\gamma, \text{jet}) = 180° \pm \Delta\phi$, where $\Delta\phi \leq 17°$. The seventh criterion constrains the value of the missing transverse momentum $P_t^{\text{miss}}$, thereby reducing the background contribution from the electroweak subprocesses $qg \to q' + W^{\pm}$ and $q\bar{q}' \to g + W^{\pm}$ followed by the decay $W^{\pm} \to e^{\pm}\nu$ (this background would lead to a sizable value of $P_t^{\text{miss}}$ [1]).

The eighth and ninth criteria in Table 1 select events where the cluster (minijet) transverse momenta $P_t^{\text{clust}}$ are low and where the absolute value of the vector sum of the transverse momenta of all recorded particles not belonging to the *photon + jet* system (this quantity is denoted by $P_t^{\text{out}}$)[9] is less than 10 GeV/$c$.

For the aforementioned three samples of generated events, Table 2 gives the numbers of signal and background events that survived the application of the selection criteria 1–9. The "Preselection" row corresponds to the first criterion, while the "After selection" row presents the results obtained after the application of criteria 1–9 from Table 1.

The origin of direct-photon candidates is shown in Table 2 in more detail. Presented in the "$\gamma^{\text{dir}}$" columns are the numbers of events that stem from the subprocesses $qg \to q + \gamma$ and $q\bar{q} \to g + \gamma$ and which remain in each interval $P_t^{\tilde{\gamma}}$ after the application of the preselection criterion and the selection criteria 2–9. Similarly, the numbers of background events caused by photons emitted from quarks involved in $2 \to 2$ hard parton–parton interactions are given in the "$\gamma^{\text{brems}}$" column of Table 2 for the same levels of selection. The numbers of events featuring photons

---

[6] Our simulation was performed for the geometry of the D0 detector.

[7] Information about the efficiency of each criterion can be found in [1].

[8] In Table 1 and in what follows, $\eta = -\ln(\tan(\theta/2))$ is the pseudorapidity defined in terms of the polar angle $\theta$ reckoned from the beam axis. We also use the azimuthal angle $\phi$ defined in the plane orthogonal to the beam axis.

[9] More correct definitions of the quantities $P_t^{\text{clust}}$ and $P_t^{\text{out}}$ are given in [1, 2], where they were introduced as new physical variables that may be useful in selecting events of clearer topology.

**Table 2.** Numbers of signal and background events left after the application of all selection criteria

| $\hat{p}_{\perp}^{\min}$, GeV/$c$ | Criterion | $\gamma^{\rm dir}$ | $\gamma^{\rm brems}$ | Photons from meson decays ($\gamma^{\rm mes}$) | | | | $e^{\pm}$ |
|---|---|---|---|---|---|---|---|---|
| | | | | $\pi^0$ | $\eta$ | $\omega$ | $K_S^0$ | |
| 40 | Preselection | 18056 | 14466 | 152927 | 56379 | 17292 | 14318 | 2890 |
| | After selection | 6238 | 686 | 824 | 396 | 112 | 104 | 24 |
| 70 | Preselection | 39340 | 63982 | 761926 | 269666 | 87932 | 63499 | 17562 |
| | After selection | 8608 | 424 | 320 | 146 | 58 | 36 | 64 |
| 100 | Preselection | 56764 | 111512 | 970710 | 346349 | 117816 | 91416 | 38872 |
| | After selection | 11452 | 280 | 124 | 92 | 24 | 24 | 136 |

**Table 3.** Efficiencies and signal-to-background ratios ($S/B$) for selected events

| $\hat{p}_{\perp}^{\min}$, GeV/$c$ | $S$ | $B$ | $\epsilon_S$, % | $\epsilon_B$, % | $S/B$ | $S/\sqrt{B}$ |
|---|---|---|---|---|---|---|
| 40 | 6238 | 2122 | $34.55 \pm 0.51$ | $0.831 \pm 0.018$ | 2.9 | 135.4 |
| 70 | 8608 | 984 | $21.88 \pm 0.26$ | $0.079 \pm 0.003$ | 8.8 | 274.4 |
| 100 | 11452 | 544 | $20.17 \pm 0.21$ | $0.033 \pm 0.001$ | 21.1 | 491.0 |

from neutral-meson decays (specifically, $\pi^0$-, $\eta$-, $\omega$- and $K_S^0$-meson decays), $\gamma^{\rm mes}$ events, are listed in the respective columns of this table.

The numbers of events involving $e^{\pm}$ that pass the selection criteria of Table 1 are given in the last column of Table 2. It should be noted that, after all selections, such events contribute 1% to the total background at $\hat{p}_{\perp}^{\min} = 40$ GeV/$c$ and 25% at $\hat{p}_{\perp}^{\min} = 100$ GeV/$c$[10] (for more details, see [1]).

The numbers in Table 3 represent the information from Tables 1 and 2 in a condensed form. The values in the "$S$" and "$B$" columns represent the total numbers of signal and background events that passed the selection criteria 1–9.

Thus, the application of the proposed set of criteria leads to selecting *photon + jet* events of clean topology, the contribution of background processes being suppressed—that is, to events where a photon is well isolated and where the activity of clusters beyond the *photon + jet* system is suppressed.[11]

It should be emphasized that, in contrast to backgrounds from other sources, the background associated with bremsstrahlung photons is irremovable. The number of such events must be thoroughly estimated for each interval of $P_t^{\tilde{\gamma}}$ by using the particle level of the simulation on the basis of event generators like PYTHIA, because the bremsstrahlung background becomes much greater than the contribution from meson decays and the $e^{\pm}$ contribution as $P_t^{\tilde{\gamma}}$ grows [1, 2].

## 3. ESTIMATE OF THE EVENT RATE

Experimental investigation of processes involving a direct photon and a jet in the final state provides a better source of information about the gluon distribution in a hadron than investigation of inclusive-photon production ("$\gamma + X$") [7–15], since, in the latter case, the cross section is an integral of the parton distributions $f_a(x_a, Q^2)$ ($a$ denotes a quark or a gluon), whereas, in the former case, the differential cross section for the process $p\bar{p} \to \gamma^{\rm dir} + {\rm jet} + X$[12] at $P_t^{\rm jet} \geq 30$ GeV/$c$ (that is, in the region where $k_t$ effects[13] can be neglected) can be expressed in terms

---

[10] The contribution of $e^{\pm}$ events can be estimated by using the efficiency of finding a track within the central region of the D0 detector ($|\eta| < 0.9$). As was determined in the Run I [6], this efficiency is 83%, in which case the fraction of $\tilde{\gamma} = e^{\pm}$ events in the total background does not exceed 5% even for $P_t^{\tilde{\gamma}} > 100$ GeV/$c$.

[11] Clusters are suppressed by the selection criteria based on the $P_t^{\rm clust}$ and $P_t^{\rm out}$ cuts (see also [1, 2]).

[12] Respective experimental data can be found in [16, 17].

[13] That is, effects due to the internal motion of partons in the proton, this motion being responsible for their transverse momentum.

**Table 4.** Rate of $gq \to \gamma^{\rm dir} + q$ events for various $Q^2$ and $x$ intervals at $L_{\rm int} = 3$ fb$^{-1}$

| $Q^2$, (GeV/$c$)$^2$ | $x$ values of a parton | | | | | | All $x$ |
|---|---|---|---|---|---|---|---|
| | 0.001–0.005 | 0.005–0.01 | 0.01–0.05 | 0.05–0.1 | 0.1–0.5 | 0.5–1.0 | 0.001–1.0 |
| 1600–2500 | 8582 | 56 288 | 245 157 | 115 870 | 203 018 | 3647 | 632 563 |
| 2500–4900 | 371 | 13 514 | 119 305 | 64 412 | 119 889 | 3196 | 320 688 |
| 4900–8100 | 0 | 204 | 17 865 | 13 514 | 26 364 | 1059 | 59 007 |
| 8100–19600 | 0 | 0 | 3838 | 5623 | 11 539 | 548 | 21 549 |
| | | | | | | | **1 033 807** |

of the parton distributions as [1, 5, 10]

$$\frac{d\sigma}{d\eta_1 d\eta_2 dP_t^2} \tag{1}$$
$$= \sum_{a,b} x_a f_a(x_a, Q^2) x_b f_b(x_b, Q^2) \frac{d\sigma}{d\hat{t}}(ab \to 34),$$

where $a, b = q, \bar{q}, g$ and $3, 4 = q, \bar{q}, g, \gamma$. The gluon distribution $f_g(x, Q^2)$ can be determined by using formula (1) and the results of independent measurements of the $q, \bar{q}$ distributions with allowance for the efficiency of selection of $\gamma^{\rm dir}$ + *jet* events and for the background contribution that passed the selection criteria from Table 1.

Signal "gluon" events associated with the subprocess $qg \to q + \gamma$ and background events associated with the subprocess $q\overline{q} \to g + \gamma$ can be selected with the same efficiencies by applying criteria 1–9 from Table 1. Over the range $40 < P_t^\gamma < 140$ GeV/$c$, the contribution of the gluon subprocess is about 70 to 90%, but it decreases with increasing $P_t^\gamma$ [1].

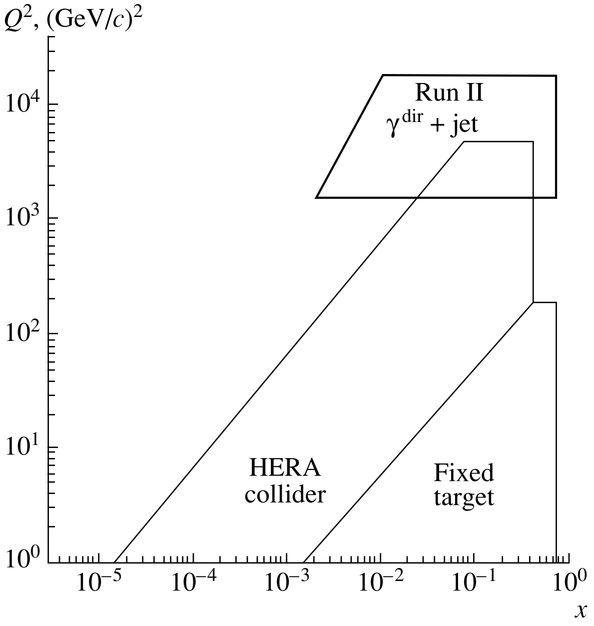

Kinematical region of the variables $x$ and $Q^2$ for the process $p\bar{p} \to \gamma^{\rm dir}$ + jet.

The $Q^2 \equiv (P_t^\gamma)^2$ and $x$ distributions of events associated with the gluon subprocess and selected by criteria 1–8 from Table 1[14] are presented in Table 4 for the Tevatron integrated luminosity of $L_{\rm int} = 3$ fb$^{-1}$. The $(x, Q^2)$ kinematical diagram in the figure shows the region that can be covered at the Tevatron in Run II. From the figure and from Table 4, it can be seen that experiments at the integrated luminosity of $L_{\rm int} = 3$ fb$^{-1}$ would make it possible to measure the gluon distribution with high statistics[15] of *photon* + *jet* events over a wide region of the variable $x$ that includes its small values. It is of particular importance that such measurements can be performed at $Q^2$ values an order of magnitude greater than those attained in experiments at the HERA collider.

## 4. CONCLUSION

It has been shown that separation of *photon* + *jet* events would make it possible to determine the gluon distribution in the proton over the range $2 \times 10^{-3} < x < 1.0$ for $1.6 \times 10^3 \le Q^2 \le 2 \times 10^4$ (GeV/$c$)$^2$ at a high statistical significance. At small $x$, the values of $Q^2$ in this range are greater than those achieved in all previous experiments.

It should be noted that, by extending to lower values of $Q^2$ the region experimentally accessible at the Tevatron with the aid of *photon* + *jet* events, one could enhance the overlap with the region studied at the HERA collider (see figure). This would make it possible to test theoretical predictions based on analytic solutions to the Dokshitzer–Gribov–Lipatov–Altarelli–Parisi equations [18].

---

[14] The application of criterion 9 from Table 1 results in only a 20% increase in the signal-to-background ratio [1].

[15] That is, commensurate with statistics in fixed-target experiments.

## ACKNOWLEDGMENTS

We are indebted to D. Denegri for inspiring our study of processes involving *photon + jet* final states. We are also grateful to G. Alexeev, P. Aurenche, M. Dittmar, M. Fontannaz, J.Ph. Guillet, M.L. Mangano, E. Pilon, H. Rohringer, S. Tapprogge, H. Weerts, and especially J. Womersley for support and enlightening comments.

## REFERENCES

1. D. V. Bandurin and N. B. Skachkov, hep-ex/0203003.
2. D. V. Bandurin, V. F. Konoplyanikov, and N. B. Skachkov, hep-ex/0207028.
3. T. Sjostrand, Comput. Phys. Commun. **82**, 74 (1994).
4. http://www-d0.fnal.gov/Run2Physics/qcd/.
5. D. V. Bandurin, V. F. Konoplyanikov, and N. B. Skachkov, Part. Nucl., Lett. **103**, 34 (2000); hep-ex/0011015.
6. D0 Collab. (B. Abbott *et al.*), Phys. Rev. Lett. **84**, 2786 (2000).
7. P. Aurenche *et al.*, in *Proceedings of the ECFA LHC Workshop, Aachen, Germany, 1990,* Ed. by G. Jarlskog and D. Rein, CERN Report No. 90-10 (Geneva, Switzerland, 1990), Vol. II.
8. P. Aurenche *et al.*, Phys. Rev. D **39**, 3275 (1989).
9. E. N. Argyres, A. P. Contogouris, N. Mebarki, and S. D. P. Vlassopulos, Phys. Rev. D **35**, 1584 (1987).
10. J. F. Owens, Rev. Mod. Phys. **59**, 465 (1987).
11. E. L. Berger and J. Qiu, Phys. Rev. D **44**, 2002 (1991).
12. S. Catani, M. Fontannaz, and E. Pilon, Phys. Rev. D **58**, 094025 (1998).
13. S. Frixione and W. Vogelsang, hep-ph/9908387.
14. E706 Collab. (L. Apanasevich *et al.*), Phys. Rev. Lett. **81**, 2642 (1998).
15. UA6 Collab. (G. Ballocchi *et al.*), Phys. Lett. B **436**, 222 (1998).
16. ISR–AFS Collab. (T. Akesson *et al.*), Z. Phys. C **34**, 293 (1987).
17. CDF Collab. (F. Abe *et al.*), Phys. Rev. D **57**, 1359 (1998).
18. A. V. Kotikov and G. Parente, Nucl. Phys. B **549**, 242 (1999).

*Translated by R. Rogalyov*

*Physics of Atomic Nuclei, Vol. 67, No. 4, 2004, pp. 693–702. From Yadernaya Fizika, Vol. 67, No. 4, 2004, pp. 715–724.*

# Study of Collective Flow Effects in CC Collisions at a Momentum of 4.2 GeV/*c* per Nucleon*

**L. V. Chkhaidze[1)]**, T. D. Djobava[1)], L. L. Kharkhelauri[1)], E. N. Kladnitskaya[2)], and A. A. Kuznetsov[2)]**

Received November 26, 2002; in final form, April 7, 2003

**Abstract**—Directed (in-plane) flows of protons, pions, and projectile light fragments ($d, t, {}^3$He, ${}^4$He) have been observed by investigating the dependence of the mean transverse momentum in the reaction plane $\langle p_x \rangle$ on the rapidity $y$ in the c.m. system for CC collisions at a momentum of 4.2 GeV/$c$ per nucleon. The comparison of our in-plane-flow results of protons with flow data for various projectile/target configurations was made using the scaled flow $F_s = F/(A_P^{1/3} + A_T^{1/3})$. $F_s$ demonstrates a common scaling behavior for flow values from different systems. From azimuthal distributions of protons and $\pi^-$ mesons, out-of-plane (squeeze-out) flow effects have been observed and the parameter $a_2$ (the measure of the anisotropic emission strength) has been extracted. The quark–gluon string model reproduces the experimental results quite well. © *2004 MAIK "Nauka/Interperiodica".*

## 1. INTRODUCTION

Multiparticle azimuthal correlations are being investigated very intensively with the goal to study the dynamics of relativistic nucleus collisions. The study of this effect in terms of the collective flow variables with respect to the reaction plane has turned out to be especially fruitful. The collective emission of particles occurs at the expansion stage of nuclear matter through the short-range repulsion between the nucleons at the expense of the compressional energy concentrated in the high-density and temperature overlap region of colliding nuclei. The collective effects lead to characteristic, azimuthally asymmetric sideward emission of the reaction products. The analysis of the main characteristics of the collective flow allows one to obtain information about the fundamental properties of nuclear matter, connected particularly to the equation of state (EOS) [1].

Two different signatures of the collective flow have been studied:

(a) the bounce-off of compressed matter in the reaction plane [a sideward deflection of the spectator fragments ("bounce-off") as well as directed flow of nucleons from the overlap region between the colliding nuclei (participants) in the reaction plane ("side-splash"), called sideward or directed flow];

(b) the squeeze-out of the participant matter out of the reaction plane—elliptic flow.

The method proposed by Danielewicz and Odyniec [2] has turned out to be the most convenient and fruitful for the investigation of collective flow phenomena, which allows one to determine the reaction plane by using the transverse momenta of participating protons. Lately, the method of Fourier expansion of azimuthal particle distributions has been widely used [3].

At present, the collective flow effects are being investigated in a wide range of energies from several hundred MeV up to hundreds of GeV. The majority of experiments are carried out using the electronic technique in $4\pi$ geometry, and only in the first experiments at Berkeley and lately at Dubna did the streamer chamber serve as the detector.

Collective flow of charged particles has been observed experimentally for the first time at BEVALAC by the Plastic Ball [4–6] and Streamer Chamber [7] collaborations. It has been studied intensively at Berkeley and GSI [8–13], at AGS [14–17], and at CERN/SPS [18–21]. At RHIC (Relativistic Heavy Ion Collider) of BNL, the STAR Collaboration recently reported the first results on the elliptic flow of charged particles at midrapidity in AuAu collisions at the energy $\sqrt{S_{NN}} = 130$ GeV [22].

At Dubna (JINR) in the 2-m Propane Bubble Chamber, the shape of the individual events of CTa

---

*This article was submitted by the authors in English.

[1)] High Energy Physics Institute, Tbilisi State University, Tbilisi, Georgia.

[2)] Joint Institute for Nuclear Research, Dubna, Moscow oblast, 141980 Russia.

**e-mail: `ida@sun20.hepi.edu.ge,ichkhaidze@yahoo.com`

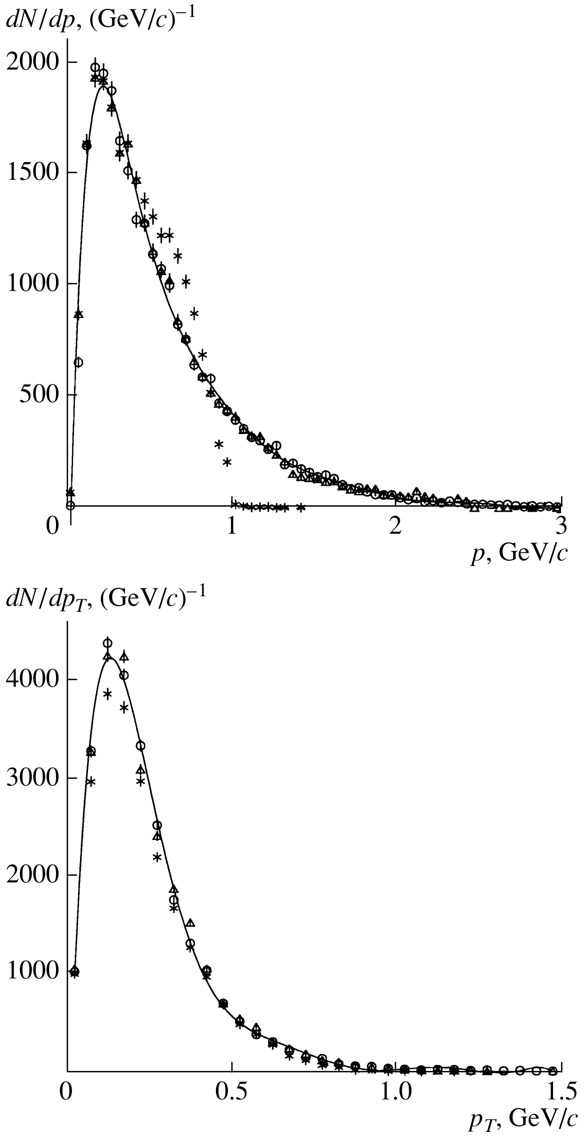

**Fig. 1.** The momentum and transverse-momentum distributions of $\pi^-$ and $\pi^+$ mesons in CC collisions. Points: ($\circ$) $\pi^-$ mesons; ($*$) $\pi^+$ mesons, identified by ionization; ($\triangle$) $\pi^+$ mesons, additional identification.

collisions at a momentum of 4.2 GeV/$c$ per nucleon has been studied in terms of the tensor of kinetic energy (sphericity) [23]. It has been shown that the angle between the axis of the ellipsoid and the beam direction $\theta_{\text{flow}}$ is 12° for high-multiplicity events.

Flows of protons and $\pi^-$ mesons have been observed at Dubna by the SKM-200-GIBS Collaboration [24, 25] in central CNe and CCu collisions at a momentum of 4.5 GeV/$c$ per nucleon. In inelastic CC collisions at a momentum of 4.2 GeV/$c$ per nucleon registered in the 2-m Propane Bubble Chamber, the flow of protons has been obtained only on part of the statistics [26]. The most complete experimental data of collective flow effects are presented in the review article [27].

## 2. EXPERIMENTAL DATA

In this paper the collective flows of protons, $\pi^-$ mesons, and projectile light fragments ($d$, $t$, $^3$He, $^4$He) in CC collisions at a momentum of 4.2 GeV/$c$ per nucleon, registered in the 2-m Propane Bubble Chamber of JINR, are studied.

The chamber was placed in a magnetic field of 1.5 T. The method of separation of CC collisions in propane, the processing of the data, identification of particles, and discussion of corrections are described in detail in [28]. The experimental data, apart from the unambiguously identified CC collisions with the probability of $\omega e = 1$, contains the sample of CC events with $\omega e = 0.21$. In the study of the inclusive characteristics of CC collisions, the distributions are obtained for the whole of C–propane collisions, taking into account the weight factor $\omega e$.

For the analysis of the collective flow of particles, the experimental data contained 15 692 unambiguously identified CC.

The study of collective flow phenomenon needs "event-by-event" analysis, which requires an exclusive analysis of each individual collision. In this connection, there has been a necessity to perform an additional identification of $\pi^+$ mesons, since in the propane chamber the $\pi^+$ mesons have been identified in a narrow interval of momenta (up to 0.5 GeV/$c$). The weight (probability) is defined statistically for particles with the momentum $p > 0.5$ GeV/$c$ with which the particle satisfies the hypothesis of $\pi^+$ meson or proton for the whole ensemble of CC collisions. However, the group of particles has remained with unseparated hypothesis ($p, \pi^+$), the most part of which form the protons. The separation of the group of CC collisions with $\omega e = 1$ and the necessity of unambiguous separation of protons and $\pi^+$ mesons have led to the difference in the momentum distributions of $\pi^-$ and $\pi^+$ mesons. To remove this difference, a correction of the $\pi^+$-meson identification has been carried out. The procedure has been performed statistically, based on the well-founded assumption that, for symmetric nuclear collisions, the distributions of $\pi^-$ and $\pi^+$ mesons are similar.

In Fig. 1, the momentum and transverse momentum distributions of $\pi^-$ and $\pi^+$ mesons are presented with the previous and additional identifications. One can see from Fig. 1 that a small difference in the momentum distribution of $\pi^+$ mesons is removed.

Only participant protons have been selected for the analysis. With this purpose, from the whole ensemble of particles, the fragments of the target

($p < 0.3$ GeV/$c$), projectile stripping fragments ($p >$ 3 GeV/$c$ and angle $\theta < 4°$), and also the light fragments of the projectile with $Z > 1$ ($^3$He, $^4$He) identified by ionization visually and $Z = 1$ ($d$, $t$) with $p > 5$ GeV/$c$ have been excluded.

The following restriction, the choice of events with the number of participant protons $N_{\text{part}} \geq 4$, is caused by the necessity to obtain reliable results at low multiplicity. In consequence, from the inelastic CC collisions, a group of 9490 semicentral collisions with 58 078 participant protons have been selected.

## 3. TRANSVERSE-FLOW ANALYSIS METHOD

The method of Danielewicz and Odyniec [2] has been used for study of collective flow of protons, based on the summation of the transverse momenta of selected particles [2]. Most experimental data at energies below 4 GeV/nucleon have been analyzed by this method. It gives satisfactory results even for small available statistics obtained by the film detectors.

The reaction plane vector $\mathbf{Q}$ in each individual event is defined only by the participant protons in the c.m. system:

$$\mathbf{Q} = \sum_{i=1}^{n} \omega_i \mathbf{p}_{Ti}, \tag{1}$$

where $p_{Ti}$ is the transverse momentum of particle $i$; the weight factor $\omega_i$ is taken as 1 for $y_i > 0$ and $-1$ for $y_i < 0$, where $y_i$ is the rapidity of particle $i$; and $n$ is the number of participant protons in the event. This choice leads to the result that the forward and backward moving particles, which are azimuthally anticorrelated if there is a collective transverse flow, will contribute equally to $\mathbf{Q}$.

The reaction plane is the plane containing the impact parameter $\mathbf{b}$ and beam axis. Taking into account that the definition of $\mathbf{b}$ experimentally is not possible, in the transverse momentum analysis method of Danielewicz and Odyniec [2], the vector $\mathbf{b}$ is replaced by $\mathbf{Q}$. If one projects the transverse momentum of each particle $p_{Ti}$ onto the total momentum, autocorrelations will arise, from which it will be very difficult to extract true dynamic correlations. To remove the autocorrelations, Danielewicz and Odyniec [2] proposed to estimate the reaction plane for each particle $j$, i.e., to project $p_{Ti}$ onto the total vector of all other particles in the same event:

$$\mathbf{Q}_j = \sum_{i \neq j}^{n} \omega_i \mathbf{p}_{Ti}. \tag{2}$$

The transverse momentum of each particle in the estimated reaction plane is calculated as

$$p'_{xj} = \{\mathbf{Q}_j \cdot \mathbf{p}_{Tj} / |\mathbf{Q}_j|\}. \tag{3}$$

The dependence of the mean transverse momentum of each particle in the reaction plane $\langle p_x \rangle$ on the rapidity $y$ is constructed. The average transverse momentum $\langle p'_x(y) \rangle$ is obtained by averaging over all events in the corresponding intervals of rapidity.

It is known [4] that the estimated reaction plane differs from the true one, due to the finite number of particles in each event. The component $p_x$ in the true reaction plane is systematically larger than the component $p'_x$ in the estimated plane; hence,

$$\langle p_x \rangle = \langle p'_x \rangle / \langle \cos \phi \rangle, \tag{4}$$

where $\phi$ is the angle between the estimated and true planes. The correction factor $k = 1/\langle \cos \phi \rangle$ is subject to a large uncertainty, especially for low multiplicity. In [2], the method for the definition of the correction factor has been proposed. Each event is randomly divided into two almost equal subevents, the vectors $\mathbf{Q}_1$ and $\mathbf{Q}_2$ are constructed, and then the distribution of the azimuthal angle between these two vectors is plotted. The dispersion of this angular distribution determines the discrepancy between the true and estimated reaction planes. The coefficient $k$ depends on the multiplicity in the event, and naturally the correction is larger at low multiplicity. It is desirable to group the events by the multiplicity intervals. Due to the limited statistics, the coefficient in this paper has been defined for the whole ensemble, averaged over all the multiplicities: $k = 1.43 \pm 0.8$.

Figure 2 shows the dependence of the corrected $\langle p_x(y) \rangle$ on $y$ for protons in CC collisions at a momentum of 4.2 GeV/$c$ per nucleon. The data exhibits $S$-shape behavior which demonstrates the collective-transverse-momentum transfer between the backward and forward hemispheres.

From the mean-transverse-momentum distributions, one can extract two main observables sensitive to the EOS. One of them is the mean transverse momentum in the reaction plane in the forward rapidity region $\langle p_x \rangle_{y>0}$. Another equivalent observable is the transverse flow $F$ determined by slope of the momentum distribution at midrapidity (at the intersection point $y = 0$), which was introduced by the Plastic-Ball team [5]:

$$F = \left. \frac{\partial \, [p_x]}{\partial y} \right|_{y_{\text{c.m.}}=0}. \tag{5}$$

$F$ is a measure of the amount of collective transverse momentum transfer in the reaction plane, i.e., intensity of nuclear interactions.

This quantity was the subject of less experimental bias than the maximum of $p_x$, and it enabled one to compare different reactions and results of different experimental setups to each other. The straight line in Fig. 2 is the result of the fit of experimental data

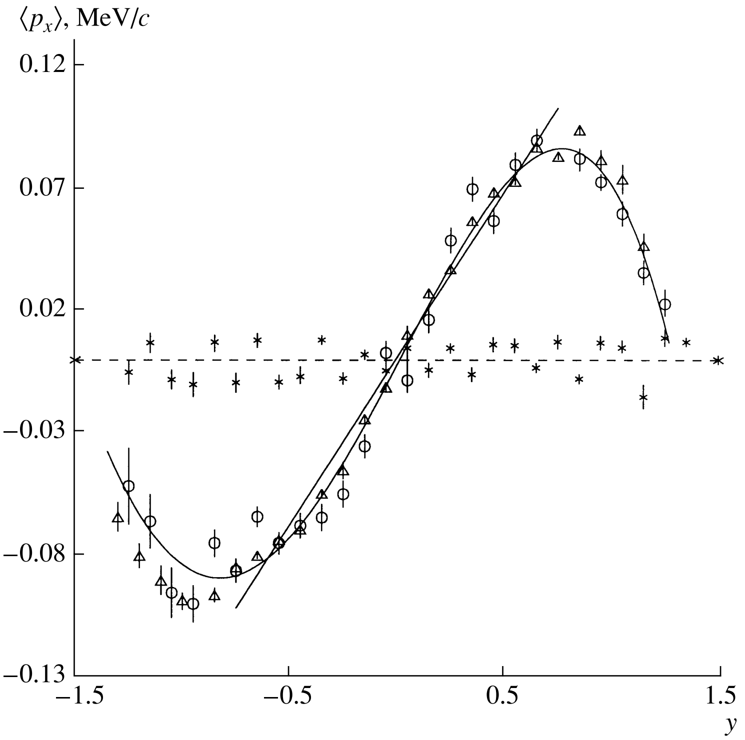

**Fig. 2.** The dependence of $\langle p_x(y) \rangle$ on $y$ for protons in CC collisions in the c.m. system. Points: (○) the experimental data, (△) QGSM generated data for fixed $b = 2.65$ fm, (∗) events composed by randomly selected tracks from different events (within the same multiplicity range). The solid line is the result of the linear approximation of experimental data in the interval of $y$ from −0.75 to 0.75. The solid curve for visual presentation of experimental events is the result of approximation by a fourth-order polynomial.

in the rapidity-$y$ interval (from −0.75 to 0.75). The protons flow $F = 136 \pm 11$ MeV/$c$. The value of $F$ is very similar to the result obtained at the SKM-200-GIBS setup at JINR in central CNe collisions at a momentum of 4.5 GeV/$c$ per nucleon [24, 25]: $F = 134 \pm 12$ MeV/$c$. The $\langle p_x \rangle$ distribution for CC collisions is more symmetric than for CNe interactions (see Fig. 1 from [24] and Fig. 1$a$ from [25]). It is worth emphasizing that CC is the lightest system of colliding nuclei in which the transverse (directed) flow of protons has been observed.

To be convinced that the observed effect is due to the manifestation of the dynamics of collisions, the following checkup has been carried out. The events have been composed by mixing randomly selected tracks from different events (within the same multiplicity range) and then the flow has been defined for these "mixed" events. One can see from Fig. 2 that, in these events, there is no correlation with the reaction plane and particles are emitted isotropically in the "mixed" events.

The mean transverse momentum in the reaction plane in the forward rapidity region $\langle p_x \rangle_{y>0}$ has been calculated for protons and the value of $\langle p_x \rangle_{y>0} = 104 \pm 9$ MeV/$c$ has been obtained. In CC collisions, selected for the flow analysis, 4464 identified light fragments with $Z > 1$ ($^3$He, $^4$He) and 4857 single-charged particles with the momentum $p > 5$ GeV/$c$ have been detected, which are deuterons and tritons with a large probability. As follows from our estimates, the fraction of $^3$He/$^4$He and also $t/d$ is the same and equals 1/4. Averaged over light fragments, the value of $\langle p_x \rangle_{y>0}$ has been obtained: $\langle p_x \rangle_{y>0} = 140 \pm 20$ MeV/$c$. Thus, the value of $\langle p_x \rangle_{y>0}$ for light fragments is 20–30% larger than for participant protons.

The experimental data of different particle flows formed in heavy-ion collisions contain the whole interval of available energies and a large set of colliding nuclei $A_P$ and $A_T$ (ArKCl, CaCa, NbNb, CNe, CCu, NiCu, CPb, ArBaI$_2$, ArPb, AuAu, PbPb, etc.). For the investigation of energy dependence of flow values for different projectile/target mass combinations, the scaled variable $F_s$ has been introduced [29], which does not depend on the mass numbers of colliding nuclei,

$$F_s = F/(A_P^{1/3} + A_T^{1/3}). \qquad (6)$$

In Fig. 3, the energy dependence of scaled flow $F_s$ of protons from different experiments is presented.

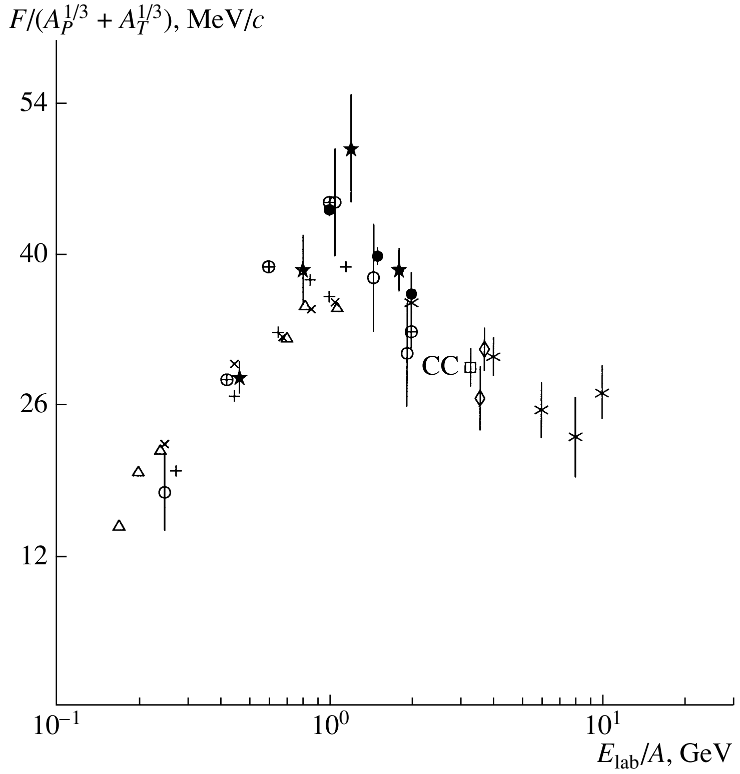

**Fig. 3.** Scaled flow values vs. beam energy per nucleon for different projectile/target systems. Points: (□) CC (this work); (×) NbNb (Plastic Ball); (△) AuAu (Plastic Ball) [30]; (○) NiNi (FOPI) [9]; (●) NiCu (EOS); (+) AuAu (EOS); (⊕) NiAu (EOS) [13, 31]; (⋆) ArPb (Streamer Chamber); the value at $E = 1.08\ A$ GeV represents the ArKCl Streamer Chamber [32, 33]; (◇) CNe, CCu [25]; (∗) AuAu (E-895) [16]; the value at $E = 10\ A$ GeV represents AuAu from E-877 [15]. To improve the distinction between data points at the same beam energy, some of the beam energy values have been shifted.

Figure 3 represents our result and the data from the EOS [13, 31], E-895 [16], E-877 [15], FOPI [9], and SKM-200-GIBS [25] experiments, along with the values derived from the Plastic Ball [30] and the Streamer Chamber experiments [32, 33] for a variety of energies and mass combinations. The point $F_s = 29.7 \pm 2.4$ MeV/$c$ is obtained in this work. One can see that the scaled flow $F_s$ follows, within the uncertainties, a common trend with an initial step rise and then a gradual decrease.

In view of the strong coupling between the nucleon and pion, it is interesting to know whether pions also have a collective flow behavior and how the pion flow is related to the nucleon flow.

For this purpose, the reaction plane has been defined for the participant protons and the transverse momentum of each $\pi^-$ meson has been projected onto this reaction plane. Figure 4 shows the dependence of $\langle p_x \rangle$ on rapidity $y$ in the c.m. system for $\pi^-$ mesons in CC collisions. This dependence has the same behavior as for the protons. The value of flow $F$ for $\pi^-$ mesons is $F = 22.2 \pm 6.1$ MeV/$c$. The straight line in Fig. 4 shows the result of the fitting. The fit was done in the interval of $y$ from $-0.6$ to 0.6. This result is very close to the $F$ of pions obtained at SKM-200-GIBS in CNe collisions at 4.5 GeV/$c$ per nucleon (see Fig. 1$a$ from [25]): $F = 29 \pm 5$ MeV/$c$.

The dependence of flow of pions $F$ on the transverse momentum has been investigated. In Table 1, the flows of pions in the whole interval of $p_T$, $0 < p_T \leq 1.0$ GeV/$c$, and in intervals of $0.1 < p_T \leq 1.0$ GeV/$c$, $0.15 < p_T \leq 1.0$ GeV/$c$, and $0.2 < p_T \leq 1.0$ GeV/$c$ are presented. The flow increases with $p_T$ from 22.2 up to 43.7 MeV/$c$. The flow of $\pi^-$ mesons in CC collisions has been observed for the first time. For CC collisions, flows of protons and pions are correlated similarly as in CNe interactions [24, 25].

Several theoretical models of nucleus–nucleus collisions at high energy have been proposed for the description of the collective flow effects. The relativistic transport model (ART 1.0) [34] and the quark–gluon string model (QGSM) are widely used. A detailed description and comparison of the QGSM with collective flow effects observed in different experiments over a wide energy range can be found in [35, 36]. It is worth mentioning that the QGSM satisfactorily describes the spectra of secondary protons and $\pi^-$ mesons in CC [37] and MgMg [38] collisions

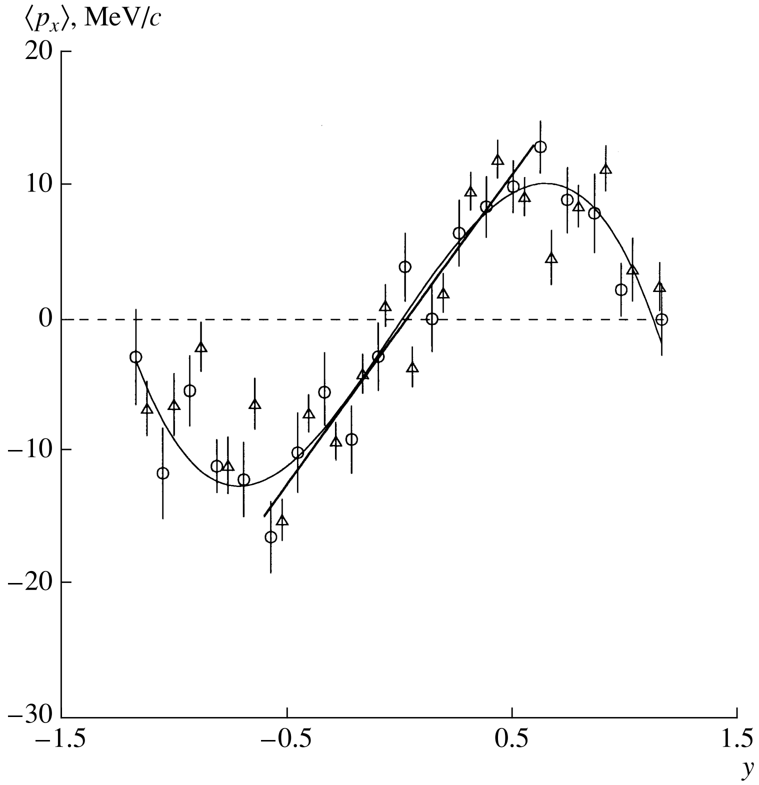

**Fig. 4.** The dependence of $\langle p_x(y)\rangle$ on $y$ for $\pi^-$ mesons in CC collisions in the c.m. system. Points: (○) the experimental data, (△) QGSM-generated data for fixed $b = 2.65$ fm. The solid line is the result of the linear approximation of experimental data in the interval of $y$ from −0.6 to 0.6. The solid curve for visual presentation of experimental events is the result of approximation by a fourth-order polynomial.

at momenta of 4.2 and 4.5 GeV/$c$ per nucleon, respectively. The model also reproduces well the flow of protons and $\pi^-$ mesons in CNe and CCu collisions at $p = 4.5$ GeV/$c$ per nucleon [24, 25]. In the present paper, the QGSM was used for a comparison with experimental data. We generated CC inelastic collisions using the COLLI Monte Carlo generator [39]. At the first step, the version of the generation program with unfixed impact parameter $b$ was used; 50 000 inelastic CC collisions at a momentum of 4.2 GeV/$c$ were generated. From the $b$ distribution, we obtained the mean value $\langle b\rangle = 3.8$ fm. Then, similarly as for the experimental data, the selection criteria of participant protons were applied to these events; namely, the fragments of the target ($p < 0.3$ GeV/$c$) and stripping fragments of the projectile ($p > 3$ GeV/$c$ and angle $\theta < 4°$) were excluded. From the analysis of generated events, the protons with deep angles greater than 60° were additionally excluded, because such vertical tracks were recorded with less efficiency in the experiment. After selection of events with the number of participant protons not less than 4, for the analysis of the flow of protons, the group of semicentral collisions with $\langle b\rangle = 2.65$ fm survived.

At the second step, 50 000 semicentral CC collisions were generated at a fixed impact parameter $\langle b\rangle = 2.65$ fm with superimposition of the above-mentioned criteria during the generation of the collisions. The dependence $\langle p_x(y)\rangle$ on $y$ for protons in CC collisions generated for fixed and unfixed impact parameters coincides within the errors.

In Fig. 2, the result of the analysis of the group of generated events with $\langle b\rangle = 2.65$ fm is presented, as well as experimental data. One can see that the model describes quite well the experimental data of protons in the central region and $F_{\text{mod}} = 145 \pm 9$ MeV/$c$ (196 942 participant protons). From the QGSM, the value of mean transverse momentum of protons in the reaction plane in the forward rapidity region $\langle p_x\rangle_{y>0}$ has been obtained: $\langle p_x\rangle_{y>0} = 114 \pm 7$ MeV/$c$.

The QGSM has also been used for comparison with the pion flow in CC collisions. One can see from Fig. 4 that the QGSM yields a flow signature similar to the experimental data. The value of $F$, obtained from the QGSM, is $F_{\text{mod}} = 23.2 \pm 3.0$ MeV/$c$.

**Table 1.** The number of $\pi^-$ mesons $N_{\pi^-}$ and the values of the parameters $F$, $a_2$, $\chi^2/N$, and $R$ for experimental (upper value) and QGSM (lower value) events

| $p_T$, GeV/$c$ | $N_{\pi^-}$ | $F$, MeV/$c$ | $a_2$ | $\chi^2/N$ | $R$ |
|---|---|---|---|---|---|
| $0 < p_T \leq 1.0$ | 20 310 | $22.2 \pm 6.1$ | $-0.037 \pm 0.011$ | 20/24 | $1.077 \pm 0.106$ |
| | 71 014 | $23.2 \pm 3.0$ | $-0.034 \pm 0.006$ | 22/24 | $1.070 \pm 0.063$ |
| $0.1 < p_T \leq 1.0$ | 16 898 | $27.0 \pm 7.1$ | $-0.051 \pm 0.012$ | 21/24 | $1.107 \pm 0.086$ |
| | 58 963 | $29.1 \pm 3.5$ | $-0.042 \pm 0.006$ | 20/24 | $1.088 \pm 0.052$ |
| $0.15 < p_T \leq 1.0$ | 13 415 | $33.5 \pm 8.6$ | $-0.067 \pm 0.013$ | 14/24 | $1.144 \pm 0.074$ |
| | 47 410 | $34.4 \pm 4.1$ | $-0.052 \pm 0.007$ | 26/24 | $1.110 \pm 0.050$ |
| $0.2 < p_T \leq 1.0$ | 10 208 | $43.7 \pm 10.2$ | $-0.083 \pm 0.015$ | 12/24 | $1.181 \pm 0.071$ |
| | 36 218 | $45.0 \pm 5.1$ | $-0.062 \pm 0.008$ | 27/24 | $1.132 \pm 0.050$ |

**Table 2.** The number of participant protons $N_{\text{part}}$ and the values of the parameters $a_2$, $\chi^2/N$, and $R$ for experimental (upper value) and QGSM (lower value) events

| $p_T$, GeV/$c$ | $N_{\text{part}}$ | $a_2$ | $\chi^2/N$ | $R$ |
|---|---|---|---|---|
| All $p_T$ | 55 752 | $-0.044 \pm 0.006$ | 28/30 | $1.092 \pm 0.050$ |
| | 189 676 | $-0.046 \pm 0.003$ | 37/30 | $1.096 \pm 0.025$ |
| $0.1 < p_T < 1.5$ | 53 197 | $-0.059 \pm 0.007$ | 35/30 | $1.125 \pm 0.045$ |
| | 180 416 | $-0.068 \pm 0.003$ | 34/30 | $1.146 \pm 0.013$ |
| $0.2 < p_T < 1.5$ | 48 442 | $-0.067 \pm 0.007$ | 33/30 | $1.144 \pm 0.040$ |
| | 169 667 | $-0.072 \pm 0.003$ | 36/30 | $1.155 \pm 0.016$ |
| $0.3 < p_T < 1.5$ | 40 057 | $-0.079 \pm 0.007$ | 32/30 | $1.171 \pm 0.034$ |
| | 151 257 | $-0.079 \pm 0.004$ | 35/30 | $1.171 \pm 0.020$ |

## 4. AZIMUTHAL ANISOTROPIC EMISSION OF PROTONS AND PIONS

The preferential emission of particles in the direction perpendicular to the reaction plane (i.e., "squeeze-out") is particularly interesting since it is the only way that nuclear matter might escape without being rescattered by spectator remnants of the projectile and target and is expected to provide direct information on the hot and dense participant region formed in high-energy nucleus—nucleus interactions. This phenomenon, predicted by hydrodynamical calculations [2], was clearly identified by the Plastic Ball Collaboration.

In order to extend these investigations, we have studied the azimuthal $\varphi$ ($\cos\varphi = p_x/p_T$) distributions of the pions and protons with respect to the reaction plane. The angle $\varphi$ is the angle of the transverse momentum of each particle in the event with respect to the reaction plane. The analysis was restricted only to the midrapidity region by applying a cut around the c.m. rapidity. Figure 5 shows the respective distribution for protons in CC collisions obtained in central rapidity region $|y| \leq 1$. The azimuthal angular distribution shows maxima at $\varphi = 90°$ and $270°$ with respect to the event plane. These maxima are associated with preferential particle emission perpendicular to the reaction plane (squeeze-out, or elliptic flow). Thus, a clear signature of an out-of-plane signal (elliptic flow) is evidenced.

To treat the data in a quantitative way, the azimuthal distributions have been fitted by a polynomial:

$$dN/d\varphi = a_0(1 + a_1\cos\varphi + a_2\cos 2\varphi). \qquad (7)$$

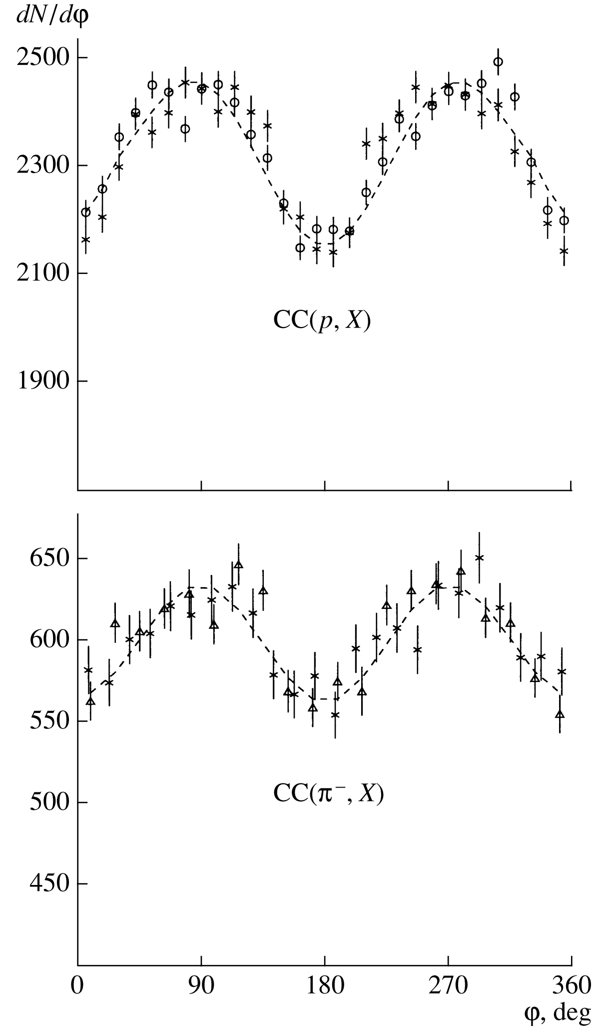

**Fig. 5.** The azimuthal distributions with respect to the reaction plane of $dN/d\varphi$ for protons and $\pi^-$ mesons. Points: (○) protons, (△) $\pi^-$ mesons, and (×) QGSM-generated data, respectively. The curves are the result of the approximation by $dN/d\varphi = a_0(1 + a_1\cos\varphi + a_2\cos 2\varphi)$.

The anisotropy factor $a_2$ is negative for out-of-plane enhancement (squeeze-out) and is the measure of the strength of the anisotropic emission. The value of the coefficient $a_2$ extracted from the azimuthal distribution of protons is $a_2 = -0.044 \pm 0.006$ (Table 2) and of pions is $a_2 = -0.037 \pm 0.011$ (Table 1). The dashed curves (Fig. 5) are the result of the fitting by (7) of the experimental distributions. The QGSM has been used for comparison with the experimental results. The QGSM data for protons and pions at fixed impact parameter $b = 2.65$ fm are also plotted in Fig. 5 and the corresponding values of $a_2$ extracted from the QGSM data are listed in Tables 1 and 2. One can see that the model describes the experimental azimuthal distributions.

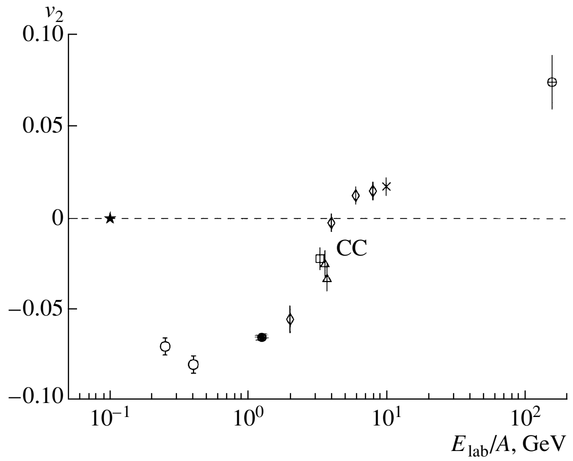

**Fig. 6.** The dependence of the elliptic flow excitation function $\nu_2$ on energy $E_{lab}/A$ obtained for protons: (□) in CC (this work), (⋆) FOPI [41], (○) MINIBALL, (●) EOS [13], (◇) E-895 [16], (∗) E-877 [15], and (⊕) NA49 [21], together with results for CNe, CCu [25] (△).

The values of $a_2$ are used to quantify the ratio $R$ of the number of particles emitted in the perpendicular direction to the number of particles emitted in the reaction plane, which represents the magnitude of the out-of-plane emission signal:

$$R = \frac{1 - a_2}{1 + a_2}. \tag{8}$$

A ratio $R$ larger than unity implies a preferred out-of-plane emission. The values of $R$ for protons and pions are listed in Tables 1 and 2. The dependence of the azimuthal anisotropy on the transverse momentum has been investigated. One can see that $a_2$ and $R$ increase for both protons and $\pi^-$ mesons with increasing cutting limit applied to the transverse momentum. Our results on the transverse momentum dependence of the azimuthal anisotropy in CC semicentral collisions are consistent with the results of SKM-200-GIBS for CNe and CCu central collisions (see Fig. 3 from [25]).

In experiments E-895 [40], E-877 [15] at AGS, and NA49 [21] at SPS (CERN), the elliptic flow is typically studied at midrapidity and quantified in terms of the second Fourier coefficient $v_2 = \langle\cos 2\varphi\rangle$. The Fourier coefficient $v_2$ is related to $a_2$ via the equation $v_2 = a_2/2$. In Fig. 6 are presented the values of $v_2$ obtained for protons in CC (this work) and in the FOPY [41], MINIBALL, EOS [13], E-895 [16], E-877 [15], and NA49 [21] collaborations together with results for CNe, CCu [25].

## 5. CONCLUSIONS

The flow effects of protons, $\pi^-$ mesons, and projectile light fragments ($d$, $t$, $^3$He, $^4$He) have been investigated in semicentral CC collisions at a momentum of 4.2 GeV/$c$ per nucleon. The transverse-momentum technique of Danielewicz and Odyniec [2] was used for data analysis. Clear evidence of directed (in-plane) and elliptic (out-of-plane, squeeze-out) flow effects for protons and $\pi^-$ mesons has been obtained.

(i) From the transverse-momentum distributions of protons and $\pi^-$ mesons with respect to the reaction plane, the flow $F$ (the measure of the collective transverse-momentum transfer in the reaction plane) has been extracted. For participant protons, the value of $F$ has been obtained: $F = 136 \pm 11$ MeV/$c$. The mean transverse momentum of protons in the reaction plane in the forward rapidity region $y > 0$ $\langle p_x \rangle_{y>0}$ has been estimated: $\langle p_x \rangle_{y>0} = 104 \pm 9$ MeV/$c$.

(ii) The comparison of our results on the proton directed (in-plane) flow with flow data for various projectile/target combinations was made using the scaled flow $F_s = F/(A_P^{1/3} + A_T^{1/3})$. $F_s$ demonstrates a common scaling behavior for flow values from different systems.

(iii) The value of $\pi^-$-meson flow $F$ is equal to $22.2 \pm 6.1$ MeV/$c$ and increases up to $43.7 \pm 10.2$ MeV/$c$ with a rise of the cut applied to transverse momentum of pions from 0 to 0.2 GeV/$c$. The flow of $\pi^-$ mesons is obtained for the first time for such a light system as CC. In-plane flow of $\pi^-$ mesons is in the same direction as for the protons.

(iv) The mean transverse momentum in the reaction plane in the forward rapidity region $y > 0$ $\langle p_x \rangle_{y>0}$ has been estimated for projectile light fragments ($d$, $t$, $^3$He, $^4$He), assuming that the fraction of $^3$He and $^4$He, and $d$ and $t$ is the same: $\langle p_x \rangle_{y>0} = 140 \pm 20$ MeV/$c$.

(v) From the azimuthal distributions of protons and $\pi^-$ mesons with respect to the reaction plane, the parameter $a_2$ (the measure of the anisotropic emission strength) has been extracted. The value of the azimuthal anisotropy coefficient of protons is $a_2 = -0.044 \pm 0.006$ and of pions is $a_2 = -0.037 \pm 0.011$. The anisotropy of $\pi^-$ mesons increases with the rise of the cut applied to the transverse momentum. The parameter $a_2$ was defined for a light CC system also for the first time.

(vi) All experimental results have been compared with the predictions of the quark–gluon string model. The model reproduces experimental data quite well.

## ACKNOWLEDGMENTS

We express our deep gratitude to V.V. Uzhinskii for interesting and valuable discussions concerning the collective flow effects and to N. Amaglobeli for his continuous support. We are very grateful to N. Amelin for providing us with the QGSM code program COLLI. One of us (L.Ch.) would like to thank the Board of Directors of the Laboratory of High Energies of JINR for the warm hospitality and also J. Lukstins and O. Rogachevsky for assistance during the preparation of the manuscript.

## REFERENCES

1. H. Stöcker *et al.*, Phys. Rev. Lett. **44**, 725 (1980); Phys. Rev. C **25**, 1873 (1982).
2. P. Danielewicz and G. Odyniec, Phys. Lett. B **157B**, 146 (1985).
3. S. Voloshin and Y. Zhang, Z. Phys. C **70**, 665 (1996).
4. H. Gustafsson *et al.*, Phys. Rev. Lett. **52**, 1590 (1984).
5. K. Doss *et al.*, Phys. Rev. Lett. **57**, 302 (1986).
6. H. Gutbrod *et al.*, Phys. Lett. B **216**, 267 (1989); Phys. Rev. C **42**, 640 (1990).
7. R. Renfordt *et al.*, Phys. Rev. Lett. **53**, 763 (1984).
8. V. Ramillien *et al.*, Nucl. Phys. A **587**, 802 (1995).
9. N. Herrmann *et al.*, Nucl. Phys. A **610**, 49 (1996).
10. Y. Leifels *et al.*, Phys. Rev. Lett. **71**, 963 (1993).
11. A. Kugler *et al.*, Phys. Lett. B **335**, 319 (1994).
12. D. Brill *et al.*, Z. Phys. A **357**, 207 (1997).
13. J. Chance *et al.*, Phys. Rev. Lett. **78**, 2535 (1997); M. D. Partlan *et al.*, Phys. Rev. Lett. **75**, 2100 (1995).
14. J. Barrette *et al.*, Phys. Rev. Lett. **73**, 2532 (1994).
15. J. Barrette *et al.*, Phys. Rev. C **56**, 3254 (1997); **55**, 1420 (1997).
16. H. Liu *et al.*, Nucl. Phys. A **638**, 451 (1998); Phys. Rev. Lett. **84**, 5488 (2000).
17. C. Ogilvie *et al.*, Nucl. Phys. A **638**, 57 (1998).
18. A. Keitz *et al.*, Phys. Lett. B **263**, 353 (1991).
19. S. Nishimura *et al.*, Nucl. Phys. A **638**, 549 (1998).
20. M. Aggarwal *et al.*, nucl-ex/9807004.
21. NA49 Collab. (H. Appelshauser *et al.*), Phys. Rev. Lett. **80**, 4136 (1998).
22. K. Ackermann *et al.*, Phys. Rev. Lett. **86**, 402 (2001).
23. A. Cheplakov *et al.*, JINR Rapid Commun., No. 2 [70]-95, 35 (1995).
24. L. Chkhaidze *et al.*, Phys. Lett. B **411**, 26 (1997).
25. L. Chkhaidze *et al.*, Phys. Lett. B **479**, 21 (2000).
26. Lj. Simic and J. Milose, J. Phys. G **27**, 183 (2001).
27. L. Chkhaidze, T. Djobava, and L. Kharkhelauri, Phys. Part. Nucl. **33**, 196 (2002).
28. A. Bondarenko *et al.*, Preprint No. P1-98-292, OIYaI (Joint Institute for Nuclear Research, Dubna, 1998).
29. A. Lang *et al.*, Z. Phys. A **340**, 287 (1991).
30. H. Gutbrod, A. Poskanzer, and H. Ritter, Rep. Prog. Phys. **52**, 1267 (1989).
31. N. Ajitanand *et al.*, Nucl. Phys. A **638**, 451 (1998); P. Danielewicz, nucl-th/9907098.
32. J. Harris *et al.*, Nucl. Phys. A **471**, 241 (1987).

33. D. Beavis *et al.*, Phys. Rev. C **45**, 299 (1992); **33**, 1113 (1986).
34. Bao-An Lee and Che Ming Ko, Phys. Rev. C **52**, 2037 (1995).
35. N. S. Amelin *et al.*, Yad. Fiz. **51**, 512 (1990) [Sov. J. Nucl. Phys. **51**, 327 (1990)]; Yad. Fiz. **52**, 272 (1990) [Sov. J. Nucl. Phys. **51**, 133 (1990)].
36. N. S. Amelin *et al.*, Phys. Rev. Lett. **67**, 1523 (1991).
37. R. N. Bekmirzaev *et al.*, Yad. Fiz. **58**, 63, 1642, 1822 (1995) [Phys. At. Nucl. **58**, 58, 1548, 1721 (1995)].
38. L. Chkhaidze *et al.*, Eur. Phys. J. A **1**, 299 (1998).
39. N. S. Amelin *et al.*, Preprint No. P2-86-837, OIYaI (Joint Institute for Nuclear Research, Dubna, 1986).
40. C. Pinkenburg *et al.*, Phys. Rev. Lett. **83**, 1295 (1999).
41. D. Pelte *et al.*, Nucl. Phys. A **622**, 573 (1997).

Physics of Atomic Nuclei, Vol. 67, No. 4, 2004, pp. 703–707. Translated from Yadernaya Fizika, Vol. 67, No. 4, 2004, pp. 725–729.

## ELEMENTARY PARTICLES AND FIELDS
## Experiment

# Properties of Proton Clusters in Inelastic CC Interactions Accompanied by the Production of $\Lambda$ and $K^0$ Particles at $p = 4.2$ GeV/$c$ per Nucleon

**R. N. Bekmirzaev**[1)*], **A. A. Kuznetsov**[**], **E. Kh. Shukurov**[1)], **and B. S. Yuldashev**[2)]

*Joint Institute for Nuclear Research, Dubna, Moscow oblast, 141980 Russia*

Received December 17, 2002; in final form, June 3, 2003

**Abstract**—Within a new relativistically invariant approach, the properties of proton clusters that are formed together with $\Lambda$ and $K^0$ particles in inelastic CC interactions at $p = 4.2$ GeV/$c$ per nucleon are investigated in the space of relative 4-velocities. The observed proton clusters are shown to be characterized by high values of the mean kinetic energy of the protons in the cluster rest frame: $\langle T_p\rangle = 100 \pm 2$ MeV. *© 2004 MAIK "Nauka/Interperiodica".*

## INTRODUCTION

In the inclusive approach, which is traditionally applied in describing multiparticle-production processes, use is made of only a small part of information about such processes.

In the present study, we apply the method proposed in [1–5], which, in contrast to the inclusive approach, enables us to incorporate the entire body of information accessible in experiments in the description of multiparticle-production processes. The new method also makes it possible to systematize complicated pictures of relativistic nuclear interactions.

The present article reports on a continuation of the series of studies initiated in [1–5] and devoted to investigating the properties of baryon clusters in various hadron–nucleus and nucleus–nucleus interactions over a wide energy range by using the dimensionless relativistically invariant quantities

$$b_{ik} = -\left(\frac{p_i}{m_i} - \frac{p_k}{m_k}\right)^2 = -(u_i - u_k)^2, \qquad (1)$$

where $p_i$ and $p_k$ are the 4-momenta of the particles under consideration, while $m_i$ and $m_k$ are their masses.

Here, we study the formation and the properties of proton clusters in inelastic CC interactions involving the production of $\Lambda$ and $K^0$ particles (CC $^{\Lambda/K}$).

## 1. EXPERIMENTAL PROCEDURE

The experimental data used were obtained with the aid of a 2-m propane bubble chamber irradiated with a beam of protons and nuclei from the synchrophasotron of the Laboratory of High Energies at the Joint Institute for Nuclear Research (JINR, Dubna). Here, we would like to highlight the following methodological features of the experiment. The lower detection threshold for protons in the chamber was $p_{\rm lab} \approx 150$ MeV/$c$. Protons could be distinguished from $\pi^+$ mesons by the range and specific ionization down to momentum values of $p_{\rm lab} \approx 800$ MeV/$c$. The admixture of $\pi^+$ mesons among positive particles did not exceed 10 to 15%. According to various estimates, the admixture of deuterons and tritons among slow protons of momentum in the region $p_{\rm lab} < 800$ MeV/$c$ did not exceed 10 to 15% either [6, 7]. A detailed account of the procedure used in processing events featuring $V^0$ particles was given in [8].

A Lorentz-invariant method in 4-velocity space was employed to single out proton clusters among all inelastic $A$C interactions. Specifically, we minimized, in events where the proton multiplicity satisfied the condition $n_p \geq 4$, the quantities

$$A_2 = \min\left[\sum (V_\alpha - u_i^\alpha)^2 - \sum (V_\beta - u_i^\beta)^2\right], \quad (2)$$

where $V_\alpha$ and $V_\beta$ are the centers of the $\alpha$ and $\beta$ clusters [they are defined as the unit 4-vectors $V_{\alpha(\beta)} = \sum u_i / \sqrt{(\sum u_i)^2}$ derived from the condition requiring that the quantity $\sum b_i = -\sum (V_{\alpha(\beta)} - u_i)^2$ be minimal] and

$$u_i^\alpha = p_i^\alpha / m_i, \quad u_i^\beta = p_i^\beta / m_i \qquad (3)$$

---

[1)] Dzhizak State Pedagogical University, Uzbekistan.

[2)] Institute of Nuclear Physics, Uzbek Academy of Sciences, pos. Ulughbek, Tashkent, 702132 Uzbekistan.

[*] e-mail: `bekmirzaev@land.ru`

[**] e-mail: `kuzn@sunhe.jinr.ru`

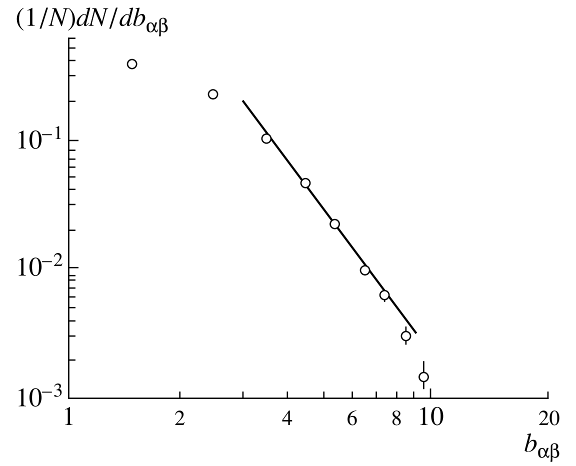

**Fig. 1.** Distribution of proton clusters with respect to the variable $b_{\alpha\beta}$ in inelastic CC interactions. The line represents a power-law fit in terms of Eq. (7).

are the 4-vectors of secondary baryons associated with the $\alpha$ and $\beta$ clusters, respectively.

Fragments of the target ($p_{\text{lab}} < 300$ MeV/$c$) and the projectile ($p_{\text{lab}} > 3$ GeV/$c$, $\theta_{\text{lab}} < 4$) were excluded from our analysis. In order to find the quantity $A_2$ with the aim of isolating two (or one) clusters in each event where the multiplicity of selected protons satisfied the condition $n_p \geq 4$, all possible partitions of the particles into two groups were considered. It was assumed that either two clusters or one cluster and one positively charged particle were formed in an event if the spacing $b_{\alpha\beta}$ between the isolated groups of baryons in 4-velocity space was not less than unity; that is,

$$b_{\alpha\beta} = -(V_\alpha - V_\beta)^2 \geq 1. \tag{4}$$

In order to specify the region of cluster formation, we used the relativistically invariant variables $x_{\text{Icl}}$ and $x_{\text{IIcl}}$ characterizing the fraction of the 4-momenta of colliding particles that is carried away by the clusters [1–5]:

$$x_{\text{Icl}} = \frac{m_{\text{cl}}^{\alpha(\beta)}(V_{\alpha(\beta)}u_{\text{II}})}{m_{\text{I}}(u_{\text{I}}u_{\text{II}})}, \tag{5}$$

$$x_{\text{IIcl}} = \frac{m_{\text{cl}}^{\alpha(\beta)}(V_{\alpha(\beta)}u_{\text{I}})}{m_{\text{II}}(u_{\text{I}}u_{\text{II}})}. \tag{6}$$

For $m_{\text{I}}$ and $m_{\text{II}}$, we took the proton mass: $m_{\text{I}} = m_{\text{II}} = m_p = 0.931$ MeV.

Large values of the variable $x_{\text{IIcl}}$ correspond to the target-fragmentation region, while large values of the variable $x_{\text{Icl}}$ correspond to the projectile-fragmentation region. In particular, it was assumed that the clusters were formed in the beam-fragmentation region if $x_{\text{Icl}} > x_{\text{IIcl}}$. In this study, we explored clusters in the target-fragmentation region ($x_{\text{IIcl}} > x_{\text{Icl}}$).

Figure 1 shows the distribution of two clusters $\alpha$ and $\beta$ formed in CC collisions versus the spacing between the clusters in 4-velocity space ($b_{\alpha\beta}$). It can be seen that, in the region $b_{\alpha\beta} > 3$, this distribution is adequately described by the power-law dependence

$$\frac{dN}{db_{\alpha\beta}} = \frac{A}{b_{\alpha\beta}^m} \tag{7}$$

with the parameter value of $m = 3.72 \pm 0.07$, which agrees with the behavior expected for nucleon clusters [3]. This universal character of the dependence was previously observed in experiments reported in [9, 10] and devoted to studying the distribution of hadron jets in soft hadron–hadron, hadron–nucleus, and deep-inelastic $\nu N$ collisions and in $e^+e^-$ annihilation. The parameter value was found to be $m \approx 3$ and to be independent of either the interaction type or the interaction energy for all collisions.

## 2. PROPERTIES OF THE INVARIANT DISTRIBUTIONS $F(b_k)$ OF PROTONS IN CLUSTERS AND OF THE INVARIANT DISTRIBUTIONS $F(b_{\text{IIcl}})$ OF CLUSTERS WITH RESPECT TO THE TARGET NUCLEUS

In order to study the properties of baryon clusters, we analyzed the invariant $F(b_k)$ distributions of protons in these clusters. These distributions can be represented as

$$F(b_k) = \frac{1}{N}\frac{2}{m_N^2}\int \frac{1}{\sqrt{b_k + b_k^2/4}}\frac{dN}{db_k d\Omega}d\Omega. \tag{8}$$

They have the following property: in the cluster rest system ($V_\alpha = 0$), the mean value $\langle b_k \rangle$ derived from Eq. (8) is unambiguously related to the mean kinetic energy of the protons in the cluster as

$$\langle b_k \rangle = \left\langle \frac{2E_k}{m_k} - 2 \right\rangle = \frac{2\langle T_k \rangle}{m_k}, \tag{9}$$

where $E_k$ and $T_k$ are, respectively, the total and the kinetic energy of the protons in the cluster rest frame.

Thus, one can determine the mean "temperature" of the protons in the clusters by analyzing the distributions in (8).

In [5] and [10], the dependences $F(b_k)$ were investigated for, respectively, $A$C and $A$Ta interactions at $p_A = 4.2$ GeV/$c$ per nucleon. In $p$C (Ta) and $d$C (Ta) collisions, the distributions of protons in clusters

Mean features of protons in clusters

| Type of interaction | Momentum, GeV/$c$ | Cluster of type 1 | | Cluster of type 2 | |
|---|---|---|---|---|---|
| | | $\langle b_k\rangle_1$ | $\langle T_k\rangle_1$, MeV | $\langle b_k\rangle_2$ | $\langle T_k\rangle_2$, MeV |
| $p$C | 4.2 | $0.133 \pm 0.004$ | $62 \pm 2$ | – | – |
| $d$C | 4.2 A | $0.147 \pm 0.002$ | $67 \pm 1$ | – | – |
| $\alpha$C | 4.2 A | $0.147 \pm 0.008$ | $67 \pm 1$ | $0.248 \pm 0.022$ | $118 \pm 10$ |
| CC | 4.2 A | $0.154 \pm 0.014$ | $72 \pm 7$ | $0.288 \pm 0.028$ | $135 \pm 13$ |
| $p$C | 10 | $0.158 \pm 0.005$ | $74 \pm 2$ | – | – |
| CC(mn) | 4.2 A | – | – | $0.256 \pm 0.005$ | $120 \pm 2$ |
| CC$^{\Lambda/K}$ | 4.2 A | – | – | $0.213 \pm 0.004$ | $100 \pm 2$ |

Note: mn stands for multinucleonic.

with respect to the variable $b_k$ can be described by the exponential form

$$F(b_k) = a_1 \exp(-b_k/\langle b_k\rangle_1). \qquad (10)$$

The mean values $\langle b_k\rangle_1$ and the corresponding mean temperatures are given in the table.

In contrast to what was observed in $p$C (Ta) and $d$C (Ta) collisions, the dependence $F(b_k)$ in $\alpha$C and CC events is described by a linear combination of two exponential functions; that is,

$$F(b_k) = a_1 \exp(-b_k/\langle b_k\rangle_1) + a_2 \exp(-b_k/\langle b_k\rangle_2), \qquad (11)$$

with the mean values $\langle b_k\rangle_1$ and $\langle b_k\rangle_2$ differing from each other by a factor close to 2 (see table). The results suggest the formation of two types of proton clusters in $\alpha$C and CC collisions: clusters of type 1 have the same temperature as those formed in $p$C (Ta) and $d$C (Ta) collisions, while clusters of type 2 have a higher temperature (see table).

Below, we analyze the dependences $F(b_k)$ for CC$^{\Lambda/K}$ events that involve the production of either a $\Lambda$ hyperon or a $K^0$ meson. The dependences $F(b_k)$ obtained experimentally for such CC interactions are shown in Fig. 2. From this figure, it can be seen that, in CC$^{\Lambda/K}$ events, the distributions of protons in clusters with respect to the variable $b_k$ are described by an exponential dependence similar to that in Eq. (10) with the mean value of $\langle b_k\rangle_2 = 0.213 \pm 0.004$ and the corresponding temperature $\langle T_k\rangle = 100 \pm 2$ MeV.

Thus, we see that, in contrast to all inelastic CC interactions, which, as was stated above, involve the formation of two types of clusters having different temperatures [5], CC$^{\Lambda/K}$ events result in the formation of predominantly a single type of proton clusters having a high temperature, this being caused by the associated production of strange particles.

In order to study the features of the formation of proton clusters accompanied by the production of strange particles (either a $\Lambda$ hyperon or a $K^0$ meson), we explored the behavior of the invariant cross section $Ed^3\sigma/dp^3$ as a function of the variable $b_{\rm IIcl}$, where $b_{\rm IIcl} = -(V_\alpha - u_{\rm II})^2$ (here, the index II refers to the target nucleus). The function $F(b_{\rm IIcl})$ is taken in a form similar to Eq. (8).

In [5], it was established that clusters formed in nucleus–nucleus interactions with different temperatures are characterized by different distributions (or spacings in 4-velocity space) with respect to the target nucleus or by different dependences on the variable $b_{\rm IIcl}$. Below, we display results characterizing the behavior of the invariant functions $F(b_{\rm IIcl})$ for clusters formed in CC$^{\Lambda/K}$ interactions.

It was found that the mean value of the quantity

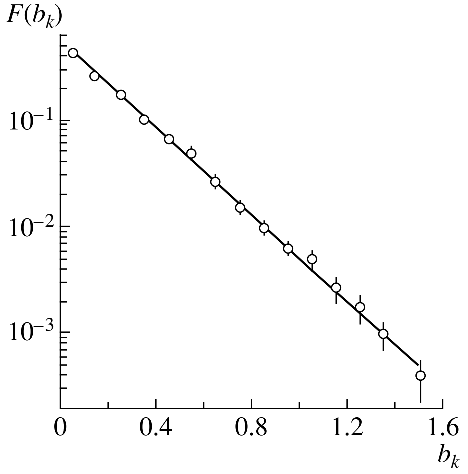

**Fig. 2.** Invariant function $F(b_k)$ for protons in clusters formed in CC$^{\Lambda/K}$ collisions. The line represents an exponential fit in terms of Eq. (10).

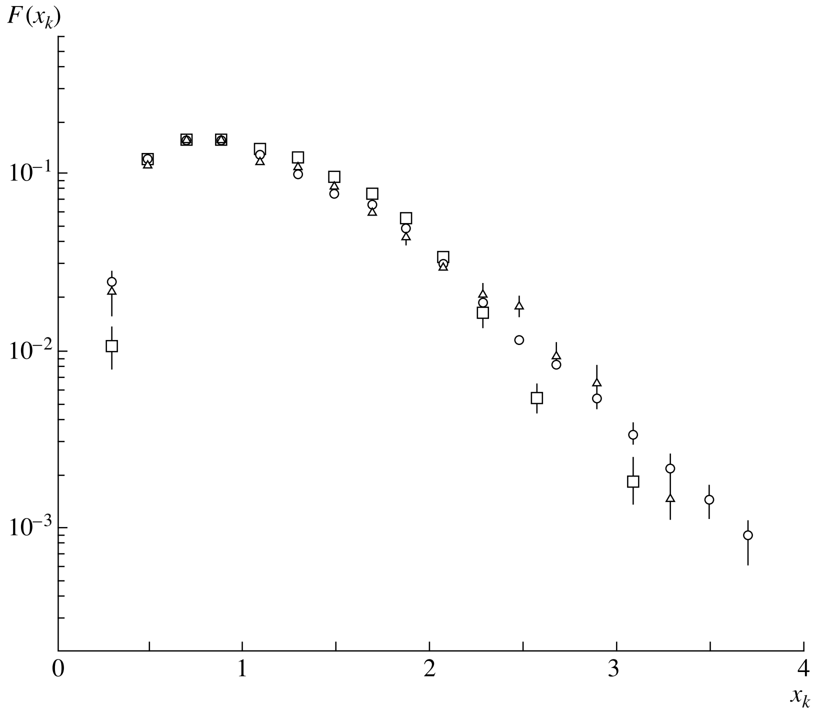

**Fig. 3.** Invariant functions $F(x_k)$ for protons in clusters formed in (□) $\alpha$C, (○) CC, and (△) $\mathrm{CC}^{\Lambda/K}$ interactions.

$b_{\mathrm{IIcl}}$ for proton clusters formed in $\mathrm{CC}^{\Lambda/K}$ interactions is $\langle b_{\mathrm{IIcl}}\rangle = 0.58 \pm 0.02$. Within the experimental errors, this result agrees well with the value that was obtained previously in [5, 11] for high-temperature proton clusters formed in $\alpha$C and CC interactions ($\langle b_{\mathrm{IIcl}}\rangle = 0.51 \pm 0.05$).

Thus, we can state that nucleon clusters having different temperatures are characterized by different spacings with respect to the target nucleus in the space of relative 4-velocities, this in turn suggesting different degrees of excitation of nuclear matter in relativistic nuclear interactions. Low-temperature nucleon clusters formed in $\alpha$C and CC interactions are characterized by the mean 4-velocity value of $\langle b_{\mathrm{IIcl}}\rangle = 0.11$–$0.14$ with respect to the target nucleus, this being in good agreement with the slope parameter $\langle b_{\mathrm{IIcl}}\rangle = 0.14 \pm 0.01$ of the function $F(b_{\mathrm{IIcl}})$ for nucleon clusters formed in $p$C collisions. Nucleon clusters of higher temperature that are formed in $\alpha$C, CC and $\mathrm{CC}^{\Lambda/K}$ interactions are characterized by a higher 4-velocity with respect to the target nucleus: $\langle b_{\mathrm{IIcl}}\rangle = 0.5$–$0.6$ [12].

## 3. PROPERTIES OF THE INVARIANT DISTRIBUTIONS $F(x_k)$ OF PROTONS IN CLUSTERS

The variable $x_k$ for protons from cluster $\alpha$ is defined as

$$x_k^\alpha = b_{\beta k}/b_{\alpha\beta} = x_k, \qquad (12)$$

where $b_{\beta k} = -(V_\beta - u_k^\alpha)^2$.

For $b_{\alpha\beta} > 1$, the variable $x_k$ in the rest system of cluster $\alpha$ ($V_\alpha = 0$) reduces to the light-cone variable $x_k^\alpha = u_{k0}^\alpha - u_{kz}^\alpha$. Here, the $z$ axis specifies the direction of the line connecting the centers of the clusters $V_\alpha$ and $V_\beta$ in three-dimensional space. It follows that the dependence of the invariant function $F$ on the variable $x_k$ means the dependence on the direction of the segment connecting the centers of the clusters $V_\alpha$ and $V_\beta$. In turn, this means that an isolated system (cluster) must decay anisotropically in the cluster rest frame with respect to the above direction.

The invariant function $F(x_k)$ can be represented in the form

$$F(x_k) = \frac{2}{m_N^2 b_{\alpha\beta}} \qquad (13)$$
$$\times \int \frac{1}{\sqrt{x_k b_{\alpha\beta} + (x_k b_{\alpha\beta})^2/4}} \frac{d\Omega}{dx_k d\Omega} d\Omega.$$

Figure 3 shows the dependences $F(x_k)$ obtained experimentally for $\alpha$C, CC, and $\mathrm{CC}^{\Lambda/K}$ interactions. It can be seen that the values of $F(x_k)$ for the interaction types being considered agree within the errors; that is, they are independent of the projectile atomic weight. Previously, it was found that, in the momentum range 4–40 GeV/$c$, $F(x_k)$ does not depend on either the projectile atomic weight or the interaction energy in $p$C, $d$C, and $\pi^-$C collisions as well. It should be noted that the dependences $F(x_k)$ for $\alpha$C, CC, and CC$^{\Lambda/K}$ interactions are broader than those for $p$C and $d$C collisions. This is a manifestation of the fact that $\alpha$C, CC, and CC$^{\Lambda/K}$ interactions feature baryon clusters of temperature higher than that in $p$C and $d$C collisions.

## CONCLUSIONS

The set of data on the properties of nucleon clusters in events featuring strange particles that was obtained in the present experiment and their comparison with the results obtained previously for the properties of nucleon clusters formed in $(p, d, \alpha$, C)C interactions at the same energies without accompanying strange particles enable us to draw the following conclusions:

(i) Nucleon clusters characterized by a high mean kinetic energy of protons in the cluster rest system, $\langle T_p \rangle = 100 \pm 2$ MeV, are formed in CC$^{\Lambda/K}$ collisions at a momentum of 4.2 GeV/$c$ (this circumstance was discovered for the first time).

(ii) The temperature and other features describing the properties of proton clusters in events involving strange particles agree, within the errors, with the respective features obtained previously in studying high-temperature nucleon clusters in strange-particle-free events induced by $\alpha$C and CC interactions at the same energies [5].

## REFERENCES

1. A. M. Baldin *et al.,* Yad. Fiz. **44**, 1209 (1986) [Sov. J. Nucl. Phys. **44**, 785 (1986)].
2. A. M. Baldin and L. A. Didenko, Kratk. Soobshch. OIYaI, No. 3-84, 5 (1984); No. 8-85, 5 (1985).
3. A. M. Baldin and A. A. Baldin, Kratk. Soobshch. OIYaI, No. 17-86, 19 (1986).
4. D. Armutliski *et al.,* Kratk. Soobshch. OIYaI, No. 4 (24)-87, 5 (1987).
5. A. M. Baldin *et al.,* Yad. Fiz. **49**, 1034 (1989) [Sov. J. Nucl. Phys. **49**, 640 (1989)].
6. BBCDHSSTTU-BW Collab., Phys. Lett. B **39B**, 571 (1972); N. Angelov *et al.,* Yad. Fiz. **25**, 1013 (1977) [Sov. J. Nucl. Phys. **25**, 539 (1977)].
7. B. P. Adyasevich, Preprint IAE-4148/2 (Kurchatov Institute of Atomic Energy, Moscow, 1985).
8. G. N. Agakishiev *et al.,* Yad. Fiz. **43**, 366 (1986) [Sov. J. Nucl. Phys. **43**, 234 (1986)].
9. V. G. Grishin *et al.,* Yad. Fiz. **52**, 183 (1990) [Sov. J. Nucl. Phys. **52**, 115 (1990)].
10. V. G. Grishin *et al.*, Preprint No. 1-89-838, OIYaI (Joint Institute for Nuclear Research, Dubna, 1989).
11. D. M. Baldin *et al.*, Preprint No. R1-90-263, OIYaI (Joint Institute for Nuclear Research, Dubna, 1990).
12. L. A. Didenko *et al.*, Preprint No. E1-91-323, OIYaI (Joint Institute for Nuclear Research, Dubna, 1991).

*Translated by V. Bukhanov*

Physics of Atomic Nuclei, Vol. 67, No. 4, 2004, pp. 708–713. Translated from Yadernaya Fizika, Vol. 67, No. 4, 2004, pp. 730–735.

## ELEMENTARY PARTICLES AND FIELDS
## Experiment

# Phenomenological Analysis of the Channels of the Production of Three and Four Alpha Particles in $^{16}$O$p$ Collisions at 3.25 GeV/$c$ per Nucleon

**E. Kh. Bazarov, V. V. Glagolev**[1]**, K. G. Gulamov, V. V. Lugovoi,**
**S. L. Lutpullaev, K. Olimov*****, A. A. Yuldashev, and B. S. Yuldashev**[2]

*Institute for Physics and Technology, Fizika-Solntse Research and Production Association, Uzbek Academy of Sciences, ul. Timiryazeva 2b, Tashkent, 700084 Republic of Uzbekistan*

Received January 15, 2003; in final form, June 18, 2003

**Abstract**—A phenomenological analysis of the channels of the production of three and four alpha particles in $^{16}$O$p$ collisions at 3.25 GeV/$c$ per nucleon is performed for the first time under conditions of $4\pi$ geometry. The experimentally observed azimuthal asymmetries and collinearity are described on the basis of a phenomenological model that assumes that the excitation of the nucleus involved is peripheral and that its decay is statistical. It is shown that the azimuthal asymmetries in question are due to the transverse motion of the fragmenting nucleus. The mean transverse momentum of alpha particles and the collinearity of their emission in the reaction plane are found to be independent of the transverse-momentum transfer to the nucleus involved. © *2004 MAIK "Nauka/Interperiodica"*.

## INTRODUCTION

For $^{16}$O$p$ interactions at 3.25 GeV/$c$ per nucleon, an analysis of the angular distributions of slow ($T <$ 10 MeV per nucleon) light fragments—$^2$H$_1$, $^3$H$_1$, and $^3$He$_2$—from these interactions in the rest frame of the oxygen nucleus [1] revealed that their inclusive cross sections increase in the limit $|\cos\theta| \to 1$. This effect was interpreted on the basis of the assumption that the fragmenting nucleus acquires an angular momentum in the interaction with a target. In [2], angular asymmetries and collinearities were observed in the channels of the production of two and three alpha particles in $^{12}$CEm interactions at 4.5 GeV/$c$ per nucleon. This experimental fact and the discrepancy between the experimental transverse-momentum spectrum of alpha particles and the predictions of the statistical fragmentation model [3] were qualitatively interpreted under the assumption that the fragmenting nucleus acquires a transverse momentum,[3] which was used as a free parameter in the calculations performed in [2], and, possibly, an angular momentum, which was not taken into account in [2]. In order to test an alternative physical pattern that could provide a quantitative explanation, we therefore performed experimental investigations, whose results were contrasted against the results of the respective original Monte Carlo calculation that differed from the calculation in [2]. The main distinctions consist in the following: the law of energy–momentum conservation is taken into account in each event to a relative precision of $10^{-6}$ (see Appendix); events are generated in accordance with the experimental probability of each exclusive channel (with the exception of that which involves pions) of the breakup of the primary nucleus; the components of the momentum transfer to the fragmenting nucleus from the target proton are generated in accordance with the Gaussian distribution; and, finally, the probability for the generation of collinearity of the momentum vectors of two alpha particles is taken into account in terms of a free model parameter (see Appendix).

We have investigated the coefficients of azimuthal asymmetry and collinearity,

$$A = (N_{\varepsilon<\pi/2} - N_{\varepsilon\geq\pi/2})/N_{0\leq\varepsilon\leq\pi}, \qquad (1)$$

$$B = (N_{\varepsilon<\pi/4} + N_{\varepsilon\geq 3\pi/4} - N_{\pi/4\leq\varepsilon\leq 3\pi/4})/N_{0\leq\varepsilon\leq\pi}, \qquad (2)$$

of the inclusive distribution with respect to the pair azimuthal angle

$$\varepsilon_{ij} = \arccos[(\mathbf{p}_{\perp i}\cdot\mathbf{p}_{\perp j})/(p_{\perp i}p_{\perp j})]$$

between the transverse-momentum vectors of the $i$th and the $j$th alpha particle from the same fragmentation event ($0 \leq \varepsilon_{ij} \leq \pi$). We have also studied the

---

[1] Joint Institute for Nuclear Research, Dubna, Moscow oblast, 141980 Russia.

[2] Institute of Nuclear Physics, Uzbek Academy of Sciences, pos. Ulughbek, Tashkent, 702132 Republic of Uzbekistan.

*e-mail: `olimov@uzsci.net`

[3] Within the phenomenological cylindrical-phase-space model.

mean values of the coefficients of azimuthal asymmetry and collinearity in individual $^{16}\mathrm{O}p$ events,

$$\langle\alpha\rangle = \sum_{k=1}^{N} \alpha_k/N, \tag{3}$$

$$\alpha_k = \sum_{i\neq j}^{n_k} \cos(\varepsilon_{ij})/(n_k(n_k-1))^{1/2},$$

$$\langle\beta\rangle = \sum_{k=1}^{N} \beta_k/N, \tag{4}$$

$$\beta_k = \sum_{i\neq j}^{n_k} cos(2\varepsilon_{ij})/(n_k(n_k-1))^{1/2},$$

where $k = 1, 2, \ldots N$ and $N$ is the number of events where the multiplicity of alpha particles belonging to the type being considered is $n_k = 3$ or 4.

Before proceeding to describe relevant experimental data and the physical foundations of our Monte Carlo calculation and to analyze the results obtained for the features of the fragmentation process that are being studied here, we will briefly list some basic properties of the quantities defined in (1)–(4) [4].

(i) If the emission of alpha particles is statistically independent and if their angular spectrum is isotropic, it is natural to expect that $A$, $B$, $\langle\alpha\rangle$, and $\langle\beta\rangle$ assume zero values and that the distribution with respect to $\varepsilon_{ij}$ is uniform in the interval [0, $\pi$].

(ii) Upon taking into account the law of energy–momentum conservation, it turns out that $A < 0$, $\langle\alpha\rangle < 0$, $B > 0$, and $\langle\beta\rangle > 0$. Concurrently, the distribution with respect to $\varepsilon_{ij}$ develops a maximum for $\varepsilon_{ij} \to \pi$.

(iii) A nonzero angular momentum of a fragmenting nucleus may lead to an increase in $B$ and $\langle\beta\rangle$ in relation to their "kinematical input" values corresponding to taking into account conservation laws for the transverse motion of a disintegrating system.

The experimental data used were obtained by exposing the 1-m hydrogen bubble chamber of the Laboratory for High Energies (Joint Institute for Nuclear Research, Dubna) to a beam of $^{16}\mathrm{O}$ nuclei accelerated at the Dubna synchrophasotron to a momentum of 3.25 GeV/$c$ per nucleon. The data sample subjected to analysis in the present study consists of 11 098 measured events of $^{16}\mathrm{O}p$ interactions. It should be emphasized that the use of beams of accelerated light nuclei in experiments with hydrogen bubble chambers makes it possible to identify all projectile fragments [5–7] by charge and mass. Under the conditions of our experiment, recoil protons are rather well identified by ionization up to momenta of about 1.2 GeV/$c$. The admixture of positively charged pions among singly charged positive particles of momentum in the region $P > 1.75$ GeV/$c$ (low boundary for the separation of protons appearing as fragmentation products) is negligible.

We have considered fully measured events that involve three or four alpha particles in the final state. For a fragment to be reliably identified by mass, its measured-track length $L$ must exceed 35 cm. If this constraint is imposed on the measured-track lengths, the accuracies in determining the fragment momenta and emission angles are within 4% (relative error) and 0.1°, respectively. The channels being considered involve the production of singly and doubly charged fragments whose mass number satisfies the condition $A \leq 4$. The mass separation of fragments was performed on the basis of the measured values of the respective momentum and charge. The momentum distributions of singly and doubly charged fragments have distinct maxima [5] at the values of $P =$ 3.25 A GeV/$c$ corresponding to hydrogen and helium isotopes. In order to perform an eventual identification of fragments by mass, we introduced the following momentum intervals: singly charged fragments of momentum in the regions $P =$ 1.75–4.75 GeV/$c$, $P =$ 4.75–7.8 GeV/$c$, and $P > 7.8$ GeV/$c$ were classified as $^1$H, $^2$H, and $^3$H, respectively, while doubly charged fragments of momentum in the regions $P <$ 10.8 GeV/$c$ and $P > 10.8$ GeV/$c$ were treated as $^3$He and $^4$He, respectively. For this choice of momentum intervals for fragment separation, the admixture of isotopes that have the closest mass values does not exceed 4 to 5%.

## EXPERIMENTAL RESULTS AND THEIR DISCUSSION

Events featuring peripheral projectile–target interactions, in which case the intranuclear-cascade contribution can be disregarded, provide favorable conditions for studying the structure of the primary nucleus and for assessing the transverse- and angular-momentum transfers to this nucleus. As was mentioned above, we therefore study the coefficients of azimuthal asymmetry ($A$) and collinearity ($B$), $\alpha_k$ and $\beta_k$ distributions in individual events, distributions with respect to the difference of the azimuthal angles of pairs of alpha particles, and transverse-momentum distributions of alpha particles from $^{16}\mathrm{O}p$ interactions for channels involving three or four alpha particles in the final state. The number of events in which three or four alpha particles were present and in which the kinematical features were measured for all charged particles and fragments whose tracks had a length satisfying the condition $L > 35$ cm proved to be 431.

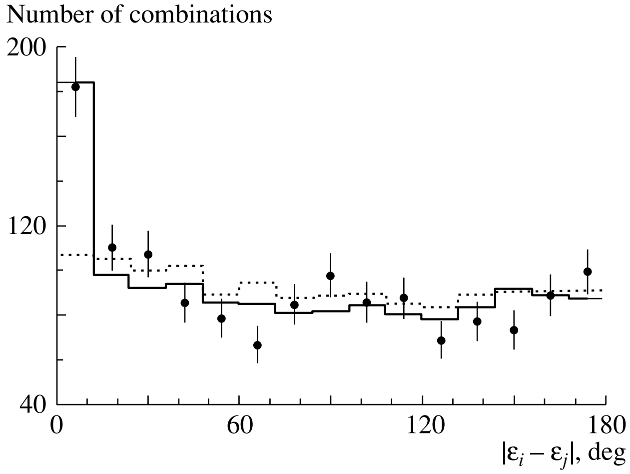

**Fig. 1.** Distribution with respect to the pair azimuthal angle ($\varepsilon_{ij}$) between the momenta of the $i$th and $j$th alpha particles. The histograms represent the results of the calculations performed on the basis of our Monte Carlo model (solid-line histogram) with and (dashed-line histogram) without allowance for the collinearity of the momentum vectors of the alpha particles forming the pair in question, the mean transverse momentum of the fragmenting nucleus being $\langle P_\perp \rangle = 0.24$ GeV/$c$.

Figure 1 displays the distribution with respect to the pair azimuthal angle ($\varepsilon_{ij}$) between the momenta of the $i$th and $j$th alpha particles. As can be seen from Fig. 1, the distribution with respect to the quantity $\varepsilon_{ij}$ is not isotropic—this distribution has a maximum in the region of small angles ($\varepsilon_{ij} < 10°$), but, within the statistical uncertainties, it becomes isotropic at larger angles. The peak in the region $\varepsilon_{ij} < 10°$ may be indicative of the presence of collinear correlations between the momenta in a pair of alpha particles. In order to test this assumption, we introduced, as a free parameter in our Monte Carlo calculations, the probability for the emergence of events featuring collinear momentum vectors in alpha-particle pairs (see Appendix).

For the case where the mean transverse momentum of the recoil nucleus is $\langle P_\perp \rangle = 0.24$ GeV/$c$ (the choice of this value is discussed below), the histograms in Fig. 1 represent the results of the calculations based on our Monte Carlo model that either (solid-line histogram) take into account or (dashed-line histogram) disregard the collinearity of the momentum vectors in the alpha-particle pair being considered. It can be seen that, in the case where the collinearity in question is disregarded, the results of the calculations disagree dramatically with experimental data for $\varepsilon_{ij} < 10°$. On the other hand, the best agreement between theoretical and experimental results is observed at the collinearity-emergence probability of 20% (solid-line histogram).

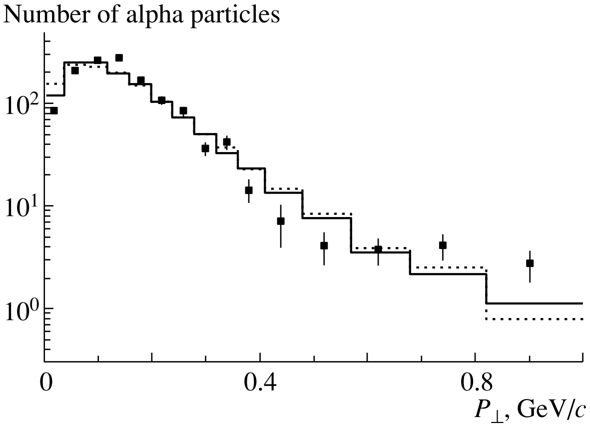

**Fig. 2.** Transverse-momentum distribution of alpha particles. The histograms represent the results of the calculations for the cases where the mean transverse momentum of the fragmenting nucleus is set to (solid-line histogram) 0.24 GeV/$c$ or (dashed-line histogram) zero.

The values obtained for the coefficients of azimuthal asymmetry and collinearity on the basis of experimental $\varepsilon_{ij}$ distributions are $A = 0.10 \pm 0.03$ and $B = 0.12 \pm 0.03$. The values calculated for these quantities with allowance for collinearity proved to be in agreement with their experimental counterparts within the statistical uncertainties: $A = 0.09 \pm 0.03$ and $B = 0.13 \pm 0.03$. Without allowance for collinearity, these coefficients proved to be compatible with zero within the statistical uncertainties: $A = -0.03 \pm 0.03$ and $B = 0.02 \pm 0.03$. In the following, a comparison of the results of model calculations with experimental data is performed with allowance for collinearity at a 20% level.

Figure 2 displays the transverse-momentum distribution of alpha particles. In this figure, the histograms represent the results of the respective calculations where the mean transverse momentum of the fragmenting nucleus was set either to (solid-line histogram) 0.24 GeV/$c$ or to (dashed-line histogram) zero. It can be seen that the shape of the calculated transverse-momentum distribution depends only slightly on the transverse momentum of the fragmenting nucleus. At $\langle P_\perp \rangle = 0.24$ GeV/$c$, the mean value of the transverse momenta of alpha particles that was calculated within our model ($0.165 \pm 0.001$ GeV/$c$) agrees with its experimental counterpart ($0.166 \pm 0.004$ GeV/$c$) within the statistical uncertainties. In response to the reduction of the mean transverse momentum of the fragmenting nucleus from $\langle P_\perp \rangle = 0.24$ GeV/$c$ to zero, the mean transverse momentum of alpha particles decreases only by 7 MeV/$c$. In view of this, the mean transverse momentum of the fragmenting nucleus was assessed not only by using the calculated values of the mean transverse momentum of alpha particles but also by fitting the theoretical $\alpha_k$ and $\beta_k$ distributions to their experimental counterparts.

Figures 3*a* and 3*b* show the experimental $\alpha_k$ and $\beta_k$ distributions in individual events of $^{16}\mathrm{O}p$ interactions. The respective mean values proved to be $\langle\alpha\rangle = 0.12 \pm 0.03$ and $\langle\beta\rangle = 0.13 \pm 0.03$.

These data suggest the existence of an azimuthal asymmetry in alpha-particle emission and a trend toward a collinearity of the transverse momenta of emitted alpha particles in the plane orthogonal to the beam axis. The collinearity observed in our experiment may be due to a nonzero angular momentum of the thermalized excited nucleus undergoing breakup.

In Figs. 3*a* and 3*b*, the histograms represent the calculated distributions with respect to $\alpha_k$ and $\beta_k$ for the cases where the mean transverse momentum of the fragmenting nucleus is (solid-line histograms) 0.24 GeV/$c$ or (dashed-line histograms) zero. From Fig. 3, it can be seen that, in either case, the calculated distributions with respect to $\alpha_k$ and $\beta_k$ reproduce their experimental counterparts quite satisfactorily.

However, the mean value for the calculated distribution with respect to $\alpha_k$ at $\langle P_\perp\rangle = 0$ proved to be $0.00 \pm 0.03$, which is compatible with the absence of asymmetry; at the same time, the analogous mean value for $\langle P_\perp\rangle = 0.24$ GeV/$c$ is $0.12 \pm 0.03$, which is indicative of a small azimuthal asymmetry complying with the experimental value.

Figure 3*b* shows that the calculated distribution with respect to $\beta_k$ is virtually independent of the transverse momentum of the fragmenting nucleus. The mean value for the calculated distribution with respect to $\beta_k$ proved to be $0.10 \pm 0.03$ for $\langle P_\perp\rangle = 0$ and $0.13 \pm 0.03$ for $\langle P_\perp\rangle = 0.24$ GeV/$c$, this indicating the presence of a small azimuthal collinearity, which is in agreement with its experimental counterpart.

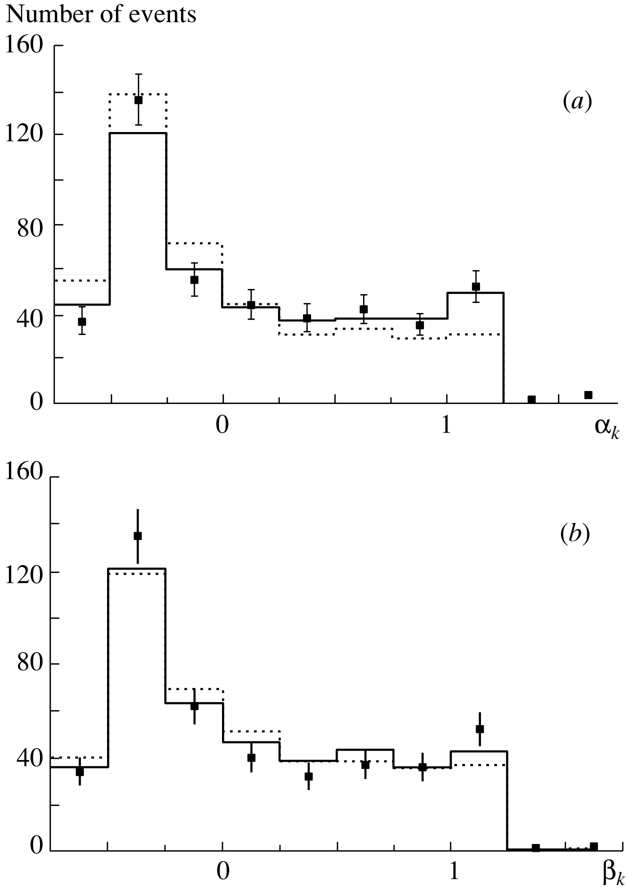

**Fig. 3.** Distributions with respect to (*a*) $\alpha_k$ and (*b*) $\beta_k$ in individual events of $^{16}\mathrm{O}p$ interactions. The histograms represent the results of the respective calculations for the cases where the mean transverse momentum of the fragmenting nucleus is (solid-line histograms) 0.24 GeV/$c$ or (dashed-line histograms) zero.

The above experimental data were also compared with the predictions of the cascade—fragmentation—evaporation model [8], where use is made of the intranuclear-cascade model [9, 10] combined with a modification of the Fermi statistical model for multiparticle production [11]. In this combined model, it is assumed that the fragmenting nucleus consists of a perfect Fermi gas. Upon the propagation of the intranuclear cascade, a statistical equilibrium is established in the nucleus, so that the probability of each channel is proportional to the respective phase space. For the light nucleus of $^{16}\mathrm{O}$, Fermi breakup—that is, an explosive disintegration of the nucleus—is assumed within the model in question to be a dominant mechanism of fragment formation. The basic results obtained from a comparison of experimental data with the predictions of the cascade—fragmentation—evaporation model are the following:

(a) The model cannot reproduce quantitatively either the above distributions of particles and events with respect to the quantities $\varepsilon_{ij}$, $\alpha_k$, $\beta_k$, and $P_\perp$ or the mean values $\langle\alpha\rangle$, $\langle\beta\rangle$, and $\langle P_\perp\rangle$. It underestimates the azimuthal asymmetry ($\langle\alpha\rangle = 0.01 \pm 0.02$) and overestimates the azimuthal collinearity by a factor of 3 ($\langle\beta\rangle = 0.39 \pm 0.03$). The model underestimates the mean transverse momentum of alpha particles ($\langle P_\perp\rangle = 0.153 \pm 0.003$ GeV/$c$); concurrently, the theoretical transverse-momentum distribution of alpha particles terminates at $P_\perp \leq 0.5$ GeV/$c$, while the experimental distribution extends to 1 GeV/$c$.

(b) Within the model, the cross sections for channels involving the production of three or four alpha particles are suppressed by a factor greater than 2.5.

The results of a phenomenological analysis of the channels of $^{16}\mathrm{O}p$ interaction at 3.25 GeV/$c$ per nucleon that result in the production of three or four alpha particles can be briefly summarized as follows:

(i) The experimentally observed small azimuthal anisotropy of alpha-particle emission in the plane orthogonal to the beam axis is due to the transverse motion of the fragmenting nucleus, the mean transverse momentum acquired by the fragmenting nucleus being $\langle P_\perp \rangle = 0.24$ GeV/$c$. In contrast to what was obtained from the calculations reported in [2], this transverse momentum has virtually no effect on the mean transverse momentum of emitted alpha particles.

(ii) The angular momentum acquired by the fragmenting nucleus is low, and it does not make a significant contribution to the experimentally observed azimuthal collinearity in the production of three or four alpha particles. This is suggested by the agreement between the results of our Monte Carlo calculations, where the fragmenting nucleus is assumed to have no angular momentum, and experimental data.

(iii) The evaporation process is dominant, while the intranuclear cascade is suppressed, which is indicative of a peripheral character of the exclusive (with respect to fragments) channels of the production of three and four alpha particles.

## APPENDIX

### *Simulation of the Exclusive (with Respect to Fragments) Channels of the Breakup of Relativistic Oxygen Nuclei into Three or Four Alpha Particles*

It was assumed that, for events considered here, all collisions between oxygen nuclei and protons are peripheral, an excited oxygen nucleus decaying isotropically in its rest frame into fragments. The generation of events was performed in accordance with the probabilities of the experimentally observed exclusive (with respect to fragments) channels of oxygen-nucleus breakup that involve three or four alpha particles. The kinematical features of neutrons were assumed to be identical to those of protons.

Following the assumption that the interactions in question are peripheral, we proceeded as follows:

(i) The generation of the excited-oxygen-nucleus mass $M^*$ was performed according to the formula

$$M^* = \sum_{i=1}^{n} M_i + \lambda r,$$

where $M_i$ stands for the fragment masses, $\lambda$ is a free parameter that is related to the excitation energy, and $r$ is a pseudorandom number that is uniformly distributed over the segment [0, 1]. The best agreement between the results of the calculations and experimental data was attained at $\lambda = 0.3$.

(ii) The generation of all three components of the $^{16}\mathrm{O}^*$ momentum in the rest frame of the primary nucleus was performed according to a Gaussian distribution that is characterized by the root-mean-square deviation $\sigma_{\mathrm{nucl}} = \gamma^*(2/\pi)^{0.5}$ [GeV/$c$], where $\gamma$ is a free parameter that takes into account the mean transverse momentum acquired by the fragmenting nucleus. The best agreement between the results of the calculations and experimental data is obtained at $\gamma = 0.24$ GeV/$c$.

Following the assumption that the breakup of an excited fragmenting nucleus is isotropic in its rest frame, we further generate all three components of the momentum of each fragment according to a Gaussian distribution such that the respective root-mean-square deviation is $\sigma_{\mathrm{frag}} = \langle P_\perp \rangle (2/\pi)^{0.5}$ [GeV/$c$], where $\langle P_\perp \rangle$ is the experimental value of the mean transverse momentum of a fragment that belongs to a given type.

In order to take into account the collinearity of the momentum vectors in a pair of alpha particles, we introduce, as an additional model parameter, the collinearity of a pair of alpha particles in each event with a probability of 20%, this parameter being determined by fitting the calculated $\varepsilon_{ij}$ distribution to its experimental counterpart (see Fig. 1). The specific procedure used here for this was as follows: after the generation of the components of the momentum of one alpha particle in a pair, the components of the momentum of the other alpha particle were generated within a range that admitted not more than a 4% distinction from the components of the momentum of the first alpha particle, the difference of the components of the momenta of the two particles being generated uniformly within the mean relative error.

In order to ensure fulfillment of the momentum-conservation law, all three momentum components were subjected to the shift

$$P_{xi} \to P_{xi} - (P_{x1} + P_{x2} + P_{x3} + \ldots + P_{xn})/n,$$

$$P_{yi} \to P_{yi} - (P_{y1} + P_{y2} + P_{y3} + \ldots + P_{yn})/n,$$

$$P_{zi} \to P_{zi} - (P_{z1} + P_{z2} + P_{z3} + \ldots + P_{zn})/n,$$

where $i = 1, 2, 3, \ldots, n$ and $n$ is the number of fragments in a given event. Additionally, we required that, in the rest frame of the recoil nucleus, the energy-conservation law be satisfied to the following accuracy:

$$[(E_1 + E_2$$

$$+ E_3 + \ldots + E_n - M_{\text{nucl}})^2/(M_{\text{nucl}})^2]^{0.5} < 10^{-6}.$$

Here, $E_i = (m_i^2 + (P'_{xi})^2 + (P'_{yi})^2 + (P'_{zi})^2)^{0.5}$ is the energy of the $i$th fragment; $m_i$ is the mass of the $i$th fragment; and $P'_{xi} = \alpha P_{xi}$, $P'_{yi} = \alpha P_{yi}$, and $P'_{zi} = \alpha P_{zi}$ are the new components of the momentum of the $i$th fragment that were obtained after multiplication by the coefficient $\alpha$, whose value was chosen in such a way as to ensure fulfillment of the condition required for the energy-conservation law to be satisfied.

Further, the components of the momenta of fragments and their energies were transformed from the excited-oxygen-nucleus rest frame $K$ to the rest frame $K_0$ of the primary target proton. These two reference frames are related to each other as follows. In the reference frame $K_0$, we rotate the $z_0$ axis in such a way that it becomes aligned with the 3-momentum $\mathbf{P}_0$ of the excited oxygen nucleus and denote this new axis by $z'$. We refer to the resulting reference frame as $K'$. In this reference frame, we choose the $y'$ axis to be directed along the vector product $[\mathbf{z} \times \mathbf{z}_0]$. Suppose that the reference frame $K'$ moves along the $z'$ axis at the velocity $\boldsymbol{\beta} = \mathbf{P}_0/E_0$, where $E_0$ and $\mathbf{P}_0$ are, respectively, the energy and the 3-momentum of the excited oxygen nucleus in the reference frame $K_0$. The excited-nucleus rest frame constructed in this way will be referred to as the reference frame $K$.

The components of the momentum of each $i$th fragment and its energy in the reference frames $K'$ and $K$ are related by the equations

$$P'_{xi} = P_{xi}, \quad P'_{yi} = P_{yi},$$

$$P'_{zi} = \gamma(P_{zi} + \beta E_i), \quad E' = \gamma(E_i + \beta P_{zi}),$$

where $\gamma = E_0/M^*$, $\beta = |\mathbf{P}_0|/E^0$, and $M^*$ is the mass of the excited oxygen nucleus. After transforming the fragment-momentum components and fragment energies from the reference frame $K$ to the reference frame $K'$, the momentum components were transformed from the reference frame $K'$ to the rest frame $K_0$ of the primary target proton by using the formulas

$$P^0_{xi} = -P'_{xi}\cos\theta\cos\varphi - P'_{yi}\sin\varphi - P'_{zi}\sin\theta\cos\varphi,$$

$$P^0_{yi} = -P'_{xi}\cos\theta\sin\varphi + P'_{yi}\cos\varphi - P'_{zi}\sin\theta\sin\varphi,$$

$$P^0_{zi} = -P'_{xi}\sin\theta - P'_{zi}\cos\theta, \quad i = 1, 2, \ldots, n,$$

where $n$ is the number of fragments in an event and

$$\cos\theta = -P_{z0}/(P_{x0}^2 + P_{y0}^2 + P_{z0}^2)^{0.5},$$

$$\sin\theta = (1 - (\cos\theta_z)^2)^{0.5},$$

$$\cos\varphi = -P_{x0}/(P_{x0}^2 + P_{y0}^2)^{0.5},$$

$$\sin\varphi = -P_{y0}/(P_{x0}^2 + P_{y0}^2)^{0.5}.$$

Here, $P_{x0}$, $P_{y0}$, and $P_{z0}$ are the components of the momentum of the excited oxygen nucleus in the rest frame $K_0$ of the primary target proton.

## REFERENCES

1. V. V. Glagolev, K. G. Gulamov, V. D. Lipin, *et al.,* Yad. Fiz. **62**, 1472 (1999) [Phys. At. Nucl. **62**, 1388 (1999)].
2. R. A. Bondarenko, K. G. Gulamov, U. G. Gulyamov, and G. M. Chernov, Yad. Fiz. **38**, 1483 (1983) [Sov. J. Nucl. Phys. **38**, 903 (1983)].
3. A. S. Goldhaber, Phys. Lett. B **53B**, 306 (1974).
4. S. A. Azimov and G. M. Chernov, *Statistical Methods in the High Energy Physics* (FAN, Tashkent, 1970), p. 108 [in Russian].
5. V. V. Glagolev, K. G. Gulamov, M. Yu. Kratenko, *et al.,* Pis'ma Zh. Éksp. Teor. Fiz. **58**, 497 (1993) [JETP Lett. **58**, 497 (1993)].
6. V. V. Glagolev, K. G. Gulamov, M. Yu. Kratenko, *et al.,* Pis'ma Zh. Éksp. Teor. Fiz. **59**, 316 (1994) [JETP Lett. **59**, 336 (1994)].
7. V. V. Glagolev, K. G. Gulamov, M. Yu. Kratenko, *et al.,* Yad. Fiz. **58**, 2005 (1995) [Phys. At. Nucl. **58**, 1896 (1995)].
8. A. S. Botvina, A. S. Iljinov, and I. N. Mishustin, Nucl. Phys. A **507**, 649 (1990); A. S. Botvina *et al.*, Preprint No. 626, IYaI (Institute for Nuclear Research, USSR Acad. Sci., Moscow, 1989).
9. V. S. Barashenkov and V. D. Toneev, *Interaction of High-Energy Particles and Nuclei with Nuclei* (Atomizdat, Moscow, 1972) [in Russian].
10. V. S. Barashenkov, A. S. Iljinov, N. M. Sobolevskiĭ, *et al.,* Usp. Fiz. Nauk **109**, 91 (1973).
11. E. Fermi, Prog. Theor. Phys. **5**, 570 (1950).

*Translated by A. Isaakyan*

Physics of Atomic Nuclei, Vol. 67, No. 4, 2004, pp. 714–718. Translated from Yadernaya Fizika, Vol. 67, No. 4, 2004, pp. 736–740.

## ELEMENTARY PARTICLES AND FIELDS
## Experiment

# Proton Production in $^{16}$O$p$ Collisions at 3.25 GeV/$c$ per Nucleon

**E. Kh. Bazarov, V. V. Glagolev[1], K. G. Gulamov, V. D. Lipin, S. L. Lutpullaev, K. Olimov*, A. A. Yuldashev, B. S. Yuldashev[2], and Kh. Sh. Khamidov[2]**

*Institute for Physics and Technology, Fizika-Solntse Research and Production Association, Uzbek Academy of Sciences, ul. Timiryazeva 2b, Tashkent, 700084 Republic of Uzbekistan*

Received January 16, 2003; in final form, June 18, 2003

**Abstract**—The momentum features of protons originating as fragments from $^{16}$O$p$ interactions at 3.25 GeV/$c$ per nucleon are analyzed for the first time under conditions of $4\pi$ geometry. It is found that the mechanisms of the production of all protons traveling in the forward direction in the rest frame of the fragmenting nucleus (with the exception of evaporated protons) do not depend on either the primary energy or the target-nucleus type, this regularity being quite universal for the formation of such protons. It is shown that there is a strong correlation between the shape of the momentum spectrum of protons appearing as fragments from such interactions, especially slow protons, and the degree of the excitation of the fragmenting nucleus. *© 2004 MAIK "Nauka/Interperiodica".*

## INTRODUCTION

According to present-day theoretical concepts, the formation of the lightest nuclear fragments (nucleons) may occur at all stages of high-energy hadron–nucleus interactions, including an intranuclear cascade, the decay of excited multinucleon fragments, evaporation of an excited nucleus, and the explosive breakup (Fermi breakup) of a thermalized residual nucleus. The interaction of primary particles with intranuclear systems, where the spacings between nucleons are very small (about or less than 1 fm), may in principle lead to the formation of so-called cumulative nucleons—that is, nucleons having momenta that are forbidden by the conventional kinematics of particle scattering on a free nucleon. Reactions involving the absorption of slow product pions or slow resonances by few-nucleon systems may be among mechanisms responsible for the production of relatively energetic nucleons. Such reactions may also lead to the production of cumulative protons if the energy of the absorbed pion or resonance is sufficiently high for this.

It is well known that the inclusive cross section for proton production in hadron–nucleus collisions is commensurate with the inelastic reaction cross section and that the majority of protons from such collisions are formed at the initial stage of the reaction, carrying primary information about the dynamics of the process. Since it is rather easy to identify secondary protons experimentally and to measure their kinematical features, investigations in these realms resulted in accumulating a vast body of data on their inclusive yield in hadron–nucleus collisions at intermediate and high energies and in establishing a number of physical regularities of their production. In particular, it was shown that, at primary momenta in the region $P_0 \geq 4$ GeV/$c$, the multiplicity distribution of protons is independent of primary energy (see, for example, [1–3]) and that their mean multiplicity $\langle n_p \rangle$ is weakly dependent on the primary-particle type and, naturally, on the mass number of the target nucleus [4], the $A$ dependence of $\langle n_p \rangle$ varying with the proton momentum. The multiplicity distribution of protons having momenta in the region $P > 0.2$ GeV/$c$ is satisfactorily described on the basis of a model that assumes that protons formed in hadron–nucleus collisions are products of independent knockout in the rescattering of primary and secondary particles [5–7]. The invariant structure function for protons (including slow, so-called evaporated, protons) is satisfactorily described in terms of a three-exponential dependence [6], this being so both in the case where the kinetic energy is taken for the argument of this function, $f(T)$, and in the case where the square of the total momentum appears as its argument, $f(P^2)$. The spectrum $f(T)$ for protons having momenta in the region $P > 0.2$ GeV/$c$ and traveling within a rather narrow angular interval is satisfactorily described by one exponential function, the slope parameter, which is independent of primary energy, being a function of the proton-emission angle [8].

---

[1] Joint Institute for Nuclear Research, Dubna, Moscow oblast, 141980 Russia.

[2] Institute of Nuclear Physics, Uzbek Academy of Sciences, pos. Ulughbek, Tashkent, 702132 Republic of Uzbekistan.

*e-mail: `olimov@uzsci.net`

1063-7788/04/6704-0714$26.00 © 2004 MAIK "Nauka/Interperiodica"

The majority of the aforementioned and other regularities of the formation of protons (including cumulative protons) were obtained by using an electronic procedure, predominantly in a narrow solid angle of proton emission, this constraining the range of useful information about the dynamics of the process being considered. The remaining data come from tracking instruments used in fixed-target experiments, the impossibility of recording slow ($P < 120$–$140$ MeV/$c$) and identifying fast ($P > 750$–$1250$ MeV/$c$) protons being a serious drawback of such methods. In view of this, it would be of great interest to obtain new experimental data where all charged particles (including slow and, to the maximum possible degree, fast protons) and nuclear fragments would be reliably identified under conditions of $4\pi$ geometry. In this respect, the conditions are the most favorable if a nucleus is taken for a projectile, while a nucleon is taken for a target.

The present study is devoted to exploring the yield of protons in $^{16}Op$ interactions at a momentum of 3.25 GeV/$c$ per projectile nucleon. The experimental data used were obtained by exposing the 1-m hydrogen bubble chamber of the Laboratory for High Energies at the Joint Institute for Nuclear Research (JINR, Dubna) to relativistic $^{16}$O nuclei accelerated at the Dubna synchrophasotron. The data sample subjected to analysis consisted of 11 098 measured $^{16}Op$ events. The homogeneity of the sample and a low density of the working liquid in the chamber made it possible to identify the charges of all secondary particles and fragments unambiguously and to measure their momenta to a high precision. Since the accuracy in determining the kinematical features of fragments depends on the length $L$ of the measured tracks, we will include in our analysis those protons appearing as fragments for which $L > 35$ cm. For such protons, the mean relative error in determining their momenta does not exceed 3.5%. The distribution of singly charged fragments with respect to $x = 1/P$ has three maxima corresponding to the hydrogen isotopes $^1$H, $^2$H, and $^3$H [9]. Positively charged particles of momentum in the range $P =$ 1.75–4.75 GeV/$c$ were identified as protons. For this separation, the admixture of positively charged pions and deuterons among particles that we identified as protons appearing as fragments did not exceed 3 to 4%. Other methodological aspects of our experiment are described in [9–11]. In the following, the momentum and energy features of protons treated as fragments are given in the antilaboratory reference frame—that is, in the reference frame comoving with the oxygen nucleus.

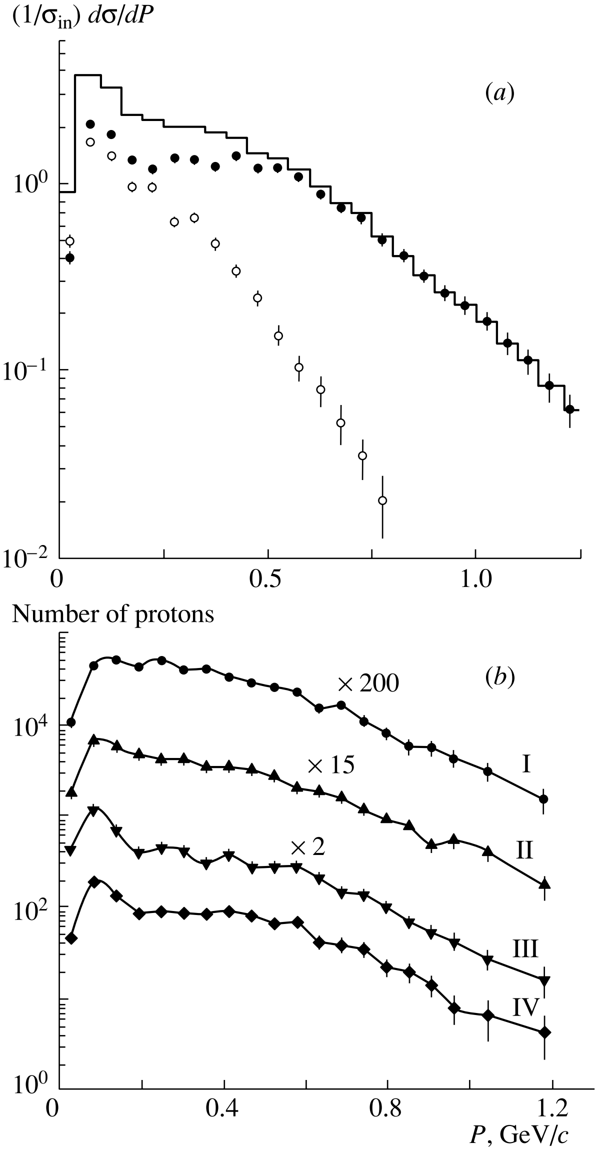

**Fig. 1.** Momentum distributions of protons from $^{16}Op$ interactions: ($a$) distributions for (histogram) all protons, (closed circles) protons traveling in the forward direction, and (open circles) protons traveling in the backward direction; ($b$) distributions for protons from four groups of events (the numbers of the groups are indicated by Roman numerals above each spectrum). Lines are drawn for the clarity of the presentation.

## EXPERIMENTAL DATA AND THEIR DISCUSSION

In analyzing the spectra of the kinematical features of protons appearing as nuclear fragments, use is usually made of their distribution with respect to the kinetic energy $T$. In order to study the structural features of the spectra in the region of low $T$, it is more convenient, however, to represent data in the form of the distribution of protons with respect to the momentum $P$. The experimental semi-inclusive momentum spectra that we obtained for protons emitted into the forward and the backward hemisphere are displayed in Fig. 1*a*. In this figure, the histogram represents the momentum distribution for all protons.

It can be seen that, irrespective of the proton-emission direction, the spectra have maxima in the vicinity of the point $P \approx 80$ MeV/$c$ and a distinct peak in the interval $P = 50$–$150$ MeV/$c$, which corresponds to the kinetic-energy range $T = 5$–$20$ MeV. This range of kinetic energies is peculiar to protons appearing as fragments emitted by an intermediate excited nucleus. In separating the mechanisms responsible for proton production in hadron–nucleus and nucleus–nucleus collisions at high energies, such protons are usually classified as evaporated protons or products of Fermi breakup. It should be emphasized, however, that, in studying the emission of light fragments in $^{16}\mathrm{O}p$ interactions, it was previously shown in [12] that the Fermi breakup model [13] is unable to describe the spectrum of protons in the region $T < 50$ MeV, especially underestimating the yield of slow protons ($T \leqslant 10$ MeV).

The momentum spectrum of protons emitted into the forward hemisphere is rather hard and has a shoulder in the momentum interval $P = 250$–$500$ MeV/$c$; at the same time, the spectrum of protons emitted into the backward hemisphere decreases monotonically in this region. Possibly, this effect is due to a significant distinction between the mechanisms responsible for the production of protons traveling in the forward and in the backward direction. The main contribution to the yield of fast protons emitted into the forward hemisphere comes from intranuclear-cascade processes, which, however, contribute only slightly to the formation of protons emitted into the backward hemisphere. Relatively fast protons emitted into the backward hemisphere, which are referred to as cumulative protons, may be produced, in particular, in the decay of a two-nucleon system in a nucleus via the absorption of a slow pion by this system. The contributions of the evaporation mechanism to the yields of forward and backward produced protons may be considered to be identical [14].

The yield of evaporated particles depends on the mass number of the primary nucleus and on the degree to which it disintegrates. The total charge of multiply charged (multinucleon) fragments may serve as a measure of the degree to which the primary nucleus disintegrates. In this connection, the shape of the momentum spectrum of protons may be expected to be correlated with the total charge of multiply charged fragments ($Z \geq 2$), and this can measure the degree to which the primary nucleus disintegrates. In order to perform such an analysis, the set of relevant events was broken down into four groups, the results obtained via this partition being displayed in Fig. 1*b*, where the Roman numerals I, II, III, and IV correspond to events in which the total charge of multiply charged fragments is less than or equal to 3, 4 and 5, 6, and 7, respectively. For the data to be conveniently arranged within the same panel, the numbers of events in groups I–III were multiplied by factors that are indicated on the respective spectra in Fig. 1*b*.

Figure 1*b* shows that there are distinct correlations between the shape of the proton momentum spectrum, especially in the region $P \leq 250$ MeV/$c$, and the total charge of multiply charged fragments in the final state. For groups I and II, one cannot notice a clear-cut peak in the vicinity of the maximum of the distribution, but such a peak begins to manifest itself for group II, albeit rather slightly. Clear-cut maxima are observed in groups III and IV, the respective peaks in the spectra being quite distinct. The absence of a peak at low momenta for groups I and II may also be due to the dominant contribution of protons formed owing to the intranuclear cascading of the primary particle and secondary particles. Thus, one can state that the shape of the proton momentum spectrum depends, especially for protons of momentum in the region $P < 250$ MeV/$c$, on the degree of the excitation of the fragmenting nucleus.

In the momentum spectrum of protons from groups III and IV, there is a distinct shoulder in the range $P = 250$–$500$ MeV/$c$, a structure similar to that which was observed in the spectrum of forward emitted protons. A similar behavior of the proton momentum spectrum was previously observed in $\pi^{-12}\mathrm{C}$ interactions at 4, 5, and 40 GeV/$c$ [15–19]; in $n^{12}\mathrm{C}$ interactions at 7 GeV/$c$ [19]; in $p^{20}\mathrm{Ne}$ collisions at 300 GeV/$c$ [6]; and in some other cases [20, 21]. This phenomenon, which shows a trend toward a stronger manifestation for relatively light nuclei [22], is caused by the presence of short-range correlations between intranuclear nucleons [20, 23]. In principle, one cannot rule out the possibility that the structure observed in the proton momentum spectrum is due, as was indicated above, to the absorption of slow pions or slow resonances by few-nucleon systems featuring short-range internucleon correlations [24–26].

For all protons in Fig. 2*a* and for protons emitted into the forward and the backward hemisphere in Fig. 2*b*, we display the invariant structure function $f(p) = (E/\sigma_{\mathrm{in}}) d^3\sigma/d\mathbf{p}^3$ versus the proton momentum. The solid curves represent the results obtained by approximating our experimental data by the function

$$f(p) = a_1 \exp(-b_1 p^2) + a_2 \exp(-b_2 p^2) + a_3 \exp(-b_3 p^2). \quad (1)$$

The dashed curves in Fig. 2*a* correspond to the contributions of each individual term in expression (1). It can be seen that the function $f(p)$ for protons is satisfactorily described by the function in (1), the fitted values of the parameters in (1) being given in the table, along with the respective data from [6] for $p^{20}$Ne interactions at 300 GeV/$c$.

By using the fitted parameter values from the table, we have determined the proton fractions described by each of the three terms in (1) for $^{16}Op$ interactions. The results proved to be $27.4 \pm 0.5$, $32.0 \pm 0.6$, and $40.6 \pm 0.7\%$. It follows that, in simulating nuclear-fragmentation processes, the evaporation mechanism of nucleon formation cannot be disregarded even for nuclei as light as $^{16}$O.

From the data presented in the table, we can see the following:

(i) The slope parameter $b_1$ is much greater for $^{16}Op$ than for $p^{20}$Ne interactions. In all probability, this is because of different conditions of slow-neutron detection in a hydrogen and in a neon–hydrogen bubble chamber.

(ii) The value of the slope parameter $b_1$ for protons emitted into the backward hemisphere is approximately 1.3 times as great as that for protons emitted into the forward hemisphere. The reliability of the values obtained for the slope parameters $b_1$ is suggested by the fact that, in response to the change in the proton momentum from $P \approx 25$ MeV/$c$ to $P \approx 250$ MeV/$c$, the value of the first exponential term in expression (1) changes by nearly four orders of magnitude.

(iii) For protons emitted into the forward hemisphere, the value of the slope parameter $b_2$ in $^{16}Op$ interactions agrees within the statistical errors with that for $p^{20}$Ne interactions.

(iv) Also, the values of the slope parameter $b_3$ for protons emitted into the forward hemisphere in the above two types of interactions comply within the statistical errors.

It should be noted that, for protons emitted into the forward hemisphere in $p^{12}$C interactions at 4.2 GeV/$c$ [27], the approximation of the structure function $f(p)$ by expression (1) leads to the value of $b_2 = 10.06 \pm 0.99\,(\text{GeV}/c)^{-2}$ for the second slope parameter, this being in agreement within the statistical errors with the respective values for $^{16}Op$ and $p^{20}$Ne interactions (see table). Unfortunately, we cannot compare the value of the third slope parameter with our data, since protons of momentum in the region $P > 750$ MeV/$c$ could not be identified in the experiment reported in [27]. These results are compatible with the experimental data of Bayukov *et al.* [8], who studied the invariant structure function $f(T)$

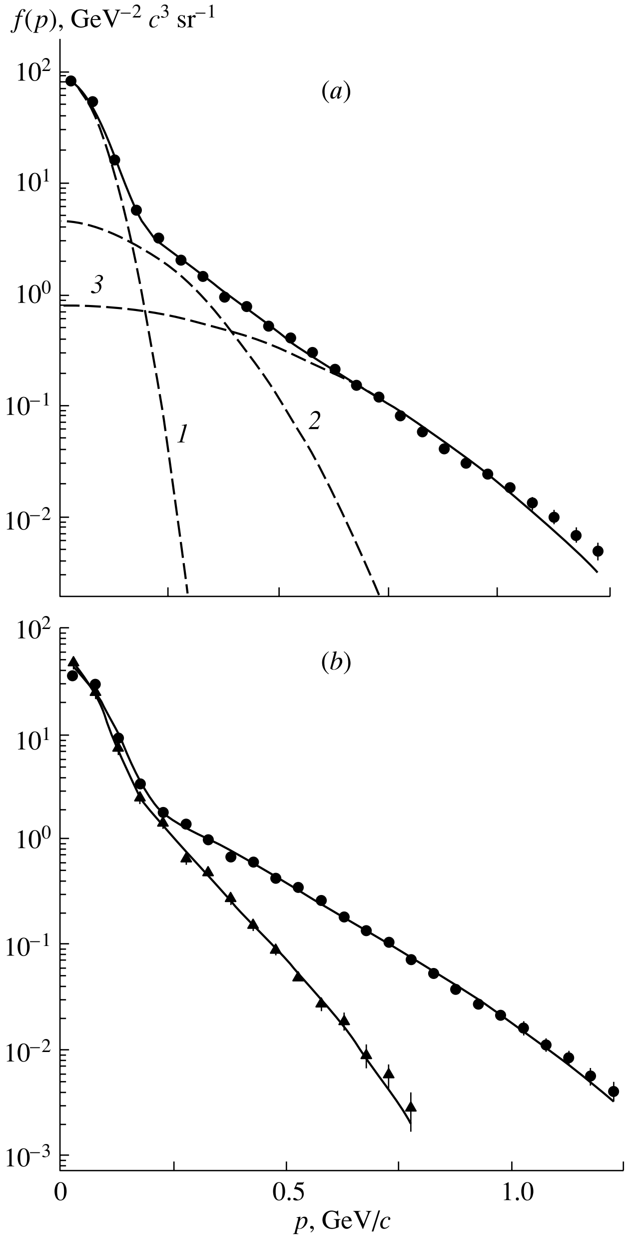

**Fig. 2.** Invariant structure function for protons versus momentum in $^{16}Op$ interactions for (*a*) all protons and (*b*) protons emitted at angles (closed circles) $0° \le \theta_p \le 90°$ and (closed triangles) $90° \le \theta_p \le 180°$. The solid curves represent the results obtained by fitting the three-exponential form in (1) to the data, while the dashed curves *1–3* correspond to the individual contributions of the exponential terms in expression (1).

Fitted values of the parameters in the approximation (1) of the invariant structure function for protons originating from $^{16}Op$ interactions at 3.25 GeV/$c$ per nucleon and $p^{20}$Ne collisions at 300 GeV/$c$ [6]

| Parameters | Interaction type | | | | |
|---|---|---|---|---|---|
| | $^{16}Op$ | | | $p^{20}$Ne | |
| | All protons | Forward emitted protons | Backward emitted protons | All protons | Forward emitted protons |
| $a_1$ | $94.46 \pm 3.47$ | $45.29 \pm 2.17$ | $49.45 \pm 2.88$ | $50.11 \pm 2.44$ | $20.53 \pm 1.63$ |
| $b_1$ | $126.1 \pm 3.8$ | $111.9 \pm 4.1$ | $149.7 \pm 8.4$ | $56.66 \pm 2.61$ | $49.19 \pm 4.29$ |
| $a_2$ | $4.55 \pm 0.30$ | $1.80 \pm 0.13$ | $3.22 \pm 0.46$ | $4.21 \pm 0.42$ | $1.93 \pm 0.43$ |
| $b_2$ | $14.57 \pm 0.91$ | $9.83 \pm 0.99$ | $24.34 \pm 3.91$ | $10.39 \pm 0.92$ | $10.19 \pm 2.41$ |
| $a_3$ | $0.84 \pm 0.07$ | $0.56 \pm 0.09$ | $0.54 \pm 0.24$ | $0.65 \pm 0.11$ | $0.77 \pm 0.15$ |
| $b_3$ | $3.71 \pm 0.12$ | $3.28 \pm 0.19$ | $8.78 \pm 1.23$ | $3.12 \pm 0.18$ | $3.30 \pm 0.19$ |
| $\chi^2$/NDF | 1.35 | 1.12 | 0.72 | 1.41 | 1.01 |

for fast protons ($T > 70$ MeV) emitted at various angles in proton interactions with various nuclei (of mass number ranging between $A = 6$ and $A = 124$) at 7.5 GeV/$c$. It turned out that, at a fixed proton emission angle, the invariant structure function $f(T)$ is satisfactorily described by a single exponential, the respective slope parameter being independent of the mass number of the fragmenting nucleus within the statistical errors.

Thus, we can conclude that the mechanism responsible for the formation of fast protons (especially of those that are emitted into the forward hemisphere) is universal—that is, it does not depend on either the primary energy or the fragmenting-nucleus type.

## REFERENCES

1. S. A. Azimov *et al.*, Nucl. Phys. B **107**, 45 (1976).
2. S. A. Azimov *et al.*, Yad. Fiz. **32**, 1560 (1980) [Sov. J. Nucl. Phys. **32**, 808 (1980)].
3. V. G. Grishin, T. Kanarek, and L. Simich, Preprint No. P1-81-676, OIYaI (Joint Institute for Nuclear Research, Dubna, 1981).
4. A.G.M.T. Collab., Preprint No. 3, FIAN (Lebedev Institute of Physics, USSR Academy of Sciences, Moscow, 1977).
5. B. Andersson, I. Otterlund, and E. Stenlund, Phys. Lett. B **73B**, 343 (1978).
6. M. L. Allaberdin, T. Ya. Inogamova, E. A. Kosonovskiĭ, *et al.,* Yad. Fiz. **39**, 662 (1984) [Sov. J. Nucl. Phys. **39**, 532 (1984)].
7. A. S. Botvina, I. Ya. Chasnicov, A. Sh. Gaitinov, *et al.*, Z. Phys. A **345**, 413 (1993).
8. Yu. D. Bayukov, A. V. Vlasov, V. B. Gavrilov, *et al.,* Preprint No. 5, ITÉF (Institute of Theoretical and Experimental Physics, Moscow, 1985).
9. V. V. Glagolev, K. G. Gulamov, M. Yu. Kratenko, *et al.,* Pis'ma Zh. Éksp. Teor. Fiz. **58**, 497 (1993) [JETP Lett. **58**, 497 (1993)].
10. V. V. Glagolev, K. G. Gulamov, M. Yu. Kratenko, *et al.,* Pis'ma Zh. Éksp. Teor. Fiz. **59**, 316 (1994) [JETP Lett. **59**, 336 (1994)].
11. V. V. Glagolev, K. G. Gulamov, M. Yu. Kratenko, *et al.,* Yad. Fiz. **58**, 2005 (1995) [Phys. At. Nucl. **58**, 1896 (1995)].
12. V. V. Glagolev, K. G. Gulamov, D. Lipin, *et al.,* Yad. Fiz. **62**, 1472 (1999) [Phys. At. Nucl. **62**, 1388 (1999)].
13. A. S. Botvina, A. S. Iljinov, and I. N. Mishustin, Nucl. Phys. A **507**, 649 (1990); A. S. Botvina *et al.*, Preprint No. 626, IYaI AN SSSR (Institute for Nuclear Research, USSR Academy of Sciences, Moscow, 1989).
14. B. S. Aladashvili, A. M. Baldin, V. V. Glagolev, *et al.,* Yad. Fiz. **27**, 704 (1978) [Sov. J. Nucl. Phys. **27**, 377 (1978)]; V. V. Glagolev *et al.,* Soobshch. OIYaI, No. P1-12907 (Dubna, 1983).
15. S. A. Azimov *et al.*, Yad. Fiz. **23**, 987 (1976) [Sov. J. Nucl. Phys. **23**, 519 (1976)].
16. N. I. Angelov *et al.,* Yad. Fiz. **33**, 190 (1981) [Sov. J. Nucl. Phys. **33**, 98 (1981)].
17. S. L. Lutpullaev, A. A. Yuldashev, and B. S. Yuldashev, Dokl. Akad. Nauk UzSSR, No. 3, 27 (1980).
18. P. P. Temnikov and V. A. Shakhbazyan, Preprint No. P1-12139, OIYaI (Joint Institute for Nuclear Research, Dubna, 1979).
19. O. B. Abdinov *et al.*, Preprint No. P1-11820, OIYaI (Joint Institute for Nuclear Research, Dubna, 1978).
20. D. J. Findlay *et al.*, Phys. Lett. B **74B**, 305 (1978).
21. J. W. Geaga *et al.*, Phys. Rev. Lett. **45**, 1993 (1980).
22. M. I. Andreĭchenko *et al.,* Pis'ma Zh. Éksp. Teor. Fiz. **37**, 446 (1983).
23. J. L. Matthers *et al.*, Phys. Rev. Lett. **38**, 8 (1977).
24. T. Nakamura *et al.*, Nucl. Phys. A **365**, 457 (1981).
25. O. B. Abdinov *et al.*, Preprint No. P1-8373, OIYaI (Joint Institute for Nuclear Research, Dubna, 1983).
26. O. B. Abdinov *et al.,* Yad. Fiz. **30**, 396 (1979) [Sov. J. Nucl. Phys. **30**, 204 (1979)].
27. E. N. Kladnitskaya and S. Yu. Sivoklokov, Preprint No. P1-88-412, OIYaI (Joint Institute for Nuclear Research, Dubna, 1988).

*Translated by A. Isaakyan*

*Physics of Atomic Nuclei, Vol. 67, No. 4, 2004, pp. 719–725. Translated from Yadernaya Fizika, Vol. 67, No. 4, 2004, pp. 741–747.*
*Original Russian Text Copyright © 2004 by Dvornikov, Studenikin.*

ELEMENTARY PARTICLES AND FIELDS
Theory

# Parametric Resonance in Neutrino Oscillations in Periodically Varying Electromagnetic Fields

**M. S. Dvornikov*** **and A. I. Studenikin****

*Moscow State University, Vorob'evy gory, Moscow, 119899 Russia*

Received November 6, 2002; in final form, May 23, 2003

**Abstract**—It is shown that a parametric resonance may arise in neutrino oscillations in varying electromagnetic fields. For two types of electromagnetic fields—an amplitude-modulated electromagnetic wave and a transverse magnetic field that is constant in time, but which has an amplitude periodically varying in space—the probabilities of the $\nu_i \leftrightarrow \nu_j$ neutrino transitions are found, and it is shown that the probability amplitudes increase with time for a specific choice of the parameters of external electromagnetic fields. *© 2004 MAIK "Nauka/Interperiodica".*

## INTRODUCTION

Since the theoretical prediction of the possibility of neutrino oscillations in 1958 [1], numerous attempts have been made to discover this phenomenon. Despite considerable advances in clarifying the problem of solar and atmospheric neutrinos (see, for example, the article of Bilenky [2], who considered the present-day status of the problem of neutrino mixing and oscillations), there is still no unambiguous corroboration of the existence of neutrino oscillations.

It is well known that, along with the Mikheev–Smirnov–Wolfenstein effect [3, 4] (and the analog of this effect for the case of spin–flavor neutrino oscillations [5, 6]), there can exist another mechanism of the enhancement of neutrino oscillations, that which is based on the parametric-resonance phenomenon [7–15].

It should be noted that the aforementioned mechanisms of the enhancement of neutrino oscillations differ from each other drastically. In the case of the Mikheev–Smirnov–Wolfenstein effect, the enhancement of the amplitude of neutrino oscillations is due to a specific choice of the parameters that describe neutrinos and external conditions (for example, matter density). It should be emphasized that these parameters are assumed to be constant—or at least slightly varying—along the neutrino path. Thus, one can ensure that the effective mixing angle is close to $\pi/4$ even at a small mixing angle in a vacuum. But in the case of a parametric resonance, the effective mixing angle is not large in general. It is assumed, however, that external parameters, such as the matter density, vary periodically along the neutrino path. The enhancement of the probability of a neutrino transition from one state to another is achieved owing to specific phase relations.

In one of the pioneering studies [16] devoted to the parametric-resonance phenomenon in elementary-particle physics, neutron–antineutron oscillations were studied in a periodically varying magnetic field. Later, the approach formulated in [16] to consider the emergence of a parametric resonance and the method for deriving an approximate solution to the equation describing the evolution of a two-level system were used to study this phenomenon in neutrino oscillations (see, for example, [7]).

The emergence of a parametric resonance in neutrino oscillations in the case of a periodically varying matter density has been repeatedly discussed in the literature. First of all, we would like to recall the study of Ermilova *et al.* [7], who presented an approximate solution to the equation describing the evolution of a neutrino beam propagating through matter whose density varies according to a harmonic law. A numerical simulation of the propagation of a neutrino beam through the Earth's substance of variable density was performed in [8]. For the case of neutrino propagation in a medium of varying density, an analytic solution to the respective equation was found in [9]. However, the effective mixing angle and the effective oscillation length were assumed to be only slightly different from their counterparts in a vacuum. The article of Krastev and Smirnov [10], who studied transitions between neutrino states with allowance for both the Mikheev–Smirnov–Wolfenstein effect and the parametric resonance and who additionally considered some astrophysical applications, is also worthy of note.

The case where the matter density changes abruptly from one constant value to another deserves

---

[*] e-mail: `maxim_dvornikov@aport.ru`

[**] e-mail: `studenik@srd.sinp.msu.ru`

particular attention since the Earth's matter density can be approximated by such a function. It is this case that was recently discussed in [11, 12], where an exact analytic solution to the equation describing the evolution of the system of neutrinos was obtained for a density profile of this type. It was found that only one period and a half of the density variation are sufficient for achieving a sizable probability of a neutrino transition from one state to another. Thus, the results of these investigations are of paramount importance for exploring the propagation of solar and atmospheric neutrinos through the Earth's substance. In this connection, we would also like to mention some recent studies devoted to an analysis of new possibilities that arise owing to the application of the neutrino-tomography method to investigating the distribution of the matter density in the Earth (see [13–15] and references therein).

In the present study, the possibility of the emergence of a parametric resonance in neutrino oscillations in a nonuniform electromagnetic field is considered for the first time. We address the case of an electromagnetic field because, from the point of view of experimentally investigating neutrino oscillations, it is much easier to create an electromagnetic field of preset configuration than to obtain a similar density profile. We consider an amplitude-modulated electromagnetic wave and a magnetic field of the planar-ondulator type—that is, a time-independent transverse magnetic field whose amplitude changes abruptly from one fixed value to another. It is shown that, in the case of an amplitude-modulated electromagnetic wave and in the case of a magnetic field of a planar-ondulator type, a parametric resonance appears for a specific choice of the parameters describing neutrinos, the electromagnetic field, and matter. The possibility of the emergence of a parametric resonance in cosmic microwave radiation is assessed. The scheme of a possible experiment aimed at studying neutrino oscillations under laboratory conditions is proposed.

## 1. NEUTRINO OSCILLATIONS IN THE FIELD OF AN ELECTROMAGNETIC WAVE

First, we consider a parametric resonance in the field of an amplitude-modulated electromagnetic wave. Our consideration is based on the evolution of the system of two neutrinos $\nu = (\nu_{j+}, \nu_{i-})$ corresponding to different helicity states and occurring in the field of an electromagnetic wave characterized by a frequency $\omega$ and a circular polarization. We note that the $(\nu_{j+}, \nu_{i-})$ states can in principle belong to different neutrino generations (for $i \neq j$). We denote by $\mathbf{e}_3$ the axis that is parallel to the direction of neutrino motion and by $\phi$ the angle between $\mathbf{e}_3$ and the direction of wave propagation. In order to describe the evolution of this system, it is necessary to use the relativistically invariant approach developed in [17].

The dynamical equation describing the evolution of $\nu$ can be written in the form of the Schrödinger equation

$$i\frac{\partial \nu}{\partial t} = H\nu. \tag{1}$$

The expression for the Hamiltonian $H$ is derived, as in [17, 18], on the basis of an expansion in terms of the small parameter $\sqrt{1-\beta^2} \ll 1$ ($\beta$ is the neutrino velocity). This yields

$$H = -\tilde{\rho}\sigma_3 - A(t)(\sigma_1 \cos\psi - \sigma_2 \sin\psi), \tag{2}$$

where $A(t) = -\mu B(t)(1 - \beta\cos\phi)$, with $B(t)$ being the wave amplitude, which, in our case, depends on time; $\psi = g\omega t(1 - (\beta/\beta_0)\cos\phi)$ is the wave phase depending on the wave velocity $\beta_0$ in a medium ($\beta_0 \leq 1$), the quantities $g = \pm 1$ corresponding to two wave-polarization states; $\mu$ is the neutrino magnetic moment; $\tilde{\rho} = V_{\text{eff}}/2 - \Delta m^2\Theta/(4E)$ {here, $E$ is the neutrino energy, $\Delta m^2$ is the difference of the masses squared between the $\nu_j$ and $\nu_i$ states, $V_{\text{eff}}$ is the difference of the effective potentials describing neutrino interaction with the medium, and $\Theta$ is a function of the vacuum mixing angle $\theta_{\text{vac}}$ (the explicit form of $\Theta$ for various types of $\nu_{i-} \leftrightarrow \nu_{j+}$ transitions can be found, for example, in [19])}; and $\sigma = (\sigma_1, \sigma_2, \sigma_3)$ are the Pauli matrices. Here, we use the natural system of units where $c = \hbar = 1$.

For an arbitrary form of the function $B(t)$, serious mathematical difficulties hinder attempts at obtaining an analytic solution to Eq. (1). In view of this, we will derive conditions under which a parametric resonance emerges in the case where the function $B(t)$ differs only slightly from a constant $B$ (the case of an amplitude-modulated electromagnetic wave); that is,

$$B(t) = B(1 + hf(t)), \tag{3}$$

where $h$ is a small ($|h| \ll 1$) constant (its sign will be fixed below) and $f(t)$ is an arbitrary bounded function of time.

For the ensuing investigation, it is convenient to introduce an evolution operator $V(t)$ that relates the state $\nu(t)$ of a neutrino at an instant $t$ to its initial state $\nu(0)$: $\nu(t) = V(t)\nu(0)$. By using the Hamiltonian in the form (2) and the time dependence of the field amplitude in the form (3), we find that $V(t)$ satisfies the equation

$$\begin{aligned} \dot{V}(t) = i[\tilde{\rho}\sigma_3 + (A + \varepsilon f(t)) \\ \times (\sigma_1\cos\psi - \sigma_2\sin\psi)]V(t), \end{aligned} \tag{4}$$

where $\varepsilon = Ah$ and $A = -\mu B(1 - \beta \cos \phi)$. We seek a solution to Eq. (4) in the form

$$V(t) = U_{\mathbf{e}_3}(t) U_{\mathbf{l}}(t) F(t), \qquad (5)$$

where $U_{\mathbf{e}_3}(t) = \exp(i\sigma_3 \dot{\psi} t/2)$ is the operator of rotation about the axis $\mathbf{e}_3$, while $U_{\mathbf{l}}(t) = \exp(i\sigma \mathbf{l} t)$ is the operator of rotation about the axis $\mathbf{l} = (A, 0, \tilde{\rho} - \dot{\psi}/2)$. Everywhere, we use the basis vectors $\mathbf{e}_{1,2,3}$, the vector $\mathbf{e}_3$ being the unit vector aligned with the neutrino velocity. We note that $U_0(t) = U_{\mathbf{e}_3}(t) U_{\mathbf{l}}(t)$ is a solution to Eq. (4) at $\varepsilon = 0$ (see [17]). For an unknown operator $F(t)$, the use of Eq. (4) leads to the equation

$$\dot{F}(t) = i\varepsilon H_\varepsilon(t) F(t), \qquad (6)$$

where

$$H_\varepsilon(t) = (\sigma \mathbf{y}(t)) f(t), \quad y_1 = 1 - 2n_3^2 \sin^2(\Omega t), \qquad (7)$$
$$y_2 = n_3 \sin(2\Omega t), \quad y_3 = 2n_1 n_3 \sin^2(\Omega t),$$

and $\mathbf{n} = n_1 \mathbf{e}_1 + n_2 \mathbf{e}_2 + n_3 \mathbf{e}_3 = \mathbf{l}/\Omega$ is a unit vector ($\Omega = |\mathbf{l}|$).

In order to investigate solutions to Eq. (6), we apply the method developed in [18]. By using the smallness of the parameter $\varepsilon$, we will seek a solution to Eq. (6) in the form

$$F = \sum_{k=0}^{\infty} \varepsilon^k F^{(k)}, \qquad (8)$$

where $F^{(0)} = \hat{1}$ is an identity matrix. For the operators $F^{(k)}$, we derive the recursion relation

$$F^{(k+1)}(t) = i \int_0^t H_\varepsilon(\tau) F^{(k)}(\tau) d\tau. \qquad (9)$$

Omitting the details of the calculations, we will present the result that is obtained for $F$ on the basis of (8) and (9). To terms linear in $\varepsilon$, we have

$$F(t) = \hat{1} + i\varepsilon(\sigma \mathbf{x}(t)) + O(\varepsilon^2), \qquad (10)$$

where

$$\mathbf{x}(t) = \int_0^t \mathbf{y}(\tau) f(\tau) d\tau. \qquad (11)$$

We note that the analogous approach to describing neutrino oscillations in a medium of periodically varying density was discussed in [20].

For the probability of $\nu_{i-} \leftrightarrow \nu_{j+}$ neutrino transitions, the application of formulas (5)–(11) yields

$$P(t) = \left| \langle \nu_{j+} | U_{\mathbf{e}_3}(t) U_{\mathbf{l}}(t) F(t) | \nu_{i-} \rangle \right|^2 \qquad (12)$$
$$= n_1^2 \sin^2(\Omega t) + 2\varepsilon n_1 \sin(\Omega t)(x_1(t) \cos(\Omega t)$$
$$+ n_3 x_2(t) \sin(\Omega t)).$$

For the purposes of the ensuing investigation, we specify the form of the function $f(t)$. It was indicated in [11] that there is some analogy between the process of neutrino oscillations and mechanical vibrations. On the basis of this fact, we chose the function $f(t)$ in the same form as in the analogous problem of a parametric resonance in mechanical vibrations [21]; that is, $f(t) = \sin(2\Omega t)$. We note that $\Omega$ is a natural frequency of a two-level vibrational system. As will be seen below, it is precisely for this choice of the function $f(t)$—that is, in the case where the frequency of $f(t)$ is twice as high as the natural frequency—that a parametric resonance manifests itself.

Let us find the probability of neutrino transitions for this specific choice of $f(t)$. After some simple algebra, we arrive at

$$P(t) = \Bigg[ n_1^2 + \varepsilon n_1 n_3^2 t \qquad (13)$$
$$+ \frac{\varepsilon n_1}{\Omega} \left( 1 - \frac{n_3^2}{2} \right) \sin(2\Omega t) \Bigg] \sin^2(\Omega t).$$

Here, we choose the sign of $\varepsilon$ in such a way that $n_1 \varepsilon > 0$ (hence, the sign of $h$ is determined by the relation $n_1 A h > 0$). In the bracketed expression on the right-hand side of (13), there then appears a term that grows linearly with time and which leads to an increase in the transition probability. This result can be interpreted as a manifestation of a parametric resonance.

We note that, from relation (13), it formally follows that, at rather large values of the observation time $t$, the transition probability $P(t)$ may exceed unity. In this connection, we recall that, in studying the phenomenon of a parametric resonance in mechanics, the amplitude of vibrations is an analog of the transition probability. The respective approach in mechanics is known to be applicable only at comparatively small amplitudes of vibrations. In accordance with the physical meaning of our solution, we can therefore conclude that, as in the case of mechanical vibrations, relation (13) is valid for a relatively small (say, about 10%) enhancement of the transition probability. Unfortunately, the qualitative description proposed here for a parametric resonance gives no way to investigate the exact behavior of the transition probability near a value of unity. However, the numerical simulation performed in [7] for the case of the parametric resonance arising in the process of neutrino interaction with a medium of periodically varying density showed that the transition probability asymptotically tends to unity, so that the condition $P(t) \leq 1$ always holds.

Let us estimate the characteristic time within which a neutrino can go over from one type to another with a probability of 10%. From relation (13), we obtain

$$t_c \sim 0.1(\varepsilon n_1). \tag{14}$$

Here, we assumed that $n_3^2 \sim 1$. This choice of the parameters will be explained below.

For the sake of comparison, we present the expression for the transition probability in the case where there is no additional excitation ($h = 0$); that is,

$$P(t)|_{h=0} = \sin^2(2\theta_{\text{eff}}) \sin^2\left(\frac{\pi t}{L_{\text{eff}}}\right), \tag{15}$$

where $L_{\text{eff}} = \pi/\Omega$ is the effective length of oscillations and $\sin^2(2\theta_{\text{eff}}) = l_1^2/(l_1^2 + l_3^2) = P_{\max}|_{h=0}$ is the maximum transition probability in the absence of additional excitations. In studying a parametric resonance, the case where $P_{\max}|_{h=0} \ll 1$—that is, the case where there are virtually no transitions between the two neutrino states (this corresponds to $n_3^2 \sim 1$)—is of particular interest. Choosing the specific case where

$$|l_1| = 0.1|l_3|, \tag{16}$$

we find that $P_{\max}|_{h=0} \approx 0.01$—that is, the transition probability cannot exceed 1% at any value of the observation time. In the case where there is an additional excitation ($h \neq 0$), the presence of the term proportional to $t$ in the expression for the transition probability makes it possible to reach values exceeding 1%.

Let us estimate the value of $x_c = t_c$ for the case specified by (16). Setting $|h| = 0.1$, we obtain

$$x_c \sim \frac{10}{|\mu B(1 - \beta\cos\phi)|}. \tag{17}$$

We note that, if the parameters describing the external electromagnetic field, the medium, and neutrinos are chosen in such a way as to correspond to relation (16), the first and the third term in (13) can be disregarded since they are much smaller than the second term. Indeed, we have

$$n_1^2 \approx 0.01; \quad |\varepsilon n_1 n_3^2 t_c| \approx 0.1;$$

$$\left|\frac{\varepsilon n_1}{\Omega}\left(1 - \frac{n_3^2}{2}\right)\sin(2\Omega t_c)\right| \approx 4 \times 10^{-4}.$$

Thus, the enhancement of the transition probability is due precisely to the parametric resonance.

## 2. NEUTRINO OSCILLATIONS IN THE FIELD OF A PLANAR ONDULATOR

Let us now consider neutrino oscillations in a magnetic field of the planar-ondulator type. The dynamical equation describing the evolution of $\nu$ is identical to Eq. (1). The expression for the Hamiltonian $H$ can be formally derived from relation (2) by making the substitutions $A(t) \to \mu B(t)$ and $\omega = 0$. The resulting expression can be written as

$$H = -\tilde{\rho}\sigma_3 - \mu B(t)\sigma_1. \tag{18}$$

It was mentioned above that, in the case of a planar ondulator, the amplitude of the magnetic field is a periodic function; that is,

$$B(t) = \begin{cases} B_1, & 0 \le t < T_1, \\ B_2, & T_1 \le t < T_1 + T_2, \end{cases} \tag{19}$$

$$B(t + T) = B(t), \quad T = T_1 + T_2, \tag{20}$$

where $B_{1,2}$ are constants. It is obvious that the Hamiltonian $H(t)$ is also a periodic function that has the same period $T$: $H(t + T) = H(t)$. Additionally, $H(t) = H_1$ if $t \in [0, T_1]$ and $H(t) = H_2$ if $t \in [T_1, T]$, where $H_{1,2}$ are constant operators. By $U_{1,2}$, we denote the evolution operators for the intervals $[0, T_1]$ and $[T_1, T]$, respectively. From the aforesaid, it can easily be seen that

$$U_a = \exp(-iH_a T_a), \quad a = 1, 2. \tag{21}$$

Hence, the evolution operator per period has the form

$$U_T = U_2 U_1. \tag{22}$$

We introduce unit vectors as

$$\begin{aligned} \mathbf{n}_a &= \frac{1}{\omega_a}(E_a, 0, -\tilde{\rho}) \\ &= (\sin 2\theta_a, 0, -\cos(2\theta_a)), \quad a = 1, 2, \end{aligned} \tag{23}$$

where $E_a = -\mu B_a$; $\omega_a = \sqrt{\tilde{\rho}^2 + E_a^2}$; and $\theta_a$ is the effective mixing angle, which takes into account the effect of the medium and of the magnetic field. By using formulas (19)–(23), we obtain the evolution operator per period in the form

$$U_T = Y - i(\sigma\mathbf{X}) = \exp(-i(\sigma\mathbf{n}_X)\Phi), \tag{24}$$

where

$$\begin{gathered} Y = c_1c_2 - (\mathbf{n}_1 \cdot \mathbf{n}_2)s_1s_2, \\ \mathbf{X} = s_1c_2\mathbf{n}_1 + s_2c_1\mathbf{n}_2 - (\mathbf{n}_1 \times \mathbf{n}_2)s_1s_2, \\ \Phi = \arcsin X = \arccos Y, \quad \mathbf{n}_X = \mathbf{X}/X, \\ X = |\mathbf{X}|. \end{gathered} \tag{25}$$

Here, we have also used the notation

$$s_a = \sin\phi_a, \quad c_a = \cos\phi_a, \quad \phi_a = \omega_a T_a, \quad a = 1, 2. \tag{26}$$

We note that $Y^2 + \mathbf{X}^2 = 1$ since $U_T$ is a unitary operator. We rewrite the vector $\mathbf{X}$ in terms of the components as

$$\mathbf{X} = \left( \frac{s_1 c_2 E_1}{\omega_1} + \frac{s_2 c_1 E_2}{\omega_2}, \tilde{\rho} \frac{s_1 s_2}{\omega_1 \omega_2} \times (E_2 - E_1), -\tilde{\rho} \left( \frac{s_1 c_2}{\omega_1} + \frac{s_2 c_1}{\omega_2} \right) \right). \quad (27)$$

The evolution operator over $n$ periods can be obtained by raising the operator $U_T$ to the power $n$:

$$U_{nT} = \exp(-i(\sigma \mathbf{n}_X) n \Phi). \quad (28)$$

The probability of a transition from the $\nu_{i-}$ state to the $\nu_{j+}$ state within the time $t$ is determined by the explicit form of the evolution operator:

$$P(t) = |\langle \nu_{j+} | U(t) | \nu_{i-} \rangle|^2. \quad (29)$$

Let us consider the case of $t = nT$. Taking into account formulas (24)–(26) and (28), we find from the general formula (29) that $P(t = nT)$ has the form

$$P(nT) = \frac{X_1^2 + X_2^2}{X_1^2 + X_2^2 + X_3^2} \sin^2(n\Phi) = \frac{X_1^2 + X_2^2}{X_1^2 + X_2^2 + X_3^2} \sin^2 \left( \Phi \frac{t}{T} \right). \quad (30)$$

Expression (30) is similar to the formula for the transition probability in the case of oscillations in a constant magnetic field. However, there is an important distinction: in the case of a constant field, the factor in front of the sine does not exceed $\sin^2(2\theta_a)$, which is in general small. In the case where $B_1 \neq B_2$, the relevant parameters can be chosen in such a way that the factor in front of the sine reduces to unity. This is a manifestation of the parametric-resonance phenomenon. To demonstrate this, we set

$$X_3^2 = \tilde{\rho}^2 \left( \frac{s_1 c_2}{\omega_1} + \frac{s_2 c_1}{\omega_2} \right)^2 = 0. \quad (31)$$

In this way, we do indeed arrive at the situation where the transition probability may reach a value of unity at some instants of time (see below).

Let us consider the situation where

$$(\mu B_a)^2 = E_a^2 \ll \tilde{\rho}^2 \quad (32)$$

(this is the case of a rather weak magnetic field), which is of interest for a possible experimental investigation of neutrino oscillations. By using relation (32), we then find that, in this case, $\tilde{\rho} \neq 0$ and formula (31) is equivalent to the condition

$$\phi_1 + \phi_2 = \pi k, \quad k \in N. \quad (33)$$

By $\Omega$, we denote the mean frequency of oscillations:

$$\Omega = \frac{\omega_1 T_1 + \omega_2 T_2}{T}. \quad (34)$$

The resonance condition (33) then reduces to the form

$$\omega_B = 2\Omega / k, \quad (35)$$

where $\omega_B = 2\pi/T$ is the frequency of variations of the magnetic-field amplitude. Formula (35) reflects the well-known property of a parametric resonance: it is excited in the case where the doubled natural frequency $2\Omega$ is an integral multiple of the frequency $\omega_B$ of variations of a parameter that characterizes the vibrational system [21].

Let us discuss expression (30) for the transition probability in more detail. If the resonance condition (33) is valid, the square of the absolute value of the vector $\mathbf{X}$ can be written in the form

$$\mathbf{X}^2_{\text{res}} = \frac{1}{\tilde{\rho}^2} (s_1^2 E_1^2 + s_2^2 E_2^2 + 2 s_1 E_1 s_2 E_2 (-1)^k). \quad (36)$$

By means of a procedure similar to that in [11], one can show that

$$\phi_a = \pi/2 + \pi k_a, \quad a = 1, 2, \quad (37)$$

where $k_a \in Z$, the additional condition $k_1 + k_2 \geq 0$ being valid, which follows from (33). Taking into account formulas (32) and (37), we find from (36) that

$$|\mathbf{X}|_{\text{res}} = \left| \frac{E_1 - E_2}{\tilde{\rho}} \right| \ll 1. \quad (38)$$

From formulas (38) and (25), it follows that $\Phi_{\text{res}} \approx |\mathbf{X}|_{\text{res}}$. If the resonance condition (33) holds, we have the following result for the transition probability:

$$P(t = nT) = \sin^2 \left( n \frac{(E_1 - E_2)}{\tilde{\rho}} \right) = \sin^2(2n(\theta_1 - \theta_2)). \quad (39)$$

Here, we have assumed that $\theta_a \ll 1$; therefore, $\sin(2\theta_a) \approx 2\theta_a$. We note that $|\tilde{\rho}| = \pi k/T$, whence it follows that expression (39) can be rewritten in the form

$$P(t = nT) = \sin^2 \left( \frac{(E_1 - E_2)}{\pi k} t \right). \quad (40)$$

It can be seen from formula (40) that the maximum enhancement of oscillations is achieved at $k = 1$. This result, which is also well known in the theory of a parametric resonance in mechanical vibrations [21], highlights once again that the construction of corresponding analogies is legitimate.

## CONCLUSION

In conclusion, we will discuss the possibility of the emergence of a parametric resonance in some periodically varying electromagnetic fields. We will now estimate the quantity $x_c$ (the characteristic distance over which a neutrino can go over from one state to another with a probability of 10%) for neutrino oscillations in the field of cosmic microwave radiation. We assume that this radiation is amplitude-modulated, in which case the application of the approach developed in Section 1 is legitimate. We can see from (17) that the most realistic values of $x_c$ are obtained if the neutrino moves in antiphase to the electromagnetic wave (at $\phi = \pi$). In this case, the electromagnetic-wave amplitude $B$ can reach a strength of $10^{-6}$ G [17]. Setting $\mu \approx 10^{-10}\mu_{\mathrm{B}}$, we find that $x_c$ is about $10^{20}$ m, which is commensurate with the galaxy size of $R_G \approx 3 \times 10^{20}$ m. Thus, we can conclude that, in this case, a parametric-resonance-induced transition of a neutrino from one state to another becomes noticeable.

Let us now discuss a possible experiment aimed at studying neutrino oscillations under laboratory conditions through the observation of a 10% decrease in the intensity of the primary neutrino beam. This experiment could consist in transmitting a neutrino beam through a chain of solenoids generating an oppositely directed magnetic field that is constant in time. In this case, it would therefore be necessary to use the results presented in Section 2 of this article, where we studied neutrino oscillations in a magnetic field of the planar-ondulator type. We consider transitions between states belonging to different generations—for example, $\nu_{e-} \leftrightarrow \nu_{\mu+}$. In this situation, we can neglect the effects of neutrino interaction with medium particles—that is, $|\tilde{\rho}| \approx \Delta m^2 \Theta/(4E)$, which is natural for experimental investigations into neutrino oscillations under terrestrial conditions. We assume that $T_1 = T_2 = D$. From relation (35), we then obtain the following expression for $D$:

$$D = \frac{2\pi k E}{\Delta m^2 \Theta}. \tag{41}$$

It was mentioned above that, in order to obtain the maximum enhancement of oscillations, it is necessary to set $k = 1$. Assuming that $\Delta m^2 = 10^{-2}$ eV$^2$, $E = 10^4$ eV, and $\theta_{\mathrm{vac}} = 0$, we obtain $D \approx 1$ m. Further, we set $B_1 = -B_2 = B$, in which case formula (39) reduces to the form

$$P(nT) = \sin^2(4n\theta), \tag{42}$$

where

$$2\theta = \mu B \Big/ \left(\frac{\Delta m^2}{4E}\right).$$

Setting $\mu = 10^{-10}\mu_{\mathrm{B}}$ and $B = 10^7$ G, we obtain $2\theta \approx 2.3 \times 10^{-5}$. It follows that the transition probability can be represented in the form

$$P(nT) \approx \sin^2(4.6 \times 10^{-5} n). \tag{43}$$

It can be seen from formula (43) that, at $n \approx 7000$, the probability reaches the desired value.

The above estimates show that, at present, the proposed experiment to study neutrino oscillations under laboratory conditions can hardly be realized.[1] However, the characteristic dimensions obtained for the proposed experimental setup, $L = 2nD \approx 14$ km, inspire the hope that, in the future, the development of experimental techniques will make it possible to approach the realization of a similar experiment.

## REFERENCES

1. B. M. Pontecorvo, Zh. Éksp. Teor. Fiz. **34**, 247 (1958) [Sov. Phys. JETP **7**, 172 (1958)].
2. S. M. Bilenky, hep-ph/0205047.
3. L. Wolfenstein, Phys. Rev. D **17**, 2369 (1978).
4. S. P. Mikheev and A. Yu. Smirnov, Yad. Fiz. **42**, 1441 (1985) [Sov. J. Nucl. Phys. **42**, 913 (1985)].
5. E. Akhmedov, Phys. Lett. B **213**, 64 (1988).
6. C.-S. Lim and W. Marciano, Phys. Rev. D **37**, 1368 (1988).
7. V. K. Ermilova, V. A. Tsarev, and V. A. Chechin, Kratk. Soobshch. Fiz., No. 5, 26 (1986).
8. V. K. Ermilova, V. A. Tsarev, and V. A. Chechin, Pis'ma Zh. Éksp. Teor. Fiz. **43**, 353 (1986) [JETP Lett. **43**, 453 (1986)].
9. E. Kh. Akhmedov, Yad. Fiz. **47**, 475 (1988) [Sov. J. Nucl. Phys. **47**, 301 (1988)].
10. P. I. Krastev and A. Yu. Smirnov, Phys. Lett. B **226**, 341 (1989).
11. E. Akhmedov, Nucl. Phys. B **538**, 25 (1999); hep-ph/9805272.
12. S. Petcov, Phys. Lett. B **434**, 321 (1998); **444**, 584(E) (1998); hep-ph/9805262; M. Chizhov and S. Petcov, Phys. Rev. Lett. **83**, 1096 (1999); hep-ph/9903399; Phys. Rev. D **63**, 073003 (2001); hep-ph/9903424.
13. T. Ohlsson and H. Snellman, Phys. Lett. B **474**, 153 (2000); **480**, 419(E) (2000); hep-ph/9912295.
14. T. Ohlsson and W. Winter, Phys. Lett. B **512**, 357 (2001); hep-ph/0105293; Europhys. Lett. **60**, 34 (2001); hep-ph/0111247.
15. A. Ioannisian and A. Smirnov, hep-ph/0201012.
16. G. D. Pusch, Nuovo Cimento A **74**, 149 (1983).

---

[1] Presently, constant magnetic fields employed in accelerator techniques can reach strengths of about $10^5$ G.

17. A. M. Egorov, A. E. Lobanov, and A. I. Studenikin, in *New Worlds in Astroparticle Physics*, Ed. by A. Mourao, M. Pimento, and P. Sa (World Sci., Singapore, 1999); hep-ph/9902447; Phys. Lett. B **491**, 137 (2000); hep-ph/9910476; A. Studenikin, hep-ph/0205200.
18. M. S. Dvornikov and A. I. Studenikin, Yad. Fiz. **64**, 1705 (2001) [Phys. At. Nucl. **64**, 1624 (2001)].
19. G. G. Likhachev and A. I. Studenikin, Zh. Éksp. Teor. Fiz. **108**, 769 (1995) [JETP **81**, 419 (1995)]; Grav. Cosm. **1**, 22 (1995).
20. P. M. Fishbane and S. G. Gasiorowicz, Phys. Rev. D **64**, 113017 (2001); hep-ph/0012230.
21. L. D. Landau and E. M. Lifshits, *Mechanics* (Nauka, Moscow, 1965; Pergamon, Oxford, 1976).

*Translated by A. Isaakyan*

Physics of Atomic Nuclei, Vol. 67, No. 4, 2004, pp. 726–742. Translated from Yadernaya Fizika, Vol. 67, No. 4, 2004, pp. 748–763.
Original Russian Text Copyright © 2004 by Kasatkin, Kirichenko.

## ELEMENTARY PARTICLES AND FIELDS
## Theory

# Field-Theory Approach to the Disintegration of Bound Systems on the Basis of a Local Gauge Nature of an Electromagnetic Field

**Yu. A. Kasatkin**[1)]* **and I. K. Kirichenko**

*Ukrainian Engineering and Pedagogical Academy, Kharkov, Ukraine*

Received April 25, 2003

**Abstract**—An approach is developed that makes it possible to take into account the structure of bound (nonlocal) matter fields in photodisintegration processes with allowance for the requirements of the fundamental principles of covariance and gauge invariance. The approach is based on employing the local $U(1)$ gauge nature of an electromagnetic field, whose vector potential is identified with a connection that performs a parallel transportation of matter-field operators in a fiber space with an interior charge symmetry along “minimum” trajectories. © *2004 MAIK “Nauka/Interperiodica”*.

## 1. INTRODUCTION

The calculation of Green’s functions—that is, vacuum expectation values of chronologically ordered products of interacting fields—is the basic problem of quantum field theory. The use of functional methods permits combining all Green’s functions into a generating functional, while the application of the reduction technique makes it possible to establish relations between Green’s functions and their contributions to the respective element of the $S$ matrix. This modern approach to deriving matrix elements for various processes is based on the use of Lagrangians for interacting fields.

In contrast to what occurs in QED, the above scheme becomes inapplicable in dealing with photon–nucleus interaction, since nuclei are strongly bound composite systems, so that it is impossible to formulate explicitly a Lagrangian that would describe the breakup of such a composite system into its constituents and, hence, to include an electromagnetic field in the respective Lagrangian by going over to covariant derivatives.

At present, there are no adequate theoretical approaches that could be used to study electromagnetic-field interaction with structural matter fields and which are based, as QED, on fulfillment of the fundamental principles of covariance, gauge invariance, and spacetime uniformity. As a result, reaction mechanisms that are unknown because of the incompleteness of the theoretical pattern are usually supplemented with not very well validated ad hoc assumptions in describing and analyzing such processes, and this leads to an unjustifiable overestimation of the contributions from some exotic mechanisms.

In the present study, we propose a theoretical approach within which the problem formulated above is solved without explicitly writing a Lagrangian for a composite system. In developing this approach, it is only assumed that two- and three-body Green’s functions for interacting fields are known from the outset as solutions to the relativistic Bethe–Salpeter equation or as solutions to quasipotential equations. It will be shown that this is sufficient for constructing the total amplitude for the process being considered (irrespective of the details of the electromagnetic structure of our strongly bound composite system), the requirements of covariance and gauge invariance being satisfied in its matrix element if intranuclear dynamics is taken consistently into account.

On the basis of the local gauge nature of an electromagnetic field and its geometric interpretation in terms of the operator of a parallel transportation of matter fields in a fiber space that possesses interior charge symmetry and where the Abelian gauge group $U(1)$ is defined, two- and three-point Green’s functions [1] for matter fields are introduced in such a way that they are invariant under the transformations of this group [2].

For particles of spin 0 and 1/2, the functional derivatives of modified two- and three-point Green’s functions with respect to the gauge-field vector potential $A_\mu(r)$, which implements a parallel transportation in the space featuring interior symmetry along the minimum trajectory $r(\lambda) = (1-\lambda)x + \lambda y$ ($\lambda \in [0;1]$) between the points at which the field operators $\Psi(x)$ and $\bar{\Psi}(y)$ are defined, make it possible to introduce, in the momentum representation, electromagnetic current vertices that describe

---

[1)] Kharkov Institute for Physics and Technology, Akademicheskaya ul. 1, Kharkov, 61108 Ukraine.

[*] e-mail: `kasatkin@itl.net.ua`

electromagnetic-field interaction with sources [2–4]. Similar manipulations for the total three-point Green's function (which involves the respective vertex operator, external legs, and two-point Green's functions) generate a gauge-invariant series for the four-point Green's function, this series consisting of the sum of three single-particle-reducible four-point Green's functions (pole part) related by crossing symmetry and a strongly connected (single-particle-irreducible) four-point Green's function (regular part).

As a consequence of the principles of local gauge invariance and spacetime uniformity, fulfillment of Ward–Takahashi identities for the functional derivatives of Green's functions is ensured, which eventually leads to the exact conservation of the electromagnetic current of the bound system being considered with allowance for its structure and its subsequent decay into constituents, irrespective of the explicit functional form used for the vertex operator. This property of the series obtained for four-point Green's functions and the subsequent application of the reduction technique to this series make it possible to establish a relation between it and the respective $S$-matrix element and to employ, in performing a numerical analysis, solutions to various quasipotential equations and to the exact Bethe–Salpeter equation for the vertex operator.

In this connection, the concept of taking into account the contribution of meson-exchange currents is treated in a novel way. Since a vertex function is a solution to a quasipotential equation whose potential is formed owing to exchanges of various mesons—in the vertex operator, this is eventually manifested in the degree of its decrease and in the character of the curvature of a curve—the further use of the vertex operator in the amplitude obtained on the basis of the requirement of invariance under the transformations of the local gauge group leads to automatically taking into account all meson exchanges via the pole and the regular part of the total amplitude. Indeed, the pole part of the amplitude is determined by the absolute values of the vertex function at each specific value of its argument, while the regular part is controlled, owing to the presence of the derivative of the vertex operator in it, by the angle of slope of the tangent. Therefore, such "inclusion" of virtual (unobservable) meson exchanges is implemented via the vertex operator and is strictly balanced with respect to taking into account single-particle (pole) and multiparticle (regular) mechanisms of the process being considered, the requirement of total-electromagnetic-current conservation being rigorously respected.

It is important to note that, in view of the condition of $S$-matrix unitarity, the partition of diagrams into gauge-closed classes obtained at the level of allowing for single-particle (generalized pole series) and multiparticle (one-loop series and so on) mechanisms may be considered, because of the absence of perturbation theory in the strong-interaction coupling constant, as a hierarchy of taking into account loop-mechanism contributions that is consecutively refined with respect to the generalized pole series that is based on a local gauge invariance. The scheme of the argument is as follows. At the level of a single-particle intermediate state, the conditions of $S$-matrix unitarity and of local gauge invariance lead to the appearance of a generalized pole series of reaction mechanisms, where, in addition to the pole (single-particle) mechanisms, multiparticle mechanisms (regular part of the amplitude) are effectively taken into account, which, taken together, ensure the exact electromagnetic-current conservation, $q_\mu J_\mu^{\mathrm{tot}} = q_\mu[J_\mu^{\mathrm{pol}} + J_\mu^{\mathrm{reg}}]_1 = 0$, apart from a component $\delta J_\mu$ that is purely transverse with respect to the photon momentum $q_\mu$, $\delta J_\mu q_\mu = 0$. At the stage of considering a single-particle intermediate state, this component is naturally equal to zero. By virtue of the principle of local gauge invariance, the inclusion of a two-particle intermediate state in addition to a single-particle intermediate state leads to the emergence of a gauge-closed one-loop set of diagrams that involves the conserved two-particle loop $[J_\mu]_2$ current, which, with respect to the generalized pole set of diagrams, can be associated with the conserved two-particle addition $[J_\mu]_2 = \delta J_\mu$ taking into account the contributions of the two-particle mechanisms to $J_\mu^{\mathrm{reg}}$. Thus, the above procedure of taking into account successive approximations on the basis of the conditions of unitarity and gauge invariance appears to be the partition of all diagrams into gauge-closed sets corresponding to the inclusion of various numbers of intermediate states, the total structural electromagnetic current being conserved—that is, $J_\mu^{\mathrm{tot}} = [J_\mu^{\mathrm{pol}} + J_\mu^{\mathrm{reg}}]_1 + [J_\mu]_2 + \ldots + [J_\mu]_i + \ldots = 0$, where $i = 1, \ldots, n$ is the number of intermediate states. Here, each term of the series for the current satisfies the requirement $q_\mu[J_\mu]_i = 0$.

## 2. INVARIANCE OF GREEN'S FUNCTIONS UNDER THE LOCAL GAUGE GROUP OF TRANSFORMATIONS

In going over from the point $x$ to the point $x + dx$, the change of the orientation of a local rest frame for the matter-field operators $\Psi(x)$ is correlated with the gauge field $A_\mu(x)$. For the system of matter fields, a local orientation of the reference frame in the space of interior variables is immaterial; that is, the fields $\Psi(x)$ and $U(x)\Psi(x)$ are physically indistinguishable. Local gauge transformations of the vector potential of an electromagnetic field, $A_\mu(x) \to A'_\mu(x) = A_\mu(x) +$

$\partial_\mu \alpha(x)$, do not change the properties of the system either.

For “global” gauge transformations $\alpha(x) = \mathrm{const}$ of the $U(1)$ group, the two-point Green’s function $D(x,y) = i\left\langle T\left(\Psi(x)\bar{\Psi}(y)\right)\right\rangle$ ($\Psi(x)$ and $\bar{\Psi}(x)$ are complex-valued matter-field operators in the Heisenberg representation and $T$ is the operator of chronological ordering) remains invariant under the matter-field transformation

$$\begin{gathered}\Psi(x) \to \Psi'(x) = \Psi(x)e^{-ie\alpha}, \\ \bar{\Psi}(x) \to \bar{\Psi}'(x) = \bar{\Psi}(x)e^{ie\alpha}, \\ A_\mu(x) \to A'_\mu(x) = A_\mu(x) + \partial_\mu\alpha(x) = A_\mu(x),\end{gathered} \tag{1}$$

where $e$ is the gauge coupling constant that fixes the relative scale of the interaction between the gauge field and the matter field.

Upon the extension of the $U(1)$ group to local gauge transformations, in which case the phase $\alpha(x)$ is an arbitrary real-valued function rather than a constant, so that the transformations in (1) become

$$\begin{gathered}\Psi(x) \to \Psi'(x) = \Psi(x)e^{-ie\alpha(x)}, \\ \bar{\Psi}(x) \to \bar{\Psi}'(x) = \bar{\Psi}(x)e^{ie\alpha(x)}, \\ A_\mu(x) \to A'_\mu(x) = A_\mu(x) + \partial_\mu\alpha(x),\end{gathered} \tag{2}$$

the Green’s function $D(x,y)$ appears to be noninvariant with respect to these transformations [1],

$$\begin{gathered}D(x,y) = i\left\langle T\left(\Psi(x)\bar{\Psi}(y)\right)\right\rangle \\ \to D'(x,y) = i\left\langle T\left(\Psi(x)e^{-ie\alpha(x)}e^{ie\alpha(y)}\bar{\Psi}(y)\right)\right\rangle,\end{gathered} \tag{3}$$

since the fields $\Psi(x)$ and $\bar{\Psi}(y)$ in (3) are defined at different spacetime points.

This situation can be remedied by invoking the principle of local gauge invariance and the concept of a parallel transportation [5] of the field $\Psi(x)$ from the point $x$ to the point $x + dx$ in the space with interior symmetry, in which case the complex field $\Psi(x) = e^{-ie\alpha(x)}\left|\Psi(x)\right|$ remains unchanged, which means that $dx_\mu[\partial_\mu + ie\partial_\mu\alpha(x)]\Psi(x) = 0$. In terms of a $U(1)$ gauge field taken in the pure gauge $A_\mu(x) = -(i/e)U(x)\partial_\mu U^{-1}(x) = \partial_\mu\alpha(x)$ with $U(x) = e^{-ie\alpha(x)}$, we have

$$dx_\mu[\partial_\mu + ieA_\mu(x)]\Psi(x) = 0, \tag{4}$$

where the orientation of the local coordinate frame is determined by the gauge field $A_\mu(x) = A^a_\mu L_a$ (for Yang–Mills fields, the gauge field $A^a_\mu(x)$ is an element of a Lie algebra) at fixed generators $L_a$. In the case of an electromagnetic field, we have $A^a_\mu(x) \to A_\mu(x)$ and $L_a \to 1$.

Solving Eq. (4) for the field $\Psi(x)$ along the path $S$ that is defined by introducing the parameter $0 \le \lambda \le 1$, we find for any point $x(\lambda)$ that

$$\begin{gathered}\Psi(x(\lambda)) = T \\ \times \left[\exp\left(-ie\int\limits_0^\lambda d\lambda' \frac{dx_\mu}{d\lambda'}A_\mu(x(\lambda'))\right)\right]\Psi(x(0)),\end{gathered} \tag{5}$$

where $T$ is the operator of ordering along the path $S$.

The two-point Green’s function that is invariant under the local gauge transformations (2) of the $U(1)$ group is

$$D(x,y,\{A\}) = i\left\langle T\left(\Psi(x)e^{ie\int\limits_x^y dr_\mu A_\mu(r)}\bar{\Psi}(y)\right)\right\rangle. \tag{6}$$

It can easily be proven that expression (6) is invariant under the transformations in (2); indeed, we have

$$\begin{gathered}D'(x,y,\{A\}) = i\left\langle T\left(\Psi'(x)e^{ie\int\limits_y^x dr_\mu A'_\mu(r)}\bar{\Psi}'(y)\right)\right\rangle \\ = i\left\langle T\left(\Psi(x)e^{-ie\alpha(x)}e^{ie\int\limits_y^x dr_\mu[A_\mu(r)+\partial_\mu\alpha(r)]}e^{ie\alpha(y)}\bar{\Psi}(y)\right)\right\rangle = i\left\langle T\left(\Psi(x)e^{ie\int\limits_y^x dr_\mu A_\mu(r)}\bar{\Psi}(y)\right)\right\rangle = D(x,y,\{A\}),\end{gathered}$$

where we have used the equality $\int_y^x dr_\mu\partial_\mu\alpha(r) = \alpha(x) - \alpha(y)$. It should be noted that, in the case where $\alpha(r)$ is an operator [1], all transformations performed above remain in force since one can make any particular assumptions on the properties of an arbitrary operator $\alpha(r)$ in the transformations in (2), the only requirement to be satisfied being that these transformations change only the longitudinal part of the photon propagator, in which case the eventual physical result would remain unaffected.

We will further calculate the functional derivative of expression (6) with respect to the vector potential $A_\mu(r)$ by employing the equality $\delta A_\rho(r')/\delta A_\mu(r) =$

$g_{\mu\rho}\delta(r'-r)$ ($g_{\mu\rho}$ is the metric tensor). We have

$$\frac{\delta}{\delta A_\mu(r)} D(x,y,\{A\})\Big|_{A=0}$$
$$= i^2 e \int\limits_y^x dr'_\mu \delta(r-r') \left\langle T\left(\Psi(x)\bar{\Psi}(y)\right)\right\rangle .$$

Choosing the minimum trajectory connecting the points $x$ and $y$ in the interior reference frame, $r'(\lambda) = (1-\lambda)y + \lambda x$, and using the relation

$$\int\limits_x^y dr'_\mu \delta(r-r') = \int\limits_0^1 d\lambda \frac{dr'_\mu(\lambda)}{d\lambda}\delta(r'(\lambda)-r),$$

we obtain [3]

$$\frac{\delta}{\delta A_\mu(r)} D(x,y,\{A\})\Big|_{A=0} \tag{7}$$
$$= ie(x-y)_\mu \int\limits_0^1 dr'_\mu \delta[y-r+\lambda(x-y)] D(x,y).$$

By virtue of translation invariance (spacetime uniformity), the two-point Green's function depends only on the difference of the 4-coordinates, $D(x,y) = D(x-y)$.

Upon going over to the momentum representation, the functional derivative (7)

$$\int \frac{\delta}{\delta A_\mu(r)} D(x,y,\{A\})\Big|_{A=0} e^{i(qr+px-p'y)} dx dy dr$$
$$= ie \int\limits_0^1 d\lambda \int dx dy dr e^{i(qr+px-p'y)} (x-y)_\mu \tag{8}$$
$$\times \delta[y-r+\lambda(x-y)] D(x-y)$$

in terms of the relative coordinate $x-y=\xi$ and the c.m. coordinate $X=(x+y)/2$ assumes the form

$$\int \frac{\delta}{\delta A_\mu(r)} D(x,y,\{A\})\Big|_{A=0} e^{i(qr+px-p'y)} dx dy dr$$
$$= (2\pi)^4 \delta(q+p-p') ie \int\limits_0^1 d\lambda \int d\xi e^{i\xi(p+\lambda q)} \xi_\mu D(\xi).$$

Considering that

$$\xi_\mu e^{i\xi(p+\lambda q)} = \frac{1}{i}\frac{\partial}{\partial(p+\lambda q)_\mu} e^{i\xi(p+\lambda q)},$$

we eventually obtain the following expression in the momentum representation:

$$\int \frac{\delta}{\delta A_\mu(r)} D(x,y,\{A\})\Big|_{A=0} e^{i(qr+px-p'y)} dx dy dr \tag{9}$$
$$= (2\pi)^4 \delta(q+p-p') e \int\limits_0^1 d\lambda \frac{\partial}{\partial p_\mu(\lambda)} D(p+\lambda q),$$

where $p(\lambda) = p + \lambda q$.

Making the same manipulations for the exact three-point Green's function (vertex operator)

$$G(x,y,z) = i\left\langle T\left(B(z)\bar{\Psi}_1(x)\bar{\Psi}_2(y)\right)\right\rangle , \tag{10}$$

which describes a transition of the charged composite field $B(z)$ having a charge $e_B$ to a state that is characterized by the field operators $\bar{\Psi}_1(x)$ and $\bar{\Psi}_2(y)$ and by the charges $e_1$ and $e_2$ ($e_1 + e_2 = e_B$), respectively, and using a natural generalization of (6), we reduce the three-point Green's function (10) to the form

$$G(x,y,z,\{A\}) \tag{11}$$
$$= i\left\langle T\left(B(z) e^{ie_1\int\limits_x^z dr_\rho A_\rho(r)} \bar{\Psi}_1(x) e^{ie_2\int\limits_y^z dr_\sigma A_\sigma(r)} \bar{\Psi}_2(y)\right)\right\rangle ,$$

which is invariant under the local gauge transformations (2).

The group of gauge transformations of the field operators in (11) and of the vector potential $A_\mu(r)$ has the form

$$B(z) \to B(z)e^{-ie_B\alpha(z)}, \quad \bar{\Psi}_1(x) \to \bar{\Psi}_1(x)e^{ie_1\,\alpha(x)}, \tag{12}$$
$$\bar{\Psi}_2(y) \to \bar{\Psi}_2(y)e^{ie_2\,\alpha(y)}, \;\; A_\mu(r) \to A_\mu(r) + \partial_\mu\alpha(r).$$

It can easily be verified that expression (11) is invariant under the transformations in (12).

We emphasize that, within the geometric treatment of gauge fields, invariance under the transformations in (12) for various coupling constants $e_i$ ($i = B, 1, 2$) fixing the relative scale of the interaction between a gauge field and various matter fields in adjoint space inevitably leads, by virtue of the principle of local gauge invariance, to the relation $e_1 + e_2 = e_B$. In other words, a local variation in the phases of matter fields—they can be considered as coordinates in charge space—is equivalent to the emergence of an extra gauge field with an additive coupling constant, which, in the conventional language in configuration space, is associated with a charge.

Calculating, as before, the functional derivative of the Green's function (11) with respect to $A_\mu(r)$,

$$\frac{\delta}{\delta A_\mu(r)} G(x,y,z,\{A\})\Big|_{A=0}$$
$$= i^2 e_1 \int\limits_x^z dr'_\rho g_{\mu\rho} \delta(r'-r) G(x,y,z,\{0\})$$

$$+ i^2 e_2 \int\limits_y^z dr'_\sigma g_{\mu\sigma}\delta(r'-r)G(x,y,z,\{0\}),$$

and parametrizing the minimum trajectories connecting the points $x$ and $y$ with the point $z$ as $r'_\rho(\lambda) = (1-\lambda)x_\rho + \lambda z_\rho$ and $r'_\sigma(\lambda) = (1-\lambda)y_\sigma + \lambda z_\sigma$, we obtain

$$\left.\frac{\delta G(x,y,z,\{A\})}{\delta A_\mu(r)}\right|_{A=0} \tag{13}$$

$$= i^2 \left\{ e_1(z-x)_\mu \int\limits_0^1 d\lambda \delta(x - r + \lambda(z-x)) \right.$$

$$\left. + \, e_2(z-y)_\mu \int\limits_0^1 d\lambda \delta(y - r + \lambda(z-y)) \right\} G(x,y,z).$$

By performing a Fourier transformation in expression (13), we finally reduce the functional derivative of the three-point Green's function to the form

$$\int\limits_0^1 d\lambda \frac{\partial}{\partial p_\mu(\lambda-1)} \{e_1 G(p_1 + (\lambda-1)q, p_2; p+\lambda q) \tag{14}$$

$$+ e_2 G(p_1, p_2 + (\lambda-1)q; p+\lambda q)\},$$

which is similar to that in (9). In expression (14), we have omitted a delta function that reflects the law of 4-momentum conservation. The momenta $p$, $p_1$, and $p_2$ correspond to the fields $B(z)$, $\bar{\Psi}_1(x)$, and $\bar{\Psi}_2(y)$, respectively, while the momentum $q$ corresponds to the electromagnetic field $A_\mu(r)$. We note that, for the first and the second term in the braced expression on the right-hand side of (14), the law of conservation of the total 4-momentum has the usual form $p_1 + (\lambda-1)q + p_2 = p_1 + p_2 + (\lambda-1)q = p + \lambda q$; upon the cancellation of the term $\lambda q$ appearing on either side of this equality, we obviously arrive at $p_1 + p_2 = p + q$.

The ensuing consideration will be performed in the momentum representation. We "include" an electromagnetic field of polarization 4-vector $\varepsilon_\mu$ and 4-momentum $q_\mu$ in the Green's function $D(p)$ for a scalar particle of momentum $p$ and mass $m$ in accordance with expression (9); that is,

$$ze\varepsilon_\mu \int\limits_0^1 d\lambda \frac{\partial}{\partial p_\mu(\lambda)} \left\{D(p+\lambda q)\right\}, \tag{15}$$

where $ze$ is the charge of the particle interacting with the field.

Owing to the fact that the photon polarization vector is transverse, $\varepsilon_\mu q_\mu = 0$ ($q^2 = 0$), the ensuing calculations are simplified upon the substitution

$$\varepsilon_\mu \int\limits_0^1 d\lambda \frac{\partial}{\partial p_\mu(\lambda)} \cdots = \varepsilon_\mu \int\limits_0^1 \frac{\partial\lambda}{\lambda}\frac{\partial}{\partial q_\mu} \cdots .$$

In [6], the integral operator (15) was used to ensure the gauge invariance of the nonrelativistic amplitude for the deuteron-photodisintegration process.

Considering that the direct and the inverse propagator satisfy the relation $DD^{-1} = D^{-1}D = I$ and differentiating this relation with respect to $q_\mu$, we obtain $\partial D/\partial q_\mu = -D \times \partial D^{-1}/\partial q_\mu \times D$. Expression (15) then takes the form

$$ze\varepsilon_\mu \int\limits_0^1 \frac{d\lambda}{\lambda}\frac{\partial}{\partial q_\mu}\{D(p+\lambda q)\}$$

$$= -ze\varepsilon_\mu \int\limits_0^1 \frac{d\lambda}{\lambda} D(p+\lambda q) \tag{16}$$

$$\times \frac{\partial}{\partial q_\mu}\left\{D^{-1}(p+\lambda q)\right\} D(p+\lambda q).$$

The explicit form of the propagator for a scalar particle, $D(p) = 1/\big(p^2 - m^2 + i0\big)$, makes it possible to perform the respective differentiation, $\partial D^{-1}(p + \lambda q)/\partial q_\mu = 2\lambda p_\mu$; as a result, we obtain

$$ze\varepsilon_\mu \int\limits_0^1 \frac{d\lambda}{\lambda}\frac{\partial}{\partial q_\mu}\{D(p+\lambda q)\} \tag{17}$$

$$= -ze\varepsilon_\mu \int\limits_0^1 \frac{d\lambda}{\lambda}\frac{2\lambda p_\mu}{\left[(p+\lambda q)^2 - m^2 + i0\right]^2}.$$

Representing the bracketed expression in the denominator on the right-hand side of (17) in the form $(p+\lambda q)^2 - m^2 + i0 = \lambda a + (1-\lambda)b$, where $a = (p+q)^2 - m^2 + i0$ and $b = p^2 - m^2 + i0$, and calculating the respective integral (we omit the factor $-ze\varepsilon_\mu$), we arrive at the relation

$$\int\limits_0^1 \frac{d\lambda}{\lambda}\frac{2\lambda p_\mu}{\left[(p+\lambda q)^2 - m^2 + i0\right]^2}$$

$$= (2p+q)_\mu \int\limits_0^1 d\lambda \frac{1}{\left[\lambda a + (1-\lambda)b\right]^2} \tag{18}$$

$$= D(p+q)\left\{(2p+q)_\mu\right\} D(p).$$

Thus, the inclusion of an electromagnetic field in the two-particle propagator reproduces, for the interaction between an electromagnetic and a charged scalar field, the vertex function that is known in QED; that is,

$$ze\varepsilon_\mu \int\limits_0^1 \frac{d\lambda}{\lambda}\frac{\partial}{\partial q_\mu}\left\{D(p+\lambda q)\right\} \tag{19}$$
$$= -zeD(p+q)\left\{\varepsilon_\mu(2p+q)_\mu\right\}D(p).$$

The substitution $\varepsilon_\mu \to q_\mu$ in (19) leads to the Ward–Takahashi identity

$$q_\mu(2p+q)_\mu = D^{-1}(p+q) - D^{-1}(p). \tag{20}$$

In the case of a spin-1/2 particle, the one-photon insertion into the two-particle Green's function $S(p)$ is made in the same way as in (15):

$$ze\varepsilon_\mu \int\limits_0^1 \frac{d\lambda}{\lambda}\frac{\partial}{\partial q_\mu}\left\{S(p+\lambda q)\right\}$$
$$= -ze\varepsilon_\mu \int\limits_0^1 \frac{d\lambda}{\lambda} S(p+\lambda q) \tag{21}$$
$$\times \frac{\partial}{\partial q_\mu}\left\{S^{-1}(p+\lambda q)\right\}S(p+\lambda q).$$

Making use of the explicit form of the propagator $S(p+\lambda q) = 1/(\hat{p}+\lambda\hat{q}-m+i0)$, where all hat-labeled 4-vectors are defined as $\hat{p} \equiv p_\mu\gamma_\mu$ ($\gamma_\mu$ are the 4×4 Dirac matrices), recalling that $p^2 \neq m^2$, and introducing $a$ and $b$ in the denominator in just the same way as in (18), we recast expression (21) into the form

$$\int\limits_0^1 d\lambda \frac{(\hat{p}+\lambda\hat{q}+m)\gamma_\mu(\hat{p}+\lambda\hat{q}+m)}{[(p+\lambda q)^2 - m^2 + i0]^2} \tag{22}$$
$$= \Biggl\{ (2p_\mu(\hat{p}+m) - b\gamma_\mu) \int\limits_0^1 d\lambda \frac{1}{[\lambda a + (1-\lambda)b]^2}$$
$$+ 2\left(p_\mu\hat{k} - (qp)\gamma_\mu\right)\int\limits_0^1 d\lambda \frac{\lambda}{[\lambda a + (1-\lambda)b]^2} \Biggr\}.$$

Calculating the relevant integrals and considering that $|a/b| \sim 1$, we arrive at

$$e\varepsilon_\mu \int\limits_0^1 d\lambda \frac{\partial S(p+\lambda q)}{\partial p_\mu(\lambda)}$$
$$= \frac{(\hat{p}+\hat{q}-m)\{-e\varepsilon_\mu\gamma_\mu\}(\hat{p}+\hat{q}-m)}{[(p+q)^2-m^2]^2(p^2-m^2)^2}$$
$$= \frac{(\hat{p}+\hat{q}-m)\{-e\varepsilon_\mu\gamma_\mu\}\left(1+\hat{q}\dfrac{\hat{p}+m}{p^2-m^2}\right)(\hat{p}-m)}{[(p+q)^2-m^2]^2(p^2-m^2)^2}$$
$$= S(p+q)\left\{-e\varepsilon_\mu\gamma_\mu\left(1+\hat{q}\frac{\hat{p}+m}{p^2-m^2}\right)\right\}S(p),$$

where $\sigma_{\mu\nu} = (\gamma_\mu\gamma_\nu - \gamma_\nu\gamma_\mu)/2$. Finally, Eq. (21) for the one-photon insertion into the Green's function leads to the following vertex function for the interaction of an electromagnetic and a charged spinor field:

$$e\varepsilon_\mu \int\limits_0^1 d\lambda \frac{\partial S(p+\lambda q)}{\partial p(\lambda)_\mu} \tag{23}$$
$$= S(p+q)\{-e\varepsilon_\mu(\gamma_\mu + \sigma_{\mu\nu}q_\nu S(p))\}S(p).$$

As in the case of a scalar field in (20), the substitution $\varepsilon_\mu \to q_\mu$ in (23) leads to the Ward–Takahashi identity

$$\hat{q} = S^{-1}(p+q) - S^{-1}(p). \tag{24}$$

As an example of the use of expression (14), we can consider a repeated inclusion of a photon having a polarization 4-vector $\varepsilon''_\nu$ and a 4-momentum $q''_\nu$ into the three-point vertex function $-ze\varepsilon'_\mu(p_1+p_2)_\mu$:

$$-ze\varepsilon''_\nu \int\limits_0^1 \frac{d\lambda}{\lambda}\frac{\partial}{\partial q''_\nu}\Bigl\{ze\varepsilon'_\mu(p_1 + (\lambda-1)q'' + p_2)_\mu$$
$$+ ze\varepsilon'_\mu(p_1+p_2+(\lambda-1)q'')_\mu\Bigr\} = -z^2e^2 2g_{\mu\nu}\varepsilon'_\mu\varepsilon''_\nu,$$

this leading to the well-known (in QED) expression for the emission (absorption) of two electromagnetic-field quanta by a charged scalar field at the same point.

Let us now consider the insertion of an electromagnetic field into the total strongly connected three-point propagator (see Fig. 1). The interaction of an electromagnetic field with the total strongly connected three-point Green's function is implemented by inserting it into the external legs (two-point Green's functions) and into the vertex function itself (three-point Green's function), the photon exercising a continuous control over the "motion" of the charge at all stages of evolution as the system goes over from the in- to the out-state, suffering qualitative and quantitative changes in the region of strong interaction. The mathematical expression that reflects the insertion of the electromagnetic field in the strongly connected three-point vertex function (Fig. 1) according to the rules specified by Eqs. (9) and (14) has the form

$$\{D(p)G(p;p_1,p_2)D(p_1)D(p_2)\} + \{e\varepsilon_\mu\} \tag{25}$$

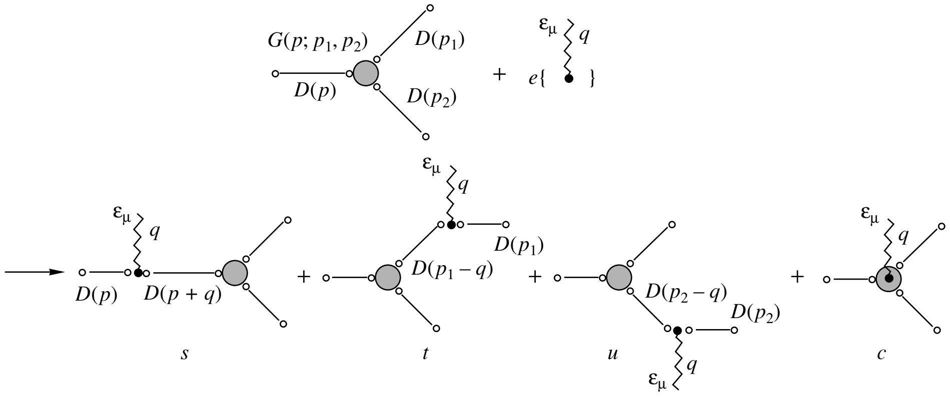

**Fig. 1.** Insertion of an electromagnetic field into the total strongly connected three-point vertex function $G(p_1, p_2; p)$. Diagrams denoted by $s$, $t$, $u$, and $c$ correspond to Mandelstam's terminology for reaction channels.

$$\begin{gathered}
\to \left\{ -e\varepsilon_\mu z \int\limits_0^1 \frac{d\lambda}{\lambda}\frac{\partial}{\partial q_\mu} D(p+\lambda q) \right\} \\
\times G(p+q;p_1,p_2)D(p_1)D(p_2) \\
+ D(p)G(p;p_1-q,p_2) \\
\times \left\{ -e\varepsilon_\mu z_1 \int\limits_0^1 \frac{d\lambda}{\lambda}\frac{\partial}{\partial q_\mu} D\left(p_1+(\lambda-1)q\right) \right\} D(p_2) \\
+ D(p)G(p;p_1,p_2-q)D(p_1) \\
\times \left\{ -e\varepsilon_\mu z_2 \int\limits_0^1 \frac{d\lambda}{\lambda}\frac{\partial}{\partial q_\mu} D\left(p_2+(\lambda-1)q\right) \right\} + D(p) \\
\times \left\{ -e\varepsilon_\mu \int\limits_0^1 \frac{d\lambda}{\lambda}\frac{\partial}{\partial q_\mu} [z_1 G(p+\lambda q;p_1+(\lambda-1)q,p_2) \right. \\
\left. + z_2 G(p+\lambda q;p_1,p_2+(\lambda-1)q)] \right\} D(p_1)D(p_2),
\end{gathered}$$

where $z_1$ and $z_2$ are the charges of the first and the second product particle in units of $e$.

As the result of including the electromagnetic field in the total three-point Green's function (vertex operator, external legs in the form of two-point Green's functions), we obtained a gauge-invariant series for four-point Green's functions, which consists of the sum of three single-particle-reducible four-point Green's functions (pole part) related by crossing symmetry and the strongly connected (single-particle-irreducible) four-point Green's function (regular part). Upon the application of the standard recipe of quantum field theory [5] to the resulting gauge-closed series of four-point Green's functions, it reduces to the corresponding $S$-matrix element, and this makes it possible to calculate the photodisintegration of strongly bound composite systems (nuclei) within a fully covariant description featuring an exactly conserved electromagnetic structural current and taking consistently into account the structure of the composite system in question.

Let us demonstrate the gauge invariance of this expression. Making the substitution $\varepsilon_\mu \to q_\mu$ in expression (25) and evaluating thereupon the integrals for the right-hand side, we obtain

$$\begin{gathered}
-ze\,[D(p+q)-D(p)] \qquad (26) \\
\times G(p+q;p_1,p_2)D(p_1)D(p_2) \\
+ D(p)G(p;p_1-q,p_2) \\
\times \left[-ez_1\left(D(p_1)-D(p_1-q)\right)\right] D(p_2) \\
+ D(p)G(p;p_1,p_2-q)D(p_1) \\
\times \left[-ez_2\left(D(p_2)-D(p_2-q)\right)\right] \\
- ez_1 D(p)\left[G(p+q;p_1,p_2)-G(p;p_1-q,p_2)\right] \\
\times D(p_1)D(p_2) \\
- ez_2 D(p)\left[G(p+q;p_1,p_2)-G(p;p_1,p_2-q)\right] \\
\times D(p_1)D(p_2).
\end{gathered}$$

Making use of the Ward–Takahashi identity (20)

$$\begin{gathered}
eq_\mu \int\limits_0^1 \frac{d\lambda}{\lambda}\frac{\partial}{\partial q_\mu}\left\{D(p+\lambda q)\right\} \\
= e\,[D(p+q)-D(p)] \\
= -eD(p+q)\left\{2(pq)\right\}D(p),
\end{gathered}$$

reducing in (26) the two-particle propagators appearing (see Fig. 1) as external legs of the diagrams [that is, multiplying expression (26) by the inverse propagators $D^{-1}(p)$, $D^{-1}(p_1)$, and $D^{-1}(p_2)$], replacing the external legs of the diagrams by the corresponding wave functions for free (on-shell) particles (in the normalization adopted here, they are equal to unity for scalar fields), and taking into account the relation

$$D(p \pm q) = \frac{1}{(p \pm q)^2 - m^2} = \pm\frac{1}{2pq}$$

we obtain the contribution of the series of Feynman diagrams to the $S$-matrix element in the form

$$\begin{gathered} ezG(p+q;p_1,p_2) - ez_1G(p;p_1-q,p_2) \\ - ez_2G(p;p_1,p_2-q) \\ - e(z_1+z_2)G(p+q;p_1,p_2) \\ + ez_1G(p;p_1-q,p_2) + ez_2G(p;p_1,p_2-q) = 0. \end{gathered}$$

Therefore, expression (25) is gauge-invariant. It is important to note that, in deriving the last equality, we nowhere used the explicit form of the vertex function $G(p;p_1,p_2)$, which describes the breakup of the composite system into its constituents. Thus, one can respect, without having any information about the nature of a composite strongly interacting system, the requirement of conservation of the total nuclear electromagnetic current, knowing only, by virtue of the general requirements of covariance and conservation laws, the functional dependence of the respective vertex function.

The physical meaning of the diagram series in Fig. 1 and of the respective mathematical expression (25) is the following. The three-point Green's function describes the transition of a strongly interacting nuclear system to a state where it is characterized by its constituents, the dynamical pattern of this transition being realized in accordance with the Bethe–Salpeter equation or its quasipotential analogs. The presence of a photon introduces a perturbation in the composite system and renders the transition in question real; at the subsequent instants, it only fixes electric-charge conservation at all stages of the evolution, having no effect on strong interaction.

In applying the developed approach to studying the photodisintegration of nuclei, there arises the problem of finding the explicit form of the argument of the vertex function $G(p;p_1,p_2)$, which describes a relativistic bound state and its subsequent breakup into constituents. A full description of this problem requires solving the relativistic Bethe–Salpeter equation. Even for the deuteron, which is a very loosely bound nuclear system, the description of a relativistic bound state in terms of the Bethe–Salpeter equation involves considerable difficulties. In view of this, use is presently made of approaches that rely on solving approximate Bethe–Salpeter equations, such as the Logunov–Tavkhelidze, Kadyshevsky–Weinberg, and Gross equations. In each specific approximation, solutions to these equations make it possible to employ the vertex function $G(p;p_1,p_2)$ without violating the covariance and gauge invariance of the total amplitude in (25). Here, we will dwell on this point at some length. As is well known, solving the aforementioned approximate equations reduces to projecting the covariant Bethe–Salpeter equation onto a spacelike hypersurface with the aim of imparting the traditional probabilistic interpretation to the resulting solutions, this implying that the vertex function $G(p;p_1,p_2)$ appears to be dependent only on the square of the relative 3-momentum, $G(\mathbf{p}^2)$. In view of this, it is necessary to go over, in the formal dependence of the vertex function, from covariant momenta to the relative 3-momentum of product constituents.

By way of example, we will now apply this scheme to the virtual breakup of a bound state at rest, its total energy being denoted by $W$. We introduce a spacelike 4-vector $K$ whose spatial component is equal to the relative 3-momentum $\mathbf{p}$; that is,

$$K = (0, \mathbf{p}) \quad \text{or} \quad \mathbf{p}^2 = -K^2. \tag{27}$$

The relationship between the 4-vector $K$ and the vectors $P$, $p_1$, and $p_2$ of the bound-state vertex function can be represented as

$$K = \frac{(Pp_2)}{P^2}p_1 - \frac{(Pp_1)}{P^2}p_2. \tag{28}$$

It is obvious that, for this choice of the 4-vector $K$, the condition $(KP) = 0$ holds.

It can easily be verified that the spacelike 4-vector $K$ constructed in this way satisfies the requirement in (27); that is,

$$\begin{gathered} K_0 = \frac{WE_2}{W^2}E_1 - \frac{WE_1}{W^2}E_2 = 0, \\ \mathbf{K} = \frac{WE_2}{W^2}\mathbf{p} + \frac{WE_1}{W^2}\mathbf{p} = \mathbf{p}, \end{gathered} \tag{29}$$

where $W = E_1 + E_2$ ($E_1$ and $E_2$ are the energies of the constituents in their c.m. frame). The functional dependence of the vertex function $G(P;p_1,p_2)$ will then have the form

$$G(P;p_1,p_2) = G(-K^2) = G(\mathbf{p}^2). \tag{30}$$

Since, in (25), each term on the right-hand side involves vertex functions at the corresponding values of the momenta, one can represent, with the aid of (28), expressions for the relative momenta as

$$\begin{aligned} P^{st}_\alpha(\lambda) &= \frac{(p+\lambda q)p_2}{(p+\lambda q)^2}(p'_1+\lambda q)_\alpha \\ &\quad - \frac{(p+\lambda q)(p'_1+\lambda q)}{(p+\lambda q)^2}p_{2\alpha} \\ &= \frac{(p+\lambda q)p_2}{(p+\lambda q)^2}(p+\lambda q)_\alpha - p_{2\alpha}, \end{aligned} \tag{31}$$

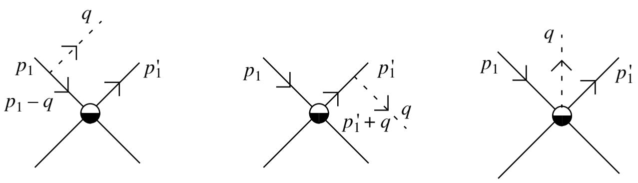

**Fig. 2.** Feynman diagrams describing the bremsstrahlung in elastic scattering.

where $p_1' = p_1 - q$, and as

$$P_\alpha^{su}(\lambda) = \frac{(p+\lambda q)(p_2'+\lambda q)}{(p+\lambda q)^2} p_{1\alpha} - \frac{(p+\lambda q)p_1}{(p+\lambda q)^2}(p_2'+\lambda q)_\alpha = p_{1\alpha} - \frac{(p+\lambda q)p_1}{(p+\lambda q)^2}(p+\lambda q)_\alpha, \tag{32}$$

where $p_2' = p_2 - q$. Setting $\lambda = 0$ in (31) and (32), we obtain the momentum for the vertex function in the first term on the right-hand side of (25); setting $\lambda = 1$, we obtain the momenta for the vertex function in the second and the third term on the right-hand side of (25).

It can easily be seen that the 4-momenta that are defined in this way according to the generally accepted terminology of the Mandelstam variables and which relate, respectively, the first diagram in Fig. 1 to the second one and the first diagram there to the third one satisfy the relations $P_\alpha^{st}(\lambda)(p+\lambda q)_\alpha = P_\alpha^{su}(\lambda)(p+\lambda q)_\alpha = 0$.

We would like to highlight a situation that has a general character for all light nuclei interacting with an electromagnetic field. For incident-photon energies below the meson-production threshold, the ratio of the incident-photon energy $q_0$ to the target-nucleus mass $M$ does not exceed 0.1 even for the deuteron, which is the lightest composite nucleus.

Further, we square the expression for the spacelike 4-momentum (31) and expand it in powers of $q_0/M$. As a result, we obtain

$$P^2(\lambda) \cong P^2 - 2\frac{(p'p_2)}{p'^2}(qP)\lambda + 2\frac{(p'p_2)(p'q)(qp_2)}{p'^4}\lambda^2 + 2\frac{(qp_2)^2}{p'^2}\lambda^2 + \dots,$$

where $P$ is the value of the relative momentum (31) at $\lambda = 0$. In this expansion, the first term does not depend either on the photon energy or on the direction of photon motion, while the second term is proportional to the ratio $q_0/M$ and depends on the direction of final-particle emission. The next terms are of order $(q_0/M)^2$; of these, some depend on the direction of final-particle emission, while others do not. Retaining, in this expansion, only terms of the first two types, we see that the momenta in (31) and (32) can be represented in the form

$$P_\alpha^{st}(\lambda) = P_\alpha - \lambda\frac{(p'p_2)}{p'^2}q_\alpha, \tag{33}$$

$$P_\alpha^{su}(\lambda) = P_\alpha + \lambda\frac{(p'p_1)}{p'^2}q_\alpha.$$

For the 4-momenta defined in this way, we have $P_\alpha^{st}(\lambda)(p+\lambda q)_\alpha \neq 0$ and $P_\alpha^{su}(\lambda)(p+\lambda q)_\alpha \neq 0$ instead of (31) and (32). This simplification in the representation (31), (32) of the relative 4-momenta permits making, in the following, a number of significant simplifications in studying specific processes.

As an illustration of inserting an electromagnetic field into the four-point Green's function, we consider the bremsstrahlung of a photon with a 4-momentum $q_\mu$ in the elastic scattering of scalar particles having identical masses $m$, momenta $p_1$ and $p_2$, and charges $z_1$ and $z_2$ (Fig. 2).

In accordance with the above scheme of including an electromagnetic field, the amplitude of the process has the form

$$\begin{aligned} M = ez_1 &\left\{ \frac{(2p_1-q)\varepsilon}{(p_1-q)^2-m^2}\Gamma(p_1-q,p_2;p_1',p_2') \right. \\ &\left. + \Gamma(p_1,p_2;p_1'+q,p_2')\frac{(2p_1'+q)\varepsilon}{(p_1'+q)^2-m^2} \right\} \\ + ez_2 &\left\{ \frac{(2p_2-q)\varepsilon}{(p_2-q)^2-m^2}\Gamma(p_1,p_2-q;p_1',p_2') \right. \\ &\left. + \Gamma(p_1,p_2;p_1',p_2'+q)\frac{(2p_2'+q)\varepsilon}{(p_2'+q)^2-m^2} \right\} \\ + e\varepsilon_\mu &\int\limits_0^1 \frac{d\lambda}{\lambda}\{z_1\Gamma[p_1-\lambda q,p_2;p_1'+(1-\lambda)q,p_2'] \\ &+ z_2\Gamma[p_1,p_2-\lambda q;p_1',p_2'+(1-\lambda)q]\}, \end{aligned} \tag{34}$$

where $\Gamma$ is the vertex function for this process.

By making the substitution $\varepsilon_\mu \to q_\mu$, it can easily be shown that expression (34) is gauge-invariant:

$$\begin{aligned} &z_1[-\Gamma(p_1-q,p_2;p_1',p_2') + \Gamma(p_1,p_2;p_1'+q,p_2') \\ &+ \Gamma(p_1-q,p_2;p_1',p_2') - \Gamma(p_1,p_2;p_1'+q,p_2')] \\ &+ z_2[-\Gamma(p_1,p_2-q;p_1',p_2') + \Gamma(p_1,p_2;p_1',p_2'+q) \\ &+ \Gamma(p_1,p_2-q;p_1',p_2') - \Gamma(p_1,p_2;p_1',p_2'+q)] = 0. \end{aligned} \tag{35}$$

The formal dependence of the vertex function $\Gamma$ in the form (34) on all 4-momenta reduces to dependence on two relative 4-momenta. The matrix element (34) can be used in further numerical calculations of elastic photon-emission (photon-absorption) processes.

## 3. GENERAL APPROACH TO THE PHOTODISINTEGRATION OF A SCALAR COMPOSITE SYSTEM

We will illustrate the proposed approach by constructing a gauge-invariant amplitude that describes the breakup of a composite nuclear system in photodisintegration reactions. Without restricting the generality in the conclusions drawn on the basis of the proposed approach, we will consider only the photodisintegration of a scalar composite particle into two scalar constituents of positive parity in the final state in order to simplify the mathematical computations.

The Feynman diagrams corresponding to this process are shown in Fig. 1.

In accordance with (25), the matrix element for the process in question has the form

$$\mathrm{M} = \sum_{i=s,t,u,c} M_i. \tag{36}$$

The amplitudes corresponding to the $s$, $t$, and $u$ pole diagrams and the $c$ contact diagram are given by

$$M_s = ez\varepsilon_\mu \frac{(2p+q)_\mu}{s-M^2} G_s(p+q; p_1, p_2), \quad s=(p+q)^2;$$

$$M_t = ez_1\varepsilon_\mu G_t(p; p_1 - q, p_2)\frac{(2p_1-q)_\mu}{t-m^2}, \tag{37}$$

$$t = (p_1-q)^2;$$

$$M_u = ez_2\varepsilon_\mu G_u(p; p_1, p_2 - q)\frac{(2p_2-q)_\mu}{u-m^2},$$

$$u = (p_2-q)^2;$$

$$M_c = e\varepsilon_\mu \int_0^1 \frac{d\lambda}{\lambda}\frac{\partial}{\partial q_\mu}\{z_1 G\left(p' - \lambda q\,; p_1 - \lambda q\,, p_2\right) \tag{38}$$

$$+ z_2 G\left(p' - \lambda q\,; p_1\,, p_2 - \lambda q\right)\},$$

where $z$, $z_1$, and $z_2$ are the respective charges in units of $e$; $p$ is the momentum of the composite particle undergoing breakup; $p_1$ and $p_2$ are the momenta of the product particles; $p' = p + q$; $M$ is the mass of the composite particle; and $m$ is the product-particle mass (it is assumed to be identical for all of the constituents).

Considering that $(\varepsilon\, q) = 0$ and expressing the Mandelstam variables in terms of the scalar products of vectors involved in this process, we recast the amplitudes in (37) and (38) into the form

$$M_s = ez\frac{(\varepsilon p)}{(qp)}G(-P_s^2), \quad M_t = -ez_1\frac{(\varepsilon p_1)}{(qp_1)}G(-P_t^2),$$

$$M_u = -ez_2\frac{(\varepsilon p_2)}{(qp_2)}G(-P_u^2), \tag{39}$$

$$M_c = e\varepsilon_\mu \int_0^1 \frac{d\lambda}{\lambda}\frac{\partial}{\partial q_\mu} \tag{40}$$

$$\times \left\{z_1 G\left(-P_{st}^2(\lambda)\right) + z_2 G\left(-P_{su}^2(\lambda)\right)\right\},$$

where

$$P_s^2 = m^2 - \frac{(p'p_2)^2}{p'^2}, \quad P_t^2 = m^2 - \frac{(pp_2)^2}{p^2},$$

$$P_u^2 = m^2 - \frac{(pp_1)^2}{p^2}, \tag{41}$$

$$P_{st}^2(\lambda) = m^2 - \frac{\left[(p'-\lambda q)p_2\right]^2}{(p'-\lambda q)^2},$$

$$P_{su}^2(\lambda) = m^2 - \frac{\left[(p'-\lambda q)p_1\right]^2}{(p'-\lambda q)^2}. \tag{42}$$

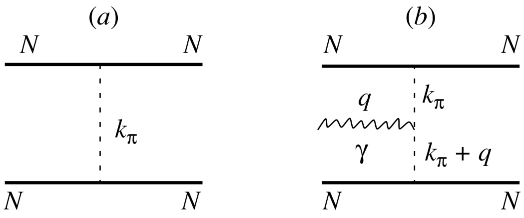

**Fig. 3.** (*a*) Lowest order diagram for scalar nucleon–nucleon interaction in the $g\psi^2\varphi$ model and (*b*) diagram for the exchange current upon the inclusion of an electromagnetic field.

In order to perform further calculations, which will be of a purely illustrative character, we will consider two versions of the functional dependence of the vertex function $G(\mathbf{p}^2)$, which are treated as solutions to two different hypothetical quasipotential equations describing the breakup of the composite system into constituents; that is,

$$G(\mathbf{p}^2) = \begin{cases} N_1 e^{-\delta \mathbf{p}^2} & \text{(I)}, \\ N_2 \dfrac{1}{\alpha_0^2 + \mathbf{p}^2} & \text{(II)}, \end{cases} \tag{43}$$

where $\mathbf{p}$ is the relative 3-momentum in the final system of product states, $N_1$ and $N_2$ are normalization factors ensuring the probabilistic interpretation of the vertex function, and $\delta$ and $\alpha_0^2$ are fixed parameters

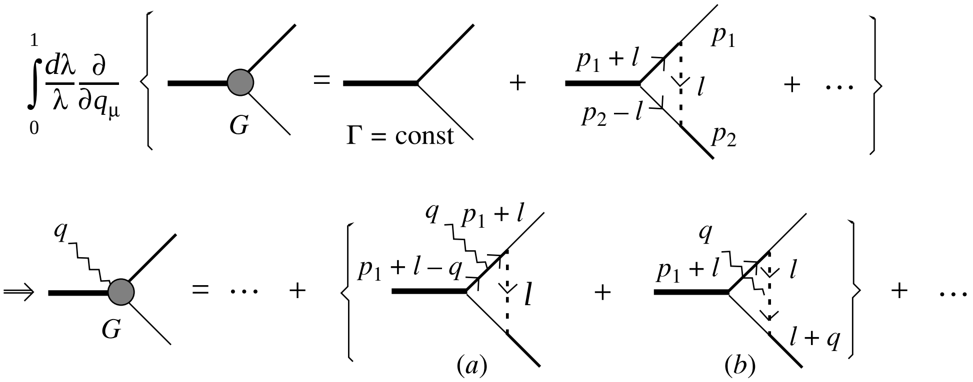

**Fig. 4.** Inclusion of an electromagnetic field in the exact strongly connected vertex function $G$. The thick lines indicate the motion of an electric charge.

ensuring the similarity of $G(\mathbf{p}^2)$ to the actual momentum distribution of constituents in the bound nuclear system.

We indicate that the distinction between the functional dependences (I) and (II) in (43) is of fundamental importance and is caused by the fact that the meson sector participating in the formation of the quasipotential for the hypothetical equation describing the strong-interaction vertex is taken into account to different degrees. We will dwell on this point at some length. We consider scalar nucleons ($\psi$) interacting in the $t$ channel through the exchange of a charged scalar meson ($\varphi$), the Lagrangian for nucleon–meson coupling being $L_{\text{int}} = g\psi^2\varphi$. In the lowest order in the coupling constant $g$, the amplitude for $NN \to NN$ scattering (Fig. 3$a$) takes the form

$$V_g^{NN\to NN}(k_\pi) = \frac{g^2}{k_\pi^2 - \mu^2},$$

where $k_\pi$ is the momentum of the respective meson and $\mu$ is its mass. Upon the substitution of this expression into formula (15), we obtain the corresponding the electromagnetic current,

$$J_\mu(k_\pi, q) = eg^2 \int_0^1 \frac{d\lambda}{\lambda}\frac{\partial}{\partial q_\mu}\left[(k_\pi + \lambda q)^2 - \mu^2\right]^{-1}$$

$$= -eg^2 \frac{(2k_\pi + q)_\mu}{(k_\pi^2 - \mu^2)\left[(k_\pi + q)^2 - \mu^2\right]}.$$

It is obvious that this current, corresponding to the diagram in Fig. 3$b$, is nothing but a meson-exchange current.

Following the same line of reasoning, we further consider the inclusion of a photon in the vertex itself. The exact strongly connected vertex function $G$ can be represented as the sum of an infinite series of diagrams (Fig. 4), where the first term represents the bare vertex ($\Gamma_{\text{const}}$), while the second term takes into account the exchange of a charged meson.

The insertion of an electromagnetic field into the vertex function $G$ takes into account photon interaction both with the constituents of the bound state and with mesons mediating the nuclear field. Denoting the momenta of the participant particles as is shown in Fig. 4 and including the electromagnetic field on the left- and on the right-hand side of the series, we arrive at

$$e\int_0^1 \frac{d\lambda}{\lambda}\frac{\partial}{\partial q_\mu} G(p + \lambda q; p_1 + \lambda q, p_2)$$

$$= eg^2\Gamma_{\text{const}} \int_0^1 \frac{d\lambda}{\lambda}\frac{\partial}{\partial q_\mu}\left\{\int \frac{d^4 l}{(2\pi)^4}\frac{1}{[(p_1 + l - \lambda q)^2 - m_1^2 + i0][l^2 - \mu^2 + i0][(p_2 - l)^2 - m_2^2 + i0]}\right.$$

$$\left. + \int \frac{d^4 l}{(2\pi)^4}\frac{1}{[(p_1 + l)^2 - m_1^2 + i0][(l - \lambda q)^2 - \mu^2 + i0][(p_2 - l)^2 - m_2^2 + i0]}\right\} + \ldots$$

$$= eg^2\Gamma_{\text{const}}\left\{\int \frac{d^4 l}{(2\pi)^4}\frac{2(p_1 + l)_\mu}{[(p_1 + l)^2 - m_1^2 + i0][(p_1 + l - q)^2 - m_1^2 + i0][l^2 - \mu^2 + i0][(p_2 - l)^2 - m_2^2 + i0]}\right.$$

$$+\int \frac{d^4l}{(2\pi)^4}\frac{2l_\mu}{[(p_1+l)^2-m_1^2+i0][l^2-\mu^2+i0][(l+q)^2-\mu^2+i0][(p_2-l)^2-m_2^2+i0]}\Bigg\}+\ldots,$$

where $m_1$ and $m_2$ are the masses of particles 1 and 2, respectively, and $p_1$ and $p_2$ are their momenta. Thus, the mechanisms corresponding to final-state interaction (Fig. 4*a*) and the exchange currents (Fig. 4*b*) corresponding to those mediators of the interaction that were originally included in the potentials describing the strongly connected vertex are taken into account in the amplitudes for electromagnetic processes, the exchange currents being strictly balanced with other mechanisms in the total amplitude.

## 4. ANALYSIS OF THE PHOTODISINTEGRATION OF A COMPOSITE NUCLEAR SYSTEM WITH ALLOWANCE FOR DYNAMICS IN THE STRONG-INTERACTION VERTEX FUNCTION

The total amplitude (36) for the process being considered has a pole and a regular part. The pole part is controlled exclusively by the absolute value of the vertex function at each point of its argument. The regular part of the amplitude is determined not only by the absolute value of the vertex function, as occurs in the pole diagrams, but also by the slope of the tangent to the curve at each point of the vertex function, since the integrand involves a derivative. In view of this, the two distribution functions (43), which were chosen above, will be studied here to reveal the role of the distribution of the contributions of the pole and the regular part to the total amplitude for each of the above distribution functions individually and the redistribution of these contributions in the total amplitude.

Our numerical calculations will be performed in the c.m. frame of primary particles, with the $z$ axis being aligned with the photon momentum $\mathbf{q}$. In this reference frame, the Lorentz condition $(\varepsilon q)=0$ is equivalent to the choice of the three-dimensional-transverse gauge. If the $xz$ coordinate plane is taken to coincide with the reaction plane, the components of the 4-momenta and of the polarization vector of particles involved in the reaction have the following form in the chosen reference frame:

$$q=(q_0;0,0,|\mathbf{q}|),\quad \varepsilon_x=(0;1,0,0),\quad \varepsilon_y=(0;0,1,0), \tag{44}$$

$$p=(E;0,0,-|\mathbf{q}|),\quad p_1=(\omega;\mathbf{p}\sin\vartheta,0,|\mathbf{p}|\cos\vartheta),\quad p_2=(\omega;-|\mathbf{p}|\sin\vartheta,0,-|\mathbf{p}|\cos\vartheta).$$

Performing differentiation with respect to the variable $q_\mu$ in the integrand in expression (40) with allowance for (41) and (42) and considering that the condition $(\varepsilon p)=0$ holds in the chosen reference frame, we reduce, for the distribution function (43-I), the total matrix element for the process being considered to the form

$$M=\sqrt{4\pi\alpha}N_1\left\{z_1\left[(\varepsilon p_2)J_1-\frac{(\varepsilon p_1)}{(qp_1)}\Phi_t\right]+z_2\left[(\varepsilon p_1)J_2-\frac{(\varepsilon p_2)}{(qp_2)}\Phi_u\right]\right\}, \tag{45}$$

where $\alpha=e^2/4\pi$,

$$\Phi_t=\exp\left\{\delta P_{st}^2(\lambda=1)\right\},\quad \Phi_u=\exp\left\{\delta P_{su}^2(\lambda=1)\right\}, \tag{46}$$

$$J_1=2\delta\int\limits_0^1 d\lambda\frac{(p'-\lambda q)p_2}{(p'-\lambda q)^2}\exp\left\{\delta P_{st}^2(\lambda)\right\},$$

$$J_2=2\delta\int\limits_0^1 d\lambda\frac{(p'-\lambda q)p_1}{(p'-\lambda q)^2}\exp\left\{\delta P_{su}^2(\lambda)\right\}.$$

For the distribution function (43-II), we similarly obtain

$$M=\sqrt{4\pi\alpha}N_2\left\{z_1\left[(\varepsilon p_2)J_1-\frac{(\varepsilon p_1)}{(qp_1)}\Phi_t\right]+z_2\left[(\varepsilon p_1)J_2-\frac{(\varepsilon p_2)}{(qp_2)}\Phi_u\right]\right\}, \tag{47}$$

$$\Phi_t=\frac{1}{\alpha_0^2-P_{st}^2(\lambda=1)},\quad \Phi_u=\frac{1}{\alpha_0^2-P_{su}^2(\lambda=1)}, \tag{48}$$

$$J_1=2\int\limits_0^1 d\lambda\frac{(p'-\lambda q)p_2}{(p'-\lambda q)^2}\frac{1}{\left[\alpha_0^2-P_{st}^2(\lambda)\right]^2},$$

$$J_2=2\int\limits_0^1 d\lambda\frac{(p'-\lambda q)p_1}{(p'-\lambda q)^2}\frac{1}{\left[\alpha_0^2-P_{su}^2(\lambda)\right]^2}.$$

For the parameters in the distribution functions (43), we choose the values of $\delta=80\ \mathrm{GeV}^{-2}$ and $\alpha_0^2=0.0094\ \mathrm{GeV}^2$ in order that our distributions be similar to actual momentum distributions in few-nucleon bound states; also, we set the normalization factors to $N_1=300$ and $N_2=1.56$ in order that the square of distribution function be normalized to unity.

The dependence of the distribution functions on the relative momentum in the range between 0 and

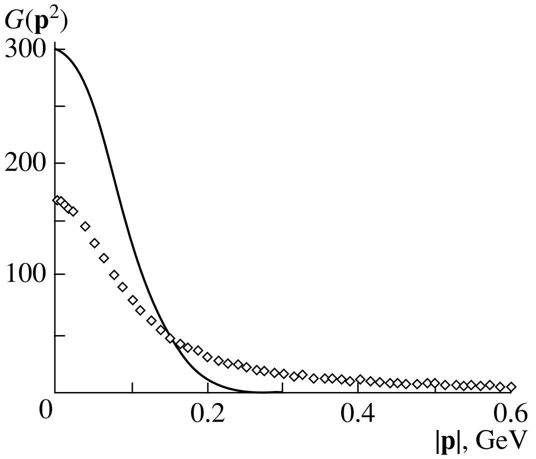

**Fig. 5.** Vertex function versus momentum (momentum distribution) according to the calculation on the basis of (43).

0.6 GeV is shown in Fig. 5, where the solid and the dotted curve correspond to the functions in (43-I) and (43-II), respectively. The quantity $G(\mathbf{p}^2)$ is given in arbitrary units, which are immaterial for the ensuing calculations. These distributions are rather hard at low momenta and behave quite specifically in the high-momentum region.

It should be emphasized that, at a momentum of about 0.15 GeV, the functions in question are equal to each other, but they have different slopes of the tangent to the curve. This value of the relative momentum in the product system corresponds to the incident-photon energy of $E_\gamma^{\text{lab}} = 42$ MeV in the laboratory frame, which is associated with the target. In order to reveal the role of the contact diagram in the amplitude of the process being considered, the differential cross sections $d\sigma(E_\gamma^{\text{lab}}, \vartheta)/d\Omega_{\text{c.m.}}$ with respect to angles were calculated here at this photon-energy value. The results are given in Fig. 6.

From Fig. 6, it can be seen that, as might have been expected, the values corresponding to the dotted curves at the energy value of $E_\gamma^{\text{lab}} = 42$ MeV are identical (in this figure and in the figures that follow, the cross-section values are given in arbitrary units). For the first distribution function (43-I), the absolute value of the contact-diagram contribution (dotted curves) to the total cross section saturates 28% of the total cross section, while the absolute value of the pole-part contribution (dotted curve) is 23% of the total cross section. For the second distribution function (43-II), the respective contributions are 7 and 52%. The regular-part contribution (dashed curves) takes different values, despite the equality of the absolute values of the vertex functions at this point (Fig. 5). The mathematical reason for this is that the values of the derivatives of the vertex functions at the point $E_\gamma^{\text{lab}} = 42$ MeV are different, which explains the different values of the differential cross section calculated on the basis of the total amplitude (solid curves). The physical meaning of this statement is that, in the amplitude, the regular part, which is responsible for the restoration of gauge invariance via the dependence on the form of the vertex function, actually takes into account different fractions of the contribution from the meson sector of the strong-interaction vertex.

We note that the cross-section fractions associated with gauge-noninvariant parts of the total amplitude (dotted and dashed curves) have no absolute meaning, since their values depend on the choice of gauge, whereas the total cross section is invariant under gauge transformations, reflecting its absolute character.

The surfaces of the differential cross section as a function of the photon energy in the laboratory frame and the cosine of the emission angle of a final particle ($x = \cos\vartheta$) are shown in Fig. 7 for angles in the range $\vartheta = 0$–$\pi$ and energies in the range $E_\gamma^{\text{lab}} = 10$–$15$ MeV. Surface *1* corresponds to the calculation performed on the basis of the total matrix element; surface *2* represents the cross section calculated without including the regular part of the amplitude; and surface *3* corresponds to the calculation that employs only the regular part of the amplitude. The cross sections in question were calculated either (Fig. 7*a*) for $z = 2$ and $z_1 = z_2 = 1$ (for example, this may correspond to the photodisintegration of a $^4$He nucleus into two scalar deuterons) or (Fig. 7*b*) for $z = z_1 = 1$ and $z_2 = 0$ (this may be the case of deuteron photodisintegration into two scalar nucleons). The difference in the behavior of the differential cross sections with respect to the variable $x$ is due to the electric-quadrupole character of real-photon absorption in the case in Fig. 7*a* and its electric-dipole character in the case in Fig. 7*b*.

As can be seen from Fig. 7, the fraction of the contribution of the pole part of the amplitude in the total amplitude remains invariable over the entire energy range being considered. The quantitative hierarchy of these contributions for the two different forms (43-I) and (43-II) of the vertex function is analyzed below.

Let us consider the calculation of the energy dependence of the differential cross section for the case where a final particle is emitted at an angle of 45°. The results of this calculation are given in Fig. 8. One can see from Fig. 8 that, for the vertex function in the form (43-I), the contribution of the contact diagram is dominant from the energy of 40 MeV. But for the vertex function in the form (43-II), it is the pole part of the amplitude that makes the main contribution to the

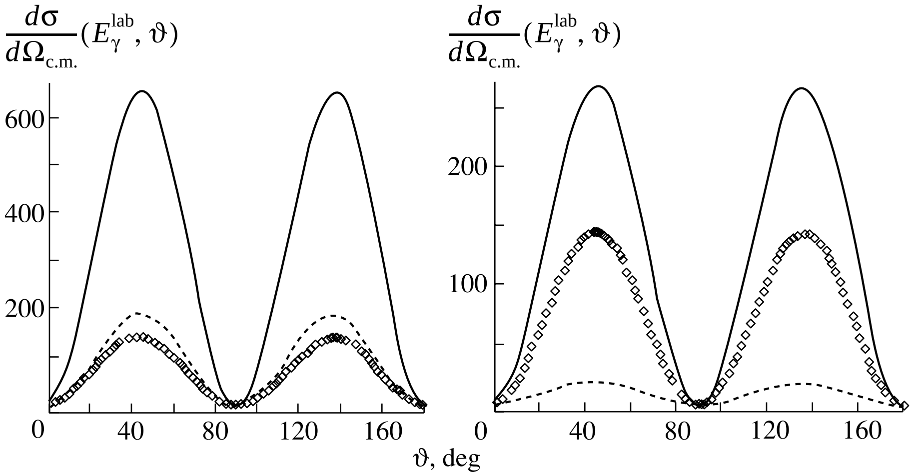

**Fig. 6.** Differential cross sections at $E_\gamma^{\text{lab}} = 42$ MeV in arbitrary units versus the emission angle of a final particle according to calculations with (left panel) the vertex function in the form (43-I) and (right panel) the vertex function in the form (43-II): (solid curves) results of the calculation with the total matrix element [Eqs. (45) and (47)], (dotted curves) results of the calculation that takes into account only the $t$ and $u$ poles, and (dashed curves) results of the calculation that takes into account only the contact diagram.

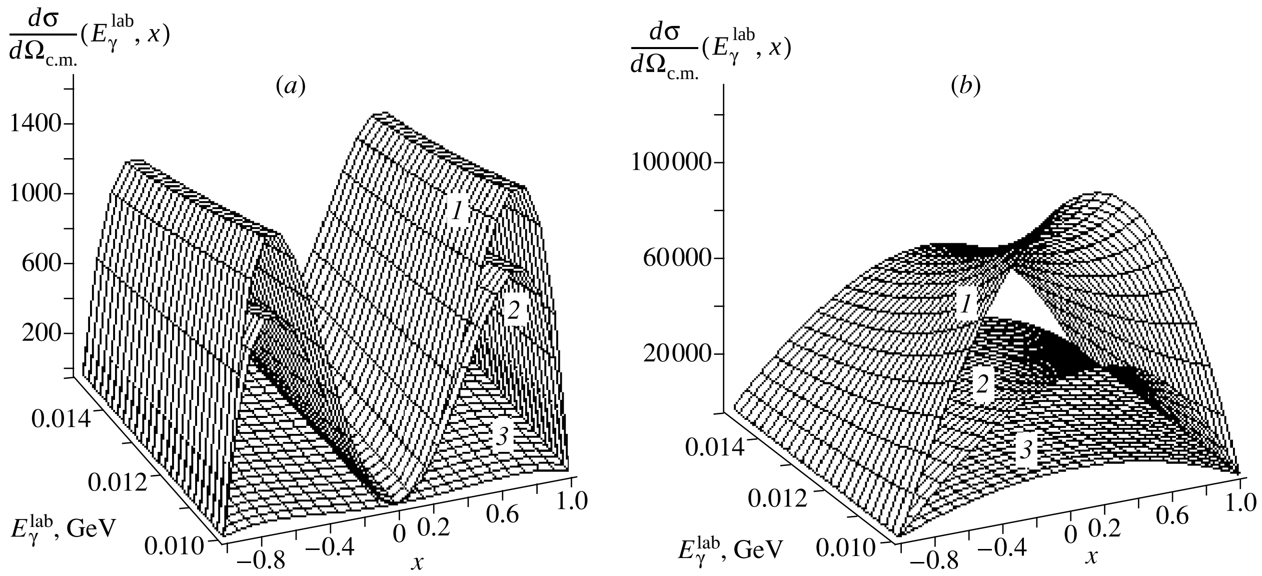

**Fig. 7.** Differential cross section $d\sigma/d\Omega_{\text{c.m.}}$ versus the photon energy in the laboratory frame and the cosine of the emission angle of a final particle ($x = \cos\vartheta$) in the energy range between 10 and 15 MeV: (surfaces *1*) differential cross section calculated on the basis of the total matrix element, (surfaces *2*) differential cross section calculated on the basis of only the pole part of the amplitude, and (surfaces *3*) differential cross section calculated on the basis of only the regular part of the amplitude. The calculations were performed at ($a$) $z = 2$ and $z_1 = z_2 = 1$ and at ($b$) $z = z_1 = 1$ and $z_2 = 0$.

cross section. The above trend toward the invariability of the relationship between the contributions of the contact and pole parts of the total amplitude persists for the second form of the momentum distribution over the entire energy range under consideration. From the above analysis of the two different model forms (43-I) and (43-II) of the vertex function, it follows that both the total amplitude and the relation between the individual contributions of the pole and regular parts, which must be consistent with each other in view of the fundamental requirement of gauge invariance, are highly sensitive to the choice of the vertex function.

There naturally arises the question of whether such a sensitivity of the cross section will be observed with respect to a different relative 4-momentum that is not spacelike this time and which appears as a solution to some other hypothetical approximate

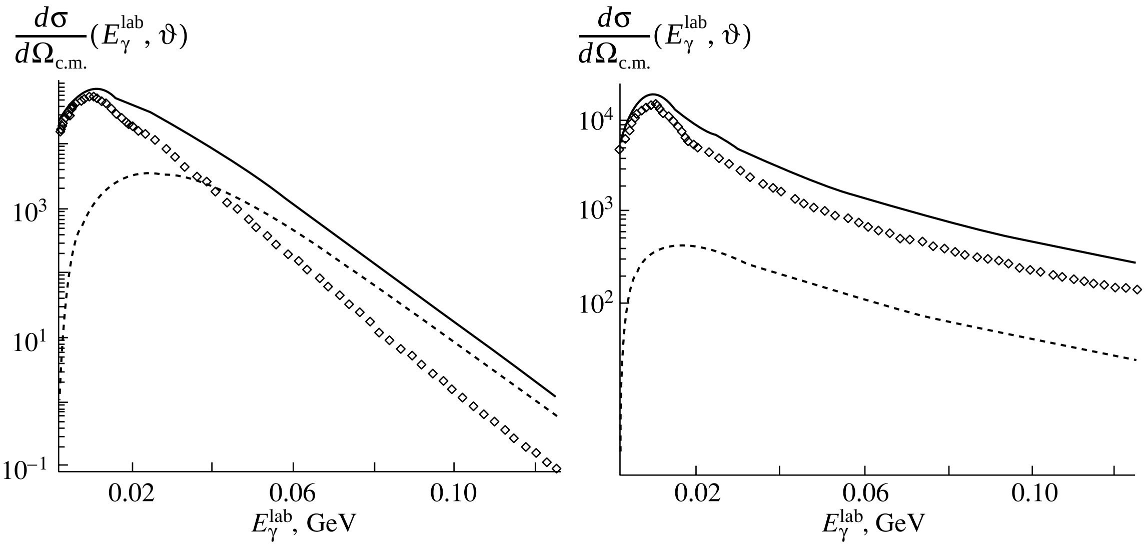

**Fig. 8.** Differential cross sections at the product-particle emission angle of $\vartheta = 45°$ versus energy according to the calculation with (left panel) the vertex function in the form (43-I) and (right panel) the vertex function in the form (43-II): (solid curves) cross sections calculated with the total matrix element [Eqs. (45) and (47)], (dotted curves) cross sections calculated with allowance for only the $t$ and $u$ poles, and (dashed curves) cross sections calculated with allowance for only the contact diagram.

Bethe–Salpeter equation under the condition that the functional dependence of the vertex functions remains unchanged. For this purpose, we choose the relative 4-momenta according to (33):

$$P_\alpha^{st}(\lambda) = P_\alpha^s - \lambda\frac{(p'p_2)}{p'^2}q_\alpha,$$

$$P_\alpha^{su}(\lambda) = P_\alpha^s + \lambda\frac{(p'p_1)}{p'^2}q_\alpha. \qquad (49)$$

As was indicated above, the inequalities $P_\alpha^{st}(\lambda)(p' - \lambda q)_\alpha \neq 0$ and $P_\alpha^{su}(\lambda)(p' - \lambda q)_\alpha \neq 0$ hold for the 4-momenta chosen in this way.

We note that, although the squares of the relative 4-momenta taken in the form (49) are not strictly spacelike, they possess the following remarkable property: irrespective of the explicit form of the vertex function $G(-P^2)$, the integrand in (38) is a total differential for this choice of the relative 4-momenta, this making it possible to evaluate the respective integral for the contact part of the amplitude analytically.

The choice of the momenta in the form (49) has yet another advantage—namely, it admits a very simple representation of these momenta in terms of the singularities of the pole amplitudes in (37); that is,

$$-P_{st}^2(\lambda) = \lambda\frac{m^2 - t}{2} + (1-\lambda)\frac{s - M^2}{4} - \alpha_0^2,$$

$$-P_{su}^2(\lambda) = \lambda\frac{m^2 - u}{2} + (1-\lambda)\frac{s - M^2}{4} - \alpha_0^2,$$

where $\alpha_0^2 = m^2 - \dfrac{M^2}{4}$.

For the choice of the relative 4-momenta according to (49), the matrix element in (36) assumes the form

$$\begin{aligned} \mathrm{M} = e\Bigg\{ & z\frac{(\varepsilon p)}{(qp)}G(-P_s^2) - z_1\frac{(\varepsilon p_1)}{(qp_1)}G(-P_t^2) \\ & - z_2\frac{(\varepsilon p_2)}{(qp_2)}G(-P_u^2) \\ & + \frac{(\varepsilon P_s)}{(qP_s)}\left[z_1 G(-P_t^2) + z_2 G(-P_u^2) - zG(-P_s^2)\right]\Bigg\}, \end{aligned} \qquad (50)$$

its more compact expression being

$$\mathrm{M} = e\varepsilon_\mu\left\{M_\mu^{(\text{pol})} + M_\mu^{(\text{reg})}\right\}, \qquad (51)$$

where $M_\mu^{(\text{pol})}$ and $M_\mu^{(\text{reg})}$ correspond to, respectively, two upper lines and the lower line in (50).

In this representation of the matrix element, we deliberately retained the Lorentz gauge in the expression for the total amplitude in order that the verification of its gauge invariance be clear. In the following, we will perform, as before, all calculations in the reference frame chosen above. At first glance, the presence of the factor $(qP_s)$ in the denominator of the contact part of expression (50) leads to a singularity there, since the scalar product $(qP_s) = -|\mathbf{q}|\,|\mathbf{p}|\cos\vartheta$ vanishes at $\vartheta = 90°$. However, this is not so. In order to demonstrate this, we represent the numerator in the form

$$\begin{aligned} & z_1 G(-P_t^2) + z_2 G(-P_u^2) - zG(-P_s^2) \\ & = z_1 G\left(-P_s^2 + 2\frac{(p'p_2)}{p'^2}(qP_s)\right) \end{aligned}$$

$$+ z_2 G\left(-P_s^2 - 2\frac{(p'p_1)}{p'^2}(qP_s)\right) - zG(-P_s^2)$$

and expand, in this expression, the vertex functions $G$ in Taylor series in the vicinity of the point $-P_s^2$ with allowance for the equality $z = z_1 + z_2$. Since this yields

$$2\left[z_1(p'p_2) - z_2(p'p_1)\right]\frac{(qP_s)}{p'^2}\frac{\partial G}{\partial(-P_s^2)} + o((qP_s)^2),$$

the $(qP_s)$ singularity is removed, which indicates that the contact contribution to the amplitude in (50) is regular for all values of the angle $\vartheta$.

It should be emphasized that the matrix element (50) can be expressed in terms of the electromagnetic-field tensor $F_{\mu\nu} = \varepsilon_\mu q_\nu - \varepsilon_\nu q_\mu$ as

$$\mathrm{M} = e\frac{F_{\mu\nu}P_{(s)\nu}}{(qP_s)}\left\{z\frac{p_\mu}{(qp)}G(-P_s^2) \right. \tag{52}$$

$$\left. - z_1\frac{p_{1\mu}}{(qp_1)}G(-P_t^2) - z_2\frac{p_{2\mu}}{(qp_2)}G(-P_u^2)\right\}$$

or as

$$\mathrm{M} = e\tilde{\varepsilon}_\mu\left\{M_\mu^{(\mathrm{pol})}\right\}, \tag{53}$$

where

$$\tilde{\varepsilon}_\mu = \frac{F_{\mu\nu}P_{s(\nu)}}{(qP_s)} = \varepsilon_\mu - \frac{(\varepsilon P_s)}{(qP_s)}q_\mu. \tag{54}$$

From expression (54), it can be seen that the gauge transformation $\varepsilon_\mu \to \varepsilon_\mu + \eta q_\mu$ leaves $\tilde{\varepsilon}_\mu$ unchanged. The distinction between expressions (53) and (51) is due to some fixed dynamical gauge transformation, where the transformation parameter $\eta$ is a function of the dynamical variable $P_s$:

$$\eta = \eta(P_s) = -\frac{(\varepsilon P_s)}{(qP_s)}. \tag{55}$$

The calculation of cross sections on the basis of the matrix element (50) with the relative 4-momenta in the form (49) leads to results that are very close to those that are obtained from the respective calculation with the 4-momenta given by (41) and (42). The distinctions between the angular and energy spectra do not exceed 4% over the entire energy range considered here.

## 5. CONCLUSION

On the basis of respecting the fundamental principles of covariance, local gauge invariance, and spacetime uniformity, we have developed an approach that extends the possibilities for applying QED to a correct investigation of the photodisintegration of strongly bound systems with allowance for their internal structure.

The approach is based on the use of the local $U(1)$-gauge nature of an electromagnetic field, whose vector potential is identified with a connection that implements a parallel transportation of matter-field operators in a fiber space featuring interior charge symmetry along "minimum" trajectories.

The introduction of two- and three-point Green's functions that describe scalar and spinor fields and which are invariant under the transformations of the local gauge group $U(1)$ and the subsequent calculation of their functional derivatives with respect to the vector potential of the gauge field have made it possible to determine electromagnetic-current vertex functions corresponding to electromagnetic-field interaction with matter fields. It has been shown that the construction of a generalized gauge-closed amplitude is achieved by calculating the functional derivative of the exact three-point Green's function, which is invariant under the transformations of the $U(1)$ group, with respect to the vector potential $A_\mu(r)$ of the gauge field at zero strength of the electromagnetic field. Upon the application of the reduction technique to the resulting series of four-point Green's functions, this series is expressed in terms of the respective contribution to the relevant $S$-matrix element. The electromagnetic structural current constructed on the basis of the reduction series of four-point Green's functions in the momentum representation is exactly conserved, irrespective of the explicit functional form of the vertex operator, this making it possible to use, for the vertex function, solutions to quasipotential equations or solutions to the exact covariant Bethe–Salpeter equation.

The regularities revealed in analyzing the photodisintegration of a scalar system are of a general character and are confirmed by specific calculations performed for actual processes involving deuterons, tritons, and $^3$He and $^4$He nuclei [4, 7–9].

## ACKNOWLEDGMENTS

We are grateful to S.I. Nagorny for stimulating discussions and enlightening comments.

## REFERENCES

1. E. M. Lifshitz and L. P. Pitaevskiĭ, *Relativistic Quantum Theory* (Nauka, Moscow, 1971; Pergamon, Oxford, 1971), Part 2.
2. Yu. A. Kasatkin and I. K. Kirichenko, Vestn. Kharkov. Univ., Ser. Fiz. **524** (3(10)), 25 (2001).
3. Yu. A. Kasatkin, I. K. Kirichenko, and A. P. Korzh, Vestn. Kharkov. Univ., Ser. Fiz. **510** (1(13)), 3 (2001).
4. S. I. Nagornyĭ, Yu. A. Kasatkin, E. V. Inopin, and I. K. Kirichenko, Yad. Fiz. **49**, 749 (1989) [Sov. J. Nucl. Phys. **49**, 465 (1989)].

5. L. Ryder, *Quantum Field Theory* (Cambridge Univ. Press, Cambridge, 1985; Mir, Moscow, 1987).
6. A. I. L'vov, Vopr. At. Nauki Tekh., Ser.: Obshch. Yad. Fiz., No. 2 (35), 53 (1986).
7. A. A. Zayats, V. A. Zolenko, Yu. A. Kasatkin, and A. P. Korzh, Yad. Fiz. **57**, 798 (1994) [Phys. At. Nucl. **57**, 747 (1994)].
8. S. I. Nagornyĭ, Yu. A. Kasatkin, and V. A. Zolenko, Yad. Fiz. **55**, 2385 (1992) [Sov. J. Nucl. Phys. **55**, 1325 (1992)].
9. S. I. Nagornyi, Yu. A. Kasatkin, and V. A. Zolenko, Yad. Fiz. **57**, 1001 (1994) [Phys. At. Nucl. **57**, 940 (1994)].

*Translated by A. Isaakyan*

*Physics of Atomic Nuclei, Vol. 67, No. 4, 2004, pp. 743–747. From Yadernaya Fizika, Vol. 67, No. 4, 2004, pp. 764–768.*
*Original English Text Copyright © 2004 by Baru, Kudryavtsev, Tarasov.*

## ELEMENTARY PARTICLES AND FIELDS
## Theory

# On Rescattering Effects in the Reaction $\pi^- d \to \pi^- d$*

**V. V. Baru[1),2)], A. E. Kudryavtsev[2)], and V. E. Tarasov[2)]****

Received January 21, 2003; in final form, April 20, 2003

**Abstract**—Rescattering corrections to the impulse approximation for the processes $\gamma d \to \pi^0 d$ and $\pi^- d \to \pi^- d$ are discussed. It is shown that the rescattering effects give a nonnegligible contribution to the real part of these amplitudes. At the same time, the contributions from the imaginary parts of impulse and rescattering corrections drastically cancel each other. This cancellation means that the processes $\pi^- d \to \pi^0 nn$ and $\gamma d \to \pi^+ nn/\pi^- pp$, when the nucleon pair is in the spin triplet state, are strongly suppressed near threshold as required by the Pauli principle. © *2004 MAIK "Nauka/Interperiodica".*

## 1. INTRODUCTION

The study of the reactions $\gamma d \to \pi^0 d$ and $\pi^- d \to \pi^- d$ near threshold has attracted continuous attention in the past few decades. Moreover, the new experimental data that appeared owing to the recent success of accelerator technologies stimulate increasing theoretical interest in this field. In this paper, we would like to concentrate on the rescattering effects (RE) and their role for these reactions. Indeed, these effects are found to be important in many of the theoretical investigations of the reaction $\gamma d \to \pi^0 d$ (see, e.g., [1–4]). However, recently in [5], the discussion about the role of these effects was renewed. In particular, it was emphasized in [5] that the contribution from the two-step process $\gamma d \to \pi^- pp \to \pi^0 d$ (see Fig. 1*a*) is totally compensated by the loop corrections to the impulse approximation (LCIA) (see Fig. 1*b*) according to the Pauli principle for the intermediate two-nucleon states. Thus, the rescattering effects in [5] do not contribute to the process of coherent $\pi^0$ photoproduction on a deuteron near threshold. Obviously, this conclusion of [5] disagrees with the results of other calculations performed, e.g., in [1–4]. Let us discuss the arguments of [5] in more detail:

(i) The final $\pi^0 d$ state has quantum numbers $J^P = 1^-$ at low energies, where the pion is in the $S$ wave with respect to the deuteron. However, the only possible state of the system $pp\pi^-$ with $l_1 = l_2 = 0$ is $0^-$ (here, $l_1$ is the orbital angular momentum of the $pp$ system and $l_2$ is the orbital momentum of the pion relative to the $pp$ system). Therefore, the $S$-wave intermediate state $pp\pi^-$ does not contribute to the process $\gamma d \to \pi^0 d$.

(ii) In other words, the contribution of the diagram in Fig. 1*a* has to be compensated by the loop corrections to the impulse approximation (Fig. 1*b*) because of antisymmetry of the wave function for the pair of intermediate nucleons.

Note that the process $\gamma d \to \pi^0 np \to \pi^0 d$ is allowed by quantum numbers. However, the amplitude $\gamma n \to \pi^0 n$ which contributes to this reaction is ~20 times smaller than the corresponding amplitude for the charged pion production.

In this paper, we are going to discuss the role of rescattering effects for the process of pion–deuteron elastic scattering at low energies. The diagrams corresponding to RE and LCIA for the $\pi d$ scattering are very similar to the ones for the reaction $\gamma d \to \pi d$ (see Fig. 1 and Figs. 2*b* and 2*c*). Therefore, we will investigate the relevance of RE and the problem of the cancellation of RE and LCIA performing the calculation of the $\pi d$-scattering amplitude.

The $\pi d$-scattering length was measured with a high accuracy [6, 7] and its value coincides with the theoretical predictions (see, e.g., [8–11]).

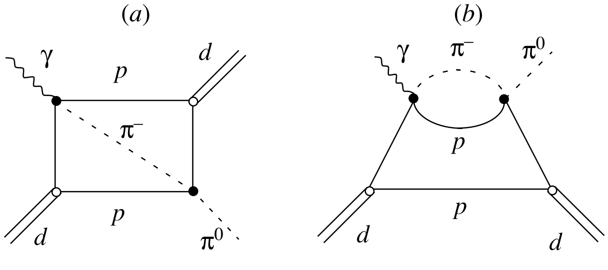

**Fig. 1.** Diagrams with intermediate negative pion rescattering contributing to the process $\gamma d \to \pi^0 d$.

---

*This article was submitted by the authors in English.

[1)]Institut für Kernphysik, Forschungszentrum Jülich, GmbH, Germany.

[2)]Institute of Theoretical and Experimental Physics, Bol'shaya Cheremushkinskaya ul. 25, Moscow, 117259 Russia.

**e-mail: `tarasov@heron.itep.ru`

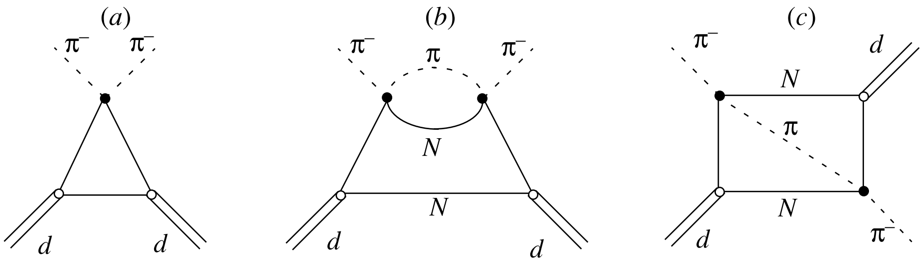

**Fig. 2.** Feynman diagrams contributing to the $\pi d$-scattering amplitude: (*a*) diagram of the first order on the $\pi N$ potential; (*b, c*) diagrams of the second order on the $\pi N$ potential.

In all these theoretical calculations, rescattering effects (including the two-step charge-exchange process $\pi^- p \to \pi^0 n \to \pi^- p$) give a significant contribution to the value of the pion–deuteron scattering length.

In what follows, we will directly demonstrate that the real part of the rescattering diagram (see Fig. 2*c*) gives a nonnegligible contribution to the pion–deuteron scattering length. It is not compensated by the real part of LCIA (see Fig. 2*b*). However, the imaginary parts of RE and LCIA cancel each other. This cancellation means that there is no contribution to observables from the $\pi NN$ states forbidden by the Pauli principle.

## 2. CALCULATION OF THE $\pi d$-SCATTERING AMPLITUDE

Below, we use a simple potential approach for the calculation of the $\pi N$-scattering amplitude. This approach was already applied to the problem of the determination of the $\pi N$-scattering length in [9]. The model utilizes a pion–nucleon potential $V_{\pi N}(\mathbf{p}, \mathbf{q})$, which is required for solving the Lippmann–Schwinger equation

$$T = V + VGT. \tag{1}$$

The $S$-wave $\pi N$ lengths $b_0$ and $b_1$ are related to the scattering length $a_{\pi N}$ by the equation

$$a_{\pi N} = b_0 + b_1 \mathbf{I} \cdot \boldsymbol{\tau}, \tag{2}$$

where $\mathbf{I}$ and $\boldsymbol{\tau}$ are isospin operators for the pion and nucleon, and $b_0$ and $b_1$ are isoscalar and isovector scattering lengths. The analyses [9, 10] of the experimental data [6, 7] show that the absolute values of $b_0$ and $b_1$ are small compared to the typical scale of the problem $\sim \mu^{-1}$ (where $\mu$ is the pion mass). Note also that $b_0 \ll b_1$. Thus, the amplitude $T$ in Eq. (1) may be perturbatively expanded in terms of the potential $V_{\pi N}(\mathbf{p}, \mathbf{q})$.

Following [9], we choose $V_{\pi N}$ in the $S$ wave in the separable form

$$V_{\pi N}(\mathbf{k}, \mathbf{q}) = -\frac{(\lambda_0 + \lambda_1 \mathbf{I} \cdot \boldsymbol{\tau})}{2m_{\pi N}} g(k) g(q), \tag{3}$$

where $g(k) = (c^2 + k^2)^{-1}$, $m_{\pi N} = m\mu/(m+\mu)$, $\mathbf{k}$ and $\mathbf{q}$ are the 3-momenta of the pion, and $m$ is the nucleon mass. The cutoff parameter $c$ characterizes the range of the $\pi N$ forces, and usually it is varied in the range $2.5\mu \le c \le 5\mu$ [9, 10]. The parameters $\lambda_0$ and $\lambda_1$ are chosen in such a way as to reproduce the scattering lengths $b_0$ and $b_1$. In what follows, we will calculate the pion–deuteron scattering amplitude up to the second order in terms of the potential $V_{\pi N}$. With this accuracy, $\lambda_0$ and $\lambda_1$ are equal to

$$\lambda_0 = \frac{c^4}{2\pi^2}\left(b_0 - \frac{c}{2}(b_0^2 + 2b_1^2)\right), \tag{4}$$

$$\lambda_1 = \frac{c^4}{2\pi^2} b_1 \left(1 - \frac{c}{2}(2b_0 - b_1)\right).$$

Corrections to these expressions are of the order of $\sim O(b_0^3, b_1^3)$, which is negligible.

Let us calculate the pion–deuteron scattering length using the potential $V_{\pi N}$ [see Eq. (3)].

### *2.1. Single-Scattering Amplitude in the Born Approximation*

The diagram corresponding to this amplitude is shown in Fig. 2*a*. The expression for the $\pi d$ amplitude $f_{\pi d}^{(1)V}$ corresponding to the sum of two diagrams with the scattering of a pion on a proton and neutron has the form

$$f_{\pi d}^{(1)V} = -\frac{\mu}{(2\pi)(1 + \mu/m_d)} \tag{5}$$

$$\times \int d\mathbf{p} \varphi_d^2(\mathbf{p}) [V_{\pi^- p} + V_{\pi^- n}].$$

Here, $\varphi_d(\mathbf{p})$ is the deuteron wave function in the momentum space with the normalization condition $\int d\mathbf{p} \varphi_d^2(\mathbf{p}) = (2\pi)^3$. Neglecting the small corrections of the order of $\sim \mu/m$, one may take the potential $V$ in Eq. (5) out of the integral and then get

$$f_{\pi d}^{1(V)} = 2\left[b_0 - \frac{c}{2}(b_0^2 + 2b_1^2)\right]. \tag{6}$$

This contribution is real, as it should be in the Born approximation. Note also that the value $f_{\pi d}^{1(V)}$ depends on the value of the parameter $c$.

### 2.2. Single Scattering in the One-Loop Approximation

The diagram for the one-loop correction to the Born approximation is shown in Fig. 2*b*. We have to calculate the sum of two diagrams with the scattering of a pion on a proton and neutron, taking into account the sum over all intermediate states. The expression for the amplitude $f_{\pi d}^{(1)VGV}$ corresponding to this sum has the form

$$f_{\pi d}^{(1)VGV} = \frac{2\mu}{1+\mu/m_d}\left[(\lambda_0^2+\lambda_1^2)I(\Delta m=0)+\lambda_1^2 I(\Delta m)\right], \tag{7}$$

$$I(\Delta m) = \int \frac{d\mathbf{p}}{2\pi}\frac{g^2\left(\dfrac{m\mathbf{k}-\mu\mathbf{p}}{m+\mu}\right)\varphi_d^2(\mathbf{p})}{(2m_{\pi N})^2}\int\frac{d\mathbf{s}g^2\left(\dfrac{m\mathbf{k}-\mu\mathbf{p}}{m+\mu}+\mathbf{s}\right)}{\left[\dfrac{(\mathbf{k}+\mathbf{s})^2}{2\mu}+\dfrac{p^2}{2m}+\dfrac{(\mathbf{p}-\mathbf{s})^2}{2m}+\varepsilon_d-\Delta m-\dfrac{k^2}{2\mu}-i0\right]}.$$

Here, $\mathbf{k}$ is the 3-momentum of the initial and final pion, $\varepsilon_d$ is the deuteron binding energy, and $\Delta m = m_{\pi^-}+m_p-m_{\pi^0}-m_n = 3.3$ MeV is the excess energy for the charge-exchange process $\pi^- p \to \pi^0 n$ in the intermediate state. For the case of elastic rescattering, $\Delta m = 0$.

The integral in Eq. (7) is calculated numerically for some values of the cutoff parameter $c$. In the limit of large $c$, i.e., when $c \gg \mu$, and for $\mu/m \ll 1$, the integral can be calculated analytically:

$$f_{\pi d}^{(1)VGV} = c(b_0^2+2b_1^2) + 2i\left[k_0(\Delta m=0)(b_0^2+b_1^2)+k_0(\Delta m)b_1^2\right], \tag{8}$$

where we introduced the notation $k_0^2 = k^2+2\mu\Delta m - 2\mu\varepsilon_d$. Note that $k \ll c$ near the threshold.

Thus, in the limit of large $c$, the resulting contribution from the impulse approximation (see Figs. 2*a* and 2*b*) to the real part of the $\pi d$-scattering amplitude is

$$\mathrm{Re} f_{\pi d}^{1} = f_{\pi d}^{1(V)} + \mathrm{Re} f_{\pi d}^{(1)VGV} = 2b_0. \tag{9}$$

This is a naive but expected result for the real part of the amplitude corresponding to the impulse approximation. The values of $\mathrm{Re} f_{\pi d}^{(1)VGV}$ for the charge-exchange process $\pi^- d \to \pi^0 nn \to \pi^- d$ are presented in the table for different values of parameter $c$. Contrary to the real part of the loop amplitude, the imaginary part of $f_{\pi d}^{(1)VGV}$ [see Eq. (8)] does not depend on $c$ as required by the unitarity.

Now, let us discuss the contribution to the pion—deuteron scattering length from the double-scattering process.

### 2.3. Double-Scattering Contribution

The double-scattering diagram is shown in Fig. 2*c*. Performing the calculation, we have the following integral for the double-scattering amplitude $f_{\pi d}^{(2)}$ (see [9] for details):

$$f_{\pi d}^{(2)} = \frac{4c^4}{(2\pi)^5}\left[(b_0^2-b_1^2)J(\Delta m=0)-b_1^2 J(\Delta m)\right], \tag{10}$$

$$J(\Delta m) = \int\frac{d\mathbf{q}_1 d\mathbf{q}_2\varphi_d(\mathbf{q}_1)\varphi_d(\mathbf{q}_2)g^2(\mathbf{k}+\mathbf{q}_1-\mathbf{q}_2)}{(\mathbf{k}+\mathbf{q}_1-\mathbf{q}_2)^2+(\mu/m)(q_1^2+q_2^2)+2\mu(\varepsilon_d-\Delta m)-k^2-i0}.$$

In the limit of large $c$ and for $\mu/m \ll 1$, this integral is reduced to the following expression:

$$f_{\pi d}^{(2)} = 2(b_0^2-b_1^2)\times\int\Psi_d^2(r)\frac{e^{-i\mathbf{k}\cdot\mathbf{r}+ik_0(\Delta m=0)r}}{r}d\mathbf{r} - 2b_1^2\int\Psi_d^2(r)\frac{e^{-i\mathbf{k}\cdot\mathbf{r}+ik_0(\Delta m)r}}{r}d\mathbf{r}, \tag{11}$$

where $\Psi_d(\mathbf{r})$ is the deuteron wave function in the coordinate space.

In the limit of small $k$ and $k_0$, i.e., near the threshold, for the real part of $f_{\pi d}^{(2)}$, we get

$$\mathrm{Re} f_{\pi d}^{(2)} = 2(b_0^2-2b_1^2)\left\langle\frac{1}{r}\right\rangle_d. \tag{12}$$

Real parts of the contributions from the diagrams shown in Figs. 2*b* and 2*c* for the charge-exchange process

| $c$ | $\mathrm{Re}f_{\pi d}^{(1)VGV}$, fm | $\mathrm{Re}f_{\pi d}^{(2)}$, fm |
|---|---|---|
| $2\mu$ | 0.0199 | −0.0084 |
| $3\mu$ | 0.0317 | −0.0098 |
| $4\mu$ | 0.0435 | −0.0104 |
| $5\mu$ | 0.0551 | −0.0107 |

This expression is well known as a static limit for the double-scattering amplitude (see, e.g., [12] and references therein).

The imaginary part of the amplitude $f_{\pi d}^{(2)}$ (11) in the same limit is

$$\mathrm{Im} f_{\pi d}^{(2)} = 2k_0(\Delta m = 0)(b_0^2 - b_1^2) - 2k_0(\Delta m) b_1^2. \tag{13}$$

Note that this contribution is negative, because $b_1 \gg b_0$.

### 2.4. Total Pion–Deuteron Amplitude

Let us discuss the value for the total pion–deuteron scattering amplitude in the limit of large $c$ ($c \gg \mu$) and for $\mu/m \ll 1$. For the imaginary part of the resulting amplitude in this limit from Eqs. (8) and (13), we get

$$\mathrm{Im} f_{\pi d} \approx 4k_0(\Delta m = 0) b_0^2. \tag{14}$$

Thus, we find that the contributions from LCIA and RE to the imaginary part of the pion–deuteron scattering amplitude cancel each other in the leading order (i.e., terms $\sim b_1^2$). The nonvanishing part of $\mathrm{Im} f_{\pi d}$ is proportional to $b_0^2$, which corresponds to the elastic rescattering process $\pi^- d \to \pi^- pn \to \pi^- d$. Note that the imaginary parts of both expressions (8) and (13) behave as two-particle phase space, i.e., proportional to $k_0 \sim Q^{1/2}$, where $Q$ is the kinetic energy of the intermediate $\pi NN$ system. However, three-particle $\pi NN$ phase space should behave as $Q^2$. This paradox can be resolved if we remind the reader that the approximation $\mu/m \ll 1$, which implies that the kinetic energies of the intermediate nucleons in Eqs. (7) and (10) are neglected, was used to obtain Eqs. (8) and (13). This approximation corresponds to the rescattering of pions on the fixed centers. That is why the imaginary parts in Eqs. (8) and (13) behave as $Q^{1/2}$. The result (14) means that the only possible final state which can be formed in the $S$ wave in the process of deuteron disintegration is $pn\pi^-$ (with total spin $S = 1$ and isospin $I = 0$ for a pair of nucleons). The virtual charge exchange does not contribute to the imaginary part of the pion–deuteron amplitude. This conclusion is in agreement with the remark of [5].

At the same time, we would like to stress that there is no complete cancellation between the real parts of the amplitudes $f_{\pi d}^{(1)VGV}$ and $f_{\pi d}^{(2)}$, i.e., the resulting contribution from LCIA and RE to the real part of the pion–deuteron scattering amplitude is not small. This conclusion, which is also correct for the process $\gamma d \to \pi^0 d$, is in contrast to the arguments of [5]. As can be seen from Eq. (8), the expression for $\mathrm{Re}f_{\pi d}^{(1)VGV}$ depends linearly on the cutoff parameter $c$ for large values of $c$ and $\mu/m \ll 1$, whereas $\mathrm{Re}f_{\pi d}^{(2)}$ in the same limit is totally determined by the deuteron wave function, i.e., independent of $c$ [see Eq. (12)]. Therefore, the cancellation of the real parts of the amplitudes $f_{\pi d}^{(1)VGV}$ and $f_{\pi d}^{(2)}$ cannot be achieved in this limit (the value $c = 2\langle |1/r| \rangle_d \approx 1.2\mu$ is obviously not realistic).

In [9], we have calculated the sum of the real parts of the diagrams presented in Fig. 2 varying the parameter $c$ in the limits $2.5\mu \le c \le 3.5\mu$. The results of our numerical calculation are shown in the table for the case where $c$ varies in a larger range and the terms $\sim O(\mu/m)$ are taken into account. In the calculation, we use the purely hadronic values for $b_0$ and $b_1$ presented in [7], i.e., $b_0 = -2.2 \times 10^{-3} m_\pi^{-1}$ and $b_1 = 90.5 \times 10^{-3} m_\pi^{-1}$. This table clearly confirms the conclusion discussed above that the real parts of the diagrams of Figs. 2*b* and 2*c* do not cancel each other.

## 3. SUMMARY

We developed a consequent potential approach to the problem of the calculation of the pion–deuteron scattering length. The $\pi d$ amplitude was calculated with inclusion of terms of the second order with respect to the pion–nucleon potential $V_{\pi N}$. The proper symmetrization of the wave function for the intermediate nucleons is taken into account automatically in our approach.

We show that there is a significant cancellation of the contributions from the imaginary parts of LCIA (Fig. 2*b*) and RE (Fig. 2*c*). This cancellation is expected. It simply reflects the fact that the process $\pi^- d \to \pi^0 nn$ is strongly suppressed near threshold, as required by the Pauli principle. However, no such cancellations take place between the real parts of these processes. The integrals for the real parts of the amplitudes (7) and (10) are quite different. In particular, they have a different dependence on the cutoff parameter $c$ in the form factor. Therefore, we see no reasons for the cancellation of $\mathrm{Re}f^{(1)VGV}_{\pi^- d}$ and $\mathrm{Re}f^{(2)}_{\pi^- d}$.

The situation for the reaction $\gamma d \to \pi^0 d$ is quite analogous to that discussed for the reaction $\pi d \to \pi d$. There are no reasons for the cancellation of the real parts of the diagrams shown in Figs. 1*a* and 1*b*. This conclusion is in agreement with the results of [1–4], where rescattering effects are found to be important for the reaction $\gamma d \to \pi^0 d$.

## ACKNOWLEDGMENTS

We would like to thank A.M. Gasparyan and V.G. Ksenzov for useful discussions.

This work was partly supported by the Russian Foundation for Basic Research (project no. 02-02-16465) and DFG–RFBR (grant no. 436 RUS 113/652/0-1).

## REFERENCES

1. J. H. Koch and R. M. Woloshin, Phys. Rev. C **16**, 1968 (1977).
2. P. Bosted and J. M. Laget, Nucl. Phys. A **296**, 413 (1978).
3. G. Fäldt, Phys. Scr. **22**, 5 (1980).
4. S. R. Beane *et al.*, Nucl. Phys. A **618**, 381 (1997).
5. M. Rekalo and E. Tomasi-Gustafsson, Phys. Rev. C **66**, 015203 (2002); nucl-th/0112063.
6. D. Chatellard *et al.*, Phys. Rev. Lett. **74**, 4157 (1995); Nucl. Phys. A **625**, 855 (1997).
7. H. Ch. Schröder *et al.*, Phys. Lett. B **469**, 25 (1995); Eur. Phys. J. C **21**, 473 (2001).
8. V. M. Kolybasov and A. E. Kudryavtsev, Nucl. Phys. B **41**, 510 (1972).
9. V. V. Baru and A. E. Kudryavtsev, Yad. Fiz. **60**, 1620 (1997) [Phys. At. Nucl. **60**, 1475 (1997)]; $\pi N$-Newsletter **12**, 64 (1997).
10. T. E. O. Ericson, B. Loiseau, and A. W. Thomas, hep-ph/0009312, submitted to Phys. Rev. C.
11. A. Deloff, Phys. Rev. C **64**, 065205 (2001); nucl-th/0104067.
12. T. Ericson and W. Weise, *Pions and Nuclei* (Clarendon Press, Oxford, 1988), p. 126.

*Physics of Atomic Nuclei, Vol. 67, No. 4, 2004, pp. 748–756. Translated from Yadernaya Fizika, Vol. 67, No. 4, 2004, pp. 769–777.*
*Original Russian Text Copyright © 2004 by Shunderuk.*

## ELEMENTARY PARTICLES AND FIELDS
## Theory

# Properties of Multi-Skyrmions and Their Quantization within a Generalized Chiral Soliton Model

**A. M. Shunderuk**[*]

*Institute for Nuclear Research, Russian Academy of Sciences,*
*pr. Shestidesyatiletiya Oktyabrya 7a, Moscow, 117312 Russia;*
*Moscow Institute for Physics and Technology,*
*Institutskiĭ proezd 9, Dolgoprudnyĭ, Moscow oblast, 141700 Russia*

Received June 2, 2003

**Abstract**—A semiclassical quantization of the Skyrme model featuring a sixth-order term in the derivatives of the chiral field in the Lagrangian is performed. The orbital, isotopic, interference, and flavor tensors of inertia are calculated. For this version of the model, numerical calculations are performed for the excitation energies of flavors in baryon systems. © *2004 MAIK "Nauka/Interperiodica".*

## 1. INTRODUCTION

The Skyrme model of baryons as chiral-field solitons makes it possible to describe mesons and baryons with the aid of the same effective Lagrangian [1], configurations characterized by different baryon numbers being considered as solutions for this effective Lagrangian that belong to different topological classes.

A unitary matrix $U(x) \in SU(2)$,

$$U = e^{if(x)\mathbf{n}(x)\cdot\boldsymbol{\tau}} = \cos f + i\sin f(\mathbf{n}\cdot\boldsymbol{\tau}),$$
$$\mathbf{n}^2 = 1,$$

that is expressed in terms of meson fields $\boldsymbol{\pi}$ and $\sigma$ according to the relations $\boldsymbol{\pi} = (F_\pi/2)\mathbf{n}\sin f$ and $\sigma = (F_\pi/2)\cos f$ is a dynamical field of the model, the constraint

$$\boldsymbol{\pi}^2 + \sigma^2 = \text{const} \quad (1)$$

being satisfied.

The boundary condition $U(|\mathbf{r}| = \infty, t) = 1$ (which corresponds to a physical vacuum) makes it possible to break down all field configurations $U(\mathbf{r})$ into topological classes according to the multiplicity of the mapping of the space $\mathbf{r} \in R^3$ into the interior-symmetry space—namely, a sphere of fixed radius in the four-dimensional space $(\boldsymbol{\pi}, \sigma)$. There exists the conserved [by virtue of the constraint (1)] topological current

$$B^\mu = \frac{1}{24\pi^2}\varepsilon^{\mu\nu\alpha\beta}\mathrm{tr}L_\nu L_\alpha L_\beta, \quad (2)$$

which determines the topological charge

$$B = \int B^0 d^3r,$$

the latter being coincident with the multiplicity of mapping. The anti-Hermitian matrix $L_\mu \equiv \partial_\mu U U^\dagger$ is a left chiral derivative. The boundary condition ensures that the topological charge $B$ is an integer. From the physical point of view, the topological charge $B$ is identified with the baryon number of the meson-field configuration [1].

In terms of the field $U$, the chirally symmetric kinetic term in the meson Lagrangian,

$$\mathcal{L}_{\text{kin}} = \frac{1}{2}(\partial_\mu\boldsymbol{\pi}\partial^\mu\boldsymbol{\pi} + \partial_\mu\sigma\partial^\mu\sigma), \quad (3)$$

has the form

$$\mathcal{L}_{\text{kin}} = \frac{F_\pi^2}{16}\mathrm{tr}\partial_\mu U\partial^\mu U^\dagger = -\frac{F_\pi^2}{16}\mathrm{tr}L_\mu L^\mu. \quad (4)$$

It is well known that a static solution to the Lagrange–Euler equation minimizes the energy functional. However, the scale transformation $\mathbf{r} \to a\mathbf{r}$ reveals that the energy functional corresponding to the Lagrangian in (4) has no minimum. A soliton can be stabilized by supplementing the Lagrangian with higher order terms in derivatives. In order to provide the possibility of performing a quantization, it is necessary to include only the first derivatives of the field $U$, with the power of the time derivative not being higher than two.

So far, attention has been given primarily to the original version of the Skyrme model [$Sk(4)$], where

---

[*] e-mail: `A.Shunderuk@umail.ru`

the soliton is stabilized by a quartic term in the derivatives,

$$\mathcal{L}_4 = \frac{1}{32e_{Sk}^2}\mathrm{tr}[L_\mu, L_\nu]^2. \tag{5}$$

Within a different model version that satisfies the aforementioned requirements, the Lagrangian involves a sixth-order term in the derivatives $[Sk(6)]$,

$$\mathcal{L}_6 = -c_6\mathrm{tr}[L_\mu, L^\nu][L_\nu, L^\alpha][L_\alpha, L^\mu]. \tag{6}$$

Previously, this Lagrangian has been investigated only at the classical level [2]. In the present study, a semiclassical quantization is performed.

The total Lagrangian of the model also involves a chiral-symmetry-breaking mass term; that is,

$$\mathcal{L} = \mathcal{L}_{\mathrm{kin}} + \mathcal{L}_4 + \mathcal{L}_6 + \mathcal{L}_m, \tag{7}$$

where

$$\mathcal{L}_m = \frac{F_\pi^2 m_\pi^2}{16}\mathrm{tr}(U + U^\dagger - 2). \tag{8}$$

All qualitative properties of classical solutions (they are discussed in the next section) are independent of the presence of the mass term in view of the smallness of the pion mass.

The generalized model involves the following four constants: $F_\pi$, the pion decay constant; $m_\pi$, the pion mass; and $e_{Sk}$ and $c_6$, free parameters that specify the coefficients in front of the $Sk(4)$ and $Sk(6)$ terms, respectively.

## 2. CLASSICAL SOLUTIONS

Numerical calculations revealed that the field configurations of lowest energy possess different symmetries for different baryon numbers $B$. These are spherical symmetry for $B = 1$, axial symmetry for $B = 2$ [3], tetrahedral symmetry for $B = 3$, cubic symmetry for $B = 4$ [4], etc. The symmetries of Skyrmions for baryon numbers up to $B = 22$ inclusive were determined in [5]. For $B > 6$, all of them, with the exception of two cases, are formed by 12 pentagons and $2B - 14$ hexagons. Configurations of icosahedral symmetry were recently found for greater baryon numbers ($B$ = 37, 47, 67, 97) [6]. Numerical calculations for $B \leq 5$ within the $Sk(6)$ version and the mixed version of the model showed that Skyrmions have the same symmetries in this case as well [2]. Within the $Sk(6)$ version of the model, a toroidal solution was found for the first time in [3].

In [7], a rational-map ansatz was proposed to describe such solutions. The classical-mass values obtained with the aid of this method agree to within about 2% with the results of numerical calculations.

The basic idea of that approach is as follows. It can be assumed that the profile function $f$ depends only on the distance to the Skyrmion center and that the unit vector $\mathbf{n}$ depends only on angular variables; that is,

$$U(\mathbf{r}) = e^{if(r)\mathbf{n}(\theta,\phi)\cdot\boldsymbol{\tau}}. \tag{9}$$

The function $\mathbf{n}(\theta, \phi)$ specifies the map having the index $\mathcal{N}$ and transforming a unit two-dimensional sphere in coordinate space into a unit two-dimensional sphere in isospin space ($S^2 \mapsto S^2$). In general, we have $\mathcal{N} = B$ for minimum-energy configurations (this corresponds to the boundary conditions $f(0) = \pi$, $f(+\infty) = 0$).

By using the stereographic projection, a unit sphere in coordinate space can be transformed into a complex plane

$$z = \tan\frac{\theta}{2}e^{i\phi} \tag{10}$$

and a unit sphere in isospin space can be transformed into its own complex plane

$$n_x = \frac{2\mathrm{Re}R}{1 + |R|^2}, \qquad n_y = \frac{2\mathrm{Im}R}{1 + |R|^2}, \tag{11}$$
$$n_z = \frac{1 - |R|^2}{1 + |R|^2}.$$

In this case, $R(z)$ will be a rational function of power $\mathcal{N}$ .

Considering that $|dR/dz|^2$ is the Jacobian of the map $z \mapsto R(z)$ , one can easily prove that the index of the map admits the integral representation

$$\mathcal{N} = \frac{1}{8\pi}\int r^2(\partial_k\mathbf{n})^2 d\Omega \tag{12}$$
$$= \frac{1}{\pi}\int\left(\frac{1 + |z|^2}{1 + |R|^2}\left|\frac{dR}{dz}\right|\right)^2\frac{dS_z}{(1 + |z|^2)^2},$$

where $(\partial_k\mathbf{n})^2 \equiv (\partial_k\mathbf{n}, \partial_k\mathbf{n})$, $k = 1\ldots3$; $dS_z$ is an area element on the complex plane; and $d\Omega$ is a solid-angle element in coordinate space,

$$d\Omega = \frac{4dS_z}{(1 + |z|^2)^2}. \tag{13}$$

We use the following notation for the corresponding integral with respect to angles:

$$\Im = \frac{1}{8\pi}\int r^4[\partial_i\mathbf{n}, \partial_k\mathbf{n}]^2 d\Omega \tag{14}$$
$$= \frac{1}{\pi}\int\left(\frac{1 + |z|^2}{1 + |R|^2}\left|\frac{dR}{dz}\right|\right)^4\frac{dS_z}{(1 + |z|^2)^2}.$$

The Cauchy–Schwarz (Buniakowski's) inequality for the integrals $\mathcal{N}$ and $\Im$ leads to $\Im \geqslant \mathcal{N}^2$; numerical calculations reveal that, for the minimum-energy configurations, $\Im \sim \mathcal{N}^2$.

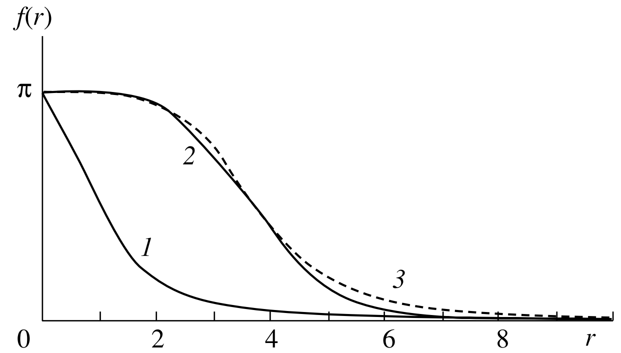

**Fig. 1.** Profile functions obtained for rational-map multi-Skyrmions at various baryon numbers by minimizing the mass functional (15) within the $Sk(6)$ version of the model ($\lambda = 1$): (curve *1*) numerical solution for $B = 1$, (curve *2*) numerical solution for $B = 17$, and (curve *3*) analytic approximation for $B = 17$. The scale along the radius was chosen to be $2/(F_\pi e)$.

Let us choose $2/(F_\pi e)$ for a unit of length and $3\pi^2 F_\pi/e$ for a unit of energy (here, $e = e_{Sk}\sqrt{1-\lambda}$ with $\lambda/(1-\lambda)^2 = 48c_6F_\pi^2e_{Sk}^4$ ). At $\lambda = 0$, we arrive at the original version of the Skyrme model [without an $Sk(6)$ term], while, at $\lambda = 1$, we obtain a pure $Sk(6)$ version [without an $Sk(4)$ term]. In the latter case, we have $e = 1/\sqrt[4]{48c_6F_\pi^2}$.

In the limit $m_\pi = 0$, the classical Skyrmion mass obtained from (7) with the aid of a rational map and reduced to a dimensionless form in the way outlined above is given by [2, 8]

$$M_{\mathrm{clas}} = \frac{1}{3\pi}\int\limits_0^\infty \left\{\left(r^2 f'^2(r) + 2Bs_f^2\right) + (1-\lambda)s_f^2\left(2Bf'^2(r) + \Im\frac{s_f^2}{r^2}\right) + \lambda\Im\frac{s_f^4}{r^2}f'^2(r)\right\}dr. \qquad (15)$$

The baryon-number density averaged over angles has the form

$$\rho_B(r) = 4\pi r^2 B^0(r) = -\frac{2B}{\pi}s_f^2 f'(r). \qquad (16)$$

Hereafter, we use the notation $s_f = \sin f$ and $c_f = \cos f$. The relevant integrals with respect to angles were evaluated with the aid of formulas (12) and (14). Thus, the problem of minimizing the classical mass has been broken down into two independent problems: that of minimizing the integral $\Im$ with respect to the angles and that of minimizing the mass functional (15), which depends only on the profile function $f(r)$.

Technically, the main difficulty consists in finding the integral $\Im$ and the specific form of the map of a sphere into a sphere. As was shown in [8, 9], the problem of minimizing the functional in (15) and studying the basic features of multi-Skyrmions versus $B$ and $\Im$ can be solved analytically to a high precision, many features of multi-Skyrmions being only slightly dependent on the angular distribution since $\Im$ either does not appear at all in the respective expressions or appears only through the factor $\sqrt[4]{\Im/B^2}$, which is close to unity. The required substitution for the profile function can be obtained on the basis of the fact that the functional in (15) is a quadratic form. The result is

$$\cos f = \frac{(r/r_0)^b - 1}{(r/r_0)^b + 1}, \qquad (17)$$

where $b$ and $r_0$ are parameters that must be determined by minimizing the mass functional (15). It is obvious that $r_0$ has the meaning of the Skyrmion radius. At $B \gg 1$, it was found that

$$r_0^{\min} \approx \sqrt[4]{\frac{4}{9}\Im}, \qquad b^{\min} \approx 2\sqrt[4]{\Im}, \qquad (18)$$

$$\frac{M_{\mathrm{clas}}^{\min}}{B} \approx \frac{4}{3\pi}\sqrt{\frac{2}{3}}\left(2 + \sqrt{\frac{\Im}{B^2}}\right)$$

in the pure $Sk(4)$ case ($\lambda = 0$) and that

$$r_0^{\min} \approx \sqrt[4]{\frac{8}{15}\Im}, \qquad b^{\min} \approx 2\sqrt{B}, \qquad (19)$$

$$\frac{M_{\mathrm{clas}}^{\min}}{B} \approx \frac{8}{3\pi}\sqrt[4]{\frac{8}{15}\frac{\Im}{B^2}}$$

in the pure $Sk(6)$ case ($\lambda = 1$).

Since $\Im \sim B^2$, the Skyrmion size is $r_0 \sim \sqrt{B}$, while the classical mass is proportional to $B$. The profile function $f(r)$ and its analytic approximation are depicted in Fig. 1.

From formulas (15) and (16), it directly follows that the energy density and the baryon-number density are nonzero only in that region of space where the profile function $f(r)$ does actually change from $\pi$ to 0—that is, inside some spherical layer $r_0 - w/2 \leqslant r \leqslant r_0 + w/2$, beyond which we have $f(r < r_0 - w/2) \approx \pi$ and $f(r > r_0 + w/2) \approx 0$. The layer width $w$ can be determined as the doubled distance between the points where $\cos f = \pm 1/2$. This yields $w = 4(r_0/b)\ln 3$—that is, the result is independent of $B$.

For Skyrmions of large baryon number, the mass and the baryon charge are therefore concentrated at the surface of a sphere whose radius grows with increasing baryon number in proportion to $\sqrt{B}$, the layer width taking the same value for Skyrmions having different baryon numbers (see Fig. 2). The mean volume energy density within the layer, $M_{\mathrm{clas}}/(4\pi r_0^2 w)$, does not depend on $B$ either [9, 10].

## 3. SEMICLASSICAL QUANTIZATION

On the basis of each static solution $U(\mathbf{r})$, one can construct, with the aid of rotations in ordinary space and in isospin space, an energy-degenerate family of configurations $U(\mathbf{r}, A, R) = AU(R\mathbf{r})A^\dagger$, where $A$ is a unitary $SU(2)$ matrix and $R$ is an orthogonal $O(3)$ matrix. In performing quantization of these zero-point modes, the model parameters $R$ and $A$ become the dynamical variables $R(t)$ and $A(t)$.

Upon the substitution of the field $\widetilde{U}(\mathbf{r}, t) = A(t)U(R(t)\mathbf{r})A^\dagger(t)$ into the Lagrangian in (7), we obtain the contribution of the rotational energy in the form

$$E_{\text{total}} = M_{\text{clas}} + E_{\text{rot}}, \qquad (20)$$

$$E_{\text{rot}} = \frac{1}{2}\Theta^I_{ab}\omega_a\omega_b + \Theta^{\text{int}}_{ab}\omega_a\Omega_b + \frac{1}{2}\Theta^J_{ab}\Omega_a\Omega_b,$$

where $\Theta^I_{ab}$ is the isospin tensor of inertia; $\Theta^J_{ab}$ is the orbital tensor of inertia; $\Theta^{\text{int}}_{ab}$ is the interference tensor of inertia; and $\omega_a$ and $\Omega_a$ are angular velocities,

$$A^\dagger\dot{A} = -\frac{i}{2}\boldsymbol{\omega}\cdot\boldsymbol{\tau}, \qquad (\dot{R}R^T)_{ik} = \varepsilon_{ijk}\Omega_j.$$

Let us introduce the isospin and angular-momentum operators ($I_i$ and $J_i$, respectively) that are conjugate to the angular velocities $\omega_i$ and $\Omega_i$ via the linear relations [11]

$$I_i = \Theta^I_{ij}\omega_j + \Theta^{\text{int}}_{ij}\Omega_j, \qquad J_i = \Theta^J_{ij}\Omega_j + \Theta^{\text{int}}_{ji}\omega_j.$$

The isospin operators $I_i$ commute with the angular-momentum operators $J_i$; taken separately, they satisfy the $SU(2)$ commutation relations:

$$[I_i, I_j] = i\varepsilon_{ijk}I_k, \qquad [J_i, J_j] = i\varepsilon_{ijk}J_k.$$

On the basis of the above, the derivation of the energy spectrum is especially straightforward for Skyrmions of large baryon number since numerical calculations show that such Skyrmions are almost spherically symmetric and since the interference tensor of inertia is much smaller for them than the isospin and orbital tensors of inertia. For $B \gg 1$, we can therefore set

$$I_i = \Theta_I\delta_{ij}\omega_j, \qquad J_i = \Theta_J\delta_{ij}\Omega_j, \qquad (21)$$

$$\Theta_{I(J)} \equiv \frac{1}{3}\Theta^{I(J)}_{aa}.$$

The rotational-energy operator is then expressed in terms of the isospin operator and the angular-momentum operator as

$$E_{\text{rot}} = \frac{I_i\omega_i + J_i\Omega_i}{2} = \frac{\mathbf{I}^2}{2\Theta_I} + \frac{\mathbf{J}^2}{2\Theta_J};$$

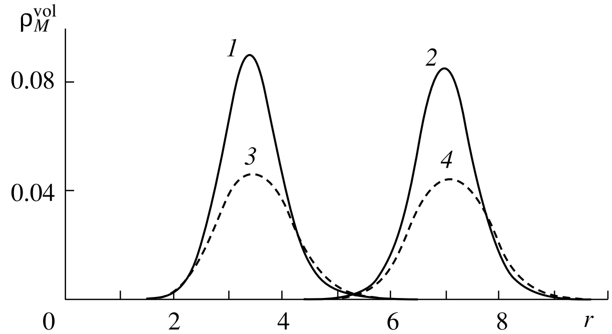

**Fig. 2.** Volume energy density for rational-map multi-Skyrmions, $\rho_M^{\text{vol}} = dM_{\text{clas}}/dV$, as a function of the radius for various baryon numbers: (curve *1*) $Sk(4)$ version, $B = 17$, and $\Im/B^2 = 1.257$; (curve *2*) $Sk(4)$ version, $B = 67$, and $\Im/B^2 = 1.250$; (curve *3*) $Sk(6)$ version, $B = 17$, and $\Im/B^2 = 1.257$; and (curve *4*) $Sk(6)$ version, $B = 67$, and $\Im/B^2 = 1.250$. The energy density and the radius are given in units of $3\pi^2F_\pi^4e^2/8$ and $2/(F_\pi e)$, respectively. The constant $e$ can have different numerical values in different versions of the model.

thus, the eventual form of the energy spectrum is

$$E_{I,J} = M_{\text{clas}} + \frac{I(I+1)}{2\Theta_I} + \frac{J(J+1)}{2\Theta_J}. \qquad (22)$$

The contributions to the tensors of inertia from the kinetic and $Sk(4)$ terms of the Lagrangian were calculated in [10] for arbitrary baryon numbers; in the next section, these results will be supplemented with the calculation of the contribution from the $Sk(6)$ term.

## 4. CALCULATION OF THE TENSORS OF INERTIA

In the $Sk(6)$ term, we now single out the part depending on time derivatives. We have

$$\begin{aligned} &\operatorname{tr}[L_\mu, L^\nu][L_\nu, L^\alpha][L_\alpha, L^\mu] \qquad (23)\\ &= -\operatorname{tr}[L_p, L_q][L_q, L_j][L_j, L_p] \\ &+ 3\operatorname{tr}[L_p, L_q][L_q, L_t][L_t, L_p], \end{aligned}$$

where $L_j = \partial_j UU^\dagger$; the indices $j, p, q$ run through the values of $1\ldots3$; and $L_t = \dot{U}U^\dagger$. Substituting the field $\widetilde{U}(\mathbf{r}, t)$ into the Lagrangian with the aid of the equality

$$\begin{aligned} \dot{\widetilde{U}} = \frac{d}{dt}AU(R\mathbf{r})A^\dagger = \dot{A}UA^\dagger + AU\dot{A}^\dagger \qquad (24)\\ + A\partial_kU\varepsilon_{kam}\Omega_a(R\mathbf{r})_mA^\dagger \end{aligned}$$

and going over from integration with respect to the fixed coordinates $\mathbf{r}$ to integration with respect to the coordinates $R(t)\mathbf{r}$ rotating with the body (we denote them again $\mathbf{r}$), we obtain

$$E^{Sk(6)}_{\text{rot}} = -3c_6\int \operatorname{tr}[L_p, L_q][L_q, L_t][L_t, L_p]d^3r, \qquad (25)$$

where we now have $L_t = [A^\dagger \dot{A}, U]U^\dagger + h_k L_k$ with $h_k = \varepsilon_{kam}\Omega_a r_m$, $U(\mathbf{r})$ having the meaning of a classical solution.

The traceless anti-Hermitian matrices $L_k$ and $L_t$ are expanded in terms of the Pauli matrices as $L_k = i\mathbf{L}_k \cdot \boldsymbol{\tau}$ and $L_t = i\mathbf{L}_t \cdot \boldsymbol{\tau}$; therefore, we have

$$\begin{aligned} &\mathrm{tr}[L_p, L_q][L_q, L_t][L_t, L_p] \qquad (26)\\ &= 8i\mathrm{tr}([\mathbf{L}_p, \mathbf{L}_q]\cdot\boldsymbol{\tau})([\mathbf{L}_q, \mathbf{L}_t]\cdot\boldsymbol{\tau})([\mathbf{L}_t, \mathbf{L}_p]\cdot\boldsymbol{\tau})\\ &= -16([\mathbf{L}_p, \mathbf{L}_q], [\mathbf{L}_q, \mathbf{L}_t], [\mathbf{L}_t, \mathbf{L}_p])\\ &= -16(\mathbf{L}_p, \mathbf{L}_q, \mathbf{L}_t)^2. \end{aligned}$$

Let us now calculate the chiral derivative with respect to time, $L_t$. The commutator appearing in it can also be expanded in terms of the Pauli matrices:

$$\begin{aligned} [A^\dagger \dot{A}, U] &= \left[-\frac{i}{2}\boldsymbol{\omega}\cdot\boldsymbol{\tau}, c_f + is_f\mathbf{n}\cdot\boldsymbol{\tau}\right] \qquad (27)\\ &= is_f[\boldsymbol{\omega}, \mathbf{n}]\cdot\boldsymbol{\tau} = is_f\mathbf{N}\cdot\boldsymbol{\tau}, \quad \mathbf{N} \equiv [\boldsymbol{\omega}, \mathbf{n}]. \end{aligned}$$

In just the same way as in [12], we denote by $\mathbf{a}^*$ the vector $\mathbf{a}$ rotated about the vector $\mathbf{n}$ through an angle $(-f)$ according to the screwdriver rule. It can easily be proven that, if $\mathbf{a}$ is orthogonal to $\mathbf{n}$, then $(\mathbf{a}\cdot\boldsymbol{\tau})U^\dagger = \mathbf{a}^*\cdot\boldsymbol{\tau}$, in which case $[A^\dagger \dot{A}, U]U^\dagger = is_f\mathbf{N}^*\cdot\boldsymbol{\tau}$. Further, we have

$$\mathbf{L}_k = \partial_k f\mathbf{n} + c_f s_f \partial_k\mathbf{n} - s_f^2[\mathbf{n}, \partial_k\mathbf{n}] = \boldsymbol{\Lambda}_k^*, \qquad (28)$$
$$\text{where } \boldsymbol{\Lambda}_k \equiv \partial_k f\mathbf{n} + s_f\partial_k\mathbf{n},$$

whence it follows that

$$\mathbf{L}_t = s_f\mathbf{N}^* + h_k\boldsymbol{\Lambda}_k^* = \boldsymbol{\Lambda}_t^*, \qquad (29)$$
$$\text{where } \boldsymbol{\Lambda}_t \equiv s_f\mathbf{N} + h_k\boldsymbol{\Lambda}_k.$$

By using the invariance of a mixed product under rotations, we can then simplify the ensuing calculations as follows:

$$(\mathbf{L}_p, \mathbf{L}_q, \mathbf{L}_t) = (\boldsymbol{\Lambda}_p^*, \boldsymbol{\Lambda}_q^*, \boldsymbol{\Lambda}_t^*) = (\boldsymbol{\Lambda}_p, \boldsymbol{\Lambda}_q, \boldsymbol{\Lambda}_t). \qquad (30)$$

We denote

$$\begin{aligned} \chi_{pqk} &\equiv (\partial_p f\mathbf{n}, \partial_q\mathbf{n}, \partial_k\mathbf{n}) \qquad (31)\\ &+ (\partial_k f\mathbf{n}, \partial_p\mathbf{n}, \partial_q\mathbf{n}) + (\partial_q f\mathbf{n}, \partial_k\mathbf{n}, \partial_p\mathbf{n}). \end{aligned}$$

The substitution of expressions (28) and (29) into the mixed product (30) then yields

$$\begin{aligned} (\boldsymbol{\Lambda}_p, \boldsymbol{\Lambda}_q, \boldsymbol{\Lambda}_t) &= -s_f^2(\boldsymbol{\omega}, \partial_p f\partial_q\mathbf{n} - \partial_q f\partial_p\mathbf{n}) \qquad (32)\\ &+ s_f^2 h_k\chi_{pqk}, \end{aligned}$$

where we have used the relation $(\partial_p\mathbf{n}, \partial_q\mathbf{n}, \mathbf{N}) = 0$, which is valid by virtue of coplanarity—all three vectors are orthogonal to $\mathbf{n}$.

Upon squaring, we find according to formulas (25) and (26) that

$$\begin{aligned} \Theta_{ab}^{I,Sk(6)} &= \int 192c_6 s_f^4\{(\partial_k f)^2\partial_i n_a\partial_i n_b \qquad (33)\\ &- \partial_k f\partial_k n_a\partial_i f\partial_i n_b\}d^3r,\\ \Theta_{ab}^{J,Sk(6)} &= \int 96c_6 s_f^4\chi_{ipq}\chi_{kpq}\varepsilon_{iam}\varepsilon_{kbn}r_m r_n d^3r,\\ \Theta_{ab}^{\mathrm{int},Sk(6)} &= -\int 96c_6 s_f^4(\partial_p f\partial_q n_a\\ &- \partial_q f\partial_p n_a)\chi_{pqk}\varepsilon_{kbn}r_n d^3r. \end{aligned}$$

The total isospin tensor of inertia can be represented as

$$\Theta_{ab}^{I} = \Theta_{ab}^{I,\mathrm{kin}} + \Theta_{ab}^{I,Sk(4)} + \Theta_{ab}^{I,Sk(6)}.$$

The expressions for the total orbital and the interference tensor of inertia can be obtained in a similar way.

Using rational maps and, therefore, taking into account the orthogonality of spherical coordinates $(\partial_k f\partial_k\mathbf{n} = 0)$, we can simplify the respective expressions, reducing them to the form

$$\begin{aligned} \Theta_{ab}^{I,Sk(6)}(\mathrm{RM}) &= \int 192c_6 s_f^4 f'^2(r)\partial_i n_a\partial_i n_b d^3r, \qquad (34)\\ \Theta_{ab}^{J,Sk(6)}(\mathrm{RM}) &= \int 192c_6 s_f^4 f'^2(r)\\ &\times \Big\{(r^2\delta_{ab} - r_a r_b)[\partial_p\mathbf{n}, \partial_q\mathbf{n}]^2\\ &- r^2(\partial_q\mathbf{n})^2(\partial_a\mathbf{n}\partial_b\mathbf{n}) + r^2(\partial_a\mathbf{n}\partial_q\mathbf{n})(\partial_b\mathbf{n}\partial_q\mathbf{n})\Big\}d^3r,\\ \Theta_{ab}^{\mathrm{int},Sk(6)}&(\mathrm{RM})\\ &= \int 192c_6 s_f^4 f'^2(r)(\mathbf{n}, \partial_k\mathbf{n}, \partial_p\mathbf{n})\partial_p n_a\varepsilon_{kbn}r_n d^3r. \end{aligned}$$

It was indicated in [10] that the traces of the isospin and orbital tensors of inertia (in the standard Skyrme model) are expressed in terms of the profile function $f(r)$, the baryon number $B$, and the integral $\Im$ with respect to angles exclusively, this making it possible to investigate, irrespective of the angular distribution, the properties of multi-Skyrmions having large baryon numbers (for example, the isoscalar magnetic moment of a Skyrmion is proportional to $1/\Theta_J$).

The above is valid for the $Sk(6)$ contributions as well. With allowance for all contributions, the moments of inertia [for the definition of $\Theta_{I(J)}$, see (21)] are given by

$$\begin{aligned} \Theta_I &= \frac{4}{9\pi}\int_0^\infty\{s_f^2 r^2 + (1-\lambda)s_f^2(f'^2 r^2 + Bs_f^2) \qquad (35)\\ &+ \lambda Bs_f^4 f'^2\}dr,\\ \Theta_J &= \frac{4}{9\pi}\int_0^\infty\{Bs_f^2 r^2 + (1-\lambda)s_f^2(Bf'^2 r^2 + \Im s_f^2) \end{aligned}$$

$$+ \lambda \Im s_f^4 f'^2 \} dr.$$

These expressions were reduced to a dimensionless form by the method described in Section 2 [the moment of inertia is measured in units of $12\pi^2/(F_\pi e^3)$]. Since $\Im \geq B^2$, it can be found by analogy with [10] that

$$\Theta_J - B\Theta_I = \frac{4}{9\pi}(\Im - B^2)$$
$$\times \int\limits_0^\infty s_f^4 \left((1-\lambda) + \lambda f'^2\right) dr \geq 0,$$
$$\Im\Theta_I - B\Theta_J = \frac{4}{9\pi}(\Im - B^2)$$
$$\times \int\limits_0^\infty r^2 s_f^2 \left(1 + (1-\lambda) f'^2\right) dr \geq 0,$$

whence we obtain

$$\frac{\Im}{B}\Theta_I \geq \Theta_J \geq B\Theta_I. \quad (36)$$

## 5. FLAVOR MOMENT OF INERTIA

It is straightforward to include a third quark in the Skyrme model—that is, to extend the symmetry to the $(u, d, s)$, $(u, d, c)$, or $(u, d, b)$ group. For this, one must take the field $U(\mathbf{r}, t)$ in the form of an $SU(3)$ matrix. In this case, the classical $SU(2)$ solution considered above takes the form

$$U(\mathbf{r}) = \left(\begin{array}{c|c} e^{if(\mathbf{r})\mathbf{n}(\mathbf{r})\cdot\boldsymbol{\tau}} & 0 \\ \hline 0 & 1 \end{array}\right).$$

In order to quantize deviations in the strange (charm, beauty) direction in the vicinity of a classical $SU(2)$ solution, we consider the time-dependent field

$$\widetilde{U}(\mathbf{r}, t) = A(t) U(\mathbf{r}) A^\dagger(t)$$

and introduce the $SU(3)$ matrix $A(t)$ through the relation $A^\dagger \dot{A} = -(i/2) v_a \lambda_a$, where $\lambda_a$ are the Gell-Mann matrices and $a = 4, \ldots, 7$. Further, we set

$$V = \begin{pmatrix} v_4 - iv_5 \\ v_6 - iv_7 \end{pmatrix},$$

in which case

$$A^\dagger \dot{A} = -\frac{i}{2}\left(\begin{array}{c|c} 0 & V \\ \hline V^\dagger & 0 \end{array}\right).$$

The corresponding rotational energy takes the form

$$E_{\text{rot}} = \frac{1}{2}\Theta_F^{(0)} |V|^2. \quad (37)$$

The objective of this section is to calculate the $Sk(6)$ contribution to the flavor moment of inertia $\Theta_F^{(0)}$ (for the quantization procedure, see [12, 13] and references therein).

Let us introduce the notation

$$W = (1 - U)V.$$

We then have

$$L_t = [A^\dagger \dot{A}, U]U^\dagger = -\frac{i}{2}\left(\begin{array}{c|c} 0 & W \\ \hline W^\dagger & 0 \end{array}\right). \quad (38)$$

Since

$$L_k = \left(\begin{array}{c|c} i\mathbf{L}_k \cdot \boldsymbol{\tau} & 0 \\ \hline 0 & 0 \end{array}\right),$$

the further calculations give

$$[L_k, L_t] = \frac{1}{2}\left(\begin{array}{c|c} 0 & (\mathbf{L}_k \cdot \boldsymbol{\tau})W \\ \hline -W^\dagger(\mathbf{L}_k \cdot \boldsymbol{\tau}) & 0 \end{array}\right), \quad (39)$$

$$[L_k, L_t][L_t, L_i] = \frac{1}{4} \quad (40)$$
$$\times \left(\begin{array}{c|c} (\mathbf{L}_k \cdot \boldsymbol{\tau})WW^\dagger(\mathbf{L}_i \cdot \boldsymbol{\tau}) & 0 \\ \hline 0 & W^\dagger(\mathbf{L}_k \cdot \boldsymbol{\tau})(\mathbf{L}_i \cdot \boldsymbol{\tau})W \end{array}\right),$$

$$\operatorname{tr}[L_i, L_k][L_k, L_t][L_t, L_i] \quad (41)$$
$$= -\frac{i}{2}\operatorname{tr}(\mathbf{L}_i \cdot \boldsymbol{\tau})([\mathbf{L}_i, \mathbf{L}_k] \cdot \boldsymbol{\tau})(\mathbf{L}_k \cdot \boldsymbol{\tau})WW^\dagger.$$

The product of linear combinations of Pauli matrices that appears in (41) is proportional to the identity matrix; that is,

$$(\mathbf{L}_i \cdot \boldsymbol{\tau})([\mathbf{L}_i, \mathbf{L}_k] \cdot \boldsymbol{\tau})(\mathbf{L}_k \cdot \boldsymbol{\tau}) = -i[\mathbf{L}_i, \mathbf{L}_k]^2$$
$$= -i[\boldsymbol{\Lambda}_i, \boldsymbol{\Lambda}_k]^2,$$

whence we obtain

$$\operatorname{tr}[L_i, L_k][L_k, L_t][L_t, L_i] = -\frac{1}{2}[\boldsymbol{\Lambda}_i, \boldsymbol{\Lambda}_k]^2 |W|^2, \quad (42)$$

where $\boldsymbol{\Lambda}_i$ is given by (28). Upon using the general formula (25) with allowance for (37), we find with the aid of the equality $|W|^2 = 2(1 - c_f)|V|^2$ that

$$\Theta_F^{(0),Sk(6)} = \int 6c_6(1 - c_f)s_f^2 \Big\{ 2(\partial_k f)^2 (\partial_i \mathbf{n})^2 \quad (43)$$
$$+ s_f^2 [\partial_i \mathbf{n}, \partial_k \mathbf{n}]^2 - 2(\partial_k f \partial_k \mathbf{n})^2 \Big\} d^3 r,$$
$$\Theta_F^{(0)} = \Theta_F^{(0),\text{kin}} + \Theta_F^{(0),Sk(4)} + \Theta_F^{(0),Sk(6)}.$$

For rational maps, the $Sk(6)$ contribution is

$$\Theta_F^{(0),Sk(6)}(\mathrm{RM}) \tag{44}$$
$$= \int_0^\infty 48\pi c_6 (1-c_f) s_f^2 \left\{ 2Bf'^2(r) + \Im \frac{s_f^2}{r^2} \right\} dr.$$

The total moment of inertia reduced to a dimensionless form in the same way as in (35) can be rewritten as

$$\Theta_F^{(0)} = \frac{1}{24\pi} \int_0^\infty (1-c_f) \tag{45}$$
$$\times \left\{ 8r^2 + (1-\lambda)(2r^2 f'^2 + 4Bs_f^2) \right.$$
$$\left. + \lambda s_f^2 \left( 2Bf'^2 + \Im \frac{s_f^2}{r^2} \right) \right\} dr.$$

## 6. FLAVOR EXCITATION ENERGIES WITHIN THE $Sk(6)$ VERSION

By using the expression derived in the preceding section for the flavor moment of inertia, one can calculate the strangeness, charm, and bottom excitation energies in nuclei (by analogy with the study of Kopeliovich and Zakrzewski [14], who considered the $Sk(4)$ version of the model). For this, it is necessary to take into account, in the Lagrangian, the flavor-symmetry-breaking contribution

$$\mathcal{L}_{\mathrm{FSB}} = \frac{F_D^2 m_D^2 - F_\pi^2 m_\pi^2}{24} \mathrm{tr}(1-\sqrt{3}\lambda_8) \tag{46}$$
$$\times (U + U^\dagger - 2) + \frac{F_D^2 - F_\pi^2}{48} \mathrm{tr}(1-\sqrt{3}\lambda_8)$$
$$\times (UL_\mu^2 + L_\mu^2 U^\dagger),$$

which proved to be sufficient for describing the mass splitting in the octet and the decuplet of baryons [15]. In formula (46), $F_D$ and $m_D$ are, respectively, the $K$-, $D$-, or $B$-meson decay constant and mass.

Within the $1/N_c$ expansion ($N_c$ is the number of colors in QCD), the expression for the Hamiltonian of the system characterized by a fixed baryon number $B$ has the form

$$H_B = M_{\mathrm{clas},B} + \omega_{F,B} a^\dagger a + \overline{\omega}_{F,B} b^\dagger b + O(1/N_c), \tag{47}$$

where $a^\dagger$ and $b^\dagger$ are the corresponding creation operators and $\omega_{F,B}$ and $\overline{\omega}_{F,B}$ are, respectively, the strangeness and antistrangeness (flavor and antiflavor) excitation energies. Upon introducing the notation $\overline{m}_D^2 = (F_D^2/F_\pi^2)m_D^2 - m_\pi^2$, the excitation energies can be represented as [14]

$$\omega_{F,B} = N_c B \frac{\mu_{F,B} - 1}{8\Theta_F}, \tag{48}$$
$$\overline{\omega}_{F,B} = N_c B \frac{\mu_{F,B} + 1}{8\Theta_F},$$
$$\mu_{F,B} = \sqrt{1 + \frac{16\Theta_F}{(N_c B)^2} (\overline{m}_D^2 \Gamma + (F_D^2 - F_\pi^2)\widetilde{\Gamma})},$$

where the new flavor moment of inertia $\Theta_F = \Theta_F^{(0)} + (F_D^2/F_\pi^2 - 1)\Gamma/4$ and the integrals

$$\Gamma = \frac{F_\pi^2}{2} \int (1-c_f) d^3r, \tag{49}$$

$$\widetilde{\Gamma} = \frac{1}{4} \int c_f \left( (\partial_k f)^2 + s_f^2 (\partial_k \mathbf{n})^2 \right) d^3r \tag{50}$$

are also functions of the baryon number $B$.

In view of the shell behavior of the classical solution at large $B$, the model is applicable only to light nuclei. This drawback (from the phenomenological point of view) can be associated, for example, with the fact that, for large baryon numbers, the rational-map ansatz (9) provides only a local minimum of the energy functional rather than the absolute one. This means that, at a specific critical value of the baryon number, $B_{\mathrm{crit}}$, there may occur a phase transition to configurations of the Skyrmion crystal type (for a discussion on this issue, see [16]). It is known that $B_{\mathrm{crit}} > 22$.

In the table, the strangeness, charm, and bottom excitation energies are given for relatively small baryon numbers. The strangeness excitation energies appear to be 30 to 50 MeV greater in the $Sk(6)$ model version than in the $Sk(4)$ case, which was considered in [10]. For charm and bottom, the corresponding values increase by 70 to 120 and 110 to 200 MeV, respectively. The distinction between the two versions of the model manifests itself most significantly here in relatively low values of $\omega_s$, $\omega_c$, and $\omega_b$ for the $B = 1$ states in the $Sk(6)$ version. On the whole, the results of the calculation show that, in the $Sk(6)$ model version, the qualitative behavior of the flavor excitation energies versus the baryon number of the original $SU(2)$ configuration is identical to that in the $Sk(4)$ case—namely, states of baryon numbers in the range 4–11 are bound most strongly. This effect can be understood on the basis of the following simple considerations. The flavor excitation energy can be represented as

$$\omega_F \sim \mathrm{const} \cdot \sqrt{\frac{\Gamma}{\Theta_F}},$$

Features of multi-Skyrmions and strangeness, charm, and bottom excitation energies for configurations of various baryon numbers $B$ within the $Sk(6)$ version of the model

| $B$ | $\Theta_F^{(0)}$, GeV$^{-1}$ | $\Gamma$, GeV$^{-1}$ | $\widetilde{\Gamma}$, GeV$^{-1}$ | $\omega_s$, MeV | $\omega_c$, MeV | $\omega_b$, MeV |
|---|---|---|---|---|---|---|
| 1 | 2.28 | 6.08 | 15.8 | 336 | 1604 | 4920 |
| 2 | 4.95 | 14.0 | 24.7 | 346 | 1635 | 4980 |
| 3 | 7.35 | 20.7 | 30.4 | 342 | 1632 | 4970 |
| 4 | 8.94 | 24.5 | 33.7 | 328 | 1612 | 4950 |
| 5 | 11.8 | 32.8 | 38.3 | 334 | 1622 | 4960 |
| 6 | 14.1 | 39.3 | 41.6 | 332 | 1622 | 4960 |
| 7 | 15.4 | 42.5 | 43.5 | 324 | 1609 | 4950 |
| 8 | 18.5 | 51.6 | 47.0 | 330 | 1620 | 4960 |
| 9 | 21.1 | 59.2 | 49.7 | 331 | 1623 | 4960 |
| 10 | 23.5 | 65.8 | 52.0 | 331 | 1624 | 4970 |
| 11 | 26.1 | 73.6 | 54.4 | 332 | 1626 | 4970 |
| 12 | 28.3 | 80.0 | 56.3 | 332 | 1626 | 4970 |
| 13 | 30.8 | 87.2 | 58.2 | 332 | 1628 | 4970 |
| 14 | 34.0 | 96.9 | 60.6 | 335 | 1633 | 4980 |
| 15 | 36.8 | 105 | 62.5 | 336 | 1635 | 4980 |
| 16 | 39.3 | 113 | 64.2 | 336 | 1636 | 4980 |
| 17 | 41.4 | 118 | 65.5 | 335 | 1635 | 4980 |
| 22 | 56.4 | 164 | 73.9 | 342 | 1647 | 5000 |
| 67 | 213 | 662 | 119 | 366 | 1690 | 5060 |

Note: The model parameters are set to the values $F_\pi = 186$ MeV, $e = 4.11$, and $m_\pi = 138$ MeV. In order to take into account flavor-symmetry breaking in the decay constants, we set $F_K/F_\pi = 1.22$, $F_D/F_\pi = 1.5$, and $F_B/F_\pi = 2$. For all $B$ values, the numerical results were obtained within the rational-map-ansatz approximation, in contrast to [10], where the results of a numerical minimization of the three-dimensional mass functional are given up to $B = 8$ [for the $Sk(4)$ version of the model].

where $\Gamma$ is proportional, according to (49), to the volume of the entire Skyrmion, while $\Theta_F$ is proportional in part to the Skyrmion volume (the kinetic-term contribution) and in part to the volume of the shell (the contribution of the $Sk(4)$ and $Sk(6)$ terms); therefore, $\omega_F$ grows with increasing baryon number. The values of $\omega_F$ for $B = 2$ and 3 are greater than those for larger baryon numbers because of a significant asymmetry of the toroidal and tetrahedral solutions (this manifests itself in relatively large values of $\Im/B^2$ for $B = 2$ and 3).

## 7. CONCLUSION

The tensors of inertia calculated within the chiral soliton model featuring a sixth-order term in the derivatives in the Lagrangian make it possible to find the free parameters of the model.

In both limiting cases considered here, $Sk(4)$ ($\lambda = 0$) and $Sk(6)$ ($\lambda = 1$), there is only one free parameter $e$ (in this version of the parametrization, the pion decay constant is fixed by the experimental value of $F_\pi = 186$ MeV). From the above, one can derive, in the $Sk(6)$ case, the coefficient of the term involving six derivatives in the Lagrangian; that is,

$$c_6 = \frac{1}{48F_\pi^2 e^4}. \qquad (51)$$

By using the formula for the energy of the isospin-$I$ single-baryon state [17],

$$E_I = M_{\text{clas}} + \frac{I(I+1)}{2\Theta_I^{B=1}}, \qquad (52)$$

the parameter $e$ can be determined on the basis of the mass difference between the delta particle and the nucleon,

$$m_\Delta - m_N = \frac{3}{2\Theta_I^{B=1}}.$$

In the $Sk(6)$ case, this yields $e = 4.11$ and $c_6 = 2.11 \times 10^{-3}$ GeV$^{-2}$. This value of the parameter $e$ was used in numerically calculating flavor excitation energies. The fact that the nucleon mass predicted by formula (52) (1400 MeV) is closer to the experimental value of 938 MeV is an appealing feature of the $Sk(6)$ version of the model; at the same time, the $Sk(4)$ version yields 1771 MeV for the nucleon mass at $e = 4.12$.

## ACKNOWLEDGMENTS

I am grateful to V.B. Kopeliovich for the formulation of the problem and stimulating discussions.

This work was supported in part by the Russian Foundation for Basic Research (project no. 01-02-16615).

## REFERENCES

1. T. H. R. Skyrme, Proc. R. Soc. London, Ser. A **260**, 127 (1961); Nucl. Phys. **31**, 556 (1962).
2. I. Floratos and B. M. A. G. Piette, Phys. Rev. D **64**, 045009 (2001); hep-th/0103126.
3. V. B. Kopeliovich and B. E. Stern, Pis'ma Zh. Éksp. Teor. Fiz. **45**, 165 (1987) [JETP Lett. **45**, 203 (1987)].
4. E. Braaten, S. Townsend, and L. Carson, Phys. Lett. B **235**, 147 (1990).
5. R. A. Battye and P. M. Sutcliffe, Phys. Rev. Lett. **86**, 3989 (2001).
6. R. A. Battye, C. J. Houghton, and P. M. Sutcliffe, hep-th/0210147.
7. C. J. Houghton, N. S. Manton, and P. M. Sutcliffe, Nucl. Phys. B **510**, 507 (1998); hep-th/9705151.
8. V. B. Kopeliovich, J. Phys. G **28**, 103 (2002).
9. V. B. Kopeliovich, Pis'ma Zh. Éksp. Teor. Fiz. **73**, 667 (2001) [JETP Lett. **73**, 587 (2001)]; hep-ph/0109229.
10. V. B. Kopeliovich, Zh. Éksp. Teor. Fiz. **120**, 499 (2001) [JETP **93**, 435 (2001)]; hep-ph/0103336.
11. V. B. Kopeliovich, Yad. Fiz. **47**, 1495 (1988) [Sov. J. Nucl. Phys. **47**, 949 (1988)]; E. Braaten and L. Carson, Phys. Rev. D **38**, 3525 (1988).
12. K. M. Westerberg and I. R. Klebanov, Phys. Rev. D **50**, 5834 (1994); hep-ph/9406383.
13. I. R. Klebanov and K. M. Westerberg, Phys. Rev. D **53**, 2804 (1996); V. B. Kopeliovich, Pis'ma Zh. Éksp. Teor. Fiz. **67**, 854 (1998) [JETP Lett. **67**, 896 (1998)]; hep-ph/9805296.
14. V. B. Kopeliovich and W. J. Zakrzewski, Pis'ma Zh. Éksp. Teor. Fiz. **69**, 675 (1999) [JETP Lett. **69**, 721 (1999)].
15. B. Schwesinger and H. Weigel, Phys. Lett. B **267**, 438 (1991); H. Weigel, Int. J. Mod. Phys. A **11**, 2419 (1996).
16. R. A. Battye and P. M. Sutcliffe, Phys. Lett. B **416**, 385 (1998); hep-th/9709221.
17. G. S. Adkins, C. R. Nappi, and E. Witten, Nucl. Phys. B **228**, 552 (1983); G. S. Adkins and C. R. Nappi, Nucl. Phys. B **233**, 109 (1984).

*Translated by A. Isaakyan*

*Physics of Atomic Nuclei, Vol. 67, No. 4, 2004, pp. 757–761. Translated from Yadernaya Fizika, Vol. 67, No. 4, 2004, pp. 778–782.*
*Original Russian Text Copyright © 2004 by Berezhnoy, Likhoded.*

## ELEMENTARY PARTICLES AND FIELDS
## Theory

# Processes $e^+e^- \to c\bar{c}c\bar{c}$ and $e^+e^- \to J/\psi + gg$ at $\sqrt{s} = 10.59$ GeV

**A. V. Berezhnoy**[1)]* **and A. K. Likhoded**[2)]

Received February 26, 2003; in final form, June 10, 2003

**Abstract**—Experimental data obtained by the BELLE Collaboration for inclusive $J/\psi$ production in the processes $e^+e^- \to J/\psi + gg$ and $e^+e^- \to J/\psi + c\bar{c}$ are discussed. These data are compared with the predictions of perturbative QCD that were obtained by two methods, that which employs information about the $J/\psi$ wave function and that which relies on the hypothesis of quark–hadron duality exclusively. Both computational methods yield results that disagree with the experimental data considerably. The dependence of the cross section for the process $e^+e^- \to J/\psi + gg$ on the effective gluon mass is studied. The cross section for the production of doubly charmed baryons $\Xi^*_{cc}$ is estimated. © *2004 MAIK "Nauka/Interperiodica".*

## 1. INTRODUCTION

At present, perturbative QCD (pQCD) makes it possible to describe hard subprocesses in hadron production adequately. The most pronounced advances in employing pQCD have been made toward obtaining deeper insight into heavy-quark and heavy-quarkonium production at high transverse momenta, where, in accordance with the factorization theorem, the process of heavy-hadron production can be broken down into two steps: (i) heavy-quark production and (ii) the hadronization of product quarks. The hadronization process can be described in terms of a common factor that involves only a weak (logarithmic) dependence on $p_T$. At low energies and transverse momenta, factorization can be severely violated because of final-state interactions. This is suggested, for example, by the asymmetry in hadronic production of different charged states of charmed particles. Since, at low energies and transverse momenta, the factorization theorem is not more than an approximation, we can expect significant deviations in this region from the predictions based on pQCD and the factorization theorem. Recent measurements of $e^+e^-$ annihilation at $\sqrt{s} = 10.6$ GeV that were performed by the BELLE Collaboration [1] indicate that the experimental values of the cross sections for pair $J/\psi + \eta_c$ production and for inclusive $J/\psi + c\bar{c}$ production are an order of magnitude larger than the respective values predicted by pQCD [2, 3]. The shape of some experimental differential cross sections for the process $J/\psi + gg$ bears no resemblance to their shape in pQCD. It was shown in [4] that allowance for the electromagnetic contribution to $J/\psi + J/\psi$ and $J/\psi + \eta_c$ production may nearly double theoretical values of the respective cross sections. Despite this, the pQCD predictions remain inconsistent with experimental data on $c\bar{c}c\bar{c}$ production. In addition to the disagreement between the theoretical and experimental values of the cross section, there is a discrepancy for the relative rate of $J/\psi$ production in the processes $e^+e^- \to J/\psi + c\bar{c}$ and $e^+e^- \to J/\psi + gg$ [1]: the experimental ratio of the $J/\psi$-production cross sections,

$$\sigma(J/\psi + c\bar{c})/\sigma(J/\psi + gg) = 0.59^{+0.15}_{-0.13} \pm 0.12, \quad (1)$$

is inconsistent with the pQCD prediction [3]

$$\sigma(J/\psi + c\bar{c})/\sigma(J/\psi + gg) \sim 0.1.$$

The cross sections $\sigma(J/\psi + c\bar{c})$ and $\sigma(J/\psi + gg)$ are of the same order in $\alpha_s$; over the energy range under consideration, their ratio depends only slightly on the scale or on model assumptions. In what follows, we consider these disagreements between the pQCD predictions and experimental data in more detail.

## 2. PROCESS $e^+e^- \to J/\psi + c\bar{c}$

The experimental value of the cross section for the process

$$e^+e^- \to J/\psi + c\bar{c} \quad (2)$$

was determined from data on the reactions $e^+e^- \to J/\psi + D^0 + X$ and $e^+e^- \to J/\psi + D^{*+} + X$. The results were [1]

$$\sigma(e^+e^- \to J/\psi + c\bar{c}) \quad (3)$$
$$= 1.1^{+0.36}_{-0.30} \pm 0.26 \text{ pb and } 0.74^{+0.28}_{-0.24} \pm 0.19 \text{ pb},$$

---

[1)] Institute of Nuclear Physics, Moscow State University, Vorob'evy gory, Moscow, 119899 Russia.
[2)] Institute for High Energy Physics, Protvino, Moscow oblast, 142284 Russia.
[*] e-mail: `aber@ttk.ru`

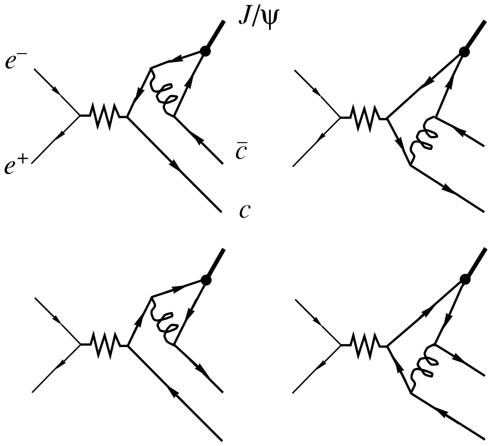

**Fig. 1.** Feynman diagrams for the process $e^+e^- \to J/\psi + c\bar{c}$.

respectively.

Theoretical estimates of the cross section for process (2) are based on considering the pQCD diagrams in Fig. 1. The amplitude of this process can be represented as the product of the amplitude for the hard production of two $c\bar{c}$ pairs and the wave functions describing $c\bar{c}$ bound states and taking into account the hadronization of the product quark—antiquark pairs. The results of the calculations performed by various authors [2, 3, 5] are in good agreement with one another, amounting to[3)]

$$\sigma(J/\psi + c\bar{c}) \simeq 6 \times 10^{-2}\ \text{pb}, \quad (4)$$

which is more than an order of magnitude smaller than the experimental value in (3). The discrepancy cannot be removed by increasing the cross section in (4) through an increase in $\alpha_s$. There is every reason to believe that the factorization hypothesis for the matrix element is not responsible for this discrepancy, because, as was shown in [2], the predictions relying on the factorization hypothesis agree well with those obtained within the approach based on quark—hadron duality, in which case neither the factorization hypothesis nor bound-state wave functions are employed.

For example, the cross section calculated for the production of a color-singlet $c\bar{c}$ pair to the same order in $\alpha_s$ as $\sigma(J/\psi + c\bar{c})$ at $2m_c \le M_{c\bar{c}} \le 2M_{D^*} + \Delta M$ ($\Delta M \simeq 0.5$–$1$ GeV), $\alpha_s = 0.24$, and $m_c = 1.4$ GeV is [2]

$$\sigma_{c\bar{c}}(\Delta M = 0.5\ \text{GeV}) = 0.13\ \text{pb}, \quad (5)$$

$$\sigma_{c\bar{c}}(\Delta M = 1.0\ \text{GeV}) = 0.16\ \text{pb}. \quad (6)$$

This result should be compared with the sum of the cross sections for the production of $S$-wave states (including the production of resonance excitations),

$$\sigma(\Sigma\eta_c,\psi) = 0.13\ \text{pb}. \quad (7)$$

A comparison of the results in (5)–(7) reveals that the rough estimates of the cross section for process (2) that are given in (5) and (6) and which are based on duality are close to the value in (7), which was obtained within a more rigorous approach. Although these values, which were deduced within the different approaches, agree with one another, each of them is an order of magnitude less than the experimental value obtained by the BELLE Collaboration (see above).

Yet another circumstance is also of importance. According to our calculations at $\alpha_s = 0.24$, $m_c = 1.4$ GeV, and $\sqrt{s} = 10.6$ GeV, the total cross section for the production of two $c\bar{c}$ pairs is

$$\sigma(c\bar{c}c\bar{c}) = 0.237\ \text{pb}, \quad (8)$$

which is only $W_{c\bar{c}} = 2 \times 10^{-4}$ of the total cross section for $c\bar{c}$-pair production at the same energy. At the $Z^0$-boson peak, where the accessible energy is an order of magnitude greater than that in the above example, $W_{c\bar{c}}$ amounts to 0.03. This behavior of the probability for the production of an additional pair is in good agreement with the pQCD predictions [7]. But it should be noted that the value in (8) is smaller than the experimental cross section for $J/\psi + c\bar{c}$ production, this in turn suggesting a strong suppression of the production of four $D$ mesons.

The contribution of electromagnetic interactions to the cross section for $c\bar{c}c\bar{c}$ production is about 2.5% of the total cross section in (8),

$$\sigma^{\text{QED}}(c\bar{c}c\bar{c}) \simeq 6.6 \times 10^{-3}\ \text{pb}.$$

This cross section is several times smaller than the cross section for the exclusive electromagnetic production of pairs of $S$-wave states, the value of the latter being taken from [4].[4)] This indicates that, on one hand, such an estimate of the cross section for exclusive pair production can be several times greater than its true value and that, on the other hand, the mechanism of $c\bar{c}c\bar{c}$ production in electromagnetic interactions differs substantially from that in QCD.

---

[3)] However, the calculations performed recently in [6] with $\alpha_s = 0.26$ give a cross-section value that is nearly twice as great.

[4)] In the recent study of Luchinsky [8], it was argued that the cross section for the exclusive electromagnetic production of pairs of $S$-wave states is only one-half of this value.

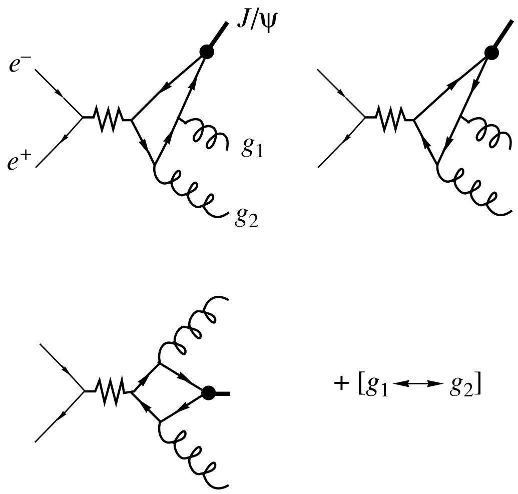

**Fig. 2.** Feynman diagrams for the process $e^+e^- \to J/\psi + gg$.

## 3. PROCESS $e^+e^- \to J/\psi + gg$

Let us consider yet another important process contributing to inclusive $J/\psi$-meson production (see Fig. 2),

$$e^+e^- \to J/\psi + gg.$$

A detailed investigation of this process was performed in [9].

Within the color-singlet model, the cross section for this process at the interaction energy of $\sqrt{s} = 10.6$ GeV and $\alpha_s = 0.24$ is

$$\sigma(J/\psi + gg) = 0.7 \text{ pb}. \tag{9}$$

By using the estimate of the cross section for $J/\psi + c\bar{c}$ production within the same model, one obtains the ratio

$$\sigma(J/\psi + c\bar{c})/\sigma(J/\psi + gg) = 6 \times 10^{-2}/0.7 \approx 0.1, \tag{10}$$

which is to be compared with the experimental value in (1). From the theoretical point of view, it is evident that the uncertainty in this ratio is less than the uncertainty in each of the cross sections involved. The reason is that the ratio in (10) is independent of the nonrelativistic matrix element for the $c\bar{c} \to J/\psi$ transition; moreover, it is independent of the factorization scale entering into $\alpha_s$ because the leading contributions to the two processes are of the same order in $\alpha_s$ and involve approximately equal virtualities.

However, a straightforward application of the cross section for color-singlet production presents some difficulties. It is well known that the pQCD predictions (at least, in the leading approximation) for the spectrum of the $gg$ system are inconsistent with experimental data at low invariant masses. Recently, this discrepancy was clearly demonstrated by considering the example of the photon spectrum in the decay $J/\psi \to \gamma + gg$. It was shown in [10] that the inclusion of higher order corrections gives rise to significant changes in the spectrum at low invariant masses of the $gg$ system. The introduction of the effective gluon mass leads to the same results. Following the ideas proposed in [11], we assigned the gluon an effective mass of 1.18 GeV in order to take into account corrections to the mass spectrum of the $gg$ system and to reproduce the photon spectrum in the decay $\Upsilon \to \gamma + X$ faithfully. In the case under consideration, the introduction of the gluon mass shifts the spectrum of two-gluon masses $m_{gg}$ to greater values, thereby reducing the cross section by a factor greater than 2 (see Fig. 3). Therefore, the ratio of the cross sections becomes

$$\sigma(J/\psi + c\bar{c})/\sigma(J/\psi + gg) \approx 0.2,$$

but this improvement does not remove the discrepancy with the experimental data.

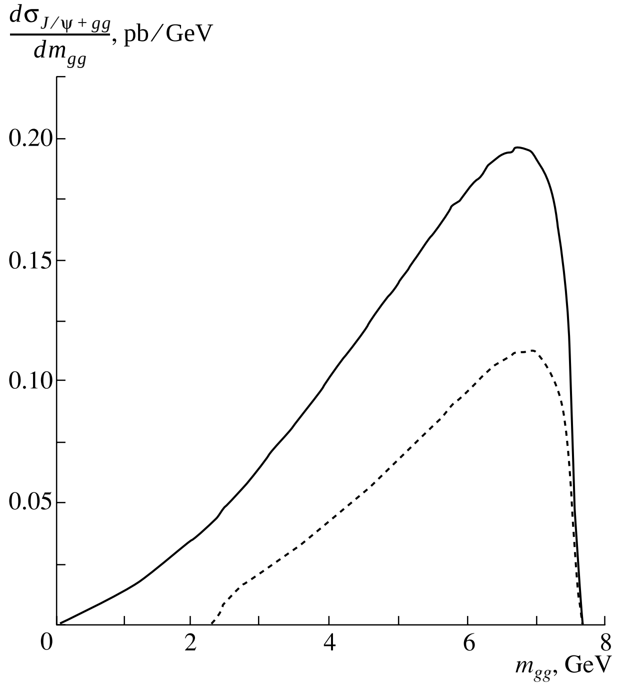

**Fig. 3.** Distribution of the cross section for $J/\psi + gg$ production in $e^+e^-$ annihilation with respect to the invariant mass $m_{gg}$ of the two-gluon system for (solid curve) massless ($m_g = 0$) and (dotted curve) massive ($m_g = 1.18$ GeV) gluons.

## 4. PRODUCTION OF DOUBLY CHARMED BARYONS

In investigating events that involve two $c\bar{c}$ pairs, proper attention must be given to studying the production of doubly charmed baryons $\Xi_{cc}^*$. The cross

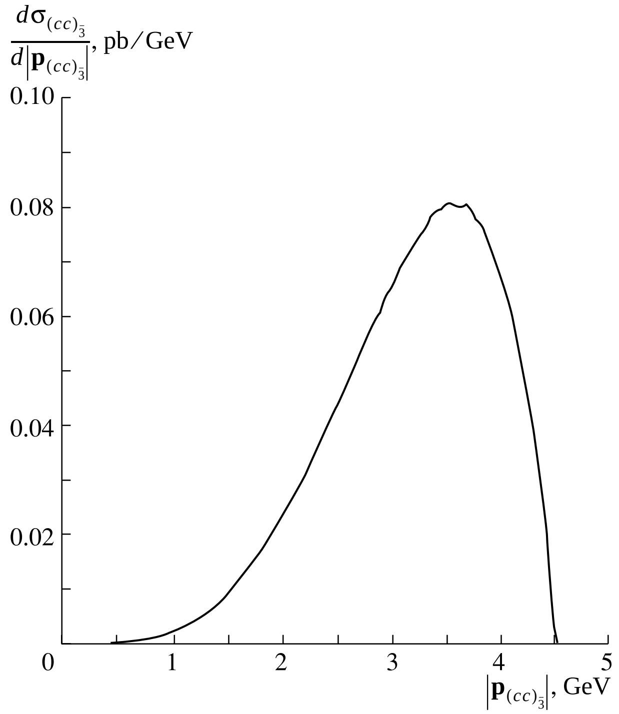

**Fig. 4.** Momentum distribution of $(cc)_{\bar{3}}$ diquarks produced in $e^+e^-$ annihilation.

section for $\Xi^*_{cc} + \bar{c}\bar{c}$ production can be estimated by the same two methods as those that were employed in calculating the associated production of $J/\psi + c\bar{c}$.

The first method is based on the factorization theorem. Within this approximation, the cross section for $\Xi^*_{cc}$ production can be represented as the product of the cross section for hard $c\bar{c}$-pair production and a coefficient that takes into account the formation of a $cc$ diquark in the color-antitriplet state. In just the same way as in the case of $J/\psi$ production, this coefficient is proportional to the square of the $cc$-diquark wave function in the $\Xi^*_{cc}$ baryon. At high energies of $e^+e^-$ collisions, the cross section for $cc$-diquark production can be represented in turn as the product of the cross section for $c\bar{c}$-pair production and the $c \to (cc)_{\bar{3}} + \bar{c}$ fragmentation function [12]. Unfortunately, this asymptotic regime is not attained at the energies of the BELLE measurements. Therefore, all subleading terms must be taken into account. With allowance for such terms, the cross section calculated at $\alpha_s = 0.24$ is

$$\sigma(\Xi^*_{cc}) = 0.15 \pm 0.01 \text{ pb}. \qquad (11)$$

A comparison with the cross section for the production of a single $c\bar{c}$ pair gives

$$\sigma(\Xi^*_{cc})/\sigma_{c\bar{c}} \sim 10^{-4}. \qquad (12)$$

The uncertainty in this estimate is mainly due to the uncertainty in the $(cc)_{\bar{3}}$-diquark wave function.

The second method for evaluating the cross section for $\Xi^*_{cc}$ production is based on the hypothesis of quark–hadron duality. In this approach, the cross section for associated baryon production is determined by the formula

$$\sigma(e^+e^- \to \Xi^*_{cc} + \bar{c}\bar{c}) = \int\limits_{2m_c}^{2m_c+\Delta M} \frac{d\sigma}{dM}((cc)_{\bar{3}} + \bar{c}\bar{c})dM.$$

For the two different energy intervals of duality, this yields

$$\sigma_{cc}(\Delta M = 0.5 \text{ GeV}) = 0.1 \text{ pb}, \qquad (13)$$
$$\sigma_{cc}(\Delta M = 1.0 \text{ GeV}) = 0.17 \text{ pb}.$$

For the luminosity of $L = 10^{34}$ cm$^2$ s$^{-1}$, the expected rate of production of doubly charmed baryons is approximately $10^4$/year. The momentum distribution of product $(cc)_{\bar{3}}$ diquarks is shown in Fig. 4.

Thus, we have shown that the inclusive cross sections for $J/\psi + c\bar{c}$ and $\Xi^*_{cc} + \bar{c}\bar{c}$ production are close in magnitude. Assuming that the large cross-section value obtained in the BELLE experiment can be explained theoretically, it is natural to expect that the rate of production of doubly charmed baryons is several times greater than the value predicted by pQCD.

## ACKNOWLEDGMENTS

We are grateful to V.V. Kiselev, M.V. Danilov, and P.N. Pakhlov for discussions.

This work was supported in part by the Russian Foundation for Basic Research (project nos. 99-02-16558, 00-15-96645, 01-02-16585), the Ministry of Education of the Russian Federation (grant no. E02-3.1-96), CRDF (grant no. MO-001-0), and the Program for Support of Scientific Schools (grant no. NSh-1303.2003.2).

## REFERENCES

1. BELLE Collab. (K. Abe *et al.*), Phys. Rev. Lett. **88**, 052001 (2002); **89**, 142001 (2002).
2. V. V. Kiselev, A. K. Likhoded, and M. V. Shevlyagin, Phys. Lett. B **332**, 411 (1994).
3. P. Cho and A. Leibovich, Phys. Rev. D **54**, 6690 (1996).
4. G. T. Bodwin, J. Lee, and E. Braaten, hep-ph/0212181; hep-ph/0212352.
5. S. Baek, P. Ko, J. Lee, and H. S. Song, J. Korean Phys. Soc. **33**, 97 (1998).
6. K.-Y. Liu, Z.-G. He, and K.-T. Chao, hep-ph/0301218.

7. V. V. Kiselev, A. K. Likhoded, and M. V. Shevlyagin, Yad. Fiz. **58**, 82 (1995) [Phys. At. Nucl. **58**, 77 (1995)].
8. A. V. Luchinsky, hep-ph/0301190.
9. J. H. Kuhn and H. Schneider, Z. Phys. C **11**, 263 (1981); Phys. Rev. D **24**, 2996 (1981); V. M. Driesen and J. H. Kuhn, Phys. Rev. D **49**, 3197 (1994); W.-Y. Keung, Phys. Rev. D **23**, 2072 (1981); F. Yuan, C.-F. Qiao, and K.-T. Chao, Phys. Rev. D **56**, 321, 1663 (1997); E. Braaten and Y.-Q. Chen, Phys. Rev. Lett. **76**, 730 (1996).
10. S. Fleming and A. Leibovich, Phys. Rev. Lett. **90**, 032001 (2003); hep-ph/0212094.
11. J. H. Field, Phys. Rev. D **66**, 013013 (2002).
12. A. F. Falk *et al.*, Phys. Rev. D **49**, 555 (1994).

*Translated by R. Rogalyov*

Physics of Atomic Nuclei, Vol. 67, No. 4, 2004, pp. 762–772. From Yadernaya Fizika, Vol. 67, No. 4, 2004, pp. 783–793.
Original English Text Copyright © 2004 by Narodetskii, Trusov.

## ELEMENTARY PARTICLES AND FIELDS
## Theory

# Ground-State Baryons in Nonperturbative Quark Dynamics*

**I. M. Narodetskii and M. A. Trusov****

*Institute of Theoretical and Experimental Physics,*
*Bol'shaya Cheremushkinskaya ul. 25, Moscow, 117259 Russia*

Received January 17, 2003; in final form, September 17, 2003

**Abstract**—We have studied the three-quark systems in an effective Hamiltonian (EH) approach, which is derived from QCD. The EH has the form of the nonrelativistic three-quark Hamiltonian with perturbative Coulomb-like and nonperturbative string interactions and a specific mass term. After outlining the approach, methods of calculating the baryon eigenenergies and some simple applications are explained in detail. With only two parameters, the string tension $\sigma = 0.15$ GeV$^2$ and the strong coupling constant $\alpha_s = 0.39$, we obtain a good description of the ground-state light and heavy baryons. Predictions of the masses of doubly heavy baryons not discovered yet are also given. In particular, a mass of 3660 MeV for the lightest $\Xi_{cc}$ baryon is found by employing the hyperspherical formalism to the three-quark confining potential with the string junction. *© 2004 MAIK "Nauka/Interperiodica".*

## 1. INTRODUCTION

Doubly heavy baryons are baryons that contain two heavy quarks, either *cc*, *bc*, or *bb*. Their existence is a natural consequence of the quark model of hadrons, and it would be surprising if they did not exist. In particular, data from the BaBar and Belle Collaborations at the SLAC and KEK $B$ factories would be good places to look for doubly charmed baryons. Recently, the SELEX, the charm hadroproduction experiment at Fermilab, reported a narrow state at $3519 \pm 1$ MeV decaying in $\Lambda_c^+ K^- \pi^+$, consistent with the weak decay of the doubly charmed baryon $\Xi_{cc}^+$ [1]. The candidate is a $6.3\sigma$ signal.

The SELEX result was recently critically discussed in [2]. Whether or not the state that SELEX reports turns out to be the first observation of doubly charmed baryons, studying their properties is important for a full understanding of the strong interaction between quarks.

Estimates for the masses and spectra of the baryons containing two or more heavy quarks have been considered by many authors [3]. The purpose of this paper is to present a consistent treatment of the results of the calculation[1)] of the masses and wave functions of the doubly heavy baryons obtained in a simple approximation within nonperturbative QCD.

The paper is organized as follows. In Section 2, we briefly review the effective Hamiltonian (EH) method. In Section 3, we discuss the hyperspherical approach, which is a very effective numerical tool to solve this Hamiltonian. In Section 4, our predictions for the ground-state spectra of doubly heavy baryons are reported and a detailed comparison with the results of other approaches is given. Section 5 contains our conclusions.

## 2. THE EFFECTIVE HAMILTONIAN IN QCD

Starting from the QCD Lagrangian and assuming the minimal-area law for the asymptotics of the Wilson loop, the Hamiltonian of the $3q$ system in the rest frame has been derived. The methodology of the approach has been reviewed recently [5] and so will be sketched here only briefly. The $Y$-shaped baryon wave function has the form

$$\begin{aligned} &B_Y(x_1, x_2, x_3, X) \qquad (1)\\ &= e_{\alpha\beta\gamma} q^\alpha(x_1, X) q^\beta(x_2, X) q^\gamma(x_3, X), \end{aligned}$$

where $q(x_i, X)$ is the extended operator of the $i$th quark at a point $x_i$; $\alpha$, $\beta$, $\gamma$ are the color indices; and $X = (0, \mathbf{X})$ is the equilibrium junction position (see below). This is the only gauge-invariant configuration possible for baryons. The starting point of the approach is the Feynman–Schwinger representation for the gauge-invariant Green's function of the three quarks propagating in the nonperturbative QCD vacuum,

$$G(x, y) = \prod_{i=1}^{3} \int_0^\infty ds_i \int Dz_i \exp(-K_i) \langle \mathcal{W} \rangle_B, \quad (2)$$

---

*This article was submitted by the authors in English.

**e-mail: `trusov@heron.itep.ru`

[1)] A preview of this calculation has been done in [4].

where $x = \{x_1, x_2, x_3\}$, $y = \{y_1, y_2, y_3\}$, $z_i = z_i(s_i)$ are the quark trajectories with $z_i(0) = x_i$, $z_i(T) = y_i$, while $s_i$ is the Fock–Schwinger proper time of the $i$th quark. Angular brackets mean averaging over the background field. The quantities $K_i$ are the kinetic energies of quarks, and all the dependence on the vacuum background field is contained in the generalized Wilson loop $\mathcal{W}$:

$$\mathcal{W} = \frac{1}{3!}\varepsilon_{ijk}\varepsilon_{lmn}U_1^{il}U_2^{jm}U_3^{kn} \tag{3}$$

with

$$U_k = P\exp\left(ig\int\limits_{C_i} A_\mu(x)dx^\mu\right), \tag{4}$$
$$k = 1, 2, 3.$$

Here, $P$ denotes the path-ordered product along the path $C_i$ in Fig. 1, where the contours run over the classical trajectories of static quarks. In this figure, three quark lines start at junction $X$ at time zero, run in the time direction from 0 to $T$ with the spatial position of quarks fixed, and join again at junction $Y$ at time $T$. There are three planes that are bounded, respectively, by one quark line, two lines connecting the junction and quark at $t = 0$ and $t = T$, and the connection line of two junctions. Under the minimal-area-law assumption, the Wilson loop configuration takes the form

$$\langle\mathcal{W}\rangle_B \propto \exp(-\sigma(S_1 + S_2 + S_3)), \tag{5}$$

where $S_i$ are the minimal areas inside the contours formed by quarks and the string-junction trajectories and $\sigma$ is the QCD string tension.

In Eq. (2), the role of the time parameter along the trajectory of each quark is played by the Fock–Schwinger proper time $s_i$. The proper and real times for each quark are related via a new quantity that eventually plays the role of the dynamical quark mass. The final result is the derivation of the EH [see Eq. (6) below].

In contrast to the standard approach of the constituent quark model, the dynamical masses $m_i$ are no longer free parameters. They are expressed in terms of the running masses $m_i^{(0)}(Q^2)$ defined at the appropriate hadronic scale of $Q^2$ from the condition of the minimum of the baryon mass as a function of $m_i$.

Technically, this has been done using the einbein (auxiliary fields) approach, which is proven to be rather accurate in various calculations for relativistic systems. Einbeins are treated as $c$-number variational parameters: the eigenvalues of the EH are minimized with respect to einbeins to obtain the physical spectrum. Such a procedure, first suggested in [6, 7], provides a reasonable accuracy for the meson ground states [8].

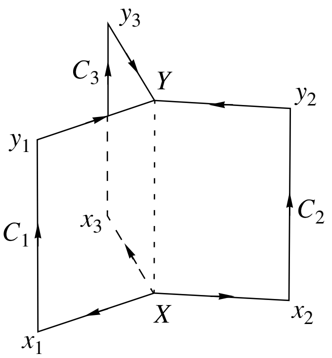

**Fig. 1.** Three-lobe Wilson loop.

This method was already applied to study baryon Regge trajectories [6] and very recently for computation of magnetic moments of light baryons [9]. The essential point adopted in [4] is that it is very reasonable that the same method should also hold for hadrons containing heavy quarks. As in [9], we take as the universal QCD parameter the string tension $\sigma$. We also include the perturbative Coulomb interaction with the frozen strong coupling constant $\alpha_s$.

From experimental point of view, a detailed discussion of the excited $QQ'q$ states is probably premature. Therefore, we consider the ground-state baryons without radial and orbital excitations, in which case tensor and spin–orbit forces do not contribute perturbatively. Then, only the spin–spin interaction survives in the perturbative approximation. In what follows, we disregard the spin–spin interaction; then, the EH has the following form:

$$H = \sum_{i=1}^{3}\left(\frac{m_i^{(0)2}}{2m_i} + \frac{m_i}{2}\right) + H_0 + V. \tag{6}$$

Here, $H_0$ is the nonrelativistic kinetic energy operator and $V$ is the sum of the perturbative one-gluon-exchange potential $V_\mathrm{C}$:

$$V_\mathrm{C} = -\frac{2}{3}\alpha_s\sum_{i<j}\frac{1}{r_{ij}},$$

where $r_{ij}$ are the distances between quarks and the string potential $V_\mathrm{string}$. The baryon mass is given by the formula

$$M_B = \min_{m_i}\langle H\rangle + C, \tag{7}$$

where $C$ is the quark self-energy correction calculated in [10]:

$$C = -\frac{2\sigma}{\pi}\sum_i\frac{\eta_i}{m_i} \tag{8}$$

with $\eta = 1$ for $q$ quark,[2] $\eta = 0.88$ for $s$ quark, $\eta = 0.234$ for $c$ quark, and $\eta = 0.052$ for $b$ quark.

The string potential calculated in [6] as the static energy of the three heavy quarks was shown to be consistent with that given by a minimum length configuration of the strings meeting in a $Y$-shaped configuration at a junction $\mathbf{X}$:

$$V_{\text{string}}(\mathbf{r}_1, \mathbf{r}_2, \mathbf{r}_3) = \sigma l_{\text{min}}, \tag{9}$$

where $l_{\text{min}}$ is the sum of the three distances $|\mathbf{r}_i|$ between quarks and the string-junction point $\mathbf{X}$. The $Y$-shaped configuration was suggested long ago [11], and since then it has been used repeatedly in many dynamical calculations [12].

## 3. SOLVING THE THREE-QUARK EQUATION

### *3.1. Jacobi Coordinates*

The baryon wave function depends on the three-body Jacobi coordinates

$$\boldsymbol{\rho}_{ij} = \sqrt{\frac{\mu_{ij}}{\mu}}(\mathbf{r}_i - \mathbf{r}_j), \tag{10}$$

$$\boldsymbol{\lambda}_{ij} = \sqrt{\frac{\mu_{ij,k}}{\mu}}\left(\frac{m_i\mathbf{r}_i + m_j\mathbf{r}_j}{m_i + m_j} - \mathbf{r}_k\right) \tag{11}$$

($i, j, k$ cyclic), where $\mu_{ij}$ and $\mu_{ij,k}$ are the appropriate reduced masses

$$\mu_{ij} = \frac{m_i m_j}{m_i + m_j}, \tag{12}$$
$$\mu_{ij,k} = \frac{(m_i + m_j)m_k}{m_i + m_j + m_k},$$

and $\mu$ is an arbitrary parameter with the dimension of mass which drops off in the final expressions. The coordinate $\boldsymbol{\rho}_{ij}$ is proportional to the separation of quarks $i$ and $j$, and coordinate $\boldsymbol{\lambda}_{ij}$ is proportional to the separation of quarks $i$ and $j$, and quark $k$. There are three equivalent ways of introducing the Jacobi coordinates, which are related to each other by linear transformations with the coefficients depending on quark masses, with the Jacobian equal to unity. In what follows, we omit indices $i, j$.

In terms of the Jacobi coordinates, the kinetic energy operator $H_0$ is written as

$$H_0 = -\frac{1}{2\mu}\left(\frac{\partial^2}{\partial\boldsymbol{\rho}^2} + \frac{\partial^2}{\partial\boldsymbol{\lambda}^2}\right) \tag{13}$$
$$= -\frac{1}{2\mu}\left(\frac{\partial^2}{\partial R^2} + \frac{5}{R}\frac{\partial}{\partial R} + \frac{K^2(\Omega)}{R^2}\right),$$

where $R$ is the six-dimensional hyperradius,

$$R^2 = \boldsymbol{\rho}^2 + \boldsymbol{\lambda}^2, \tag{14}$$

$\Omega$ furnishes five residuary angular coordinates, and $K^2(\Omega)$ is angular momentum operator whose eigenfunctions (hyperspherical harmonics) are

$$K^2(\Omega)Y_{[K]} = -K(K+4)Y_{[K]} \tag{15}$$

with $K$ being the grand orbital momentum. In terms of $Y_{[K]}$, the wave function $\psi(\boldsymbol{\rho}, \boldsymbol{\lambda})$ can be written in a symbolic shorthand as

$$\psi(\boldsymbol{\rho}, \boldsymbol{\lambda}) = \sum_K \psi_K(R) Y_{[K]}(\Omega).$$

In the hyperradial approximation, which we shall use below, $K = 0$ and $\psi = \psi(R)$. Such a wave function is obviously completely symmetric under quark permutations. Note that the centrifugal potential in the Schrödinger equation for the reduced radial function $\chi(R) = R^{5/2}\psi_K(R)$ with a given $K$

$$\frac{(K+2)^2 - 1/4}{R^2}$$

is not zero even for $K = 0$.

The Coulomb potential can be expressed directly in terms of Jacobi coordinates,

$$V_{\text{C}} = -\frac{2\alpha_s}{3}\sum_{i<j}\sqrt{\frac{\mu_{ij}}{\mu}}\frac{1}{|\boldsymbol{\rho}_{ij}|}, \tag{16}$$

while for the string potential the situation is not so simple. We will construct it in the next section.

### *3.2. String-Junction Point*

Now, we turn to the definition of the minimal length string $Y$-shaped configuration. Let $\varphi_{ijk}$ be the angle between the line from quark $i$ to quark $j$ and that from quark $j$ to quark $k$. One should distinguish two cases. In the first case, all $\varphi_{ijk}$ are smaller than 120°, and the equilibrium junction position $\mathbf{X}$ coincides with the so-called Torrichelli point of the triangle at whose vertices three quarks are situated. To find this point, consider a scalar function of a point inside a triangle $\triangle ABC$, defined as a sum of distances between this point and the triangle vertices:

$$\mathcal{L}(\mathbf{r}) = |\mathbf{r} - \mathbf{r}_A| + |\mathbf{r} - \mathbf{r}_B| + |\mathbf{r} - \mathbf{r}_C|. \tag{17}$$

The position of the minimum of the function $\mathcal{L}$ is calculated from the condition $d\mathcal{L}/d\mathbf{r} = \mathbf{0}$, i.e.,

$$\frac{\mathbf{r} - \mathbf{r}_A}{|\mathbf{r} - \mathbf{r}_A|} + \frac{\mathbf{r} - \mathbf{r}_B}{|\mathbf{r} - \mathbf{r}_B|} + \frac{\mathbf{r} - \mathbf{r}_C}{|\mathbf{r} - \mathbf{r}_C|} \tag{18}$$
$$= -\mathbf{n}_A - \mathbf{n}_B - \mathbf{n}_C = \mathbf{0},$$

---

[2] Here and throughout the paper, $q$ denotes a light quark $u$ or $d$.

where $\mathbf{n}_{A,B,C}$ are the unit vectors from the minimum point directed to the vertices of the triangle. It follows from Eq. (18) that this condition can be realized only in the case where angles between vectors $\mathbf{n}_A$, $\mathbf{n}_B$, and $\mathbf{n}_C$ are equal to 120°. If $\varphi_{ijk}$ are all smaller than 120°, this point exists and is the unique one. From this point, all sides of the triangle are seen at an angle of 120°. In the second case, when $\varphi_{ijk}$ is equal to or greater than 120°, the lowest energy configuration has the junction at the position of quark $j$.

The geometrical construction of the Torrichelli point is presented in Fig. 2. One should plot three equilateral triangles $\triangle AFB$, $\triangle BDC$, and $\triangle CEA$ on the sides of the initial triangle $\triangle ABC$. It is easy to prove the following statements:

The straight lines $AD$, $BE$, $CF$ intersect at a unique point $T$;

$$AD = BE = CF = AT + BT + CT;$$

$$\angle ATF = \angle BTF = \angle BTD = \angle CTD = \angle CTE = \angle ATE = \pi/3.$$

Now one can easily obtain an expression for a radius-vector of the Torrichelli point in terms of the lengths $l_i$ of the segments between this point and the $i$th quark (segments $AT$, $BT$, $CT$ on Fig. 2), and the quark positions $\mathbf{r}_i$ (points $A$, $B$, $C$ on Fig. 2) [13]:

$$\mathbf{X} = \frac{l_2 l_3 \mathbf{r}_1 + l_1 l_3 \mathbf{r}_2 + l_1 l_2 \mathbf{r}_3}{l_2 l_3 + l_1 l_3 + l_1 l_2}. \tag{19}$$

An equivalent expression for $\mathbf{X}$ in terms of the center-of-mass position $\mathbf{R}_{\text{c.m.}}$ and vectors $\boldsymbol{\rho}$ and $\boldsymbol{\lambda}$ is [14]

$$\mathbf{X} = \mathbf{R}_{\text{c.m.}} + \alpha\boldsymbol{\rho} + \beta\boldsymbol{\lambda} \tag{20}$$

with

$$\alpha = \frac{1}{2}\sqrt{\frac{\mu}{\mu_{ij}}}\left(\frac{m_j - m_i}{m_i + m_j} - \frac{1}{\sqrt{3}}\frac{4t + (3 - t^2)\cot\chi}{1 + t^2}\right),$$

$$\beta = \frac{\sqrt{\mu\mu_{ij,k}}}{m_i + m_j} + \sqrt{\frac{\mu}{3\mu_{ij}}}\frac{\rho}{2\lambda\sin\chi}\frac{3 - t^2}{1 + t^2},$$

where

$$t = \left(2\lambda\sin\chi + \sqrt{\frac{3\mu_{ij,k}}{\mu_{ij}}}\rho\right) \Bigg/ \left(2\lambda\cos\chi + \sqrt{\frac{3\mu_{ij,k}}{\mu_{ij}}}\frac{m_j - m_i}{m_i + m_j}\rho\right),$$

and $\chi$ is the angle between $\boldsymbol{\rho}$ and $\boldsymbol{\lambda}$, $0 \le \chi \le \pi$. It can easily be seen that the dependence on $m_i$ in Eq. (20) is apparent and $\mathbf{X}$ does not depend on quark masses, just as it should be.

After definition of the string-junction point, one can calculate the explicit expression for $l^2_{\text{min}}$ in terms of the Jacobi coordinates [15]. Introducing the variable $\theta = \arctan(\rho/\lambda)$, $0 \le \theta \le \pi/2$, one obtains for the case $\varphi_{ijk} < 120°$

$$l^2_{\text{min}} = \mu R^2\cos^2\theta\Bigg(\frac{(m_1^3 - m_2^3)\tan^2\theta}{m_1 m_2(m_1^2 - m_2^2)} + \left(\frac{m_2 - m_1}{m_2 + m_1}\cos\chi + \sqrt{3}\sin\chi\right)\frac{\tan\theta}{m} + \frac{1}{\mu_{12,3}}\Bigg), \tag{21}$$

where $m^2 = m_1 m_2 m_3/(m_1 + m_2 + m_3)$. If $m_1 = m_2 = m_3$, this expression coincides with that derived in [6]. When $\varphi_{ijk} > 120°$, the lowest energy configuration has the junction at the position of quark $j$ and

$$l_{\text{min}} = r_{ij} + r_{jk}, \tag{22}$$

where

$$r_{12} = R\sin\theta\sqrt{\frac{\mu}{\mu_{12,3}}}, \tag{23}$$

$$r_{13} = R\cos\theta\sqrt{\frac{\mu}{\mu_{12,3}}} \times \sqrt{\frac{m^2}{m_1^2}\tan^2\theta + \frac{2m}{m_1}\tan\theta\cos\chi + 1},$$

$$r_{23} = R\cos\theta\sqrt{\frac{\mu}{\mu_{12,3}}} \times \sqrt{\frac{m^2}{m_2^2}\tan^2\theta - \frac{2m}{m_2}\tan\theta\cos\chi + 1}.$$

The boundaries corresponding to the condition $\varphi_{ijk} = 120°$ in the $(\chi, \theta)$ plane are

$$\theta_{1(2)}(\chi) = \arctan(m_{1(2)}(\mp\cos\chi - \sin\chi/\sqrt{3})/m), \tag{24}$$

$$\theta_3(\chi) = \arctan(m_2(f(\chi) + \sqrt{f^2(\chi) + 4\varkappa})/2m),$$

where

$$f(\chi) = (1 - \varkappa)\cos\chi + (1 + \varkappa)\sin\chi/\sqrt{3} \tag{25}$$

and $\varkappa = m_1/m_2$. These boundaries are shown in Fig. 3 for the case of equal quark masses.

For simplicity, the string junction point is often chosen to coincide with the c.m. coordinate. In this case,

$$V_{\text{string}} = \sigma\sum_{(i,j,k)}\frac{1}{m_k}\sqrt{\mu\mu_{ij,k}}|\boldsymbol{\lambda}_{ij}| \tag{26}$$

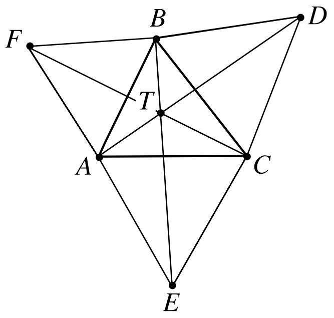

**Fig. 2.** The geometrical construction of the Torrichelli point $T$ for an arbitrary triangle $\triangle ABC$. The triangles $\triangle AFB$, $\triangle BDC$, and $\triangle CEA$ are equilateral.

($i, j, k$ cyclic). Accuracy of this approximation that greatly simplifies the calculations was discussed in [6, 15]. We shall comment on this point later on.

### *3.3. Hyperradial Approximation*

Introducing the variable $x = \sqrt{\mu}R$ and averaging the interaction $U = V_{\text{C}} + V_{\text{string}}$ over the six-dimensional sphere $\Omega_6$, one obtains the Schrödinger equation for $\chi(x)$:

$$\frac{d^2\chi(x)}{dx^2} + 2\left[E_0 + \frac{a}{x} - bx - \frac{15}{8x^2}\right]\chi(x) = 0. \quad (27)$$

Because the wave function $\psi$ must be finite, at the origin $\chi(x) \sim \mathcal{O}(x^{5/2})$ as $x \to 0$. As $x \to \infty$, one can neglect the Coulomb-like and centrifugal terms, and Eq. (27) becomes

$$\frac{d^2\chi(z)}{dz^2} - z\chi(z) = 0, \quad z = (2b)^{1/3}x. \quad (28)$$

This is the familiar Airy equation whose solution $\text{Ai}(z)$ behaves at infinity as

$$\text{Ai}(z) \sim \frac{1}{2}\pi^{-1/2}z^{-1/4}\exp\left(-\frac{2}{3}z^{3/2}\right), \quad (29)$$
$$\text{Re}z \geq 0.$$

In Eq. (27), $E_0$ is the ground-state eigenvalue and

$$a = R\sqrt{\mu}\int V_{\text{C}}(\mathbf{r}_1, \mathbf{r}_2, \mathbf{r}_3)d\Omega_6, \quad (30)$$
$$b = \frac{1}{R\sqrt{\mu}}\int V_{\text{string}}(\mathbf{r}_1, \mathbf{r}_2, \mathbf{r}_3)d\Omega_6.$$

Using expression (16) for the $V_{\text{C}}$, the coefficient $a$ can be easily calculated:

$$a = \frac{2\alpha_s}{3}\frac{16}{3\pi}\left(\sum_{i<j}\sqrt{\mu_{ij}}\right), \quad (31)$$

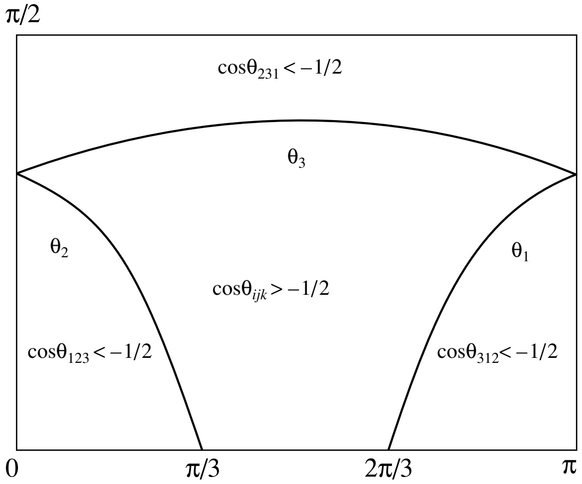

**Fig. 3.** The four regions in the $(\chi, \theta)$ plane corresponding to $\varphi_{ijk} \geq 120°$ and $\varphi_{ijk} \leq 120°$ for the case of equal quark masses.

while the analytical result for the coefficient $b$ cannot be obtained except for the equal-quark-mass system $m_1 = m_2 = m_3 = m$, in which case a straightforward calculation yields

$$b = \frac{4}{15}\frac{\sigma}{\sqrt{m}}\left(-\sqrt{3} + \frac{12\sqrt{2}}{\pi}\right. \quad (32)$$
$$\left. + \frac{3\sqrt{3}}{\pi}\arccos\frac{1}{5}\right) \approx 1.58\frac{\sigma}{\sqrt{m}}.$$

On the contrary, in the approximation (26), the coefficient $b$ can be found analytically for the case of different quark masses. The result is

$$b = \sigma\frac{32}{15\pi}\left(\sum_{(i,j,k)}\frac{\sqrt{\mu_{ij,k}}}{m_k}\right) \quad (33)$$

($i, j, k$ cyclic).

Let us explain the numerical coefficients in (31) and (33) in more detail. To this end, we introduce the angle $\theta$ as in (21) such that

$$\rho = R\sin\theta, \quad \lambda = R\cos\theta, \quad (34)$$
$$0 \leq \theta \leq \frac{\pi}{2},$$

and write the volume element $d^3\rho d^3\lambda$ as

$$d^3\rho d^3\lambda \quad (35)$$
$$= (4\pi)^2\rho^2\lambda^2 d\rho d\lambda = (4\pi)^2R^5\sin^2\theta\cos^2\theta dRd\theta.$$

The volume of the six-dimensional sphere is

$$\Omega_6 = (4\pi)^2\int\limits_0^{\pi/2}\sin^2\theta\cos^2\theta d\theta = (4\pi)^2\frac{\pi}{16} = \pi^3.$$
$$(36)$$

Then averaging the Coulomb and string terms yields

$$\left\langle \frac{1}{\rho} \right\rangle = \frac{1}{\pi^3}\frac{1}{R}(4\pi)^2 \int\limits_0^{\pi/2} \sin\theta\cos^2\theta d\theta = \frac{16}{3\pi}\frac{1}{R}, \quad (37)$$

$$\langle \lambda \rangle = \frac{1}{\pi^3}R(4\pi)^2 \int\limits_0^{\pi/2} \sin^2\theta\cos^3\theta d\theta = \frac{32}{15\pi}R. \quad (38)$$

Combining together expressions (16), (26), (30), (37), and (38) leads to (31) and (33).

### *3.4. Analytic Results for Light Baryons*

We can eliminate all dimensional parameters from Eq. (27) by a substitution $y = b^{1/3}x$, which leads us to the equation

$$\frac{d^2\chi}{dy^2} + 2\left(\mathcal{E} - y + \frac{\delta}{y} - \frac{15}{8y^2}\right) = 0, \quad (39)$$

where

$$\mathcal{E} = E_0 b^{-2/3}, \quad \delta = ab^{-1/3}.$$

The eigenvalue of Eq. (39) can be found using ordinary perturbation theory, the Coulomb term $(-\delta/y)$ being considered as a small perturbation. This approximation works well for a nucleon containing three light quarks with the running mass equal to zero. In this case, there is only one dynamical quark mass $m$. Thus, the task is greatly simplified and one can obtain analytic expressions for $m$ and $M_B$ via two parameters, $\sigma$ and $\alpha_s$, as expansions in powers of $\alpha_s$.

Omitting the intermediate details outlined in the Appendix, we quote here the result with accuracy up to $\alpha_s^2$:

$$m = \sqrt{\sigma} \cdot 0.959(1 + 0.270\alpha_s + 0.117\alpha_s^2 + \dots), \quad (40)$$

$$M_B = \sqrt{\sigma} \cdot 5.751(1 - 0.270\alpha_s - 0.039\alpha_s^2 + \dots), \quad (41)$$

or

$$M_B = 6m(1 - 0.540\alpha_s - 0.083\alpha_s^2 + \dots) + C, \quad (42)$$

i.e., the Coulomb-like correction to $M_B$ comprises approximately 20%.

### *3.5. Semiclassical Solution*

For the purpose of illustration, the problem is first solved semiclassically rather than using quantum mechanics. This approach is based on the well-known fact that interplay between the centrifugal term and the confining potential produces an effective potential minimum specific to the three-body problem. The numerical solution of (27) for the ground-state eigenenergy may be reproduced on a percent level of accuracy by using the parabolic approximation [16] for the effective potential

$$U(x) = -\frac{a}{x} + bx + \frac{15}{8x^2}.$$

This approximation provides an analytical expression for the eigenenergy. The potential $U(x)$ has the minimum at a point $x = x_0$ defined by the condition $U'(x_0) = 0$, i.e.,

$$bx_0^3 + ax_0 - 15/4 = 0. \quad (43)$$

Expanding $U(x)$ in the vicinity of the minimum, one obtains

$$U(x) \approx U(x_0) + \frac{1}{2}U''(x_0)(x - x_0)^2,$$

i.e., the potential of the harmonic oscillator with the frequency $\omega = \sqrt{U''(x_0)}$. Therefore, the ground-state energy eigenvalue is

$$E_0 \approx U(x_0) + \frac{1}{2}\omega. \quad (44)$$

### *3.6. Variational Solution*

Another method of solving Eq. (27) is the minimization of the baryon energy using a simple variational ansatz

$$\chi(x) \sim x^{5/2}e^{-p^2x^2}, \quad (45)$$

where $p$ is the variational parameter. Then, using the three-quark Hamiltonian, one can get an approximate expression for the ground-state energy: $E_0 \approx \min_p E_0(p)$, where

$$E_0(p) = \langle\chi|H|\chi\rangle = 3p^2 - a\frac{3}{4}\sqrt{\frac{\pi}{2}}p + b\frac{15}{16}\sqrt{\frac{\pi}{2}}\frac{1}{p}. \quad (46)$$

### *3.7. Analytic Results for $(Qud)$ Baryons*

For the heavy quarks ($Q = c$ and $b$), the variation in the values of their masses $m_Q$ is marginal. This is illustrated by the simple analytical results for $(Qud)$ baryons [17]. These results were obtained from the approximate solution of equation

$$\frac{\partial E_0(m_1, m_2, m_3, p)}{\partial p} = 0, \quad (47)$$

**Table 1.** Summary of variational calculations for the various baryon states in the approximation $\mathbf{X} = \mathbf{R}_{\text{c.m.}}$

| Baryon | $m_1$ | $m_2$ | $m_3$ | $E_0$ | $M_B$ |
|---|---|---|---|---|---|
| $(qqq)$ | 0.372 | 0.372 | 0.372 | 1.433 | 1.221 |
| $(qqs)$ | 0.377 | 0.377 | 0.415 | 1.404 | 1.314 |
| $(qss)$ | 0.381 | 0.420 | 0.420 | 1.377 | 1.405 |
| $(sss)$ | 0.424 | 0.424 | 0.424 | 1.350 | 1.493 |
| $(qqc)$ | 0.424 | 0.424 | 1.464 | 1.178 | 2.538 |
| $(qsc)$ | 0.427 | 0.465 | 1.467 | 1.153 | 2.613 |
| $(ssc)$ | 0.468 | 0.468 | 1.469 | 1.129 | 2.686 |
| $(qqb)$ | 0.446 | 0.446 | 4.819 | 1.093 | 5.909 |
| $(qsb)$ | 0.448 | 0.487 | 4.820 | 1.067 | 5.978 |
| $(ssb)$ | 0.490 | 0.490 | 4.821 | 1.042 | 6.046 |
| $(qcc)$ | 0.459 | 1.498 | 1.498 | 0.914 | 3.712 |
| $(scc)$ | 0.499 | 1.499 | 1.499 | 0.890 | 3.777 |
| $(qcb)$ | 0.477 | 1.524 | 4.834 | 0.793 | 7.021 |
| $(scb)$ | 0.517 | 1.525 | 4.834 | 0.770 | 7.083 |
| $(qbb)$ | 0.495 | 4.854 | 4.854 | 0.606 | 10.260 |
| $(sbb)$ | 0.534 | 4.855 | 4.855 | 0.583 | 10.318 |

where $E_0$ is given by Eq. (46) in the form of an expansion in the small parameters

$$\xi = \frac{\sqrt{\sigma}}{m_Q^{(0)}} \text{ and } \alpha_s, \tag{48}$$

where $m_Q^{(0)}$ is the heavy-quark running mass.

Omitting the intermediate steps, one obtains [17]

$$E_0 = 3\sqrt{\sigma}\left(\frac{6}{\pi}\right)^{1/4}\left(1 + A\xi - \frac{5}{3}B\alpha_s + \dots\right), \tag{49}$$

$$m_q = \sqrt{\sigma}\left(\frac{6}{\pi}\right)^{1/4}(1 - A\xi + B\alpha_s + \dots), \tag{50}$$

$$m_Q = m_Q^{(0)}(1 + \mathcal{O}(\xi^2, \alpha_s^2, \alpha_s\xi) + \dots), \tag{51}$$

where for the Gaussian variational ansatz (45)

$$A = \frac{\sqrt{2} - 1}{2}\left(\frac{6}{\pi}\right)^{1/4} \approx 0.24, \tag{52}$$

$$B = \frac{4 + \sqrt{2}}{18}\sqrt{\frac{6}{\pi}} \approx 0.42.$$

Note that the corrections of the first order in $\xi$ and $\alpha_s$ are absent in expression (51) for $m_Q$. The accuracy of this approximation is illustrated in Table 1 of [14].

## 4. BARYON MASSES

### 4.1. Quark Dynamical Masses

We first calculate the dynamical masses $m_i$ retaining only the string potential in the EH (6). This procedure is in agreement with the strategy adopted in [9]. The masses $m_i$ are then obtained from the equation

$$\frac{\partial M_B^{(0)}}{\partial m_i} = 0, \tag{53}$$

where

$$M_B^{(0)} = \sum_{i=1}^{3}\left(\frac{m_i^{(0)2}}{2m_i} + \frac{m_i}{2}\right) + E_0(m_1, m_2, m_3; \alpha_s = 0). \tag{54}$$

Then we add the one-gluon-exchange Coulomb potential and solve Eq. (27) to obtain the ground-state eigenvalues $E_0(m_1, m_2, m_3; \alpha_s)$ for a given $\alpha_s$. The physical mass $M_B$ of a baryon is [10]

$$M_B = \sum_{i=1}^{3}\left(\frac{m_i^{(0)2}}{2m_i} + \frac{m_i}{2}\right) + E_0(m_1, m_2, m_3; \alpha_s) + C. \tag{55}$$

We use the values of parameters $\sigma = 0.15$ GeV$^2$ (this value has been found in a recent lattice study [18]), $\alpha_s = 0.39$, $m_q^{(0)} = 0.009$ GeV $(q = u, d)$, $m_s^{(0)} = 0.17$ GeV, $m_c^{(0)} = 1.4$ GeV, and $m_b^{(0)} = 4.8$ GeV. The results for various baryons, obtained using various approximations, are given in Tables 1–3. Table 1 contains the results obtained using the variational solution of Eq. (27) with the approximate three-quark potential (26). In Table 2, the results obtained using exact numerical solution of Eq. (27) and the same approximation, $\mathbf{X} = \mathbf{R}_{\text{c.m.}}$, are presented. Table 3 contains the results obtained by the numerical integration of (27) with the three-quark potential in the form (21), (22). Comparing the results of Tables 1 and 2, we observe a good accuracy of the variational solution: the difference between variational and exact results for $M_B$ does not exceed 10–15 MeV for all baryons from the lightest to doubly heavy ones. The approximation $\mathbf{X} = \mathbf{R}_{\text{c.m.}}$ leads to an ~5% increase in the coefficient $b$ in (27) and, as a consequence, an increase in the baryon masses by ~70 MeV.

Note that there is no good theoretical reason why quark masses $m_i$ need to be the same in different baryons. Inspection of Table 1 shows that the masses of the light quarks ($u$, $d$, or $s$) are increased by ~100 MeV in going from light to heavy baryons. The dynamical masses of light quarks $m_{u,d,s} \sim \sqrt{\sigma} \sim$

**Table 2.** Summary of numerical calculations for the various baryon states in the approximation $\mathbf{X} = \mathbf{R}_{\text{c.m.}}$

| Baryon | $m_1$ | $m_2$ | $m_3$ | $E_0$ | $M_B$ |
|---|---|---|---|---|---|
| $(qqq)$ | 0.372 | 0.372 | 0.372 | 1.427 | 1.212 |
| $(qqs)$ | 0.376 | 0.376 | 0.415 | 1.398 | 1.306 |
| $(qss)$ | 0.381 | 0.419 | 0.419 | 1.370 | 1.397 |
| $(sss)$ | 0.423 | 0.423 | 0.423 | 1.344 | 1.485 |
| $(qqc)$ | 0.424 | 0.424 | 1.464 | 1.170 | 2.530 |
| $(qsc)$ | 0.426 | 0.465 | 1.466 | 1.146 | 2.604 |
| $(ssc)$ | 0.467 | 0.467 | 1.468 | 1.122 | 2.677 |
| $(qqb)$ | 0.445 | 0.445 | 4.820 | 1.085 | 5.900 |
| $(qsb)$ | 0.448 | 0.487 | 4.820 | 1.059 | 5.970 |
| $(ssb)$ | 0.488 | 0.488 | 4.820 | 1.035 | 6.037 |
| $(qcc)$ | 0.458 | 1.497 | 1.497 | 0.905 | 3.702 |
| $(scc)$ | 0.497 | 1.498 | 1.498 | 0.882 | 3.767 |
| $(qcb)$ | 0.475 | 1.523 | 4.833 | 0.784 | 7.010 |
| $(scb)$ | 0.515 | 1.523 | 4.837 | 0.760 | 7.072 |
| $(qbb)$ | 0.490 | 4.850 | 4.850 | 0.596 | 10.245 |
| $(sbb)$ | 0.530 | 4.856 | 4.856 | 0.571 | 10.303 |

400–500 MeV qualitatively agree with the results of [19] obtained from the analysis of the heavy–light ground-state mesons.

While studying Table 3 is sufficient to have an appreciation of the accuracy of our predictions, a few comments should be added. We expect the accuracy of the baryon predictions to be $\sim$ 5–10%, which is partly due to the approximations employed in the derivations of the EH itself [5] and partly due to the error associated with the variational nature of the hyperspherical approximation. From this point of view, the overall agreement with data is quite satisfactory. For example, we get $\frac{1}{2}(N + \Delta)_{\text{theory}} = 1144$ MeV vs. $\frac{1}{2}(N + \Delta)_{\text{exp}} = 1085$ MeV (a 5% increase in $\alpha_s$ would correctly give the $(N, \Delta)$ center of gravity), $\frac{1}{4}(\Lambda + \Sigma + 2\Sigma^*) = 1242$ MeV vs. the experimental value of 1267 MeV. We also find $\Xi_{\text{theory}} = 1336$ MeV (without hyperfine splitting) vs. $\Xi_{\text{exp}} = 1315$ MeV and $\Xi^c_{\text{theory}} = 2542$ MeV vs. $\Xi^c_{\text{exp}} = 2584$ MeV. On the other hand, our study shows some difficulties in reproducing the $\Omega$-hyperon mass.

**Table 3.** Summary of numerical calculations for the various baryon states with exact treatment of the string-junction point

| Baryon | $m_1$ | $m_2$ | $m_3$ | $E_0$ | $M_B$ |
|---|---|---|---|---|---|
| $(qqq)$ | 0.362 | 0.362 | 0.362 | 1.392 | 1.144 |
| $(qqs)$ | 0.367 | 0.367 | 0.407 | 1.362 | 1.242 |
| $(qss)$ | 0.371 | 0.411 | 0.411 | 1.335 | 1.336 |
| $(sss)$ | 0.415 | 0.415 | 0.415 | 1.307 | 1.426 |
| $(qqc)$ | 0.406 | 0.406 | 1.470 | 1.142 | 2.464 |
| $(qsc)$ | 0.409 | 0.448 | 1.471 | 1.116 | 2.542 |
| $(ssc)$ | 0.452 | 0.452 | 1.473 | 1.090 | 2.621 |
| $(qqb)$ | 0.425 | 0.425 | 4.825 | 1.054 | 5.823 |
| $(qsb)$ | 0.429 | 0.469 | 4.826 | 1.026 | 5.903 |
| $(ssb)$ | 0.471 | 0.471 | 4.826 | 1.000 | 5.975 |
| $(qcc)$ | 0.444 | 1.494 | 1.494 | 0.876 | 3.659 |
| $(scc)$ | 0.485 | 1.496 | 1.496 | 0.851 | 3.726 |
| $(qcb)$ | 0.465 | 1.512 | 4.836 | 0.753 | 6.969 |
| $(scb)$ | 0.505 | 1.514 | 4.837 | 0.729 | 7.032 |
| $(qbb)$ | 0.488 | 4.847 | 4.847 | 0.567 | 10.214 |
| $(sbb)$ | 0.526 | 4.851 | 4.851 | 0.544 | 10.273 |

### *4.2. Doubly Heavy Baryons*

In Table 4, we compare the spin-averaged masses (computed without the spin–spin term) of the lowest doubly heavy baryons to the predictions of other models [20–22] as well as variational calculations of [4] for which the center-of-gravity of nonstrange baryons and hyperons was essentially a free parameter. Most of the recent predictions were obtained in a light quark–heavy-diquark model [20, 21], in which case the spin-averaged values are $M = \frac{1}{3}(M_{1/2} + 2M_{3/2})$.

**Table 4.** Comparison of various predictions for ground-state masses (in units of GeV) of doubly heavy baryons

| Baryon | [15] | [4] | [20] | [21] | [22] |
|---|---|---|---|---|---|
| $\Xi_{cc}$ | 3.66 | 3.69 | 3.57 | 3.69 | 3.70 |
| $\Omega_{cc}$ | 3.73 | 3.86 | 3.66 | 3.84 | 3.80 |
| $\Xi_{cb}$ | 6.97 | 6.96 | 6.87 | 6.96 | 6.99 |
| $\Omega_{cb}$ | 7.03 | 7.13 | 6.96 | 7.15 | 7.07 |
| $\Xi_{bb}$ | 10.21 | 10.16 | 10.12 | 10.23 | 10.24 |
| $\Omega_{bb}$ | 10.27 | 10.34 | 10.19 | 10.38 | 10.34 |

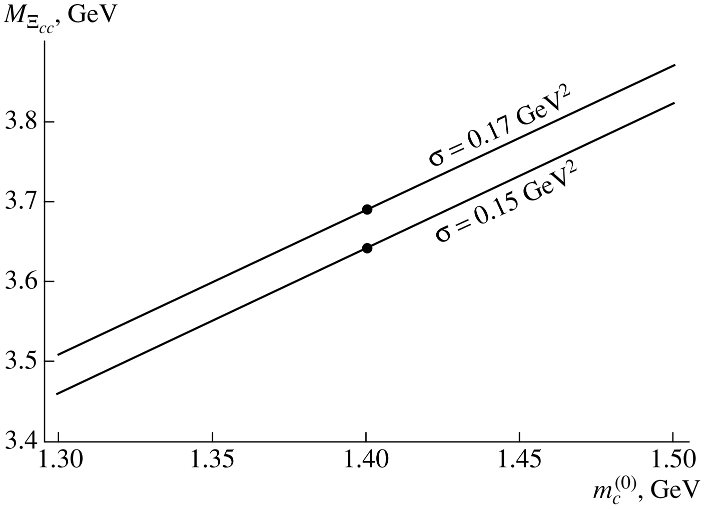

**Fig. 4.** Mass of $\Xi^+_{cc}$ as a function of the running $c$-quark mass for $\sigma = 0.15$ and $0.17$ GeV$^2$. Closed circles refer to the case $m_c^{(0)} = 1.4$ GeV.

Note that the wave function calculated in the hyperspherical approximation shows the marginal diquark clustering in the doubly heavy baryons. This is primarily a kinematic effect related to the fact that, in this approximation, the difference between the various mean values $\bar{r}_{ij}$ in a baryon is due to the factor $\sqrt{1/\mu_{ij}}$, which varies between $\sqrt{2/m_i}$ for $m_i = m_j$ and $\sqrt{1/m_i}$ for $m_i \ll m_j$. In general, in spite of the completely different physical picture, we find a reasonable agreement within 100 MeV between different predictions for the ground-state masses of the doubly heavy baryons. Our prediction for $M_{ccu}$ is 3.66 GeV with the perturbative hyperfine splitting $\Xi^*_{ccu} - \Xi_{ccu} \sim 40$ MeV.

The change in $\sigma$ to 0.17 GeV$^2$ increases the mass of $\Xi_{cc}$ by $\sim 30$ MeV. The hyperfine splitting with the spin-1/2 states is calculated using Fermi–Breit spin–spin interaction [23]. It produces an additional shift of the $\Xi_{cc}$ mass of $\approx -20$ MeV. Note that the mass of $\Xi_{cc}$ is rather sensitive to the value of the running $c$-quark mass $m_c^{(0)}$ (see Fig. 4).

## 5. CONCLUSIONS

We have outlined a novel approach to baryon spectroscopy that is based on a single framework of the effective Hamiltonian that is consistent with QCD. This model uses the stringlike picture of confinement and perturbative one-gluon-exchange potential. The main advantage of this work is demonstration of the fact that it is possible to describe all the baryons in terms of the only two parameters inherent to QCD, namely, $\sigma$ and $\alpha_s$.

## ACKNOWLEDGMENTS

This work was supported in part by NATO (grant no. PST.CLG.978710) and by the Russian Foundation for Basic Research (project nos. 03-02-17345 and 02-02-17379).

## APPENDIX

### *The Approximate Calculation of the Mass of the Three-Light-Quark System in the Hyperspherical Formalism*

Let us consider the case where each quark has a zero current mass and the constituent mass $m$, which is the same for all three quarks. Then the mass of the system is the minimum of the function $\mathcal{H}(m)$: $\mathcal{M} = \min_m \mathcal{H}(m)$, where[3]

$$\mathcal{H}(m) = \frac{3m}{2} + E, \tag{A.1}$$

and $E$ is the energy level defined from the ordinary Schrödinger equation [see Eq. (27)]:

$$\frac{d^2\chi}{dx^2} + 2\left(E + \frac{\beta\sqrt{m}}{x} - \frac{\gamma}{\sqrt{m}}x - \frac{15}{8x^2}\right)\chi = 0, \tag{A.2}$$

where

$$\beta = \frac{16\sqrt{2}}{3\pi}\alpha_s \approx 2.401\alpha_s, \tag{A.3}$$

$$\gamma = \frac{32\sqrt{6}}{15\pi}\sigma \approx 1.663\sigma. \tag{A.4}$$

---

[3] For simplicity we omit here and below the corrections $C$.

Let us replace the variable $x$ by a dimensionless variable $y$: $y = (\gamma^2/m)^{1/6}x$. Then,

$$\frac{d^2\chi}{dy^2} + 2\left(\mathcal{E} + \frac{\delta}{y} - y - \frac{15}{8y^2}\right)\chi = 0, \qquad (A.5)$$

where $\mathcal{E}$ and $\delta$ are dimensionless parameters:

$$\mathcal{E} = E\left(\frac{m}{\gamma^2}\right)^{1/3}, \quad \delta = \beta\left(\frac{m^2}{\gamma}\right)^{1/3}.$$

We will calculate the eigenvalues of Eq. (A.5) using second-order perturbation theory, considering the Coulomb term $(-\delta/y)$ in the potential as a small perturbation. The unperturbed equation is

$$\frac{d^2f}{dy^2} + 2\left(\lambda - y - \frac{15}{8y^2}\right)f = 0. \qquad (A.6)$$

It contains no physical parameters, so its solution is a pure mathematical task. Let us denote the eigenvalues of Eq. (A.6) as $\{\lambda_i\}$,

$$0 < \lambda_0 < \lambda_1 < \ldots,$$

and the corresponding normalized eigenfunctions as $\{f_i(y)\}$. In what follows, we will use the notation

$$\xi = \int\limits_0^{+\infty} \frac{1}{y} f_0^2(y)dy, \quad \xi > 0,$$

$$\eta = \sum_{i=1}^{\infty}\left(\int\limits_0^{+\infty}\frac{1}{y}f_i(y)f_0(y)dy\right)^2 \Big/ (\lambda_i - \lambda_0), \;\; \eta > 0.$$

The approximate numerical values of these parameters are

$$\lambda_0 \approx 3.030, \qquad (A.7)$$

$$\xi \approx 0.553, \qquad (A.8)$$

$$\eta \approx 0.028. \qquad (A.9)$$

The ground level of Eq. (A.5) can be approximately calculated as follows:

$$\mathcal{E} \approx \lambda_0 - \delta\xi - \delta^2\eta. \qquad (A.10)$$

The small parameter here is the ratio $\delta\xi/\lambda_0$. To estimate this quantity, one can solve the problem in the zero approximation without the Coulomb term. Thus,

$$\mathcal{E} \approx \lambda_0,$$

$$E \approx \lambda_0\left(\frac{\gamma^2}{m}\right)^{1/3},$$

$$\mathcal{H} \approx \frac{3}{2}m + \lambda_0\left(\frac{\gamma^2}{m}\right)^{1/3}.$$

$\mathcal{H}$ has a single minimum, defined by the equation $\partial\mathcal{H}/\partial m = 0$, i.e.,

$$\frac{3}{2} - \frac{1}{3}\lambda_0\gamma^{2/3}m^{-4/3} = 0.$$

Thus, $m = (2\lambda_0/9)^{3/4}\sqrt{\gamma}$, and finally

$$\frac{\delta\xi}{\lambda_0} = \frac{\beta\xi}{\lambda_0}\left(\frac{m^2}{\gamma}\right)^{1/3} = \frac{2\beta\xi}{3\sqrt{2\lambda_0}} \approx 0.360\alpha_s.$$

For $\alpha_s = 0.4$, one has $\delta\xi/\lambda_0 \approx 0.14 \ll 1$. This verifies the correctness of using perturbation theory in this problem.

Now, using Eq. (A.10), we can calculate the constituent mass $m$ and the mass of the state $\mathcal{M}$. For the energy level, we have

$$E = \left(\frac{\gamma^2}{m}\right)^{1/3}\mathcal{E} = \left(\frac{\gamma^2}{m}\right)^{1/3}\lambda_0 - (\gamma m)^{1/3}\beta\xi - m\beta^2\eta.$$

It is convenient to use the positive dimensionless parameter $q = m^{1/3}\gamma^{-1/6}$, so that $m = \sqrt{\gamma}q^3$. Then,

$$E = \sqrt{\gamma}(\lambda_0 q^{-1} - \beta\xi q - \beta^2\eta q^3),$$

and substituting it into Eq. (A.1), we find

$$\mathcal{H} = \sqrt{\gamma}\left(\lambda_0 q^{-1} - \beta\xi q + \left(\frac{3}{2} - \beta^2\eta\right)q^3\right).$$

$\mathcal{H}$ has a single minimum, defined from the condition $\partial\mathcal{H}/\partial q|_{q=q_0} = 0$, i.e.,

$$\left(\frac{9}{2} - 3\beta^2\eta\right)q_0^2 - \beta\xi - \frac{\lambda_0}{q_0^2} = 0. \qquad (A.11)$$

After calculating $q_0$, one can find the constituent mass $m = \sqrt{\gamma}q_0^3$ and the mass of the system $\mathcal{M}$:

$$\mathcal{M} = \mathcal{H}(q_0) = \frac{2\sqrt{\gamma}}{3}\left(\frac{2\lambda_0}{q_0} - \beta\xi q_0\right).$$

Equation (A.11) can be easily solved:

$$q_0 = \sqrt{\frac{\beta\xi + \sqrt{\beta^2\xi^2 + 2\lambda_0(9 - 6\beta^2\eta)}}{9 - 6\beta^2\eta}}. \qquad (A.12)$$

On expanding the right-hand side of this equation taking $\beta$ as a small parameter

$$q_0 \approx \frac{(2\lambda_0)^{1/4}}{\sqrt{3}}\left(1 + \frac{\xi\beta}{6\sqrt{2\lambda_0}} + \left(\frac{\xi^2}{144\lambda_0} + \frac{\eta}{6}\right)\beta^2\right),$$

we easily get formulas for the constituent mass,

$$m \approx \sqrt{\gamma}\frac{(2\lambda_0)^{3/4}}{3\sqrt{3}}\left(1 + \frac{\xi\beta}{2\sqrt{2\lambda_0}} + \left(\frac{\xi^2}{16\lambda_0} + \frac{\eta}{2}\right)\beta^2\right), \qquad (A.13)$$

and for the state mass,

$$\mathcal{M} \approx \sqrt{\gamma}(2\lambda_0)^{3/4}\frac{2}{\sqrt{3}}\left(1 - \frac{\xi\beta}{2\sqrt{2\lambda_0}} - \left(\frac{\xi^2}{48\lambda_0} + \frac{\eta}{6}\right)\beta^2\right). \quad (A.14)$$

Substituting into Eqs. (A.13) and (A.14) numerical values according to formulas (A.3), (A.4), and (A.7)–(A.9), we obtain

$$m \approx \sqrt{\sigma} \cdot 0.959(1 + 0.270\alpha_s + 0.117\alpha_s^2), \quad (A.15)$$

$$\mathcal{M} \approx \sqrt{\sigma} \cdot 5.751(1 - 0.270\alpha_s - 0.039\alpha_s^2). \quad (A.16)$$

For $\sigma = 0.15$ GeV$^2$ and $\alpha_s = 0.4$, one has $m \approx 0.418$ GeV and $\mathcal{M} \approx 1.973$ GeV.

## REFERENCES

1. M. Mattson *et al.*, Phys. Rev. Lett. **89**, 112001 (2002).
2. V. V. Kiselev and A. K. Likhoded, hep-ph/0208231.
3. K. Anikeev *et al.*, See references [111–124] in hep-ph/0201071.
4. I. M. Narodetskii and M. A. Trusov, Yad. Fiz. **65**, 949 (2002) [Phys. At. Nucl. **65**, 917 (2002)]; hep-ph/0104019.
5. Yu. A. Simonov, Yad. Fiz. **66**, 363 (2003) [Phys. At. Nucl. **66**, 338 (2003)]; hep-ph/0205334.
6. M. Fabre de la Ripelle and Yu. A. Simonov, Ann. Phys. (N.Y.) **212**, 235 (1991).
7. A. Yu. Dubin, A. B. Kaidalov, and Yu. A. Simonov, Phys. Lett. B **323**, 41 (1994).
8. V. L. Morgunov, A. V. Nefediev, and Yu. A. Simonov, Phys. Lett. B **459**, 653 (1999).
9. B. O. Kerbikov and Yu. A. Simonov, Phys. Rev. D **62**, 093016 (2000).
10. Yu. A. Simonov, Phys. Lett. B **515**, 137 (2001).
11. X. Artru, Nucl. Phys. B **85**, 442 (1975); H. G. Dosch and V. Mueller, Nucl. Phys. B **116**, 470 (1976).
12. J. Carlson, J. Kogut, and V. R. Pandharipande, Phys. Rev. D **27**, 233 (1983); N. Isgur and J. Paton, Phys. Rev. D **31**, 2910 (1985).
13. S. Capstick and P. R. Page, Phys. Rev. C **66**, 065204 (2002); nucl-th/0207027.
14. I. M. Narodetskii and M. A. Trusov, Nucl. Phys. B (Proc. Suppl.) **115**, 20 (2003); hep-ph/0209044.
15. I. M. Narodetskii, A. N. Plekhanov, and A. I. Veselov, JETP Lett. **77**, 58 (2003); hep-ph/0212358.
16. Yu. S. Kalashnikova, I. M. Narodetskii, and Yu. A. Simonov, Yad. Fiz. **46**, 1181 (1987) [Sov. J. Nucl. Phys. **46**, 689 (1987)].
17. I. M. Narodetskii and M. A. Trusov, in *Proceedings of the 9th International Conference on the Structure of Baryons (Baryons-2002), Newport News, VA, USA, 2002*; hep-ph/0307131.
18. T. T. Takahashi, H. Matsufuru, Y. Nemoto, and H. Suganuma, Phys. Rev. Lett. **86**, 18 (2001).
19. Yu. S. Kalashnikova and A. Nefediev, Phys. Lett. B **492**, 91 (2000).
20. S. S. Gershtein, V. V. Kiselev, A. K. Likhoded, and A. I. Onishchenko, Phys. Rev. D **62**, 050421 (2000).
21. D. Ebert, R. N. Faustov, V. D. Galkin, and A. P. Matvienko, Phys. Rev. D **66**, 014008 (2002).
22. E. Bagan *et al.*, Z. Phys. C **64**, 57 (1994).
23. A. De Rujula, H. Georgy, and S. L. Glashow, Phys. Rev. D **12**, 147 (1975).

Physics of Atomic Nuclei, Vol. 67, No. 4, 2004, pp. 773–803. From Yadernaya Fizika, Vol. 67, No. 4, 2004, pp. 794–824.
Original English Text Copyright © 2004 by A. Anisovich, V. Anisovich, Markov, Matveev, Sarantsev.

**ELEMENTARY PARTICLES AND FIELDS**
**Theory**

# Quark–Antiquark Composite Systems: The Bethe–Salpeter Equation in the Spectral-Integration Technique*

**A. V. Anisovich, V. V. Anisovich**, V. N. Markov, M. A. Matveev, and A. V. Sarantsev**

*Petersburg Nuclear Physics Institute, Russian Academy of Sciences, Gatchina, 188350 Russia*

Received May 22, 2003

**Abstract**—The Bethe–Salpeter equations for the quark–antiquark composite systems, $q\bar{q}$, are written in terms of spectral integrals. For the $q\bar{q}$ mesons characterized by the mass $M$, spin $J$, and radial quantum number $n$, the equations are presented for the following $(n, M^2)$ trajectories: $\pi_J$, $\eta_J$, $a_J$, $f_J$, $\rho_J$, $\omega_J$, $h_J$, and $b_J$. *© 2004 MAIK "Nauka/Interperiodica".*

## 1. INTRODUCTION

The relativistic description of composite systems was always an actual and challenging task. The most frequently used technique, which takes into account the relativism of the constituents, is the Bethe–Salpeter equation [1]. But in the standard formulation of the Bethe–Salpeter equation, when the Feynman integration technique with mass-off-shell amplitudes is used, one faces problems in describing multiparticle channels and high-spin states. A more appropriate technique for the high-spin composite systems is the dispersion-relation approach, in particular, the most developed $N/D$ method [2]. However, our experience and intuition are based on the consideration of the potential-type interactions, i.e., those which are associated with the particle-exchange mechanism. In terms of the $N/D$ method, one can easily relate the nearest left-hand side singularity of the $N$ function to the $t$-channel (or $u$-channel) meson-exchange diagram, but the reconstruction of the full set of left-hand singularities, when the interaction is given by the particle exchange or potential forces, is not a simple problem. Here, we present the Bethe–Salpeter equation in terms of the spectral-integral technique, which has advantages of both approaches discussed above:

(i) In the spectral integrals, the mass-on-shell amplitudes are used.

(ii) The interaction terms are written in the potential or particle-exchange form.

Moreover, in the spectral-integral technique, one can use the energy-dependent forces as well.

In [3–5], the dispersion-relation approach was applied to the description of the deuteron, a two-nucleon composite system, by treating nucleon–nucleon forces in terms of separable interactions. By using the interaction in a separable form, one can work with mass-on-shell amplitudes and meson-exchange interactions. The expansion of the one-meson exchange diagrams in a series of separable interaction factors was developed in [6]. The principal points in the transformation of the standard Bethe–Salpeter equation to the dispersion-relation representation for the case of separable vertices were clarified in [7]. However, the representation of the meson-exchange diagram as a finite set of separable vertices works successfully for mesons with nonzero mass only. For the long-range interaction, like confinement forces, the separable-vertex approach fails, thus forcing us to use not the standard $N/D$ method but the spectral-integral technique.

The important ingredient of the dispersion relation and spectral-integration methods is the moment-operator expansion. The elements of the moment-operator-expansion technique were presented in [3, 4, 8], and a systematic presentation of the technique may be found in [9].

The Bethe–Salpeter equation in the spectral integral representation is written here for quark–antiquark systems. Our attention is focused on the light-quark bound states, $q\bar{q}$, where $q = u, d, s$: for the sake of simplicity, we consider here the systems built by quark and antiquark with equal masses: $u\bar{d}$, $u\bar{u}$, $d\bar{d}$, $s\bar{s}$. The treatment of heavy-quark composite systems, $c\bar{c}$ and $b\bar{b}$, can be performed similarly.

The necessity to deal with a full set of equations for the light-quark composite systems is governed by the rich information on the light-meson radiative decays that appeared recently [10–12]. The radiative decay

---

[*] This article was submitted by the authors in English.

[**] e-mail: `anisovich@thd.pnpi.spb.ru`

data make it possible to restore the wave functions of mesons involved in reactions. The corresponding relativistic technique based on the consideration of the form-factor amplitudes in terms of the double spectral integrals was developed in [13] for pseudoscalar $q\bar{q}$ mesons, and it was generalized for scalar and tensor $q\bar{q}$ mesons in [14]. Finding the meson wave functions in the spectral-integral form (or in the light-cone variables—see [13, 14] for details) opens the way for direct reconstruction of the quark–antiquark interactions. The spectral-integral representation of the Bethe–Salpeter equation gives us the possibility to find the interaction forces directly, provided the masses and wave functions of composite systems are known: this problem is discussed in Section 2 by using a simplified example of composite particles with spinless constituents.

For the reconstruction of $q\bar{q}$ forces, it is important for the light-quark $q\bar{q}$ states to lie on linear trajectories in the $(n, M^2)$ plane, where $n$ is the radial quantum number of the meson with mass $M$ [15]. In more detail, the $q\bar{q}$ states can be classified, within spectroscopic notation, as the $n^{2S+1}L_J$ levels, where $S$, $L$, and $J$ refer to the spin, orbital, and total momenta, respectively. The analysis of spectra in the mass region 1950–2400 MeV performed in [16] fixed more than thirty new mesons which belong to the meson groups with positive- and negative-charge parities $(C = +/-)$. Namely, for the $(C = +)$ states, one has

$$\begin{aligned}
{}^1S_0 q\bar{q} &\to \quad \pi \text{ mesons}, \ \eta \text{ mesons}, \ \eta' \text{ mesons}; \qquad (1)\\
{}^1D_2 q\bar{q} &\to \quad \pi_2 \text{ mesons}, \ \eta_2 \text{ mesons};\\
{}^3P_0 q\bar{q} &\to \quad a_0 \text{ mesons}, \ f_0 \text{ mesons};\\
{}^3P_2 q\bar{q} &\to \quad a_2 \text{ mesons}, \ f_2 \text{ mesons};\\
{}^3P_1 q\bar{q} &\to \quad a_1 \text{ mesons};\\
{}^3F_2 q\bar{q} &\to \quad a_2 \text{ mesons}, \ f_2 \text{ mesons};\\
{}^3F_3 q\bar{q} &\to \quad a_3 \text{ mesons};\\
{}^3F_4 q\bar{q} &\to \quad a_4 \text{ mesons}, \ f_4 \text{ mesons};
\end{aligned}$$

and for the $(C = -)$ states,

$$\begin{aligned}
{}^3S_1 q\bar{q} &\to \quad \rho \text{ mesons}, \ \omega \text{ mesons}, \ \phi \text{ mesons}; \qquad (2)\\
{}^3D_1 q\bar{q} &\to \quad \rho \text{ mesons};\\
{}^3D_3 q\bar{q} &\to \quad \rho_3 \text{ mesons};\\
{}^1P_1 q\bar{q} &\to \quad h_1 \text{ mesons}, \ b_1 \text{ mesons};\\
{}^1F_3 q\bar{q} &\to \quad b_3 \text{ mesons}.
\end{aligned}$$

The mesons measured in [16], as well as those accumulated in the compilation [17], being classified versus radial quantum number $n$, can be put, with sufficiently good accuracy, on linear trajectories in the $(n, M^2)$ plane:

$$M^2 = M_0^2 + \mu^2(n-1), \qquad n = 1, 2, 3, \ldots, \qquad (3)$$

with the universal slope $\mu^2 \simeq 1.3$ GeV$^2$ [15]. The linearity of trajectories, leading and daughter ones, was observed for the $(J, M^2)$ plane too [15].

The linearity of trajectories on the $(n, M^2)$ and $(J, M^2)$ planes is in good agreement with large-$r$ behavior of the confinement potential, $V(r) \sim \alpha r$; e.g., see [7], where the calculation of $q\bar{q}$ states from the groups (1) and (2) has been carried out.

At the same time, it is necessary to emphasize that, for the low-mass states, one can expect a violation of the trajectory linearity. For example, the $\pi$ meson is just an exception that is not surprising because of a particular role of the pion. The standard explanation is that the pion, being a low-mass particle, is determined by the instanton-induced forces (see [18, 19] and references therein), although one cannot exclude an alternative modeling of the short-range forces. The problem of short-range forces is stressed by systematics of scalar states: the $K$-matrix analysis of $\pi\pi$, $K\bar{K}$, $\eta\eta$, and $\eta\eta'$ spectra [20] tells us that the lightest scalar–isoscalar state belongs to the flavor octet, but in the model calculations [18, 19], the lightest state is close to the flavor singlet. We hope that a precise reconstruction of the $q\bar{q}$ forces can be facilitated by using the Bethe–Salpeter equation for the $q\bar{q}$ states in the spectral-integral form.

Thus, we focus our attention on the reconstruction of the $q\bar{q}$ interaction, on the basis of the following triad:

(1) the Bethe–Salpeter equation in the spectral-integral form,

(2) the linearity of trajectories on the $(n, M^2)$ and $(J, M^2)$ planes,

(3) the use of wave functions for low- and moderate-mass $q\bar{q}$ states found in the study of meson radiative decays.

The important point is that radiative decays can give us information about meson wave functions which are now studied in the mass region 1000–1800 MeV: just the mesons from this region are determined by short-$r$ and intermediate-$r$ forces, and only the forces from this $r$ region are not known sufficiently well, thus being a subject of discussions and hypotheses.

The paper is organized as follows. In Section 2, we recall basic statements of the Bethe–Salpeter equation written in terms of the standard Feynman diagram technique, give the elements of the dispersion-relation $N/D$ method, and clarify the interplay of these two methods by using separable vertices. The spectral-integral representation of the

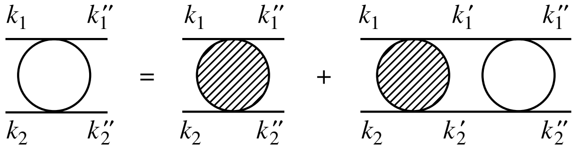

**Fig. 1.** Nonhomogeneous Bethe–Salpeter equation for the scattering amplitude; dashed block is the interaction kernel.

Bethe–Salpeter equation is also written for the case of scalar constituents.

In Section 3, the $q\bar{q}$ system is considered: the Bethe–Salpeter equations are written for the light-quark mesons which belong to the following $(n, M^2)$-trajectories: $\pi_J$, $\eta_J$, $a_J$, $f_J$, $\rho_J$, $\omega_J$, $h_J$, and $b_J$.

In Appendices A, B, and C, the necessary auxiliary formulas are presented which were used for deriving the equations. In Appendix D, we collect equations which are rather cumbersome, these being the Bethe–Salpeter equations for $\omega$, $\phi$, $a_2$, and $f_2$ trajectories.

## 2. SCALAR CONSTITUENTS: DISPERSION-RELATION METHOD AND THE BETHE–SALPETER EQUATION FOR COMPOSITE PARTICLES

In this section, we compare the Bethe–Salpeter equation for composite particles written with the use of Feynman diagrams with the equation in terms of the dispersion relations with separable vertices. This comparison gives us a guide for the transformation of Bethe–Salpeter equation with separable vertices into the spectral-integral Bethe–Salpeter equation with arbitrary meson-exchange-type interaction.

To simplify the consideration, we deal here with scalar particles as constituents.

### *2.1. Bethe–Salpeter Equation in the Feynman Diagram Technique*

Written in terms of the Feynman diagrams, the nonhomogeneous Bethe–Salpeter equation in the momentum representation reads

$$A(k_1, k_2; k''_1, k''_2) = V(k_1, k_2; k''_1, k''_2) \tag{4}$$
$$+ \int \frac{d^4k'_1 d^4k'_2}{i(2\pi)^4} V(k_1, k_2; k'_1, k'_2)$$
$$\times \frac{\delta^4(k'_1 + k'{}_2 - P)}{(m^2 - k'^2_1 - i0)(m^2 - k'^2_2 - i0)}$$
$$\times A(k'_1, k'_2; k''_1 k''_2).$$

It is shown in Fig. 1 in diagram form, and one can see there the notation for particle momenta. In (4), the constituents obey the momentum-conservation constraint

$$k_1 + k_2 = k'_1 + k'_2 = k''_1 + k''_2 = P,$$

and $V(k_1, k_2; k'_1, k'_2)$ is the irreducible kernel, i.e., the block without two-particle intermediate states (dashed block in Fig. 1).

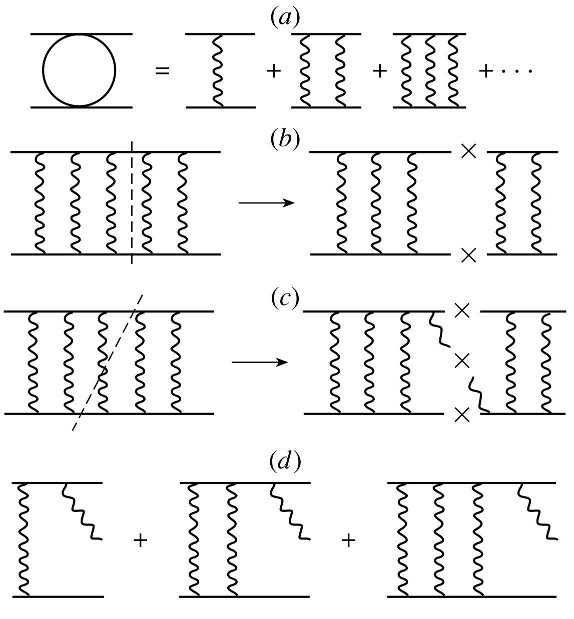

**Fig. 2.** ($a$) Presentation of the scattering amplitude as a set of ladder diagrams with the $t$-channel meson exchange interaction; ($b$, $c$) cuttings of the ladder diagrams; ($d$) meson production processes which are determined by ladder diagrams.

The scattering amplitude $A(k_1, k_2; k''_1, k''_2)$ determined by the Bethe–Salpeter Eq. (4) is the mass-off-shell amplitude. Even if we set $k^2_1 = k''^2_1 = k^2_2 = k''^2_2 = m^2$ on the left-hand side of Eq. (4), the right-hand side contains the amplitude $A(k'_1, k'_2; k''_1, k''_2)$ for $k'^2_1 \neq m^2, k'^2_2 \neq m^2$.

Let us draw the kernel $V$ as a meson-exchange diagram; then, by iterating Eq. (4), we represent $A(k_1, k_2; k''_1, k''_2)$ as an infinite set of ladder diagrams of Fig. 2$a$. For further investigation, it is important to fix intermediate states in the scattering amplitude. The ladder diagrams have two-particle intermediate states that can appear as real states at the c.m. energies squared $s = P^2 > 4m^2$, which corresponds to the cutting of ladder diagrams across the lines related to the constituents (see Fig. 2$b$).

Such a two-particle state manifests itself as a singularity of the scattering amplitude at $s = 4m^2$. However, the amplitude $A(k_1, k_2; k''_1, k''_2)$ considered as a function of $s$ has not only this singularity but also an infinite set of singularities which correspond to the ladder-diagram cuts across meson lines associated with the forces: an example of such a cutting is shown

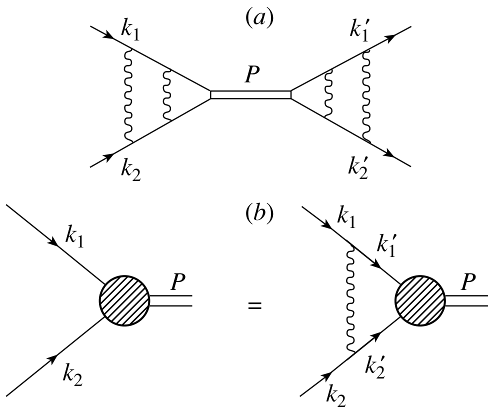

**Fig. 3.** (*a*) Scattering amplitude near the pole related to the bound state; (*b*) Bethe–Salpeter equation for the bound state.

in Fig. 2*c*. The diagrams which appear after the cutting procedure are the meson-production diagrams (e.g., see Fig. 2*d*).

Thus, in the complex $s$ plane, the amplitude $A(k_1, k_2; k_1'', k_2'')$ has the following singularity:

$$s = 4m^2, \tag{5}$$

which is related to the rescattering process. The other singularities are related to the meson production processes with cuts originating at

$$s = (2m + n\mu)^2, \qquad n = 1, 2, 3, \ldots. \tag{6}$$

The four-point amplitude depends on six variables as follows:

$$k_1^2, k_2^2, k_1''^2, k_2''^2, \tag{7}$$
$$s = (k_1 + k_2)^2 = (k_1'' + k_2'')^2,$$
$$t = (k_1 - k_1'')^2 = (k_2 - k_2'')^2.$$

The seventh variable $u = (k_1 - k_2'')^2 = (k_1'' - k_2)^2$ is not independent because of the relation

$$s + t + u = k_1^2 + k_2^2 + k_1''^2 + k_2''^2. \tag{8}$$

If the interaction creates a bound state, then the infinite set of ladder diagrams should produce the pole singularity in the amplitude. Near the pole, the scattering amplitude is determined by diagrams of the type in Fig. 3*a*, which means that, in graphical form, the equation for composite system reads as Fig. 3*b*. In terms of the Feynman integral, it is as follows:

$$A(k_1, k_2; P) = \int \frac{d^4k_1' d^4k_2'}{i(2\pi)^4} V(k_1, k_2; k_1', k_2') \tag{9}$$
$$\times \frac{\delta^4(k_1' + k_2' - P)}{(m^2 - k_1'^2 - i0)(m^2 - k_2'^2 - i0)} A(k_1', k_2'; P).$$

The homogeneous Bethe–Salpeter Eq. (9), like the nonhomogeneous one, works upon the mass-off-shell amplitudes; the multimeson production channels in (9) exist, and they are strongly related to the meson-exchange forces.

### *2.2. Scattering Amplitude in the Dispersion-Relation N/D Method*

Let us summarize analytic properties of the discussed scattering amplitudes for two spinless particles (with the mass $m$) which interact through the exchange of another spinless particle (with the mass $\mu$) (Fig. 2*a*). This amplitude, $A(s, t)$, has $s$- and $t$-channel singularities. In the $t$ plane, there are singularities at $t = \mu^2, 4\mu^2, 9\mu^2$, etc., which correspond to one- or multimeson exchanges. In the $s$ plane, the amplitude has a singularity at $s = 4m^2$ (elastic rescattering) and singularities at $s = (2m + n\mu)^2$, where $n = 1, 2, \ldots$, which corresponds to the production of $n$ mesons with the mass $\mu$. For the bound state with mass $M$, there exists a pole singularity at $s = M^2$. If the mass of this bound state $M > 2m$, this is a resonance, and the corresponding pole is located on the second sheet of the complex $s$ plane.

The dispersion-relation $N/D$ method deals with partial-wave amplitudes. The $s$-channel partial amplitudes depend on $s$ only. They have all the $s$-channel singularities of $A(s, t)$, namely, the right-hand-side singularities at $s = M^2$, $s = 4m^2$, $s = (2m + \mu)^2$, and so on (see Fig. 4).

Left-hand-side singularities of the partial amplitudes are related to the $t$-channel singularities of $A(s, t)$. The $S$-wave partial amplitude is equal to

$$A(s) = \int_{-1}^{1} \frac{dz}{2} A(s, t(z)), \tag{10}$$

where $t(z) = -2(s/4 - m^2)(1 - z)$ and $z = \cos\theta$. The left-hand singularities correspond to

$$t(z = -1) = (n\mu)^2, \tag{11}$$

and they are located at $s = 4m^2 - \mu^2$, $s = 4m^2 - 4\mu^2$, and so on.

The $N/D$ method provides us with the possibility to construct the relativistic two-particle scattering amplitude in the region of low and intermediate energies, where multiparticle production processes are not important; this region is shown in Fig. 4 by a dashed line. If the threshold singularity at $s = (2m + \mu)^2$ is not strong (one-meson production process is suppressed), the region of partial amplitude under consideration can be expanded up to the next threshold.

The unitarity condition for the partial-wave scattering amplitude (we consider the $S$-wave amplitude as an example) reads

$$\operatorname{Im} A(s) = \rho(s)|A(s)|^2. \tag{12}$$

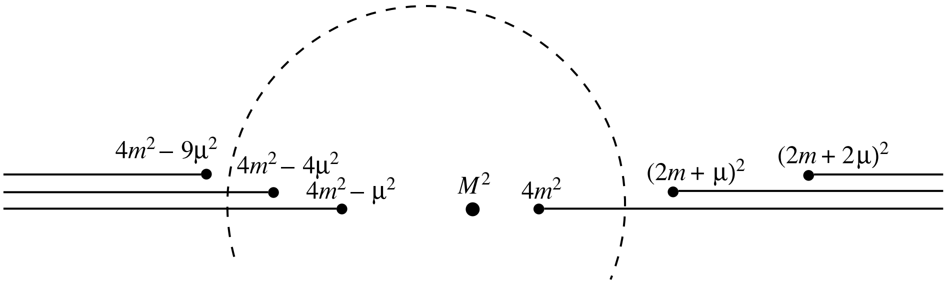

**Fig. 4.** The partial-wave amplitude singularities in the complex-$s$ plane.

Here, $\rho(s)$ is the two-particle phase space integrated at fixed $s$:

$$\rho(s) = \int d\Phi_2(P; k'_1, k'_2) = \frac{1}{16\pi}\sqrt{\frac{s-4m^2}{s}}, \quad (13)$$

$$d\Phi_2(P; k'_1, k'_2) = \frac{1}{2}(2\pi)^4\delta^4(P - k'_1 - k'_2) \times \frac{d^3k'_1}{(2\pi)^3 \cdot 2k'_{10}} \frac{d^3k'_2}{(2\pi)^3 \cdot 2k'_{20}}.$$

In the $N/D$ method, the amplitude $A(s)$ is represented as

$$A(s) = \frac{N(s)}{D(s)}, \quad (14)$$

where $N(s)$ has left-hand singularities only, whereas $D(s)$ has right-hand ones only. So the $N$ function is real in the physical region, $s > 4m^2$. The unitarity condition can be rewritten as follows:

$$\mathrm{Im}\, D(s) = -\rho(s)N(s). \quad (15)$$

The solution to this equation is

$$D(s) = 1 - \int\limits_{4m^2}^{\infty} \frac{ds'}{\pi}\frac{\rho(s')N(s')}{s'-s} \equiv 1 - B(s). \quad (16)$$

In Eq. (16), we suppose that CDD poles [21] are absent and we normalize $N(s)$ by the condition $D(s) \to 1$ as $s \to \infty$.

In principle, Eqs. (14), (16) provide us with a complete description of partial amplitude in the low-$s$ region: the amplitude is determined by the $N$ function being a set of left-hand singularities which are due to one-meson exchange ($s = 4m^2 - \mu^2$), two-meson exchange ($s = 4m^2 - 4\mu^2$), and so on. The right-hand singularities in Eqs. (14), (16) are uncoupled to the left-hand ones, opposite to the Feynman diagram approach given by (4). It is important for the description of realistic processes to have the left-hand and right-hand singularities uncoupled: a well-known example provides us with the $pn$ amplitude, with the deuteron quantum numbers, where the production of pions is suppressed (right-hand singularity at $s = (2m + \mu_\pi)^2$ is weak), while the forces related to the pion exchange are significant (left-hand singularity at $s = 4m^2 - \mu_\pi^2$ is strong).

### 2.3. N/D Method and Separable Interaction

The $N/D$ method gives us the mass-on-shell partial amplitude, provided the $N$ function is known. However, the $N$ functions have rather intricate properties: they depend on the total number of $t$- and $u$-channel exchanges and do not obey the factorization constraints; i.e., for different reactions, the $N$ functions may be independently different. As was stressed above, the spectral-integral representation for the Bethe–Salpeter equation, keeping the advantages of the dispersion-relation method, is free from this problem: it uses $t$- and $u$-channel exchanges, with universal interaction blocks.

As the first step in rewriting the Bethe–Salpeter equation in the spectral-integral form, let us consider separable interaction as an example. For this purpose, we rewrite Eqs. (14), (16) introducing the vertex function

$$g(s) = \sqrt{N(s)}. \quad (17)$$

Here, we assume that $N(s)$ is positive (the cases with negative $N(s)$ or with changing-sign $N(s)$ need the introduction of several vertices). Thus, the partial wave amplitude $A(s)$ written in terms of the separable vertex $g(s)$ is given by the following series:

$$A(s) = g(s)[1 + B(s) + B^2(s) + B^3(s) + \cdots]g(s). \quad (18)$$

Its graphical interpretation is shown by Fig. 5.

This set of diagrams can be rewritten in the form of the Bethe–Salpeter equation:

$$A(s) = g^2(s) + g(s)\int\limits_{4m^2}^{\infty} \frac{ds'}{\pi} g(s')\frac{\rho(s')}{s'-s}A(s', s), \quad (19)$$

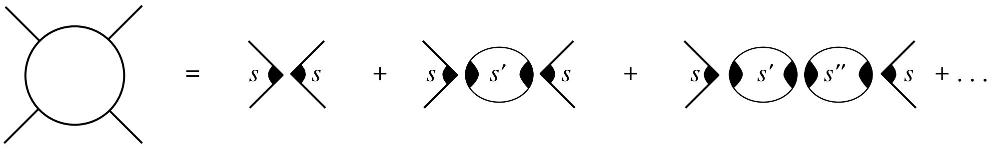

**Fig. 5.** Scattering amplitude in the dispersion-relation approach as a set of loop diagrams with separable vertices; there is no energy conservation in the intermediate states, $s \neq s' \neq s''$, and so on.

where $A(s', s)$ is the energy-off-shell amplitude which enters the intermediate state of the diagrams of Fig. 5; one has for the energy-on-shell amplitude $A(s, s) = A(s)$. The interaction block is written as follows:

$$V(s', s) = g(s')g(s). \tag{20}$$

Therefore, the Bethe–Salpeter equation is to be applied for the amplitude $A(s', s)$; it reads

$$A(s', s) = g(s')g(s) + g(s') \times \int\limits_{4m^2}^{\infty} \frac{ds''}{\pi} g(s'') \frac{\rho(s'')}{s'' - s} A(s'', s). \tag{21}$$

If the bound state exists, the amplitude contains a pole singularity at $s = M^2$. Considering Eq. (21) near the pole and neglecting the nonpole terms, we have the following equation for the bound state vertex:

$$G(s', M^2) = g(s') \times \int\limits_{4m^2}^{\infty} \frac{ds''}{\pi} g(s'') \frac{\rho(s'')}{s'' - M^2} G(s'', M^2), \tag{22}$$

where

$$G(s', M^2) = \left[\frac{A(s', s)(M^2 - s)}{G(s)}\right]_{s \to M^2}. \tag{23}$$

The Bethe–Salpeter equation (22) gives us a guide for the consideration of the general case, when the interaction is of the meson-exchange type. But beforehand, we need to consider in more detail the representation of the loop diagram.

### *2.4. Loop Diagram*

The loop diagram $B(s)$ plays the decisive role for the two-meson amplitude, so let us compare in detail the dispersion and Feynman integral expressions for $B(s)$.

Namely, the Feynman expression for $B_{\mathrm{F}}(s)$, with a special choice of separable interaction $G(4k_\perp^2 + 4m^2)$, is proven to be equal to the dispersion integral representation, where the four-vector $k_\perp$ is defined as follows:

$$2k_\perp = k_1 - k_2 - \frac{k_1^2 - k_2^2}{P^2}(k_1 + k_2). \tag{24}$$

In this section, we use the total-momentum vector $P = k_1 + k_2$, so it is convenient to write here $P^2$ but not $s$.

The Feynman expression for the loop diagram reads

$$B_{\mathrm{F}}(P^2) = \frac{1}{(2\pi)^4 i} \times \int \frac{d^4k_2 G^2(4(Pk_2)^2/P^2 - 4k_2^2 + 4m^2)}{(m^2 - k_2^2 - i0)(m^2 - (P - k_2)^2 - i0)}. \tag{25}$$

Since it is more convenient to treat a composite system with light-cone variables, they are hereafter

$$k_- = \frac{1}{\sqrt{2}}(k_{20} - k_{2z}); \tag{26}$$

$$k_+ = \frac{1}{\sqrt{2}}(k_{20} + k_{2z}); \qquad \mathbf{k}_{2\perp} = \mathbf{k}_T.$$

We choose the reference frame where $P_T = 0$. Then,

$$Pk_2 = P_+k_- + P_-k_+, \tag{27}$$

and Eq. (25) takes the form

$$B_{\mathrm{F}}(P^2) = \frac{1}{(2\pi)^4 i} \int \frac{dk_+ dk_- d^2k_T}{(2k_+k_- - m_T^2 + i0)(P^2 - 2(P_+k_- + P_-k_+) + 2k_+k_- - m_T^2 + i0)}, \tag{28}$$

where $m_T^2 = m^2 + k_T^2$. It should be mentioned that, if $G \equiv 1$, we can perform the integration over $k_-$ right now, closing the integration contour around the pole

$$k_- = \frac{m_T^2 - i0}{2k_+}, \tag{29}$$

and we obtain the standard dispersion representation for the Feynman loop graph ($x = k_+/P_+$):

$$\frac{1}{(2\pi)^4 i}\int d^2k_T \int\limits_0^1 dx \frac{-2\pi i}{2x(P^2 - m_T^2/x - P^2x + i0)}$$
$$= \int \frac{ds}{\pi(s - P^2 - i0)} \int \frac{dx dk_T^2}{x(1-x)} \qquad (30)$$
$$\times \frac{\delta(s - m_T^2/[x(1-x)])}{16\pi} = \int\limits_{4m^2}^{\infty} \frac{ds\rho(s)}{\pi(s - P^2 - i0)}.$$

The dispersion integral (30) is divergent at $s \to \infty$ due to $G = 1$, and it is the function $G$ which makes $B_{\mathrm{F}}$ convergent in Eq. (25). Convergence of the integral (30) can be restored by the subtraction procedure.

For $G \neq 1$, some additional steps are needed to obtain the dispersion representation; namely, we introduce new variables $\xi_+$ and $\xi_-$:

$$P_+k_- + P_-k_+ = \sqrt{P^2}\xi_+, \qquad (31)$$
$$P_+k_- - P_-k_+ = \sqrt{P^2}\xi_-.$$

With these variables, Eq. (25) takes the form

$$B_{\mathrm{F}}(P^2) = \frac{1}{(2\pi)^4 i}\int \frac{G^2(4(\xi_-^2 + m_T^2))d\xi_+ d\xi_- d^2k_T}{(\xi_+^2 - \xi_-^2 - m_T^2 + i0)(P^2 - 2\sqrt{P^2}\xi_+ + \xi_+^2 - \xi_-^2 - m_T^2 + i0)} \qquad (32)$$
$$= \int dk_T^2 \int\limits_0^{\infty} 2d\xi_- \pi G^2(4(\xi_-^2 + m_T^2)) \int\limits_{-\infty}^{\infty} \frac{d\xi_+}{[\xi_+^2 - (\xi_-^2 + m_T^2) + i0][(\xi_+ - \sqrt{P^2})^2 - (\xi_-^2 + m_T^2) + i0]}.$$

The integration over $\xi_+$ is performed by closing the integration contour in the upper half-plane, so the two poles, $\xi_+ = -\sqrt{\xi_-^2 + m_T^2} + i0$ and $\xi_+ = \sqrt{P^2} - \sqrt{\xi_-^2 + m_T^2} + i0$, contribute. The introduction of a new variable $s = 4(\xi_-^2 + m_T^2)$ yields

$$B_{\mathrm{F}}(P^2) = \int\limits_{4m^2}^{\infty} \frac{dsG^2(s)}{\pi(s - P^2)} \frac{1}{16\pi}\sqrt{1 - \frac{4m^2}{s}}, \qquad (33)$$

which is the dispersion representation of Eq. (16).

Thus, the hypothesis of separable interaction gives us an opportunity to solve the Bethe–Salpeter equation easily. Within this hypothesis, we can use different techniques: either Feynman integration, or spectral-integral representation, or light-cone variables.

### *2.5. Spectral-Integral Representation and Interaction Forces*

The introduction of a separable interaction is not the only way to make the Bethe–Salpeter equation easily solvable. The main point in handling the Bethe–Salpeter equation is to control the right-hand-side singularities, especially those related to multimeson production, at $s = (2m + \mu)^2$, $s = (2m + 2\mu)^2, \ldots$, and it is the spectral-integration technique which enables us to control the multimeson production processes.

The spectral integral representation is based on the following cornerstones: (i) constituent particles in the intermediate states are mass-on-shell ($k_1'^2 = m^2$ and $k_2'^2 = m^2$ in Fig. 1); (ii) there is no energy conservation in the interaction processes ($s \neq s' \neq s''$ in Fig. 5).

Based on these statements, we consider potential interaction, or the particle-exchange interaction, by using the spectral-integral diagrams. Consider as an example the interaction associated with the $t$-channel exchange of a meson with the mass $\mu$:

$$V(k_1, k_1') = \frac{g^2}{\mu^2 - t}, \quad t = (k_1 - k_1')^2. \qquad (34)$$

In the c.m. system, which is the most convenient for our consideration, we have for the four-momenta of the constituent particles

$$k_1 = (k_0, \mathbf{k}) = \left(\frac{\sqrt{s}}{2}, \mathbf{n}\sqrt{\frac{s}{4} - m^2}\right), \qquad (35)$$
$$k_1' = (k_0', \mathbf{k}') = \left(\frac{\sqrt{s'}}{2}, \mathbf{n}'\sqrt{\frac{s'}{4} - m^2}\right),$$

where $\mathbf{n}^2 = \mathbf{n}'^2 = 1$. The interaction block $V(k_1, k_1')$ can be expanded in a series with respect to $z = (\mathbf{n} \cdot \mathbf{n}')$. In this way, we can obtain the interaction for different partial waves. For example, the interaction in the wave with the angular momentum $L = 0$ is equal to

$$V_0(s,s') = \int\limits_{-1}^{1} \frac{dz}{2} V(k_1, k_1'). \qquad (36)$$

Actually, Eqs. (34)–(36) allow us to generalize the procedure with the separable interaction considered above. Indeed, expanding (36) in a series with respect to orthogonal functions, one has

$$V_0(s,s') = \sum_n g_n(s) g_n(s'), \qquad (37)$$

which is a separable interaction in a generalized form, assuming the choice of functions allows one to use a restricted number of terms in (37). Separable interaction taken in such a form was used in [3, 4] for the description of nucleon–nucleon interactions by considering the deuteron within the dispersion-relation technique.

### *2.6. Spectral-Integral Representation of the Bethe–Salpeter Equation for Composite System*

First, we consider the case of $L = 0$ for scalar constituents with equal masses, though not identical. The bound system is treated as a composite system of these constituents. Furthermore, the case $L \neq 0$ is considered in detail.

**2.6.1. Bethe–Salpeter equation for vertex function with $L = 0$.** The equation for the vertex *composite system* → *constituents*, shown graphically in Fig. 3*b*, reads

$$G(s) = \int\limits_{4m^2}^{\infty} \frac{ds'}{\pi} \int d\Phi_2(P'; k_1', k_2') \qquad (38)$$

$$\times V(k_1, k_2; k_1', k_2') \frac{G(s')}{s' - M^2 - i0},$$

where the phase space is determined by Eq. (13). Scalar constituents are supposed to be not identical, so we do not write an additional identity factor 1/2 in the phase space.

Equation (38) written in the spectral-representation form deals with the energy off-shell states $s' = (k_1' + k_2')^2 \neq M^2$, $s = (k_1 + k_2)^2 \neq M^2$, and $s \neq s'$; the constituents are mass-on-shell, $k_1'^2 = m^2$ and $k_2'^2 = m^2$. We can use the alternative expression for the phase space

$$d\Phi_2(P'; k_1', k_2') = \rho(s') \frac{dz}{2} \equiv d\Phi(k'), \qquad (39)$$

$$z = \frac{(kk')}{\sqrt{k^2}\sqrt{k'^2}},$$

where $k = (k_1 - k_2)/2$ and $k' = (k_1' - k_2')/2$. Then,

$$G(s) = \int\limits_{4m^2}^{\infty} \frac{ds'}{\pi} \int d\Phi(k') \qquad (40)$$

$$\times V(s, s', (kk')) \frac{G(s')}{s' - M^2 - i0}.$$

In the c.m. system, $(kk') = -\mathbf{k} \cdot \mathbf{k}'$ and $\sqrt{k^2} = \sqrt{-\mathbf{k}^2} = i|\mathbf{k}|$ and $\sqrt{k'^2} = \sqrt{-\mathbf{k}'^2} = i|\mathbf{k}'|$, so $z = \mathbf{k} \cdot \mathbf{k}'/(|\mathbf{k}||\mathbf{k}'|)$. The phase space and spectral integrations can be written as follows:

$$\int\limits_{4m^2}^{\infty} \frac{ds'}{\pi} \int d\Phi_2(P'; k_1', k_2') = \int \frac{d\mathbf{k}'}{(2\pi)^3 k_0'}, \qquad (41)$$

where $k_0' = \sqrt{m^2 + \mathbf{k}'^2}$. In the c.m. system, Eq. (38) reads

$$G(s) = \int \frac{d\mathbf{k}'}{(2\pi)^3 k_0'} V(s, s', -(\mathbf{k} \cdot \mathbf{k}')) \frac{G(s')}{s' - M^2 - i0}. \qquad (42)$$

**2.6.2. Bethe–Salpeter equation for the ($L = 0$) wave function.** Now consider the wave function of the composite system,

$$\psi(s) = \frac{G(s)}{s - M^2}. \qquad (43)$$

To this end, the identity transformation on Eq. (40) should be done as follows:

$$(s - M^2) \frac{G(s)}{s - M^2} \qquad (44)$$

$$= \int\limits_{4m^2}^{\infty} \frac{ds'}{\pi} \int d\Phi(k') V(s, s', (kk')) \frac{G(s')}{s' - M^2}.$$

Using wave functions, Eq. (44) can be written as follows:

$$(s - M^2)\psi(s) \qquad (45)$$

$$= \int\limits_{4m^2}^{\infty} \frac{ds'}{\pi} \int d\Phi_2(k') V(s, s', (kk')) \psi(s').$$

Finally, using $\mathbf{k}'^2$ and $\mathbf{k}^2$ instead of $s'$ and $s$, $\psi(s) \to \psi(\mathbf{k}^2)$, we have

$$(4\mathbf{k}^2 + 4m^2 - M^2)\psi(\mathbf{k}^2) \qquad (46)$$

$$= \int \frac{d\mathbf{k}'}{(2\pi)^3 k_0'} V(s, s', -\mathbf{k} \cdot \mathbf{k}') \psi(\mathbf{k}'^2).$$

This is a basic equation for the set of states with $L = 0$. The set is formed by levels with different radial excitations $n = 1, 2, 3, \ldots$, and relevant wave functions are as follows: $\psi_1(\mathbf{k}^2)$, $\psi_2(\mathbf{k}^2)$, $\psi_3(\mathbf{k}^2)$, ….

The wave functions are normalized and orthogonal to each other. The normalization/orthogonality condition reads

$$\int \frac{d\mathbf{k}}{(2\pi)^3 k_0}\psi_n(\mathbf{k}^2)\psi_{n'}(\mathbf{k}^2) = \delta_{nn'}. \tag{47}$$

Here, $\delta_{nn'}$ is the Kronecker symbol. Equation (47) is due to the consideration of the charge form factors of composite systems with the gauge-invariance requirement imposed (see [13] for details). This normalization/orthogonality condition looks as in quantum mechanics.

Therefore, the Bethe–Salpeter equation for the $S$-wave mesons reads

$$4(\mathbf{k}^2 + m^2)\psi_n(\mathbf{k}^2) \tag{48}$$

$$-\int\limits_0^\infty \frac{d\mathbf{k}'^2}{\pi} V_0(\mathbf{k}^2, \mathbf{k}'^2)\phi(\mathbf{k}'^2)\psi_n(\mathbf{k}'^2) = M_n^2\psi_n(\mathbf{k}^2),$$

where

$$\phi(\mathbf{k}'^2) = \frac{1}{4\pi}\frac{|\mathbf{k}'|}{k_0'}. \tag{49}$$

The $\psi_n(\mathbf{k}^2)$ presents a full set of wave functions which are orthogonal and normalized:

$$\int\limits_0^\infty \frac{d\mathbf{k}^2}{\pi}\psi_a(\mathbf{k}^2)\phi(\mathbf{k}^2)\psi_b(\mathbf{k}^2) = \delta_{ab}. \tag{50}$$

The function $V_0(\mathbf{k}^2, \mathbf{k}'^2)$ is the projection of potential $V(s, s', (kk'))$ on the $S$ wave:

$$V_0(\mathbf{k}^2, \mathbf{k}'^2) = \int \frac{d\Omega_{\mathbf{k}}}{4\pi}\int \frac{d\Omega_{\mathbf{k}'}}{4\pi} V(s, s', -\mathbf{k}\cdot\mathbf{k}'). \tag{51}$$

Let us expand $V_0(\mathbf{k}^2, \mathbf{k}'^2)$ with respect to a full set of wave functions:

$$V_0(\mathbf{k}^2, \mathbf{k}'^2) = \sum_{a,b}\psi_a(\mathbf{k}^2)v_{ab}^{(0)}\psi_b(\mathbf{k}'^2), \tag{52}$$

where numerical coefficients $v_{ab}^{(0)}$ are defined by the inverse transformation as follows:

$$v_{ab}^{(0)} = \int\limits_0^\infty \frac{d\mathbf{k}^2}{\pi}\frac{d\mathbf{k}'^2}{\pi}\psi_a(\mathbf{k}^2)\phi(\mathbf{k}^2) \tag{53}$$

$$\times V_0(\mathbf{k}^2, \mathbf{k}'^2)\phi(\mathbf{k}'^2)\psi_b(\mathbf{k}'^2).$$

Taking account of series (52), Eq. (48) is rewritten as follows:

$$4(\mathbf{k}^2 + m^2)\psi_n(\mathbf{k}^2) - \sum_a \psi_a(\mathbf{k}^2)v_{an}^{(0)} \tag{54}$$

$$= M_n^2\psi_n(\mathbf{k}^2).$$

Such a transformation should be carried out on the kinetic-energy term; it is also expanded in a series with respect to a full set of wave functions:

$$4(\mathbf{k}^2 + m^2)\psi_n(\mathbf{k}^2) = \sum_a K_{na}\psi_a(\mathbf{k}^2), \tag{55}$$

where

$$K_{na} = \int\limits_0^\infty \frac{d\mathbf{k}^2}{\pi}\psi_a(\mathbf{k}^2)\phi(\mathbf{k}^2)4(\mathbf{k}^2 + m^2)\psi_n(\mathbf{k}^2). \tag{56}$$

Finally, the Bethe–Salpeter equation takes the form

$$\sum_a K_{na}\psi_a(\mathbf{k}^2) - \sum_a v_{na}^{(0)}\psi_a(\mathbf{k}^2) = M_n^2\psi_n(\mathbf{k}^2). \tag{57}$$

We take into account that $v_{na}^{(0)} = v_{an}^{(0)}$.

Equation (57) is a standard homogeneous equation:

$$\sum_a s_{na}\psi_a(\mathbf{k}^2) = M_n^2\psi_n(\mathbf{k}^2), \tag{58}$$

with $s_{na} = K_{na} - v_{na}^{(0)}$. The values $M^2$ are defined as zeros of the determinant

$$\det|\hat{s} - M^2 I| = 0, \tag{59}$$

where $I$ is the unity matrix.

**2.6.3. The Bethe–Salpeter equation for the states with arbitrary angular momentum *L*.** For the wave function with arbitrary angular momentum $\psi^{(L)}_{(n)\mu_1\ldots\mu_L}(s)$, we use the following ansatz:

$$\psi^{(L)}_{(n)\mu_1\ldots\mu_L}(s) = X^{(L)}_{\mu_1\ldots\mu_L}(k)\psi_n^{(L)}(s). \tag{60}$$

The momentum operator $X^{(L)}_{\mu_1\ldots\mu_L}(k)$ was introduced in [9]; we recall its features in Appendix A.

The Bethe–Salpeter equation for the $(L, n)$ state, presented in a form similar to (48), reads

$$4(\mathbf{k}^2 + m^2)X^{(L)}_{\mu_1\ldots\mu_L}(k)\psi_n^{(L)}(\mathbf{k}^2) - X^{(L)}_{\mu_1\ldots\mu_L}(k)$$

$$\times \int\limits_0^\infty \frac{d\mathbf{k}'^2}{\pi} V_L(s, s')X_L^2(k'^2)\phi(\mathbf{k}'^2)\psi_n^{(L)}(\mathbf{k}'^2) \tag{61}$$

$$= M_n^2 X^{(L)}_{\mu_1\ldots\mu_L}(k)\psi_n^{(L)}(\mathbf{k}^2),$$

where

$$X_L^2(k'^2) = \int \frac{d\Omega_{\mathbf{k}'}}{4\pi}(X^{(L)}_{\nu_1\ldots\nu_L}(k'))^2 \tag{62}$$

$$= \alpha(L)(k'^2)^L = \alpha(L)(-\mathbf{k}'^2)^L,$$

$$\alpha(L) = \frac{(2L-1)!!}{L!}, \quad \alpha(0) = 1. \tag{63}$$

The potential is expanded in a series with respect to the product of operators $X^{(L)}_{\mu_1\ldots\mu_L}(k)X^{(L)}_{\mu_1\ldots\mu_L}(k')$, that is,

$$V(s,s',(kk')) = \sum_{L,\mu_1\ldots\mu_L} X^{(L)}_{\mu_1\ldots\mu_L}(k) \qquad (64)$$
$$\times V_L(s,s')X^{(L)}_{\mu_1\ldots\mu_L}(k'),$$
$$X^2_L(k^2)V_L(s,s')X^2_L(k'^2)$$
$$= \int \frac{d\Omega_{\mathbf{k}}}{4\pi}\frac{d\Omega_{\mathbf{k}'}}{4\pi} X^{(L)}_{\nu_1\ldots\nu_L}(k)V(s,s',(kk'))$$
$$\times X^{(L)}_{\nu_1\ldots\nu_L}(k').$$

Therefore, formula (61) reads as follows:

$$4(\mathbf{k}^2+m^2)\psi^{(L)}_n(\mathbf{k}^2) \qquad (65)$$
$$-\int_0^\infty \frac{d\mathbf{k}'^2}{\pi}V_L(s,s')\alpha(L)(-\mathbf{k}'^2)^L\phi(\mathbf{k}'^2)\psi^{(L)}_n(\mathbf{k}'^2)$$
$$= M^2_n\psi^{(L)}_n(\mathbf{k}^2).$$

As compared to (48), this equation contains the additional factor $X^2_L(k'^2)$; still, the same factor is in the normalization condition, so it would be reasonable to insert it into the phase space. Finally, we have

$$4(\mathbf{k}^2+m^2)\psi^{(L)}_n(\mathbf{k}^2) \qquad (66)$$
$$-\int_0^\infty \frac{d\mathbf{k}'^2}{\pi}\widetilde{V}_L(s,s')\phi_L(\mathbf{k}'^2)\psi^{(L)}_n(\mathbf{k}'^2)$$
$$= M^2_n\psi^{(L)}_n(\mathbf{k}^2),$$

where

$$\phi_L(\mathbf{k}'^2) = \alpha(L)(\mathbf{k}'^2)^L\phi(\mathbf{k}'^2), \qquad (67)$$
$$\widetilde{V}_L(s,s') = (-1)^L V_L(s,s').$$

The normalization condition for a set of wave functions with orbital momentum $L$ reads

$$\int_0^\infty \frac{d\mathbf{k}^2}{\pi}\psi^{(L)}_a(\mathbf{k}^2)\phi_L(\mathbf{k}^2)\psi^{(L)}_b(\mathbf{k}^2) = \delta_{ab}. \qquad (68)$$

One can see that it is similar to the case of $L=0$, the only difference consisting in the redefinition of the phase space $\phi \to \phi_L$. The Bethe–Salpeter equation reads

$$\sum_a s^{(L)}_{na}\psi^{(L)}_a(\mathbf{k}^2) = M^2_{n,L}\psi^{(L)}_n(\mathbf{k}^2), \qquad (69)$$

with

$$s^{(L)}_{na} = K^{(L)}_{na} - v^{(L)}_{na}, \qquad (70)$$
$$v^{(L)}_{ab} = \int_0^\infty \frac{d\mathbf{k}^2}{\pi}\frac{d\mathbf{k}'^2}{\pi}\psi^{(L)}_a(\mathbf{k}^2)\phi_L(\mathbf{k}^2)$$
$$\times \widetilde{V}_L(s,s')\phi_L(\mathbf{k}'^2)\psi^{(L)}_b(\mathbf{k}'^2),$$
$$K^{(L)}_{na} = \int_0^\infty \frac{d\mathbf{k}^2}{\pi}\psi^{(L)}_a(\mathbf{k}^2)\phi_L(\mathbf{k})\cdot 4(\mathbf{k}^2+m^2)\psi^{(L)}_n(\mathbf{k}^2).$$

Using radial-excitation levels, one can reconstruct the potential in the $L$ wave and, then, reconstruct, with the help of (64), the $t$-dependent potential.

## 3. QUARK–ANTIQUARK COMPOSITE SYSTEMS

For the $q\bar{q}$ system, the Bethe–Salpeter equation for the wave function with the total momentum $J$, angular momentum $L = |\mathbf{J}-\mathbf{S}|$, and quark–antiquark spin $S$ can be conventionally written as follows:

$$(s-M^2)\widehat{\Psi}^{(S,L,J)}_{(n)\mu_1\cdots\mu_J}(k) \qquad (71)$$
$$= \int \frac{d^3k'}{(2\pi)^3k'_0}\widehat{V}(s,s',(kk'))\widehat{\Psi}^{(S,L,J)}_{(n)\mu_1\cdots\mu_J}(k'),$$

where

$$k = \frac{1}{2}(k_1-k_2), s = (k_1+k_2)^2, \qquad (72)$$
$$k' = \frac{1}{2}(k'_1-k'_2), s' = (k'_1+k'_2)^2.$$

The wave-function operator with fixed quantum numbers is presented as

$$\widehat{\Psi}^{(S,L,J)}_{(n)\mu_1\cdots\mu_J}(k) = \widehat{Q}^{(S,L,J)}_{\mu_1\cdots\mu_J}(k)\psi^{(S,L,J)}_n(k^2), \qquad (73)$$

where $\widehat{Q}$ is the moment operator for the $q\bar{q}$ system.

The potential operator can be decomposed as follows:

$$\widehat{V}(s,s',(kk')) = \sum_I V^{(0)}_I(s,s',(kk'))\widehat{O}_I \otimes \widehat{O}_I, \qquad (74)$$

where $I = S, V, T, A, P$ is a full set of Dirac matrices in the $t$ channel,

$$\widehat{O}_I = I,\ \gamma_\mu,\ i\sigma_{\mu\nu},\ i\gamma_\mu\gamma_5,\ \gamma_5. \qquad (75)$$

The potential operator $\widehat{V}(s,s',(kk'))$ can be decomposed in the $s$ channel by using the Fierz transformation:

$$\widehat{V}(s,s',(kk')) \qquad (76)$$
$$= \sum_I\sum_c \widehat{V}^{(0)}_I(s,s',(kk'))C_{Ic}(\widehat{O}_c\otimes\widehat{O}_c),$$

where $C_{Ic}$ are coefficients of the Fierz matrix:

$$C = \begin{pmatrix} \frac{1}{4} & \frac{1}{4} & \frac{1}{8} & \frac{1}{4} & \frac{1}{4} \\ 1 & -\frac{1}{2} & 0 & \frac{1}{2} & -1 \\ 3 & 0 & -\frac{1}{2} & 0 & 3 \\ 1 & \frac{1}{2} & 0 & -\frac{1}{2} & -1 \\ \frac{1}{4} & -\frac{1}{4} & \frac{1}{8} & -\frac{1}{4} & \frac{1}{4} \end{pmatrix}. \tag{77}$$

Denoting

$$V_c(s,s',(kk')) = \sum_I \widehat{V}_I^{(0)}(s,s',(kk'))C_{Ic}, \tag{78}$$

we have

$$\begin{aligned} &\widehat{V}(s,s',(kk')) \\ &= \sum_c (\widehat{O}_c \otimes \widehat{O}_c) V_c(s,s',(kk')) = (I \otimes I) \\ &\times V_S(s,s',(kk')) + (\gamma_\mu \otimes \gamma_\mu) V_V(s,s',(kk')) \\ &+ (i\sigma_{\mu\nu} \otimes i\sigma_{\mu\nu}) V_T(s,s',(kk')) \\ &+ (i\gamma_\mu\gamma_5 \otimes i\gamma_\mu\gamma_5) V_A(s,s',(kk')) \\ &+ (\gamma_5 \otimes \gamma_5) V_P(s,s',(kk')). \end{aligned} \tag{79}$$

Let us multiply Eq. (71) by the operator $\widehat{Q}^{(S,L,J)}_{\mu_1\ldots\mu_J}(k)$ and convolute over the spin-momentum indices. After the redefinition $\widehat{V}(s,s',(kk')) \to (\hat{k}'_1 + m')\widehat{V}(s,s',(kk'))(-\hat{k}'_2 + m')$, one has

$$\begin{aligned} &(s - M^2)\mathrm{tr}\left[\widehat{\Psi}^{(S,L,J)}_{(n)\mu_1\ldots\mu_J}(k)(\widehat{k}_1 + m) \right. \\ &\left. \times \widehat{Q}^{(S,L,J)}_{\mu_1\ldots\mu_J}(k)(-\widehat{k}_2 + m)\right] \\ &= \sum_c \mathrm{tr}\left[\widehat{O}_c(\widehat{k}_1 + m)\widehat{Q}^{(S,L,J)}_{\mu_1\ldots\mu_J}(k)(-\widehat{k}_2 + m)\right] \\ &\times \int \frac{d^3k'}{(2\pi)^3 k'_0} V_c(s,s',(kk'))\mathrm{tr}\left[(\widehat{k}'_1 + m') \right. \\ &\left. \times \widehat{O}_c(-\widehat{k}'_2 + m')\widehat{\Psi}^{(S,L,J)}_{(n)\mu_1\ldots\mu_J}(k')\right]. \end{aligned} \tag{80}$$

Here, we define $m'$ as ${k'_1}^2 = {k'_2}^2 = m'^2$. We have four states with the $q\bar{q}$ spins $S = 0$ and $S = 1$:

(i) $S = 0$, $L = J$,

(ii) $S = 1$, $L = J + 1, J, J - 1$.

These states are constructed from the operators [9] as follows:

$$\widehat{Q}^{(0,J,J)}_{\mu_1\ldots\mu_J}(k) = i\gamma_5 X^{(J)}_{\mu_1\ldots\mu_J}(k), \tag{81}$$

$$\widehat{Q}^{(1,J+1,J)}_{\mu_1\ldots\mu_J}(k) = \gamma^\perp_\alpha X^{(J+1)}_{\mu_1\ldots\mu_J\alpha}(k), \tag{82}$$

$$\widehat{Q}^{(1,J,J)}_{\mu_1\ldots\mu_J}(k) = \varepsilon_{\alpha\nu_1\nu_2\nu_3}\gamma^\perp_\alpha P_{\nu_1} Z^{(J)}_{\nu_2\mu_1\ldots\mu_J,\nu_3}(k), \tag{83}$$

$$\widehat{Q}^{(1,J-1,J)}_{\mu_1\ldots\mu_J}(k) = \gamma^\perp_\alpha Z^{(J-1)}_{\mu_1\ldots\mu_J,\alpha}(k). \tag{84}$$

For these operators, the wave functions read

for $J = L + 1$,

$$\widehat{\Psi}^{(1,J-1,J)}_{(n)\mu_1\ldots\mu_J}(k) = \widehat{Q}^{(1,J-1,J)}_{\mu_1\ldots\mu_J}(k)\psi_n^{(1,J-1,J)}(k^2); \tag{85}$$

for $J = L - 1$,

$$\widehat{\Psi}^{(1,J+1,J)}_{(n)\mu_1\ldots\mu_J}(k) = \widehat{Q}^{(1,J+1,J)}_{\mu_1\ldots\mu_J}(k)\psi_n^{(1,J+1,J)}(k^2); \tag{86}$$

for $S = 1$, $L = J \pm 1$, $J$,

$$\begin{aligned} \widehat{\Psi}^{(1,(J\pm1),J)}_{(n)\mu_1\ldots\mu_J}(k) &= A_j\widehat{\Psi}^{(1,J-1,J)}_{(n)\mu_1\ldots\mu_J}(k) \\ &+ B_j\widehat{\Psi}^{(1,J+1,J)}_{(n)\mu_1\ldots\mu_J}(k), \end{aligned} \tag{87}$$

where $A_j$ and $B_j$ are the mixing coefficients with $j = 1, 2$.

These wave functions are normalized as follows:

$$\begin{aligned} &\int \frac{d^3k}{(2\pi)^3 k_0}(-1) \\ &\times \mathrm{tr}\left[\widehat{\Psi}^{(S',L'_{j'},J')}_{(n')\mu_1\ldots\mu_J}(k)(\widehat{k}_1 + m) \right. \\ &\left. \times \widehat{\Psi}^{(S,L_j,J)}_{(n)\mu_1\ldots\mu_J}(k)(-\widehat{k}_2 + m)\right] \\ &= (-1)^J \delta_{S',S}\delta_{L'_{j'},L_j}\delta_{J',J}\delta_{n',n}. \end{aligned} \tag{88}$$

### 3.1. *Equation for (S = 0, J = L) State*

The equation for the state with $S = 0$, $J = L$ reads

$$\begin{aligned} &(s - M^2)X^{(J)}_{\mu_1\ldots\mu_J}(k) \\ &\times \mathrm{tr}\left[i\gamma_5(\widehat{k}_1 + m)i\gamma_5(-\widehat{k}_2 + m)\right] X^{(J)}_{\mu_1\ldots\mu_J}(k) \\ &\times \psi_n^{(0,J,J)}(k^2) = X^{(J)}_{\mu_1\ldots\mu_J}(k) \\ &\times \sum_c \mathrm{tr}\left[\widehat{F}_c(\widehat{k}_1 + m)i\gamma_5(-\widehat{k}_2 + m)\right] \\ &\times \int \frac{d^3k'}{(2\pi)^3 k'_0} V_c(s,s',(kk'))\mathrm{tr}\left[i\gamma_5(\widehat{k}'_1 + m') \right. \\ &\left. \times \widehat{F}_c(-\widehat{k}'_2 + m')\right] X^{(J)}_{\mu_1\ldots\mu_J}(k')\psi_n^{(0,J,J)}(k'^2). \end{aligned} \tag{89}$$

Now consider the left-hand side of Eq. (89). Using the traces presented in Appendix B and convolution of operators from Appendix C, we have

$$\begin{aligned} &X^{(J)}_{\mu_1\ldots\mu_J}(k) \\ &\times \mathrm{tr}\left[i\gamma_5(\widehat{k}_1 + m)i\gamma_5(-\widehat{k}_2 + m)\right] X^{(J)}_{\mu_1\ldots\mu_J}(k) \\ &= X^{(J)}_{\mu_1\ldots\mu_J}(k)(-2s)X^{(J)}_{\mu_1\ldots\mu_J}(k) = -2s\alpha(J)k^{2J}. \end{aligned}$$

The right-hand side of the equation is calculated in two steps: first, we summarize with respect to $c$:

$$
\begin{aligned}
&A(s,s',(kk')) \qquad (90)\\
&= \sum_{c=T,A,P} A_c(s,s',(kk'))V_c(s,s',(kk'))\\
&= \sum_{c=T,A,P} \mathrm{tr}\left[\widehat{F}_c(\widehat{k}_1+m)i\gamma_5(-\widehat{k}_2+m)\right]\\
&\times \mathrm{tr}\left[i\gamma_5(\widehat{k}'_1+m')\widehat{F}_c(-\widehat{k}'_2+m')\right]V_c(s,s',(kk')).
\end{aligned}
$$

In Appendix B, the trace calculations are presented, and the values $A_c(s,s',(kk'))$ are given. In this way, the sum is written as follows:

$$
\begin{aligned}
&A(s,s',(kk')) \qquad (91)\\
&= \sum_{c=T,A,P} A_c(s,s',(kk'))V_c(s,s',(kk'))\\
&= -4\sqrt{ss'}\Big[\sqrt{ss'}V_P(s,s',(kk'))\\
&+ 4mm'V_A(s,s',(kk')) + 8(kk')V_T(s,s',(kk'))\Big].
\end{aligned}
$$

At the second step, the convolution of operators is performed by using equations of Appendix C and recurrent formulas for the Legendre polynomials

$$
zP_J(z) = \frac{J+1}{2J+1}P_{J+1}(z) + \frac{J}{2J+1}P_{J-1}(z),
$$

which allows us to write the Bethe–Salpeter equation in terms of the Legendre polynomials (recall that $z = (kk')/(\sqrt{k^2}\sqrt{k'^2})$ and $\sqrt{k^2} = i\sqrt{s/4-m^2}$, $\sqrt{k'^2} = i\sqrt{s'/4-m'^2}$). For the exceptional case $J=0$, we set $P_{-1}(z)=0$. As a result, we get

$$
\begin{aligned}
&X^{(J)}_{\mu_1\ldots\mu_J}(k)A(s,s',(kk'))X^{(J)}_{\mu_1\ldots\mu_J}(k') \qquad (92)\\
&= \alpha(J)\left(\sqrt{k^2}\sqrt{k'^2}\right)^J(-4\sqrt{ss'})\\
&\times\Big[8\frac{J+1}{2J+1}\sqrt{k^2}\sqrt{k'^2}P_{J+1}(z)V_T(s,s',(kk'))\\
&+ (\sqrt{ss'}V_P(s,s',(kk'))\\
&+ 4mm'V_A(s,s',(kk')))P_J(z)\\
&+ 8\frac{J}{2J+1}\sqrt{k^2}\sqrt{k'^2}P_{J-1}(z)V_T(s,s',(kk'))\Big].
\end{aligned}
$$

Substituting the obtained expressions into Eq. (89), we obtain

$$
\begin{aligned}
&(s-M^2)(-2s)\alpha(J)k^{2J}\psi_n^{(0,J,J)}(k^2) \qquad (93)\\
&= \int\frac{d^3k'}{(2\pi)^3k'_0}(-4\sqrt{ss'})\alpha(J)\left(\sqrt{k^2}\sqrt{k'^2}\right)^J\\
&\times\Big[8\frac{J+1}{2J+1}\sqrt{k^2}\sqrt{k'^2}P_{J+1}(z)V_T(s,s',(kk'))\\
&+ \Big(\sqrt{ss'}V_P(s,s',(kk'))\\
&+ 4mm'V_A(s,s',(kk'))\Big)P_J(z)\\
&+ 8\frac{J}{2J+1}\sqrt{k^2}\sqrt{k'^2}P_{J-1}(z)\\
&\times V_T(s,s',(kk'))\Big]\psi_n^{(0,J,J)}(k'^2).
\end{aligned}
$$

Expanding the interaction block in the Legendre polynomial series,

$$
\begin{aligned}
&V_c(s,s',(kk')) = \sum_J V_c^{(J)}(s,s')P_J(z) \qquad (94)\\
&= \sum_J \widetilde{V}_c^{(J)}(s,s')\alpha(J)\left(-\sqrt{k^2}\sqrt{k'^2}\right)^J P_J(z),
\end{aligned}
$$

and integrating over angle variables on the right-hand side by taking into account the standard normalization condition $\int_{-1}^{1}(dz/2)P_J^2(z) = 1/(2J+1)$, we have finally

$$
\begin{aligned}
&(s-M^2)\psi_n^{(0,J,J)}(s) \qquad (95)\\
&= \int\limits_{4m'^2}^{\infty}\frac{ds'}{\pi}\rho(s')(-k'^2)^J 2\sqrt{\frac{s'}{s}}\\
&\times\Big[-8\frac{J+1}{2J+1}\xi(J+1)k^2k'^2\widetilde{V}_T^{(J+1)}(s,s')\\
&+ \sqrt{ss'}\xi(J)\widetilde{V}_P^{(J)}(s,s') + 4mm'\xi(J)\widetilde{V}_A^{(J)}(s,s')\\
&- 8\frac{J}{2J+1}\xi(J-1)\widetilde{V}_T^{(J-1)}(s,s')\Big]\psi_n^{(0,J,J)}(s'),
\end{aligned}
$$

where

$$
\begin{aligned}
&\int\limits_{-1}^{1}\frac{dz}{2}P_J(z)V_c(s,s',(kk')) \qquad (96)\\
&= \int\limits_{-1}^{1}\frac{dz}{2}P_J(z)\sum_{J'}\widetilde{V}_c^{(J')}(s,s')P_{J'}(z)\alpha(J')\\
&\times\left(-\sqrt{k^2}\sqrt{k'^2}\right)^{J'} = \frac{\alpha(J)}{2J+1}\widetilde{V}_c^{(J)}(s,s')\\
&\times\left(-\sqrt{k^2}\sqrt{k'^2}\right)^J = \xi(J)\widetilde{V}_c^{(J)}(s,s')\\
&\times\left(-\sqrt{k^2}\sqrt{k'^2}\right)^J,
\end{aligned}
$$

$$
\xi(J) = \frac{\alpha(J)}{2J+1} = \frac{(2J-1)!!}{(2J+1)\cdot J!}.
$$

**3.1.1. Equation for the pion $(M^2, n)$ trajectory.** The pion states which belong to the pion

$(M^2, n)$ trajectory obey the following equation:

$$(s-M^2)\psi^{(0,0,0)}_{\pi,n}(s) = \int\limits_{4m^2}^{\infty} \frac{ds'}{\pi}\rho(s')\cdot 2\sqrt{\frac{s'}{s}} \times \Big[ -\frac{8}{3}k^2k'^2\widetilde{V}^{(1)}_T(s,s') + \sqrt{ss'}\widetilde{V}^{(0)}_P(s,s') + 4m^2\widetilde{V}^{(0)}_A(s,s')\Big]\psi^{(0,0,0)}_{\pi,n}(s'). \quad (97)$$

Recall that $n$ is the radial quantum number, and the following states with different $n$ are located on the discussed $(M^2, n)$ trajectory: $\pi(140)$ with $n=1$, $\pi(1300)$ with $n=2$, $\pi(1800)$ with $n=3$, $\pi(2070)$ with $n=4$, $\pi(2360)$ with $n=5$, and so on.

The wave functions of the states lying on the $(M^2, n)$ trajectory satisfy the orthogonality/normalization constraint

$$\int\limits_{4m^2}^{\infty} \frac{ds}{\pi}\rho(s)\cdot 2s\psi^{(0,0,0)}_{\pi,n'}(s)\psi^{(0,0,0)}_{\pi,n}(s) = \delta_{n',n}. \quad (98)$$

The factor $2s$ is due to summing over the spin variables of quarks.

Expanding the interaction block over the full set of radial wave functions, we can transform (97) into a system of linear equations of the type of Eq. (58).

**3.1.2. Equation for the $\eta$ $(M^2, n)$ trajectory.** The $\eta$ states have two components, $n\bar n = (u\bar u + d\bar d)/\sqrt{2}$ and $s\bar s$. We write $\eta_n = \cos\Theta_n n\bar n + \sin\Theta_n s\bar s$ and $\eta'_n = -\sin\Theta_n n\bar n + \cos\Theta_n s\bar s$. For the lightest mesons $\eta(550)$ and $\eta'(958)$, one has $\cos\Theta_1 = \simeq 0.8$ and $\sin\Theta_1 \simeq -0.6$.

Correspondingly, we have two equations for the wave functions which describe the $n\bar n$ and $s\bar s$ components:

$$(s-M^2)\psi^{(0,0,0)}_{\eta(n\bar n),n}(s)\cos\Theta_n \quad (99)$$
$$= \int\limits_{4m^2}^{\infty} \frac{ds'}{\pi}\rho(s')\cdot 2\sqrt{\frac{s'}{s}}\Big[ -\frac{8}{3}k^2k'^2\widetilde{V}^{(1)}_{(n\bar n\to n\bar n),T}(s,s') + \sqrt{ss'}\widetilde{V}^{(0)}_{(n\bar n\to n\bar n),P}(s,s') + 4m^2\widetilde{V}^{(0)}_{(n\bar n\to n\bar n),A}(s,s')\Big]\psi^{(0,0,0)}_{\eta(n\bar n),n}(s')\cos\Theta_n$$
$$+ \int\limits_{4m_s^2}^{\infty} \frac{ds'}{\pi}\rho_s(s')\cdot 2\sqrt{\frac{s'}{s}}\Big[ -\frac{8}{3}k^2k_s'^2\widetilde{V}^{(1)}_{(s\bar s\to n\bar n),T}(s,s') + \sqrt{ss'}\widetilde{V}^{(0)}_{(s\bar s\to n\bar n),P}(s,s') + 4mm_s\widetilde{V}^{(0)}_{(s\bar s\to n\bar n),A}(s,s')\Big]\psi^{(0,0,0)}_{\eta(s\bar s),n}(s')\sin\Theta_n,$$

where $\rho_s(s')$ refers to the $s\bar s$ phase space and $\sqrt{k_s'^2} = i\sqrt{s'/4 - m_s^2}$. The second equation, for the $s\bar s$ component, reads

$$(s-M^2)\psi^{(0,0,0)}_{\eta(s\bar s),n}(s)\sin\Theta_n \quad (100)$$
$$= \int\limits_{4m^2}^{\infty} \frac{ds'}{\pi}\rho(s')\cdot 2\sqrt{\frac{s'}{s}}\Big[ -\frac{8}{3}k_s^2k'^2\widetilde{V}^{(1)}_{(n\bar n\to s\bar s),T}(s,s') + \sqrt{ss'}\widetilde{V}^{(0)}_{(n\bar n\to s\bar s),P}(s,s') + 4mm_s\widetilde{V}^{(0)}_{(n\bar n\to s\bar s),A}(s,s')\Big]\psi^{(0,0,0)}_{\eta(n\bar n),n}(s')\cos\Theta_n$$
$$+ \int\limits_{4m_s^2}^{\infty} \frac{ds'}{\pi}\rho_s(s')\cdot 2\sqrt{\frac{s'}{s}}\Big[ -\frac{8}{3}k_s^2k_s'^2\widetilde{V}^{(1)}_{(s\bar s\to s\bar s),T}(s,s') + \sqrt{ss'}\widetilde{V}^{(0)}_{(s\bar s\to s\bar s),P}(s,s') + 4m_s^2\widetilde{V}^{(0)}_{(s\bar s\to s\bar s),A}(s,s')\Big]\psi^{(0,0,0)}_{\eta(s\bar s),n}(s')\sin\Theta_n.$$

The wave functions $\psi^{(0,0,0)}_{\eta(n\bar n),n}(s)$ and $\psi^{(0,0,0)}_{\eta(s\bar s),n}(s)$ satisfy the normalization condition within an obvious change of the integration region for the $s\bar s$ component: $4m^2 \to 4m_s^2$.

The following states are located on the $\eta$ and $\eta'$ $(M^2, n)$ trajectories:

(i) $\eta$ trajectory: $\eta(550)$ with $n=1$, $\eta(1295)$ with $n=2$, $\eta(1700)$ with $n=3$, $\eta(2010)$ with $n=4$, $\eta(2320)$ with $n=5$, and so on;

(ii) $\eta'$ trajectory: $\eta'(958)$ with $n=1$, $\eta(1440)$ with $n=2$, $\eta(1820)$ with $n=3$, and so on.

**3.1.3. Equation for the $b_1$ $(M^2, n)$ trajectory.** The equation for the states with $S=0$, $L=1$, $J=1$ reads

$$(s-M^2)\psi^{(0,1,1)}_{b_1,n}(s) \quad (101)$$
$$= -\int\limits_{4m^2}^{\infty} \frac{ds'}{\pi}\rho(s')k'^2\frac{2}{3}\sqrt{\frac{s'}{s}}\Big[ -\frac{24}{5}k^2k'^2\widetilde{V}^{(2)}_T(s,s') + \sqrt{ss'}\widetilde{V}^{(1)}_P(s,s') + 4m^2\widetilde{V}^{(1)}_A(s,s') - 8\widetilde{V}^{(0)}_T(s,s')\Big]\psi^{(0,1,1)}_{b_1,n}(s').$$

The following states are located on the $b_1$ $(M^2, n)$ trajectories: $b_1(1235)$ with $n=1$, $b_1(1640)$ at $n=2$, $b_1(1970)$ with $n=3$, $b_1(2210)$ with $n=4$, and so on.

The wave functions of the $b_1$ states lying on the $(M^2, n)$ trajectory satisfy the orthogonality/normalization constraint

$$\int\limits_{4m^2}^{\infty} \frac{ds}{\pi}\rho(s) \cdot 2sk^2\ \psi^{(0,1,1)}_{b_1,n'}(s)\psi^{(0,1,1)}_{b_1,n}(s) = \delta_{n',n}. \tag{102}$$

**3.1.4. Equation for the $h_1$ $(M^2, n)$ trajectory.** The $h_1$ states have two components, $n\bar n = (u\bar u + d\bar d)/\sqrt{2}$ and $s\bar s$; we write $h_{1,n} = \cos\Theta_n n\bar n + \sin\Theta_n s\bar s$. Correspondingly, we have two equations for the wave-function $n\bar n$ component:

$$\begin{aligned}
&(s - M^2)\psi^{(0,1,1)}_{h_1(n\bar n),n}(s)\cos\Theta_n \qquad (103)\\
&= -\int\limits_{4m^2}^{\infty} \frac{ds'}{\pi}\rho(s')k'^2\frac{2}{3}\sqrt{\frac{s'}{s}}\\
&\times\bigg[-\frac{24}{5}k^2k'^2\widetilde V^{(2)}_{(n\bar n\to n\bar n),T}(s,s')\\
&+\sqrt{ss'}\widetilde V^{(1)}_{(n\bar n\to n\bar n),P}(s,s') + 4m^2\widetilde V^{(1)}_{(n\bar n\to n\bar n),A}(s,s')\\
&-8\widetilde V^{(0)}_{(n\bar n\to n\bar n),T}(s,s')\bigg]\psi^{(0,1,1)}_{h_1(n\bar n),n}(s')\cos\Theta_n\\
&-\int\limits_{4m_s^2}^{\infty} \frac{ds'}{\pi}\rho_s(s')k_s'^2\frac{2}{3}\sqrt{\frac{s'}{s}}\\
&\times\bigg[-\frac{24}{5}k^2k_s'^2\widetilde V^{(2)}_{(s\bar s\to n\bar n),T}(s,s')\\
&+\sqrt{ss'}\widetilde V^{(1)}_{(s\bar s\to n\bar n),P}(s,s') + 4mm_s\widetilde V^{(1)}_{(s\bar s\to n\bar n),A}(s,s')\\
&-8\widetilde V^{(0)}_{(s\bar s\to n\bar n),T}(s,s')\bigg]\psi^{(0,1,1)}_{h_1(s\bar s),n}(s')\sin\Theta_n,
\end{aligned}$$

where $\rho_s(s')$ refers to the $s\bar s$ phase space and $\sqrt{k_s'^2} = i\sqrt{s'/4 - m_s^2}$. For the $s\bar s$ component, we have

$$\begin{aligned}
&(s - M^2)\psi^{(0,1,1)}_{h_1(s\bar s),n}(s)\sin\Theta_n \qquad (104)\\
&= -\int\limits_{4m^2}^{\infty} \frac{ds'}{\pi}\rho(s')k'^2\frac{2}{3}\sqrt{\frac{s'}{s}}\\
&\times\bigg[-\frac{24}{5}k_s^2k'^2\widetilde V^{(2)}_{(n\bar n\to s\bar s),T}(s,s')\\
&+\sqrt{ss'}\widetilde V^{(1)}_{(n\bar n\to s\bar s),P}(s,s') + 4mm_s\widetilde V^{(1)}_{(n\bar n\to s\bar s),A}(s,s')\\
&-8\widetilde V^{(0)}_{(n\bar n\to s\bar s),T}(s,s')\bigg]\psi^{(0,1,1)}_{h_1(n\bar n),n}(s')\cos\Theta_n\\
&-\int\limits_{4m_s^2}^{\infty} \frac{ds'}{\pi}\rho_s(s')k_s'^2\frac{2}{3}\sqrt{\frac{s'}{s}}\\
&\times\bigg[-\frac{24}{5}k_s^2k_s'^2\widetilde V^{(2)}_{(s\bar s\to s\bar s),T}(s,s')\\
&+\sqrt{ss'}\widetilde V^{(1)}_{(s\bar s\to s\bar s),P}(s,s') + 4m_s^2\widetilde V^{(1)}_{(s\bar s\to s\bar s),A}(s,s')\\
&-8\widetilde V^{(0)}_{(s\bar s\to s\bar s),T}(s,s')\bigg]\psi^{(0,1,1)}_{h_1(s\bar s),n}(s')\sin\Theta_n.
\end{aligned}$$

The wave functions $\psi^{(0,1,1)}_{h_1(n\bar n),n}(s)$ and $\psi^{(0,1,1)}_{h_1(s\bar s),n}(s)$ satisfy the normalization condition within the obvious change of the integration region for the $s\bar s$ component: $4m^2 \to 4m_s^2$.

The following states are located on the $h_1$ $(M^2, n)$ trajectories:

(i) $h_1(1170)$ with $n = 1$, $h_1(1600)$ with $n = 2$, $h_1(2000)$ with $n = 3$, $h_1(2270)$ with $n = 4$, and so on;

(ii) $h_1(1390)$ with $n = 1$, $h_1(1780)$ with $n = 2$, $h_1(2120)$ with $n = 3$, and so on.

**3.1.5. Equation for the $\pi_2$ $(M^2, n)$ trajectories.** The equation for the $\pi_2$ states ($S = 0$, $L = 2$, $J = 2$) reads

$$\begin{aligned}
&(s - M^2)\psi^{(0,2,2)}_{\pi_2,n}(s) \qquad (105)\\
&= \int\limits_{4m^2}^{\infty} \frac{ds'}{\pi}\rho(s')k'^4\frac{3}{5}\sqrt{\frac{s'}{s}}\bigg[-\frac{40}{7}k^2k'^2\widetilde V^{(3)}_T(s,s')\\
&+\sqrt{ss'}\widetilde V^{(2)}_P(s,s') + 4m^2\widetilde V^{(2)}_A(s,s')\\
&-\frac{32}{9}\widetilde V^{(1)}_T(s,s')\bigg]\psi^{(0,2,2)}_{\pi_2,n}(s').
\end{aligned}$$

The following states are located on the $\pi_2$ $(M^2, n)$ trajectory [15]: $\pi_2(1670)$ with $n = 1$, $\pi_2(2005)$ with $n = 2$, $\pi_2(2245)$ with $n = 3$, and so on.

The wave functions of the $\pi_2$ states satisfy the orthogonality/normalization constraint

$$\int\limits_{4m^2}^{\infty} \frac{ds}{\pi}\rho(s)k^4 \cdot 2s\alpha(2)\psi^{(0,2,2)}_{\pi,n'}(s)\psi^{(0,2,2)}_{\pi,n}(s) = \delta_{n',n}, \tag{106}$$

where $\alpha(2)$ is determined by Eq. (63).

**3.1.6. Equation for the $\eta_2$ $(M^2, n)$ trajectory.** The $\eta_2$ states have two components, $n\bar n = (u\bar u + d\bar d)/\sqrt{2}$ and $s\bar s$. We write $\eta_{2,n} = \cos\Theta_n n\bar n + \sin\Theta_n s\bar s$, and, correspondingly, we have two equations for the wave functions:

$$\begin{aligned}
&(s - M^2)\psi^{(0,2,2)}_{\eta_2(n\bar n),n}(s)\cos\Theta_n \qquad (107)\\
&= \int\limits_{4m^2}^{\infty} \frac{ds'}{\pi}\rho(s')k'^4\frac{3}{5}\sqrt{\frac{s'}{s}}
\end{aligned}$$

$$\times\Big[-\frac{40}{7}k^2k'^2\widetilde V^{(3)}_{(n\bar n\to n\bar n),T}(s,s')$$
$$+\sqrt{ss'}\widetilde V^{(2)}_{(n\bar n\to n\bar n),P}(s,s')+4m^2\widetilde V^{(2)}_{(n\bar n\to n\bar n),A}(s,s')$$
$$-\frac{32}{9}\widetilde V^{(1)}_{(n\bar n\to n\bar n),T}(s,s')\Big]\psi^{(0,2,2)}_{\eta_2(n\bar n),n}(s')\cos\Theta_n$$
$$+\int\limits_{4m_s^2}^{\infty}\frac{ds'}{\pi}\rho_s(s')k_s'^4\frac{3}{5}\sqrt{\frac{s'}{s}}$$
$$\times\Big[-\frac{40}{7}k^2k_s'^2\widetilde V^{(3)}_{(s\bar s\to n\bar n),T}(s,s')$$
$$+\sqrt{ss'}\widetilde V^{(2)}_{(s\bar s\to n\bar n),P}(s,s')+4mm_s\widetilde V^{(2)}_{(s\bar s\to n\bar n),A}(s,s')$$
$$-\frac{32}{9}\widetilde V^{(1)}_{(s\bar s\to n\bar n),T}(s,s')\Big]\psi^{(0,2,2)}_{\eta_2(s\bar s),n}(s')\sin\Theta_n$$

and

$$(s-M^2)\psi^{(0,2,2)}_{\eta_2(s\bar s),n}(s)\sin\Theta_n \tag{108}$$
$$=\int\limits_{4m^2}^{\infty}\frac{ds'}{\pi}\rho(s')k'^4\frac{3}{5}\sqrt{\frac{s'}{s}}$$
$$\times\Big[-\frac{40}{7}k_s^2k'^2\widetilde V^{(3)}_{(n\bar n\to s\bar s),T}(s,s')$$
$$+\sqrt{ss'}\widetilde V^{(2)}_{(n\bar n\to s\bar s),P}(s,s')+4mm_s\widetilde V^{(2)}_{(n\bar n\to s\bar s),A}(s,s')$$
$$-\frac{32}{9}\widetilde V^{(1)}_{(n\bar n\to s\bar s),T}(s,s')\Big]\psi^{(0,2,2)}_{\eta_2(n\bar n),n}(s')\cos\Theta_n$$
$$+\int\limits_{4m_s^2}^{\infty}\frac{ds'}{\pi}\rho_s(s')k_s'^4\frac{3}{5}\sqrt{\frac{s'}{s}}$$
$$\times\Big[-\frac{40}{7}k_s^2k_s'^2\widetilde V^{(3)}_{(s\bar s\to s\bar s),T}(s,s')$$
$$+\sqrt{ss'}\widetilde V^{(2)}_{(s\bar s\to s\bar s),P}(s,s')+4m_s^2\widetilde V^{(2)}_{(s\bar s\to s\bar s),A}(s,s')$$
$$-\frac{32}{9}\widetilde V^{(1)}_{(s\bar s\to s\bar s),T}(s,s')\Big]\psi^{(0,2,2)}_{\eta_2(s\bar s),n}(s')\sin\Theta_n.$$

The wave functions $\psi^{(0,2,2)}_{\eta_2(n\bar n),n}(s)$ and $\psi^{(0,2,2)}_{\eta_2(s\bar s),n}(s)$ satisfy the normalization condition (106), with obvious change of the integration region for the $s\bar s$ component: $4m^2\to 4m_s^2$.

The following states are located on the $\eta_2\ (M^2,n)$ trajectory [15]: $\eta_2(1645)$ with $n=1$, $\eta_2(2030)$ with $n=2$, $\eta_2(2250)$ with $n=3$, and so on.

**3.1.7. Equation for the $b_3$ $(M^2,n)$ trajectory.** The equation for the $b_3$ mesons ($S=0$, $L=3$, $J=3$) is as follows:

$$(s-M^2)\psi^{(0,3,3)}_{b_3,n}(s) \tag{109}$$
$$=-\int\limits_{4m^2}^{\infty}\frac{ds'}{\pi}\rho(s')k'^6\frac{5}{7}\sqrt{\frac{s'}{s}}\Big[-\frac{56}{9}k^2k'^2\widetilde V^{(4)}_T(s,s')$$
$$+\sqrt{ss'}\widetilde V^{(3)}_P(s,s')+4m^2\widetilde V^{(3)}_A(s,s')$$
$$-\frac{72}{25}\widetilde V^{(2)}_T(s,s')\Big]\psi^{(0,3,3)}_{b_3,n}(s').$$

According to [15], the following states are located on the $b_3\ (M^2,n)$ trajectory in the mass region below 2400 MeV: $b_3(2020)$ with $n=1$, $b_3(2245)$ with $n=2$, and so on.

The wave functions of the states laying on the $(M^2,n)$ trajectory satisfy the orthogonality/normalization constraint

$$\int\limits_{4m^2}^{\infty}\frac{ds}{\pi}\rho(s)k^6\cdot 2s\alpha(3)\psi^{(0,3,3)}_{b_3,n'}(s)\psi^{(0,3,3)}_{b_3,n}(s)=\delta_{n',n}. \tag{110}$$

The factor $\alpha(3)$ is given by Eq. (63).

### *3.2. Equation for the $(S=1,\ J=L)$ State*

The equation for the $(S=1,\ J=L)$ state reads

$$(s-M^2)\varepsilon_{\beta\nu_1\nu_2\nu_3}P_{\nu_1}Z^{(J)}_{\nu_2\mu_1\cdots\mu_J,\nu_3}(k) \tag{111}$$
$$\times\,\mathrm{tr}\Big[\gamma^\perp_\alpha(\widehat k_1+m)\gamma^\perp_\beta(-\widehat k_2+m)\Big]$$
$$\times\,\varepsilon_{\alpha\xi_1\xi_2\xi_3}P_{\xi_1}Z^{(J)}_{\xi_2\mu_1\cdots\mu_J,\xi_3}(k)\psi^{(1,J,J)}_n(s)$$
$$=\varepsilon_{\beta'\nu_1\nu_2\nu_3}P_{\nu_1}Z^{(J)}_{\nu_2\mu_1\cdots\mu_J,\nu_3}(k)$$
$$\times\sum_c\mathrm{tr}\Big[\widehat F_c(\widehat k_1+m)\gamma^\perp_{\beta'}(-\widehat k_2+m)\Big]$$
$$\times\int\frac{d^3k'}{(2\pi)^3k'_0}V_c(s,s',(kk'))$$
$$\times\,\mathrm{tr}\Big[\gamma^\perp_{\alpha'}(\widehat k'_1+m')\widehat F_c(-\widehat k'_2+m')\Big]$$
$$\times\,\varepsilon_{\alpha'\xi_1\xi_2\xi_3}P_{\xi_1}Z^{(J)}_{\xi_2\mu_1\cdots\mu_J,\xi_3}(k')\psi^{(1,J,J)}_n(s').$$

The left-hand side of the equation is calculated by using the trace and operator convolutions given in Appendices B and C:

$$\varepsilon_{\beta\nu_1\nu_2\nu_3}P_{\nu_1}Z^{(J)}_{\nu_2\mu_1\cdots\mu_J,\nu_3}(k) \tag{112}$$
$$\times\,\mathrm{tr}\Big[\gamma^\perp_\alpha(\widehat k_1+m)\gamma^\perp_\beta(-\widehat k_2+m)\Big]$$
$$\times\,\varepsilon_{\alpha\xi_1\xi_2\xi_3}P_{\xi_1}Z^{(J)}_{\xi_2\mu_1\cdots\mu_J,\xi_3}(k)$$
$$=-2s^2\frac{J(2J+3)^2}{(J+1)^3}\alpha(J)k^{2J}.$$

As before, the right-hand side is calculated in two steps.

(i) We calculate traces:

$$B_{\beta'\alpha'}(s,s',(kk')) \tag{113}$$
$$= \sum_{c=T,A,V,S} (B_c)_{\beta'\alpha'}(s,s',(kk'))V_c(s,s',(kk'))$$
$$= \sum_{c=T,A,V,S} \mathrm{tr}\left[\widehat{F}_c(\widehat{k}_1+m)\gamma^{\perp}_{\beta'}(-\widehat{k}_2+m)\right]$$
$$\times\, \mathrm{tr}\left[\gamma^{\perp}_{\alpha'}(\widehat{k}'_1+m')\widehat{F}_c(-\widehat{k}'_2+m')\right]V_c(s,s',(kk')).$$

Following the items presented in Appendix B, we write

$$B_{\beta'\alpha'}(s,s',(kk')) = g^{\perp}_{\beta'\alpha'}\cdot 4\sqrt{ss'} \tag{114}$$
$$\times\left[\sqrt{ss'}V_V(s,s',(kk')) + 8mm'V_T(s,s',(kk'))\right.$$
$$\left.+\,4\sqrt{k^2}\sqrt{k'^2}zV_A(s,s',(kk'))\right] + 64mm'k^{\perp}_{\beta'}k'^{\perp}_{\alpha'}$$
$$\times\, V_S(s,s',(kk')) - 16k'^{\perp}_{\beta'}k^{\perp}_{\alpha'}\sqrt{ss'}V_A(s,s',(kk'))$$
$$+\,16\left[s'k^{\perp}_{\beta'}k^{\perp}_{\alpha'} + sk'^{\perp}_{\beta'}k'^{\perp}_{\alpha'} + 4z\sqrt{k^2}\sqrt{k'^2}k^{\perp}_{\beta'}k'^{\perp}_{\alpha'}\right]$$
$$\times\, V_V(s,s',(kk')).$$

(ii) The convolutions of the trace factor $B_{\beta'\alpha'}(s,s',(kk'))$ with angular momentum wave functions are presented in Appendix C; we have

$$\varepsilon_{\beta'\nu_1\nu_2\nu_3}P_{\nu_1}Z^{(J)}_{\nu_2\mu_1\cdots\mu_J,\nu_3}(k) \tag{115}$$
$$\times\, B_{\beta'\alpha'}(s,s',(kk'))\varepsilon_{\alpha'\xi_1\xi_2\xi_3}P_{\xi_1}Z^{(J)}_{\xi_2\mu_1\cdots\mu_J,\xi_3}(k')$$
$$= \alpha(J)\left(\sqrt{k^2}\sqrt{k'^2}\right)^J(-4ss')\frac{J(2J+3)^2}{(J+1)^3}$$
$$\times\left[4\frac{J}{2J+1}\sqrt{k^2}\sqrt{k'^2}P_{J+1}(z)V_A(s,s',(kk'))\right.$$
$$+\left(\sqrt{ss'}V_V(s,s',(kk'))\right.$$
$$\left.+\,8mm'V_T(s,s',(kk'))\right)P_J(z)$$
$$\left.+\,4\frac{J+1}{2J+1}\sqrt{k^2}\sqrt{k'^2}P_{J-1}(z)V_A(s,s',(kk'))\right].$$

Inserting these expressions into Eq. (111), we obtain

$$(s-M^2)(-2s^2)k^{2J}\psi^{(1,J,J)}_n(s) \tag{116}$$
$$= \int\frac{d^3k'}{(2\pi)^3k'_0}(-4ss')\left(\sqrt{k^2}\sqrt{k'^2}\right)^J$$
$$\times\left[4\frac{J}{2J+1}\sqrt{k^2}\sqrt{k'^2}P_{J+1}(z)V_A(s,s',(kk'))\right.$$
$$+\sqrt{ss'}V_V(s,s',(kk'))P_J(z)$$
$$+\,8mm'V_T(s,s',(kk'))P_J(z)$$
$$\left.+\,4\frac{J+1}{2J+1}\sqrt{k^2}\sqrt{k'^2}P_{J-1}(z)V_A(s,s',(kk'))\right]$$
$$\times\,\psi^{(1,J,J)}_n(s').$$

Expanding the interaction block according to (94) and integrating both sides over $\int_{-1}^{1}dz/2$, we get

$$(s-M^2)\psi^{(1,J,J)}_n(s) \tag{117}$$
$$= \int\limits_{4m'^2}^{\infty}\frac{ds'}{\pi}\rho(s')(-k'^2)^J\cdot 2\frac{s'}{s}$$
$$\times\left[-4\frac{J}{2J+1}\xi(J+1)k^2k'^2\widetilde{V}^{(J+1)}_A(s,s')\right.$$
$$+\sqrt{ss'}\xi(J)\widetilde{V}^{(J)}_V(s,s') + 8mm'\xi(J)\widetilde{V}^{(J)}_T(s,s')$$
$$\left.-\,4\frac{J+1}{2J+1}\xi(J-1)\widetilde{V}^{(J-1)}_A(s,s')\right]\psi^{(1,J,J)}_n(s').$$

The normalization condition for the $(S=1,\ J=L)$ wave functions reads

$$\int\limits_{4m^2}^{\infty}\frac{ds}{\pi}\rho(s)k^{2J}\cdot 2s^2\frac{J(2J+3)^2}{(J+1)^3}\alpha(J) \tag{118}$$
$$\times\,\psi^{(1,J,J)}_{n'}(s)\psi^{(1,J,J)}_n(s) = \delta_{n',n}.$$

### 3.2.1. Equation for the $a_1$ $(M^2, n)$ trajectory.

The $a_1$ states $(S=1,\ L=1,\ J=1)$ obey the Bethe–Salpeter equation

$$(s-M^2)\psi^{(1,1,1)}_{a_1,n}(s) \tag{119}$$
$$= -\int\limits_{4m^2}^{\infty}\frac{ds'}{\pi}\rho(s')k'^2\frac{2}{3}\frac{s'}{s}\left[-\frac{6}{5}k^2k'^2\widetilde{V}^{(2)}_A(s,s')\right.$$
$$+\sqrt{ss'}\widetilde{V}^{(1)}_V(s,s') + 8m^2\widetilde{V}^{(1)}_T(s,s')$$
$$\left.-\,8\widetilde{V}^{(0)}_A(s,s')\right]\psi^{(1,1,1)}_{a_1,n}(s').$$

The following states are located on the $a_1$ $(M^2,n)$ trajectory [15]: $a_1(1230)$ with $n=1$, $a_1(1640)$ with $n=2$, $a_1(1960)$ with $n=3$, $a_1(2270)$ with $n=4$, and so on.

The wave functions of the $a_1$ states satisfy the orthogonality/normalization condition

$$\int\limits_{4m^2}^{\infty}\frac{ds}{\pi}\rho(s)k^2\cdot 2s^2\frac{25}{8}\alpha(1)\psi^{(1,1,1)}_{a_1,n'}(s)\psi^{(1,1,1)}_{a_1,n}(s)$$
$$= \delta_{n',n}. \tag{120}$$

### 3.2.2. Equation for the $a_3$ $(M^2, n)$ trajectory.

For the $a_3$ mesons $(S=1,\ L=3,\ J=3)$, the Bethe–Salpeter equation reads

$$(s-M^2)\psi^{(1,3,3)}_{a_3,n}(s) \tag{121}$$

$$\begin{aligned}&= -\int\limits_{4m^2}^{\infty} \frac{ds'}{\pi}\rho(s')k'^6\frac{5}{7}\frac{s'}{s}\bigg[-\frac{7}{3}k^2k'^2\widetilde{V}_A^{(4)}(s,s')\\ &\quad + \sqrt{ss'}\widetilde{V}_V^{(3)}(s,s') + 8m^2\widetilde{V}_T^{(3)}(s,s')\\ &\quad - \frac{48}{25}\widetilde{V}_A^{(2)}(s,s')\bigg]\psi^{(1,3,3)}_{a_3,n}(s').\end{aligned}$$

Two $a_3$ states were seen: $a_3(2030)$ with $n = 1$ and $a_3(2275)$ with $n = 2$ [15].

The orthogonality/normalization constraint reads

$$\int\limits_{4m^2}^{\infty}\frac{ds}{\pi}\rho(s)k^6 s\frac{243}{32}\alpha(3)\psi^{(1,3,3)}_{a_3,n'}(s)\psi^{(1,3,3)}_{a_3,n}(s) = \delta_{n',n}. \tag{122}$$

### *3.3. Equations for the $(S = 1, J = L \pm 1)$ States*

We have two equations for two states with $S = 1$ and $J = L \pm 1$ for $J > 0$. The corresponding wave functions are denoted as $A_j\widehat{\Psi}^{(1,J-1,J)}_{(n)\mu_1\ldots\mu_J}(k) + B_j\widehat{\Psi}^{(1,J+1,J)}_{(n)\mu_1\ldots\mu_J}(k)$ with $j = 1, 2$. These wave functions are orthogonal to one another. Normalization and orthogonality conditions give three constraints for four mixing parameters $A_j$ and $B_j$.

Each wave function obeys two equations:

$$\begin{aligned}&(s - M^2)X^{(J+1)}_{\mu_1\ldots\mu_J\beta}(k)\\ &\times \mathrm{tr}\left[\gamma^{\perp}_{\alpha}(\widehat{k}_1 + m)\gamma^{\perp}_{\beta}(-\widehat{k}_2 + m)\right]\\ &\times (A_j Z^{(J-1)}_{\mu_1\ldots\mu_J,\alpha}(k)\psi^{(1,J-1,J)}_n(k^2)\\ &+ B_j X^{(J+1)}_{\mu_1\ldots\mu_J\alpha}(k)\psi^{(1,J+1,J)}_n(k^2)) = X^{(J+1)}_{\mu_1\ldots\mu_J\beta'}(k)\\ &\times \sum_c \mathrm{tr}\left[\widehat{F}_c(\widehat{k}_1 + m)\gamma^{\perp}_{\beta'}(-\widehat{k}_2 + m)\right]\\ &\times \int\frac{d^3k'}{(2\pi)^3k'_0}V_c(s,s',(kk'))\mathrm{tr}\left[\gamma^{\perp}_{\alpha'}(\widehat{k}'_1 + m')\right.\\ &\left.\times \widehat{F}_c(-\widehat{k}'_2 + m')\right](A_j Z^{(J-1)}_{\mu_1\ldots\mu_J,\alpha'}(k')\psi^{(1,J-1,J)}_n(k'^2)\\ &+ B_j X^{(J+1)}_{\mu_1\ldots\mu_J\alpha'}(k')\psi^{(1,J+1,J)}_n(k'^2))\end{aligned} \tag{123}$$

and

$$\begin{aligned}&(s - M^2)Z^{(J-1)}_{\mu_1\ldots\mu_J,\beta}(k)\\ &\times \mathrm{tr}\left[\gamma^{\perp}_{\alpha}(\widehat{k}_1 + m)\gamma^{\perp}_{\beta}(-\widehat{k}_2 + m)\right]\\ &\times (A_j Z^{(J-1)}_{\mu_1\ldots\mu_J,\alpha}(k)\psi^{(1,J-1,J)}_n(k^2)\\ &+ B_j X^{(J+1)}_{\mu_1\ldots\mu_J\alpha}(k)\psi^{(1,J+1,J)}_n(k^2)) = Z^{(J-1)}_{\mu_1\ldots\mu_J,\beta'}(k)\\ &\times \sum_c \mathrm{tr}\left[\widehat{F}_c(\widehat{k}_1 + m)\gamma^{\perp}_{\beta'}(-\widehat{k}_2 + m)\right]\\ &\times \int\frac{d^3k'}{(2\pi)^3k'_0}V_c(s,s',(kk'))\mathrm{tr}\left[\gamma^{\perp}_{\alpha'}(\widehat{k}'_1 + m')\right.\\ &\left.\times \widehat{F}_c(-\widehat{k}'_2 + m')\right](A_j Z^{(J-1)}_{\mu_1\ldots\mu_J,\alpha'}(k')\psi^{(1,J-1,J)}_n(k'^2)\\ &+ B_j X^{(J+1)}_{\mu_1\ldots\mu_J\alpha'}(k')\psi^{(1,J+1,J)}_n(k'^2)).\end{aligned} \tag{124}$$

First, let us consider (123); on the left-hand side of (123), one has two convolutions:

$$\begin{aligned}&X^{(J+1)}_{\mu_1\ldots\mu_J\beta}(k)\mathrm{tr}\left[\gamma^{\perp}_{\alpha}(\widehat{k}_1 + m)\gamma^{\perp}_{\beta}(-\widehat{k}_2 + m)\right]\\ &\times X^{(J+1)}_{\mu_1\ldots\mu_J\alpha}(k) = 2\alpha(J)k^{2(J+1)}\left[\frac{2J+1}{J+1}s + 4k^2\right],\\ &X^{(J+1)}_{\mu_1\ldots\mu_J\beta}(k)\mathrm{tr}\left[\gamma^{\perp}_{\alpha}(\widehat{k}_1 + m)\gamma^{\perp}_{\beta}(-\widehat{k}_2 + m)\right]\\ &\times Z^{(J-1)}_{\mu_1\ldots\mu_J,\alpha}(k) = 8\alpha(J)k^{2(J+1)}.\end{aligned} \tag{125}$$

The left-hand side of (124) also contains two convolutions:

$$\begin{aligned}&Z^{(J-1)}_{\mu_1\ldots\mu_J,\beta}(k)\mathrm{tr}\left[\gamma^{\perp}_{\alpha}(\widehat{k}_1 + m)\gamma^{\perp}_{\beta}(-\widehat{k}_2 + m)\right]\\ &\times X^{(J+1)}_{\mu_1\ldots\mu_J\alpha}(k) = 8\alpha(J)k^{2(J+1)},\\ &Z^{(J-1)}_{\mu_1\ldots\mu_J,\beta}(k)\mathrm{tr}\left[\gamma^{\perp}_{\alpha}(\widehat{k}_1 + m)\gamma^{\perp}_{\beta}(-\widehat{k}_2 + m)\right]\\ &\times Z^{(J-1)}_{\mu_1\ldots\mu_J,\alpha}(k) = 2\alpha(J)k^{2(J-1)}\left[\frac{2J+1}{J}s + 4k^2\right].\end{aligned} \tag{126}$$

The right-hand sides of Eqs. (123) and (124) are determined by convolutions of the trace factor $B_{\beta'\alpha'}(s,s',(kk'))$ [see Eqs. (113) and (114)] with angular-momentum wave functions; the corresponding formulas are presented in Appendix C. Following them, one has for the right-hand side of (123)

$$\begin{aligned}&X^{(J+1)}_{\mu_1\ldots\mu_J\beta'}(k)B_{\beta'\alpha'}(s,s',(kk'))\\ &\times X^{(J+1)}_{\mu_1\ldots\mu_J\alpha'}(k') = 4\alpha(J)\left(\sqrt{k^2}\sqrt{k'^2}\right)^{J+1}\\ &\times\Bigg(\bigg[\frac{2J+1}{J+1}\sqrt{ss'}(\sqrt{ss'}V_V(s,s',(kk'))\\ &\quad + 8mm'V_T(s,s',(kk')))\\ &\quad + 4s'k^2V_V(s,s',(kk')) + 4sk'^2V_V(s,s')\\ &\quad + 16\frac{J+1}{2J+1}k^2k'^2V_V(s,s',(kk'))\bigg]\\ &\times P_{J+1}(z) + \bigg[16mm'V_S(s,s',(kk'))\\ &\quad + 4\frac{J}{J+1}\sqrt{ss'}V_A(s,s',(kk'))\bigg]\sqrt{k^2}\sqrt{k'^2}P_J(z)\\ &\quad + 16\frac{J}{2J+1}k^2k'^2V_V(s,s',(kk'))P_{J-1}(z)\Bigg)\end{aligned} \tag{127}$$

and

$$X^{(J+1)}_{\mu_1\ldots\mu_J\beta'}(k)B_{\beta'\alpha'}(s,s',(kk')) \tag{128}$$

$$\begin{aligned}
&\times Z^{(J-1)}_{\mu_1\ldots\mu_J,\alpha'}(k') = 16\alpha(J)k^2\left(\sqrt{k^2}\sqrt{k'^2}\right)^{J-1}\\
&\times\left(\left[s+4\frac{J+1}{2J+1}k^2\right]k'^2P_{J+1}(z)V_V(s,s',(kk'))\right.\\
&+\left[-\sqrt{ss'}V_A(s,s',(kk'))+4mm'V_S(s,s',(kk'))\right]\\
&\times\sqrt{k^2}\sqrt{k'^2}P_J(z)+\left[s'+4\frac{J}{2J+1}k'^2\right]\\
&\left.\times k^2P_{J-1}(z)V_V(s,s',(kk'))\right).
\end{aligned}$$

For the right-hand side of (124), one has

$$\begin{aligned}
&Z^{(J-1)}_{\mu_1\ldots\mu_J,\beta'}(k)B_{\beta'\alpha'}(s,s',(kk')) \qquad (129)\\
&\times X^{(J+1)}_{\mu_1\ldots\mu_J\alpha'}(k') = 16\alpha(J)k'^2\left(\sqrt{k^2}\sqrt{k'^2}\right)^{J-1}\\
&\times\left(\left[s'+4\frac{J+1}{2J+1}k'^2\right]k^2P_{J+1}(z)V_V(s,s',(kk'))\right.\\
&+\left[-\sqrt{ss'}V_A(s,s',(kk'))+4mm'V_S(s,s',(kk'))\right]\\
&\times\sqrt{k^2}\sqrt{k'^2}P_J(z)+\left[s+4\frac{J}{2J+1}k^2\right]\\
&\left.\times k'^2P_{J-1}(z)V_V(s,s',(kk'))\right)
\end{aligned}$$

and

$$\begin{aligned}
&Z^{(J-1)}_{\mu_1\ldots\mu_J,\beta'}(k)B_{\beta'\alpha'}(s,s',(kk')) \qquad (130)\\
&\times Z^{(J-1)}_{\mu_1\ldots\mu_J,\alpha'}(k') = 4\alpha(J)\left(\sqrt{k^2}\sqrt{k'^2}\right)^{J-1}\\
&\times\left(16\frac{J+1}{2J+1}k^2k'^2P_{J+1}(z)V_V(s,s',(kk'))\right.\\
&+\left[16mm'V_S(s,s',(kk'))\right.\\
&\left.+4\sqrt{ss'}\frac{J+1}{J}V_A(s,s',(kk'))\right]\sqrt{k^2}\sqrt{k'^2}P_J(z)\\
&+\left[\frac{2J+1}{J}\sqrt{ss'}(\sqrt{ss'}V_V(s,s',(kk'))\right.\\
&+8mm'V_T(s,s',(kk')))\\
&+4s'k^2V_V(s,s',(kk'))+4sk'^2V_V(s,s',(kk'))\\
&\left.\left.+16\frac{J}{2J+1}k^2k'^2V_V(s,s',(kk'))\right]P_{J-1}(z)\right).
\end{aligned}$$

On the right-hand sides of Eqs. (123) and (124), we expand the interaction blocks in the Legendre polynomial series (94) and integrate over angle variables $\int_{-1}^{1}dz/2$. As a result, Eq. (123) reads

$$\begin{aligned}
&(s-M^2)\left[4\psi_n^{(1,J-1,J)}(k^2)A_j\right. \qquad (131)\\
&\left.+\left(\frac{2J+1}{J+1}s+4k^2\right)\psi_n^{(1,J+1,J)}(k^2)B_j\right]\\
&=\int\limits_{4m'^2}^{\infty}\frac{ds'}{\pi}\rho(s')\cdot 8(-k'^2)^{J-1}\psi_n^{(1,J-1,J)}(k'^2)A_j\\
&\times\left[\xi(J+1)\left(s+4\frac{J+1}{2J+1}k^2\right)k'^4\widetilde{V}_V^{(J+1)}(s,s')\right.\\
&+\xi(J)\sqrt{ss'}k'^2\widetilde{V}_A^{(J)}(s,s')\\
&-4mm'k'^2\xi(J)\widetilde{V}_S^{(J)}(s,s')+\xi(J-1)\\
&\left.\times\left(s'+4\frac{J}{2J+1}k'^2\right)\widetilde{V}_V^{(J-1)}(s,s')\right]\\
&+\int\limits_{4m'^2}^{\infty}\frac{ds'}{\pi}\rho(s')\cdot 2(-k'^2)^{J+1}\psi_n^{(1,J+1,J)}(k'^2)B_j\\
&\times\left[8mm'\frac{2J+1}{J+1}\xi(J+1)\sqrt{ss'}\widetilde{V}_T^{(J+1)}(s,s')\right.\\
&+\xi(J+1)\left(\frac{2J+1}{J+1}ss'+4s'k^2+4sk'^2\right.\\
&\left.+16\frac{J+1}{2J+1}k^2k'^2\right)\widetilde{V}_V^{(J+1)}(s,s')\\
&-16mm'\xi(J)\widetilde{V}_S^{(J)}(s,s')\\
&-4\frac{J}{J+1}\xi(J)\sqrt{ss'}\widetilde{V}_A^{(J)}(s,s')\\
&\left.+16\frac{J}{2J+1}\xi(J-1)\widetilde{V}_V^{(J-1)}(s,s')\right].
\end{aligned}$$

The second Eq. (124) reads

$$\begin{aligned}
&(s-M^2)\left[\left(\frac{2J+1}{J}s+4k^2\right)\right. \qquad (132)\\
&\left.\times\psi_n^{(1,J-1,J)}(k^2)A_j+4k^4\psi_n^{(1,J+1,J)}(k^2)B_j\right]\\
&\times\int\limits_{4m'^2}^{\infty}\frac{ds'}{\pi}\rho(s')\cdot 2(-k'^2)^{J-1}\psi_n^{(1,J-1,J)}(k'^2)A_j\\
&\times\left[8mm'\frac{2J+1}{J}\xi(J-1)\sqrt{ss'}\widetilde{V}_T^{(J-1)}(s,s')\right.\\
&+\xi(J-1)\left(\frac{2J+1}{J}ss'+4s'k^2+4sk'^2\right.\\
&\left.+16\frac{J}{2J+1}k^2k'^2\right)\widetilde{V}_V^{(J-1)}(s,s')\\
&-16mm'\xi(J)k^2k'^2\widetilde{V}_S^{(J)}(s,s')\\
&-4\frac{J+1}{J}\xi(J)\sqrt{ss'}k^2k'^2\widetilde{V}_A^{(J)}(s,s')
\end{aligned}$$

$$
\begin{aligned}
&+ 16\frac{J+1}{2J+1}\xi(J+1)k^4k'^4\widetilde{V}_V^{(J+1)}(s,s')\Big] \\
&+ \int\limits_{4m'^2}^{\infty}\frac{ds'}{\pi}\rho(s')\cdot 8(-k'^2)^{J+1}\psi_n^{(1,J+1,J)}(k'^2)B_j \\
&\times\Big[\xi(J+1)\Big(s'+4\frac{J+1}{2J+1}k'^2\Big)k^4\widetilde{V}_V^{(J+1)}(s,s') \\
&\quad + \xi(J)\sqrt{ss'}k^2\widetilde{V}_A^{(J)}(s,s') \\
&\quad - 4mm'\xi(J)k^2\widetilde{V}_S^{(J)}(s,s') + \xi(J-1) \\
&\quad \times\Big(s+4\frac{J}{2J+1}k^2\Big)\widetilde{V}_V^{(J-1)}(s,s')\Big].
\end{aligned}
$$

Normalization and orthogonality conditions determined by Eq. (87) are as follows:

$$
\begin{aligned}
&\int\limits_{4m^2}^{\infty}\frac{ds}{\pi}\rho(s)\Big[A_j^2\left(\psi_n^{(1,J-1,J)}(k^2)\right)^2 \\
&\times 2\alpha(J)(-k^2)^{(J-1)}\left(\frac{2J+1}{J}s+4k^2\right) \\
&+ 2A_jB_j\psi_n^{(1,J-1,J)}(k^2)\psi_n^{(1,J+1,J)}(k^2) \\
&\times 8\alpha(J)(-k^2)^{(J+1)} + B_j^2\left(\psi_n^{(1,J+1,J)}(k^2)\right)^2 \\
&\times 2\alpha(J)(-k^2)^{(J+1)}\left(\frac{2J+1}{J+1}s+4k^2\right)\Big] = 1, \\
&j = 1,2,
\end{aligned}
\tag{133}
$$

and

$$
\begin{aligned}
&\int\limits_{4m^2}^{\infty}\frac{ds}{\pi}\rho(s)\Big[A_1A_2\left(\psi_n^{(1,J-1,J)}(k^2)\right)^2 \\
&\times 2\alpha(J)(-k^2)^{(J-1)}\left(\frac{2J+1}{J}s+4k^2\right) \\
&+ (A_1B_2+A_2B_1)\psi_n^{(1,J-1,J)}(k^2)\psi_n^{(1,J+1,J)}(k^2) \\
&\times 8\alpha(J)(-k^2)^{(J+1)} + B_1B_2\left(\psi_n^{(1,J+1,J)}(k^2)\right)^2 \\
&\times 2\alpha(J)(-k^2)^{(J+1)}\left(\frac{2J+1}{J+1}s+4k^2\right)\Big] = 0.
\end{aligned}
\tag{134}
$$

Let us emphasize again that all the above equations are written for the case $J > 0$.

**3.3.1. Equation for the $a_0$ $(M^2, n)$ trajectory.** For the $(S = 1, L = 1, J = 0)$ state, we have only one level $L = J + 1$; the wave function of this state obeys the equation

$$
\begin{aligned}
&(s-M^2)(s+4k^2)\psi_{a_0,n}^{(1,1,0)}(s) \\
&= -\int\limits_{4m'^2}^{\infty}\frac{ds'}{\pi}\rho(s')\cdot 2k'^2\psi_{a_0,n}^{(1,1,0)}(s') \\
&\times\left[\frac{8}{3}m^2\sqrt{ss'}\widetilde{V}_T^{(1)}(s,s') + \frac{1}{3}(ss'+4s'k^2+4sk'^2\right. \\
&\left.+ 16k^2k'^2)\widetilde{V}_V^{(1)}(s,s') - 16m^2\widetilde{V}_S^{(0)}(s,s')\right].
\end{aligned}
\tag{135}
$$

According to [15], the following states are located on the $a_0$ $(M^2, n)$ trajectory: $a_0(980)$ with $n = 1$, $a_0(1520)$ with $n = 2$, $a_0(1830)$ with $n = 3$, $a_0(2120)$ with $n = 3$, and so on.

The normalization reads

$$
\int\limits_{4m^2}^{\infty}\frac{ds}{\pi}\rho(s)\left(\psi_{a_0,n}^{(1,1,0)}(s)\right)^2\cdot 2(-k^2)(s+4k^2) = 1.
\tag{136}
$$

**3.3.2. Equation for the $f_0$ $(M^2, n)$ trajectory.** The $f_0$ states have two flavor components, $n\bar{n}$ and $s\bar{s}$; correspondingly, we have two equations for two wave functions

$$
\begin{aligned}
&(s-M^2)(s+4k^2)\psi_{a_0(n\bar{n}),n}^{(1,1,0)}(s)\cos\Theta_n \\
&= -\int\limits_{4m^2}^{\infty}\frac{ds'}{\pi}\rho(s')\cdot 2k'^2\psi_{a_0(n\bar{n}),n}^{(1,1,0)}(s')\cos\Theta_n \\
&\times\left[\frac{8}{3}m^2\sqrt{ss'}\widetilde{V}_{(n\bar{n}\to n\bar{n}),T}^{(1)}(s,s') + \frac{1}{3}(ss'+4s'k^2\right. \\
&\quad + 4sk'^2+16k^2k'^2)\widetilde{V}_{(n\bar{n}\to n\bar{n}),V}^{(1)}(s,s') \\
&\quad\left. - 16m^2\widetilde{V}_{(n\bar{n}\to n\bar{n}),S}^{(0)}(s,s')\right] \\
&- \int\limits_{4m_s^2}^{\infty}\frac{ds'}{\pi}\rho_s(s')\cdot 2k_s'^2\psi_{a_0(s\bar{s}),n}^{(1,1,0)}(s')\sin\Theta_n \\
&\times\left[\frac{8}{3}mm_s\sqrt{ss'}\widetilde{V}_{(s\bar{s}\to n\bar{n}),T}^{(1)}(s,s')\right. \\
&\quad + \frac{1}{3}(ss'+4s'k^2+4sk_s'^2+16k^2k_s'^2) \\
&\left.\times\widetilde{V}_{(s\bar{s}\to n\bar{n}),V}^{(1)}(s,s') - 16mm_s\widetilde{V}_{(s\bar{s}\to n\bar{n}),S}^{(0)}(s,s')\right]
\end{aligned}
\tag{137}
$$

and

$$
\begin{aligned}
&(s-M^2)(s+4k^2)\psi_{a_0(s\bar{s}),n}^{(1,1,0)}(s)\sin\Theta_n \\
&= -\int\limits_{4m^2}^{\infty}\frac{ds'}{\pi}\rho(s')\cdot 2k'^2\psi_{a_0(n\bar{n}),n}^{(1,1,0)}(s')\cos\Theta_n \\
&\times\left[\frac{8}{3}mm_s\sqrt{ss'}\widetilde{V}_{(n\bar{n}\to s\bar{s}),T}^{(1)}(s,s') + \frac{1}{3}(ss'+4s'k_s^2\right. \\
&\quad + 4sk'^2+16k_s^2k'^2)\widetilde{V}_{(n\bar{n}\to s\bar{s}),V}^{(1)}(s,s') \\
&\quad\left. - 16mm_s\widetilde{V}_{(n\bar{n}\to s\bar{s}),S}^{(0)}(s,s')\right]
\end{aligned}
\tag{138}
$$

$$
\begin{aligned}
&- \int\limits_{4m_s^2}^{\infty} \frac{ds'}{\pi}\rho_s(s') \cdot 2k_s'^2 \psi^{(1,1,0)}_{a_0(s\bar{s}),n}(s') \sin\Theta_n \\
&\times \left[\frac{8}{3}m_s^2\sqrt{ss'}\widetilde{V}^{(1)}_{(s\bar{s}\to s\bar{s}),T}(s,s') + \frac{1}{3}(ss' + 4s'k_s^2 \right. \\
&\quad + 4sk_s'^2 + 16k_s^2k_s'^2)\widetilde{V}^{(1)}_{(s\bar{s}\to s\bar{s}),V}(s,s') \\
&\quad \left. - 16m_s^2\widetilde{V}^{(0)}_{(s\bar{s}\to s\bar{s}),S}(s,s')\right].
\end{aligned}
$$

The following states are located on two $f_0\,(M^2,n)$ trajectories [15]:

(i) $f_0(980)$ with $n=1$, $f_0(1500)$ with $n=2$, $f_0(2005)$ with $n=3$, $f_0(2240)$ with $n=4$, and so on;

(ii) $f_0(1300)$ with $n=1$, $f_0(1750)$ with $n=2$, $f_0(2105)$ with $n=3$, $f_0(2330)$ with $n=4$, and so on.

**3.3.3. Equation for the $\rho\ (M^2, n)$ trajectory.** The two equations read

$$
\begin{aligned}
&(s-M^2)\left[4\psi^{(1,0,1)}_{\rho,n}(s)A_j \right. \\
&\quad \left. + \left(\frac{3}{2}s + 4k^2\right)\psi^{(1,2,1)}_{\rho,n}(s)B_j\right] \\
&= \int\limits_{4m^2}^{\infty} \frac{ds'}{\pi}\rho(s') \cdot 8\psi^{(1,0,1)}_{\rho,n}(s')A_j \\
&\times \left[\frac{3}{10}\left(s + \frac{8}{3}k^2\right)k'^4\widetilde{V}^{(2)}_V(s,s') \right. \\
&\quad + \frac{1}{3}\sqrt{ss'}k'^2\widetilde{V}^{(1)}_A(s,s') - \frac{4}{3}m^2k'^2\widetilde{V}^{(1)}_S(s,s') \\
&\quad \left. + \left(s' + \frac{4}{3}k'^2\right)\widetilde{V}^{(0)}_V(s,s')\right] \\
&+ \int\limits_{4m^2}^{\infty} \frac{ds'}{\pi}\rho(s') \cdot 2k'^4\psi^{(1,2,1)}_{\rho,n}(s')B_j \\
&\times \left[m^2\frac{18}{5}\sqrt{ss'}\widetilde{V}^{(2)}_T(s,s') + \frac{3}{10}\left(\frac{3}{2}ss' + 4s'k^2 \right.\right. \\
&\quad \left. + 4sk'^2 + \frac{32}{3}k^2k'^2\right)\widetilde{V}^{(2)}_V(s,s') \\
&\quad - m^2\frac{16}{3}\widetilde{V}^{(1)}_S(s,s') - \frac{2}{3}\sqrt{ss'}\widetilde{V}^{(1)}_A(s,s') \\
&\quad \left. + \frac{16}{3}\widetilde{V}^{(0)}_V(s,s')\right]
\end{aligned}
\tag{139}
$$

and

$$
\begin{aligned}
&(s-M^2)\left[(3s+4k^2)\psi^{(1,0,1)}_{\rho,n}(s)A_j \right. \\
&\quad \left. + 4k^4\psi^{(1,2,1)}_{\rho,n}(s)B_j\right] \\
&= \int\limits_{4m^2}^{\infty} \frac{ds'}{\pi}\rho(s') \cdot 2\psi^{(1,0,1)}_{\rho,n}(s')A_j \\
&\times \left[24m^2\sqrt{ss'}\widetilde{V}^{(0)}_T(s,s') + \left(3ss' \right.\right. \\
&\quad \left. + 4s'k^2 + 4sk'^2 + \frac{16}{3}k^2k'^2\right)\widetilde{V}^{(0)}_V(s,s') \\
&\quad - m^2\frac{16}{3}k^2k'^2\widetilde{V}^{(1)}_S(s,s') - \frac{8}{3}\sqrt{ss'}k^2k'^2\widetilde{V}^{(1)}_A(s,s') \\
&\quad \left. + \frac{16}{5}k^4k'^4\widetilde{V}^{(2)}_V(s,s')\right] \\
&+ \int\limits_{4m^2}^{\infty} \frac{ds'}{\pi}\rho(s') \cdot 8k'^4\psi^{(1,2,1)}_{\rho,n}(s')B_j \\
&\times \left[\frac{3}{10}\left(s' + \frac{8}{3}k'^2\right)k^4\widetilde{V}^{(2)}_V(s,s') \right. \\
&\quad + \frac{1}{3}\sqrt{ss'}k^2\widetilde{V}^{(1)}_A(s,s') - m^2\frac{4}{3}k^2\widetilde{V}^{(1)}_S(s,s') \\
&\quad \left. + \left(s + \frac{4}{3}k^2\right)\widetilde{V}^{(0)}_V(s,s')\right].
\end{aligned}
\tag{140}
$$

The following states are located on the $\rho\,(M^2,n)$ trajectories [15]:

(i) $\rho(770)$ with $n=1$, $\rho(1450)$ with $n=2$, $\rho(1830)$ with $n=3$, $\rho(2110)$ with $n=4$, and so on;

(ii) $\rho(1700)$ with $n=1$, $\rho(1990)$ with $n=2$, $\rho(2285)$ with $n=3$, and so on.

The normalization and orthogonality conditions are as follows:

$$
\begin{aligned}
&\int\limits_{4m^2}^{\infty} \frac{ds}{\pi}\rho(s)\left[A_j^2(\psi^{(1,0,1)}_{\rho,n}(s))^2 \cdot 2(3s+4k^2) \right. \\
&\quad + 2A_jB_j\psi^{(1,0,1)}_{\rho,n}(s)\psi^{(1,2,1)}_{\rho,n}(s) \cdot 8k^4 \\
&\quad \left. + B_j^2(\psi^{(1,2,1)}_{\rho,n}(s))^2 \cdot 2k^4\left(\frac{3}{2}s + 4k^2\right)\right] = 1, \\
&\qquad j = 1, 2,
\end{aligned}
\tag{141}
$$

and

$$
\begin{aligned}
&\int\limits_{4m^2}^{\infty} \frac{ds}{\pi}\rho(s)\left[A_1A_2(\psi^{(1,0,1)}_{\rho,n}(s))^2 \right. \\
&\times 2(3s+4k^2) + (A_1B_2 + A_2B_1)\psi^{(1,0,1)}_{\rho,n}(s) \\
&\times \psi^{(1,2,1)}_{\rho,n}(s) \cdot 8k^4 + B_1B_2(\psi^{(1,2,1)}_{\rho,n}(s))^2 \\
&\left. \times 2k^4\left(\frac{3}{2}s + 4k^2\right)\right] = 0.
\end{aligned}
\tag{142}
$$

## ACKNOWLEDGMENTS

We are grateful to D.V. Bugg, L.G. Dakhno, D.I. Melikhov, V.A. Nikonov, H.R. Petry, and V.V. Vereshagin for helpful and stimulating discussions.

This work was supported by the Russian Foundation for Basic Research, project nos. 01-02-17861 and 01-02-17152. One of us (V.N.M.) thanks INTAS (project no. 2000-587) and "Dynasty Foundation" for support and Prof. H.R. Petry for the hospitality in ITKP (Bonn).

## APPENDIX A

### *Angular-Momentum Operators*

Here, we present the angular-momentum operator $X^{(L)}_{\mu_1\mu_2\ldots\mu_{L-1}\mu_L}(k)$ and briefly recall its properties; a full presentation of the angular-momentum operators can be found in [9].

The operator $X^{(L)}_{\mu_1\mu_2\ldots\mu_{L-1}\mu_L}(k)$ is constructed by using relative momentum of mesons in the space orthogonal to the total momentum $P$:

$$k^\perp_\mu = k_\nu g^\perp_{\nu\mu}, \quad g^\perp_{\nu\mu} = g_{\nu\mu} - \frac{P_\nu P_\mu}{s}, \qquad (A.1)$$
$$g_{\mu\nu} = (1,-1,-1,-1).$$

In the c.m. system, where $P = (P_0, \mathbf{P}) = (\sqrt{s}, \mathbf{0})$, the vector $k^\perp$ is spacelike: $k^\perp = (0, \mathbf{k})$. We determine the operator $X^{(L)}_{\mu_1\mu_2\ldots\mu_{L-1}\mu_L}(k)$ as symmetrical and traceless. It is easy to construct it for the lowest values of $L = 0, 1, 2, 3$:

$$X^{(0)} = 1, \qquad X^{(1)}_\mu = k^\perp_\mu, \qquad (A.2)$$
$$X^{(2)}_{\mu_1\mu_2} = \frac{3}{2}\left(k^\perp_{\mu_1}k^\perp_{\mu_2} - \frac{1}{3}(k^\perp)^2 g^\perp_{\mu_1\mu_2}\right),$$
$$X^{(3)}_{\mu_1\mu_2\mu_3} = \frac{5}{2}\left[k^\perp_{\mu_1}k^\perp_{\mu_2}k^\perp_{\mu_3} - \frac{(k^\perp)^2}{5} \times \left(g^\perp_{\mu_1\mu_2}k^\perp_{\mu_3} + g^\perp_{\mu_1\mu_3}k^\perp_{\mu_2} + g^\perp_{\mu_2\mu_3}k^\perp_{\mu_1}\right)\right].$$

Correspondingly, the generalization of $X^{(L)}_{\mu_1\ldots\mu_L}$ for $L > 1$ reads

$$X^{(L)}_{\mu_1\ldots\mu_L} = k^\perp_\alpha Z^{(L-1)}_{\mu_1\ldots\mu_L,\alpha}, \qquad (A.3)$$
$$Z^{(L-1)}_{\mu_1\ldots\mu_L,\alpha} = \frac{2L-1}{L^2}\left(\sum_{i=1}^{L} X^{(L-1)}_{\mu_1\ldots\mu_{i-1}\mu_{i+1}\ldots\mu_L} g^\perp_{\mu_i\alpha} - \frac{2}{2L-1}\sum_{\substack{i,j=1\\ i<j}}^{L} g^\perp_{\mu_i\mu_j} X^{(L-1)}_{\mu_1\ldots\mu_{i-1}\mu_{i+1}\ldots\mu_{j-1}\mu_{j+1}\ldots\mu_L\alpha}\right).$$

It is seen that the operator $X^{(L)}_{\mu_1\mu_2\ldots\mu_{L-1}\mu_L}(k)$ constructed in accordance with (A.3) is symmetrical,

$$X^{(L)}_{\mu_1\ldots\mu_i\ldots\mu_j\ldots\mu_L} = X^{(L)}_{\mu_1\ldots\mu_j\ldots\mu_i\ldots\mu_L}, \qquad (A.4)$$

and it works in the space orthogonal to $P$:

$$P_{\mu_i} X^{(L)}_{\mu_1\ldots\mu_i\ldots\mu_L} = 0. \qquad (A.5)$$

The angular-momentum operator $X^{(L)}_{\mu_1\ldots\mu_L}$ is traceless over any two indices:

$$g_{\mu_i\mu_j} X^{(L)}_{\mu_1\ldots\mu_i\ldots\mu_j\ldots\mu_L} = g^\perp_{\mu_i\mu_j} X^{(L)}_{\mu_1\ldots\mu_i\ldots\mu_j\ldots\mu_L} = 0. \qquad (A.6)$$

The tracelessness property given by (A.6) is obvious for the lowest order operators entering (A.2), for example, $g^\perp_{\mu_1\mu_2} X^{(2)}_{\mu_1\mu_2} = 0$ (recall that $g^\perp_{\mu_1\mu_2} g^\perp_{\mu_1\mu_2} = 3$).

The convolution equality reads

$$X^{(L)}_{\mu_1\ldots\mu_L} k^\perp_{\mu_L} = (k^\perp)^2 X^{(L-1)}_{\mu_1\ldots\mu_{L-1}}. \qquad (A.7)$$

Using (A.7), we rewrite the recurrent equation (A.3) in the form

$$X^{(L)}_{\mu_1\ldots\mu_L} = \frac{2L-1}{L^2} \times \sum_{i=1}^{L} k^\perp_{\mu_i} X^{(L-1)}_{\mu_1\ldots\mu_{i-1}\mu_{i+1}\ldots\mu_L} - \frac{2(k^\perp)^2}{L^2}\sum_{\substack{i,j=1\\ i<j}}^{L} g^\perp_{\mu_i\mu_j} X^{(L-2)}_{\mu_1\ldots\mu_{i-1}\mu_{i+1}\ldots\mu_{j-1}\mu_{j+1}\ldots\mu_L}. \qquad (A.8)$$

On the basis of this recurrent equation and taking into account the tracelessness of $X^{(L)}_{\mu_1\ldots\mu_L}$, one can write the normalization condition for the moment-$L$ operator as follows:

$$X^{(L)}_{\mu_1\ldots\mu_L}(k) X^{(L)}_{\mu_1\ldots\mu_L}(k) = \alpha(L)(k^\perp)^{2L}, \qquad (A.9)$$
$$\alpha(L) = \prod_{l=1}^{L} \frac{2l-1}{l} = \frac{(2L-1)!!}{L!}.$$

The iteration of (A.8) gives us the following expression for the operator $X^{(L)}_{\mu_1\ldots\mu_L}$:

$$X^{(L)}_{\mu_1\ldots\mu_L}(k) = \frac{(2L-1)!!}{L!} \qquad (A.10)$$
$$\times \Big[k^\perp_{\mu_1}k^\perp_{\mu_2}k^\perp_{\mu_3}k^\perp_{\mu_4}\ldots k^\perp_{\mu_L} - \frac{(k^\perp)^2}{2L-1} \times \left(g^\perp_{\mu_1\mu_2}k^\perp_{\mu_3}k^\perp_{\mu_4}\ldots k^\perp_{\mu_L} + g^\perp_{\mu_1\mu_3}k^\perp_{\mu_2}k^\perp_{\mu_4}\ldots k^\perp_{\mu_L} + \ldots\right)$$
$$+ \frac{(k^\perp)^4}{(2L-1)(2L-3)} \times \left(g^\perp_{\mu_1\mu_2}g^\perp_{\mu_3\mu_4}k^\perp_{\mu_5}k^\perp_{\mu_6}\ldots k^\perp_{\mu_L}\right.$$

$$+ g^{\perp}_{\mu_1\mu_2} g^{\perp}_{\mu_3\mu_5} k^{\perp}_{\mu_4} k^{\perp}_{\mu_6} \ldots k^{\perp}_{\mu_L} + \ldots) + \ldots \Big].$$

One can introduce a projection operator $O^{\mu_1\ldots\mu_L}_{\nu_1\ldots\nu_L}$ for the partial wave with the angular momentum $L$. The operator is defined by the following relations:

$$X^{(L)}_{\mu_1\ldots\mu_L}(k) O^{\mu_1\ldots\mu_L}_{\nu_1\ldots\nu_L} = X^{(L)}_{\nu_1\ldots\nu_L}(k), \qquad \text{(A.11)}$$
$$O^{\mu_1\ldots\mu_L}_{\alpha_1\ldots\alpha_L} O^{\alpha_1\ldots\alpha_L}_{\nu_1\ldots\nu_L} = O^{\mu_1\ldots\mu_L}_{\nu_1\ldots\nu_L}.$$

For the sets of indices $\mu_1 \ldots \mu_L$ and $\nu_1 \ldots \nu_L$, the operator $O$ has all the properties of the operator $X^{(L)}$: it is symmetrical and traceless,

$$O^{\mu_1\mu_2\ldots\mu_L}_{\nu_1\nu_2\ldots\nu_L} = O^{\mu_2\mu_1\ldots\mu_L}_{\nu_1\nu_2\ldots\nu_L} = O^{\mu_1\mu_2\ldots\mu_L}_{\nu_2\nu_1\ldots\nu_L}, \qquad \text{(A.12)}$$
$$O^{\mu_1\mu_1\ldots\mu_L}_{\nu_1\nu_2\ldots\nu_L} = O^{\mu_1\mu_2\ldots\mu_L}_{\nu_1\nu_1\ldots\nu_L} = 0.$$

The projection operator $O$ can be constructed as a product of the operators $X^{(L)}_{\mu_1\ldots\mu_L}(k) X^{(L)}_{\nu_1\ldots\nu_L}(k)$ integrated over angular variables of the momentum $k^{\perp}$, so we have a convolution of the $(2L+1)$-dimensional vectors, which provide us with an irreducible representation of the Lorentz group in the $k^{\perp}/|k^{\perp}|$ space. Thus,

$$\xi(L) O^{\mu_1\ldots\mu_L}_{\nu_1\ldots\nu_L} = \frac{1}{(k^{\perp})^{2L}} \int \frac{d\Omega}{4\pi} X^{(L)}_{\mu_1\ldots\mu_L}(k) X^{(L)}_{\nu_1\ldots\nu_L}(k), \qquad \text{(A.13)}$$

where $\xi(L)$ is a normalization factor fixed below. Using the definition of the projection operator $O^{\mu_1\ldots\mu_L}_{\nu_1\ldots\nu_L}$, we have

$$k_{\mu_1} \ldots k_{\mu_L} O^{\mu_1\ldots\mu_L}_{\nu_1\ldots\nu_L} = \frac{1}{\alpha(L)} X^{(L)}_{\nu_1\ldots\nu_L}(k). \qquad \text{(A.14)}$$

This equation represents the basic property of the operator: it projects any index-$L$ operator into a partial-wave operator with the angular momentum $L$.

Multiplying Eq. (A.13) by the product $X^{(L)}_{\mu_1\ldots\mu_L}(q) X^{(L)}_{\nu_1\ldots\nu_L}(q)$, we get

$$\xi(L) X^{(L)}_{\nu_1\ldots\nu_L}(q) X^{(L)}_{\nu_1\ldots\nu_L}(q) \qquad \text{(A.15)}$$
$$= (q^{\perp})^{2L} \alpha^2(L) \int\limits_{-1}^{1} \frac{dz}{2} P^2_L(z),$$

which gives the normalization constant in (A.13):

$$\xi(L) = \frac{\alpha(L)}{2L+1} = \frac{(2L-1)!!}{(2L+1) \cdot L!}. \qquad \text{(A.16)}$$

Summation in the projection operator over upper and lower indices performed in (A.13) gives us the following reduction formula:

$$O^{\mu_1\ldots\mu_{L-1}\mu_L}_{\nu_1\ldots\nu_{L-1}\mu_L} = \frac{2L+1}{2L-1} O^{\mu_1\ldots\mu_{L-1}}_{\nu_1\ldots\nu_{L-1}}. \qquad \text{(A.17)}$$

Likewise, the summation over all indices gives us

$$O^{\mu_1\ldots\mu_L}_{\mu_1\ldots\mu_L} = 2L + 1, \qquad \text{(A.18)}$$

which can be proven using formula (A.13). On the basis of Eq. (A.14), one gets

$$X^{(L)}_{\mu_1\ldots\mu_{L-1}\mu_L} O^{\mu_1\ldots\mu_{L-1}}_{\nu_1\ldots\nu_{L-1}} = X^{(L)}_{\nu_1\ldots\nu_{L-1}\mu_L}. \qquad \text{(A.19)}$$

Generally, one can write

$$X^{(L)}_{\mu_1\ldots\mu_i\mu_{i+1}\ldots\mu_L} O^{\mu_1\ldots\mu_i}_{\nu_1\ldots\nu_i} = X^{(L)}_{\nu_1\ldots\nu_i\mu_{i+1}\mu_L}. \qquad \text{(A.20)}$$

## APPENDIX B

### *Traces of the Loop Diagrams*

Here, we present the traces which are used for the calculations of loop diagrams. Recall that, in the spectral-integral representation, there is no energy conservation, $s \neq s'$, where $P^2 = s$ and $P'^2 = s'$, but all constituents are mass-on-shell:

$$k_1^2 = k_2^2 = m^2, \qquad k_1'^2 = k_2'^2 = m'^2.$$

The following notation is used for the quark momenta:

$$k_\nu = \frac{1}{2}(k_1 - k_2)_\nu, \quad k'_\nu = \frac{1}{2}(k'_1 - k'_2)_\nu, \qquad \text{(B.1)}$$
$$k^{\perp}_\mu = k_\nu g^{\perp}_{\nu\mu} = k_\mu, \quad k'^{\perp}_\mu = k'_\nu g^{\perp}_{\nu\mu} = k'_\mu.$$

We follow the definition of matrices:

$$\gamma_5 = -i\gamma^0\gamma^1\gamma^2\gamma^3, \quad \sigma_{\mu\nu} = \frac{1}{2}\left[\gamma_\mu\gamma_\nu\right].$$

#### *Traces for the $S = 0$ States*

For the $S = 0$ states, we have the following nonzero traces:

$$T'_P = \mathrm{tr}\left[i\gamma_5(k'_1 + m')\gamma_5(-k'_2 + m')\right] = 2is', \quad \text{(B.2)}$$
$$T'_A = \mathrm{tr}\left[i\gamma_5(k'_1 + m')i\gamma_\mu\gamma_5(-k'_2 + m')\right]$$
$$= -4m'P'_\mu,$$
$$T'_T = \mathrm{tr}\left[i\gamma_5(k'_1 + m')i\sigma_{\mu\nu}(-k'_2 + m')\right]$$
$$= -4i\epsilon_{\mu\nu\alpha\beta}P'_\alpha k'_\beta,$$

and

$$T_P = \mathrm{tr}\left[i\gamma_5(-k_2 + m)\gamma_5(k_1 + m)\right] = 2is, \quad \text{(B.3)}$$
$$T_A = \mathrm{tr}\left[i\gamma_5(-k_2 + m)i\gamma_\mu\gamma_5(k_1 + m)\right]$$
$$= 4mP_\mu,$$
$$T_T = \mathrm{tr}\left[i\gamma_5(-k_2 + m)i\sigma_{\mu\nu}(k_1 + m)\right]$$
$$= 4i\epsilon_{\mu\nu\alpha\beta}P_\alpha k_\beta.$$

The convolutions of the traces $A_P = (T_P T'_P)$, $A_A = (T_A T'_A)$, $A_T = (T_T T'_T)$ are equal to

$$A_P = -4ss', \qquad \text{(B.4)}$$
$$A_A = -16mm'(PP'),$$
$$A_T = -32(PP')(kk').$$

### *Traces for the $S = 1$ States*

For the $S = 1$ states, the traces are equal to

$$T'_S = \mathrm{tr}\left[\gamma^{\perp}_{\alpha'}(k'_1 + m')I(-k'_2 + m')\right] \qquad \text{(B.5)}$$
$$= 8m'k'_{\alpha'},$$
$$T'_V = \mathrm{tr}\left[\gamma^{\perp}_{\alpha'}(k'_1 + m')\gamma_\mu(-k'_2 + m')\right]$$
$$= 2(g^{\perp}_{\alpha'\mu}s' + 4k'_{\alpha'}k'_\mu),$$
$$T'_A = \mathrm{tr}\left[\gamma^{\perp}_{\alpha'}(k'_1 + m')i\gamma^{\perp}_\mu\gamma_5(-k'_2 + m')\right]$$
$$= 4\epsilon_{\alpha'\mu\alpha\beta}k'_\alpha P'_\beta,$$
$$T'_T = \mathrm{tr}\left[\gamma^{\perp}_{\alpha'}(k'_1 + m')i\sigma_{\mu\nu}(-k'_2 + m')\right]$$
$$= 4m'i\left[g^{\perp}_{\alpha'\nu}P'_\mu - g^{\perp}_{\alpha'\mu}P'_\nu\right],$$

and

$$T_S = \mathrm{tr}\left[\gamma^{\perp}_{\beta}(-k_2 + m)I(k_1 + m)\right] \qquad \text{(B.6)}$$
$$= 8mk_\beta,$$
$$T_V = \mathrm{tr}\left[\gamma^{\perp}_{\beta}(-k_2 + m)\gamma_\mu(k_1 + m)\right]$$
$$= 2\left[g^{\perp}_{\mu\beta}s + 4k_\beta k_\mu\right],$$
$$T_A = \mathrm{tr}\left[\gamma^{\perp}_{\beta}(-k_2 + m)i\gamma_\mu\gamma_5(k_1 + m)\right]$$
$$= -4\epsilon_{\beta\mu\alpha'\beta'}k_{\alpha'}P_{\beta'},$$
$$T_T = \mathrm{tr}\left[\gamma^{\perp}_{\beta}(-k_2 + m)i\sigma_{\mu\nu}(k_1 + m)\right]$$
$$= 4mi\left[g^{\perp}_{\beta\mu}P_\nu - g^{\perp}_{\beta\nu}P_\mu\right].$$

The corresponding convolutions $B_c = (T_c T'_c)$ read

$$(B_S)_{\beta'\alpha'} = 64mm'k_{\beta'}k'_{\alpha'}, \qquad \text{(B.7)}$$
$$(B_V)_{\beta'\alpha'} = 4\left[ss'g^{\perp}_{\beta'\alpha'} + 4s'k_{\beta'}k_{\alpha'} + 4sk'_{\beta'}k'_{\alpha'}\right.$$
$$\left. + 16(kk')k_{\beta'}k'_{\alpha'}\right],$$
$$(B_A)_{\beta'\alpha'} = -16(PP')\left[k'_{\beta'}k_{\alpha'} - (kk')g^{\perp}_{\beta'\alpha'}\right],$$
$$(B_T)_{\beta'\alpha'} = 32(PP')mm'g^{\perp}_{\beta'\alpha'}.$$

## APPENDIX C

### *Convolutions of the Trace Factors*

Here, we present the convolutions of the angular-momentum factors. We work with $k^{\perp}_\mu = k_\nu g^{\perp}_{\nu\mu} = k_\mu$ and $k'^{\perp}_\mu = k'_\nu g^{\perp}_{\nu\mu} = k'_\mu$ and introduce

$$z = \frac{(kk')}{\sqrt{k^2}\sqrt{k'^2}}. \qquad \text{(C.1)}$$

The convolutions for the $S = 1$ states read

$$X^{(J)}_{\mu_1\mu_2\cdots\mu_J}(k)X^{(J)}_{\mu_1\mu_2\cdots\mu_J}(k') \qquad \text{(C.2)}$$
$$= \alpha(J)\left(\sqrt{k^2}\sqrt{k'^2}\right)^J P_J(z).$$

Analogous convolutions for $S = 1$ states are written as follows:

$$X^{(J+1)}_{\mu_1\mu_2\cdots\mu_J\beta}(k)X^{(J+1)}_{\mu_1\mu_2\cdots\mu_J\alpha}(k') \qquad \text{(C.3)}$$
$$= \frac{\alpha(J)}{J+1}\left(\sqrt{k^2}\sqrt{k'^2}\right)^J\left[\frac{\sqrt{k'^2}}{\sqrt{k^2}}A_{P_{J,J+1}}(z)k_\beta k_\alpha\right.$$
$$+ \frac{\sqrt{k^2}}{\sqrt{k'^2}}B_{P_{J,J+1}}(z)k'_\beta k'_\alpha + C_{P_{J,J+1}}(z)k_\beta k'_\alpha$$
$$\left.+ D_{P_{J,J+1}}(z)k'_\beta k_\alpha + \left(\sqrt{k^2}\sqrt{k'^2}\right)E_{P_{J,J+1}}(z)g^{\perp}_{\beta\alpha}\right],$$

$$X^{(J+1)}_{\mu_1\mu_2\cdots\mu_J\beta}(k)Z^{(J-1)}_{\mu_1\mu_2\cdots\mu_J,\alpha}(k') \qquad \text{(C.4)}$$
$$= -\frac{\alpha(J)}{J}\frac{1}{k'^2}\left(\sqrt{k^2}\sqrt{k'^2}\right)^J\left[\frac{\sqrt{k'^2}}{\sqrt{k^2}}A_{P_{J,J+1}}(z)k_\beta k_\alpha\right.$$
$$+ \frac{\sqrt{k^2}}{\sqrt{k'^2}}(B_{P_{J,J+1}}(z) - (2J+1)A_J(z))k'_\beta k'_\alpha$$
$$+ (C_{P_{J,J+1}}(z) - (2J+1)B_J(z))k_\beta k'_\alpha$$
$$\left.+ D_{P_{J,J+1}}(z)k'_\beta k_\alpha + \left(\sqrt{k^2}\sqrt{k'^2}\right)E_{P_{J,J+1}}(z)g^{\perp}_{\beta\alpha}\right],$$

$$Z^{(J-1)}_{\mu_1\mu_2\cdots\mu_J,\beta}(k)Z^{(J-1)}_{\mu_1\mu_2\cdots\mu_J,\alpha}(k') \qquad \text{(C.5)}$$
$$= \frac{J+1}{J^2}\alpha(J)\left(\sqrt{k^2}\sqrt{k'^2}\right)^{J-2}$$
$$\times\left[\frac{\sqrt{k'^2}}{\sqrt{k^2}}(A_{P_{J,J+1}}(z) - (2J+1)A_J(z))k_\beta k_\alpha\right.$$
$$+ \frac{\sqrt{k^2}}{\sqrt{k'^2}}(B_{P_{J,J+1}}(z) - (2J+1)A_J(z))k'_\beta k'_\alpha$$
$$+ \left(C_{P_{J,J+1}}(z) + \frac{(2J+1)^2}{J+1}P_J(z)\right.$$
$$\left. - 2(2J+1)B_J(z)\right)k_\beta k'_\alpha + D_{P_{J,J+1}}(z)k'_\beta k_\alpha$$
$$\left.+ (\sqrt{k^2}\sqrt{k'^2})E_{P_{J,J+1}}(z)g^{\perp}_{\beta\alpha}\right],$$

$$\epsilon_{\beta\nu_1\nu_2\nu_3}P_{\nu_1}Z^{(J)}_{\nu_2\mu_1\cdots\mu_J,\nu_3}(k)\epsilon_{\alpha\lambda_1\lambda_2\lambda_3}P'_{\lambda_1} \qquad \text{(C.6)}$$
$$\times Z^{(J)}_{\lambda_2\mu_1\cdots\mu_J,\lambda_3}(k') = \frac{(2J+3)^2}{(J+1)^3}\alpha(J)$$
$$\times\left(\sqrt{k^2}\sqrt{k'^2}\right)^{J-1}(PP')\left[-\sqrt{k^2}\sqrt{k'^2}((z^2-1)\right.$$
$$\times D_{P_{J,J+1}}(z) + zE_{P_{J,J+1}}(z))g^{\perp}_{\beta\alpha} - D_{P_{J,J+1}}(z)$$

$$\times\left(\frac{\sqrt{k'^2}}{\sqrt{k^2}}k_\beta k_\alpha+\frac{\sqrt{k^2}}{\sqrt{k'^2}}k'_\beta k'_\alpha-zk_\beta k'_\alpha\right)$$
$$\left.+\left(zD_{P_{J,J+1}}(z)+E_{P_{J,J+1}}(z)\right)k'_\beta k_\alpha\right],$$

and

$$X^{(J)}_{\mu_1\cdots\mu_J}(k)\epsilon_{\alpha\nu_1\nu_2\nu_3}P'_{\nu_1}Z^{(J)}_{\nu_2\mu_1\cdots\mu_J,\nu_3}(k') \tag{C.7}$$
$$=\frac{2J+3}{J+1}\alpha(J)\left(\sqrt{k^2}\sqrt{k'^2}\right)^{J-1}A_{P_{J,J+1}}(z)\epsilon_{\alpha P'kk'}.$$

Here,

$$A_{P_{J,J+1}}(z)=B_{P_{J,J+1}}(z) \tag{C.8}$$
$$=-\frac{2zP_J(z)+\left[Jz^2-(J+2)\right]P_{J+1}(z)}{(1-z^2)^2},$$
$$C_{P_{J,J+1}}(z)=\frac{\left[(1-J)z^2+(J+1)\right]P_J(z)}{(1-z^2)^2}$$
$$+\frac{\left[(2J+1)z^2-(2J+3)\right]zP_{J+1}(z)}{(1-z^2)^2},$$
$$D_{P_{J,J+1}}(z)=\frac{\left[(J+2)z^2-J\right]P_J(z)-2zP_{J+1}(z)}{(1-z^2)^2},$$
$$E_{P_{J,J+1}}(z)=\frac{zP_J(z)-P_{J+1}(z)}{(1-z^2)},$$
$$A_J=\frac{P_{J+1}(z)-zP_J(z)}{1-z^2},$$
$$B_J=\frac{P_J(z)-zP_{J+1}(z)}{1-z^2},$$
$$\epsilon_{\alpha P'kk'}=\epsilon_{\alpha\beta\mu\nu}P'^{\beta}k^{\mu}k'^{\nu}.$$

We also need more complicated convolutions, namely, for the factors $K_\beta X^{(J+1)}_{\mu_1\mu_2\cdots\mu_J\beta}(k)\times X^{(J+1)}_{\mu_1\mu_2\cdots\mu_J\alpha}(k')K_\alpha$, where $K=k,k'$:

$$k_\beta X^{(J+1)}_{\mu_1\mu_2\cdots\mu_J\beta}(k)X^{(J+1)}_{\mu_1\mu_2\cdots\mu_J\alpha}(k')k_\alpha \tag{C.9}$$
$$=k^2\alpha(J)\left(\sqrt{k^2}\sqrt{k'^2}\right)^{J+1}P_{J+1}(z),$$
$$k_\beta X^{(J+1)}_{\mu_1\mu_2\cdots\mu_J\beta}(k)X^{(J+1)}_{\mu_1\mu_2\cdots\mu_J\alpha}(k')k'_\alpha$$
$$=\alpha(J)\left(\sqrt{k^2}\sqrt{k'^2}\right)^{J+2}P_J(z),$$
$$k'_\beta X^{(J+1)}_{\mu_1\mu_2\cdots\mu_J\beta}(k)X^{(J+1)}_{\mu_1\mu_2\cdots\mu_J\alpha}(k')k'_\alpha$$
$$=k'^2\alpha(J)\left(\sqrt{k^2}\sqrt{k'^2}\right)^{J+1}P_{J+1}(z),$$
$$k'_\beta X^{(J+1)}_{\mu_1\mu_2\cdots\mu_J\beta}(k)X^{(J+1)}_{\mu_1\mu_2\cdots\mu_J\alpha}(k')k_\alpha$$
$$=\alpha(J)\left(\sqrt{k^2}\sqrt{k'^2}\right)^{J+2}$$
$$\times\left[\frac{2J+1}{J+1}zP_{J+1}(z)-\frac{J}{J+1}P_J(z)\right],$$
$$g^{\perp}_{\beta\alpha}X^{(J+1)}_{\mu_1\mu_2\cdots\mu_J\beta}(k)X^{(J+1)}_{\mu_1\mu_2\cdots\mu_J\alpha}(k')$$
$$=\frac{2J+1}{J+1}\alpha(J)\left(\sqrt{k^2}\sqrt{k'^2}\right)^{J+1}P_{J+1}(z);$$

for the factors $K_\beta X^{(J+1)}_{\mu_1\mu_2\cdots\mu_J\beta}(k)Z^{(J-1)}_{\mu_1\mu_2\cdots\mu_J,\alpha}(k')K_\alpha$:

$$k_\beta X^{(J+1)}_{\mu_1\mu_2\cdots\mu_J\beta}(k)Z^{(J-1)}_{\mu_1\mu_2\cdots\mu_J,\alpha}(k')k_\alpha \tag{C.10}$$
$$=k^4\alpha(J)\left(\sqrt{k^2}\sqrt{k'^2}\right)^{J-1}P_{J-1}(z),$$
$$k_\beta X^{(J+1)}_{\mu_1\mu_2\cdots\mu_J\beta}(k)Z^{(J-1)}_{\mu_1\mu_2\cdots\mu_J,\alpha}(k')k'_\alpha$$
$$=k^2\alpha(J)\left(\sqrt{k^2}\sqrt{k'^2}\right)^{J}P_J(z),$$
$$k'_\beta X^{(J+1)}_{\mu_1\mu_2\cdots\mu_J\beta}(k)Z^{(J-1)}_{\mu_1\mu_2\cdots\mu_J,\alpha}(k')k'_\alpha$$
$$=\alpha(J)\left(\sqrt{k^2}\sqrt{k'^2}\right)^{J+1}P_{J+1}(z),$$
$$k'_\beta X^{(J+1)}_{\mu_1\mu_2\cdots\mu_J\beta}(k)Z^{(J-1)}_{\mu_1\mu_2\cdots\mu_J,\alpha}(k')k_\alpha$$
$$=k^2\alpha(J)\left(\sqrt{k^2}\sqrt{k'^2}\right)^{J}P_J(z),$$
$$g^{\perp}_{\beta\alpha}X^{(J+1)}_{\mu_1\mu_2\cdots\mu_J\beta}(k)Z^{(J-1)}_{\mu_1\mu_2\cdots\mu_J,\alpha}(k')=0;$$

for the factors $K_\beta Z^{(J-1)}_{\mu_1\mu_2\cdots\mu_J,\beta}(k)Z^{(J-1)}_{\mu_1\mu_2\cdots\mu_J,\alpha}(k')K_\alpha$:

$$k_\beta Z^{(J-1)}_{\mu_1\mu_2\cdots\mu_J,\beta}(k)Z^{(J-1)}_{\mu_1\mu_2\cdots\mu_J,\alpha}(k')k_\alpha \tag{C.11}$$
$$=k^2\alpha(J)\left(\sqrt{k^2}\sqrt{k'^2}\right)^{J-1}P_{J-1}(z),$$
$$k_\beta Z^{(J-1)}_{\mu_1\mu_2\cdots\mu_J,\beta}(k)Z^{(J-1)}_{\mu_1\mu_2\cdots\mu_J,\alpha}(k')k'_\alpha$$
$$=\alpha(J)\left(\sqrt{k^2}\sqrt{k'^2}\right)^{J}P_J(z),$$
$$k'_\beta Z^{(J-1)}_{\mu_1\mu_2\cdots\mu_J,\beta}(k)Z^{(J-1)}_{\mu_1\mu_2\cdots\mu_J,\alpha}(k')k'_\alpha$$
$$=k'^2\alpha(J)\left(\sqrt{k^2}\sqrt{k'^2}\right)^{J-1}P_{J-1}(z),$$
$$k'_\beta Z^{(J-1)}_{\mu_1\mu_2\cdots\mu_J,\beta}(k)Z^{(J-1)}_{\mu_1\mu_2\cdots\mu_J,\alpha}(k')k_\alpha=\alpha(J)$$
$$\times\left(\sqrt{k^2}\sqrt{k'^2}\right)^{J}\left[\frac{2J+1}{J}zP_{J-1}(z)-\frac{J+1}{J}P_J(z)\right],$$
$$g^{\perp}_{\beta\alpha}Z^{(J-1)}_{\mu_1\mu_2\cdots\mu_J,\beta}(k)Z^{(J-1)}_{\mu_1\mu_2\cdots\mu_J,\alpha}(k')$$
$$=\frac{2J+1}{J}\alpha(J)\left(\sqrt{k^2}\sqrt{k'^2}\right)^{J-1}P_{J-1}(z);$$

and for the factors $K_\beta\epsilon_{\beta\nu_1\nu_2\nu_3}P_{\nu_1}Z^{(J)}_{\nu_2\mu_1\cdots\mu_J,\nu_3}(k)\times\epsilon_{\alpha\lambda_1\lambda_2\lambda_3}P'_{\lambda_1}Z^{(J)}_{\lambda_2\mu_1\cdots\mu_J,\lambda_3}(k')K_\alpha$:

$$k_\beta\epsilon_{\beta\nu_1\nu_2\nu_3}P_{\nu_1}Z^{(J)}_{\nu_2\mu_1\cdots\mu_J,\nu_3}(k)\epsilon_{\alpha\lambda_1\lambda_2\lambda_3}P'_{\lambda_1} \tag{C.12}$$
$$\times Z^{(J)}_{\lambda_2\mu_1\cdots\mu_J,\lambda_3}(k')k_\alpha=0,$$

$$k_\beta \epsilon_{\beta\nu_1\nu_2\nu_3} P_{\nu_1} Z^{(J)}_{\nu_2\mu_1\cdots\mu_J,\nu_3}(k)\epsilon_{\alpha\lambda_1\lambda_2\lambda_3}P'_{\lambda_1} \times Z^{(J)}_{\lambda_2\mu_1\cdots\mu_J,\lambda_3}(k')k'_\alpha = 0,$$

$$k'_\beta \epsilon_{\beta\nu_1\nu_2\nu_3} P_{\nu_1} Z^{(J)}_{\nu_2\mu_1\cdots\mu_J,\nu_3}(k)\epsilon_{\alpha\lambda_1\lambda_2\lambda_3}P'_{\lambda_1} \times Z^{(J)}_{\lambda_2\mu_1\cdots\mu_J,\lambda_3}(k')k'_\alpha = 0,$$

$$k'_\beta \epsilon_{\beta\nu_1\nu_2\nu_3} P_{\nu_1} Z^{(J)}_{\nu_2\mu_1\cdots\mu_J,\nu_3}(k)\epsilon_{\alpha\lambda_1\lambda_2\lambda_3}P'_{\lambda_1} \times Z^{(J)}_{\lambda_2\mu_1\cdots\mu_J,\lambda_3}(k')k_\alpha = \frac{(2J+3)^2}{(J+1)^3}\alpha(J) \times \left(\sqrt{k^2}\sqrt{k'^2}\right)^{J+1}(PP')\left[zP_J(z) - P_{J+1}(z)\right],$$

$$g^{\perp}_{\beta\alpha} \epsilon_{\beta\nu_1\nu_2\nu_3} P_{\nu_1} Z^{(J)}_{\nu_2\mu_1\cdots\mu_J,\nu_3}(k)\epsilon_{\alpha\lambda_1\lambda_2\lambda_3}P'_{\lambda_1} \times Z^{(J)}_{\lambda_2\mu_1\cdots\mu_J,\lambda_3}(k') = -\frac{J(2J+3)^2}{(J+1)^3}\alpha(J) \times \left(\sqrt{k^2}\sqrt{k'^2}\right)^{J}(PP')P_J(z).$$

## APPENDIX D

### *The Bethe–Salpeter Equations for the $\omega$, $\phi$, $a_2$, and $f_2$ Trajectories*

Here, we present the Bethe–Salpeter equations for the $\omega$, $\phi$, $a_2$, and $f_2$ trajectories. Though the explicit form of these equations is rather cumbersome, the investigation of these trajectories is informative for the reconstruction of quark–antiquark forces.

#### *Equations for the $a_2$ $(M^2, n)$ Trajectories*

The following states are located on two $(n, M^2)$ trajectories for the $a_2$ states $M \le 2400$ MeV [15]:

(i) $a_2(1320)$ with $n = 1$, $a_2(1660)$ with $n = 2$, $a_2(1950)$ with $n = 3$, $a_2(2255)$ with $n = 4$;

(ii) $a_2$ trajectory: $a_2(2030)$ with $n = 1$, $a_2(2310)$ with $n = 2$.

Correspondingly, we have two coupled equations for two wave functions:

$$(s - M^2)\Big[4\psi^{(1,1,2)}_{a_2,n}(s)A_j + \left(\frac{5}{3}s + 4k^2\right)\psi^{(1,3,2)}_{a_2,n}(s)B_j\Big] \tag{D.1}$$

$$= \int\limits_{4m^2}^{\infty}\frac{ds'}{\pi}\rho(s')\cdot 8(-k'^2)\psi^{(1,1,2)}_{a_2,n}(s')A_j \times \left[\frac{5}{14}\left(s + \frac{12}{5}k^2\right)k'^4\widetilde{V}^{(3)}_V(s,s') + \frac{3}{10}\sqrt{ss'}k'^2\widetilde{V}^{(2)}_A(s,s') - \frac{6}{5}m^2k'^2\widetilde{V}^{(2)}_S(s,s') + \frac{1}{3}\left(s' + \frac{8}{5}k'^2\right)\widetilde{V}^{(1)}_V(s,s')\right]$$

$$- \int\limits_{4m^2}^{\infty}\frac{ds'}{\pi}\rho(s')\cdot 2k'^6\psi^{(1,3,2)}_{a_2,n}(s')B_j \times \Big[m^2\frac{100}{21}\sqrt{ss'}\widetilde{V}^{(3)}_T(s,s') + \frac{5}{14} \times \left(\frac{5}{3}ss' + 4s'k^2 + 4sk'^2 + \frac{48}{5}k^2k'^2\right)\widetilde{V}^{(3)}_V(s,s') - m^2\frac{24}{5}\widetilde{V}^{(2)}_S(s,s') - \frac{4}{5}\sqrt{ss'}\widetilde{V}^{(2)}_A(s,s') + \frac{32}{15}\widetilde{V}^{(1)}_V(s,s')\Big]$$

and

$$(s - M^2)\Big[\left(\frac{5}{2}s + 4k^2\right)\psi^{(1,1,2)}_{a_2,n}(s)A_j + 4k^4\psi^{(1,3,2)}_{a_2,n}(s)B_j\Big] \tag{D.2}$$

$$= \int\limits_{4m^2}^{\infty}\frac{ds'}{\pi}\rho(s')\cdot 2(-k'^2)\psi^{(1,1,2)}_{a_2,n}(s')A_j \times \Big[m^2\frac{20}{3}\sqrt{ss'}\widetilde{V}^{(1)}_T(s,s') + \frac{1}{3}\left(\frac{5}{2}ss' + 4s'k^2 + 4sk'^2 + \frac{32}{5}k^2k'^2\right)\widetilde{V}^{(1)}_V(s,s') - m^2\frac{24}{5}k^2k'^2\widetilde{V}^{(2)}_S(s,s') - \frac{9}{5}\sqrt{ss'}k^2k'^2\widetilde{V}^{(2)}_A(s,s') + \frac{24}{7}k^4k'^4\widetilde{V}^{(3)}_V(s,s')\Big]$$

$$- \int\limits_{4m^2}^{\infty}\frac{ds'}{\pi}\rho(s')\cdot 8k'^6\psi^{(1,3,2)}_{a_2,n}(s')B_j \times \left[\frac{5}{14}\left(s' + \frac{12}{5}k'^2\right)k^4\widetilde{V}^{(3)}_V(s,s') + \frac{3}{10}\sqrt{ss'}k^2\widetilde{V}^{(2)}_A(s,s') - m^2\frac{6}{5}k^2\widetilde{V}^{(2)}_S(s,s') + \frac{1}{3}\left(s + \frac{8}{5}k^2\right)\widetilde{V}^{(1)}_V(s,s')\right].$$

The normalization and orthogonality conditions read

$$\int\limits_{4m^2}^{\infty}\frac{ds}{\pi}\rho(s)\Big[A_j^2(\psi^{(1,1,2)}_{a_2,n}(s))^2 \cdot 2\alpha(2)(-k^2) \tag{D.3}$$

$$\times\left(\frac{5}{2}s+4k^2\right)+2A_jB_j\psi^{(1,1,2)}_{a_2,n}(s)\psi^{(1,3,2)}_{a_2,n}(s)$$
$$\times 8\alpha(2)(-k^6)+B_j^2(\psi^{(1,3,J)}_{a_2,n}(s))^2$$
$$\times 2\alpha(2)(-k^6)\left(\frac{5}{3}s+4k^2\right)\Bigg]=1$$

and

$$\int\limits_{4m^2}^{\infty}\frac{ds}{\pi}\rho(s)\Bigg[A_1A_2(\psi^{(1,1,2)}_{a_2,n}(s))^2 \tag{D.4}$$
$$\times 2\alpha(2)(-k^2)\left(\frac{5}{2}s+4k^2\right)$$
$$+(A_1B_2+A_2B_1)\psi^{(1,1,2)}_{a_2,n}(s)\psi^{(1,3,2)}_{a_2,n}(s)$$
$$\times 8\alpha(2)(-k^6)+B_1B_2(\psi^{(1,3,2)}_{a_2,n}(s))^2\cdot 2\alpha(2)(-k^6)$$
$$\times\left(\frac{5}{3}s+4k^2\right)\Bigg]=0.$$

*Equations for the $\omega$ and $\phi$ $(M^2,n)$ Trajectories*

We have four trajectories in this sector with the following states located on the $(n,M^2)$ trajectories [15]:

(i) $S$-wave dominant states: $\omega(780)$ with $n=1$, $\omega(1420)$ with $n=2$, $\omega(1800)$ with $n=3$, $\omega(2150)$ with $n=4$;

(ii) $D$-wave dominant states: $\omega(1640)$ with $n=1$, $\omega(1920)$ with $n=2$, $\omega(2295)$ with $n=3$;

(iii) $S$-wave dominant states: $\phi(1020)$ with $n=1$, $\phi(1660)$ with $n=2$, $\phi(1950)$ with $n=3$;

(iv) $D$-wave dominant states: $\phi(1700)$ with $n=1$.

Correspondingly, we have four coupled equations for four wave functions.

The first one reads as follows:

$$(s-M^2)\Bigg[4\psi^{(1,0,1)}_{\omega(n\bar n),n}(s)A_j\cos\Theta_n \tag{D.5}$$
$$+\left(\frac{3}{2}s+4k^2\right)\psi^{(1,2,1)}_{\omega(n\bar n),n}(s)B_j\cos\Theta'_n\Bigg]$$
$$=\int\limits_{4m^2}^{\infty}\frac{ds'}{\pi}\rho(s')\cdot 8\psi^{(1,0,1)}_{\omega(n\bar n),n}(s')A_j\cos\Theta_n$$
$$\times\Bigg[\frac{3}{10}\left(s+\frac{8}{3}k^2\right)k'^4\widetilde V^{(2)}_{(n\bar n\to n\bar n),V}(s,s')$$
$$+\frac{1}{3}\sqrt{ss'}k'^2\widetilde V^{(1)}_{(n\bar n\to n\bar n),A}(s,s')$$
$$-\frac{4}{3}m^2k'^2\widetilde V^{(1)}_{(n\bar n\to n\bar n),S}(s,s')$$
$$+\left(s'+\frac{4}{3}k'^2\right)\widetilde V^{(0)}_{(n\bar n\to n\bar n),V}(s,s')\Bigg]$$
$$+\int\limits_{4m^2}^{\infty}\frac{ds'}{\pi}\rho(s')\cdot 2k'^4\psi^{(1,2,1)}_{\omega(n\bar n),n}(s')B_j\cos\Theta'_n$$
$$\times\Bigg[m^2\frac{18}{5}\sqrt{ss'}\widetilde V^{(2)}_{(n\bar n\to n\bar n),T}(s,s')$$
$$+\frac{3}{10}\left(\frac{3}{2}ss'+4s'k^2+4sk'^2+\frac{32}{3}k^2k'^2\right)$$
$$\times\widetilde V^{(2)}_{(n\bar n\to n\bar n),V}(s,s')-m^2\frac{16}{3}\widetilde V^{(1)}_{(n\bar n\to n\bar n),S}(s,s')$$
$$-\frac{2}{3}\sqrt{ss'}\widetilde V^{(1)}_{(n\bar n\to n\bar n),A}(s,s')+\frac{16}{3}\widetilde V^{(0)}_{(n\bar n\to n\bar n),V}(s,s')\Bigg]$$
$$+\int\limits_{4m_s^2}^{\infty}\frac{ds'}{\pi}\rho_s(s')\cdot 8\psi^{(1,0,1)}_{\omega(s\bar s),n}(s')A_j\sin\Theta_n$$
$$\times\Bigg[\frac{3}{10}\left(s+\frac{8}{3}k^2\right)k_s'^4\widetilde V^{(2)}_{(s\bar s\to n\bar n),V}(s,s')$$
$$+\frac{1}{3}\sqrt{ss'}k_s'^2\widetilde V^{(1)}_{(s\bar s\to n\bar n),A}(s,s')$$
$$-\frac{4}{3}mm_sk_s'^2\widetilde V^{(1)}_{(s\bar s\to n\bar n),S}(s,s')$$
$$+\left(s'+\frac{4}{3}k_s'^2\right)\widetilde V^{(0)}_{(s\bar s\to n\bar n),V}(s,s')\Bigg]$$
$$+\int\limits_{4m_s^2}^{\infty}\frac{ds'}{\pi}\rho_s(s')\cdot 2k_s'^4\psi^{(1,2,1)}_{\omega(s\bar s),n}(s')B_j\sin\Theta'_n$$
$$\times\Bigg[mm_s\frac{18}{5}\sqrt{ss'}\widetilde V^{(2)}_{(s\bar s\to n\bar n),T}(s,s')$$
$$+\frac{3}{10}\left(\frac{3}{2}ss'+4s'k^2+4sk_s'^2+\frac{32}{3}k^2k_s'^2\right)$$
$$\times\widetilde V^{(2)}_{(s\bar s\to n\bar n),V}(s,s')-mm_s\frac{16}{3}\widetilde V^{(1)}_{(s\bar s\to n\bar n),S}(s,s')$$
$$-\frac{2}{3}\sqrt{ss'}\widetilde V^{(1)}_{(s\bar s\to n\bar n),A}(s,s')+\frac{16}{3}\widetilde V^{(0)}_{(s\bar s\to n\bar n),V}(s,s')\Bigg];$$

the second one:

$$(s-M^2)\Bigg[4\psi^{(1,0,1)}_{\omega(s\bar s),n}(s)A_j\sin\Theta_n \tag{D.6}$$
$$+\left(\frac{3}{2}s+4k_s^2\right)\psi^{(1,2,1)}_{\omega(s\bar s),n}(s)B_j\sin\Theta'_n\Bigg]$$
$$=\int\limits_{4m^2}^{\infty}\frac{ds'}{\pi}\rho(s')\cdot 8\psi^{(1,0,1)}_{\omega(n\bar n),n}(s')A_j\cos\Theta_n$$
$$\times\Bigg[\frac{3}{10}\left(s+\frac{8}{3}k_s^2\right)k'^4\widetilde V^{(2)}_{(n\bar n\to s\bar s),V}(s,s')$$
$$+\frac{1}{3}\sqrt{ss'}k'^2\widetilde V^{(1)}_{(n\bar n\to s\bar s),A}(s,s')$$

$$
\begin{aligned}
&- \frac{4}{3} m m_s k'^2 \widetilde{V}^{(1)}_{(n\bar n\to s\bar s),S}(s,s') \\
&+ \left(s' + \frac{4}{3}k'^2\right)\widetilde{V}^{(0)}_{(n\bar n\to s\bar s),V}(s,s')\Big] \\
&+ \int\limits_{4m^2}^{\infty} \frac{ds'}{\pi}\rho(s')\cdot 2k'^4\psi^{(1,2,1)}_{\omega(n\bar n),n}(s')B_j\cos\Theta'_n \\
&\times\Big[m m_s \frac{18}{5}\sqrt{ss'}\widetilde{V}^{(2)}_{(n\bar n\to s\bar s),T}(s,s') \\
&+\frac{3}{10}\left(\frac{3}{2} ss' + 4s'k_s^2 + 4sk'^2 + \frac{32}{3}k_s^2k'^2\right) \\
&\times \widetilde{V}^{(2)}_{(n\bar n\to s\bar s),V}(s,s') - m m_s\frac{16}{3}\widetilde{V}^{(1)}_{(n\bar n\to s\bar s),S}(s,s') \\
&-\frac{2}{3}\sqrt{ss'}\widetilde{V}^{(1)}_{(n\bar n\to s\bar s),A}(s,s') + \frac{16}{3}\widetilde{V}^{(0)}_{(n\bar n\to s\bar s),V}(s,s')\Big] \\
&+\int\limits_{4m_s^2}^{\infty} \frac{ds'}{\pi}\rho_s(s')\cdot 8\psi^{(1,0,1)}_{\omega(s\bar s),n}(s')A_j\sin\Theta_n \\
&\times\Big[\frac{3}{10}\left(s+\frac{8}{3} k_s^2\right)k_s'^4\widetilde{V}^{(2)}_{(s\bar s\to s\bar s),V}(s,s') \\
&+\frac{1}{3}\sqrt{ss'}k_s'^2\widetilde{V}^{(1)}_{(s\bar s\to s\bar s),A}(s,s') \\
&-\frac{4}{3} m_s^2 k_s'^2 \widetilde{V}^{(1)}_{(s\bar s\to s\bar s),S}(s,s') \\
&+\left(s'+\frac{4}{3} k_s'^2\right)\widetilde{V}^{(0)}_{(s\bar s\to s\bar s),V}(s,s')\Big] \\
&+\int\limits_{4m_s^2}^{\infty} \frac{ds'}{\pi}\rho_s(s')\cdot 2k_s'^4\psi^{(1,2,1)}_{\omega(s\bar s),n}(s')B_j\sin\Theta'_n \\
&\times\Big[m_s^2\frac{18}{5}\sqrt{ss'}\widetilde{V}^{(2)}_{(s\bar s\to s\bar s),T}(s,s') \\
&+\frac{3}{10}\left(\frac{3}{2} ss' + 4s'k_s^2+4sk_s'^2+\frac{32}{3}k_s^2k_s'^2\right) \\
&\times\widetilde{V}^{(2)}_{(s\bar s\to s\bar s),V}(s,s') - m_s^2\frac{16}{3}\widetilde{V}^{(1)}_{(s\bar s\to s\bar s),S}(s,s') \\
&-\frac{2}{3}\sqrt{ss'}\widetilde{V}^{(1)}_{(s\bar s\to s\bar s),A}(s,s')+\frac{16}{3}\widetilde{V}^{(0)}_{(s\bar s\to s\bar s),V}(s,s')\Big];
\end{aligned}
$$

the third one:

$$
\begin{aligned}
&(s-M^2)[(3s+4k^2)\psi^{(1,0,1)}_{\omega(n\bar n),n}(s) \\
&\times A_j\cos\Theta_n + 4k^4\psi^{(1,2,1)}_{\omega(n\bar n),n}(s)B_j\cos\Theta'_n] \\
&=\int\limits_{4m^2}^{\infty}\frac{ds'}{\pi}\rho(s')\cdot 2\psi^{(1,0,1)}_{\omega(n\bar n),n}(s')A_j\cos\Theta_n \\
&\times\Big[24m^2\sqrt{ss'}\widetilde{V}^{(0)}_{(n\bar n\to n\bar n),T}(s,s') + \Big(3ss'+4s'k^2 \\
&+4sk'^2+\frac{16}{3}k^2k'^2\Big)\widetilde{V}^{(0)}_{(n\bar n\to n\bar n),V}(s,s') \\
&-m^2\frac{16}{3}k^2k'^2\widetilde{V}^{(1)}_{(n\bar n\to n\bar n),S}(s,s') \\
&-\frac{8}{3}\sqrt{ss'}k^2k'^2\widetilde{V}^{(1)}_{(n\bar n\to n\bar n),A}(s,s') \\
&+\frac{16}{5}k^4k'^4\widetilde{V}^{(2)}_{(n\bar n\to n\bar n),V}(s,s')\Big] \\
&+\int\limits_{4m^2}^{\infty} \frac{ds'}{\pi}\rho(s')\cdot 8k'^4\psi^{(1,2,1)}_{\omega(n\bar n),n}(s')B_j\cos\Theta'_n \\
&\times\Big[\frac{3}{10}\left(s'+\frac{8}{3}k'^2\right)k^4\widetilde{V}^{(2)}_{(n\bar n\to n\bar n),V}(s,s') \\
&+\frac{1}{3}\sqrt{ss'}k^2\widetilde{V}^{(1)}_{(n\bar n\to n\bar n),A}(s,s') \\
&-m^2\frac{4}{3}k^2\widetilde{V}^{(1)}_{(n\bar n\to n\bar n),S}(s,s') \\
&+\left(s+\frac{4}{3}k^2\right)\widetilde{V}^{(0)}_{(n\bar n\to n\bar n),V}(s,s')\Big] \\
&+\int\limits_{4m_s^2}^{\infty}\frac{ds'}{\pi}\rho_s(s')\cdot 2\psi^{(1,0,1)}_{\omega(s\bar s),n}(s')A_j\sin\Theta_n \\
&\times\Big[24mm_s\sqrt{ss'}\widetilde{V}^{(0)}_{(s\bar s\to n\bar n),T}(s,s')+\Big(3ss' \\
&+4s'k^2+4sk_s'^2+\frac{16}{3}k^2k_s'^2\Big)\widetilde{V}^{(0)}_{(s\bar s\to n\bar n),V}(s,s') \\
&-mm_s\frac{16}{3}k^2k_s'^2\widetilde{V}^{(1)}_{(s\bar s\to n\bar n),S}(s,s') \\
&-\frac{8}{3}\sqrt{ss'}k^2k_s'^2\widetilde{V}^{(1)}_{(s\bar s\to n\bar n),A}(s,s') \\
&+\frac{16}{5}k^4k_s'^4\widetilde{V}^{(2)}_{(s\bar s\to n\bar n),V}(s,s')\Big] \\
&+\int\limits_{4m_s^2}^{\infty}\frac{ds'}{\pi}\rho_s(s')\cdot 8k_s'^4\psi^{(1,2,1)}_{\omega(s\bar s),n}(s')B_j\sin\Theta'_n \\
&\times\Big[\frac{3}{10}\left(s'+\frac{8}{3}k_s'^2\right)k^4\widetilde{V}^{(2)}_{(s\bar s\to n\bar n),V}(s,s') \\
&+\frac{1}{3}\sqrt{ss'}k^2\widetilde{V}^{(1)}_{(s\bar s\to n\bar n),A}(s,s') \\
&-mm_s\frac{4}{3}k^2\widetilde{V}^{(1)}_{(s\bar s\to n\bar n),S}(s,s') \\
&+\left(s+\frac{4}{3}k^2\right)\widetilde{V}^{(0)}_{(s\bar s\to n\bar n),V}(s,s')\Big];
\end{aligned}
\tag{D.7}
$$

and the fourth equation:

$$(s-M^2)\Big[(3s+4k_s^2)\psi^{(1,0,1)}_{\omega(s\bar s),n}(s) \qquad \text{(D.8)}$$

$$\times A_j\sin\Theta_n + 4k_s^4\psi^{(1,2,1)}_{\omega(s\bar s),n}(s)B_j\sin\Theta'_n\Big]$$

$$=\int\limits_{4m^2}^{\infty}\frac{ds'}{\pi}\rho(s')\cdot 2\psi^{(1,0,1)}_{\omega(n\bar n),n}(s')A_j\cos\Theta_n$$

$$\times\Big[24mm_s\sqrt{ss'}\widetilde V^{(0)}_{(n\bar n\to s\bar s),T}(s,s')+\Big(3ss'$$

$$+4s'k_s^2+4sk'^2+\frac{16}{3}k_s^2k'^2\Big)\widetilde V^{(0)}_{(n\bar n\to s\bar s),V}(s,s')$$

$$-mm_s\frac{16}{3}k_s^2k'^2\widetilde V^{(1)}_{(n\bar n\to s\bar s),S}(s,s')$$

$$-\frac{8}{3}\sqrt{ss'}k_s^2k'^2\widetilde V^{(1)}_{(n\bar n\to s\bar s),A}(s,s')$$

$$+\frac{16}{5}k_s^4k'^4\widetilde V^{(2)}_{(n\bar n\to s\bar s),V}(s,s')\Big]$$

$$+\int\limits_{4m^2}^{\infty}\frac{ds'}{\pi}\rho(s')\cdot 8k'^4\psi^{(1,2,1)}_{\omega(n\bar n),n}(s')B_j\cos\Theta'_n$$

$$\times\Big[\frac{3}{10}\Big(s'+\frac{8}{3}k'^2\Big)k_s^4\widetilde V^{(2)}_{(n\bar n\to s\bar s),V}(s,s')$$

$$+\frac{1}{3}\sqrt{ss'}k_s^2\widetilde V^{(1)}_{(n\bar n\to s\bar s),A}(s,s')$$

$$-mm_s\frac{4}{3}k_s^2\widetilde V^{(1)}_{(n\bar n\to s\bar s),S}(s,s')$$

$$+\Big(s+\frac{4}{3}k_s^2\Big)\widetilde V^{(0)}_{(n\bar n\to s\bar s),V}(s,s')\Big]$$

$$+\int\limits_{4m_s^2}^{\infty}\frac{ds'}{\pi}\rho_s(s')\cdot 2\psi^{(1,0,1)}_{\omega(s\bar s),n}(s')A_j\sin\Theta_n$$

$$\times\Big[24m_s^2\sqrt{ss'}\widetilde V^{(0)}_{(s\bar s\to s\bar s),T}(s,s')+\Big(3ss'$$

$$+4s'k_s^2+4sk_s'^2+\frac{16}{3}k_s^2k_s'^2\Big)\widetilde V^{(0)}_{(s\bar s\to s\bar s),V}(s,s')$$

$$-m_s^2\frac{16}{3}k_s^2k_s'^2\widetilde V^{(1)}_{(s\bar s\to s\bar s),S}(s,s')$$

$$-\frac{8}{3}\sqrt{ss'}k_s^2k_s'^2\widetilde V^{(1)}_{(s\bar s\to s\bar s),A}(s,s')$$

$$+\frac{16}{5}k_s^4k_s'^4\widetilde V^{(2)}_{(s\bar s\to s\bar s),V}(s,s')\Big]$$

$$+\int\limits_{4m_s^2}^{\infty}\frac{ds'}{\pi}\rho_s(s')\cdot 8k_s'^4\psi^{(1,2,1)}_{\omega(s\bar s),n}(s')B_j\sin\Theta'_n$$

$$\times\Big[\frac{3}{10}\Big(s'+\frac{8}{3}k_s'^2\Big)k_s^4\widetilde V^{(2)}_{(s\bar s\to s\bar s),V}(s,s')$$

$$+\frac{1}{3}\sqrt{ss'}k_s^2\widetilde V^{(1)}_{(s\bar s\to s\bar s),A}(s,s')$$

$$-m_s^2\frac{4}{3}k_s^2\widetilde V^{(1)}_{(s\bar s\to s\bar s),S}(s,s')$$

$$+\Big(s+\frac{4}{3}k_s^2\Big)\widetilde V^{(0)}_{(s\bar s\to s\bar s),V}(s,s')\Big].$$

### *Equations for the $f_2$ $(n,M^2)$ Trajectories*

The $f_2$ mesons lay on the following four trajectories in the $(n,M^2)$ plane [15]:

(i) dominantly $P$-wave states: $f_2(1285)$ with $n=1$, $f_2(1640)$ at $n=2$, $f_2(1950)$ with $n=3$, $f_2(2210)$ with $n=4$;

(ii) dominantly $P$-wave states: $f_2(1525)$ with $n=1$, $f_2(1790)$ with $n=2$;

(iii) dominantly $F$-wave states: $f_2(2020)$ with $n=1$, $f_2(2290)$ with $n=2$;

(iv) dominantly $F$-wave state: $f_2(2200)$ with $n=1$.

We have four equations for these four sets of states: the first one,

$$(s-M^2)\Big[4\psi^{(1,1,2)}_{f_2(n\bar n),n}(s)A_j\cos\Theta_n \qquad \text{(D.9)}$$

$$+\Big(\frac{5}{3}s+4k^2\Big)\psi^{(1,3,2)}_{f_2(n\bar n),n}(s)B_j\cos\Theta'_n\Big]$$

$$=\int\limits_{4m^2}^{\infty}\frac{ds'}{\pi}\rho(s')\cdot 8(-k'^2)\psi^{(1,1,2)}_{f_2(n\bar n),n}(s')A_j\cos\Theta_n$$

$$\times\Big[\frac{5}{14}\Big(s+\frac{12}{5}k^2\Big)k'^4\widetilde V^{(3)}_{(n\bar n\to n\bar n),V}(s,s')$$

$$+\frac{3}{10}\sqrt{ss'}k'^2\widetilde V^{(2)}_{(n\bar n\to n\bar n),A}(s,s')$$

$$-\frac{6}{5}m^2k'^2\widetilde V^{(2)}_{(n\bar n\to n\bar n),S}(s,s')$$

$$+\frac{1}{3}\Big(s'+\frac{8}{5}k'^2\Big)\widetilde V^{(1)}_{(n\bar n\to n\bar n),V}(s,s')\Big]$$

$$-\int\limits_{4m^2}^{\infty}\frac{ds'}{\pi}\rho(s')\cdot 2k'^6\psi^{(1,3,2)}_{f_2(n\bar n),n}(s')B_j\cos\Theta'_n$$

$$\times\Big[m^2\frac{100}{21}\sqrt{ss'}\widetilde V^{(3)}_{(n\bar n\to n\bar n),T}(s,s')$$

$$+\frac{5}{14}\Big(\frac{5}{3}ss'+4s'k^2+4sk'^2+\frac{48}{5}k^2k'^2\Big)$$

$$\times\widetilde V^{(3)}_{(n\bar n\to n\bar n),V}(s,s')-m^2\frac{24}{5}\widetilde V^{(2)}_{(n\bar n\to n\bar n),S}(s,s')$$

$$
\begin{aligned}
&- \frac{4}{5}\sqrt{ss'}\widetilde{V}^{(2)}_{(n\bar{n}\to n\bar{n}),A}(s,s') \\
&+ \frac{32}{15}\widetilde{V}^{(1)}_{(n\bar{n}\to n\bar{n}),V}(s,s')\Bigg] \\
&+ \int\limits_{4m_s^2}^{\infty} \frac{ds'}{\pi}\rho_s(s') \cdot 8(-k_s'^2)\psi^{(1,1,2)}_{f_2(s\bar{s}),n}(s')A_j \sin\Theta_n \\
&\times \left[\frac{5}{14}\left(s + \frac{12}{5}k^2\right)k_s'^4\widetilde{V}^{(3)}_{(s\bar{s}\to n\bar{n}),V}(s,s')\right. \\
&+ \frac{3}{10}\sqrt{ss'}k_s'^2\widetilde{V}^{(2)}_{(s\bar{s}\to n\bar{n}),A}(s,s') \\
&- \frac{6}{5}mm_s k_s'^2\widetilde{V}^{(2)}_{(s\bar{s}\to n\bar{n}),S}(s,s') \\
&\left.+ \frac{1}{3}\left(s' + \frac{8}{5}k_s'^2\right)\widetilde{V}^{(1)}_{(s\bar{s}\to n\bar{n}),V}(s,s')\right] \\
&- \int\limits_{4m_s^2}^{\infty} \frac{ds'}{\pi}\rho_s(s') \cdot 2k_s'^6\psi^{(1,3,2)}_{f_2(s\bar{s}),n}(s')B_j \sin\Theta'_n \\
&\times \Bigg[mm_s\frac{100}{21}\sqrt{ss'}\widetilde{V}^{(3)}_{(s\bar{s}\to n\bar{n}),T}(s,s') \\
&+ \frac{5}{14}\left(\frac{5}{3}ss' + 4s'k^2 + 4sk_s'^2 + \frac{48}{5}k^2k_s'^2\right) \\
&\times \widetilde{V}^{(3)}_{(s\bar{s}\to n\bar{n}),V}(s,s') - mm_s\frac{24}{5}\widetilde{V}^{(2)}_{(s\bar{s}\to n\bar{n}),S}(s,s') \\
&- \frac{4}{5}\sqrt{ss'}\widetilde{V}^{(2)}_{(s\bar{s}\to n\bar{n}),A}(s,s') \\
&+ \frac{32}{15}\widetilde{V}^{(1)}_{(s\bar{s}\to n\bar{n}),V}(s,s')\Bigg];
\end{aligned}
$$

the second one,

$$
\begin{aligned}
&(s - M^2)\Bigg[4\psi^{(1,1,2)}_{f_2(s\bar{s}),n}(s)A_j \sin\Theta_n \qquad \text{(D.10)} \\
&+ \left(\frac{5}{3}s + 4k_s^2\right)\psi^{(1,3,2)}_{f_2(s\bar{s}),n}(s)B_j \sin\Theta'_n\Bigg] \\
&= \int\limits_{4m^2}^{\infty} \frac{ds'}{\pi}\rho(s') \cdot 8(-k'^2)\psi^{(1,1,2)}_{f_2(n\bar{n}),n}(s')A_j \cos\Theta_n \\
&\times \left[\frac{5}{14}\left(s + \frac{12}{5}k_s^2\right)k'^4\widetilde{V}^{(3)}_{(n\bar{n}\to s\bar{s}),V}(s,s')\right. \\
&+ \frac{3}{10}\sqrt{ss'}k'^2\widetilde{V}^{(2)}_{(n\bar{n}\to s\bar{s}),A}(s,s') \\
&- \frac{6}{5}mm_s k'^2\widetilde{V}^{(2)}_{(n\bar{n}\to s\bar{s}),S}(s,s') \\
&\left.+ \frac{1}{3}\left(s' + \frac{8}{5}k'^2\right)\widetilde{V}^{(1)}_{(n\bar{n}\to s\bar{s}),V}(s,s')\right] \\
&- \int\limits_{4m^2}^{\infty} \frac{ds'}{\pi}\rho(s') \cdot 2k'^6\psi^{(1,3,2)}_{f_2(n\bar{n}),n}(s')B_j \cos\Theta'_n \\
&\times \Bigg[mm_s\frac{100}{21}\sqrt{ss'}\widetilde{V}^{(3)}_{(n\bar{n}\to s\bar{s}),T}(s,s') + \frac{5}{14}\Bigg(\frac{5}{3}ss' \\
&+ 4s'k_s^2 + 4sk'^2 + \frac{48}{5}k_s^2k'^2\Bigg)\widetilde{V}^{(3)}_{(n\bar{n}\to s\bar{s}),V}(s,s') \\
&- mm_s\frac{24}{5}\widetilde{V}^{(2)}_{(n\bar{n}\to s\bar{s}),S}(s,s') \\
&- \frac{4}{5}\sqrt{ss'}\widetilde{V}^{(2)}_{(n\bar{n}\to s\bar{s}),A}(s,s') \\
&+ \frac{32}{15}\widetilde{V}^{(1)}_{(n\bar{n}\to s\bar{s}),V}(s,s')\Bigg] \\
&+ \int\limits_{4m_s^2}^{\infty} \frac{ds'}{\pi}\rho_s(s') \cdot 8(-k_s'^2)\psi^{(1,1,2)}_{f_2(s\bar{s}),n}(s')A_j \sin\Theta_n \\
&\times \left[\frac{5}{14}\left(s + \frac{12}{5}k_s^2\right)k_s'^4\widetilde{V}^{(3)}_{(s\bar{s}\to s\bar{s}),V}(s,s')\right. \\
&+ \frac{3}{10}\sqrt{ss'}k_s'^2\widetilde{V}^{(2)}_{(s\bar{s}\to s\bar{s}),A}(s,s') \\
&- \frac{6}{5}m_s^2k_s'^2\widetilde{V}^{(2)}_{(s\bar{s}\to s\bar{s}),S}(s,s') \\
&\left.+ \frac{1}{3}\left(s' + \frac{8}{5}k_s'^2\right)\widetilde{V}^{(1)}_{(s\bar{s}\to s\bar{s}),V}(s,s')\right] \\
&- \int\limits_{4m_s^2}^{\infty} \frac{ds'}{\pi}\rho_s(s') \cdot 2k_s'^6\psi^{(1,3,2)}_{f_2(s\bar{s}),n}(s')B_j \sin\Theta'_n \\
&\times \Bigg[m_s^2\frac{100}{21}\sqrt{ss'}\widetilde{V}^{(3)}_{(s\bar{s}\to s\bar{s}),T}(s,s') \\
&+ \frac{5}{14}\left(\frac{5}{3}ss' + 4s'k_s^2 + 4sk_s'^2 + \frac{48}{5}k_s^2k_s'^2\right) \\
&\times \widetilde{V}^{(3)}_{(s\bar{s}\to s\bar{s}),V}(s,s') - m_s^2\frac{24}{5}\widetilde{V}^{(2)}_{(s\bar{s}\to s\bar{s}),S}(s,s') \\
&- \frac{4}{5}\sqrt{ss'}\widetilde{V}^{(2)}_{(s\bar{s}\to s\bar{s}),A}(s,s') \\
&+ \frac{32}{15}\widetilde{V}^{(1)}_{(s\bar{s}\to s\bar{s}),V}(s,s')\Bigg],
\end{aligned}
$$

the third one;

$$
\begin{aligned}
&(s - M^2)\Bigg[\left(\frac{5}{2}s + 4k^2\right)\psi^{(1,1,2)}_{f_2(n\bar{n}),n}(s) \qquad \text{(D.11)} \\
&\times A_j \cos\Theta_n + 4k^4\psi^{(1,3,2)}_{f_2(n\bar{n}),n}(s)B_j \cos\Theta'_n\Bigg] \\
&= \int\limits_{4m^2}^{\infty} \frac{ds'}{\pi}\rho(s') \cdot 2(-k'^2)\psi^{(1,1,2)}_{f_2(n\bar{n}),n}(s')A_j \cos\Theta_n
\end{aligned}
$$

$$
\begin{aligned}
&\times \Big[m^2 \frac{20}{3}\sqrt{ss'}\widetilde{V}^{(1)}_{(n\bar{n}\to n\bar{n}),T}(s,s') \\
&+ \frac{1}{3}\left(\frac{5}{2}ss' + 4s'k^2 + 4sk'^2 + \frac{32}{5}k^2k'^2\right) \\
&\times \widetilde{V}^{(1)}_{(n\bar{n}\to n\bar{n}),V}(s,s') - m^2\frac{24}{5}k^2k'^2\widetilde{V}^{(2)}_{(n\bar{n}\to n\bar{n}),S} \\
&\times (s,s') - \frac{9}{5}\sqrt{ss'}k^2k'^2\widetilde{V}^{(2)}_{(n\bar{n}\to n\bar{n}),A}(s,s') \\
&+ \frac{24}{7}k^4k'^4\widetilde{V}^{(3)}_{(n\bar{n}\to n\bar{n}),V}(s,s')\Big] \\
&- \int\limits_{4m^2}^{\infty}\frac{ds'}{\pi}\rho(s')\cdot 8k'^6\psi^{(1,3,2)}_{f_2(n\bar{n}),n}(s')B_j\cos\Theta'_n \\
&\times \left[\frac{5}{14}\left(s' + \frac{12}{5}k'^2\right)k^4\widetilde{V}^{(3)}_{(n\bar{n}\to n\bar{n}),V}(s,s')\right. \\
&+ \frac{3}{10}\sqrt{ss'}k^2\widetilde{V}^{(2)}_{(n\bar{n}\to n\bar{n}),A}(s,s') \\
&- m^2\frac{6}{5}k^2\widetilde{V}^{(2)}_{(n\bar{n}\to n\bar{n}),S}(s,s') \\
&\left.+ \frac{1}{3}\left(s + \frac{8}{5}k^2\right)\widetilde{V}^{(1)}_{(n\bar{n}\to n\bar{n}),V}(s,s')\right] \\
&+ \int\limits_{4m_s^2}^{\infty}\frac{ds'}{\pi}\rho_s(s')\cdot 2(-k'^2_s)\psi^{(1,1,2)}_{f_2(s\bar{s}),n}(s')A_j\sin\Theta_n \\
&\times \Big[mm_s\frac{20}{3}\sqrt{ss'}\widetilde{V}^{(1)}_{(s\bar{s}\to n\bar{n}),T}(s,s') \\
&+ \frac{1}{3}\left(\frac{5}{2}ss' + 4s'k^2 + 4sk'^2_s + \frac{32}{5}k^2k'^2_s\right) \\
&\times \widetilde{V}^{(1)}_{(s\bar{s}\to n\bar{n}),V}(s,s') - mm_s\frac{24}{5}k^2k'^2_s\widetilde{V}^{(2)}_{(s\bar{s}\to n\bar{n}),S} \\
&\times (s,s') - \frac{9}{5}\sqrt{ss'}k^2k'^2_s\widetilde{V}^{(2)}_{(s\bar{s}\to n\bar{n}),A}(s,s') \\
&+ \frac{24}{7}k^4k'^4_s\widetilde{V}^{(3)}_{(s\bar{s}\to n\bar{n}),V}(s,s')\Big] \\
&- \int\limits_{4m_s^2}^{\infty}\frac{ds'}{\pi}\rho_s(s')\cdot 8k'^6_s\psi^{(1,3,2)}_{f_2(s\bar{s}),n}(s')B_j\sin\Theta'_n \\
&\times \left[\frac{5}{14}\left(s' + \frac{12}{5}k'^2_s\right)k^4\widetilde{V}^{(3)}_{(s\bar{s}\to n\bar{n}),V}(s,s')\right. \\
&+ \frac{3}{10}\sqrt{ss'}k^2\widetilde{V}^{(2)}_{(s\bar{s}\to n\bar{n}),A}(s,s') \\
&- mm_s\frac{6}{5}k^2\widetilde{V}^{(2)}_{(s\bar{s}\to n\bar{n}),S}(s,s') \\
&\left.+ \frac{1}{3}\left(s + \frac{8}{5}k^2\right)\widetilde{V}^{(1)}_{(s\bar{s}\to n\bar{n}),V}(s,s')\right];
\end{aligned}
$$

and the fourth equation,

$$
\begin{aligned}
&(s - M^2)\Big[\left(\frac{5}{2}s + 4k_s^2\right)\psi^{(1,1,2)}_{f_2(s\bar{s}),n}(s) \qquad \text{(D.12)} \\
&\times A_j\sin\Theta_n + 4k_s^4\psi^{(1,3,2)}_{f_2(s\bar{s}),n}(s)B_j\sin\Theta'_n\Big] \\
&= \int\limits_{4m^2}^{\infty}\frac{ds'}{\pi}\rho(s')\cdot 2(-k'^2)\psi^{(1,1,2)}_{f_2(n\bar{n}),n}(s')A_j\cos\Theta_n \\
&\times \Big[mm_s\frac{20}{3}\sqrt{ss'}\widetilde{V}^{(1)}_{(n\bar{n}\to s\bar{s}),T}(s,s') \\
&+ \frac{1}{3}\left(\frac{5}{2}ss' + 4s'k_s^2 + 4sk'^2 + \frac{32}{5}k_s^2k'^2\right) \\
&\times \widetilde{V}^{(1)}_{(n\bar{n}\to s\bar{s}),V}(s,s') - mm_s\frac{24}{5}k_s^2k'^2\widetilde{V}^{(2)}_{(n\bar{n}\to s\bar{s}),S} \\
&\times (s,s') - \frac{9}{5}\sqrt{ss'}k_s^2k'^2\widetilde{V}^{(2)}_{(n\bar{n}\to s\bar{s}),A}(s,s') \\
&+ \frac{24}{7}k_s^4k'^4\widetilde{V}^{(3)}_{(n\bar{n}\to s\bar{s}),V}(s,s')\Big] \\
&- \int\limits_{4m^2}^{\infty}\frac{ds'}{\pi}\rho(s')\cdot 8k'^6\psi^{(1,3,2)}_{f_2(n\bar{n}),n}(s')B_j\cos\Theta'_n \\
&\times \left[\frac{5}{14}\left(s' + \frac{12}{5}k'^2\right)k_s^4\widetilde{V}^{(3)}_{(n\bar{n}\to s\bar{s}),V}(s,s')\right. \\
&+ \frac{3}{10}\sqrt{ss'}k_s^2\widetilde{V}^{(2)}_{(n\bar{n}\to s\bar{s}),A}(s,s') \\
&- mm_s\frac{6}{5}k_s^2\widetilde{V}^{(2)}_{(n\bar{n}\to s\bar{s}),S}(s,s') \\
&\left.+ \frac{1}{3}\left(s + \frac{8}{5}k_s^2\right)\widetilde{V}^{(1)}_{(n\bar{n}\to s\bar{s}),V}(s,s')\right] \\
&+ \int\limits_{4m_s^2}^{\infty}\frac{ds'}{\pi}\rho_s(s')\cdot 2(-k'^2_s)\psi^{(1,1,2)}_{f_2(s\bar{s}),n}(s')A_j\sin\Theta_n \\
&\times \Big[m_s^2\frac{20}{3}\sqrt{ss'}\widetilde{V}^{(1)}_{(s\bar{s}\to s\bar{s}),T}(s,s') \\
&+ \frac{1}{3}\left(\frac{5}{2}ss' + 4s'k_s^2 + 4sk'^2_s + \frac{32}{5}k_s^2k'^2_s\right) \\
&\times \widetilde{V}^{(1)}_{(s\bar{s}\to s\bar{s}),V}(s,s') - m_s^2\frac{24}{5}k_s^2k'^2_s\widetilde{V}^{(2)}_{(s\bar{s}\to s\bar{s}),S} \\
&\times (s,s') - \frac{9}{5}\sqrt{ss'}k_s^2k'^2_s\widetilde{V}^{(2)}_{(s\bar{s}\to s\bar{s}),A}(s,s') \\
&+ \frac{24}{7}k_s^4k'^4_s\widetilde{V}^{(3)}_{(s\bar{s}\to s\bar{s}),V}(s,s')\Big] \\
&- \int\limits_{4m_s^2}^{\infty}\frac{ds'}{\pi}\rho_s(s')\cdot 8k'^6_s\psi^{(1,3,2)}_{f_2(s\bar{s}),n}(s')B_j\sin\Theta'_n
\end{aligned}
$$

$$\times \left[\frac{5}{14}\left(s' + \frac{12}{5}k_s'^2\right) k_s^4 \widetilde{V}^{(3)}_{(s\bar{s}\to s\bar{s}),V}(s,s') + \frac{3}{10}\sqrt{ss'}k_s^2\widetilde{V}^{(2)}_{(s\bar{s}\to s\bar{s}),A}(s,s') - m_s^2\frac{6}{5}k_s^2\widetilde{V}^{(2)}_{(s\bar{s}\to s\bar{s}),S}(s,s') + \frac{1}{3}\left(s + \frac{8}{5}k_s^2\right)\widetilde{V}^{(1)}_{(s\bar{s}\to s\bar{s}),V}(s,s')\right].$$

## REFERENCES

1. E. Salpeter and H. A. Bethe, Phys. Rev. **84**, 1232 (1951); E. Salpeter, Phys. Rev. **91**, 994 (1953).
2. G. F. Chew, *The Analytic S Matrix* (Benjamin, New York, 1966); G. F. Chew and S. Mandelstam, Phys. Rev. **119**, 467 (1960).
3. V. V. Anisovich, M. N. Kobrinsky, D. I. Melikhov, and A. V. Sarantsev, Nucl. Phys. A **544**, 747 (1992).
4. A. V. Anisovich and V. A. Sadovnikova, Yad. Fiz. **55**, 2657 (1992) [Sov. J. Nucl. Phys. **55**, 1483 (1992)]; Yad. Fiz. **57**, 1393 (1994) [Phys. At. Nucl. **57**, 1322 (1994)]; Eur. Phys. J. A **2**, 199 (1998).
5. A. V. Anisovich and A. V. Sarantsev, Yad. Fiz. **55**, 2163 (1992) [Sov. J. Nucl. Phys. **55**, 1200 (1992)].
6. A. V. Kapitanov and A. V. Sarantsev, Yad. Fiz. **56** (1), 156 (1993) [Phys. At. Nucl. **56**, 89 (1993)].
7. V. V. Anisovich, D. I. Melikhov, B. Ch. Metsch, and H. R. Petry, Nucl. Phys. A **563**, 549 (1993).
8. V. V. Anisovich, in *Hadron Spectroscopy and the Confinement Problem*, Ed. by D. V. Bugg (Plenum Press, New York, 1996).
9. A. V. Anisovich, V. V. Anisovich, V. N. Markov, *et al.*, J. Phys. G **28**, 15 (2002).
10. M. N. Kinzle-Focacci, in *Proceedings of the VIII Blois Workshop, Protvino, Russia, 1999*, Ed. by V. A. Petrov and A. V. Prokudin (World Sci., Singapore, 2000).
11. V. A. Schegelsky, in *Open Session of HEP Division of PNPI: On the Eve of the XXI Century, 2000*.
12. CMD-2 Collab. (R. R. Akhmetshin *et al.*), Phys. Lett. B **462**, 371, 380 (1999); SND Collab. (M. N. Achasov *et al.*), Phys. Lett. B **485**, 349 (2000).
13. V. V. Anisovich, D. I. Melikhov, and V. A. Nikonov, Phys. Rev. D **52**, 5295 (1995); Phys. Rev. D **55**, 2918 (1997); A. V. Anisovich, V. V. Anisovich, D. V. Bugg, and V. A. Nikonov, Phys. Lett. B **456**, 80 (1999); A. V. Anisovich, V. V. Anisovich, L. Montanet, and V. A. Nikonov, Eur. Phys. J. A **6**, 247 (1999).
14. A. V. Anisovich, V. V. Anisovich, and V. A. Nikonov, Eur. Phys. J. A **12**, 103 (2001); A. V. Anisovich, V. V. Anisovich, V. N. Markov, and V. A. Nikonov, Yad. Fiz. **65**, 523 (2002) [Phys. At. Nucl. **65**, 497 (2002)]; A. V. Anisovich, V. V. Anisovich, M. A. Matveev, and V. A. Nikonov, Yad. Fiz. **66**, 946 (2003) [Phys. At. Nucl. **66**, 914 (2003)].
15. A. V. Anisovich, V. V. Anisovich, and A. V. Sarantsev, Phys. Rev. D **62**, 051502 (2000); A. V. Anisovich, V. V. Anisovich, V. A. Nikonov, and A. V. Sarantsev, in *PNPI XXX, Scientific Highlights, Theoretical Physics Division, Gatchina, Russia, 2001*, p. 58; V. V. Anisovich, hep-ph/0110326.
16. A. V. Anisovich, C. A. Baker, C. J. Batty, *et al.*, Phys. Lett. B **449**, 114 (1999); **452**, 173 (1999); **452**, 180 (1999); **452**, 187 (1999); **472**, 168 (2000); **476**, 15 (2000); **477**, 19 (2000); **491**, 40 (2000); **491**, 47 (2000); **496**, 145 (2000); **507**, 23 (2001); **508**, 6 (2001); **513**, 281 (2001); **517**, 261 (2001); **517**, 273 (2001); Nucl. Phys. A **651**, 253 (1999); **662**, 319 (2000); **662**, 344 (2000).
17. PDG Group (D. E. Groom *et al.*), Eur. Phys. J. C **15**, 1 (2000).
18. R. Ricken, M. Koll, D. Merten, *et al.*, Eur. Phys. J. A **9**, 221 (2000).
19. R. D. Carlitz and D. B. Creamer, Ann. Phys. (N.Y.) **118**, 429 (1979); E. V. Shuryak, Nucl. Phys. B **203**, 93 (1982); V. V. Anisovich, S. M. Gerasyuta, and A. V. Sarantsev, Int. J. Mod. Phys. A **6**, 625 (1991).
20. V. V. Anisovich and A. V. Sarantsev, hep-ph/0204328.
21. L. Castillejo, F. J. Dyson, and R. H. Dalitz, Phys. Rev. **101**, 453 (1956).

*Physics of Atomic Nuclei, Vol. 67, No. 4, 2004, pp. 804–807. Translated from Yadernaya Fizika, Vol. 67, No. 4, 2004, pp. 825–828.*
*Original Russian Text Copyright © 2004 by Dyatlov.*

## ELEMENTARY PARTICLES AND FIELDS
## Theory

# Vacuum Stability in Nambu–Jona-Lasinio Models

**I. T. Dyatlov**

*Petersburg Nuclear Physics Institute, Russian Academy of Sciences, Gatchina, 188350 Russia*

Received May 15, 2003

**Abstract**—In Nambu–Jona-Lasinio models for a dynamical breakdown of chiral symmetry, unrenormalized divergences hinder a direct comparison of vacuum energies of different solutions. The choice of a stable vacuum in the presence of several solutions to the equations for fermion masses can nevertheless be performed since, for unstable states, tachyons appear in the spectrum of composite scalar bosons. *© 2004 MAIK "Nauka/Interperiodica".*

The Nambu–Jona-Lasinio model provides a unique four-dimensional example of the formation of a relativistic condensate and fermion masses upon a dynamical breakdown of chiral symmetry [1]. The Nambu–Jona-Lasinio system is being widely used to simulate mechanisms proposed for explaining phenomena that occur in the real world—the emergence of a light-flavor quark condensate in QCD (for an overview, see [2] and references therein), the dynamical breakdown of weak symmetry, and the generation of fermion masses in models involving the composite Higgs boson of the Standard Model [3]—and to study the possible phase transitions in multiflavor models [4].

These considerations are based on the unrenormalized four-fermion Nambu–Jona-Lasinio interaction [see formula (1) below]. It can be treated as an effective interaction that describes the dynamics of the system at energies below some value $M$. The results depend on $M$, and the cutoff $M$ is a real physical constant for the Nambu–Jona-Lasinio system. Because of divergences, we must restrict ourselves to contributions constructed from one or (maximally) two ([5]) loops, this being equivalent to considering systems featuring a large number of components ("flavors," $N_c$) of fermions.

A phase transition associated with the breakdown of chiral symmetry means that the system moves to a new stable vacuum and to a minimum of the effective potential energy. For the unrenormalized interaction, it is not possible, however, to calculate the potential energy reliably, so that stability must be established indirectly. In their pioneering study, Y. Nambu and G. Jona-Lasinio [1] proposed employing, as a criterion of stability, the shift of the cellar of free fermions as they acquire mass. However, this shift diverges quadratically, and the Nambu–Jona-Lasinio system is a system of interacting particles.

For multiflavor systems, the gap equations that determine fermion masses admit many solutions, which correspond to various versions of chiral-symmetry breaking. In a phase transition, it is possible that only some of the fermions acquire mass simultaneously. A system may involve a few Nambu–Jona-Lasinio four-fermion interactions [4, 6], and some of them may be subcritical.

In this study, it will be shown that, in such systems, the stability of a vacuum upon the transition can be established (in the same $N_c \gg 1$ approximation) by studying the properties of composite bosons formed by fermion–antifermion pairs.

In order to clarify this point, we consider the Nambu–Jona-Lasinio model of $N_f$ chiral $(R, L)$ fermions $q^c_{Ri}(x)$ and $q^c_{Li}(x)$ ($i = 1, 2, \ldots, N_f$ is the flavor index; $c = 1, 2, \ldots, N_c \gg 1$) invariantly interacting with one another $[U_R(N_f) \times U_L(N_f)]$ [4]:

$$V(x) = G\left(\bar{q}^c_{Ri} q^c_{Lk}\right)\left(\bar{q}^{c'}_{Lk} q^{c'}_{Ri}\right). \qquad (1)$$

In the leading (in $N_c$) approximation, the equation for fermion masses that is conventional for Nambu–Jona-Lasinio models has the form

$$m_i = \frac{GN_c}{8\pi^2} \int \frac{d^4p}{\pi^2 i} \frac{m_i}{m_i^2 - p^2}. \qquad (2)$$

The right-hand side of this equation is the contribution of the diagram in Fig. 1$a$. It is this equation that is referred to as a gap equation. The integral in (2) implies some cutoff of the quadratic divergence, qualitative properties of solutions to the Nambu–Jona-Lasinio equation being independent of the cutoff.

The existence of an $m_i \neq 0$ solution to Eq. (2) implies the breakdown of chiral symmetry and the transition to a new vacuum involving a condensate $\langle \bar{q}_R q_L \rangle$. This is possible only at rather large values of $G$. In order to prove this, one can calculate the

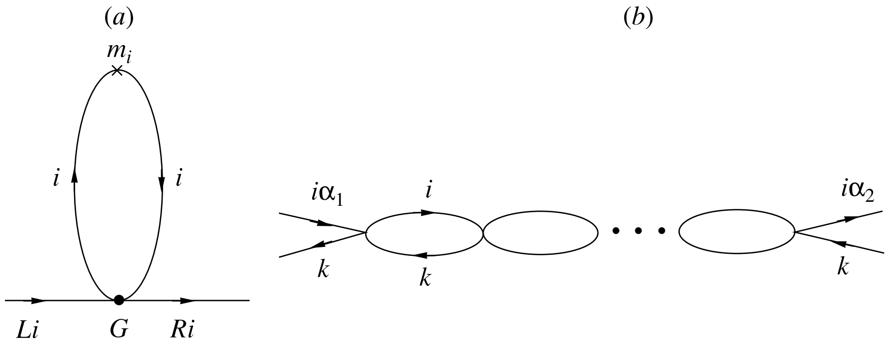

**Fig. 1.** Diagrams for (*a*) the fermion mass and (*b*) the fermion scattering amplitude.

integral in (2) for some cutoff. The simplest version leads to the known expression [1–4]

$$m_i = m_i \frac{GN_cM^2}{8\pi^2}\left(1 - \frac{m_i^2}{M^2}\ln\frac{M^2}{m_i^2}\right), \qquad (3)$$

whence one can see that the condition $GN_cM^2/8\pi^2 > 1$ is necessary for the existence of $m_i \neq 0$ solutions.

However, a solution to Eq. (2) could impart mass only to part of fermions ($n$), this corresponding to the breakdown of the chiral group:

$$U_R(N_f)U_L(N_f) \qquad (4)$$
$$\to U_R(N_f - n)U_L(N_f - n)U_{R+L}(n).$$

Such a transition is accompanied by the appearance of massless Goldstone scalars whose number is

$$2N_f^2 - 2(N_f - n)^2 - n^2 = n(4N_f - 3n). \qquad (5)$$

Let us study the question of which fermions form Goldstone particles and the question of whether all transitions in (4) are possible.

For this purpose, we consider the expression for the amplitude describing the scattering of a fermion on an antifermion with given helicities. In the leading (in $N_c$) approximation, the amplitude is equal to the contribution of the sum of diagrams belonging to the type in Fig. 1*b*. It is convenient to analyze the dimensionless amplitude $B(q)$, factoring out the quantity $G$. The one-loop contribution written in the form of the $R, L$ helicity matrix of initial–final particles [according to (1), antiparticles have the opposite helicity] then takes the form

$$A_{\alpha_1\alpha_2}(q) = A_1(q)\delta_{\alpha_1\alpha_2} + A_2(q)\delta_{\alpha_1 -\alpha_2}, \qquad (6)$$
$$\alpha = R, L;$$
$$\{A_1(q); A_2(q)\} = -\frac{GN_c}{8\pi^2}$$
$$\times \int \frac{d^4p}{\pi^2 i}\frac{\left\{p^2 - \dfrac{q^2}{4}; m_1m_2\right\}}{\left[m_1^2 - \left(p - \dfrac{q}{2}\right)^2\right]\left[m_2^2 - \left(p + \dfrac{q}{2}\right)^2\right]}.$$

Here, the quantities $A_1$ and $A_2$ are calculated at arbitrary masses of constituent particles—this will simplify the ensuing exposition.

The dimensionless amplitude $B$ is obviously given by

$$B(q) = (1 - A(q))^{-1}. \qquad (7)$$

It can easily be seen that any element of the matrix $B$ involves the expressions $[1 - A_1(q) \pm A_2(q)]_1$ in the denominator. The zeros of these expressions define the scalar (or pseudoscalar) bosons of the model. We rewrite the numerators in the integrands on the right-hand side of (6) as

$$p^2 - \frac{q^2}{4} \pm m_1m_2 = \frac{1}{2}\left[\left(p - \frac{q}{2}\right)^2 - m_1^2\right] \qquad (8)$$
$$+ \frac{1}{2}\left[\left(p + \frac{q}{2}\right)^2 - m_2^2\right] + \frac{1}{2}(m_1 \pm m_2)^2.$$

In the expressions $1 - A_1 \pm A_2$, we replace unity by the ratio of the right-hand side of Eq. (2) to $m_i$. At $m_i \equiv m$, which is a solution to the gap equation, we obtain

$$1 - A_1(q) \pm A_2(q) = \frac{GN_c}{16\pi^2} \qquad (9)$$
$$\times \int \frac{d^4p}{\pi^2 i}\left\{\left[\frac{1}{m^2 - p^2} - \frac{1}{m_1^2 - \left(p - \frac{q}{2}\right)^2}\right]\right.$$
$$+ \left[\frac{1}{m^2 - p^2} - \frac{1}{m_2^2 - \left(p + \frac{q}{2}\right)^2}\right]$$
$$\left. + \frac{(m_1 \pm m_2)^2 - q^2}{\left[m_1^2 - \left(p - \frac{q}{2}\right)^2\right]\left[m_2^2 - \left(p + \frac{q}{2}\right)^2\right]}\right\}.$$

We note that, in (9), there are no quadratically divergent integrals. The arbitrariness induced by the cutoff reduces to a constant.

Let us introduce the notation

$$x_{1,2} = \frac{1}{2}\left(1 + \frac{m_2^2 - m_1^2}{-q^2}\right) \qquad (10)$$

$$\pm\sqrt{\frac{1}{4}\left(1+\frac{m_2^2-m_1^2}{-q^2}\right)^2+\frac{m_1^2}{-q^2}},$$

and calculate four dimensional integrals with respect to $p$ in (9). We have

$$I(m_1,m_2,q) \tag{11}$$
$$=\int\frac{d^4p}{\pi^2 i}\frac{1}{\left[m_1^2-\left(p-\frac{q}{2}\right)^2\right]\left[m_2^2-\left(p+\frac{q}{2}\right)^2\right]}$$
$$=\ln\frac{M^2}{m_1m_2}+r+\frac{1-x_1-x_2}{2}\ln\frac{m_1}{m_2}$$
$$+\frac{x_1-x_2}{2}\ln\frac{(1-x_1)x_2}{(1-x_2)x_1}.$$

In the linearly divergent integral, we single out the part depending on $m_1$ and $m_2$; that is,

$$\frac{1}{2}+I_1(m_1,m_2,q) \tag{12}$$
$$=\int\frac{d^4p}{\pi^2 i}\frac{(q-2p)q}{q^2}\frac{1}{(m_1^2-p^2)[m_2^2-(p-q)^2]}$$
$$=\frac{1}{2}+(1-x_1-x_2)+x_1(1-x_1)\ln\frac{x_1-1}{x_1}$$
$$+x_2(1-x_2)\ln\frac{x_2-1}{x_2}.$$

It can easily be seen that the substitution $m_1\leftrightarrow m_2$ leads to $x_1\leftrightarrow 1-x_2$. The function $I$ is symmetric under the substitution $m_1\leftrightarrow m_2$, while the function $I_1$ is antisymmetric. The quantity $r$ simulates the dependence on the cutoff factor; for example, the use of the cutoff factor $(M^2/(M^2+p^2))^n$ in the integrals in (11) and (12) leads to $r=\sum_{k=1}^{n-1}k^{-1}$. It is this cutoff that leads to the term 1/2 in formula (12). At spacelike $q^2<0$, the functions $I$ and $I_1$ are real-valued.

For the quantity under study in (9), we obtain

$$1-A_1(q)\pm A_2(q) \tag{13}$$
$$=\frac{GN_c}{16\pi^2}\left\{(m_1^2-m^2)I\left(m,m_1,\frac{q}{2}\right)\right.$$
$$+(m_2^2-m^2)I\left(m,m_2,\frac{q}{2}\right)$$
$$+[(m_1\pm m_2)^2-q^2]I(m_1,m_2,q)$$
$$\left.-\frac{q^2}{4}\left[1+I_1\left(m,m_1,\frac{q}{2}\right)+I_1\left(m,m_2,\frac{q}{2}\right)\right]\right\}.$$

Further, we consider the possible versions of the amplitudes.

(i) Scattering of massive fermions, $m=m_1=m_2$, and $I_1=0$. For any $(i,k)$ pair from $n$ massive flavors, there exists one massive boson $(\bar{q}_{Ri}q_{Lk}+\bar{q}_{Lk}q_{Ri})/\sqrt{2}$ and one massless particle $(\bar{q}_{Ri}q_{Lk}-\bar{q}_{Lk}q_{Ri})/(\sqrt{2}i)$, $i,k\le n$. In all, there arise here $n^2$ massive and $n^2$ massless scalar–pseudoscalar particles.

(ii) Scattering of massive fermions on massless ones, $m=m_1$ and $m_2=0$ [here, $A_2(q)=0$]:

$$1-A_1(q) \tag{14}$$
$$=\frac{GN_c}{16\pi^2}\left\{-m^2\left[I\left(m,0,\frac{q}{2}\right)-I(m,0,q)\right]\right.$$
$$\left.-q^2I(m,0,q)-\frac{q^2}{4}\left[1+I_1\left(m,0,\frac{q}{2}\right)\right]\right\}.$$

For $q^2\to 0$, $I_1(m,0,0)=-(1/2)$ and $I(m,0,0)= =\ln(M^2/m^2)+r$, so that we have a zero in formula (14) in this limit. These are real Goldstone particles with positive residues. Their composition is the following:

$$\bar{q}_{Ri}q_{Lk},\ \bar{q}_{Lk}q_{Ri},\ \bar{q}_{Li}q_{Rk},\ \bar{q}_{Rk}q_{Li}, \tag{15}$$
$$i=1,2,\ldots,n,\qquad k=n+1,\ldots,N_f.$$

In all, there arise here $4n(N_f-n)$ massless bosons. The number of all massless particles is given by expression (5), as is expected to be for the transition in question.

Thus, there is every reason to believe that, in the system specified by Eq. (1), there can occur quite a wide variety of phase transitions according to (4). There arises the question of whether all of these lead to stable states.

To answer this question, we investigate the scattering of two massless fermions on each other.

(iii) This is the case of $m\ne 0$ and $m_1=m_2=0$. For the denominator in the expression for the amplitude, we have

$$1-A_1(q)=\frac{GN_c}{16\pi^2}\left\{-2m^2I\left(m,0,\frac{q}{2}\right)\right. \tag{16}$$
$$\left.-q^2I(0,0,q)-\frac{q^2}{4}\left[1-2I_1\left(m,0,\frac{q}{2}\right)\right]\right\}.$$

Upon the substitution of the corresponding quantities from (11) and (12), we obtain

$$1-A_1(q)=\frac{GN_c}{16\pi^2}\left\{-2m^2\left(\ln\frac{M^2}{m^2}+r-1\right)\right. \tag{17}$$
$$\left.-q^2\left(\ln\frac{M^2}{-q^2}+r+\frac{1}{2}\right)\right\}.$$

The spectrum of this amplitude involves tachyons: $q^2\simeq -2m^2$. Yet another root of expression (17) falls beyond the region of applicability of the model: $q^2\simeq -\left(M^2+2m^2\ln\frac{M^2}{m^2}\right)$.

The total number of states characterized by a negative square of the mass is equal to $(N_f - n)^2$. This indicates that the vacua where $n \neq N_f$ are unstable. The only stable system arises upon a transition to the state where all fermions of the model acquire mass.

In our consideration, we have avoided quadratic divergences and the arbitrariness in the cutoff at $M \gg m$ does not affect our qualitative conclusions.

## ACKNOWLEDGMENTS

This work was supported in part by the Russian Foundation for Basic Research (project no. 01-02-17216).

## REFERENCES

1. Y. Nambu and G. Jona-Lasinio, Phys. Rev. **122**, 345 (1961).
2. P. S. Klevansky, Rev. Mod. Phys. **64**, 649 (1992).
3. W. A. Bardeen, C. T. Hill, and M. Lindner, Phys. Rev. D **41**, 1647 (1990).
4. R. S. Chivukula, M. Golden, and E. H. Simmons, Phys. Rev. Lett. **70**, 1587 (1993); W. A. Bardeen, C. T. Hill, and D. U. Jungnickel, Phys. Rev. D **49**, 1437 (1994); I. T. Dyatlov, Yad. Fiz. **60**, 1650 (1997) [Phys. At. Nucl. **60**, 1504 (1997)].
5. V. Dmitrašinović, H. J. Schulze, and R. Tegen, Ann. Phys. (N.Y.) **238**, 332 (1995).
6. I. T. Dyatlov, Yad. Fiz. **64**, 1738 (2001) [Phys. At. Nucl. **64**, 1657 (2001)].

*Translated by A. Isaakyan*

Physics of Atomic Nuclei, Vol. 67, No. 4, 2004, pp. 808–814. Translated from Yadernaya Fizika, Vol. 67, No. 4, 2004, pp. 829–836.
Original Russian Text Copyright © 2004 by Baranov, Slad.

## ELEMENTARY PARTICLES AND FIELDS
## Theory

# Production of Triply Charmed $\Omega_{ccc}$ Baryons in $e^+e^-$ Annihilation

**S. P. Baranov*** **and V. L. Slad****

*Lebedev Institute of Physics, Russian Academy of Sciences, Leninskiĭ pr. 53, Moscow, 117924 Russia*

Received January 27, 2003; in final form, October 7, 2003

**Abstract**—The total and differential cross sections for the production of triply charmed $\Omega_{ccc}$ baryons in $e^+e^-$ annihilation are calculated at the $Z$-boson pole. *© 2004 MAIK "Nauka/Interperiodica".*

## 1. INTRODUCTION

Investigation into the properties of baryons containing two or three heavy $c$ and $b$ quarks, the features of their production at operating accelerators and those under construction, and their lifetimes and decay modes is topical in particle physics, but these issues have not yet received adequate study. All that is currently known in these realms from experiments amounts to the claim [1] that a doubly charmed baryon $\Xi_{cc}^+$ was observed in experiments with a beam of charged hyperons at FERMILAB. Theoretical investigations of baryons containing two heavy quarks are reviewed, for example, in [2]. Calculations available in the literature that deal with the cross sections for the production of baryons containing two heavy quarks treat primarily processes described in the fourth order of standard perturbation theory—that is, processes leading to the production of respective diquarks [3]. Only in [4] were sixth-order calculations performed, where the process $e^+e^- \to s\bar{s}c\bar{c}b\bar{b}$ was associated with the production of an $\Omega_{scb}$ baryon in $e^+e^-$ collisions. The production of baryons involving three heavy quarks has not yet been considered.

The present article reports on a continuation of the investigation begun in [4], providing a description of some features of the process involving the production of triply charmed baryons $\Omega_{ccc}$ in $e^+e^-$ annihilation. This case has nothing to do with the production $cc$ diquarks, because they can transform, with a probability close to unity, only into $\Xi_{ccu}^{++}$ or $\Xi_{ccd}^{+}$ baryons, a negligible fraction of these diquarks going over to $\Omega_{ccc}$ baryons. As a matter of fact, calculations in the sixth order of perturbation theory for the elementary process $e^+e^- \to ccc\bar{c}\bar{c}\bar{c}$ are the only possibility of theoretically studying triply charmed baryons. The main contribution to the amplitude of this process comes from 504 Feynman diagrams. In relation to the production of $\Omega_{scb}$ baryons, which was considered previously and where all components have different flavors, the calculations for $\Omega_{ccc}$ baryons are complicated by the need for taking into account the interference between identical particles.

In studying the production of $\Omega_{ccc}$ baryons in proton–proton collisions, it would be necessary to consider an order of magnitude greater number of Feynman diagrams corresponding to the subprocesses $q\bar{q} \to ccc\bar{c}\bar{c}\bar{c}$ and $gg \to ccc\bar{c}\bar{c}\bar{c}$. Moreover, the description of baryon production in hadron–hadron collisions would require a much greater effort in calculating the contributions to the amplitude of the production process from various parton color states than in the case of $e^+e^-$ annihilation.

In present study, the unification of three charmed quarks into an $\Omega_{ccc}$ baryon is described within the well-known nonrelativistic approximation [5]. Upon obtaining numerical results for the cross sections describing $\Omega_{ccc}$-baryon production, we analyze the possibility of constructing their approximate analytic description in terms of one known fragmentation function or another.

## 2. AMPLITUDE OF $\Omega_{ccc}$-BARYON PRODUCTION IN $e^+e^-$ ANNIHILATION

We assume that the amplitude of the production of triply charmed baryons $\Omega_{ccc}$ in $e^+e^-$ annihilation corresponds to the elementary process

$$e^+(k_1) + e^-(k_2) \to c(p_1, \xi_1) + c(p_2, \xi_2) \qquad (1)$$
$$+ c(p_3, \xi_3) + \bar{c}(p_4, \chi_1) + \bar{c}(p_5, \chi_2) + \bar{c}(p_6, \chi_3),$$

where $k_1$ and $k_2$ are the 4-momenta of colliding particles; $p_1, \ldots, p_6$ are the 4-momenta of product partons; and $\xi_i$ and $\chi_j$ $(i, j = 1, 2, 3)$ are the color indices of quarks and antiquarks, respectively. As usual, we disregard the contribution of the electroweak interaction of quarks to the amplitude of process (1), since it is an order of magnitude less than the corresponding contribution of QCD interaction. Thereupon, all

---

*e-mail: `baranov@sci.lebedev.ru`
**e-mail: `vslad@sci.lebedev.ru`

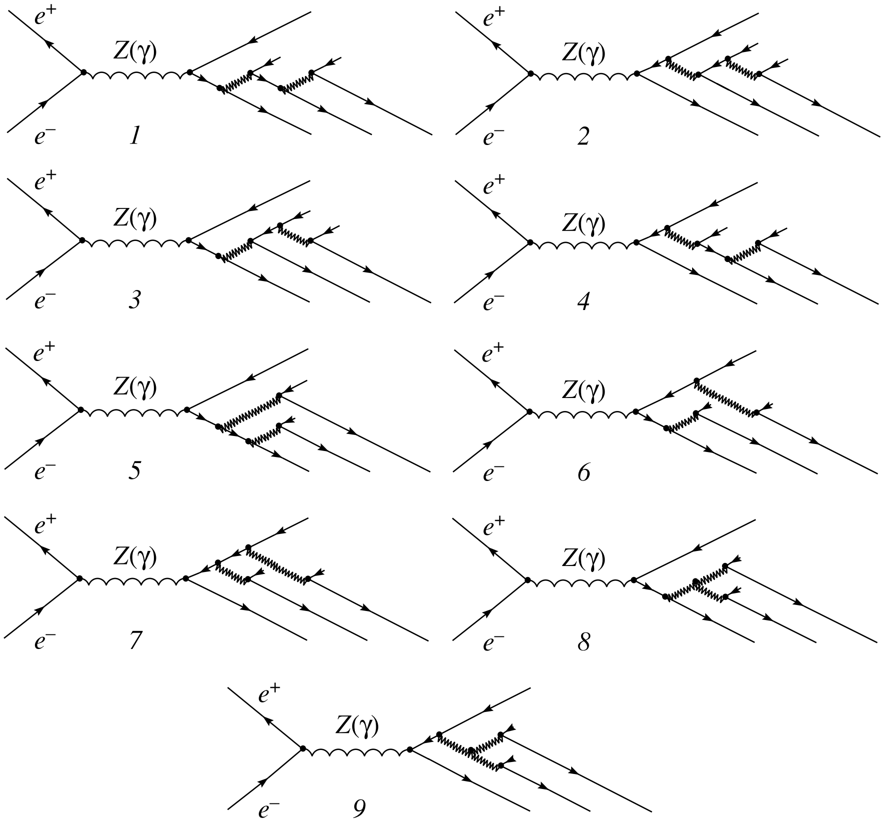

**Fig. 1.** Basic Feynman diagrams for the process $e^+ + e^- \to c + c + c + \bar{c} + \bar{c} + \bar{c}$.

Feynman diagrams to be taken into account for process (1) reduce to the nine basic diagrams in Fig. 1, which correspond to different positions of the quark–gluon vertices. Thirty-six nonequivalent dispositions of quark and antiquark lines characterized by specific 4-momenta, polarizations, and color indices are possible for each of the basic diagrams *1*–*7*, and 18 nonequivalent dispositions of such lines are possible for the basic diagrams *8* and *9*. Since a collision between an electron and a positron leads to annihilation into either a photon or a $Z$ boson, the total number of relevant Feynman diagrams is 576.

First, we consider the color structure of the amplitude of $\Omega_{ccc}$-baryon production. Since an electron, a positron, and any baryon are singlets with respect to the $SU(3)_c$ color group, three product antiquarks $\bar{c}$ must also form an $SU(3)_c$-singlet state. Therefore, the final state of process (1) must be fully antisymmetric in the color indices of the three charmed quarks bound into an $\Omega_{ccc}$ baryon and in the color indices of the three product charmed antiquarks. This requirement, together with the requirement of an appropriate normalization, is satisfied by introducing, in the amplitude of process (1), the product $(\varepsilon^{\xi_1\xi_2\xi_3}/\sqrt{6})(\varepsilon^{\chi_1\chi_2\chi_3}/\sqrt{6})$ of antisymmetric tensors and performing summation over the color indices of $\xi_i$ and $\chi_j$ $(i, j = 1, 2, 3)$.

We set $T^a = \lambda^a/2$, where $\lambda^a$ $(a = 1, \ldots, 8)$ are the Gell-Mann matrices, and denote by $N$ the total number of such permutations of different pairs of color indices of quarks and antiquarks that transform the sets $(\xi_1, \xi_2, \xi_3)$ and $(\chi_1, \chi_2, \chi_3)$ into the sets $(\xi_{i_1}, \xi_{i_2}, \xi_{i_3})$ and $(\chi_{i_1}, \chi_{i_2}, \chi_{i_3})$, respectively. The color factors associated with diagrams of the types *1*–*7* can then be found by means of direct analytic calculations. The result is

$$\sum_{a,b,\zeta}\sum_{\xi_1,\xi_2,\xi_3}\sum_{\chi_1,\chi_2,\chi_3}\frac{1}{6}\varepsilon^{\xi_1\xi_2\xi_3}\varepsilon^{\chi_1\chi_2\chi_3} \tag{2}$$

$$\times T^a_{\xi_{i_1}\chi_{j_1}} T^a_{\xi_{i_2}\zeta} T^b_{\zeta\chi_{j_2}} T^b_{\xi_{i_3}\chi_{j_3}} = (-1)^N \frac{4}{9}.$$

In the sum in expression (2), the index $\xi_1$ appears twice (as it must)—directly in the tensor $\varepsilon^{\xi_1\xi_2\xi_3}$ and indirectly as the substitute of one of the indices $\xi_{i_1}$, $\xi_{i_2}$, and $\xi_{i_3}$. The same is true for the other Greek indices in the above sum, with the exception of $\zeta$, and for the zeroth color factors corresponding to diagrams of types *8* and *9*, for which we have

$$\sum_{a,b,c}\sum_{\xi_1,\xi_2,\xi_3}\sum_{\chi_1,\chi_2,\chi_3}\varepsilon^{\xi_1\xi_2\xi_3}\varepsilon^{\chi_1\chi_2\chi_3} \tag{3}$$

$$\times f^{abc} T^{a}_{\xi_{i_1}\chi_{j_1}} T^{b}_{\xi_{i_2}\chi_{j_2}} T^{c}_{\xi_{i_3}\chi_{j_3}} = 0,$$

where $f^{abc}$ are the structure constants of the $SU(3)$ group. The proof of the equality in (3) is given in [4]. This equality means that the total contribution to the amplitude of the process in (1) from the diagrams involving three-gluon vertices vanishes. Thus, the number of contributing diagrams reduces to 504.

Since the contribution to the amplitude of process (1) from the diagram that differs from a specific diagram by a permutation of $N$ fermion pairs involves the Feynman factor $(-1)^N$, it can be concluded, with allowance for (2), that all terms appearing in the amplitude of $\Omega_{ccc}$-baryon production have the same sign.

It should be noted that, in our calculations, we used an additional simplifying approximation, setting the $c$-quark mass to zero in all expressions entering into the numerators of fermion propagators and in all traces. At the same time, we set $m_c = 1.5$ GeV and $p_i^2 = 2.25\ \mathrm{GeV}^2$ $(i = 1, \ldots, 6)$ in all of the denominators of the propagators of virtual particles and in the expression for the final-state phase space (of course, the amplitude containing zero $c$-quark mass in the denominator would diverge). But if we used a nonzero $c$-quark mass everywhere in the amplitude and in the square of the relevant matrix element, the volume of information to be saved in the computer memory and the time required for the compilation of codes and for numerical calculations of the cross sections would grow enormously, which would render the problem in question unsolvable with our means.

In order to estimate the effect of the above approximation on the accuracy of the numerical results, we repeated the calculation of the cross section for $\Omega_{scb}$-baryon production in a similar approximation and compared the results obtained in this way with the results of the full calculation performed in [4]. It turned out that the cross sections obtained for $\Omega_{scb}$-baryon production within the "massive" and "massless" (for all quarks simultaneously) approximations differ only by 8%. It seems reasonable to expect an inaccuracy on the same order of magnitude for $\Omega_{ccc}$-baryon production as well. Anyway, this inaccuracy does not exceed other theoretical uncertainties associated, for example, with the choice of the renormalization scale in the strong-interaction coupling constant or with the wave function for the triply charmed heavy baryon. Thus, this approximation appears to be numerically justified.

Taking into account the aforesaid, we can represent the matrix element for process (1) in the form

$$\mathcal{M} = \frac{g_s^4 g^2}{9\cos^2\theta_W (s - M_Z^2 + iM_Z\Gamma_Z)} D^Z - \frac{4g_s^4 e^2}{9s} D^{\gamma}, \tag{4}$$

where

$$\begin{aligned}
D^Z = \sum_{\substack{i,\,j,\,k\,\in\,\{1,2,3\} \\ i \neq j \neq k}} \; \sum_{\substack{i',\,j',\,k'\,\in\,\{1,2,3\} \\ i' \neq j' \neq k'}} \{[(p_j \qquad (5)\\
+ p_i + p_{i'})^2 - m_c^2]^{-1}[(k_1 + k_2 - p_{k'})^2 - m_c^2]^{-1}\\
\times (p_i + p_{i'})^{-2}(p_i + p_j + p_{i'} + p_{j'})^{-2}\\
\times \bar{u}(\mathbf{p}_j)\gamma^{\nu}(\hat{p}_j + \hat{p}_i + \hat{p}_{i'})\gamma_{\delta} v(-\mathbf{p}_{j'})\\
\times \bar{u}(\mathbf{p}_k)\gamma^{\delta}(\hat{k}_1 + \hat{k}_2 - \hat{p}_{k'})\\
\times \gamma_{\varepsilon}(g_V^c - g_A^c\gamma_5) v(-\mathbf{p}_{k'})\\
+ [(p_{j'} + p_i + p_{i'})^2 - m_c^2]^{-1}\\
\times [(k_1 + k_2 - p_k)^2 - m_c^2]^{-1}\\
\times (p_i + p_{i'})^{-2}(p_i + p_j + p_{i'} + p_{j'})^{-2}\bar{u}(\mathbf{p}_j)\\
\times \gamma_{\delta}(-\hat{p}_{j'} - \hat{p}_i - \hat{p}_{i'})\gamma^{\nu} v(-\mathbf{p}_{j'})\\
\times \bar{u}(\mathbf{p}_k)\gamma_{\varepsilon}(-\hat{k}_1 - \hat{k}_2 + \hat{p}_k)\\
\times \gamma^{\delta}(g_V^c - g_A^c\gamma_5) v(-\mathbf{p}_{k'})\\
+ [(p_{j'} + p_i + p_{i'})^2 - m_c^2]^{-1}\\
\times [(k_1 + k_2 - p_{k'})^2 - m_c^2]^{-1}\\
\times (p_i + p_{i'})^{-2}(p_i + p_j + p_{i'} + p_{j'})^{-2}\bar{u}(\mathbf{p}_j)\\
\times \gamma_{\delta}(-\hat{p}_{j'} - \hat{p}_i - \hat{p}_{i'})\gamma^{\nu} v(-\mathbf{p}_{j'})\\
\times \bar{u}(\mathbf{p}_k)\gamma^{\delta}(\hat{k}_1 + \hat{k}_2 - \hat{p}_{k'})\gamma_{\varepsilon}(g_V^c - g_A^c\gamma_5) v(-\mathbf{p}_{k'})\\
+ [(p_j + p_i + p_{i'})^2 - m_c^2]^{-1}\\
\times [(k_1 + k_2 - p_k)^2 - m_c^2]^{-1}\\
\times (p_i + p_{i'})^{-2}(p_i + p_j + p_{i'} + p_{j'})^{-2}\bar{u}(\mathbf{p}_j)\\
\times \gamma^{\nu}(\hat{p}_j + \hat{p}_i + \hat{p}_{i'})\gamma_{\delta} v(-\mathbf{p}_{j'})\\
\times \bar{u}(\mathbf{p}_k)\gamma_{\varepsilon}(-\hat{k}_1 - \hat{k}_2 + \hat{p}_k)\\
\times \gamma^{\delta}(g_V^c - g_A^c\gamma_5) v(-\mathbf{p}_{k'})\\
+ [(p_j + p_{j'} + p_k)^2 - m_c^2]^{-1}\\
\times [(k_1 + k_2 - p_{k'})^2 - m_c^2]^{-1}\\
\times (p_i + p_{i'})^{-2}(p_j + p_{j'})^{-2}\bar{u}(\mathbf{p}_j)\gamma_{\delta} v(-\mathbf{p}_{j'})\\
\times \bar{u}(\mathbf{p}_k)\gamma^{\delta}(\hat{p}_j + \hat{p}_{j'} + \hat{p}_k)\\
\times \gamma^{\nu}(\hat{k}_1 + \hat{k}_2 - \hat{p}_{k'})\gamma_{\varepsilon}(g_V^c - g_A^c\gamma_5) v(-\mathbf{p}_{k'})\\
+ [(p_j + p_{j'} + p_k)^2 - m_c^2]^{-1}\\
\times [(p_i + p_{i'} + p_{k'})^2 - m_c^2]^{-1}\\
\times (p_i + p_{i'})^{-2}(p_j + p_{j'})^{-2}\bar{u}(\mathbf{p}_j)\gamma_{\delta} v(-\mathbf{p}_{j'})\bar{u}(\mathbf{p}_k)\\
\times \gamma^{\delta}(\hat{p}_j + \hat{p}_{j'} + \hat{p}_k)\gamma_{\varepsilon}(-\hat{p}_i - \hat{p}_{i'} - \hat{p}_{k'})\\
\times \gamma^{\nu}(g_V^c - g_A^c\gamma_5) v(-\mathbf{p}_{k'})\\
+ [(p_i + p_{i'} + p_{k'})^2 - m_c^2]^{-1}\\
\times [(k_1 + k_2 - p_k)^2 - m_c^2]^{-1}(p_i + p_{i'})^{-2}\\
\times (p_j + p_{j'})^{-2}\bar{u}(\mathbf{p}_j)\gamma_{\delta} v(-\mathbf{p}_{j'})\bar{u}(\mathbf{p}_k)\\
\times \gamma_{\varepsilon}(-\hat{k}_1 - \hat{k}_2 + \hat{p}_k)\gamma^{\delta}(-\hat{p}_i - \hat{p}_{i'} - \hat{p}_{k'})
\end{aligned}$$

$$\times \gamma^{\nu}(g_V^c - g_A^c\gamma_5)v(-\mathbf{p}_{k'})\}$$
$$\times \bar{u}(\mathbf{p}_i)\gamma_{\nu}v(-\mathbf{p}_{i'})\bar{v}(-\mathbf{k}_1)\gamma^{\varepsilon}(g_V^e - g_A^e\gamma_5)u(\mathbf{k}_2),$$

while the expression for $D^{\gamma}$ can be derived from $D^Z$ by means of the substitutions $g_V^e \to 1$, $g_A^e \to 0$, $g_V^c \to Q_c = 2/3$, and $g_A^c \to 0$. Summation in (5) corresponds to 36 permutations of quark and antiquark lines in diagrams of types *1–7*.

## 3. METHOD OF ORTHOGONAL AMPLITUDES

In order to derive the expression that is obtained for the square of the matrix element ($\overline{|\mathcal{M}|^2}$) upon summation over the final-fermion polarizations and averaging over the polarizations of colliding particles, we use the method of orthogonal amplitudes and the REDUCE computer system for analytic calculations. The method of orthogonal amplitudes was proposed in [6] and was employed in calculations referring to $\Omega_{scb}$-baryon production in $e^+e^-$ collisions [4].

A simple and mathematically rigorous validation of the method of orthogonal amplitudes is the following (to the best of our knowledge, it has not yet been given anywhere). Suppose that four-component spinors $u(\mathbf{p})$ and $u(\mathbf{p}')$ describing particles of mass $m$ and $m'$, respectively, their 4-momenta being $p$ and $p'$ ($p^2 = m^2, p'^2 = m'^2$), obey the Dirac equation. Of the four linear homogeneous equations for the components of the spinor $u(\mathbf{p})$ [$u(\mathbf{p}')$], only two are independent; therefore, each of the four components under consideration can be represented as a linear combination of two arbitrary independent constants, denoted here by $X$ and $Y$ ($X'$ and $Y'$). Any quantity of the form $\bar{u}(\mathbf{p}')Ru(\mathbf{p})$, where $R$ is an operator specified in terms of the $\gamma$ matrices and their contractions with some 4-vectors, can be represented as a linear combination of four independent elements $XX'^*$, $XY'^*$, $YX'^*$, and $YY'^*$. Therefore, quantities of the form $\bar{u}(\mathbf{p}')Ru(\mathbf{p})$ can be treated as vectors of a linear four-dimensional space $L$ spanned by the above elements. Any four linearly independent quantities of the form $w_n \equiv \bar{u}(\mathbf{p}')O_n u(\mathbf{p})$, where the operator $O_n$ is either unity, $\gamma_5$, $\hat{V}$, $\hat{V}'\gamma_5$, or $(\hat{V}''\hat{V}''' - \hat{V}'''\hat{V}'')/2$ (with $V$, $V'$, $V''$, and $V'''$ being arbitrary 4-vectors), can be taken for basis vectors of the space $L$. The scalar product $(w_n, w_{n'})$ of vectors $w_n$ and $w_{n'}$ belonging to the linear space $L$ is defined as the product $w_n w_{n'}^*$ summed over the polarizations of fermions that are described by the spinors $u(\mathbf{p})$ and $u(\mathbf{p}')$.

Here, we take, for basis vectors of the space $L$, four quantities $w_n$ specified by the operators $O_1 = 1$, $O_2 = \hat{K}$, $O_3 = \hat{Q}$, and $O_4 = \hat{K}\hat{Q}$, with the 4-vectors $K$ and $Q$ here being orthogonal to the 4-momenta $p$ and $p'$ and to each other—that is, $K_{\mu}p^{\mu} = 0$, $K_{\mu}p'^{\mu} = 0$, $Q_{\mu}p^{\mu} = 0$, $Q_{\mu}p'^{\mu} = 0$, and $K_{\mu}Q^{\mu} = 0$. Otherwise, the 4-vectors $K$ and $Q$ are arbitrary. They can be specified, for example, by the relations $K^{\mu} = \varepsilon^{\mu\nu\rho\sigma}p_{\nu}p'_{\rho}a_{\sigma}$ and $Q^{\mu} = \varepsilon^{\mu\nu\rho\sigma}p_{\nu}p'_{\rho}K_{\sigma}$, where the 4-vector $a_{\sigma}$ is entirely arbitrary. From the orthogonality of the 4-vectors $K$ and $Q$, it follows that $\hat{K}\hat{Q} = (\hat{K}\hat{Q} - \hat{Q}\hat{K})/2$. The four quantities $w_n$ used are orthogonal to one another, $(w_n, w_{n'}) = C_n\delta_{nn'}$, $C_n \neq 0$, this proving their linear independence and justifying the name "orthogonal amplitudes." Thus, it was shown that any quantity of the form $\bar{u}(\mathbf{p}')Ru(\mathbf{p})$ can be represented as a linear combination of orthogonal amplitudes.

In order to solve the problem of calculating the square of the matrix element, we first introduce basic orthogonal amplitudes as

$$\begin{aligned} w_{i1} &= \bar{u}(\mathbf{p}_i)v(-\mathbf{p}_{3+i}), \qquad (6)\\ w_{i2} &= \bar{u}(\mathbf{p}_i)\hat{K}_i v(-\mathbf{p}_{3+i}),\\ w_{i3} &= \bar{u}(\mathbf{p}_i)\hat{Q}_i v(-\mathbf{p}_{3+i}),\\ w_{i4} &= \bar{u}(\mathbf{p}_i)\hat{K}_i\hat{Q}_i v(-\mathbf{p}_{3+i}),\\ w_{e_1} &= \bar{v}(-\mathbf{k}_1)u(\mathbf{k}_2),\\ w_{e_2} &= \bar{v}(-\mathbf{k}_1)\hat{K}_e u(\mathbf{k}_2),\\ w_{e_3} &= \bar{v}(-\mathbf{k}_1)\hat{Q}_e u(\mathbf{k}_2),\\ w_{e_4} &= \bar{v}(-\mathbf{k}_1)\hat{K}_e\hat{Q}_e u(\mathbf{k}_2), \end{aligned}$$

where $i = 1, 2, 3$. We would like to note that the pair combinations of the spinors $\bar{u}(\mathbf{p}_i)$ and $v(-\mathbf{p}_j)$ can be chosen in six equivalent ways.

On the basis of the quantities in (6), we construct 256 orthogonal amplitudes as

$$w_{nrst} = w_{1n}w_{2r}w_{3s}w_{e_t}, \qquad (7)$$

where $n, r, s, t = 1, 2, 3, 4$.

The expansion of the matrix element (4) in the amplitudes given by (7) has the form

$$\mathcal{M} = \sum_{n,r,s,t=1}^{4} c_{nrst}w_{nrst}. \qquad (8)$$

In order to derive the coefficients $c_{nrst}$ in this expansion, we multiply both sides of (8) by the factor $w_{n'r's't'}$, take the sum of the result over the polarizations of all of the fermions, and make use of the orthogonality of different amplitudes. As a result, we arrive at

$$c_{nrst} = \left\{\sum_{\text{polariz}} \mathcal{M}w_{nrst}^*\right\} / (w_{nrst}, w_{nrst}), \qquad (9)$$

where $(w_{nrst}, w_{nrst})$ is an analog of the scalar product defined above in the linear space $L$—that is, the sum of the squared modulus of the amplitude $w_{nrst}$ over the polarization of all fermions. Since $w_{nrst}$ involves arbitrariness associated with the choice of the 4-vectors $K$ and $Q$ in (6), there is also arbitrariness in the coefficients $c_{nrst}$ in (9). The substitution of these coefficients into (8) leads to an identity whose left-hand side is determined unambiguously. Thus, summation on the right-hand side of (8) removes the above ambiguity.

Since electrons and positrons are treated as massless particles and since the charmed-quark mass is set to zero in the numerators of each term of the amplitude for process (1) and in respective traces, it is clear that 192 of the 256 coefficients in expansion (8) vanish, because they are linear combinations of the traces of an odd number of the Dirac $\gamma$ matrices. We further list 64 orthogonal amplitudes in formula (7) that generate nonzero expansion coefficients: $t = 2, 3$, with either $n, r, s = 2, 3$, or one of the indices $n, r, s$ is equal to 2 or 3, while the other two belong to the set $\{1, 4\}$.

It can clearly be seen that the expression obtained for the square of the matrix element upon summation over the polarizations of final fermions and averaging over the polarizations of initial particles takes the form

$$\overline{|\mathcal{M}|^2} = \frac{1}{4}\sum_{n,r,s,t} |c_{nrst}|^2 |w_{nrst}|^2. \qquad (10)$$

In actual calculations by the method of orthogonal amplitudes, we compose one REDUCE code for traces and tensor contractions that corresponds to 504 terms in any quantity $\mathcal{M}w^*_{nrst}$ and then, by means of any text editor (for example, “joe”), perform obvious changes necessary for obtaining the REDUCE code for calculating all 64 nonzero quantities $\mathcal{M}w^*_{nrst}$.

## 4. CROSS SECTIONS FOR $\Omega_{ccc}$-BARYON PRODUCTION AT THE $Z$ POLE IN $e^+e^-$ ANNIHILATION

In describing the $\Omega_{ccc}$ baryon as a bound state of three charmed quarks, we use the nonrelativistic approximation [5]. This means that we disregard the relative velocities of the $c$ quarks confined within the baryon—that is, in the laboratory frame, the velocities and momenta of all three $c$ quarks produced in process (1) are taken to be identical and equal to one-third of the momentum $p$ of the $\Omega_{ccc}$ baryon having the mass $M = 3m_c$. With allowance for the unification of three charmed quarks into the baryon, the phase space of process (1) effectively becomes the 4-particle phase space of the process

$$e^+(k_1) + e^-(k_2) \to \Omega_{ccc}(p) + \bar{c}(p_4) + \bar{c}(p_5) + \bar{c}(p_6). \qquad (11)$$

The differential cross section for process (11) takes the form

$$d\sigma = \frac{(2\pi)^4\overline{|\mathcal{M}|^2}}{2s}\frac{|\psi(0)|^2}{M^2} \qquad (12)$$
$$\times\, \delta^4(k_1 + k_2 - p - p_4 - p_5 - p_6)$$
$$\times \frac{d^3p}{(2\pi)^3 2E}\frac{d^3p_4}{(2\pi)^3 2E_4}\frac{d^3p_5}{(2\pi)^3 2E_5}\frac{d^3p_6}{(2\pi)^3 2E_6},$$

where $\psi(0)$ is the value that the respective wave function takes in the case where all three $c$ quarks forming the $\Omega_{ccc}$ baryon are located at the same point, so that their relative coordinates are zero. The numerical value of $|\psi(0)|^2$ is taken to be identical to that in [7], where it was

$$|\psi(0)|^2 = 0.36 \times 10^{-3}\ \mathrm{GeV}^6. \qquad (13)$$

In calculating the total and differential cross sections, we employed codes for numerical integration that are based on the Monte Carlo method and which are contained in the CompHEP package [8], which is broader. It appeared that the maximum computational errors in the differential cross sections came from the first iteration. Therefore, only the total cross section was calculated in the first iteration, while both the total cross section and the differential cross sections were determined in the next five iterations. Each iteration involved 200 000 Monte Carlo calls on the integrand. The errors in calculating the total cross section amounted to 1.0%, while the errors in calculating the differential cross sections were predominantly 2 to 3% (this is reflected below in the text and in the figures). As was indicated above, the error associated with the disregard of the charmed-quark mass in the numerators of the amplitude for process (1) and in the traces is a few percent. Moreover, we additionally tested the consistency of the cross-section values for two different admissible choices of the 4-vectors $K_e^\mu, Q_e^\mu, K_i^\mu$, and $Q_i^\mu$ $(i = 1, 2, 3)$ used to construct the quantities in (6), which specify the orthogonal amplitudes (7).

In addition to statistical errors, the calculations contain unavoidable theoretical uncertainties. First, there is the uncertainty associated with the running strong-interaction coupling constant as a function of the renormalization scale. Since all of the calculations were performed at an energy value that corresponds to the $Z$-boson pole ($\sqrt{s} = 91.2$ GeV), it is reasonable to specify the coupling-constant values as follows: $\alpha_s = \alpha_s(M_Z/2) = 0.134$ and $\alpha = \alpha(M_Z) = 1/128.0$; accordingly, $\sin^2\theta_\mathrm{W} = \sin^2\theta_\mathrm{W}(M_Z) = 0.2240$. However, it is not evident why it is $M_Z$, and not, for example, the invariant mass of some product quark pair or even the $\Omega_{ccc}$-baryon mass, that should be chosen for the characteristic scale of strong interaction. Since the cross section for process

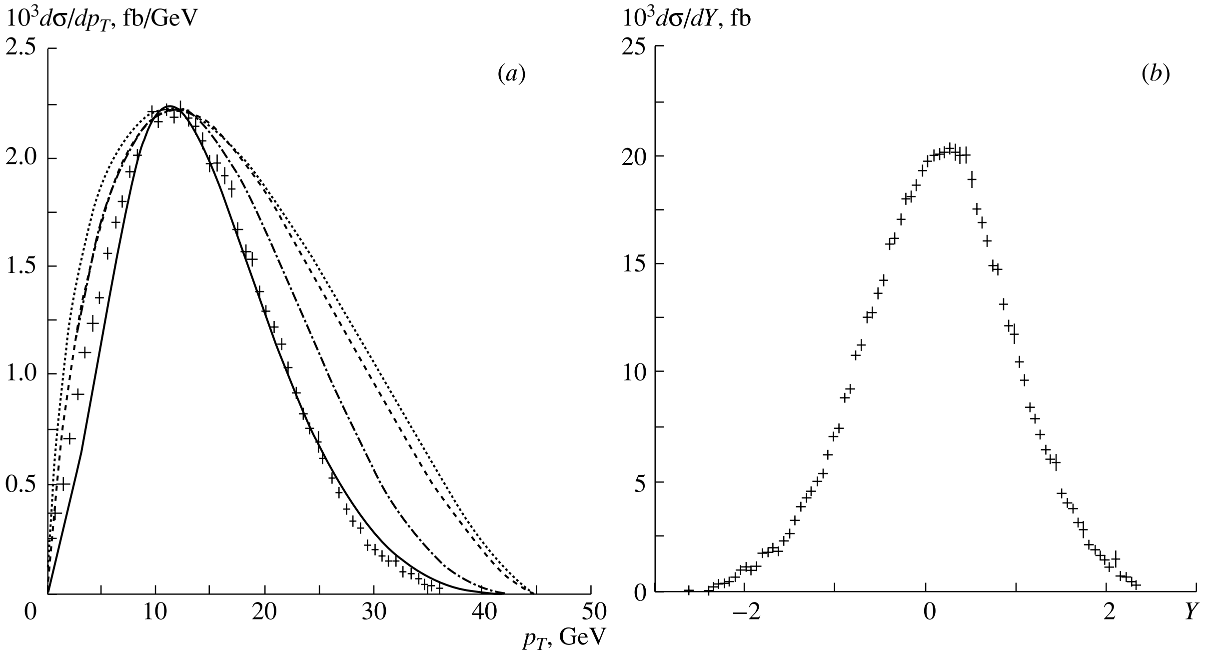

**Fig. 2.** Differential cross sections for $\Omega_{ccc}$-baryon production in $e^+e^-$ annihilation at the $Z$ pole with respect to the ($a$) transverse momentum $p_T$ and ($b$) rapidity $Y$. The results of Monte Carlo calculations and the errors in them are represented by crosses. The curves in Fig. 1$a$ correspond to expression (17) calculated with the fragmentation functions in the form (solid curve) (21) at $a = 2.4$ and $c = 0.70$, (dash-dotted curve) (18) at $\varepsilon = 0.92$, (dashed curve) (19) at $\varepsilon = 3.0$, and (dotted curve) (20) at $\alpha = 0.8$.

(11) is proportional to the fourth power of the strong-interaction coupling constant, this source of errors is the most important. Second, the accuracy of the potential model employed as a basis for calculating the baryon-wave-function value $\psi(0)$ is uncertain.

For the chosen set of model parameters, the total cross section for the process ($\sigma_{\rm tot}$) and the forward–backward production asymmetry at the $Z$-boson pole are

$$\sigma_{\rm tot} = 0.0404 \pm 0.0004 \text{ fb}, \tag{14}$$

$$A_{\rm FB} = (\sigma_F - \sigma_B)/(\sigma_F + \sigma_B) = 0.101 \pm 0.005, \tag{15}$$

where $\sigma_F$ ($\sigma_B$) is the cross section for the production of an $\Omega_{ccc}$ baryon moving in the forward (backward) direction with respect to the electron-momentum direction. The cross-section value in (14) is close to that of the total cross section for $\Omega_{scb}$-baryon production in $e^+e^-$ collisions ($0.0534 \pm 0.0014$ fb) if the strange-quark mass is set to 300 MeV [4].

The differential cross sections with respect to the transverse momentum $p_T$ and the rapidity $Y$ of $\Omega_{ccc}$ baryons are presented in Fig. 2. The distribution $d\sigma/dY$ peaks at a small positive value of $Y$, while $d\sigma/dp_T$ has a maximum at $p_T \approx 12$ GeV. Note that the maximum of the differential cross section with respect to the transverse momentum of $\Omega_{ccc}$ baryons occurs at a $p_T$ value much lower than that for $\Omega_{scb}$ baryons produced under the same conditions, in which case $d\sigma/dp_T$ peaks within the $p_T$ interval 23–26 GeV.

It is desirable to associate our numerical results with some simple analytic form, which we will seek among well-known fragmentation functions [9–12]. It is clear that the production of a triply charmed baryon can hardly be interpreted as a fragmentation process, since each of the three $c$ quarks can be treated, on equal footing, as a fragmenting quark produced at the $\gamma/Z$ vertex and since the interference between identical quarks is likely to be significant in the process being considered. However, we accept not the physical concept of the fragmentation model but its mathematical form used in processing experimental data on $e^+e^-$ annihilation (see, for example, [13]); namely, we set

$$\frac{d\sigma}{dz} = \sigma_{c\bar{c}} D_{c\to\Omega_{ccc}}(z), \tag{16}$$

where $\sigma_{c\bar{c}}$ is the total cross section for the process $e^+e^- \to c\bar{c}$, while $D_{c\to\Omega_{ccc}}(z)$ is the respective fragmentation function. Instead of the variable $z$, its approximate value $x_p = p/p_{\rm max}$ is used below.

Neglecting a small asymmetry in the angular distribution of $\Omega_{ccc}$ baryons, we arrive at the following relation between the differential cross section with respect to the transverse momentum and the fragmentation function:

$$\frac{d\sigma}{dp_T} = \frac{4\sigma_{c\bar{c}} p_T}{s} \int\limits_{2p_T/\sqrt{s}}^{1} \frac{D_{c\to\Omega_{ccc}}(z)dz}{z\sqrt{z^2 - 4p_T^2/s}}. \qquad (17)$$

We now compare our numerical results with those obtained according to expression (17) with various fragmentation functions. First, we consider the Peterson function [9]

$$D(z) \sim \frac{1}{z}\left(1 - \frac{1}{z} - \frac{\varepsilon}{1-z}\right)^{-2}, \qquad (18)$$

which is often used in processing experimental data on charmed-hadron production in $e^+e^-$ annihilation [14]. Also, this function provides a good approximation to numerical results on $\Omega_{scb}$-baryon production in $e^+e^-$ annihilation [4]. The best fit to our calculations (dash-dotted curve in Fig. 2*a*) corresponds to $\varepsilon = 0.92$. The agreement is clearly poor. The best fits with the Collins–Spiller fragmentation function [10]

$$D(z) \sim \left(\frac{1-z}{z} + \varepsilon\frac{2-z}{z}\right) \qquad (19)$$
$$\times (1+z^2)\left(1 - \frac{1}{z} - \frac{\varepsilon}{1-z}\right)^{-2}$$

at $\varepsilon = 3.0$ and with the fragmentation function [11]

$$D(z) \sim z^{\alpha}(1-z) \qquad (20)$$

at $\alpha = 0.8$ are also unsatisfactory. The results of the calculations according to (17) with the functions in (19) and (20) are displayed in Fig. 2*a* (dashed and dotted curves, respectively).

An acceptable analytic form for our numerical results is provided by the LUND fragmentation function [12]

$$D(z) \sim \frac{1}{z}(1-z)^a \exp\left(-\frac{c}{z}\right) \qquad (21)$$

at the parameters $a = 2.4 \pm 0.2$ and $c = 0.70 \pm 0.03$. The corresponding results calculated according to (17) are represented by the solid curve in Fig. 2*a*.

It should be noted that the fragmentation functions (19)–(21), along with the functions in (18), were employed by the OPAL Collaboration [15] in processing experimental data on $B$-meson production.

## REFERENCES

1. SELEX Collab. (M. Mattson *et al.*), Phys. Rev. Lett. **89**, 112001 (2002).
2. V. V. Kiselev and A. K. Likhoded, Usp. Fiz. Nauk **172**, 497 (2002).
3. A. V. Berezhnoy, V. V. Kiselev, and A. K. Likhoded, Yad. Fiz. **59**, 909 (1996) [Phys. At. Nucl. **59**, 870 (1996)]; S. P. Baranov, Phys. Rev. D **54**, 3228 (1996); **56**, 3046 (1997); A. V. Berezhnoy, V. V. Kiselev, A. K. Likhoded, and A. I. Onishchenko, Yad. Fiz. **60**, 2048 (1997) [Phys. At. Nucl. **60**, 1875 (1997)]; A. V. Bereznoy, V. V. Kiselev, A. K. Likhoded, and A. T. Onishchenko, Phys. Rev. D **57**, 4385 (1997).
4. S. P. Baranov and V. L. Slad, Yad. Fiz. **66**, 1778 (2003) [Phys. At. Nucl. **66**, 1730 (2003)].
5. C.-H. Chang, Nucl. Phys. B **172**, 425 (1980); R. Baier and R. Rückl, Phys. Lett. B **102B**, 384 (1981); D. Jones, Phys. Rev. D **23**, 1521 (1981).
6. R. E. Prange, Phys. Rev. **110**, 240 (1958).
7. E. Bagan, H. G. Dosch, P. Godzinsky, *et al.*, Z. Phys. C **64**, 57 (1994).
8. A. Pukhov *et al.*, hep-ph/9908288.
9. C. Peterson, D. Schlatter, J. Schmitt, and P. M. Zerwas, Phys. Rev. D **27**, 105 (1983).
10. P. Collins and T. Spiller, J. Phys. G **11**, 1289 (1985).
11. V. D. Kartvelischvili, A. K. Likhoded, and V. A. Petrov, Phys. Lett. B **78B**, 615 (1978).
12. B. Andersson, G. Gustafson, and B. Söderberg, Z. Phys. C **20**, 317 (1983).
13. ARGUS Collab. (H. Albrecht *et al.*), Phys. Lett. B **207**, 109 (1988); **247**, 121 (1990).
14. Particle Data Groups (D. E. Groom *et al.*), Eur. Phys. J. C **15**, 1 (2000).
15. OPAL Collab. (G. Alexander *et al.*), Phys. Lett. B **364**, 93 (1995); OPAL Collab. (G. Abbiendi *et al.*), hep-ex/0210031.

*Translated by O. Chernavskaya*

*Physics of Atomic Nuclei, Vol. 67, No. 4, 2004, pp. 815–823. Translated from Yadernaya Fizika, Vol. 67, No. 4, 2004, pp. 837–845.*
*Original Russian Text Copyright © 2004 by Berezhnoy, Kiselev, Likhoded.*

# Production of a Charmed-Meson Pair in Photon–Photon Interaction

**A. V. Berezhnoy[1)]*, V. V. Kiselev, and A. K. Likhoded**

*Institute for High Energy Physics, Protvino, Moscow oblast, 142284 Russia*

Received September 6, 2002; in final form, June 10, 2003

**Abstract**—The cross section for the exclusive production of a pair of charmed mesons in photon–photon interaction is calculated on the basis of the constituent model. The resulting predictions are compared with the predictions of heavy-quark effective theory. It is shown that the light valence quark of the $D$ meson plays a significant role not only in hadronization but also in the process leading to the production of a heavy $c$ quark. Moreover, it is shown that, because of the strong interaction of a primary photon field with the charge of a light quark, a similar situation persists even in the limit $m_Q \to \infty$, whence it follows that the application of heavy-quark effective theory to the case of photon–photon interaction is incorrect, since one of the dominant mechanisms of the production of heavy mesons is disregarded in this case. *© 2004 MAIK "Nauka/Interperiodica".*

## INTRODUCTION

In the past few years, much work has been done at the LEP accelerator to study photon–photon interactions experimentally—in particular, charmed-particle production in these interactions. In this connection, as well as in connection with prospects for commissioning the largest $e^+e^-$ collider TESLA at DESY, it is desirable to discuss in detail problems associated with photon–photon interaction at high energies. In the present study, we will dwell on some questions concerning the photon–photon interaction of heavy quarks—namely, we will discuss special features of the exclusive and inclusive production of a pair of charmed mesons and estimate the contribution of these reactions to the total cross section for charm production. By applying the constituent quark model, we will show that the light valence quark of the $D$ meson plays a significant role both in hadronization and in the hard production of a heavy quark. Because of the strong interaction between the photon field and the charge of a light quark, this is so even in the limit $m_Q \to \infty$. Therefore, calculations within heavy-quark effective theory are incorrect for these processes, since they disregard one of the dominant interaction mechanisms.

We note that, even for the exclusive pair production of charmed mesons, where, in the case of $e^+e^-$ annihilation, the constituent quark model and effective quark theory make consistent predictions for $m_Q \to \infty$, the results obtained within the constituent quark model for $\gamma\gamma$ interaction at reasonable values of the masses of the light and heavy quarks forming the $D$ meson differ rather strongly from their counterparts in heavy-quark effective theory.

The ensuing exposition is organized as follows. In Section 1, we analyze the role of a finite mass of a light quark in $e^+e^-$ annihilation. Further, we consider the exclusive production of $D$ mesons in $\gamma\gamma$ interaction in Section 2 and their inclusive production in Section 3. In the last section, we present conclusions and general comments based on the investigation described in this article.

## 1. PAIR PRODUCTION OF CHARMED MESONS IN $e^+e^-$ ANNIHILATION

We begin our investigation by discussing the production of heavy mesons in $e^+e^-$ annihilation because this is the simplest process, which has been most comprehensively considered in the literature.

For the first time, the special features of the interaction between a heavy and a light quark were used in the study reported in [1] and devoted to calculating the $D$-meson yield in $e^+e^-$ annihilation. The disregard of the spin–spin interaction between a heavy and a light quark—it is suppressed in proportion to $1/m_Q$—made it possible there to obtain the following interesting threshold relation for the pair production of $D$ and $D^*$ mesons (see Appendix):

$$\sigma_{D\bar{D}} : \sigma_{D\bar{D}^*+D^*\bar{D}} : \sigma_{D^*\bar{D}^*} = 1 : 4 : 7. \qquad (1)$$

That study was one of the first attempts at formulating heavy-quark effective theory.

A comprehensive analysis of the exclusive production of $D\bar{D}$ pairs in $e^+e^-$ interaction was performed in

---

[1)] Institute of Nuclear Physics, Moscow State University, Vorob'evy gory, Moscow, 119899 Russia.

*e-mail: `aber@ttk.ru`

[2] on the basis of the constituent quark model, which is more adequate. We recall that the constituent quark model is based on the assumption that, in the parton distributions of a meson, there are terms corresponding to valence quarks and the assumption that both these valence quarks are produced in a hard process, whereupon they form a meson.

The analytic expressions describing the cross sections for the exclusive production of pairs of pseudoscalar ($(Q\bar{q})_P$) and vector ($(Q\bar{q})_V$) mesons have the form [2]

$$\sigma(e^+e^- \to (Q\bar{q})_P(\bar{Q}q)_P) \tag{2}$$
$$= \frac{\pi^3\alpha_s^2(4m_q^2)\alpha_{\rm em}^2}{3^7\cdot 4m_q^6}\frac{m_Q^2}{M^2}f_P^4(1-v^2)^3v^3$$
$$\times\left\{3e_Q\left(\frac{2m_q}{m_Q}-1+v^2\right)-3e_q\right.$$
$$\left.\times\left[2-(1-v^2)\frac{m_q}{m_Q}\right]\frac{m_q^3\alpha_s(4m_Q^2)}{m_Q^3\alpha_s(4m_q^2)}\right\}^2,$$

$$\sigma(e^+e^- \to (Q\bar{q})_P(\bar{Q}q)_V) \tag{3}$$
$$= \frac{\pi^3\alpha_s^2(4m_q^2)\alpha_{\rm em}^2}{3^7\cdot 4m_q^6}\frac{4m_Q^2}{M^2}f_P^2f_V^2(1-v^2)^3v^3$$
$$\times\left[3e_Q+3e_q\frac{m_q^3\alpha_s(4m_Q^2)}{m_Q^3\alpha_s(4m_q^2)}\right]^2,$$

$$\sigma(e^+e^- \to (Q\bar{q})_V(\bar{Q}q)_V) = \frac{\pi^3\alpha_s^2(4m_q^2)\alpha_{\rm em}^2}{3^7\cdot 4m_q^6} \tag{4}$$
$$\times f_V^4(1-v^2)^3v^3\left[3e_Q-3e_q\frac{m_q^3\alpha_s(4m_Q^2)}{m_Q^3\alpha_s(4m_q^2)}\right]^2$$
$$\times\left[3(1-v^2)+(1+v^2)(1-a)^2\right.$$
$$\left.+\frac{a^2}{2}(1-v^2)(1-3v^2)\right],$$

where $m_q$ and $m_Q$ are the masses of, respectively, a light and a heavy quark; $f_P$ and $f_V$ are the constants that characterize the leptonic decay of, respectively, a pseudoscalar and a vector meson; $M = m_q + m_Q$; $v = \sqrt{1-4M^2/s}$; and the parameter $a$ is given by

$$a = \frac{m_Q}{M}\frac{1-\dfrac{e_q}{e_Q}\dfrac{m_q^4}{m_Q^4}\dfrac{\alpha_s(4m_Q^2)}{\alpha_s(4m_q^2)}}{1-\dfrac{e_q}{e_Q}\dfrac{m_q^3}{m_Q^3}\dfrac{\alpha_s(4m_Q^2)}{\alpha_s(4m_q^2)}}.$$

In the limit $m_Q \to \infty$, the cross sections at the threshold satisfy the relation

$$\sigma_{PP}:\sigma_{PV}:\sigma_{VV} = 1:4\frac{f_V^2}{f_P^2}:7\frac{f_V^4}{f_P^4}. \tag{5}$$

If one disregards the distinction between the values of $f_V$ and $f_P$, the ratios in (5) become identical to those in (1).

Heavy-quark effective theory predicts a ratio that, at the threshold, also coincides with that in (1); that is,

$$(1+h):\frac{s}{M^2}:3\left(1+\frac{s}{3M}+h\right),$$

where $h$ is a correction that appears upon taking into account the next order in $\alpha_s$:

$$h = -\frac{2\alpha_s}{3\pi}\sqrt{1-\frac{4M^2}{s}}$$
$$\times\ln\left(\frac{s}{2M^2}-1+\frac{s}{2M^2}\sqrt{1-\frac{4M^2}{s}}\right).$$

Expressions (2)–(4) for the cross sections receive contributions from four Feynman diagrams in Fig. 1, which are of second order both in $\alpha_s$ and in $\alpha_{\rm em}$. These diagrams are broken down into two gauge-invariant pairs. One pair corresponds to the interaction of a virtual photon with a heavy quark and is proportional to its charge (two upper diagrams in Fig. 1). For this pair, $\alpha_s$ is taken at the scale $4m_q^2$, since the gluon propagator in these diagrams involves two light quarks. The second pair (two lower diagrams in Fig. 1) corresponds to the interaction of a virtual photon with a light quark and is proportional to its charge. For this pair, $\alpha_s$ is taken at the scale $4m_Q^2$. It is obvious that the second contribution is suppressed by the factor $m_q^2/m_Q^2$ owing to the gluon propagator involving a pair of heavy quarks.

From formulas (2)–(4), it can be seen that, for $m_Q \to \infty$, one can neglect the interaction of a light quark with an initial virtual photon. It should be noted that the contribution of this interaction is negligible even at the masses of the quarks that form a $D$ meson.[2] Nevertheless, the spin–spin interaction remains significant, and this leads to a strong violation of relation (1). Instead of it, we have

$$\sigma_{D\bar{D}}:\sigma_{D\bar{D}^*+D^*\bar{D}}:\sigma_{D^*\bar{D}^*} \approx 1:8:14.$$

Thus, the production of a $D\bar{D}$ pair in $e^+e^-$ annihilation occurs as follows. A hard process produces a pair of heavy quarks, which, thereupon, undergoes

---

[2] In [2], the mass values were set to $m_c = 1.8$ GeV and $m_q = 0.2$ GeV.

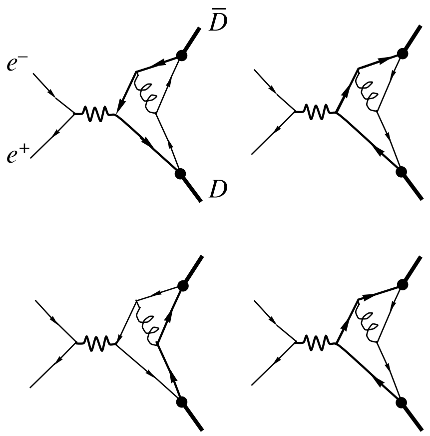

**Fig. 1.** Diagrams for the production of $D$ and $\bar{D}$ mesons in $e^+e^-$ annihilation.

hadronization via the interaction with the sea of light quarks. We recall that the inclusive production of $D$ mesons in $e^+e^-$ annihilation, where the fragmentation mechanism is operative [3], proceeds in a similar way. Thus, the role of light quarks in the hard production of $c$ quarks in $e^+e^-$ annihilation is insignificant. On the contrary, the presence of light quarks drastically changes the pattern of heavy-quark production in photon–photon interaction (see below).

## 2. EXCLUSIVE PRODUCTION OF A $D\bar{D}$ PAIR IN PHOTON–PHOTON INTERACTION

Within the constituent quark model, the exclusive production of two charmed mesons in photon–photon interaction is described by the 20 tree Feynman diagrams in Fig. 2.[3] These diagrams can be partitioned into three gauge-invariant groups. The first corresponds to the situation where a pair of light quarks is produced from the fermion line of a heavy quark (Fig. 2, diagrams *1–6*). The contribution of this group is proportional to the square of the heavy-quark charge. In the second group of diagrams (Fig. 2, diagrams *7–12*), the production of a heavy quark occurs, on the contrary, via the emission of a pair of heavy quarks from the fermion line of the light quark. This contribution is proportional to the square of the light-quark charge. These diagrams feature a gluon propagator involving the emitted pair, so that the diagrams proportional to the square of the light-quark charge are suppressed by the factor $m_q^2/m_Q^2$.

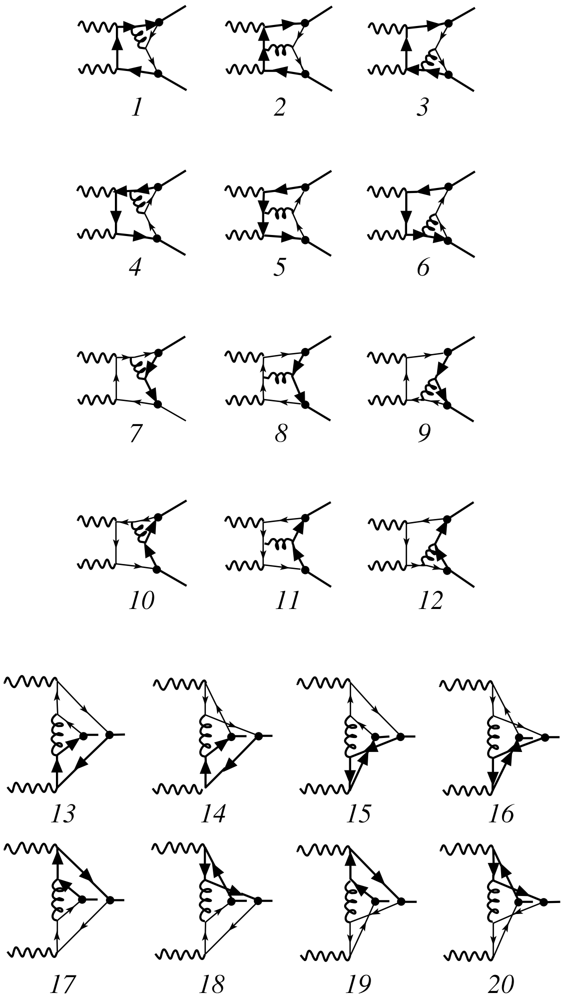

**Fig. 2.** Diagrams describing the production of two heavy mesons in photon–photon interaction.

In $e^+e^-$ annihilation, there are no diagrams contributing to the production of charmed mesons in photon–photon interaction and belonging to the third group (Fig. 2, diagrams *13–20*). In this group, each pair of quarks is connected to its own photon. Owing to this contribution, the interaction of a light quark with the initial photon is not suppressed.

Indeed, our calculations reveal that, in contrast to what occurs in $e^+e^-$ interaction, a light constituent quark plays a significant role in the exclusive production of a pair of charmed mesons in photon–photon interaction, generating a discrepancy between the predictions of heavy-quark effective theory and the constituent quark model, this discrepancy being present even in the limit $m_Q \to \infty$. In other words, the interaction of the light constituent quark with the initial photon is so strong that heavy-quark effective theory is inapplicable in this case.

Nevertheless, the agreement between the constituent quark model and heavy-quark effective theory is recovered if we set, in our calculations, the light-quark charge to zero (this corresponds to discarding

---

[3] A detailed description of the method of calculations, which is similar to that applied here, can be found in [4] (see Appendix there).

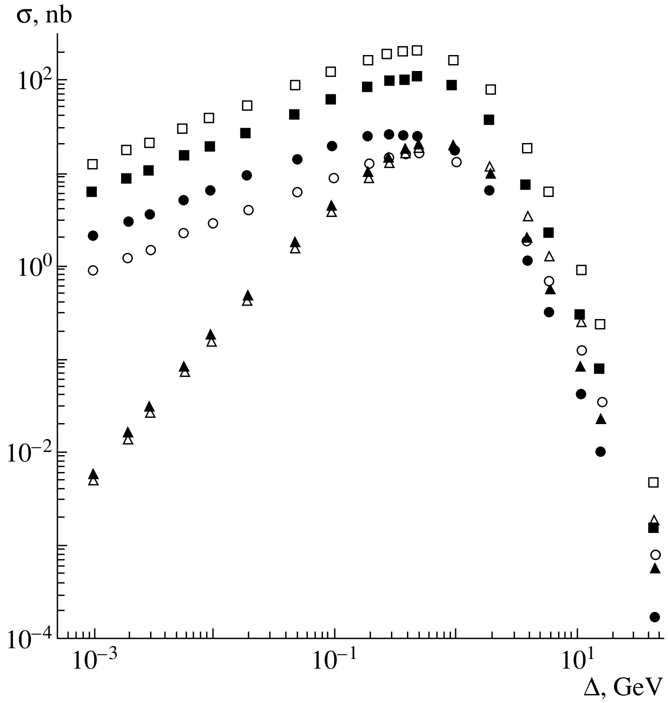

**Fig. 3.** Exclusive cross sections (○) $\sigma_{PP}$, (△) $\sigma_{PV}$, and (□) $\sigma_{VV}$ for the production of a pair of charged charmed mesons in photon–photon interaction versus $\Delta = \sqrt{s} - \sqrt{s_{\rm thr}}$. The respective closed symbols represent the analogous dependences at zero charge of a light quark.

the diagrams of the second and the third group). At zero light-quark charge and for $m_Q \to \infty$, we obtained, at the threshold, the ratio

$$\sigma_{PP} : \sigma_{PV} : \sigma_{VV} = 1 : 0 : 3, \qquad (6)$$

which was predicted in [5], where the approach proposed in [1] was applied to the case of photon–photon production (see Appendix). But the fact that the light-quark charge is nonzero considerably affects the character of $D\bar{D}$-pair production. Moreover, we find that $\sigma_{VV}/\sigma_{PP} \to \infty$ for $m_Q \to \infty$ and for $2m_Q/\sqrt{s} \to 1$.

Therefore, the idea that exclusive production proceeds via the process where the production of a heavy-quark pair is followed by hadronization is incorrect, as in the case of inclusive production [6].

In Fig. 3, the open symbols represent the exclusive cross sections for the production of a pair of charged charmed mesons in photon–photon interaction, $\sigma_{PP}$, $\sigma_{PV}$, and $\sigma_{VV}$, versus $\Delta = \sqrt{s} - \sqrt{s_{\rm thr}}$ at the following parameter values:

$$m_c = 1.5 \text{ GeV}, \quad m_q = 0.3 \text{ GeV}, \quad \alpha_s = 0.3.$$

In just the same way as in $e^+e^-$ annihilation, the cross sections $\sigma_{PP}$, $\sigma_{PV}$, and $\sigma_{VV}$ are proportional to $f_P^4$, $f_P^2 f_V^2$, and $f_V^4$, respectively.

The constants $f_P$ and $f_V$ are known from sum rules and lattice calculations, where $f_P \sim f_V \sim$ 200–300 MeV. We can use these values in our model. However, the absolute normalization of the cross sections depends, in our model, not only on these constants but also on the light-quark mass. A variation in the light-quark mass may lead to a change in the normalization.

At the same time, the cross section can be normalized by using the probability of $c \to D^*$ fragmentation in $e^+e^-$ interaction at high energies ($W(c \to D^*) = 0.22$). In this case, the quantities $m_q$ and $f$ appear to be correlated, and we obtain a scatter of the normalization within a factor of 2 to 2.5. In this approach, however, the constant $f$ proves to be overestimated at all reasonable values of the light-quark mass. We believe that this is because the contributions from the decays of higher excitations—for example, from the decay $D^{**} \to D^* + X$—are taken effectively into account in inclusive production,. Thus, the question of the absolute normalization of exclusive channels remains open in the approach used here, so that the dependences in Fig. 3 can be treated as an upper limit. But this is immaterial for all of the conclusions concerning the relative yield of $D$ mesons.

We note that, in the vicinity of the threshold, we have $\Delta \approx |k|^2/M$, where $|k|$ is the absolute value of the final meson 3-momentum in the c.m. frame. The presentation of the $\Delta$ dependences of the cross sections in Fig. 3 on a doubly logarithmic scale enables one to see that

$$\sigma_{VV}, \sigma_{PP} \sim \Delta^{1/2} \sim |k|,$$

$$\sigma_{PV} \sim \Delta^{3/2} \sim |k|^3.$$

This behavior is a clear consequence of the fact that, in $\gamma\gamma$ interaction, the threshold production of $D\bar{D}$ and $D^*\bar{D}^*$ pairs occurs in the $S$ wave ($L = 0$), while the production of $D\bar{D}^*$ pairs occurs in the $P$ wave ($L = 1$). Indeed, it is well known that, in such reactions, the threshold behavior obeys the law

$$\sigma \sim |k|^{2L+1}. \qquad (7)$$

Since, in our approach, Feynman diagrams describe quarks forming a charmed meson, the twisting of final mesons in the proper wave occurs automatically. Therefore, the observable behavior of the cross sections in the threshold region provides an additional corroboration of the correctness of our calculations.

From Fig. 3, one can see that the ratio in (6), which was obtained within heavy-quark effective theory, is strongly violated. Our calculations show that, in the threshold region,

$$\sigma_{PP} : \sigma_{PV} : \sigma_{VV} \approx 1 : 0 : 13.4.$$

It is interesting to consider the case where the coupling between light quarks and the initial photon can be disregarded, which corresponds to setting the electric charge of the light quark to zero. In Figure 3, the closed symbols represent the results of the calculations of the same cross sections at zero light-quark charge. It can easily be seen that, in this case, the cross-section ratio $\sigma_{PP} : \sigma_{PV} : \sigma_{VV}$ is in nearly perfect agreement with the predictions in (6). As the energy increases, there naturally arise deviations from this ratio. It is interesting to note that the contribution of the interaction with the light-quark charge can be either positive (as in the case of $D^*\bar{D}^*$-pair production) or negative (as in the case of $D\bar{D}$- or $D^*\bar{D}$-pair production). We also note that this contribution is minimal in absolute value for $D^*\bar{D}$-pair production, where mesons are formed in the $P$ wave.

The fact that the production of neutral mesons proceeds in a completely different way than the production of charged mesons additionally emphasizes the important role of the light quark in the production of charmed mesons. This can be observed in Fig. 4, where the $\Delta$ dependences of the cross section for the production of neutral mesons (closed symbols) are presented along with the same dependences for charged mesons (open symbols). One can see that, for charged mesons, the threshold ratio is $\sigma_{D^+D^-} : \sigma_{D^{+*}D^{-*}} \approx 1 : 13.4$, while, for neutral mesons, it is $\sigma_{D^0\bar{D}^0} : \sigma_{D^{0*}\bar{D}^{0*}} \approx 1 : 2.7$. It should also be noted that the minimum distinction between the results for charged and neutral mesons is observed in the threshold production of $D\bar{D}^*$ pairs—that is, in the case where the mesons are produced in the $P$ wave.

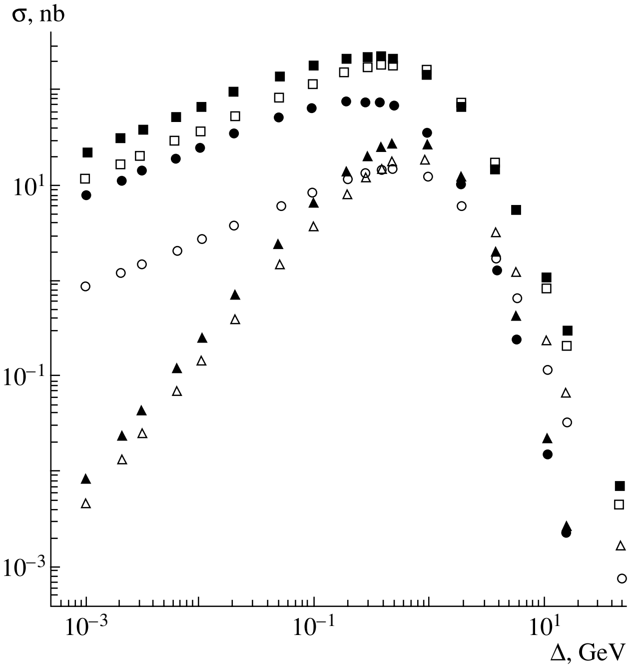

**Fig. 4.** Cross section for the production of (closed symbols) neutral $D$ mesons as a function of $\Delta$ along with the same dependence for (open symbols) charged mesons: (●, ○) $\sigma_{PP}$, (▲, △) $\sigma_{PV}$, and (■, □) $\sigma_{VV}$.

The distinctions between the production of neutral and charged $B$ mesons may be even more significant. The cross section for the production of neutral $B$ mesons versus $\Delta = \sqrt{s} - \sqrt{s_{\text{thr}}}$ is given in Fig. 5 at $m_b = 5$ GeV and $m_q = 0.2$ GeV. On the basis of an analysis of Fig. 4, it can be concluded that, in the case of $D$-meson production, the $\Delta$ dependences of the cross sections have qualitatively the same shape for neutral and charged particles, but this is not so for the production of $B$ mesons. Figure 5 shows that, in the production of two pseudoscalar mesons $B^+$ and $B^-$, the cross section displays an interference dip at $\Delta \approx 0.12$ GeV ($|k| \approx 0.8$ GeV), but there is no such dip in the production of a pair of neutral pseudoscalar mesons $B^0$ and $\bar{B}^0$.

Thus, we can conclude that, in the production of heavy mesons in photon–photon interaction, the light-quark contribution must be taken into account even in the threshold region. Models that disregard this contribution cannot provide even a qualitative description of the process under consideration. Our analysis of the production of a heavy-meson pair in photon–photon interaction reveals that naive concepts borrowed from the experience gained in study-

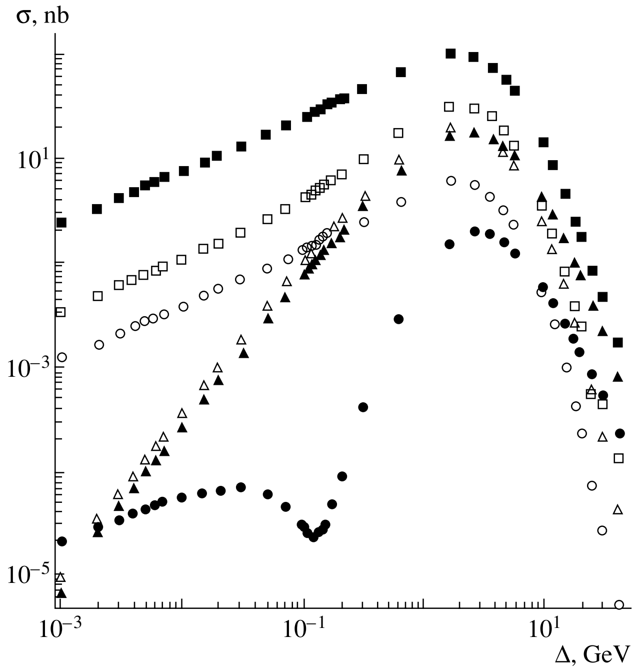

**Fig. 5.** Cross sections for the production of (closed symbols) charged and (open symbols) neutral $B$ mesons versus $\Delta$: (●, ○) $\sigma_{PP}$, (▲, △) $\sigma_{PV}$, and (■, □) $\sigma_{VV}$.

ing $e^+e^-$ annihilation are not correct: in the processes $\gamma\gamma \to D\bar{D}$ and $\gamma\gamma \to B\bar{B}$, the role of light quarks is significant both in the soft process of hadronization and in the hard production of a pair of heavy quarks. Experimental data on threshold production would shed light on the dynamics of the production of mesons featuring heavy quarks, but, unfortunately, there are no such data at the present time.

## 3. INCLUSIVE PRODUCTION OF HEAVY MESONS IN PHOTON–PHOTON INTERACTION

As was mentioned above, the exclusive production of heavy mesons is of great interest from the point of view of a comparison of the predictions of various models; however, the potential of experiments along these lines of investigation is severely limited. At the present time, the majority of relevant measurements are being performed for the inclusive production of $D$ mesons. The calculations performed in the next-to-leading order of QCD both for massive [7] and for massless [8] $c$ quarks satisfactorily reproduce respective experimental data. Since the effect of light quarks on $c$-quark production is disregarded, the yield of $D^*$ mesons within these approaches is independent of the meson type: $\sigma_{D^{*0}} = \sigma_{D^{*+}}$.

Let us now consider the predictions of our model for the inclusive production of heavy mesons, which is described by the same diagrams in Fig. 2, the only difference being that, now, the second pair of heavy and light quarks is not combined into a meson. In this way, we take into account the resonance part of the spectrum for one pair of quarks and a continuum for the other pair. In just the same way as in calculating the cross section for the exclusive production of charmed mesons, we will use the parameter values that previously made it possible to reproduce the HERA data on the photoproduction of $D^*$ mesons [6]. In these estimates, we will also take into account the octet contribution, which is obviously absent in the case of exclusive production. In the inclusive production of $D$ mesons in photon–photon interaction, the contribution of the $c\bar{q}$ octet differs from the singlet contribution only by a factor. If one describes octet production by using the same parameter values as in [6], its contribution will be about 16% of the total cross section for the inclusive production of $D$ mesons.

From Fig. 6, it can be seen that the cross section for the inclusive production of $D$ mesons is on the same order of magnitude as the value obtained in the L3 experiment [9]. It was indicated above that, even in exclusive production, the light-quark charge plays a significant role in the photon structure and, for the ratio $\sigma_{D^{*+}}/\sigma_{D^{*0}}$, leads to a value different from unity. Our calculations show that the inclusive yield of $D^{*0}$ mesons is approximately twice as great as the yield of $D^{*+}$ mesons. In contrast to this, the fragmentation models predict $\sigma_{D^{*0}}/\sigma_{D^{*+}} = 1$.

This figure also shows that, at energies in excess of 15 GeV, in which case the contribution of large invariant $c\bar{q}$ masses becomes significant, the total charm-production cross section calculated within our model (triangles in Fig. 6) begins to decrease, falling short of the experimental data. In this kinematical region, the contribution of a continuum must be taken into account along with the contribution of the resonance part of the $c\bar{q}$ spectrum. In calculating this contribution, we do not couple now light quarks to $c$ quarks and consider, within our model, the total inclusive production cross section to $O(\alpha_s^2\alpha^2)$ terms (in Fig. 6, the cross section calculated with allowance for the continuum contribution is represented by boxes). We expect that the yields of charged and neutral mesons will be identical in this case. Thus, the ratio $\sigma_{D^0}/\sigma_{D^+}$ could be a good signature of the production mechanism. In terms of the structure functions, the inclusion of this mechanism corresponds to taking into account the hadron structure of the photon. The diagrams in Fig. 2 make it possible to take into account the perturbative part of the photon structure only partly. It can be seen that we underestimate the cross section. Therefore, an additional contribution to the photon structure function must be included.

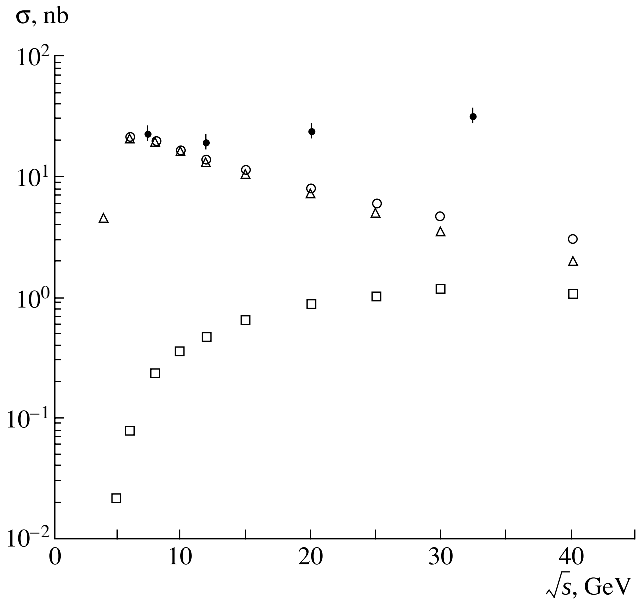

**Fig. 6.** Cross section for charm production in $\gamma\gamma \to c\bar{c} + X$ (○) processes along with the experimental data obtained by the L3 Collaboration [9] (●). The notation for the remaining symbols is explained in the main body of the text.

The calculations performed in [7, 8] show that the inclusion of such a contribution provides a satisfactory description of experimental data.

## CONCLUSION

Within the model formulated above, we have analyzed, in the vicinity of the threshold, both the exclusive production of a pair of mesons featuring a heavy quark and their inclusive production at high energies. In the threshold region, we have calculated the relative yield of various meson pairs and found that this ratio depends greatly on whether the light-quark degree of freedom is taken into account in $\gamma\gamma$ collisions. At zero electric charge of the light quark, we have obtained cross-section estimates that are consistent with the present-day idea of the meson-production process as that in which the production of heavy quarks is followed by their hadronization. At actual values of the charges, there is a strong deviation from the predictions of heavy-quark effective theory. From our analysis of the production of a heavy-meson pair in photon–photon interaction, it therefore follows that naive concepts borrowed from the investigation of $e^+e^-$ annihilation are not valid. In the processes $\gamma\gamma \to D\bar{D}$ and $\gamma\gamma \to B\bar{B}$, the role of light quarks is significant both in the soft hadronization process and in the hard process of the production of a heavy-quark pair. Within our model, we cannot, unfortunately, use the same values of the constants $f_P$ and $f_V$ in calculating the cross sections for the exclusive and inclusive channels. The use of the $f_P$ and $f_V$ values borrowed from the description of the process $\gamma p \to D^* + X$ leads to a strong overestimation of the cross sections in the threshold region. We assume that this is because the values employed for the constants in describing the inclusive process effectively involve the contribution from the decays of higher states—for example, from the decay $D^{**} \to D^* + X$—and are therefore inapplicable to the case of exclusive production. Nevertheless, our model predicts the relations between the aforementioned contributions to the production of various pairs of heavy mesons ($D^0\bar{D}^0$, $D^{0*}\bar{D}^0$, $D^{0*}\bar{D}^{0*}$, $D^0\bar{D}^{0*}$, $D^+D^-$, $D^+D^{-*}$, $D^-D^{+*}$, $D^{+*}D^{-*}$), the dependence of the cross sections on the interaction energy, and the shapes of various differential distributions. Within the same model, we have calculated the cross section for the inclusive production of charmed mesons in photon–photon interaction.

The cross section corresponding to the resonance contribution of the $c\bar{q}$ system and to the contribution of a continuum for the other quark pair has been calculated with the same parameter values as those used in describing charm production in the process $\gamma p \to D^* + X$ [6] (HERA). At low energies of $\gamma\gamma$ interaction, the results are consistent with experimental data. This is not unexpected for us because the contribution of low energies of $\gamma g$ interaction is significant in describing the HERA data on the photoproduction of $D^*$ mesons. As the energy increases, the contribution of the continuum grows, in which case the calculations must rely on a procedure identical to that in [7, 8], where the increase in the cross section for the reaction $\gamma\gamma \to c\bar{c}$ was explained by the presence of light constituents in the structure of the primary photon.

## ACKNOWLEDGMENTS

This work was supported in part by the Russian Foundation for Basic Research (project nos. 99-02-16558, 00-15-96645, 01-02-16585), by the Ministry of Education of the Russian Federation (grant no. E02-3.1-96), and by the CRDF (grant no. MO-001-0) and was performed within the Program for Support of Scientific Schools (grant no. NSh-1303.2003.2).

## APPENDIX

In this appendix, we will show how the threshold ratio $\sigma_{PP} : \sigma_{PV} : \sigma_{VV}$ for the production of heavy mesons in $e^+e^-$ annihilation and in $\gamma\gamma$ interaction can be obtained within heavy-quark effective theory. We adopt the following notation: $Q_{+(-)}$ is the wave function for a heavy quark having the spin projection $+1/2$ $(-1/2)$ onto the chosen axis; $\bar{Q}_{+(-)}$ is the heavy-antiquark wave function; and $q_{+(-)}$ and $\bar{q}_{+(-)}$ are, respectively, the light-quark and the light-antiquark wave function.

Within heavy-quark effective theory, the production of heavy quarks in $e^+e^-$ annihilation proceeds via the decay of a virtual photon; therefore, they are in the $1^-$ state. For such a state, the spin part of the wave function can be expressed in terms of the spinor quark wave functions as

$$\hat{\Psi}_{Q\bar{Q}} = \left(\Psi^{+1}_{Q\bar{Q}}, \Psi^{0}_{Q\bar{Q}}, \Psi^{-1}_{Q\bar{Q}}\right) = \left(Q_+\bar{Q}_+, \frac{Q_+\bar{Q}_- + Q_-\bar{Q}_+}{\sqrt{2}}, Q_-\bar{Q}_-\right).$$

Light quarks, which, within heavy-quark effective theory, do not interact with heavy quarks via spins, must be in the $0^+$ state. In the $P$ wave, this state can be constructed as

$$\psi_{q\bar{q}} = (n_{-1}\Psi^{+1}_{q\bar{q}} + n_0\Psi^{0}_{q\bar{q}} + n_{+1}\Psi^{-1}_{q\bar{q}})/\sqrt{3},$$

where $\hat{n}$ is the orbital part of the wave function for the system of two light quarks and $\hat{\Psi}_{q\bar{q}}$ is its spin part,

$$\hat{\Psi}_{q\bar{q}} = \left(\Psi^{+1}_{q\bar{q}}, \Psi^{0}_{q\bar{q}}, \Psi^{-1}_{q\bar{q}}\right) = \left(q_+\bar{q}_+, \frac{q_+\bar{q}_- + q_-\bar{q}_+}{\sqrt{2}}, q_-\bar{q}_-\right).$$

Thus, the total wave function has the form

$$\hat{\Psi} = \hat{\Psi}_{Q\bar{Q}} \cdot \left(n_{-1}\Psi^{+1}_{q\bar{q}} + n_0\Psi^{0}_{q\bar{q}} + n_{+1}\Psi^{-1}_{q\bar{q}}\right)/\sqrt{3}. \tag{A.1}$$

On the right-hand side of the last equation, there appear the products of the spinor quark wave functions, $Q_{+(-)}\bar{q}_{+(-)}$ and $\bar{Q}_{+(-)}q_{+(-)}$. They can be expressed in terms of the spin wave functions for final mesons. For example, the pseudoscalar-meson wave function has the form

$$P = (Q_+\bar{q}_- - Q_-\bar{q}_+)/\sqrt{2}. \tag{A.2}$$

For the components of the vector meson, we have

$$V_{+1} = Q_+\bar{q}_+, \tag{A.3}$$

$$V_0 = (Q_+\bar{q}_- + Q_-\bar{q}_+)/\sqrt{2}, \tag{A.4}$$

$$V_{-1} = Q_-\bar{q}_-. \tag{A.5}$$

From Eqs. (A.2) and (A.4), it follows that

$$Q_+\bar{q}_- = (V_0 + P)/\sqrt{2}, \tag{A.6}$$

$$Q_-\bar{q}_+ = (V_0 - P)/\sqrt{2}. \tag{A.7}$$

By using Eqs. (A.3) and (A.5)–(A.7), we obtain the following expressions for the components of the total wave function (A.1):

$$\Psi^{+1} = \frac{1}{2\sqrt{3}}\Big(n_{+1}P\bar{P} + \{n_{+1}P\bar{V}_0 + n_{+1}V_0\bar{P} + n_0P\bar{V}_{+1} + n_0V_{+1}\bar{P}\} + [n_{+1}V_0\bar{V}_0 + n_0V_0\bar{V}_{+1} + n_0V_{+1}\bar{V}_0 + 2n_{-1}V_{+1}\bar{V}_{+1}]\Big), \tag{A.8}$$

$$\Psi^{0} = \frac{1}{2\sqrt{3}}\Big(-n_0P\bar{P} + \{n_{+1}P\bar{V}_{-1} + n_{+1}V_{-1}\bar{P} - n_{-1}P\bar{V}_{+1} - n_{-1}V_{+1}\bar{P}\} + [n_{+1}V_0\bar{V}_{-1} + n_{+1}V_{-1}\bar{V}_0 + n_0V_0\bar{V}_0 + n_0V_{+1}\bar{V}_{-1} + n_0V_{-1}\bar{V}_{+1} + n_{-1}V_{+1}\bar{V}_0 + n_{-1}V_0\bar{V}_{+1}]\Big), \tag{A.9}$$

$$\Psi^{-1} = \frac{1}{2\sqrt{3}}\Big(n_{-1}P\bar{P} - \{n_{-1}P\bar{V}_0 + n_{-1}V_0\bar{P} + n_0P\bar{V}_{-1} + n_0V_{-1}\bar{P}\} + [n_{-1}V_0\bar{V}_0 + n_0V_0\bar{V}_{-1} + n_0V_{-1}\bar{V}_0 + 2n_{+1}V_{-1}\bar{V}_{-1}]\Big). \tag{A.10}$$

We assume that the spins of heavy and light quarks do not interact with one another or with the orbital angular momentum; therefore, all terms on the right-hand sides of Eqs. (A.8)–(A.10) make the same contributions to the square of the total wave function $\hat{\Psi}$. Since these terms are orthogonal, the result in (5) becomes obvious.

In the case of $\gamma\gamma$ interaction, two primary photons can be in the $0^+$, the $0^-$, or the $2^+$ state, only the $0^+$ state being produced in the $S$ wave. It is the $0^+$ state that will be considered below, since only the contributions corresponding to the minimal number of a wave [see Eq. (7)] survive at the threshold. This state can be formed by the two pseudoscalar functions

$$\Psi_{Q\bar{Q}} = \frac{Q_+\bar{Q}_- - Q_-\bar{Q}_+}{\sqrt{2}} \text{ and } \Psi_{q\bar{q}} = \frac{q_+\bar{q}_- - q_-\bar{q}_+}{\sqrt{2}}$$

as follows:

$$\Psi = \Psi_{Q\bar{Q}} \cdot \Psi_{q\bar{q}}. \tag{A.11}$$

By transforming expression (A.11) with the aid of (A.3) and (A.5)–(A.7), we obtain

$$\Psi = (-P\bar{P} + V_0\bar{V}_0 - V_{-1}\bar{V}_{+1} - V_{+1}\bar{V}_{-1})/2,$$

whence one can easily derive the aforementioned relationship for threshold production in photon–photon interaction; that is,

$$\sigma_{PP} : \sigma_{PV} : \sigma_{VV} = 1 : 0 : 3.$$

## REFERENCES

1. A. De Rújula, H. Georgi, and S. L. Glashow, Phys. Rev. Lett. **37**, 398 (1976).
2. V. V. Kiselev, Int. J. Mod. Phys. A **10**, 465 (1995).
3. V. G. Kartvelishvili, A. K. Likhoded, and V. A. Petrov, Phys. Lett. B **78B**, 615 (1978).
4. A. V. Berezhnoy and A. K. Likhoded, hep-ph/0204268.
5. V. G. Kartvelishvili and A. K. Likhoded, Pis'ma Zh. Éksp. Teor. Fiz. **26**, 54 (1977) [JETP Lett. **26**, 46 (1977)].
6. A. V. Berezhnoy, V. V. Kiselev, and A. K. Likhoded, Phys. Rev. D **62**, 074013 (2000).
7. S. Frixione, M. Krämer, and E. Laenen, Nucl. Phys. B **571**, 169 (2000); J. Phys. G **26**, 723 (2000).
8. J. Binnewies, B. A. Kniehl, and G. Kramer, Phys. Rev. D **53**, 6110 (1996); **58**, 014014 (1998).
9. L3 Collab. (M. Acciarri *et al.*), Phys. Lett. B **514**, 19 (2001).

*Translated by A. Isaakyan*

*Physics of Atomic Nuclei, Vol. 67, No. 4, 2004, pp. 824–836. Translated from Yadernaya Fizika, Vol. 67, No. 4, 2004, pp. 846–858.*
*Original Russian Text Copyright © 2004 by Zotov, Lipatov.*

**ELEMENTARY PARTICLES AND FIELDS**
**Theory**

# Investigation of the Balitsky–Fadin–Kuraev–Lipatov Dynamics of Gluon Distributions in the Inelastic Production of $J/\psi$ Mesons at the HERA Collider

**N. P. Zotov*** **and A. V. Lipatov**[1)]

*Institute of Nuclear Physics, Moscow State University, Vorob'evy gory, Moscow, 119899 Russia*

Received November 15, 2002; in final form, May 26, 2003

**Abstract**—The inelastic photo- and electroproduction of $J/\psi$ mesons at the HERA collider are considered within the semihard ($k_T$-factorization) QCD approach and the color-singlet model. The total, differential, and double-differential cross sections for the inelastic production of $J/\psi$ mesons are investigated versus the Pomeron intercept $\Delta$, which is the basic parameter of low-$x$ physics; also studied here is the spin alignment parameter $\alpha$ versus the square of the transverse momentum, $\mathbf{p}^2_{\psi T}$, and the variable $z$. The theoretical results obtained in the present study are compared with the latest experimental data of the H1 and ZEUS Collaborations. It is shown that experimental investigations of the polarization properties of $J/\psi$ mesons at the HERA collider for $Q^2 < 1$ GeV$^2$ may provide an additional test of the Balitsky–Fadin–Kuraev–Lipatov dynamics of gluon distributions. © *2004 MAIK "Nauka/Interperiodica"*.

## 1. INTRODUCTION

Recently, the H1 and ZEUS Collaborations obtained new experimental data [1–3] on the inelastic photo- and electroproduction of $J/\psi$ mesons at the HERA collider. It is well known that, in the fixed order of perturbative QCD, the ordinary parton model runs into some difficulties both in a qualitative and in a quantitative description of the production of heavy quarks and quarkonia. In the present study, the semihard ($k_T$-factorization) QCD approach [4] will therefore be used to describe experimental data reported [1–3]. By semihard processes, one usually means reactions where the characteristic scale $\mu \sim m_Q$ (where $m_Q$ is the heavy-quark mass) of the hard parton-scattering subprocess is much less than $\sqrt{s}$ (the total energy of colliding particles in the c.m. frame), but it is much greater than the parameter $\Lambda_{\rm QCD}$—that is, $\Lambda_{\rm QCD} \ll \mu \ll \sqrt{s}$—in which case the QCD running coupling constant remains small: $\alpha_{\rm QCD}(\mu^2) \ll 1$. The condition $\mu \ll \sqrt{s}$ implies that the cross sections for such processes are determined by the behavior of the gluon structure functions in the proton at low values of the variable $x$, $x \simeq m_Q/\sqrt{s} \ll 1$. At such values of $x$, the parton-model assumption that the cross sections for the relevant subprocesses and the hadron structure functions factorize is violated, so that it is necessary to take into account the dependence of the amplitude for a hard scattering subprocess on the virtuality and on the longitudinal polarization of gluons [5–7].

The gluon distributions in the proton, $xG(x, \mu^2)$, can be derived from the Dokshitzer–Gribov–Lipatov–Altarelli–Parisi (DGLAP) evolution equations [8]. In the leading-logarithm approximation, one takes into account the contributions of the form $\alpha_s^n \ln^n(\mu^2/\Lambda^2_{\rm QCD})$.

As the c.m. energy of colliding particles, $\sqrt{s}$, increases, however, contributions of order $\alpha_s^n \ln^n(s/\Lambda^2_{\rm QCD}) \sim \alpha_s^n \ln^n(1/x)$, which are disregarded in the DGLAP equations, begin to play an ever more pronounced role. Summation of diagrams involving terms of order $\alpha_s^n \ln^n(1/x)$ leads to unintegrated gluon distributions (that is, distributions that are dependent on the transverse momentum $\mathbf{q}_T$) $\Phi(x, \mathbf{q}_T^2)$ satisfying the Balitsky–Fadin–Kuraev–Lipatov (BFKL) [9] evolution equations. The inclusion of all leading logarithmic and doubly logarithmic contributions leads to an additional dependence of the unintegrated gluon distributions on $\mu^2$.

Cross sections for physical processes are determined by a convolution of unintegrated gluon distributions with the off-shell matrix element for the relevant hard subprocess [5–7]. In addition, the polarization tensor $L^{\mu\nu}$ for virtual gluons in the matrix element for the subprocess of photon–gluon or gluon–gluon fusion is prescribed by the semihard

---

[1)] Moscow State University, Vorob'evy gory, Moscow, 119899 Russia; e-mail: `lipatov@theory.sinp.msu.ru`

[*] e-mail: `zotov@theory.sinp.msu.ru`

approach to have the form [4]

$$L^{\mu\nu} = q_T^{\mu} q_T^{\nu} / \mathbf{q}_T^2. \tag{1}$$

The semihard approach was previously used to describe a number of processes [5, 10–26]. We note that calculations within the theory of semihard processes lead to some observable effects that do not emerge in other approaches—namely, a faster growth of cross sections in relation to what is obtained from calculations within the usual parton model [12–15] and the broadening of transverse-momentum ($p_T$) spectra in relation to the results produced by the parton model, this flattening becoming more significant as the energy increases [10–21].

We emphasize that calculations of cross sections for the production of heavy quarks and quarkonia within the usual parton model to a fixed order of perturbative QCD lead to some difficulties in the description of experimental data as they become vaster and more precise. For example, it was found that, for the production of $J/\psi$ and $\Upsilon$ mesons in proton–antiproton interactions, the cross sections calculated within the usual parton model fall short of experimental data by more than one order of magnitude [27, 28]. This fact gave impetus to intensive theoretical investigations into such processes—in particular, it was required to introduce additional mechanisms through which $c\bar{c}$ states undergo transitions to $J/\psi$ mesons (so-called color-octet model [29]). The color-octet model claims to provide a complete description of quarkonium-production processes both in proton–antiproton and electron–proton interactions, but it immediately ran into the problem of describing the photoproduction of $J/\psi$ mesons [30, 31] at the HERA collider energies, where the contribution of the color-octet mechanism is insignificant or is even at odds with experimental data [32, 33]. Another feature peculiar to the color-octet model is associated with the polarization properties of $J/\psi$ mesons produced in proton–antiproton interactions at the Tevatron. If, as is expected, a dominant contribution to the production of $J/\psi$ mesons comes from gluon fragmentation into octet $c\bar{c}$ pairs, then $J/\psi$ mesons must predominantly have a transverse polarization at high transverse momenta, but this contradicts experimental data, which are indicative of the absence of polarization of product $J/\psi$ mesons or of their longitudinal polarization.

The color-octet model was also used in [34, 35] to describe the deep-inelastic electroproduction of $J/\psi$ mesons at the HERA collider, but the results obtained in those two studies contradict each other [35]. The results of the calculations performed in [36–39] within the usual parton model to a fixed order of perturbation theory and within the color-singlet model differ from experimental data by a factor greater than two.

The inelastic production of $J/\psi$ mesons at the HERA collider was studied in [17–19] within the semihard QCD approach and the color-singlet model. The theoretical predictions obtained in [17] simulated an experimental analysis of the polarization properties of $J/\psi$ mesons at HERA energies. In [18, 19], we studied the dependence of the total and differential cross sections for the production of $J/\psi$ mesons on various sets of unintegrated gluon distributions. Results obtained in [19] show that the latest experimental data of the H1 Collaboration [1] can be described within the semihard QCD approach at a realistic value of the $c$-quark mass, $m_c = 1.55$ GeV.

The present article reports on a continuation of the investigation into the inelastic photo- and electroproduction of $J/\psi$ mesons at the HERA collider within the semihard QCD approach. In particular, it is of considerable interest to explore the sensitivity of the total and differential cross sections for the production of $J/\psi$ mesons to the Pomeron intercept $\Delta$, which is a basic parameter of low-$x$ physics, and to study the polarization properties of final $J/\psi$ mesons versus the transverse momentum squared $\mathbf{p}_{\psi T}^2$ and the variable $z$.

The ensuing exposition is organized as follows. In Section 2, we give expressions for the total and differential cross sections for the inelastic photo- and electroproduction of $J/\psi$ mesons within the $k_T$-factorization approach and within the color-singlet model. Also, some features of unintegrated gluon distributions used in the present study are discussed there. In Section 3, we present the results of our numerical calculations and compare them with the latest experimental data of the H1 [1, 2] and ZEUS [3] Collaborations. In Section 4, we briefly summarize the basic results and conclusions obtained in the present study.

## 2. PRODUCTION OF $J/\psi$ MESONS WITHIN THE SEMIHARD QCD APPROACH

### 2.1. Kinematics

By $p_e$ and $p_p$, we denote the 4-momenta of the primary electron and proton, respectively (Fig. 1). In the subsequent calculations, we will use the Sudakov decomposition, which, for the process $ep \to e' J/\psi X$, has the form

$$\begin{gathered} p_\psi = \alpha_1 p_e + \beta_1 p_p + p_{\psi T}, \\ p_g = \alpha_2 p_e + \beta_2 p_p + p_{gT}, \\ q_1 = x_1 p_e + q_{1T}, \quad q_2 = x_2 p_p + q_{2T}, \end{gathered} \tag{2}$$

where

$$\begin{gathered} p_\psi^2 = m_\psi^2, \quad p_g^2 = 0, \\ q_1^2 = q_{1T}^2 = -Q^2, \quad q_2^2 = q_{2T}^2. \end{gathered} \tag{3}$$

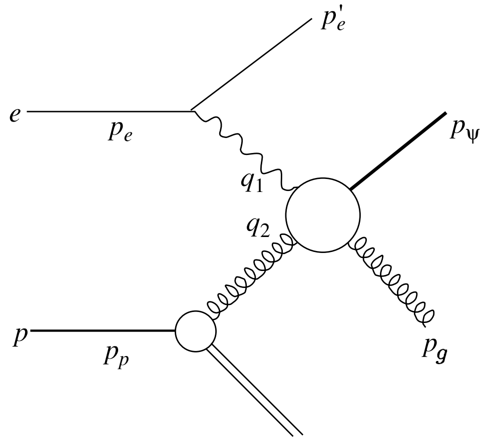

**Fig. 1.** Diagram for the deep-inelastic production of $J/\psi$ mesons in electron–proton interactions.

Here, $p_\psi$ and $p_g$ are the 4-momenta of the $J/\psi$ meson and the final gluon, respectively; $q_1$ and $q_2$ are the 4-momenta of the initial virtual photon and the initial gluon, respectively; $p_{\psi T}$, $p_{gT}$, $q_{1T}$, and $q_{2T}$ are the transverse 4-momenta of the corresponding particles; and $m_\psi$ is the $J/\psi$-meson mass. Disregarding the masses of the initial particles, we find in the electron–proton c.m. frame that

$$p_e = \sqrt{s}/2(1,0,0,1), \quad p_p = \sqrt{s}/2(1,0,0,-1), \tag{4}$$

where $p_e^2 = p_p^2 = 0$ and $(p_e \cdot p_p) = s/2$. The Sudakov variables are given by

$$\alpha_1 = \frac{m_{\psi T}}{\sqrt{s}} \exp(y_\psi), \quad \alpha_2 = \frac{|\mathbf{p}_{gT}|}{\sqrt{s}} \exp(y_g), \tag{5}$$
$$\beta_1 = \frac{m_{\psi T}}{\sqrt{s}} \exp(-y_\psi), \quad \beta_2 = \frac{|\mathbf{p}_{gT}|}{\sqrt{s}} \exp(-y_g),$$

where $m_{\psi T}^2 = m_\psi^2 + \mathbf{p}_{\psi T}^2$ and $y_\psi$ and $y_g$ are the rapidities of, respectively, the $J/\psi$ meson and the final gluon in the c.m. frame of colliding particles. Using the law of energy–momentum conservation, we can easily obtain the relations

$$x_1 = \alpha_1 + \alpha_2, \quad x_2 = \beta_1 + \beta_2, \tag{6}$$
$$\mathbf{q}_{1T} + \mathbf{q}_{2T} = \mathbf{p}_{\psi T} + \mathbf{p}_{gT}.$$

In describing $J/\psi$-meson production, use is often made of the variable $z = (p_\psi \cdot p_p)/(q_1 \cdot p_p)$. In the proton rest frame, we have $z = E_\psi/E_\gamma$.

### *2.2. Differential Cross Section for the Inelastic Electroproduction of $J/\psi$ Mesons*

Within the semihard QCD approach, the differential cross section for the process $ep \to e'J/\psi X$ can be represented in the form

$$d\sigma(ep \to e'J/\psi X) = \frac{dx_2}{x_2}\Phi(x_2, \mathbf{q}_{2T}^2, \mu^2)\frac{d\phi_2}{2\pi} \tag{7}$$
$$\times\, d\mathbf{q}_{2T}^2 d\hat{\sigma}(eg^* \to e'J/\psi g'),$$

where $\phi_2$ is the azimuthal angle of the initial virtual gluon; $\Phi(x_2, \mathbf{q}_{2T}^2, \mu^2)$ is the unintegrated gluon distribution; and

$$d\hat{\sigma}(eg^* \to e'J/\psi g') = \frac{(2\pi)^4}{2x_2 s} \tag{8}$$
$$\times \sum |M|^2_{\mathrm{SHA}}(eg^* \to e'J/\psi g')$$
$$\times \frac{d^3p_e'}{(2\pi)^3 \cdot 2p_e'^{\,0}} \frac{d^3p_\psi}{(2\pi)^3 \cdot 2p_\psi^0} \frac{d^3p_g}{(2\pi)^3 \cdot 2p_g^0}$$
$$\times\, \delta^{(4)}(p_e + q_2 - p_e' - p_\psi - p_g),$$

with $\sum |M|^2_{\mathrm{SHA}}(eg^* \to e'J/\psi g')$ being the matrix element calculated for the hard-scattering subprocess $eg^* \to e'J/\psi g'$ within the semihard QCD approach. In (8), the symbol $\sum$ denotes averaging over the polarizations of the initial particles and summation over the polarizations of the final particles. From expressions (7) and (8), one can easily obtain the final expression for the differential cross section describing the process $ep \to e'J/\psi X$ within the semihard QCD approach. The result is

$$d\sigma(ep \to e'J/\psi X) = \frac{1}{128\pi^3}\frac{\Phi(x_2, \mathbf{q}_{2T}^2, \mu^2)}{(x_2 s)^2(1-x_1)} \tag{9}$$
$$\times \frac{dz}{z(1-z)} dy_\psi \sum |M|^2_{\mathrm{SHA}}(eg^* \to e'J/\psi g') d\mathbf{p}_{\psi T}^2$$
$$\times\, dQ^2 d\mathbf{q}_{2T}^2 \frac{d\phi_1}{2\pi}\frac{d\phi_2}{2\pi}\frac{d\phi_\psi}{2\pi},$$

where $\phi_1$ and $\phi_\psi$ are the azimuthal angles of the initial virtual photon and the $J/\psi$ meson, respectively.

### *2.3. Differential Cross Section for the Inelastic Photoproduction of $J/\psi$ Mesons*

Within the semihard QCD approach, the differential cross section for the process $\gamma p \to J/\psi X$ can be represented in the form

$$d\sigma(\gamma p \to J/\psi X) = \frac{dx_2}{x_2}\Phi(x_2, \mathbf{q}_{2T}^2, \mu^2) \tag{10}$$
$$\times \frac{d\phi_2}{2\pi} d\mathbf{q}_{2T}^2 d\hat{\sigma}(\gamma g^* \to J/\psi g'),$$

where $d\hat{\sigma}(\gamma g^* \to J/\psi g')$ is the differential cross section for the hard parton subprocess of photon–gluon fusion. For $Q^2 \to 0$ and $x_1 \to 1$, the use of the same procedure as in the preceding section makes it possible to obtain an expression that describes the cross section for the inelastic electroproduction of $J/\psi$ mesons within the semihard approach. The result is

$$d\sigma(\gamma p \to J/\psi X) = \frac{1}{16\pi(x_2 s)^2} \tag{11}$$

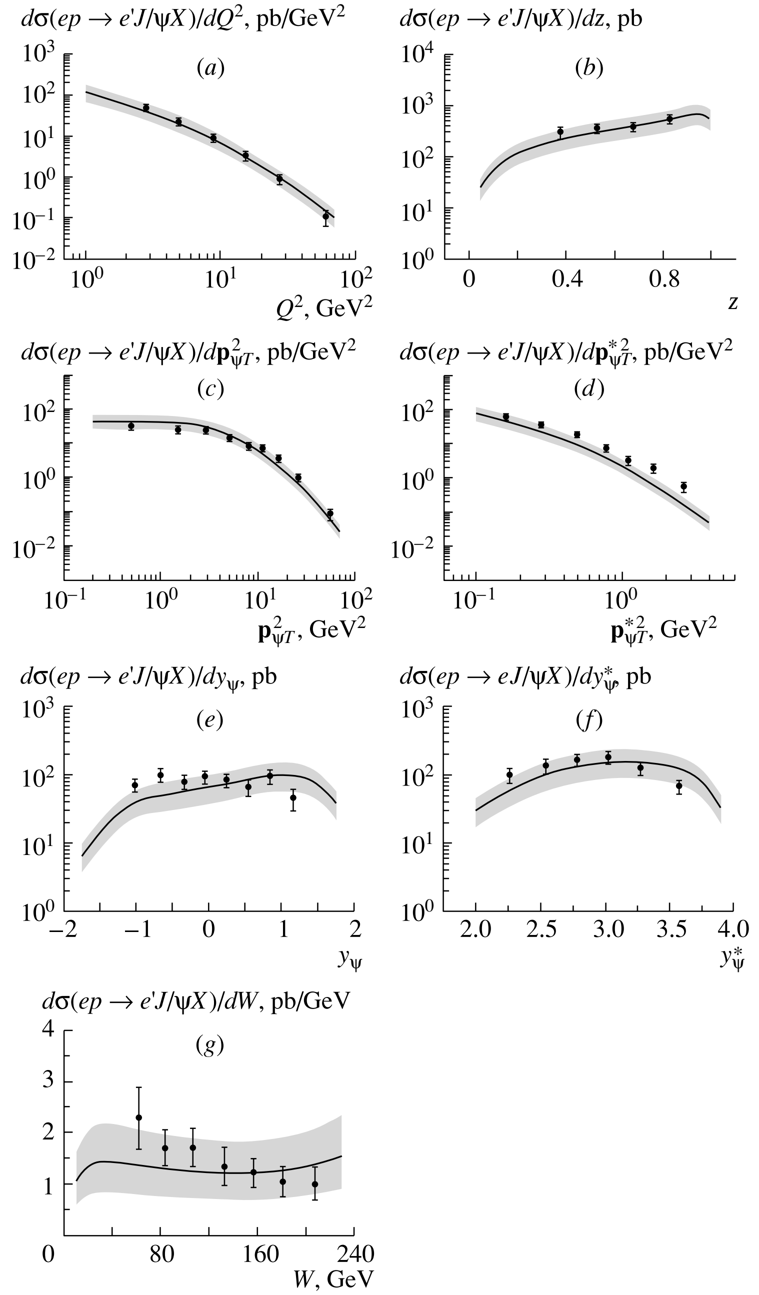

**Fig. 2.** Differential cross sections for the inelastic electroproduction of $J/\psi$ mesons versus various kinematical variables in the kinematical region specified by the inequalities $2 < Q^2 < 100$ GeV$^2$, $50 < W < 225$ GeV, $0.3 < z < 0.9$, and $\mathbf{p}^{*2}_{\psi T} > 1$ GeV$^2$ at $\sqrt{s} = 314$ GeV and $\Lambda_{\rm QCD} = 250$ MeV. The boundaries of the shaded regions correspond to the minimum ($\Delta = 0.2$) and the maximum ($\Delta = 0.53$) value of the Pomeron intercept; the solid curve corresponds to the intermediate value of $\Delta = 0.35$. The points represent experimental data of the H1 Collaboration [1].

$$\times \Phi(x_2, \mathbf{q}^2_{2T}, \mu^2)\frac{dz}{z(1-z)}$$

$$\times \sum |M|^2_{\rm SHA}(\gamma g^* \to J/\psi g')d\mathbf{p}^2_{\psi T}d\mathbf{q}^2_{2T}\frac{d\phi_2}{2\pi}\frac{d\phi_\psi}{2\pi}.$$

The matrix elements for the corresponding hard subprocesses, $\sum |M|^2_{\rm SHA}(eg^* \to e'J/\psi g')$ and $\sum |M|^2_{\rm SHA}(\gamma g^* \to J/\psi g')$ in (9) and (11), respectively, were given in [18, 19].

We note that, within the ordinary parton model, the expressions for the differential cross sections for the photo- and electroproduction of $J/\psi$ mesons can be obtained from formulas (9) and (11) in the limit $\mathbf{q}^2_{2T} \to 0$ by averaging over the transverse directions specified by the vector $\mathbf{q}_{2T}$.

### *2.4. Unintegrated Gluon Distributions*

In order to investigate the sensitivity of the total and differential cross sections for the production of $J/\psi$ mesons to the choice of value for the Pomeron intercept $\Delta$, we will use here the so-called JB parametrization of the gluon distribution,[2] which was obtained by solving the BFKL equations in [41]. The method proposed in [41] for deriving unintegrated gluon distributions relies on directly solving the BFKL equations in the leading approximation, with the collinear gluon density $xG(x,\mu^2)$ from the Glück–Reya–Vogt set [42] being taken for the initial condition. Technically, the unintegrated gluon distributions are calculated in this case as the convolution of the collinear gluon distribution $xG(x,\mu^2)$ with a universal weight factor [41]; that is,

$$\Phi(x,\mathbf{q}_T^2,\mu^2) = \int\limits_x^1 \varphi(\eta,\mathbf{q}_T^2,\mu^2)\frac{x}{\eta}G\left(\frac{x}{\eta},\mu^2\right)d\eta, \tag{12}$$

$$\varphi(\eta,\mathbf{q}_T^2,\mu^2) = \begin{cases} \dfrac{\bar{\alpha}_s}{\eta\mathbf{q}_T^2}J_0\left(2\sqrt{\bar{\alpha}_s\ln(1/\eta)\ln(\mu^2/\mathbf{q}_T^2)}\right) & \text{for } \mathbf{q}_T^2 \le \mu^2 \\ \dfrac{\bar{\alpha}_s}{\eta\mathbf{q}_T^2}I_0\left(2\sqrt{\bar{\alpha}_s\ln(1/\eta)\ln(\mathbf{q}_T^2/\mu^2)}\right) & \text{for } \mathbf{q}_T^2 > \mu^2, \end{cases} \tag{13}$$

where $J_0$ and $I_0$ are Bessel functions of, respectively, a real and an imaginary argument. The parameter $\bar{\alpha}_s = 3\alpha_s/\pi$, which appears in (13), is related to the Pomeron intercept $\Delta$: in the leading order of perturbation theory, we have $\Delta = 4\bar{\alpha}_s\ln 2 \simeq 0.53$, but, in the next-to-leading order, the expression for the Pomeron intercept in terms of the parameter $\alpha_s$ assumes the form $\Delta = 4\bar{\alpha}_s\ln 2 - N\bar{\alpha}_s^2$ and takes negative values, since $N \sim 18$ [43, 44]. However, various summation procedures proposed in recent years [44, 45] lead to positive values of $\Delta \sim 0.2$–$0.3$. A close value of $\Delta = 0.35$ was obtained in [20] in describing the $\mathbf{p}_T$ spectrum in the inclusive electroproduction of $D^*$ mesons at the HERA collider within the semihard QCD approach.[3] In this study, we will consider $\Delta$ as a free parameter varying between 0.2 and 0.53.

## 3. RESULTS OF THE CALCULATIONS

In this section, we present the results of our numerical calculations and compare them with the latest experimental data of the H1 [1, 2] and ZEUS [3] Collaborations.

We note that the absolute normalization of the cross sections calculated by formulas (9) and (11) depends on the choice of values for the $J/\psi$-meson wave function at the origin, $\psi(0)$; the $c$-quark mass, $m_c$; and the factorization scale, $\mu$. The wave-function value at the origin, $\psi(0)$, can be calculated within the potential model or can be obtained from the experimentally measured leptonic-decay width $\Gamma(J/\psi \to \mu^+\mu^-)$. Following [47], we will use the value of $|\psi(0)|^2 = 0.0876\ \text{GeV}^3$ in our calculations. In addition, we set the factorization scale to $\mu^2 = \mathbf{q}_{2T}^2$ [5, 18, 19].

At present, the problem of choosing a value for the $c$-quark mass remains open. On one hand, we have $m_c = m_\psi/2 = 1.55$ GeV in the nonrelativistic QCD approximation, which is used for the $J/\psi$ wave function in the color-singlet model. On the other hand, a somewhat smaller value of $m_c = 1.4$ GeV was obtained in [34, 48] from a comparison of the results of calculations within ordinary perturbative QCD with experimental data. In our previous study [18], we investigated, in greater detail, the $m_c$ dependence of the results of our calculations of the cross sections for $J/\psi$-meson production and found that the shift of the $c$-quark mass $m_c$ from 1.55 to 1.4 GeV leads to an increase in the absolute values of the calculated cross sections by a factor of about 1.5. This change in the normalization is due to the change in the phase space corresponding to the final $J/\psi$ meson, a variation in the value of $m_c$ in the amplitude of the parton subprocess affecting the results of the calculations only slightly [18]. Since the value of $m_c = 1.4$ GeV in the phase space of the final state corresponds to an unphysical value of the $J/\psi$-meson mass, we will use

---

[2] The dependence of the total and differential cross sections for the production of $J/\psi$ mesons at the HERA collider on various sets of unintegrated gluon distributions was investigated in our previous studies [18, 19]. Special features of various parametrizations were considered in detail, for example, in the review article of Andersson *et al.* [40].

[3] We note that the use of the JB parametrization (at the value of $\Delta = 0.35$) and the KMS parametrization [46] (which effectively takes into account about 70% of next-to-leading-order corrections to the value of $\Delta$) in the calculations leads to approximately identical results [18, 19].

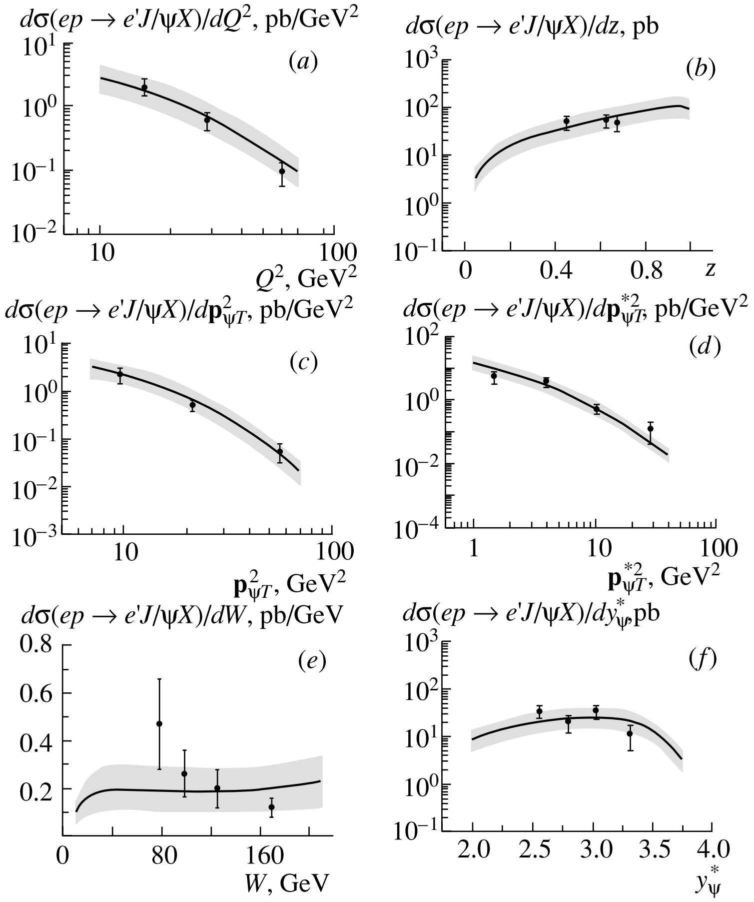

**Fig. 3.** Differential cross sections for the inelastic electroproduction of $J/\psi$ mesons versus various kinematical variables in the kinematical region specified by the inequalities $12 < Q^2 < 100$ GeV$^2$, $50 < W < 180$ GeV, $\mathbf{p}_{\psi T}^2 > 6.4$ GeV$^2$, $0.3 < z < 0.9$, and $\mathbf{p}_{\psi T}^{*2} > 1$ GeV$^2$ at $\sqrt{s} = 314$ GeV and $\Lambda_{\text{QCD}} = 250$ MeV. The notation is identical to that in Fig. 2.

the more realistic value of $m_c = 1.55$ GeV [19] in our study.

### *3.1. Electroproduction of $J/\psi$ Mesons at the HERA Collider*

In formula (9), the limits of integration with respect to the variables $\mathbf{p}_{\psi T}^2$ and $Q^2$, the rapidity $y_\psi$, and the variable $z$ are related to the boundaries of two kinematical regions where the H1 Collaboration obtained experimental data on the inelastic electroproduction of $J/\psi$ mesons [1]: $2 < Q^2 < 100$ GeV$^2$, $50 < W < 225$ GeV, $0.3 < z < 0.9$, and $\mathbf{p}_{\psi T}^{*2} > 1$ GeV$^2$ (first region) and $12 < Q^2 < 100$ GeV$^2$, $50 < W < 180$ GeV, $\mathbf{p}_{\psi T}^2 > 6.4$ GeV$^2$, $0.3 < z < 0.9$ and $\mathbf{p}_{\psi T}^{*2} > 1$ GeV$^2$ (second region).[4]

The results of our calculations are displayed in Figs. 2–4. The differential cross sections for the inelastic electroproduction of $J/\psi$ mesons versus various kinematical variables in the first kinematical region are shown in Fig. 2 for $\sqrt{s} = 314$ GeV and $\Lambda_{\text{QCD}} = 250$ MeV. The boundaries of the shaded regions correspond to the minimum ($\Delta = 0.2$) and the maximum ($\Delta = 0.53$) value of the Pomeron intercept; the solid curve corresponds to the intermediate value of $\Delta = 0.35$. It can be seen from Fig. 2 that, for all of the distributions, with the exception of the $\mathbf{p}_{\psi T}^{*2}$ distribution, the experimental points lie within the shaded regions. We note that the $W$ distribution of $J/\psi$ mesons is the most sensitive to the intercept value (Fig. 2*g*). The curves corresponding to the intercept value of $\Delta = 0.35$ are in good agreement with experimental data. However, the value of $\Delta = 0.53$ is preferable in describing the $\mathbf{p}_{\psi T}^{*2}$ spectrum. But for this choice of $\Delta$, the experimental points of the $W$, $y_\psi$, and $y_\psi^*$ distributions of $J/\psi$ mesons lie somewhat lower than the theoretical curves (Figs. 2*e*–2*g*).

---

[4] By $\mathbf{p}_{\psi T}^{*2}$ and $y_\psi^*$, we hereafter denote, respectively, the square of the transverse momentum and the rapidity of $J/\psi$ mesons in the $\gamma^* p$ c.m. frame.

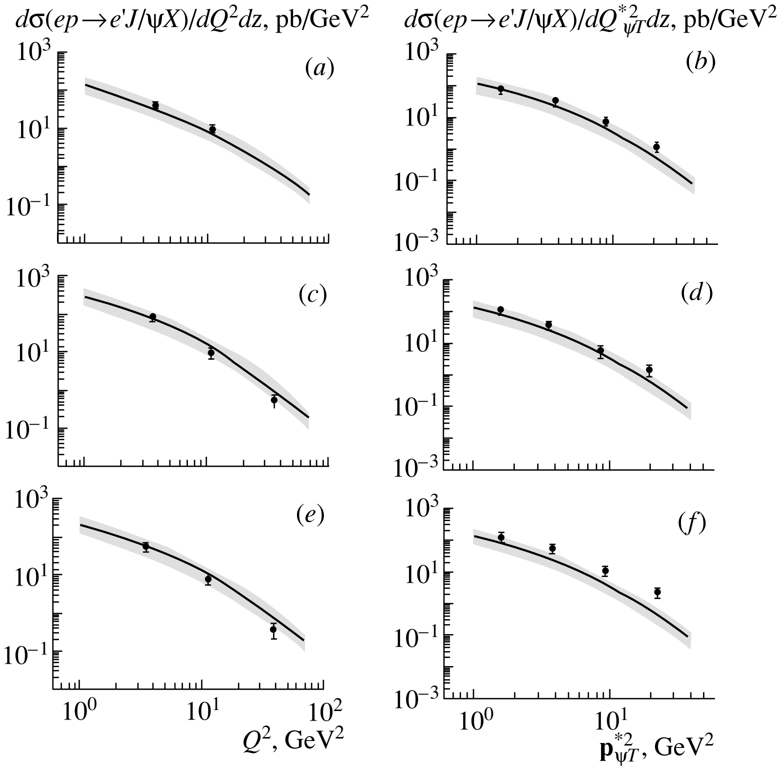

**Fig. 4.** Double-differential cross sections for the inelastic electroproduction of $J/\psi$ mesons versus $Q^2$ and $\mathbf{p}_{\psi T}^{*2}$ in the kinematical regions specified by the inequalities $2 < Q^2 < 100$ GeV$^2$; $50 < W < 225$ GeV; ($a$, $b$) $0.3 < z \leq 0.6$, ($c$, $d$) $0.6 < z \leq 0.75$, and ($e$, $f$) $0.75 < z < 0.9$; and $\mathbf{p}_{\psi T}^{*2} > 1$ GeV$^2$ at $\sqrt{s} = 314$ GeV and $\Lambda_{\text{QCD}} = 250$ MeV. The notation is identical to that in Fig. 2.

The differential cross sections for the inelastic electroproduction of $J/\psi$ mesons versus various kinematical variables in the second kinematical region are given in Fig. 3 for $\sqrt{s} = 314$ GeV and $\Lambda_{\text{QCD}} = 250$ MeV. In this kinematical region, all experimental points lie within the shaded regions, whose boundaries correspond to the intercept values of $\Delta = 0.2$ and $\Delta = 0.53$. We note that, in this region, the $\mathbf{p}_{\psi T}^{*2}$ distribution of product $J/\psi$ mesons is well described at $\Delta = 0.35$ (Fig. 3$d$).

In Fig. 4, the double-differential cross sections $d\sigma/dQ^2dz$ and $d\sigma/d\mathbf{p}_{\psi T}^{*2}dz$ for the inelastic electroproduction of $J/\psi$ mesons versus $Q^2$ and $\mathbf{p}_{\psi T}^{*2}$ in the first kinematical region are presented at $\sqrt{s} = 314$ GeV and $\Lambda_{\text{QCD}} = 250$ MeV. As can be seen from Fig. 4, all experimental points lie within the shaded region, whose boundaries correspond to the intercept values of $\Delta = 0.2$ and $\Delta = 0.53$. This is not so only at large values of the variable $z$ (Fig. 4$f$). In this region, however, an additional contribution may come, for example, from diffraction processes; however, a consideration of such additional contributions is beyond the scope of this study. We also note that, in the region of low $z$, $z < 0.3$, the contribution of mechanisms associated with the QCD structure of the photon becomes significant [49].

As can be seen from Figs. 2–4, the experimental data of the H1 Collaboration [1] lie within the shaded region (with the exception of the data in Fig. 2$d$ and Fig. 4$f$), which corresponds to the calculations within the semihard QCD approach without taking into account the octet mechanisms of the fragmentation of $c\bar{c}$ quark pairs into $J/\psi$ particles at the minimum and the maximum Pomeron intercept values of $\Delta = 0.2$ and $\Delta = 0.53$, respectively. The theoretical curves obtained at the intermediate value of $\Delta = 0.35$ are in good agreement with experimental data.

### 3.2. Photoproduction of $J/\psi$ Mesons at the HERA Collider

The limits of integration with respect to the transverse momentum squared $\mathbf{p}_{\psi T}^2$ and the variable $z$ in formula (11) are related to the boundaries of two kinematical regions where the H1 [2] and ZEUS [3] Collaborations obtained experimental data on the inelastic photoproduction of $J/\psi$ mesons. These kinematical regions are specified by the inequalities $60 < W < 240$ GeV, $0.3 < z < 0.9$, and

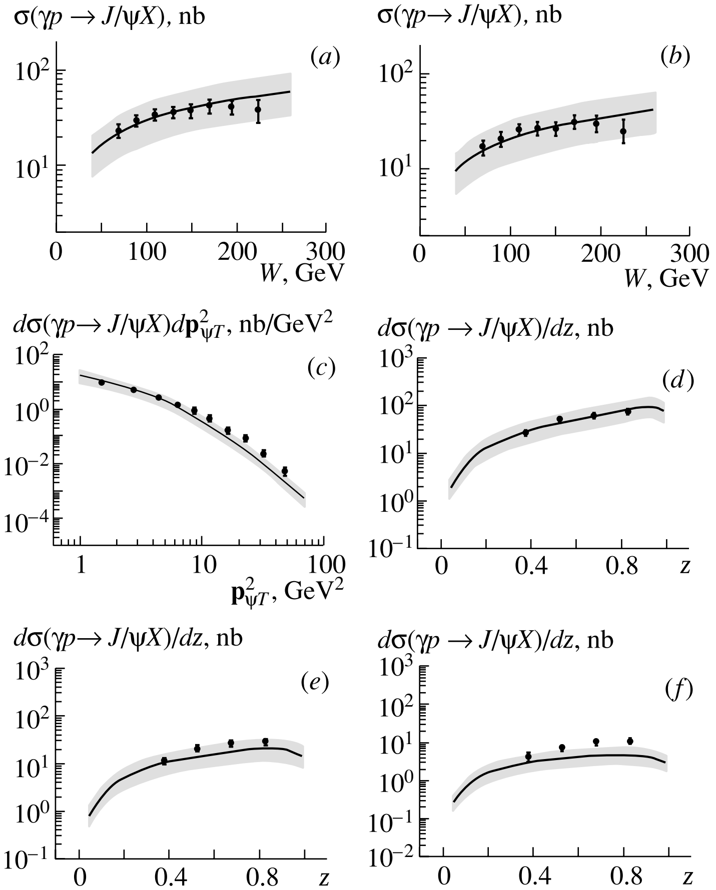

**Fig. 5.** (*a*, *b*) Total and (*c*–*f*) differential cross sections for the inelastic photoproduction of $J/\psi$ mesons versus various kinematical variables in the kinematical region specified by the inequalities $60 < W < 240$ GeV, $0.3 < z < 0.9$ ($0.3 < z < 0.8$ in Fig. 5*b*), and $1 < \mathbf{p}^2_{\psi T} < 60$ GeV$^2$ ($\mathbf{p}^2_{\psi T} > 1$ in Fig. 5*d*, $\mathbf{p}^2_{\psi T} > 2$ in Fig. 5*e*, and $\mathbf{p}^2_{\psi T} > 3$ GeV$^2$ in Fig. 5*f*) at $\Lambda_{\text{QCD}} =$ 250 MeV. The notation is identical to that in Fig. 2.

$1 < \mathbf{p}^2_{\psi T} < 60$ GeV$^2$ (first region) [2] and $50 < W <$ 180 GeV, $0.4 < z < 0.9$, and $\mathbf{p}^2_{\psi T} > 1$ GeV$^2$ (second region) [3].

The results of our calculations are shown in Figs. 5–7. In Figs. 5 and 6, the total and differential cross sections for the inelastic photoproduction of $J/\psi$ mesons versus various kinematical variables are given at $\Lambda_{\text{QCD}} = 250$ MeV and various values of $\Delta$. The displayed experimental data were obtained by the H1 (Fig. 5) and ZEUS (Fig. 6) Collaborations. From Figs. 5 and 6, it can be seen that the total cross section for $J/\psi$-meson photoproduction is the most sensitive to the choice of the parameter $\Delta$. As in the case of electroproduction, the experimental data are well described at $\Delta = 0.35$; however, the value of $\Delta = 0.53$ is preferable at rather high values of the transverse momentum of $J/\psi$ mesons (see Figs. 5*c*, 6*b*). The same (large) value of the intercept is required for describing the $z$ distribution of $J/\psi$ mesons for $\mathbf{p}^2_{\psi T} > 2$ and 3 GeV$^2$ (Figs. 5*e*, 6*e*, and 5*f*). We also note that, in just the same way as in the case of electroproduction, the contribution of mechanisms associated with the QCD structure of the photon becomes significant in the region $z < 0.3$ [49].

In Fig. 7, the double-differential cross sections $d\sigma/d\mathbf{p}^2_{\psi T}dz$ for the inelastic photoproduction of $J/\psi$ mesons versus $\mathbf{p}^2_{\psi T}$ at various values of the parameter $\Delta$ are given for the regions (Fig. 7*a*) $0.3 < z \leq 0.6$, (Fig. 7*b*) $0.6 < z \leq 0.75$, and (Fig. 7*c*) $0.75 < z <$ 0.9 at $\Lambda_{\text{QCD}} = 250$ MeV. One can easily see that the theoretical curves obtained at the intermediate value of $\Delta = 0.35$ agree well with the experimental data.

As can be seen from Figs. 5–7, the experimental data of the H1 [2] and ZEUS [3] Collaborations also lie within the shaded region (with the exception of the data in Fig. 5*f*) corresponding to the calculations within the semihard QCD approach without taking into account the octet mechanisms of the fragmentation of $c\bar{c}$ quark pairs into $J/\psi$ particles at the minimum and the maximum Pomeron intercept values of

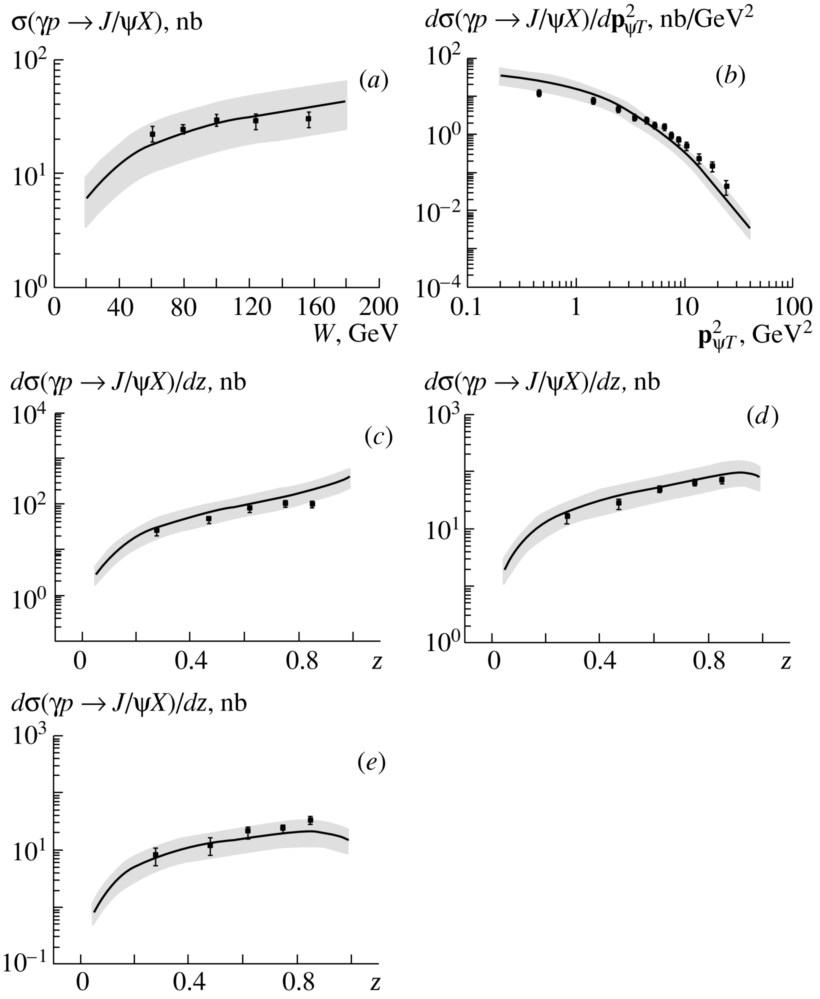

**Fig. 6.** (*a*) Total and (*b*–*e*) differential cross sections for the inelastic photoproduction of $J/\psi$ mesons versus various kinematical variables in the kinematical region specified by the inequalities $50 < W < 180$ GeV, $0.4 < z < 0.9$, and $\mathbf{p}^2_{\psi T} > 1$ GeV$^2$ (without cuts on $\mathbf{p}^2_{\psi T}$ in Fig. 6*c*, $\mathbf{p}^2_{\psi T} > 1$ GeV$^2$ in Fig. 6*d*, and $\mathbf{p}^2_{\psi T} > 2$ GeV$^2$ in Fig. 6*e*) at $\Lambda_{\mathrm{QCD}} = 250$ MeV. The notation for the curves is identical to that in Fig. 2. Points represent experimental data of the ZEUS Collaboration [3].

$\Delta = 0.2$ and $\Delta = 0.53$, respectively. As in the case of electroproduction, the theoretical curves obtained at the intermediate value of $\Delta = 0.35$ agree fairly well with the experimental data, although, at high values of the $J/\psi$-meson transverse momentum, the value of $\Delta = 0.53$ is preferable. The total cross section for the photoproduction of $J/\psi$ mesons is the most sensitive to the choice of value for the Pomeron intercept.

### *3.3. Polarization Properties of J/ψ Mesons at the HERA Collider*

As was shown in [17–19], the calculations within the standard parton model and within the semihard QCD approach lead to markedly different results for the polarization features of $J/\psi$ mesons produced at the HERA collider. In order to investigate the polarization properties of final $J/\psi$ mesons, we will calculate here, within the semihard approach and within the usual parton model, the spin-alignment parameter $\alpha$ as a function of $\mathbf{p}^2_{\psi T}$ and the variable $z$,

$$\alpha(\omega) = \frac{d\sigma/d\omega - 3d\sigma_L/d\omega}{d\sigma/d\omega + d\sigma_L/d\omega}, \qquad (14)$$

where $\sigma_L$ is the cross section for the production of longitudinally polarized $J/\psi$ mesons and $\omega = \mathbf{p}^2_{\psi T}, z$. The spin-alignment parameter $\alpha$ is related to the angular distribution of leptons from the decay process $J/\psi \to \mu^+\mu^-$ by the equation

$$\frac{d\Gamma(J/\psi \to \mu^+\mu^-)}{d\cos\theta} \sim 1 + \alpha\cos^2\theta, \qquad (15)$$

where $\theta$ is the polar emission angle of the final muon $\mu^+$ in the $J/\psi$ rest frame. The values of $\alpha = 1$ and $\alpha = -1$ correspond, respectively, to the transverse and to the longitudinal polarization of the product $J/\psi$ meson.

In [18], we investigated in detail the $Q^2$ dependence of the parameter $\alpha$. We found that, in view of the presence of an additional contribution to the cross section for the production of $J/\psi$ mesons of helicity $\lambda = 0$ from longitudinally polarized initial virtual photons, it is impossible to draw a definitive conclusion on the degree to which the virtuality of the initial gluon affects the cross section for the production of longitudinally polarized $J/\psi$ mesons. At small photon-virtuality values of $Q^2 < 1$ GeV$^2$, the contribution of longitudinally polarized photons becomes insignificant, however, which must lead to qualitative distinctions between the polarization properties of the product $J/\psi$ meson that are calculated within the usual parton model and within the semihard QCD approach [17, 18]. In the present study, we investigate the parameter $\alpha$ as a function of $\mathbf{p}^2_{\psi T}$ and the variable $z$ for the inelastic photoproduction of $J/\psi$ mesons at the HERA collider.

The results of our calculations are given in Figs. 8 and 9. The spin-alignment parameter $\alpha$ as a function of $z$ and $|\mathbf{p}_{\psi T}|$ in the kinematical region specified by the inequalities $60 < W < 240$ GeV, $0.3 < z < 0.9$, and $1 < \mathbf{p}^2_{\psi T} < 60$ GeV$^2$ is shown in Fig. 8 according to the calculations at $\Lambda_{\text{QCD}} = 250$ MeV. The experimental data displayed there were obtained by the H1 Collaboration [2]. Curve *1* corresponds to the calculations within the usual parton model with the gluon distribution $xG(x, \mu^2)$ from the Glück–Reya–Vogt set [42], while curve *2* represents the results obtained within the theory of semihard processes by using the JB unintegrated gluon distribution at the value of $\Delta = 0.35$. One can see from Fig. 8 that the predictions of the usual parton model and of the semihard QCD approach for the $z$ dependence of $\alpha$ are similar, but that the respective predictions for the dependence $\alpha(|\mathbf{p}_{\psi T}|)$ differ significantly both in shape and in absolute value. Despite rather large experimental uncertainties, curve *2* calculated within the semihard QCD approach is in better agreement with the experimental data of the H1 Collaboration (Fig. 8*b*) than curve *1*.

Figure *9* shows the parameter $\alpha$ as a function of $|\mathbf{p}_{\psi T}|$ according to the calculation at $\Lambda_{\text{QCD}} =$ 250 MeV for the kinematical regions specified by the inequalities $50 < W < 180$ GeV and (Figs. 9*a*, 9*c*) $0.4 < z < 0.9$ and (Figs. 9*b*, 9*d*) $0.4 < z < 1.0$. The displayed experimental data were obtained by the ZEUS Collaboration [3] in (Figs. 9*a*, 9*b*) the target reference frame and (Figs. 9*c*, 9*d*) the so-called helicity reference frame [3, 50]. The results of the calculations performed on the basis of the semihard QCD approach are in good agreement with the experimental data reported in [3], although the experimental uncertainties were quite large there. Curve *1*, which was calculated within the standard parton model, lies below the experimental data at low values of $|\mathbf{p}_{\psi T}|$ and above them at high values of $|\mathbf{p}_{\psi T}|$.

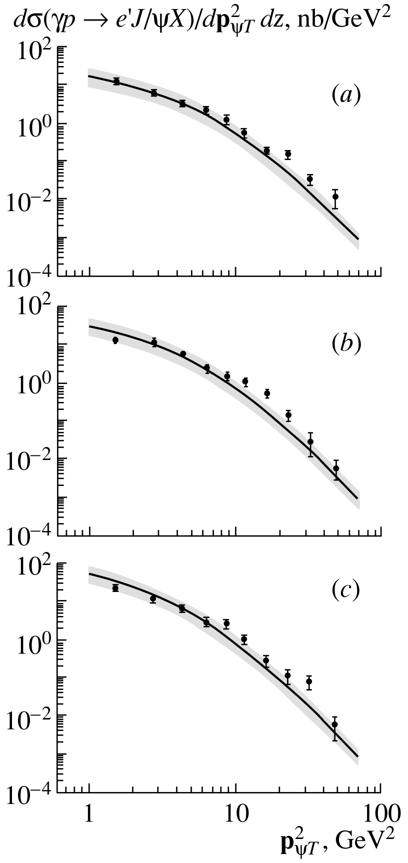

**Fig. 7.** Double-differential cross sections for the inelastic photoproduction of $J/\psi$ mesons versus $\mathbf{p}^2_{\psi T}$ in the kinematical regions (*a*) $0.3 < z \le 0.6$, (*b*) $0.6 < z \le 0.75$, and (*c*) $0.75 < z < 0.9$ at $\Lambda_{\text{QCD}} = 250$ MeV. The notation is identical to that in Fig. 5.

Thus, we conclude that, if next-to-leading-order corrections to the predictions of the parton model for the cross section describing the production of longitudinally polarized $J/\psi$ particles (these corrections have yet to be calculated) do not introduce significant changes in the behavior of the spin-alignment parameter $\alpha(|\mathbf{p}_{\psi T}|)$, experimental investigation of the polarization properties of $J/\psi$ mesons at the HERA collider will provide yet another test of the BFKL dynamics of gluon distributions.

We also note that, over a wide region of the variables $\mathbf{p}^2_{\psi T}$ and $z$, the predictions of the semihard QCD approach for the polarization properties of $J/\psi$

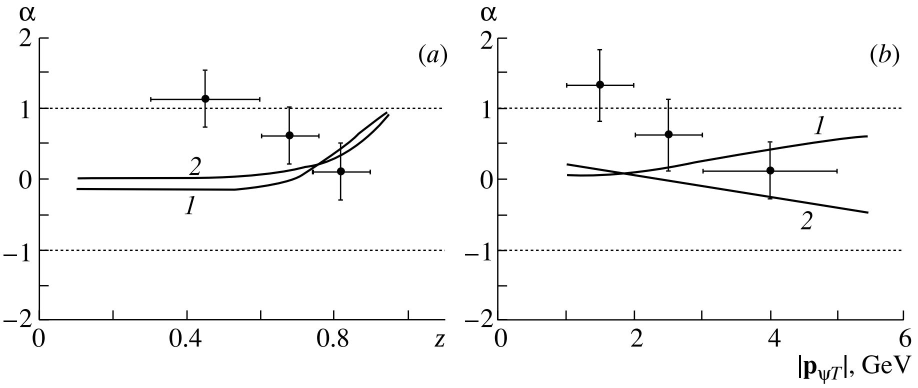

**Fig. 8.** Spin-alignment parameter $\alpha$ versus the variables $z$ and $|\mathbf{p}_{\psi T}|$ in the kinematical region specified by the inequalities $60 < W < 240$ GeV, $0.3 < z < 0.9$, and $1 < \mathbf{p}^2_{\psi T} < 60$ GeV$^2$ at $\Lambda_{\rm QCD} = 250$ MeV: (curve *1*) results of the calculation on the basis of the usual parton model with the gluon distribution $xG(x, \mu^2)$ from the Glück–Reya–Vogt set and (curve *2*) results of the calculation based on the theory of semihard processes and performed with the JB unintegrated gluon distribution at $\Delta = 0.35$. Points represent experimental data of the H1 Collaboration [2].

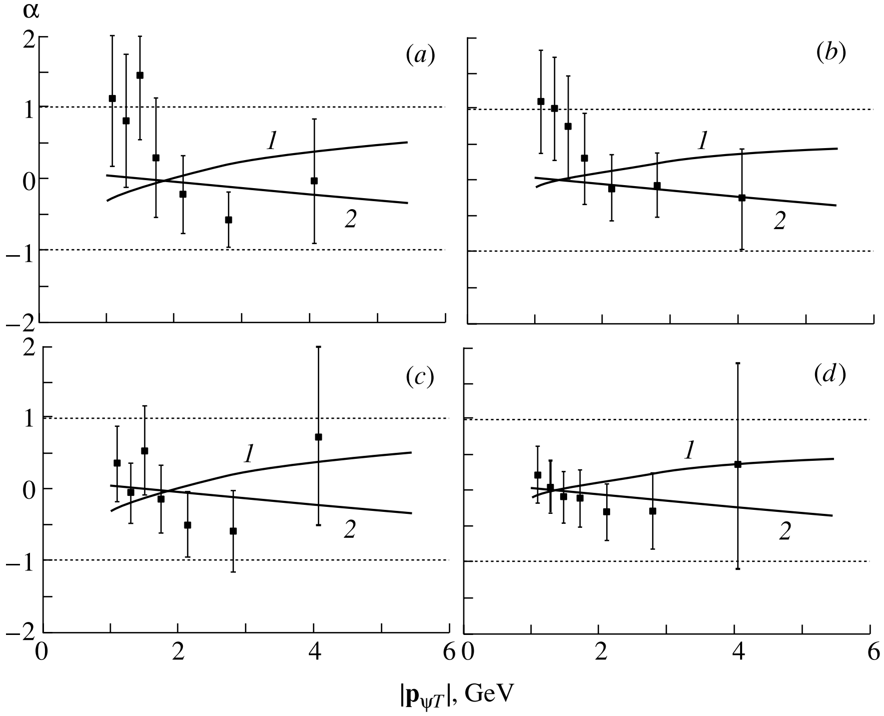

**Fig. 9.** Spin-alignment parameter $\alpha$ as a function of $|\mathbf{p}_{\psi T}|$ in the kinematical region specified by the inequalities $50 < W < 180$ GeV and ($a$, $c$) $0.4 < z < 0.9$ and ($b$, $d$) $0.4 < z < 1.0$ at $\Lambda_{\rm QCD} = 250$ MeV. The points represent experimental data of the ZEUS Collaboration [3], which were obtained in ($a$, $b$) the target reference frame and ($c$, $d$) the so-called helicity reference frame. The notation for the curves is identical to that in Fig. 8.

mesons are virtually independent of the Pomeron intercept $\Delta$.

## 4. CONCLUSION

The inelastic photo- and electroproduction of $J/\psi$ mesons at the HERA collider have been considered within the semihard QCD approach. We have investigated the dependence of the total and differential cross sections for the production of $J/\psi$ mesons on the Pomeron intercept $\Delta$, which is a basic parameter of low-$x$ physics, and the dependence of the polarization properties of final $J/\psi$ mesons on their transverse momenta $\mathbf{p}^2_{\psi T}$ and on the variable $z$. The calculations within the semihard QCD approach have been performed at realistic values of the $c$-quark mass and the $J/\psi$-meson wave function at the origin ($m_c = 1.55$ GeV and $|\psi(0)|^2 = 0.0876\ \mathrm{GeV}^3$, respectively) at $\Lambda_{\mathrm{QCD}} = 250$ MeV without taking into account the octet mechanisms of the fragmentation of $c\bar{c}$ quark pairs into $J/\psi$ particles. It has been shown that a rather good description of the latest experimental data of the H1 and ZEUS Collaborations can be attained by choosing the Pomeron intercept value of $\Delta = 0.35$. The $W$ distribution for the electroproduction of $J/\psi$ mesons and the total cross section for their photoproduction are the most sensitive to the choice of intercept value; at the same time, the polarization properties of $J/\psi$ mesons are virtually independent of the Pomeron intercept $\Delta$ over a wide region of the transverse momentum squared $\mathbf{p}^2_{\psi T}$ and the variable $z$. It has been shown that experimental investigation of the polarization properties of $J/\psi$ mesons at the HERA collider may provide an additional test of the BFKL dynamics of gluon distributions.

## ACKNOWLEDGMENTS

We are grateful to S.P. Baranov for enlightening discussions on various aspects of the semihard QCD approach. A.V. Lipatov gratefully acknowledges the assistance of V.A. Saleev at the initial stage of this research.

This work was supported in part by the Russian Foundation for Basic Research (project no. 02-02-17513) and by INTAS (grant no. YSF 2002-399).

## REFERENCES

1. H1 Collab. (C. Adloff *et al.*), Eur. Phys. J. C **25**, 41 (2002).
2. H1 Collab. (C. Adloff *et al.*), Eur. Phys. J. C **25**, 25 (2002).
3. ZEUS Collab. (S. Chekanov *et al.*), Eur. Phys. J. C **27**, 173 (2003).
4. L. V. Gribov, E. M. Levin, and M. G. Ryskin, Phys. Rep. **100**, 1 (1983).
5. E. M. Levin, M. G. Ryskin, Yu. M. Shabel'skiĭ, and A. G. Shuvaev, Yad. Fiz. **53**, 1059 (1991) [Sov. J. Nucl. Phys. **53**, 657 (1991)].
6. S. Catani, M. Ciafaloni, and F. Hautmann, Nucl. Phys. B **366**, 135 (1991).
7. J. C. Collins and R. K. Ellis, Nucl. Phys. B **360**, 3 (1991).
8. V. N. Gribov and L. N. Lipatov, Yad. Fiz. **15**, 781 (1972) [Sov. J. Nucl. Phys. **15**, 438 (1972)]; L. N. Lipatov, Yad. Fiz. **20**, 181 (1974) [Sov. J. Nucl. Phys. **20**, 94 (1975)]; G. Altarelli and G. Parisi, Nucl. Phys. B **126**, 298 (1977); Yu. M. Dokshitzer, Zh. Éksp. Teor. Fiz. **19**, 1216 (1977) [Sov. Phys. JETP **46**, 641 (1977)].
9. E. A. Kuraev, L. N. Lipatov, and V. S. Fadin, Zh. Éksp. Teor. Fiz. **17**, 840 (1976) [Sov. Phys. JETP **44**, 443 (1976)]; **18**, 377 (1977) [**45**, 199 (1977)]; Yu. Yu. Balitskiĭ and L. N. Lipatov, Yad. Fiz. **28**, 1597 (1978) [Sov. J. Nucl. Phys. **28**, 822 (1978)].
10. M. G. Ryskin and Yu. M. Shabelski, Z. Phys. C **69**, 269 (1996).
11. M. G. Ryskin, Yu. M. Shabelski, and A. G. Shuvaev, Yad. Fiz. **64**, 2080 (2001) [Phys. At. Nucl. **64**, 1995 (2001)].
12. V. A. Saleev and N. P. Zotov, Mod. Phys. Lett. A **9**, 151 (1994).
13. V. A. Saleev and N. P. Zotov, Mod. Phys. Lett. A **11**, 25 (1996).
14. A. V. Lipatov and N. P. Zotov, Mod. Phys. Lett. A **15**, 695 (2000).
15. A. V. Lipatov, V. A. Saleev, and N. P. Zotov, Mod. Phys. Lett. A **15**, 1727 (2000).
16. S. P. Baranov, A. V. Lipatov, and N. P. Zotov, in *Proceedings of the 9th International Workshop on DIS and QCD (DIS'2001), Bologna, Italy, 2001*; hep-ph/0106229.
17. S. P. Baranov, Phys. Lett. B **428**, 377 (1998).
18. N. P. Zotov and A. V. Lipatov, Yad. Fiz. **66**, 1807 (2003) [Phys. At. Nucl. **66**, 1760 (2003)]; hep-ph/0208237.
19. A. V. Lipatov and N. P. Zotov, Eur. Phys. J. C **27**, 87 (2003).
20. S. P. Baranov and N. P. Zotov, Phys. Lett. B **458**, 389 (1999); **491**, 111 (2000).
21. S. P. Baranov and M. Smižanská, Phys. Rev. D **62**, 014012 (2000).
22. P. Hägler, R. Kirschner, A. Schäfer, *et al.*, Phys. Rev. D **62**, 071502 (2000).
23. H. Jung, Phys. Rev. D **65**, 034015 (2002); hep-ph/0110034.
24. P. Hägler, R. Kirschner, A. Schäfer, *et al.*, Phys. Rev. D **63**, 077501 (2001); F. Yuan and K.-T. Chao, Phys. Rev. D **63**, 034006 (2001); hep-ph/0009224.
25. H. Jung, in *Proceedings of "Photon'2001", Ascona, Switzerland, 2001*; hep-ph/0110345.
26. S. P. Baranov, H. Jung, L. Jonsson, *et al.*, Eur. Phys. J. C **24**, 425 (2002); hep-ph/0203025.
27. E. Braaten and S. Fleming, Phys. Rev. Lett. **74**, 3327 (1995); E. Braaten and T. C. Yuan, Phys. Rev. D **52**, 6627 (1995).
28. P. Cho and A. K. Leibovich, Phys. Rev. D **53**, 6203 (1996).
29. G. Bodwin, E. Braaten, and G. Lepage, Phys. Rev. D **51**, 1125 (1995); **55**, 5853 (1997).
30. M. Cacciari and M. Kramer, Phys. Rev. Lett. **76**, 4128 (1996).
31. P. Ko, J. Lee, and H. Song, Phys. Rev. D **54**, 4312 (1996); **60**, 119902 (1999).
32. H1 Collab. (S. Aid *et al.*), Nucl. Phys. B **472**, 3 (1996).
33. ZEUS Collab. (J. Breitweg *et al.*), Z. Phys. C **76**, 599 (1997).
34. S. Fleming and T. Mehen, Phys. Rev. D **57**, 1846 (1998).

35. B. Kniehl and L. Zwirner, Nucl. Phys. B **621**, 337 (2002); hep-ph/0112199.
36. J. Korner, J. Cleymans, M. Kuroda, and G. Gounaris, Phys. Lett. B **114B**, 195 (1982).
37. J.-Ph. Guillet, Z. Phys. C **39**, 75 (1988).
38. H. Merabet, J. Mathiot, and R. Mendez-Galain, Z. Phys. C **62**, 639 (1994).
39. F. Yuan and K.-T. Chao, Phys. Rev. D **63**, 034017 (2001).
40. Small-$x$ Collab. (B. Andersson *et al.*), Eur. Phys. J. C **25**, 77 (2002); hep-ph/0204115.
41. J. Blumlein, DESY 95-121.
42. M. Glück, E. Reya, and A. Vogt, Z. Phys. C **67**, 433 (1995).
43. V. S. Fadin and L. N. Lipatov, Phys. Lett. B **429**, 127 (1998); M. Ciafaloni and G. Camici, Phys. Lett. B **430**, 349 (1998).
44. G. D. Salam, J. High Energy Phys. **9807**, 019 (1998); hep-ph/9806482.
45. S. J. Brodsky, V. S. Fadin, V. T. Kim, *et al.*, Pis'ma Zh. Éksp. Teor. Fiz. **70**, 161 (1999) [JETP Lett. **70**, 155 (1999)]; hep-ph/9901229.
46. J. Kwiecinski, A. D. Martin, and A. M. Stasto, Phys. Rev. D **56**, 3991 (1997).
47. M. Kramer, Nucl. Phys. B **459**, 3 (1996).
48. P. Ball, M. Beneke, and V. Braun, Phys. Rev. D **52**, 3929 (1995).
49. H. Jung, G. Schuler, and J. Terron, DESY-92-028.
50. CDF Collab. (T. Affolder *et al.*), Phys. Rev. Lett. **85**, 2886 (2000).

*Translated by A. Isaakyan*

*Physics of Atomic Nuclei, Vol. 67, No. 4, 2004, pp. 837–845. Translated from Yadernaya Fizika, Vol. 67, No. 4, 2004, pp. 859–867.*
*Original Russian Text Copyright © 2004 by Baranov, Zotov, Lipatov.*

## ELEMENTARY PARTICLES AND FIELDS
## Theory

# Production of Heavy Quarks on Protons within the Semihard QCD Approach

**S. P. Baranov**[1), **N. P. Zotov**[*], and **A. V. Lipatov**[**]

*Institute of Nuclear Physics,*
*Moscow State University, Vorob'evy gory, Moscow, 119899 Russia*

Received December 27, 2002; in final form, May 26, 2003

**Abstract**—The inclusive production of heavy quarks in $p\bar{p}$ interactions at the Tevatron and LHC energies is considered within the semihard QCD approach. The dependence of the total and differential cross sections for the production of $b$ quarks and $B$ mesons (and of muons originating from the subsequent semileptonic decay $B \to \mu\nu_\mu X$) on various samples of unintegrated gluon distributions is studied. The results obtained by calculating azimuthal correlations between the transverse momenta of final particles are presented. The theoretical results are compared with the latest experimental data obtained by the D0 and CDF Collaborations at the Tevatron. © *2004 MAIK "Nauka/Interperiodica".*

## 1. INTRODUCTION

Recently, the D0 and CDF Collaborations obtained new experimental data [1–5] on the inclusive production of $b$ quarks at the Tevatron. Since the customary parton model in a fixed order of perturbative QCD runs into difficulties in describing the production of heavy quarks [6], we will apply here the so-called semihard [7, 8] (or $k_T$-factorization) QCD approach [9, 10] in analyzing these data from [1–5]. By semihard processes, one usually means those where the characteristic energy scale $\mu \sim m_T$ of a hard parton-scattering subprocess (here, $m_T$ is the transverse mass of a heavy quark) is substantially lower than the total c.m. collision energy $\sqrt{s}$, but it is much higher than the parameter $\Lambda_{\rm QCD}$; that is, $\Lambda_{\rm QCD} \ll \mu \ll \sqrt{s}$. In this case, the QCD running coupling constant remains small: $\alpha_s(\mu^2) \ll 1$. Fulfillment of the condition $\mu \ll \sqrt{s}$ means that relevant cross sections are determined by the behavior of the gluon structure functions of the proton in the region of small values of the variable $x$ ($x \simeq m_T/\sqrt{s} \ll 1$). In this region of $x$, it is necessary to take into account the dependence of the amplitude of the hard-scattering subprocess on the virtuality and on the longitudinal polarization of gluons [8–10].

The gluon distribution in the proton, $xG(x, \mu^2)$, can be obtained from the Dokshitzer–Gribov–Lipatov–Altarelli–Parisi (DGLAP) evolution equations [11], which take into account (in the leading-logarithm approximation) contributions of the form $\alpha_s^n \ln^n(\mu^2/\Lambda_{\rm QCD}^2)$.

With increasing c.m. collision energy $\sqrt{s}$, however, contributions of order $\alpha_s^n \ln^n(s/\Lambda_{\rm QCD}^2) \sim \alpha_s^n \ln^n(1/x)$, which are disregarded in the DGLAP equations, begin to play a significant role. Summation of $\alpha_s^n \ln^n(1/x)$ terms leads to unintegrated (that is, transverse-momentum-dependent) gluon distributions $\Phi(x, \mathbf{q}_T^2)$ (where $\mathbf{q}_T$ is the transverse momentum) that satisfy the Balitsky–Fadin–Kuraev–Lipatov (BFKL) evolution equations [12]. The inclusion of all leading logarithmic and doubly logarithmic contributions results in an additional dependence of unintegrated gluon distributions on $\mu^2$.

In contrast to what was done in the customary parton model, the cross section for physical processes is determined by the convolution of unintegrated gluon distributions with the matrix element for the off-shell hard subprocess [8–10]. Accordingly, the polarization tensor $L^{\mu\nu}$ for virtual gluons in the matrix element for photon–gluon or gluon–gluon fusion is taken in the form [7]

$$L^{\mu\nu} = q_T^\mu q_T^\nu / \mathbf{q}_T^2. \qquad (1)$$

The semihard approach was previously used to describe a number of processes [8, 13–23]. We emphasize that calculations within the theory of semihard processes predict observable effects that are absent in the customary parton model: a faster growth of cross sections [19], the broadening of $p_T$ spectra [8, 13–21], and other polarization properties of final particles [18, 20, 21].

---

[1)] Lebedev Institute of Physics, Russian Academy of Sciences, Leninskiĭ pr. 53, Moscow, 117924 Russia; e-mail: `baranov@sci.lebedev.ru`

[*] e-mail: `zotov@theory.sinp.msu.ru`

[**] e-mail: `lipatov@theory.sinp.msu.ru`

1063-7788/04/6704-0837$26.00 © 2004 MAIK "Nauka/Interperiodica"

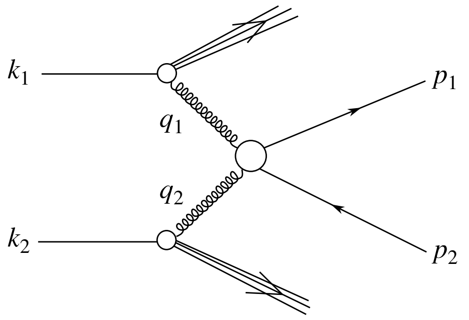

**Fig. 1.** Heavy-quark-production process $p\bar{p} \to Q\bar{Q}X$.

The production of heavy ($c$, $b$) quarks on protons was already considered within the semihard QCD approach [8, 13–18]. However, the authors of [13–16] used different matrix elements for hard subprocesses, and it is difficult to compare these matrix elements with one another. The matrix elements given in [8] contain misprints. Moreover, the results obtained in [13–16] contradict those in [17]. The matrix elements obtained in [18] for the hard subprocess of gluon–gluon fusion independently of previous studies are in numerical agreement with the matrix elements presented in [9]. The theoretical results reported in [18] are in good agreement with experimental data on the cross section for $b$-quark production that were obtained by the D0 [5] and CDF [3] Collaborations.

In the present study, we perform a more thorough analysis of the inclusive production of heavy quarks at high energies within the semihard QCD approach. We calculate the total and differential cross sections for the production of $b$ quarks and $B$ mesons (and of muons that originate from the subsequent semileptonic decay $B \to \mu\nu_\mu X$) and compare the results of our calculations with recent experimental data obtained by the D0 [4, 5] and CDF [1–3] Collaborations. In addition, we present results obtained by calculating the azimuthal correlations between the transverse momenta of final particles and study the sensitivity of our results to various sets of unintegrated gluon distributions and other parameters of the semihard approach. We pay special attention to the role of unintegrated gluon distributions that were used in [19–23]. Finally, we predict the values of the total cross sections for the processes $p\bar{p} \to b\bar{b}X \to \mu\mu X$ and $p\bar{p} \to b\bar{b}X \to \mu\bar{b}X$ at the LHC energies.

The ensuing exposition is organized as follows. In Section 2, we quote the expressions obtained in [18] for the total and differential cross sections for the inclusive production of heavy quarks on protons within the semihard approach and discuss some special features of the unintegrated gluon distributions used. In Section 3, we present our numerical results and compare them with the latest experimental data of the D0 [4, 5] and CDF [1–3] Collaborations. In Section 4, we briefly summarize the main results and conclusions of our study.

## 2. CROSS SECTION FOR THE PRODUCTION OF HEAVY QUARKS IN THE SEMIHARD QCD APPROACH

### *2.1. Kinematics*

We denote by $k_1$ and $k_2$ the 4-momenta of primary protons (Fig. 1). In the ensuing calculations, we use the Sudakov decomposition, which, for the heavy-quark-production process $p\bar{p} \to Q\bar{Q}X$, assumes the form

$$p_1 = \alpha_1 k_1 + \beta_1 k_2 + p_{1T}, \quad p_2 = \alpha_2 k_1 + \beta_2 k_2 + p_{2T}, \tag{2}$$
$$q_1 = x_1 k_1 + q_{1T}, \qquad q_2 = x_2 k_2 + q_{2T},$$

where

$$p_1^2 = p_2^2 = m_Q^2, \quad q_1^2 = q_{1T}^2, \quad q_2^2 = q_{2T}^2. \tag{3}$$

Here, $p_1$ and $p_2$ are the 4-momenta of final heavy quarks; $q_1$ and $q_2$ are the 4-momenta of virtual gluons; and $p_{1T}$, $p_{2T}$, $q_{1T}$, and $q_{2T}$ are the transverse momenta of the corresponding particles. Neglecting the proton mass and going over to the c.m. frame of colliding particles, we have

$$k_1 = \sqrt{s}/2\,(1,0,0,1), \qquad k_2 = \sqrt{s}/2\,(1,0,0,-1), \tag{4}$$

whence it follows that $k_1^2 = k_2^2 = 0$ and $(k_1 \cdot k_2) = s/2$. The Sudakov variables are

$$\alpha_1 = \frac{m_{1T}}{\sqrt{s}}\exp(y_1), \qquad \alpha_2 = \frac{m_{2T}}{\sqrt{s}}\exp(y_2), \tag{5}$$
$$\beta_1 = \frac{m_{1T}}{\sqrt{s}}\exp(-y_1), \qquad \beta_2 = \frac{m_{2T}}{\sqrt{s}}\exp(-y_2),$$

where $m_{1,2T}^2 = m_Q^2 + \mathbf{p}_{1,2T}^2$ and $y_1$ and $y_2$ are the rapidities of the corresponding heavy quarks in the c.m. frame of colliding particles. From the law of energy–momentum conservation, we readily obtain

$$x_1 = \alpha_1 + \alpha_2, \qquad x_2 = \beta_1 + \beta_2, \tag{6}$$
$$\mathbf{q}_{1T} + \mathbf{q}_{2T} = \mathbf{p}_{1T} + \mathbf{p}_{2T}.$$

### *2.2. Differential Cross Section for the Production of Heavy Quarks on Protons*

Basic formulas necessary for respective calculations were derived in [18]. Here, we will quote some of them. The differential cross section for inclusive heavy-quark production on protons within the semihard QCD approach has the form

$$d\sigma(p\bar{p} \to Q\bar{Q}X) = \frac{1}{16\pi(x_1x_2s)^2} \times \Phi(x_1, \mathbf{q}_{1T}^2, \mu^2)\Phi(x_2, \mathbf{q}_{2T}^2, \mu^2) \times \sum |M|^2_{\text{SHA}}(g^*g^* \to Q\bar{Q})dy_1dy_2 \times d\mathbf{p}_{2T}^2 d\mathbf{q}_{1T}^2 d\mathbf{q}_{2T}^2 \frac{d\phi_1}{2\pi}\frac{d\phi_2}{2\pi}\frac{d\phi_Q}{2\pi}, \quad (7)$$

where $\Phi(x_1, \mathbf{q}_{1T}^2, \mu^2)$ and $\Phi(x_2, \mathbf{q}_{2T}^2, \mu^2)$ are unintegrated gluon distributions, $\sum |M|^2_{\text{SHA}}(g^*g^* \to Q\bar{Q})$ is the square of the matrix element calculated for the subprocess of gluon–gluon fusion within the semihard QCD approach, $\phi_1$ and $\phi_2$ are the azimuthal angles of virtual gluons, and $\phi_Q$ is the azimuthal angle of the product heavy quark. In (7), the symbol $\sum$ denotes averaging over the polarizations of initial particles according to (1) and summation over the polarization of final particles. We note that the explicit expression for the squared matrix element $\sum |M|^2_{\text{SHA}}(g^*g^* \to Q\bar{Q})$ is given in [18].

The expression describing the differential cross section for heavy-quark production in the customary parton model can be obtained from (7) in the limit $\mathbf{q}_{1,2T}^2 \to 0$ by averaging over transverse directions specified by the vectors $\mathbf{q}_{1,2T}$; that is,

$$d\sigma(p\bar{p} \to Q\bar{Q}X) = \frac{1}{16\pi(x_1x_2s)^2} \times x_1G(x_1, \mu^2)x_2G(x_2, \mu^2) \times \sum |M|^2_{\text{PM}}(gg \to Q\bar{Q})dy_1dy_2d\mathbf{p}_{1T}^2\frac{d\phi_Q}{2\pi}, \quad (8)$$

where $\sum |M|^2_{\text{PM}}(gg \to Q\bar{Q})$ is the square of the matrix element calculated for the subprocess of gluon–gluon fusion, $gg \to Q\bar{Q}$, within the customary parton model (see [18]) and, as usual, $\sum$ denotes averaging over the polarizations of initial quarks and summation over the polarizations of final quarks.

### *2.3. Unintegrated Gluon Distributions*

Here, we will use various parametrizations of the unintegrated gluon distributions.[2]

The first one is the so-called JB parametrization obtained by solving the BFKL equations [25]. The method proposed in [25] for deriving unintegrated gluon distributions is based on directly solving the BFKL equations in the leading approximation with the collinear gluon density $xG(x, \mu^2)$ taken for an initial condition. In our calculations, we use the expression for $xG(x, \mu^2)$ from the Glück–Reya–Vogt set [26]. Specifically, the unintegrated gluon distributions are calculated as convolutions of the collinear gluon density $xG(x, \mu^2)$ with the universal weight factor [25]; that is,

$$\Phi(x, \mathbf{q}_T^2, \mu^2) = \int_x^1 \varphi(\eta, \mathbf{q}_T^2, \mu^2)\frac{x}{\eta}G\left(\frac{x}{\eta}, \mu^2\right)d\eta, \quad (9)$$

$$\varphi(\eta, \mathbf{q}_T^2, \mu^2) = \begin{cases} \dfrac{\bar{\alpha}_s}{\eta\mathbf{q}_T^2}J_0\left(2\sqrt{\bar{\alpha}_s\ln(1/\eta)\ln(\mu^2/\mathbf{q}_T^2)}\right) & \text{for } \mathbf{q}_T^2 \le \mu^2 \\ \dfrac{\bar{\alpha}_s}{\eta\mathbf{q}_T^2}I_0\left(2\sqrt{\bar{\alpha}_s\ln(1/\eta)\ln(\mathbf{q}_T^2/\mu^2)}\right) & \text{for } \mathbf{q}_T^2 > \mu^2, \end{cases} \quad (10)$$

where $J_0$ and $I_0$ are Bessel functions of, respectively, a real and an imaginary argument. The parameter $\bar{\alpha}_s = 3\alpha_s/\pi$ in (10) is related to the Pomeron intercept $\Delta$: in the leading order of perturbation theory, $\Delta = 4\bar{\alpha}_s\ln 2 \simeq 0.53$, but, in the next-to-leading order, we have $\Delta = 4\bar{\alpha}_s\ln 2 - N\bar{\alpha}_s^2 < 0$, because $N \sim 18$ [27]. However, various summation procedures proposed in [28, 29] lead to positive values of $\Delta \sim 0.2$–$0.3$. In [30], the close value of $\Delta = 0.35$ was obtained in describing the $\mathbf{p}_T$ spectrum in the inclusive electroproduction of $D^*$ mesons at the HERA collider within the semihard QCD approach. Here, we will use the value of $\Delta = 0.35$.[3]

Another parametrization of unintegrated gluon

---

[2] More details concerning special features of various parametrizations are given, for example, in the review article of Andersson *et al.* [24].

[3] The same value of the parameter $\Delta$ was used in describing experimental data of the H1 and ZEUS Collaborations for the photo- and electroproduction of $J/\psi$ mesons at HERA [20, 21] and in studying the behavior of structure functions for deep-inelastic scattering [$F_2^c(x, Q^2)$, $F_L^c(x, Q^2)$, and $F_L(x, Q^2)$] in the region of small $x$ within the semihard QCD approach [22, 23].

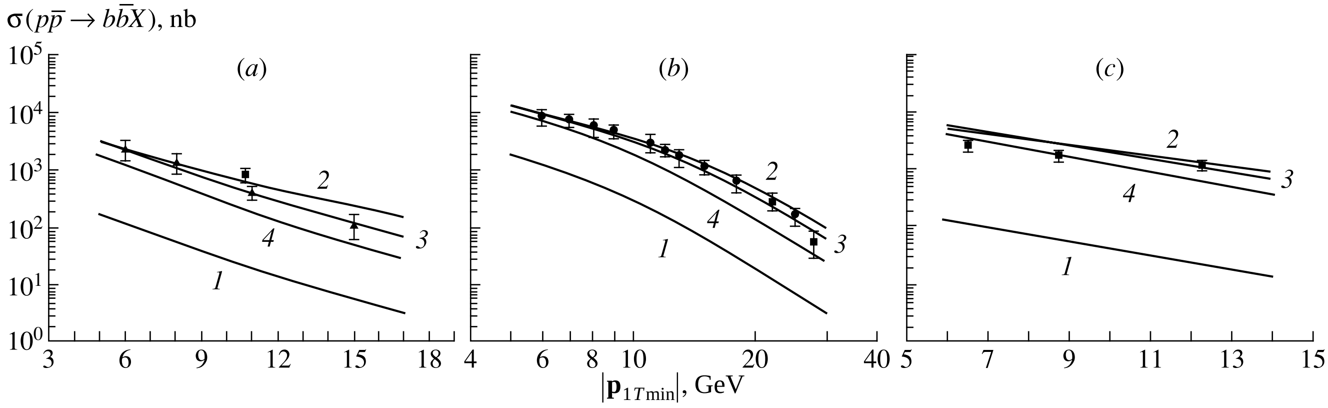

**Fig. 2.** Cross section for $b$-quark production as a function of $|\mathbf{p}_{1T\mathrm{min}}|$ for the kinematical regions specified by the inequalities ($a$) $|y_1| < 1.5$ and $|y_2| < 1.5$, at $\sqrt{s} = 630$ GeV, ($b$) $|y_1| < 1$ at $\sqrt{s} = 1800$ GeV, and ($c$) $|y_1| < 1$ and $|y_2| < 1$ at $\sqrt{s} = 1800$ GeV: (curve *1*) results of the calculations on the basis of the customary parton model with the gluon distribution $xG(x, \mu^2)$ from the standard Glück–Reya–Vogt set [26]; (*2*, *3*, and *4*) results obtained within the theory of semihard processes by using the unintegrated gluon distributions JB, KMS, and (11), respectively; and (points) experimental data obtained by the (▲) UA1 [35], (●) D0 [5], and (■) CDF [3] Collaborations.

distributions (here, it will be referred to as the KMS parametrization) was obtained in [31] by solving the generalized BFKL–DGLAP equation allowing for additional kinematical restrictions in the evolution of the gluon cascade [32]. As was shown in [33], this approach effectively takes into account about 70% of next-to-leading-order corrections to the Pomeron intercept $\Delta$.

Our calculations will also employ the gluon distribution obtained by a mere differentiation of the collinear gluon density $xG(x, \mu^2)$ [7, 12, 34]:

$$\Phi(x, \mathbf{q}_T^2) = \left. \frac{dxG(x, \mu^2)}{d\mu^2} \right|_{\mu^2 = \mathbf{q}_T^2}. \qquad (11)$$

In our calculations, we use the expression for $xG(x, \mu^2)$ from the standard Glück–Reya–Vogt set [26]. We note that the parametrization in (11) (in contrast to the JB and KMS distributions) takes into account only terms of orders $\alpha_s^n \ln^n(\mu^2/\Lambda^2_{\mathrm{QCD}})$ and $\alpha_s^n \ln^n(1/x) \ln^n(\mu^2/\Lambda^2_{\mathrm{QCD}})$. It is interesting to compare the JB gluon distribution and that in (11) because they result from different (BFKL and DGLAP) evolutions of the same collinear density $xG(x, \mu^2)$.

The limits of integration with respect to the transverse momentum $\mathbf{p}_{1T}^2$ and the heavy-quark rapidities $y_1$ and $y_2$ in (7) are related to the boundaries of the kinematical regions where the D0 and CDF Collaborations obtained their experimental data [1–5]. The region of integration with respect to $\mathbf{q}_{1T}^2$ and $\mathbf{q}_{2T}^2$ is broken down into four parts. For $\mathbf{q}_{1T}^2 > Q_0^2$ and $\mathbf{q}_{2T}^2 > Q_0^2$, we perform the calculations according to (7), while, for $\mathbf{q}_{1T}^2 \leq Q_0^2$ and $\mathbf{q}_{2T}^2 \leq Q_0^2$, we set $\mathbf{q}_{1T}^2 = 0$ and $\mathbf{q}_{2T}^2 = 0$ in the scattering amplitude and substitute $\sum |M|^2_{\mathrm{PM}}(gg \to Q\bar{Q})$ for $\sum |M|^2_{\mathrm{SHA}}(g^* g^* \to Q\bar{Q})$. The contribution from the region specified by the inequalities $\mathbf{q}_{1T}^2 \leq Q_0^2$ and $\mathbf{q}_{2T}^2 > Q_0^2$ and the region specified by the inequalities $\mathbf{q}_{1T}^2 > Q_0^2$ and $\mathbf{q}_{2T}^2 \leq Q_0^2$ is calculated in the same way by using the unintegrated distribution function $\Phi(x, \mathbf{q}_T^2, \mu^2)$ for one of the gluons and the collinear density $xG(x, \mu^2)$ for the other one. The choice of the critical value $Q_0^2$ is related to the requirement that the coupling constant $\alpha_s(\mu^2)$ be small in the region $\mathbf{q}_{1,2T}^2 \geq Q_0^2$. In our calculations, we took $Q_0^2 = 1$ GeV$^2$ [20, 21], so that $\alpha_s(\mu^2) \leq 0.26$.

## 3. RESULTS OF THE CALCULATIONS

In this section, we present the results of our numerical calculations and compare them with the latest experimental data of the D0 [4, 5], CDF [1–3], and UA1 [35] Collaborations.

The results of the theoretical calculations depend on the choice of gluon distributions, the heavy-quark mass $m_Q$, the characteristic energy scale $\mu^2$ in the running QCD coupling constant $\alpha_s(\mu^2)$, and the fragmentation function describing the transition of $b$ quarks to $B$ mesons. For example, a special choice of the fragmentation function was used in [6] as a means for increasing the cross section for $B$-meson production in the observed transverse-momentum region. In subsequent calculations, we set the $b$-quark mass to $m_b = 4.75$ GeV and the characteristic

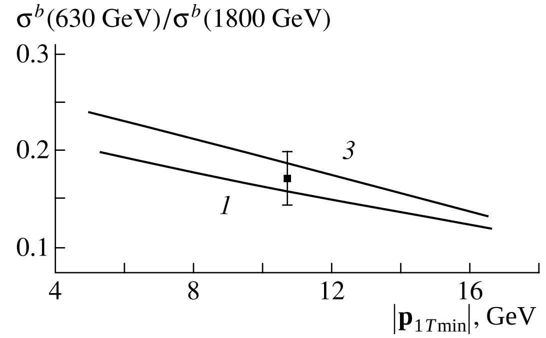

**Fig. 3.** Ratio of the cross sections for $b$-quark production at $\sqrt{s} = 630$ and 1800 GeV as a function of $|\mathbf{p}_{1T\min}|$ (the notation for the curves is identical to that in Fig. 2). The point represents the experimental value obtained by the CDF Collaboration [1].

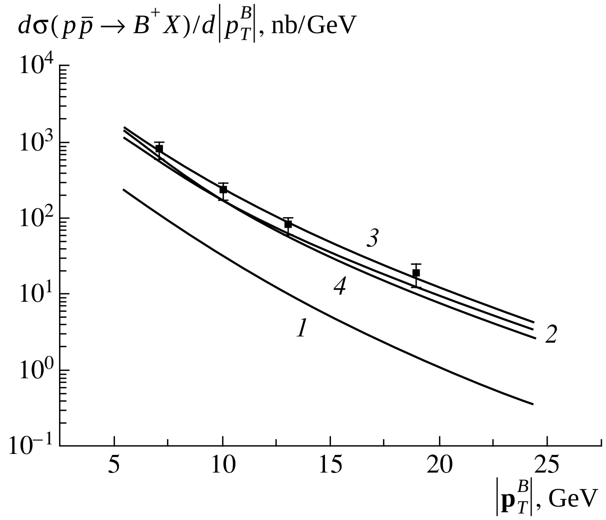

**Fig. 4.** Transverse-momentum ($|\mathbf{p}_T^B|$) distribution of $B^+$ mesons in the kinematical region $|y^B| < 1$ at $\sqrt{s} = 1800$ GeV (the notation for the curves is identical to that in Fig. 2). The points represent experimental data of the CDF Collaboration [2].

factorization scale to $\mu^2 = \mathbf{q}_{1,2T}^2$ [8, 15, 20, 21][4] and employ, for $b$-quark fragmentation to $B$ mesons, the Peterson fragmentation function [36] with the parameter value of $\epsilon = 0.006$, which is typical of $b$ quarks.

Figures 2–9 illustrate the results of our calculations. Figure 2 displays the calculated total cross section for $b$-quark production as a function of $|\mathbf{p}_{1T\min}|$ for various kinematical regions specified by the inequalities (i) $|y_1| < 1.5$ and $|y_2| < 1.5$ at $\sqrt{s} =$ 630 GeV (Fig. 2*a*), (ii) $|y_1| < 1$ at $\sqrt{s} = 1800$ GeV (Fig. 2*b*), and (iii) $|y_1| < 1$ and $|y_2| < 1$ at $\sqrt{s} =$ 1800 GeV (Fig. 2*c*). Curve *1* represents the results of the calculations on the basis of the customary parton model with the gluon distribution $xG(x, \mu^2)$ from the standard Glück–Reya–Vogt set [26], while curves *2*, *3*, and *4* correspond to the calculations within the theory of semihard processes with the unintegrated gluon distributions JB, KMS, and (11), respectively. We see from Fig. 2 that the results of the calculations within the semihard approach (curves *2*, *3*) are in very good agreement with the latest experimental data of the D0 and CDF Collaborations. Curve *4*, which represents results disregarding contributions of order $\alpha_s^n \ln^n(1/x)$, lies somewhat below the experimental data (Figs. 2*a*, 2*b*), the respective magnitudes differing by a factor of about 2. We also note that curves *2* and *3* are more smoothly sloping than curve *1*, but that curves *4* and *1* have virtually the same shape. The calculations on the basis of the customary parton model in the next-to-leading order underestimate the experimental data by a factor of about 2 [3, 5]. The calculations within the $k_T$-factorization approach [17] also underestimate the experimental cross section for $b$-quark production; their results are below those obtained here (although they coincide with our results in shape) owing to choice of different values of the parameters—in particular, a larger value of the $b$-quark mass ($m_b = 5$ GeV).

Figure 3 shows the ratio of the cross sections for $b$-quark production at $\sqrt{s} = 630$ and 1800 GeV as a function of $|\mathbf{p}_{1T\min}|$. We can see that the CDF experimental data on the ratio of the cross sections for $b$-quark production are described equally well by the calculations on the basis of the customary parton model in the leading order of perturbation theory and by the calculations within the semihard QCD approach. It should be noted that the ambiguity in choosing the $b$-quark mass $m_b$ and the factorization scale $\mu^2$ has a much weaker effect on the ratio of the cross sections for $b$-quark production at different values of $\sqrt{s}$ than on the magnitude of the cross sections [1].

Within the semihard QCD approach and the ordinary theory of electroweak interactions, one can also try to describe experimental data obtained by the D0 and CDF Collaborations at the Tevatron for the production of $B$ mesons in $p\bar{p}$ collisions [2] and their subsequent semileptonic decay $B \to \mu\nu_\mu X$ [4, 5]. Figure 4 displays the transverse-momentum ($|\mathbf{p}_T^B|$) dis-

---

[4] For this choice of $\mu^2$, the inelastic photo- and electroproduction of $J/\psi$ mesons at HERA were described in [20, 21] within the semihard QCD approach without introducing the additional (octet) mechanisms of the fragmentation of $c\bar{c}$ quark pairs into $J/\psi$ mesons, the $c$-quark mass being set to the realistic value of $m_c = 1.55$ GeV [20, 21]. The effect of the factorization scale $\mu^2$ on the cross section for heavy-quark production in $p\bar{p}$ interactions is discussed in more detail, for example, in [14].

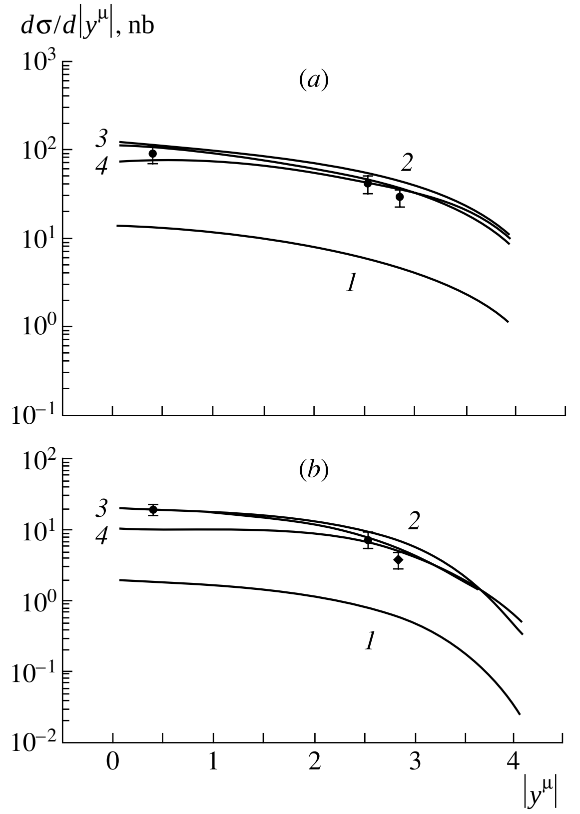

**Fig. 5.** Calculated distribution of muons (produced in the semileptonic decay $B \to \mu\nu_\mu X$) with respect to the absolute value of the rapidity ($|y^\mu|$) for $|\mathbf{p}_T^\mu| > (a)$ 5 and ($b$) 8 GeV (the notation for the curves is identical to that in Fig. 2). The points represent experimental data of the D0 Collaboration [4].

tribution of $B^+$ mesons in the kinematical region $|y^B| < 1$ at $\sqrt{s} = 1800$ GeV. It can clearly be seen that the theoretical curves obtained within the semihard approach are in excellent agreement with the experimental data. The effect of broadening of the transverse-momentum distributions in the production of $B$ mesons—this effect is typical of the $k_T$-factorization approach—does not manifest itself as clearly as in the case of $b$-quark production because of its partial compensation in the fragmentation of $b$ quarks into $B$ mesons. The values obtained within the customary parton model in the next-to-leading order are below the experimental data by a factor of about 3 [2].

The distribution of muons (produced in the semileptonic decay $B \to \mu\nu_\mu X$) with respect to the absolute value of the rapidity ($|y^\mu|$) is given in Fig. 5 according to the calculation performed for $|\mathbf{p}_T^\mu| >$ 5 GeV (Fig. 5*a*) and $|\mathbf{p}_T^\mu| > 8$ GeV (Fig. 5*b*). It is clear that the results of the calculations within the semihard approach (curves *2–4*) are in good agreement with the experimental data of the D0 Collaboration. In the central region ($|y^\mu| < 1$), curve *4* corresponding to the parametrization in (11), which disregards contributions of order $\alpha_s^n \ln^n(1/x)$, lies slightly below curves *2* and *3* (the difference is approximately 1.5-fold in magnitude).

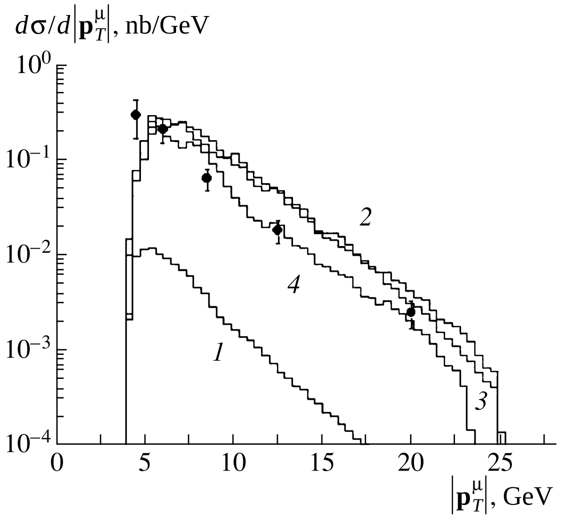

**Fig. 6.** Transverse-momentum distribution of the leading muon in the kinematical region specified by the inequalities $4 < |\mathbf{p}_{1,2T}^\mu| < 25$ GeV, $|\eta_{1,2}^\mu| < 0.8$, and $6 < m^{\mu\mu} <$ 35 GeV (the notation for the histograms corresponds to the notation for the curves in Fig. 2). The points represent experimental data of the D0 Collaboration [5].

Figure 6 displays the transverse-momentum distribution of the leading muon (which has the highest value of the transverse momentum $|\mathbf{p}_T^\mu|$) in the kinematical region specified by the inequalities $4 < |\mathbf{p}_{1,2T}^\mu| < 25$ GeV, $|\eta_{1,2}^\mu| < 0.8$, and $6 < m^{\mu\mu} <$ 35 GeV (where $\eta^\mu$ and $m^{\mu\mu}$ are the muon pseudorapidity and the dimuon invariant mass, respectively). We see that histograms *2* and *3* slightly overestimate the experimental data of the D0 Collaboration at $|\mathbf{p}_T^\mu| > 10$ GeV.

For the kinematical region $2.4 < y^\mu < 3.2$, Fig. 7 shows the double-differential cross section $d\sigma/d|\mathbf{p}_T^\mu|dy^\mu$ for the production of final muons as a function of the transverse momentum $|\mathbf{p}_T^\mu|$. It is clear from Fig. 7 that the experimental data of the D0 Collaboration are well described on the basis of the semihard QCD approach. It is worth noting that curves *2–4* have virtually the same shape. The values obtained within the customary parton model in the next-to-leading order are below the experimental data by a factor of about 4 [4].

Additional information about parton-interaction dynamics in hadron collisions can be extracted from the azimuthal correlations between the transverse momenta $\mathbf{p}_{1T}$ and $\mathbf{p}_{2T}$ of final heavy quarks (or between the transverse momenta of muons produced

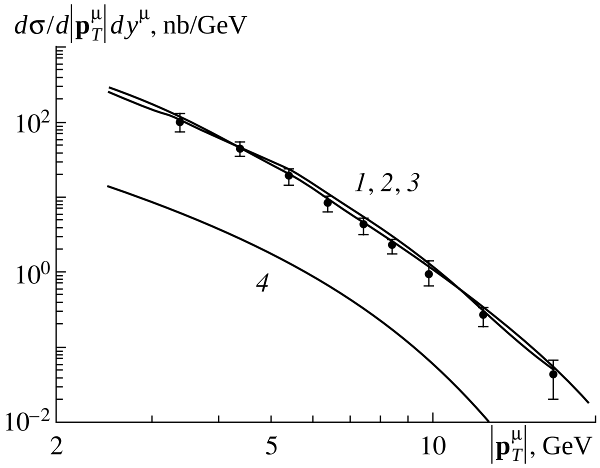

**Fig. 7.** Double-differential cross section $d\sigma/d|\mathbf{p}_T^\mu|dy^\mu$ for the production of final muons as a function of the absolute value of the transverse momentum ($|\mathbf{p}_T^\mu|$) in the kinematical region $2.4 < y^\mu < 3.2$ (the notation for the curves is identical to that in Fig. 2). The points represent experimental data of the D0 Collaboration [4].

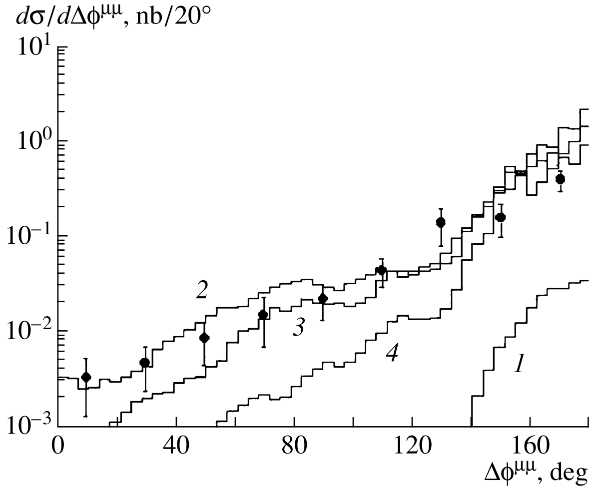

**Fig. 8.** Distribution of muons with respect to the angle $\Delta\phi^{\mu\mu}$ between the transverse momenta $\mathbf{p}_{1T}^\mu$ and $\mathbf{p}_{2T}^\mu$ in the kinematical region specified by the inequalities $4 < |\mathbf{p}_{1,2T}^\mu| < 25$ GeV, $|\eta_{1,2}^\mu| < 0.8$, and $6 < m^{\mu\mu} < 35$ GeV (the notation for the histograms corresponds to the notation for the curves in Fig. 2). The points represent experimental data of the D0 Collaboration [5].

in the semileptonic decay of $B$ mesons) [8, 13–15, 17]. In the leading order of perturbation theory in the customary parton model, we have $\mathbf{p}_{1T} = -\mathbf{p}_{2T}$; therefore, the distribution of heavy quarks with respect to the angle $\Delta\phi^{b\bar{b}}$ between the corresponding transverse momenta is proportional to the delta function $\delta(\Delta\phi^{b\bar{b}} - \pi)$. Nontrivial azimuthal correlations between the transverse momenta $\mathbf{p}_{1T}$ and $\mathbf{p}_{2T}$ of final particles arise upon taking into account the transverse momenta $\mathbf{q}_{1T}$ and $\mathbf{q}_{2T}$ of initial virtual gluons within the semihard QCD approach.

Figure 8 displays the distribution with respect to the angle $\Delta\phi^{\mu\mu}$ between the muon transverse momenta $\mathbf{p}_{1T}^\mu$ and $\mathbf{p}_{2T}^\mu$ for $4 < |\mathbf{p}_{1,2T}^\mu| < 25$ GeV, $|\eta_{1,2}^\mu| < 0.8$, and $6 < m^{\mu\mu} < 35$ GeV. It is clear from Fig. 8 that the results obtained by using the semihard approach with the JB and KMS unintegrated gluon distributions are in good agreement with the latest experimental data of the D0 Collaboration. The shape of histogram *4* differs from the shapes of histograms *2* and *3*; moreover, we see that, at small values of this angle ($\Delta\phi^{\mu\mu} \sim 0$), the parametrization in (11) predicts, for the differential cross section $d\sigma/d\Delta\phi^{\mu\mu}$, a value that is much smaller than the experimental cross section. This distinction between histogram *4*, on one hand, and histograms *2* and *3*, on the other hand, indicates the importance of $\alpha_s^n \ln^n(1/x)$ contributions in this region. Thus, the dependence on the choice of unintegrated gluon distributions manifests itself most clearly in the description of the azimuthal correlations between the transverse momenta of final particles. As might have been expected, the calculations on the basis of the customary parton model in the leading order of perturbation theory predict a sharp peak in the region around $\Delta\phi^{\mu\mu} \sim \pi$ (Fig. 8).

In the present study, we have also calculated the total cross sections $\sigma(p\bar{p} \to b\bar{b}X \to \mu\mu X)$ and $\sigma(p\bar{p} \to b\bar{b}X \to \mu\bar{b}X)$ versus the energy $\sqrt{s}$ in two kinematical regions that can be covered with the aid of the ATLAS detector [37]: these are the region specified by the inequalities $|\mathbf{p}_{1,2T}^\mu| > 6$ GeV and $|y_{1,2}^\mu| < 2.5$ (Fig. 9*a*) and the region specified by the inequalities $|\mathbf{p}_{1T}^\mu| > 6$ GeV and $|y_1^\mu| < 2.5$ (Fig. 9*b*). The predicted values of the cross sections at the LHC energy are tentative to some extent, because we did not take into account the saturation of gluon distributions that is widely discussed in the literature [8, 13, 14]. We note, however, that such predictions will remain tentative in any case because it is impossible to establish unambiguously the region of $x$ values at which saturation effects may be operative.

## 4. CONCLUSION

The inclusive production of heavy quarks in $p\bar{p}$ collisions at Tevatron and LHC energies has been considered here within the semihard QCD approach. We have studied the dependence of the total and the differential cross sections for the production of $b$ quarks and $B$ mesons (and of muons originating from the subsequent semileptonic decay $B \to \mu\nu_\mu X$) on various sets of unintegrated gluon distributions.

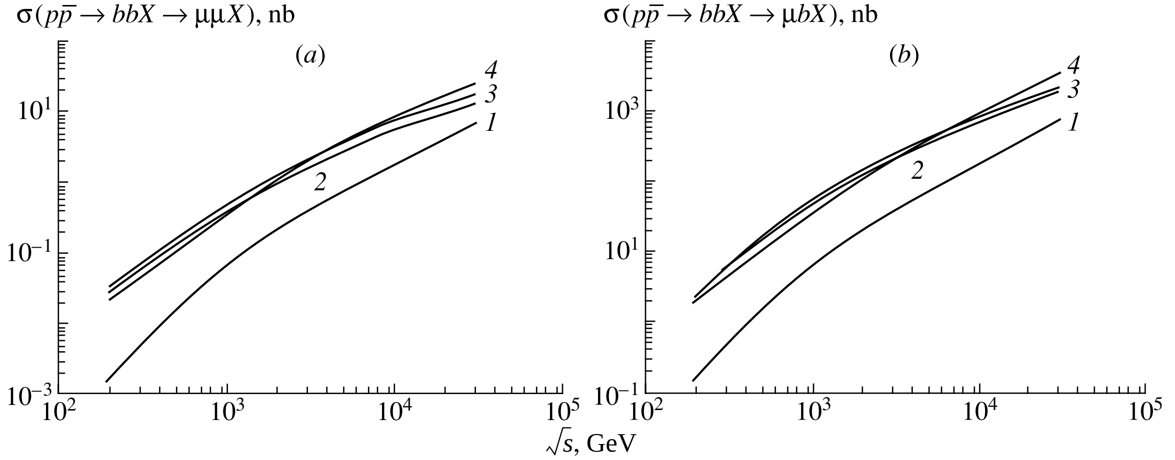

**Fig. 9.** Total cross sections $\sigma(p\bar{p} \to b\bar{b}X \to \mu\mu X)$ and $\sigma(p\bar{p} \to b\bar{b}X \to \mu\bar{b}X)$ versus the energy $\sqrt{s}$ for $(a)$ $|\mathbf{p}^{\mu}_{1,2T}| > 6$ GeV and $|y^{\mu}_{1,2}| < 2.5$ and $(b)$ $|\mathbf{p}^{\mu}_{1T}| > 6$ GeV and $|y^{\mu}_{1}| < 2.5$ (the notation for the curves is identical to that in Fig. 2).

We have presented the results obtained by calculating various azimuthal correlations between the transverse momenta of final particles. In our calculations, particular attention has been given to the role of gluon distributions. Our theoretical results obtained with the JB and KMS gluon distributions (at the $b$-quark mass of $m_b = 4.75$ GeV, the factorization scale of $\mu^2 = \mathbf{q}_T^2$, and $\Lambda_{\text{QCD}} = 250$ MeV) are in good agreement with the latest experimental data of the D0 and CDF Collaborations. The azimuthal correlations between the transverse momenta of final particles are the most sensitive to the choice of unintegrated gluon distributions. Our analysis of these correlations gives reasons to believe that the JB and KMS distributions should be preferred to the parametrization in (11). We have predicted the values of the total cross sections for the processes $p\bar{p} \to b\bar{b}X \to \mu\mu X$ and $p\bar{p} \to b\bar{b}X \to \mu\bar{b}X$ at the LHC energy.

## ACKNOWLEDGMENTS

This work was supported by the Russian Foundation for Basic Research (project no. 02-02-17513) and INTAS (YSF grant no. 2002-399).

## REFERENCES

1. CDF Collab. (D. Acosta *et al.*), hep-ex/0206019.
2. CDF Collab. (D. Acosta *et al.*), Phys. Rev. D **65**, 052005 (2002).
3. CDF Collab. (F. Abe *et al.*), Phys. Rev. D **55**, 2546 (1997).
4. D0 Collab. (B. Abbott *et al.*), hep-ex/9907029.
5. D0 Collab. (B. Abbott *et al.*), Phys. Lett. B **487**, 264 (2000); hep-ex/9905024.
6. M. Cacciari and P. Nason, Phys. Rev. Lett. **89**, 122003 (2002); hep-ph/0204025.
7. L. V. Gribov, E. M. Levin, and M. G. Ryskin, Phys. Rep. **100**, 1 (1983).
8. E. M. Levin, M. G. Ryskin, Yu. M. Shabel'skiĭ, and A. G. Shuvaev, Yad. Fiz. **53**, 1059 (1991) [Sov. J. Nucl. Phys. **53**, 657 (1991)].
9. S. Catani, M. Ciafaloni, and F. Hautmann, Nucl. Phys. B **366**, 135 (1991); S. Catani and F. Hautmann, Nucl. Phys. B **427**, 475 (1994).
10. J. C. Collins and R. K. Ellis, Nucl. Phys. B **360**, 3 (1991).
11. V. N. Gribov and L. N. Lipatov, Yad. Fiz. **15**, 781 (1972) [Sov. J. Nucl. Phys. **15**, 438 (1972)]; L. N. Lipatov, Yad. Fiz. **20**, 181 (1974) [Sov. J. Nucl. Phys. **20**, 94 (1975)]; G. Altarelli and G. Parisi, Nucl. Phys. B **126**, 298 (1977); Yu. M. Dokshitzer, Zh. Éksp. Teor. Fiz. **73**, 1216 (1977) [Sov. Phys. JETP **46**, 641 (1977)].
12. E. A. Kuraev, L. N. Lipatov, and V. S. Fadin, Sov. Phys. JETP **44**, 443 (1976); **45**, 199 (1977); Yu. Yu. Balitskiĭ and L. N. Lipatov, Yad. Fiz. **28**, 1597 (1978) [Sov. J. Nucl. Phys. **28**, 822 (1978)].
13. M. G. Ryskin and Yu. M. Shabelski, Z. Phys. C **69**, 269 (1996).
14. M. G. Ryskin, Yu. M. Shabelski, and A. G. Shuvaev, Yad. Fiz. **64**, 2080 (2001) [Phys. At. Nucl. **64**, 1995 (2001)]; hep-ph/9907507; hep-ph/0007238.
15. P. Hägler, R. Kirschner, A. Schäfer, *et al.*, Phys. Rev. D **62**, 071502 (2000).
16. H. Jung, Phys. Rev. D **65**, 034015 (2002); hep-ph/0110034.
17. S. P. Baranov and M. Smižanská, Phys. Rev. D **62**, 014012 (2000).
18. N. P. Zotov, A. V. Lipitov, and V. A. Saleev, Yad. Fiz. **66**, 786 (2003) [Phys. At. Nucl. **66**, 755 (2003)].
19. V. A. Saleev and N. P. Zotov, Mod. Phys. Lett. A **9**, 151 (1994); **11**, 25 (1996); A. V. Lipatov and N. P. Zotov, Mod. Phys. Lett. A **15**, 695 (2000); A. V. Lipatov,

V. A. Saleev, and N. P. Zotov, Mod. Phys. Lett. A **15**, 1727 (2000).

20. N. P. Zotov and A. V. Lipatov, Yad. Fiz. **66**, 1807 (2003) [Phys. At. Nucl. **66**, 1760 (2003)]; hep-ph/0208237.
21. A. V. Lipatov and N. P. Zotov, Eur. Phys. J. C **27**, 87 (2003).
22. A. V. Kotikov, A. V. Lipatov, G. Parente, and N. P. Zotov, Eur. Phys. J. C **26**, 51 (2002).
23. A. V. Kotikov, A. V. Lipatov, and N. P. Zotov, Eur. Phys. J. C **27**, 219 (2003).
24. Small-$x$ Collab. (B. Andersson *et al.*), Eur. Phys. J. C **25**, 77 (2002); hep-ph/0204115.
25. J. Blümlein, DESY 95-121.
26. M. Glück, E. Reya, and A. Vogt, Z. Phys. C **67**, 433 (1995).
27. V. S. Fadin and L. N. Lipatov, Phys. Lett. B **429**, 127 (1998); M. Ciafaloni and G. Camici, Phys. Lett. B **430**, 349 (1998).
28. G. D. Salam, J. High Energy Phys. **9807**, 019 (1998); hep-ph/9806482.
29. S. J. Brodsky, V. S. Fadin, V. T. Kim, *et al.*, Pis'ma Zh. Éksp. Teor. Fiz. **70**, 161 (1999) [JETP Lett. **70**, 155 (1999)]; hep-ph/9901229.
30. S. P. Baranov and N. P. Zotov, Phys. Lett. B **458**, 389 (1999); **491**, 111 (2000).
31. J. Kwiecinski, A. D. Martin, and A. M. Stasto, Phys. Rev. D **56**, 3991 (1997).
32. J. Kwiecinski, A. D. Martin, and P. J. Sutton, Phys. Rev. D **52**, 1445 (1995); Z. Phys. C **71**, 585 (1996).
33. J. Kwiecinski, A. D. Martin, and J. J. Outhwaite, Eur. Phys. J. C **9**, 611 (1999).
34. N. N. Nikolaev and B. G. Zakharov, Phys. Lett. B **333**, 250 (1994).
35. C. Albajar *et al.*, Z. Phys. C **61**, 41 (1994).
36. C. Peterson, D. Schlatter, I. Schmitt, and P. Zerwas, Phys. Rev. D **27**, 105 (1983).
37. ATLAS Collab. (W. Armstrong *et al.*), CERN/LHCC/94-43.

*Translated by M. Kobrinsky*

Physics of Atomic Nuclei, Vol. 67, No. 4, 2004, pp. 846–855. From Yadernaya Fizika, Vol. 67, No. 4, 2004, pp. 868–877.
Original English Text Copyright © 2004 by Simonov.

# Resolution of the Pion Puzzle: The QCD String in Nambu–Goldstone Mesons[*]

**Yu. A. Simonov**[**]

*Institute of Theoretical and Experimental Physics,*
*Bol'shaya Cheremushkinskaya ul. 25, Moscow, 117259 Russia*

Received October 14, 2003

**Abstract**—Pions and kaons have a double nature: the chiral dynamics of Nambu–Goldstone bosons together with the usual string dynamics common to all mesons. To uncover the interplay of both dynamics, the effective chiral Lagrangian is derived from the QCD Lagrangian using the field correlator method, and the pion self-energy (mass) operator is written explicitly. The latter contains an infinite number of poles, but is normalized to zero at zero momentum because of spontaneous chiral symmetry breaking. As a result, one obtains the Gell-Mann–Oakes–Renner relation for the ground-state pion and (slightly shifted by chiral dynamics) the usual spectrum of radially excited pions starting with $\pi(1300)$. *© 2004 MAIK "Nauka/Interperiodica".*

## 1. INTRODUCTION

The basic puzzle of the pion is that it is massless in the chiral limit as a Nambu–Goldstone (NG) boson, while it contains necessarily (because of confinement) a piece of the QCD string, weighing 1 GeV per 1 fm, i.e., around 0.6 GeV for its size. A naive quark model tells us that the pion differs from the $\rho$ meson only by spin–spin interaction, and a natural mass estimate, neglecting the NG mechanism, would give $m_\pi \approx 0.4$ GeV. A similar consideration with some larger (by 200–300 MeV) resulting mass also holds for the kaon. A question arises: What is the explicit cancellation mechanism which provides the vanishing pion mass (in the chiral limit)?

To get a hint to the solution of the puzzle, one may consider the NJL [1] or the instanton model [2], where the pion mass indeed vanishes in the chiral limit, while the constituent quark mass occurs due to the specific four-quark interaction.

However, in both models, confinement is absent, and in a sense the puzzle stated in the title also disappears. One can reformulate the problem with the NG mechanism, saying that in the NJL and instanton model the natural scale of meson mass is twice the constituent mass, i.e., around 0.6 GeV, while the NG meson in the pion channel has zero mass. Indeed, in both models, one can use relations for the constituent mass to prove that the denominator of the pion Green's function vanishes at zero momentum.

The situation in QCD is more complicated, however. The four-quark interaction, basic for spontaneous chiral symmetry breaking (CSB), occurs in QCD due to confinement (i.e., due to the presence of specific gluon-field correlators) and is associated with the QCD string [3, 4]. Therefore, all quarks and antiquarks are connected by the strings and the notion of a free quark with the constituent mass is not possible in QCD. Nevertheless, one can do the bosonization of the four-quark term, and as a result one obtains effective scalar and pseudoscalar fields from bilinear $q\bar{q}$ combinations [3].

The specific feature of the confining QCD phase is that the scalar field condensate is in the QCD string (scalar confining interaction in the effective operator) and defines quark mass operator $M$.

The outcome of this approach is the quark–meson effective Lagrangian $L_{\text{QML}}$ and the effective chiral Lagrangian $L_{\text{ECL}}$, containing only effective meson fields. In [3], these Lagrangians have been derived in the simplified situation when light quarks are moving in the field of the heavy antiquark. Below, we derive $L_{\text{QML}}$ and $L_{\text{ECL}}$ in a most general situation without heavy sources. Moreover, we expand $L_{\text{ECL}}$ in powers of pionic fields and demonstrate the vanishing of the pion mass in the chiral limit due to cancellation of two terms in the Green's function. For nonzero quark masses, we recover the Gell-Mann–Oakes–Renner (GOR) relation for the pion mass.

To study the interrelation between the quark and chiral degrees of freedom, the total Green's function is written in the PS channel which contains both nonchiral meson poles (as obtained, e.g., from the

---

[*] This article was submitted by the author in English.

[**] e-mail: `simonov@heron.itep.ru`

QCD string Hamiltonian [5] or quark potential models) and the pion chiral propagator poles. It is shown that, due to the interplay between both types of poles, the lowest $q\bar{q}$ nonchiral pole is replaced by the chiral pion pole, while all others are slightly shifted downwards ("the chiral shift") starting with the first radially excited pion state. In this nontrivial and remarkable way, one recovers the experimental spectrum in the whole pion channel.

The paper is organized as follows. In the next section, we derive $L_{\rm QML}$ and $L_{\rm ECL}$ following the procedure outlined in [3]. In Section 3, the pion quadratic terms in $L_{\rm ECL}$ are discussed and GOR relations are derived. In Section 4, the $q\bar{q}$ Green's function is written in the PS channel and its pole structure is investigated in detail and compared to the experimental spectrum of the pion and its radial excitations. In Section 5, the situation in the pion channel is compared to the vector channel, while Section 6 contains a discussion and possible development of this approach.

## 2. EFFECTIVE QUARK LAGRANGIAN

As was discussed in the previous section, one can obtain the effective quark Lagrangian by averaging over background gluonic fields. We shall repeat this procedure following [3, 4], now paying special attention to the case of light quarks. The QCD partition function for quarks and gluons can be written as

$$Z = \int DAD\psi D\psi^+ \exp[L_0 + L_1 + L_{\rm int}], \quad (1)$$

where we use the Euclidean metric and define

$$L_0 = -\frac{1}{4}\int d^4x (F^a_{\mu\nu})^2, \quad (2)$$

$$L_1 = -i\int {}^f\psi^+(x)(\hat{\partial} + m_f)\,{}^f\psi(x) d^4x, \quad (3)$$

$$L_{\rm int} = \int {}^f\psi^+(x) g\hat{A}(x)\,{}^f\psi(x) d^4x. \quad (4)$$

Here and in what follows, ${}^f\psi_{a\alpha}$ denotes a quark operator with flavor $f$, color $a$, and bispinor index $\alpha$.

To express $A_\mu(x)$ through $F_{\mu\nu}$, one can use the generalized contour gauge [6] with the contour $C(x)$ from the point $x$ to $x_0$, which can also lie at infinity,

$$A_\mu(x) = \int\limits_C F_{\lambda\beta}(z)\frac{\partial z_\beta(s,x)}{\partial x_\mu}\frac{\partial z_\lambda}{\partial s} ds. \quad (5)$$

Now, one can integrate out gluonic field $A_\mu(x)$. One obtains

$$Z = \int D\psi D\psi^+ \exp\{L_1 + L_{\rm eff}\}, \quad (6)$$

where the effective quark Lagrangian $L_{\rm eff}$ is defined as

$$\exp L_{\rm eff} = \langle \exp\int {}^f\psi^+ \hat{A}\,{}^f\psi d^4x\rangle_A. \quad (7)$$

Using cluster expansion, $L_{\rm eff}$ can be written as an infinite sum containing averages $\langle(\hat{A})^k\rangle_A$. At this point, one can exploit the Gaussian approximation, neglecting all correlators $\langle(\hat{A})^k\rangle$ for degrees higher than $k = 2$. Numerical accuracy of this approximation was discussed in [7] and tested in [8]. One expects that, for static quarks, corrections to the Gaussian approximation amount to less than 1%.

The resulting effective Lagrangian is quartic in $\psi$,

$$L^{(4)}_{\rm eff} = \frac{1}{2N_c}\int d^4x d^4y\, {}^f\psi^+_{a\alpha}(x) \quad (8)$$
$$\times\, {}^f\psi_{b\beta}(x)\, {}^g\psi^+_{b\gamma}(y)\, {}^g\psi_{a\delta}(y) J_{\alpha\beta,\gamma\delta}(x,y) + O(\psi^6),$$

$$J_{\alpha\beta,\gamma\delta}(x,y) = (\gamma_\mu)_{\alpha\beta}(\gamma_\nu)_{\gamma\delta} J_{\mu\nu}(x,y), \quad (9)$$

and $J_{\mu\nu}$ is expressed as

$$J_{\mu\nu}(x,y) = g^2\int\limits_C^x \frac{\partial u_\omega}{\partial x_\mu} du_\varepsilon \int\limits_C^y \frac{\partial v_{\omega'}}{\partial y_\nu} dv_{\varepsilon'} \quad (10)$$
$$\times\, \frac{1}{N_c}{\rm tr}\langle F_{\varepsilon\omega}(u) F_{\varepsilon'\omega'}(v)\rangle.$$

Lagrangian $L_{\rm eff}$ (8) is written in the contour gauge [6].

It can be identically rewritten in the gauge-invariant form if one substitutes parallel transporters $\Phi(x, x_0), \Phi(y, x_0)$ (identically equal to unity in this gauge) into (8) and (10), multiplying each $\psi(x)$ and $\psi(y)$, respectively, and in (10) replacing $F(u)$ by $\Phi(x_0, u)F(u)\Phi(u, x_0)$ and similarly for $F(v)$.

After that, $L_{\rm eff}$ becomes gauge-invariant, but in general contour-dependent, if one keeps only the quartic term (8) and neglects all higher terms. The final results of this paper do not depend on the choice of contour (more discussion of the contour fixation is given in Appendix 1).

Up to this point, we have made only one approximation—we have neglected all field correlators except the Gaussian one. Now, we must make another approximation—assume large-$N_c$ expansion and keep the lowest term. As was shown in [4], this enables one to replace in (8) the colorless product

$$ {}^f\psi_b(x)\, {}^g\psi^+_b(y)$$
$$= {\rm tr}({}^f\psi(x)\Phi(x, x_0)\Phi(x_0, y)\, {}^g\psi^+(y))$$

by the quark Green's function,

$${}^f\psi_{b\beta}(x)\, {}^g\psi^+_{b\gamma}(y) \to \delta_{fg} N_c S_{\beta\gamma}(x,y), \quad (11)$$

and $L_{\text{eff}}^{(4)}$ assumes the form

$$L_{\text{eff}}^{(4)} = -i\int d^4x d^4y\, {}^f\psi_{a\alpha}^+(x)\, {}^fM_{\alpha\delta}(x,y)\, {}^f\psi_{a\delta}(y), \tag{12}$$

where the quark mass operator is

$${}^fM_{\alpha\delta}(x,y) = -iJ_{\mu\nu}(x,y)(\gamma_\mu\, {}^fS(x,y)\gamma_\nu)_{\alpha\delta}. \tag{13}$$

From (6) and (12), it is evident that ${}^fS$ satisfies the equation

$$(-i\hat{\partial}_x - im_f)\, {}^fS(x,y) - i\int {}^fM(x,z)d^4z\, {}^fS(z,y) = \delta^{(4)}(x-y). \tag{14}$$

Equations (13) and (14) were first derived in [4]. From (6) and (12), one can realize that, at large $N_c$, the $q\bar{q}$ and $3q$ dynamics is expressed through the quark mass operator (13), which should contain both confinement and CSB.

At this point, it is necessary to stress the important difference of Eqs. (13) and (14) from the standard Dyson–Schwinger equations. In contrast to the latter, the mass operator ${}^fM$ and the quark Green's function $S$ are not one-body operators, but contain the string in the kernel $J_{\mu\nu}(x,y)$. The string extends from the midpoint of $(x,y)$ to the point $x_0$ {the distance $x-y$ is of the order of $T_g$—the gluon correlation length of the correlator $\langle F(u)F(v)\rangle$ in (10), which defines the width of the QCD string [9]}. It is convenient to specialize the contour $C(x,x_0)$ of the contour gauge (5) in such a way that it passes from the point $x$ to the trajectory of the center of mass of a gauge-invariant system, e.g., of the $\bar{q}q$ meson. Then the string in the mass operator of the quark $M_q$ extends from $x$ to the c.m. position of $(\bar{q}q)$, while the string in $M_{\bar{q}}$ extends from the position of the antiquark to the c.m. position. In [3, 4], the antiquark was taken to be infinitely heavy, so that one could consider only one string in $M_q$.

Nonlinear Eqs. (13) and (14) were studied in [4] and it was shown that there is a solution with the scalar confining interaction for ${}^fM(x,y)$, which implies CSB, and in [4] the first estimates were given for the chiral condensate $\langle\bar{q}q\rangle$: $\langle\bar{q}q\rangle \sim -c\sigma^{3/2}$, $\sigma$ is a string tension, and $c = 0.5$–$0.7$ depending on the nonlocality of the mass operator ${}^fM$; however, convergence of the series defining the constant $c$ was rather slow.

To discuss the NG modes and the CSB effects in more detail, we shall use the bosonization method of [3] in our general setting. The only difference from [3] is that we are using the most general contour gauge (5) with the contour prescription for the final gauge-invariant quantity (like Green's function), which ensures the minimal area world sheet for the string and hence for the total action of the system.

Now, instead of the large-$N_c$ substitution (11), one can do the bosonization of the $4q$ Lagrangian (8) in the same way as it was done in [3] for the heavy–light meson case. Leaving the details to the Appendix 2, one can write the resulting quark–meson Lagrangian for $n_f = 2$ keeping only scalar–isoscalar and pionic effective fields as follows:

$$\begin{aligned} L_{\text{QML}} = \int d^4x \int d^4y \{ {}^f\psi_{a\alpha}^+(x) \\ \times [(i\hat{\partial} + im_f)_{\alpha\beta}\delta_{fg}\delta^4(x-y) \\ + iM_{\alpha\beta}^{(fg)}(x,y)]\, {}^g\psi_{a\beta}(y) - [\chi^{(0,S)}(x,y)\chi^{(0,S)}(y,x) \\ + \chi_a^{(1,\text{PS})}(x,y)\chi_a^{(1,\text{PS})}(y,x)]J(x,y)\}, \end{aligned} \tag{15}$$

where

$$\begin{aligned} M_{\alpha\beta}^{(fg)}(x,y) = (\chi^{(0,S)}(x,y)\delta_{\alpha\beta}t_{fg}^{(0)} \\ + \chi_a^{(1,\text{PS})}(x,y)(i\gamma_5)_{\alpha\beta}t_{fg}^{(a)})J(x,y). \end{aligned} \tag{16}$$

It is convenient to use another parametrization of the pionic field, replacing $\chi^{(0,S)}$ and $\chi_a^{(1,\text{PS})}$ by $M_S$ and $\phi_a$:

$$\begin{aligned} M_{\alpha\beta}^{(fg)}(x,y) = M_S(x,y) \\ \times \exp(i\gamma_5 t^a\phi_a(x,y))_{\alpha\beta}^{(fg)} \equiv M_S(x,y)\hat{U}_{\alpha\beta}^{(fg)}(x,y). \end{aligned} \tag{17}$$

Then, (15) can be rewritten as

$$\begin{aligned} L_{\text{QML}} = \int d^4x \int d^4y \{ {}^f\psi_{a\alpha}^+(x) \\ \times [(i\hat{\partial} + im_f)_{\alpha\beta}\delta^{(4)}(x-y)\delta_{fg} \\ + iM_S\hat{U}_{\alpha\beta}^{(fg)}(x,y)]\, {}^g\psi_{a\beta}(y) \\ - 2n_f[J(x,y)]^{-1}M_S^2(x,y)\}. \end{aligned} \tag{18}$$

The partition function with $L_{\text{QML}}$ assumes the form

$$Z = \int D\psi D\psi^+ DM_S D\phi_a \exp L_{\text{QML}}. \tag{19}$$

One can integrate over quark fields in (19) yielding the effective chiral Lagrangian $L_{\text{ECL}}$:

$$Z = \int DM_S D\phi_a \exp L_{\text{ECL}}, \tag{20}$$

where it is assumed that $L_{\text{ECL}}$ is considered in the nonsinglet channels and therefore the chiral anomaly contribution can be neglected. $L_{\text{ECL}}$ has the form

$$\begin{aligned} L_{\text{ECL}} = -2n_f \int d^4x \int d^4y (J(x,y))^{-1}M_S^2(x,y) \\ + N_c \text{tr}\log[(i\hat{\partial} + im_f)\hat{1} + iM_S\hat{U}]. \end{aligned} \tag{21}$$

Here, tr refers to the flavor, Lorentz indices and coordinates, and $\hat{1}_{fg} = \delta_{fg}$, and the expression in the square brackets in (21) is an $n_f \times n_f$ matrix. To find the minimum of $L_{\text{ECL}}$ as a functional of $M_S$, $\phi_a$, one obtains the stationary point equations, yielding

$$\frac{\delta L_{\text{ECL}}}{\delta M_S(x,y)} = -4n_f(J(x,y))^{-1}M_S(x,y) - N_c\text{tr}(S_\phi i e^{i\gamma_5\hat{\phi}}) = 0, \qquad (22)$$

$$\frac{\delta L_{\text{ECL}}}{\delta \phi_a(x,y)} = N_c\text{tr}(S_\phi M_S e^{i\gamma_5\hat{\phi}}\gamma_5 t_a) = 0, \qquad (23)$$

where $S_\phi = -[(i\hat{\partial} + im_f)\hat{1} + iM_S\hat{U}]^{-1}$. The solutions to (22) and (23) are $\phi_a^{(0)} = 0$ and $M_S = M_S^{(0)}$, where $M_S^{(0)}$ satisfies relation

$$iM_S^{(0)}(x,y) = \frac{N_c}{4}\text{tr}(SJ(x,y)) = (\gamma_\mu S\gamma_\nu)_{\text{sc}}J_{\mu\nu}(x,y), \qquad (24)$$

the subscript "sc" implies taking the Lorentz scalar part of the operator, and $S \equiv S_\phi(\phi_a = 0)$. Note that Eq. (24) coincides with (13) if one neglects in $M_S$, as we have done before, all terms except scalars.

This remarkable feature demonstrates a completely new meaning of the scalar condensate in QCD: while in nonconfining models like the NJL or instanton model the scalar condensate, like Higgs condensate, is constant everywhere, in QCD the scalar condensate is concentrated in the string—i.e., in $M_S(x,y)$—and is actually the dominant part of the string itself.

This is of course the consequence of the fact that, in QCD, the CSB is due to confinement, and the effective meson fields are nonzero just where the confining kernel $M_S(x,y)$ is present.

## 3. THE PION MASS

In this section, it will be proved that the pion is massless, as it should be for the NG meson in the chiral limit, and that, for nonzero quark mass, one has the GOR relation [10]. To this end, we consider the pionic part of the $L_{\text{ECL}}$ (21) and expand it in powers of the pionic field $\phi_a$ up to the second order.

One has

$$\begin{aligned}-W(\phi) &\equiv N_c\text{tr}\log[(i\hat{\partial} + im_f)\hat{1} + iM_S\hat{U}] \qquad (25)\\ &= N_c\text{tr}\log[(i\hat{\partial} + im_f + iM_S)\hat{1} + \Delta]\\ &= N_c\text{tr}\log((i\hat{\partial} + im_f + iM_S)\hat{1}) + N_c\text{tr}[(i\partial + im_f + iM_S)^{-1}\Delta] - \frac{1}{2}N_c\text{tr}[(i\hat{\partial} + im_f + iM_S)^{-1}\Delta(i\hat{\partial} + im_f + iM_S)^{-1}\Delta].\end{aligned}$$

Here, $\Delta = (-\hat{\phi}\gamma_5 - \frac{i}{2}\hat{\phi}^2)M_S$, $\hat{\phi} \equiv \phi_a t_a$. One can rewrite the quadratic in $\phi_a$ terms as

$$W^{(2)}(\phi) = \frac{1}{2}\int\frac{d^4k}{(2\pi)^4}\frac{d^4k'}{(2\pi)^4}\phi_a(k)\hat{N}(k,k')\phi_a(k'). \qquad (26)$$

To simplify derivation, we shall neglect the isospin violation and nonlocality, replace $m_f \to (m_u + m_d)/2 \equiv m$, and write $M_S(x,y) \to M_S(x)\delta^{(4)}(x-y)$, $\phi_a(x,y) \to \phi_a(x)$. In [4], it was shown that $M_S(x,y)$ indeed has this property at least at large distances, where also $M_S^{(0)}(x) = \sigma|\mathbf{x}|$.

From (26) and (25), one obtains

$$\begin{aligned}\hat{N}(k,k') &= \frac{N_c}{2}\int dx e^{i(k+k')x}\text{tr}(\Lambda M_S)_{xx} \qquad (27)\\ &+ \frac{N_c}{2}\int d^4(x-y)d^4\left(\frac{x+y}{2}\right)\\ &\times e^{\frac{i}{2}(k+k')(x+y)+\frac{i}{2}(k-k')(y-x)}\\ &\times \text{tr}[\Lambda(x,y)M_S(y)\bar{\Lambda}(y,x)M_S(x)],\end{aligned}$$

where we have defined

$$\Lambda = (\hat{\partial} + m + M_S)^{-1}, \qquad (28)$$
$$\bar{\Lambda} = (\hat{\partial} - m - M_S)^{-1}.$$

One can use translation invariance of the traces in (27) to rewrite (26) as

$$W^{(2)}(\phi) = \frac{N_c}{2}\int\phi_a(k)\phi_a(-k)\bar{N}(k)\frac{d^4k}{(2\pi)^4} \qquad (29)$$

with

$$\bar{N}(k) = \frac{1}{2}\text{tr}\{(\Lambda M_S)_0 + \int d^4z e^{ikz}\Lambda(0,z)M_S(z)\bar{\Lambda}(z,0)M_S(0)\}. \qquad (30)$$

The pion mass is proportional to $\bar{N}(0)$, which can be written after some algebraic manipulations as (see Appendix 3 for details of derivation)

$$\bar{N}(0) = \frac{1}{2}\text{tr}(\Lambda M_S\bar{\Lambda}(\hat{\partial} - m)) \qquad (31)$$
$$= \frac{m}{4}\text{tr}(\Lambda - \bar{\Lambda}) = \frac{1}{2}m\text{tr}\Lambda + O(m^2).$$

Note here that, in the chiral limit $m \to 0$, one has $m_\pi^2 \sim N(0,0) = 0$. In all calculations resulting in (30) and (31), use is made of reflection symmetry, which allows one to replace $(-\hat{\partial})$ by $(\hat{\partial})$. A similar calculation was done earlier in [11], where instantons were used to create the four-quark operators in the background of gluon fields, but the phenomenon of the CSB due to confinement was absent.

Since the quark condensate as defined in Minkowskian spacetime $\langle\psi\bar{\psi}\rangle_{\rm M}$ is connected to tr$\Lambda$ as (trace is taken over bispinor indices)

$$\langle\psi\bar{\psi}\rangle_{\rm M} = i\langle\psi\psi^{+}\rangle_{\rm E} = iN_c \mathrm{tr} S(x,y) = -2N_c \mathrm{tr}\Lambda, \tag{32}$$

one has for the pion mass with the usual normalization $\phi_a = 2\pi_a/f_\pi$, $f_\pi = 93$ MeV,

$$\begin{aligned} 2m_\pi^2 f_\pi^2 &= (m_u + m_d)|\langle\psi\bar{\psi}\rangle_{\rm M}| \\ &= (m_u + m_d)|\langle\bar{u}u + \bar{d}d\rangle|, \end{aligned} \tag{33}$$

which in the standard GOR relation [10].

## 4. THE PION GREEN'S FUNCTION

To obtain the pion Green's function, one can use the partition function (19) to calculate the correlator of the PS currents $J_a^{(5)}(x) = \psi^{+}(x)\gamma_5 t_a \psi(x)$,

$$\begin{aligned} G_{ab}(x,y) &= \frac{1}{Z}\int D\psi D\psi^{+} DM_S D\phi \\ &\times \exp(L^{(2)}_{\rm QML}) J_a^{(5)}(x) J_b^{(5)}(y). \end{aligned} \tag{34}$$

Integrating over $D\psi D\psi^{+}$, one gets the standard expression

$$\begin{aligned} G_{ab}(x,y) &= \frac{1}{Z} \\ \times \int DM_S D\phi e^{L^{(2)}_{\rm ECL}} &\{\mathrm{tr}[S_\phi(x,y)\gamma_5 t_b S_\phi(y,x)\gamma_5 t_a] \\ &- \mathrm{tr}(S_\phi(x,x)\gamma_5 t_a)\mathrm{tr}(S_\phi(y,y)\gamma_5 t_b)\}, \end{aligned} \tag{35}$$

where $S_\phi(x,y)$ is defined in (23) and depends on $M_S$ and $\phi_a$. Our following discussion is similar in some respects to the line of reasoning in [11]; however, instantons are omitted in (35) since the CSB occurs due to confinement, as is demonstrated above explicitly by Eq. (24).

Equation (35) contains two terms with one and two trace operators in the curly brackets, which can be called the connected and disconnected terms, respectively. The integration over $DM_S$ can be done using the stationary condition (24), while for the integration in $D\phi$ one expands $L^{(2)}_{\rm ECL}$ in $\phi_a$ around the stationary point $\phi_a^{(0)} = 0$, keeping the second-order terms. In what follows, $M_S$ will be replaced by the stationary point value $M_S^{(0)}$ without changing notation. Using now the expansion for $S_\phi$

$$\begin{aligned} S_\phi(x,y) &= S(x,y) \\ &+ S(x,z)M_S\gamma_5\hat{\phi}(z)S(z,y) + O(\phi^2) \end{aligned} \tag{36}$$

and noticing that $\phi_a = 2\pi_a/f_\pi$ and $f_\pi = O(N_c^{1/2})$, one can deduce that the emission or absorption of the pion contains a factor $N_c^{-1/2}$, or, in other words, the coupling constant $g_{\pi q\bar{q}} = O(N_c^{-1/2})$. Therefore, in the large-$N_c$ limit, one should take into account the lowest number of pion exchanges, and we shall neglect pion fields in the connected term in (35), replacing $S_\phi$ by $S \equiv S_\phi(\phi = 0)$ and keeping only the first-order term (36) in the disconnected term of (35). Integrating now over $D\phi$, one obtains from both terms the contribution, proportional to $N_c$,

$$\begin{aligned} G_{ab}(x,y) &= N_c G^{(0)}_{ab}(x,y) \\ &- \frac{N_c^2}{f_\pi^2} G^{(M)}_{ac}(x,z) G^{(0)}_\pi(z,u) G^{(M)}_{cb}(u,y), \end{aligned} \tag{37}$$

where we have defined

$$G^{(0)}_{ab}(x,y) \equiv \frac{1}{2}G^{(0)}\delta_{ab} \equiv \mathrm{tr}[S(x,y)\gamma_5 t_b S(y,x)\gamma_5 t_a], \tag{38}$$

$$\begin{aligned} G^{(M)}_{ab}(x,y) &\equiv \frac{1}{2}G^{(M)}\delta_{ab} \\ &\equiv \mathrm{tr}[\gamma_5 t_a S(x,y) M_S \gamma_5 t_b S(y,x)], \end{aligned} \tag{39}$$

$$G^{(0)}_\pi(x,y) = \int \frac{d^4k}{(2\pi)^4}\frac{e^{ik(x-y)}f_\pi^2}{N_c\bar{N}(k)}, \tag{40}$$

and the sign tr implies Lorentz, flavor, and coordinate summation (integration).

Therefore the total Green's function looks like

$$\begin{aligned} G(x,y) &= N_c\Big\{G^{(0)}(x,y) \\ &- \frac{N_c}{2f_\pi^2}G^{(M)}(x,z)G^{(0)}_\pi(z,u)G^{(M)}(u,y)\Big\}. \end{aligned} \tag{41}$$

Using (30) and going over to momentum space, one has

$$G(k) = N_c\left\{G^{(0)}(k) - \frac{G^{(M)}(k)G^{(M)}(k)}{G^{(MM)}(k) + \mathrm{tr}(\Lambda M_S)}\right\}. \tag{42}$$

Here, $G^{(MM)}(k) \equiv \mathrm{tr}(SM_S\gamma_5 SM_S\gamma_5)_k$, where the subscript $k$ implies the Fourier transform, which according to (30) and (31) is

$$\begin{aligned} \bar{N}(k) &= \frac{1}{2}(G^{(MM)}(k) + \mathrm{tr}(\Lambda M_S)) \\ &= (m_\pi^2 + k^2)\frac{f_\pi^2}{4N_c} + O(k^4). \end{aligned} \tag{43}$$

Therefore, (42) contains the pion pole in the second term on the right-hand side of (42).

The question arises as to what happens with the poles of $G^{(0)}(k)$. Actually, here appears the lowest pole in the PS channel, which one can call the quark model (QM) pion, usually situated around 400 MeV. This pole is present in all three Green's functions $G^{(0)}(k), G^{(M)}(k)$, and $G^{(MM)}(k)$, and if one contracts all $M_S$ factors in the numerator and denominator of (42), one can easily see that the QM pole is canceled between the first and the second term in the curly brackets.

To make this cancellation more transparent, one can again use the large-$N_c$ argument and represent $G^{(0)}(k)$, $G^{(M)}(k)$, and $G^{(MM)}(k)$ as series of poles, e.g.,

$$G^{(0)}(k) = -\sum_{n=0}^{\infty} \frac{c_n^2}{k^2+m_n^2}, \tag{44}$$

$$G^{(M)}(k) = -\sum_{n=0}^{\infty} \frac{c_n c_n^{(M)}}{k^2+m_n^2},$$

$$G^{(MM)}(k) = -\sum_{n=0}^{\infty} \frac{(c_n^{(M)})^2}{k^2+m_n^2},$$

where $c_n^{(M)}$ differs from $c_n$ by the presence of the operator $M$ inside the matrix element, at the initial or final point of the Green's function, e.g., for $G^{(MM)}(k)$:

$$G^{(MM)}(k) \tag{45}$$

$$= \int \mathrm{tr}(\gamma_5 M_S(x) S(x,y) \gamma_5 M_S(y) S(y,x)) e^{ik(x-y)}$$

$$\times d^4(x-y).$$

The presence of the scalar quasi-local in time operator $M_S(x)$ cannot change the spectrum of bound states in $G^{(M)}(k)$ and $G^{(MM)}(k)$ as compared to $G^{(0)}(k)$, where operators $M_S(x)$ are absent, and therefore all three functions should have the same set of poles.

Now the vanishing of $\bar{N}(0)$ for $m=0$ implies that, in the chiral limit, one can write the denominator in (42) as

$$G^{(MM)}(k) + \mathrm{tr}\Lambda M_S = G^{(MM)}(k) \tag{46}$$

$$- G^{(MM)}(0) = k^2 \sum_{n=0}^{\infty} \frac{(c_n^{(M)})^2}{(m_n^2+k^2)m_n^2}.$$

Hence, the total Green's function can be written as (in the chiral limit, $m \to 0$)

$$G(k) = \frac{\Psi(k)}{k^2 \Phi(k)}, \tag{47}$$

where

$$\Psi(k) = \sum_{n=0}^{\infty} \frac{c_n}{k^2+m_n^2} \tag{48}$$

$$\times \sum_{k=0}^{\infty} \frac{c_n (c_k^{(M)})^2 k^2/m_k^2 + c_n^{(M)} c_k c_k^{(M)}}{k^2+m_k^2},$$

$$\Phi(k) = -\sum_{n=0}^{\infty} \frac{(c_n^M)^2}{m_n^2(k^2+m_n^2)}. \tag{49}$$

From the structure of (47), one can easily see that double poles at $k^2 = -m_n^2$ are canceled in $\Psi(k)$, so that only simple poles are retained, which are compensated by the same poles of $\Phi(k)$, so that the ratio $\Psi(k)/\Phi(k)$ does not have poles at $k^2 = -m_n^2$, $n = 0, 1, 2, \ldots$.

Clearly, $G(k)$ has a pole at $k^2 = 0$, which is the expected pion pole of the chiral limit, which is shifted to the position $k^2 = -m_\pi^2$, with $m_\pi^2$ defined in (33). Now, the question arises as to where the next pole in $G(k)$ appears.

To this end, one can take into account the properties of the hadron spectrum in the linearly confining vacuum, found in the vector channel in [12] and in general in [5, 13, 14], which are obtained without chiral effects, i.e., exactly pertinent to $m_n, c_n^{(M)}$. It was found that the spectrum of radially excited mesons in the large-$N_c$ limit satisfies the approximate relation

$$m_n^2 \simeq 4\pi\sigma n + \Delta m, \tag{50}$$

$$\Delta m(J^{PC} = 0^{-+}) \simeq 0.4\ \mathrm{GeV},$$

while $c_n^{(M)}$ is roughly independent of $n$. The latter is due to the fact that $c_n^{(M)} \sim \psi_n(\mathbf{r}=0)$ and for the linear interaction $\psi_n(0)$ does not depend on $n$.

Using these properties, one can find zeros of $\Phi(k)$ in the $k^2$ plane $k^2 = (k^{(0)})^2$, which correspond to the poles in $G(k)$. One has from (49)

$$(k^{(0)})^2 = -m_1^2(1-\delta_1), \tag{51}$$

$$-m_2^2(1-\delta_2), \ldots, -m_n^2(1-\delta_n), \ldots,$$

where the chiral shifts of the levels are $\delta_1 \simeq [c_1^2 m_0^2(m_1^2 - m_0^2)]/[m_1^2(c_0^2 m_1^2 + c_1^2 m_0^2)]$, $\delta_2 \simeq O(m_0^2)$, etc. Hence, the first excited pion pole is close to the position of the first excited pole obtained in the QM approach without taking into account chiral effects. The same is true for higher excited states. It is interesting that the ground QM state with mass $m_0 \approx 0.4$ GeV disappears from the total spectrum of the full Green's function $G(k)$ and is replaced by the correct chiral-generated pole at $m_\pi$ given in (33). This is exactly what one should expect on physical grounds, and it is rewarding that our simple Eq. (42) reproduces this physically reasonable result.

The calculation of the radially excited states in the framework of the QCD string approach was recently done in [14]. For the first radially excited state, the $1/N_c$ corrections are not large and the spin-averaged mass was found to be $\bar{M}_{\rm av} = 1.45$ GeV with $\sigma = 0.18$ GeV$^2$ (the only input). The pion mass is shifted downwards by roughly 0.105 GeV due to hyperfine interaction and the resulting theoretical pion mass $m_1$ is around 1.35 GeV, which after subtraction of the chiral shift $\delta_1$ exactly coincides with the experimental mass value of $\pi(1300)$.

## 5. DISCUSSION: PHOTON AND PION SELF-ENERGY OPERATORS

The pion Green's function

$$G_\pi^{(0)}(k) \sim \frac{1}{N(k)} \sim \frac{1}{G^{(MM)}(k) - G^{(MM)}(0)}, \quad (52)$$

which is obtained from the effective Lagrangian $L_{\rm ECL}$ [Eq. (21)], contains an infinite number of poles in the denominator due to the self-energy operator, the role of the latter being played by $G^{(MM)}(k)$. These poles are due to confinement only while chiral effects (pion emission and absorption) are switched off in $G^{(MM)}(k)$ [hence the superscript (0)].

Now, by construction—and this is the consequence of the spontaneous CSB—in the pion Green's function, only the difference $G^{(MM)}(k) - G^{(MM)}(0)$ enters in the denominator, which is $O(k^2)$ in the chiral limit ($m = 0$) for $k \to 0$.

The situation here is similar to the case of the photon propagator with the self-energy operator due to the hadron intermediate states, as it enters in the process $e^+e^- \to$ hadrons. Indeed, the full transverse photon Green's function $D(k^2)$ can be written as

$$D(k^2) = \frac{4\pi}{k^2 - \mathcal{P}(k^2)}, \quad (53)$$

$$\mathcal{P}_{\mu\nu}(k) = \left(g_{\mu\nu} - \frac{k_\mu k_\nu}{k^2}\right)\mathcal{P}(k^2)$$

with the renormalization conditions $\mathcal{P}(k^2 = 0) = \mathcal{P}'(k^2 = 0) = 0$. $\mathcal{P}(k^2)$ is connected to the vacuum polarization operator $\Pi(k^2)$ via $\mathcal{P}(k^2) \sim e^2 k^2 \Pi(k^2)$, and $\mathrm{Im}\Pi(k^2)$ is proportional to the hadronic ratio $R(k^2)$ of the process $e^+e^- \to$ hadrons.

Using the same reasoning as in [12], one can express for large $N_c$ the operator $\Pi(k^2)$ as a sum over hadronic poles—radial excitations in the vector channel with masses $m_n(v)$, $\Pi(k^2) = \sum a_n/[k^2 + m_n^2(v)]$. As a result, the structure of the photon Green's function (53) becomes similar to that of the pion Green's function (52): an infinite sum of poles in the denominator renormalized by subtractions to vanish for $k = 0$. The latter condition comes from the spontaneous CSB (the NG theorem) in case of the pion and from gauge invariance in case of the photon. It seems that one could use the same Eq. (42) for both cases with similar conclusions for the spectrum.

However, at this point, the similarity stops. Indeed, in the case of the photon, the mixing between photon and vector-meson states is governed by $\alpha = 1/137$ and is small, and the number of states does not change; it consists of all vector-meson states plus photon. In this case, the vector-meson states are shifted only slightly, as can be seen from (53), yielding the condition for poles; $\Pi(k^2) = \mathrm{const}/e^2$ and as a result $k_n^2 = (k_n^{(0)})^2 + d_n e^2$.

In case of the pion, the situation is different; the pion and hadron resonances in the self-energy part are not coupled by a small coupling constant, but rather enter in the denominator with a large coefficient such that it exactly cancels the lowest hadron state, trading it for the chiral pion. Therefore, the total spectrum consists of the almost massless pion and all its radial excitations, while the lowest nonchiral state disappears from the spectrum. This is rewarding, since the chiral pion is made of the same $\bar{q}q$ degrees of freedom as the nonchiral states, and the number of states should not increase because some states are treated differently.

This is not true for the photon, since the photon has a different nature and origin as compared to hadron states in $\Pi(k^2)$.

## 6. CONCLUSIONS AND OUTLOOK

The purpose of this paper is twofold. First of all, it is necessary to understand for the system of light quarks how confinement spontaneously provides the chiral symmetry breaking. For the heavy–light system, this was first shown in [4] and developed making use of Green's functions and the Dirac formalism. Later, in [3], the same connection between confinement and CSB was established using the familiar bosonization technique, but again for the heavy–light systems. In the present paper, the bosonization is used and the resulting effective chiral Lagrangian is obtained for the light–light systems in Eqs. (18)–(21). It is remarkable that the stationary point Eqs. (22), (23) yield a nonlinear equation for the mass operator (24), with the self-consistent solution (already discussed in [4]) containing the scalar string between quark and antiquark. This is similar to the NJL and the instanton models, where in the absence of confinement also the stationary point solution brings about the scalar condensate and this appears spontaneously, implying CSB. The difference is that, in the case of confinement, this scalar condensate resides not in all space but in strings and also gives CSB.

Another important purpose of the paper is to clarify the problem of the pion mass: while for all other mesons the QCD string approach and also the constituent quark model give a reasonable description of the spectrum, the spectrum of pions (and also of kaons and $\eta$, $\eta'$) is strikingly different, with a very large mass gap between $\pi(139)$ and $\pi(1300)$. In the present paper, we have derived the total Green's function in the PS channel, containing both chiral and confining properties. It was shown for the first time that the effective chiral Lagrangian derived directly from the QCD Lagrangian produces the pion mass satisfying the Gell-Mann–Oakes–Renner relation. Moreover, it was demonstrated that poles of the total Green's function correspond exactly to the physical picture: namely, the lowest QM pole $m_0^2$ moves into the pseudo-NG position, while all the higher poles shift only slightly, reproducing the experimental picture.

For reasons of simplicity, only the pion was considered above. It is not difficult to extend the formalism to $SU(3)$ and to treat $\eta$ and kaons, and the pion and kaon Regge trajectories. The $\eta'$ case includes the chiral anomaly and connection to the gluonic (glueball) channel, and this study is planned for the future.

Another part of the work that still remains undone is the study of the pion wave function and of the role of confinement in its dynamics.

## ACKNOWLEDGMENTS

I am grateful to S.M. Fedorov and N.O. Agasian for useful remarks.

This work was supported by the Russian Foundation for Basic Research (project no. 00-15-96786) and INTAS (grant nos. 00-00110 and 00-00366).

## APPENDIX 1

The gauge-invariant form of (8) and (10) is obtained by insertion of the parallel transporters $\Phi_C(z, x_0)$ into all $\psi$ in (8) and replacing $F(z)$ by $\Phi_C(x_0, z)F(z)\ \Phi_C(z, x_0)$. The resulting effective $4q$ Lagrangian (8) will depend on the shape of the contour $C$. It is clear that the whole sum of all-order correlators $\sum_{n=4,6,\ldots}^{\infty} L_{\text{eff}}^{(n)} \equiv L_{\text{eff}}$ does not depend on the shape of $C$. Thus, with $L_{\text{eff}}$, one can choose any contour $C(x)$ and, in particular, select a contour $C(x)$ in such a way as to produce the minimal area surface for the world sheet of the string, or, in the Lagrangian formalism, to form the string (contour) of minimal length between the quark at one end and antiquark at the other end of the string.

For this minimal string (minimal area surface), it is legitimate to drop all terms in $L_{\text{eff}}$ except $L_{\text{eff}}^{(4)}$, since the difference (for the minimal area) is expected to be of the order of 1% according to [7, 8].

A similar problem occurs in the cluster expansion of the Wilson loop, when one keeps only the lowest correlators, leading to the (erroneous) surface dependence of the result. Note that only for the minimal area surface are higher correlators negligible. Therefore, the Gaussian approximation is valid when the minimal area surface is fixed beforehand. The situation here is the same as with the sum of QCD perturbation series, which depends on the normalization mass $\mu$ for any finite number of terms in the series. This unphysical dependence is usually treated by fixing $\mu$ at some physically reasonable value $\mu_0$ (of the order of the inverse size of the system).

Similarly, the physical choice of the contour corresponds to the minimization of the meson (baryon) mass over the class of strings generated by contours $C$ in the same way as the choice of $\mu = \mu_0$ corresponds to the minimization of the dropped higher perturbative terms.

As a practical outcome, we shall keep the set of contours $C$ until the end and finally use it to minimize the string between the quarks.

## APPENDIX 2

### *Derivation of the Effective Quark–Meson Lagrangian $L_{QML}$*

We start with the white quark bilinears, as in [3],

$$\Psi^{fg}_{\alpha\varepsilon}(x,y) \equiv {}^f\psi^+_{a\alpha}(x)\,{}^g\psi_{a\varepsilon}(y) \qquad \text{(A.1)}$$
$$= {}^f\psi^+_{a'\alpha}(x)\Phi_{a'a}(x,Y)\Phi_{ac}(Y,y)\,{}^g\psi_{c\varepsilon}(y),$$

and introduce the isospin generators $t^{(n)}_{fg}$:

$$\sum_{n=0}^{n_f^2-1} t^{(n)}_{fg}t^{(n)}_{ij} = \frac{1}{2}\delta_{fj}\delta_{gi}; \qquad \text{(A.2)}$$
$$t^{(0)} = \frac{1}{\sqrt{2n_f}}\hat{1}, \quad \mathrm{tr}(t^{(n)}t^{(k)}) = \frac{1}{2}\delta_{nk}.$$

Hence, the bilinears in (8) can be written as

$$\Psi^{fg}_{\alpha\varepsilon}(x,y)\Psi^{gf}_{\gamma\beta}(y,x) = 2\sum_{n=0}^{n_f^2-1}\Psi^{(n)}_{\alpha\varepsilon}(x,y)\Psi^{(n)}_{\gamma\beta}(y,x), \qquad \text{(A.3)}$$

where we have defined

$$\Psi^{(n)}_{\alpha\varepsilon}(x,y) \equiv {}^f\psi^+_{a\alpha}(x)t^{(n)}_{fg}\,{}^g\psi_{a\varepsilon}(y). \qquad \text{(A.4)}$$

Now, one can use the Fierz transformation for the combination $\gamma^\mu\gamma^\nu$ (see Appendix 3 of [3]):

$$(\gamma^\mu)_{\alpha\beta}(\gamma^\nu)_{\gamma\delta} = \frac{1}{4}\sum_A \Delta_A(\gamma^\mu\gamma_A\gamma^\nu)_{\alpha\delta}(\gamma_A)_{\gamma\beta}, \tag{A.5}$$

where $\Delta_A = -1$ for $\gamma_A = \gamma_5\gamma_\mu$ and $\Delta_A = 1$ otherwise. We shall be interested here only in scalar and pseudoscalar combinations on the right-hand side of (A.5); hence, one can write

$$(\gamma^\mu)_{\alpha\beta}(\gamma^\nu)_{\gamma\delta} \tag{A.6}$$

$$= \frac{1}{4}\delta_{\mu\nu}\{\hat{1}_{\alpha\delta}\hat{1}_{\gamma\beta} + (i\gamma_5)_{\alpha\delta}(i\gamma_5)_{\gamma\beta}\} + \ldots$$

$$\equiv \frac{1}{4}\delta_{\mu\nu}\{O^{(S)}_{\alpha\delta}O^{(S)}_{\gamma\beta} + O^{(\mathrm{PS})}_{\alpha\delta}O^{(\mathrm{PS})}_{\gamma\beta}\}\ldots,$$

where the ellipsis in (A.6) and in what follows implies the contribution of all other combinations. As a result, one has for $L^{(4)}_{\mathrm{eff}}$ [Eq. (8)]

$$L^{(4)}_{\mathrm{eff}} = -\int d^4x\int d^4y\{\Psi^{(n,S)}(x,y) \tag{A.7}$$

$$\times\,\Psi^{(n,S)}(y,x) + \Psi^{(n,\mathrm{PS})}(x,y)$$

$$\times\,\Psi^{(n,\mathrm{PS})}(y,x)\}J(x,y) + \ldots,$$

where $J(x,y) \equiv \frac{1}{N_c}J_{\mu\mu}(x,y)$ and

$$\Psi^{(n,S),(n,\mathrm{PS})}(x,y) = \frac{1}{2}\Psi^{(n)}_{\alpha\beta}(\hat{1}_{\alpha\beta},(i\gamma_5)_{\alpha\beta}). \tag{A.8}$$

Now, the Hubbard–Stratonovich transformation is written symbolically through effective nonlocal bosonic fields $\chi^{(n,S)}(x,y)$, $\chi^{(n,\mathrm{PS})}(x,y)$ as follows:

$$e^{-\Psi J\Psi} = \int(\det J)^{1/2}D\chi \tag{A.9}$$

$$\times\exp(-\chi J\chi + i\Psi J\chi + i\chi J\Psi);$$

and the partition function assumes the form

$$Z = \int D\psi D\psi^+ D\chi\exp L_{\mathrm{QML}}, \tag{A.10}$$

where the effective quark–meson Lagrangian is

$$L_{\mathrm{QML}} = \int d^4x\int d^4y\{{}^f\psi^+_{a\alpha}(x) \tag{A.11}$$

$$\times\,[(i\hat{\partial} + im_f)_{\alpha\beta}\delta_{fg}\delta^{(4)}(x-y)$$

$$+\,iM^{(fg)}_{\alpha\beta}(x,y)]\,{}^g\psi_{a\beta}(y)$$

$$-\sum_{k=S,\mathrm{PS}}\chi^{(n,k)}(x,y)J(x,y)\chi^{(n,k)}(y,x)\}$$

and the effective quark-mass operator is

$$M^{(fg)}_{\alpha\beta}(x,y) \tag{A.12}$$

$$= \sum_{\substack{n\,=\,0,\,\ldots,\,n_f^2\,-\,1\\ k\,=\,S,\,\mathrm{PS}}}\chi^{(n,k)}(x,y)O^{(k)}_{\alpha\beta}t^{(n)}_{fg}J(x,y).$$

## APPENDIX 3

### *Derivation of the GOR Relation (33)*

We start with the definition (30), (31), which can be rewritten identically as

$$\bar{N}(0) = \frac{1}{2}\mathrm{tr}[\Lambda M_S\bar{\Lambda}(\hat{\partial} - m - M_S) \tag{A.13}$$

$$+\,\Lambda M_S\bar{\Lambda}M_S] = \frac{1}{2}\mathrm{tr}[\Lambda M_S\bar{\Lambda}(\hat{\partial} - m)].$$

Inserting, for the factor $M_S$, into the last equality of (A.13) the expression

$$M_S = \frac{1}{2}(\Lambda^{-1} - \bar{\Lambda}^{-1} - 2m), \tag{A.14}$$

one immediately obtains

$$\bar{N}(0) = \frac{1}{2}\mathrm{tr}(A + B + C), \tag{A.15}$$

where

$$A \equiv \frac{1}{2}(\bar{\Lambda} - \Lambda)\hat{\partial}, \quad B \equiv \frac{m}{2}(\Lambda - \bar{\Lambda}),$$

$$C = -m\Lambda\bar{\Lambda}(\hat{\partial} - m).$$

It is easy to see that $A$ vanishes, since it is odd with respect to the spacetime reflection, and $C$ is $O(m^2)$. The term $B$ yields the answer given in Eq. (31).

## REFERENCES

1. Y. Nambu and G. Jona-Lasinio, Phys. Rev. **122**, 345 (1961); S. P. Klevansky, Rev. Mod. Phys. **64**, 650 (1992).
2. D. Diakonov and V. Petrov, Nucl. Phys. B **272**, 457 (1986); for a review and earlier references see Th. Shaefer and E. V. Shuryak, Rev. Mod. Phys. **70**, 323 (1998).
3. Yu. A. Simonov, Phys. Rev. D **65**, 094018 (2002); hep-ph/0201170.
4. Yu. A. Simonov, Yad. Fiz. **60**, 2252 (1997) [Phys. At. Nucl. **60**, 2069 (1997)]; hep-ph/9704301; Yu. A. Simonov and J. A. Tjon, Phys. Rev. D **62**, 014501, 094511 (2000).
5. Yu. A. Simonov, in *Lisbon 1999, QCD: Perturbative or Nonperturbative?*, p. 60; hep-ph/9911237.
6. V. I. Shevchenko and Yu. A. Simonov, Phys. Lett. B **437**, 146 (1998); L. Lukaszuk, E. Leader, and A. Johansen, Nucl. Phys. B **562**, 291 (1999); for original formulaton see S. V. Ivanov and G. P. Korchemsky, Phys. Lett. B **154B**, 197 (1985); S. V. Ivanov, G. P. Korchemsky, and A. V. Radyushkin, Yad. Fiz. **44**, 230 (1986) [Sov. J. Nucl. Phys. **44**, 145 (1986)].

7. V. I. Shevchenko and Yu. A. Simonov, Phys. Rev. Lett. **85**, 1811 (2000); hep-ph/0001299; hep-ph/0104135.
8. G. S. Bali, Phys. Rev. D **62**, 114503 (2000); S. Deldar, Phys. Rev. D **62**, 034509 (2000).
9. L. Del Debbio, A. Di Giacomo, and Yu. A. Simonov, Phys. Lett. B **332**, 111 (1994); D. S. Kuzmenko and Yu. A. Simonov, Phys. Lett. B **494**, 81 (2000).
10. M. Gell-Mann, R. L. Oakes, and B. Renner, Phys. Rev. **175**, 2195 (1968); S. L. Glashow and S. Weinberg, Phys. Rev. Lett. **20**, 224 (1968).
11. Yu. A. Simonov, Yad. Fiz. **57**, 1491 (1994) [Phys. At. Nucl. **57**, 1418 (1994)].
12. A. M. Badalian and Yu. A. Simonov, Phys. At. Nucl. **60**, 630 (1997).
13. A. M. Badalian and B. L. G. Bakker, Phys. Rev. D **66**, 034025 (2002).
14. A. M. Badalian, B. L. G. Bakker, and Yu. A. Simonov, Phys. Rev. D **66**, 034026 (2002); hep-ph/0204088.

Physics of Atomic Nuclei, Vol. 67, No. 4, 2004, pp. 856–871. Translated from Yadernaya Fizika, Vol. 67, No. 4, 2004, pp. 878–893.
Original Russian Text Copyright © 2004 by Loginov, Stibunov.

## ELEMENTARY PARTICLES AND FIELDS
## Theory

# Reduction of the Bethe–Salpeter Equation for the Amplitude of the Scattering of Spin-1 Particles to a Set of Integral Equations for Invariant Functions

**A. Yu. Loginov*** **and V. N. Stibunov**

*Institute of Nuclear Physics, Tomsk Polytechnic University, Tomsk, 634004 Russia*

Received November 1, 2002; in final form, March 25, 2003

**Abstract**—The Bethe–Salpeter equation for massive spin-1 particles is considered. The amplitude for the scattering of spin-1 particles is expanded in relativistically invariant tensors. The coefficients in the transformation of helicity amplitudes into invariant functions for the scattering amplitude are found. The set of integral equations for these invariant functions is derived, and the partial-wave expansion of this set is performed. An equivalent set of integral equations for partial-wave helicity amplitudes is presented. *© 2004 MAIK "Nauka/Interperiodica".*

**1.** The Bethe–Salpeter equation was originally formulated in QED [1, 2] in order to describe two-particle bound states in the case where neither particle can be considered as a source of an external field. However, the range of applicability of this equation is not exhausted by QED. The Bethe–Salpeter equation can also be formulated within other renormalizable models of quantum field theory, such as the $\phi^3$ and $\phi^4$ models or scalar electrodynamics [3]. Moreover, the Bethe–Salpeter equation can be used in describing strong interactions—for example, in $\pi N$ and $NN$ scattering [4–6], in $NN$–$N\Delta$ reactions [7, 8], and in other processes beyond renormalizable theories. This equation is also used to describe the electromagnetic interactions of hadrons—for example, in the electron scattering by a deuteron [9, 10]. The properties of scalar and vector mesons within the constituent quark model can also be described in terms of the Bethe–Salpeter equation [11–13]. In applications, Bethe–Salpeter equations are considered most frequently for the amplitudes of reactions involving spinless and spin-1/2 particles [14–16].

In the present study, we will consider the Bethe–Salpeter equation for the amplitude of elastic vector-particle scattering—that is, processes of the $1^- + 1^- \to 1^- + 1^-$ type. Our main objective here is to reduce the Bethe–Salpeter equation for the amplitude of the scattering of spin-1 particles to a set of integral equations for invariant functions. The scattering of spin-1 particles corresponds, for example, to the interaction of vector mesons, the scattering of a vector meson on a deuteron, or the elastic scattering of deuterons.

This article is organized as follows. In Section 2, we present a general expression for the $P$- and $T$-invariant amplitude of $1^- + 1^- \to 1^- + 1^-$ reactions. In Section 3, the Bethe–Salpeter equation is reduced to a set of integral equations for invariant functions with the aid of the coefficients in the transformation of helicity amplitudes into invariant functions. In Section 4, we perform a partial-wave expansion of the set of four-dimensional integral equations and obtain a set of two-dimensional integral equations. In Section 5, an alternative set of two-dimensional integral equations is given for partial-wave helicity amplitudes. In the Appendix, we present the coefficients in the transformation of helicity amplitudes into invariant functions and the matrix of the set of two-dimensional integral equations for partial-wave helicity amplitudes.

**2.** Let us consider the general structure of the amplitude for the scattering of two spin-1 particles of negative intrinsic parity, $1^- + 1^- \to 1^- + 1^-$. We denote by $k_1$ and $q_1$ the primary momenta of the particles involved, by $k_2$ and $q_2$ their final momenta, by $u$ and $v$ the polarization 4-vectors of the primary particles, and by $u'$ and $v'$ the polarization 4-vectors of the final particles. In order to reveal the symmetry of the amplitude under spatial reflection and time inversion, it is convenient to use a symmetric and an antisymmetric combination of the momenta:

$$P = k_1 + q_1 = k_2 + q_2, \qquad (1)$$

$$p_1 = \frac{1}{2}(k_1 - q_1), \quad p_2 = \frac{1}{2}(k_2 - q_2).$$

---

[*] e-mail: `loginov@npi.tpu.ru`

1063-7788/04/6704-0856$26.00 © 2004 MAIK "Nauka/Interperiodica"

The invariant variables $s$, $t$, and $u$ can be expressed in terms of $P$, $p_1$, and $p_2$ as

$$s = P^2, \quad t = (k_1 - k_2)^2 = (p_1 - p_2)^2, \qquad (2)$$
$$u = (k_1 - q_2)^2 = (p_1 + p_2)^2,$$
$$s + t + u = 2(m_1^2 + m_2^2).$$

We assume that the interaction between the particles is $P$- and $T$-invariant. The general expression for the amplitude of a reaction involving particles of arbitrary spin has the form

$$T(p_2, p_1; P) = \sum_i f_i(p_2, p_1; P) R^i(p_2, p_1; P), \quad (3)$$

where $f_i(p_2, p_1; P)$ are invariant functions depending on the 4-momenta of the primary and final particles only through the invariant variables $s$ and $t$ and $R^i(p_2, p_1; P)$ are invariant spin combinations composed from the 4-momenta and wave functions of all particles participating in the reaction. In order to construct the reaction amplitude, it is necessary to determine the number of independent invariant functions that are involved in expression (3). It is equal to the number of independent helicity reaction amplitudes with allowance for $P$ and $T$ invariance. The total number of helicity amplitudes for a reaction of the $1^- + 1^- \to 1^- + 1^-$ type is $(2s_1 + 1)(2s_2 + 1)(2s_3 + 1)(2s_4 + 1) = 81$. From the $P$ invariance of the interaction, it follows that these amplitudes satisfy the relations

$$T_{\lambda_3\lambda_4,\lambda_1\lambda_2} = \eta(-1)^{(\lambda_1-\lambda_2)-(\lambda_3-\lambda_4)} T_{-\lambda_3-\lambda_4,-\lambda_1-\lambda_2}, \quad (4)$$

where $\eta = \eta_1\eta_2\eta_3\eta_4(-1)^{s_3+s_4-s_1-s_2}$, $\eta_i$ and $s_i$ being, respectively, the intrinsic parities and intrinsic spins of the particles involved; $\lambda_1$ and $\lambda_2$ are the helicities of the vector particles in the initial state; and $\lambda_3$ and $\lambda_4$ are their helicities in the final state . It can easily be seen that the number of independent helicity amplitudes then reduces to 41. Further constraints on the number of independent helicity amplitudes follow from the $T$ invariance of the interaction. For elastic processes, $T$ invariance leads to the following relations between the helicity amplitudes:

$$T_{\lambda_3\lambda_4,\lambda_1\lambda_2} = (-1)^{(\lambda_1-\lambda_2)-(\lambda_3-\lambda_4)} T_{\lambda_1\lambda_2,\lambda_3\lambda_4}. \quad (5)$$

This reduces the number of independent helicity amplitudes to 25. For independent helicity amplitudes, we can choose the following:

$$T_{11,11}, T_{11,10}, T_{11,1-1}, T_{11,01}, T_{11,00}, T_{11,0-1}, \qquad (6)$$
$$T_{11,-11}, T_{11,-10}, T_{11,-1-1}, T_{10,10}, T_{10,1-1},$$
$$T_{10,01}, T_{10,00}, T_{10,0-1}, T_{10,-11}, T_{10,-10}, T_{1-1,1-1},$$
$$T_{1-1,01}, T_{1-1,00}, T_{1-1,0-1}, T_{1-1,-11}, T_{01,01}, T_{01,00},$$
$$T_{01,0-1}, T_{00,00}.$$

We must now specify 25 independent invariant spin combinations $R^i(p_2, p_1; P)$ appearing in expression (3). Since $s$, $t$, and $u$ are $P$- and $T$-invariant, $f_i(p_2, p_1; P)$ are also $P$- and $T$-invariant. Therefore, the invariant spin combinations $R^i(p_2, p_1; P) = u'^{*\mu} v'^{*\nu} R^i_{\mu\nu\alpha\beta} u^\alpha v^\beta$, where $R^i_{\mu\nu\alpha\beta}$ are 4-tensors of rank 4, must also be $P$- and $T$-invariant. For the 4-tensors $R^i_{\mu\nu\alpha\beta}$ satisfying $P$ and $T$ invariance, one can take

$$R^1_{\mu\nu\alpha\beta} = p_{1\mu} p_{1\nu} p_{2\alpha} p_{2\beta}, \qquad (7)$$
$$R^2_{\mu\nu\alpha\beta} = p_{1\mu} P_\nu p_{2\alpha} p_{2\beta} + p_{1\mu} p_{1\nu} p_{2\alpha} P_\beta,$$
$$R^3_{\mu\nu\alpha\beta} = P_\mu p_{1\nu} p_{2\alpha} p_{2\beta} + p_{1\mu} p_{1\nu} P_\alpha p_{2\beta},$$
$$R^4_{\mu\nu\alpha\beta} = P_\mu P_\nu p_{2\alpha} p_{2\beta} + p_{1\mu} p_{1\nu} P_\alpha P_\beta,$$
$$R^5_{\mu\nu\alpha\beta} = p_{1\mu} P_\nu p_{2\alpha} P_\beta,$$
$$R^6_{\mu\nu\alpha\beta} = p_{1\mu} P_\nu P_\alpha p_{2\beta} + P_\mu p_{1\nu} p_{2\alpha} P_\beta,$$
$$R^7_{\mu\nu\alpha\beta} = P_\mu P_\nu p_{2\alpha} P_\beta + p_{1\mu} P_\nu P_\alpha P_\beta,$$
$$R^8_{\mu\nu\alpha\beta} = P_\mu p_{1\nu} P_\alpha p_{2\beta},$$
$$R^9_{\mu\nu\alpha\beta} = P_\mu P_\nu P_\alpha p_{2\beta} + P_\mu p_{1\nu} P_\alpha P_\beta,$$
$$R^{10}_{\mu\nu\alpha\beta} = P_\mu P_\nu P_\alpha P_\beta,$$
$$R^{11}_{\mu\nu\alpha\beta} = g_{\mu\nu} p_{2\alpha} p_{2\beta} + p_{1\mu} p_{1\nu} g_{\alpha\beta},$$
$$R^{12}_{\mu\nu\alpha\beta} = g_{\mu\nu} p_{2\alpha} P_\beta + p_{1\mu} P_\nu g_{\alpha\beta},$$
$$R^{13}_{\mu\nu\alpha\beta} = g_{\mu\nu} P_\alpha p_{2\beta} + P_\mu p_{1\nu} g_{\alpha\beta},$$
$$R^{14}_{\mu\nu\alpha\beta} = g_{\mu\nu} P_\alpha P_\beta + P_\mu P_\nu g_{\alpha\beta},$$
$$R^{15}_{\mu\nu\alpha\beta} = p_{1\mu} g_{\nu\beta} p_{2\alpha},$$
$$R^{16}_{\mu\nu\alpha\beta} = P_\mu g_{\nu\beta} p_{2\alpha} + p_{1\mu} g_{\nu\beta} P_\alpha,$$
$$R^{17}_{\mu\nu\alpha\beta} = P_\mu g_{\nu\beta} P_\alpha,$$
$$R^{18}_{\mu\nu\alpha\beta} = g_{\mu\beta} p_{1\nu} p_{2\alpha} + p_{1\mu} g_{\nu\alpha} p_{2\beta},$$
$$R^{19}_{\mu\nu\alpha\beta} = g_{\mu\beta} P_\nu p_{2\alpha} + p_{1\mu} g_{\nu\alpha} P_\beta,$$
$$R^{20}_{\mu\nu\alpha\beta} = g_{\mu\beta} p_{1\nu} P_\alpha + P_\mu g_{\nu\alpha} p_{2\beta},$$
$$R^{21}_{\mu\nu\alpha\beta} = g_{\mu\beta} P_\nu P_\alpha + P_\mu g_{\nu\alpha} p_\beta,$$
$$R^{22}_{\mu\nu\alpha\beta} = g_{\mu\alpha} p_{1\nu} p_{2\beta},$$
$$R^{23}_{\mu\nu\alpha\beta} = g_{\mu\alpha} P_\nu p_{2\beta} + g_{\mu\alpha} p_{1\nu} P_\beta,$$
$$R^{24}_{\mu\nu\alpha\beta} = g_{\mu\alpha} P_\nu P_\beta, \quad R^{25}_{\mu\nu\alpha\beta} = g_{\mu\alpha} g_{\nu\beta},$$

where $g_{\mu\nu}$ is a metric tensor. It can be seen from expressions (4) and (5) that the relations of $P$ and $T$ invariance for the helicity amplitudes of the elastic scattering of spin-1 particles coincide if the products of the intrinsic parities of the particles involved, $\eta_1\eta_2\eta_3\eta_4$, are identical. For such reactions, the numbers of independent helicity amplitudes also coincide. Therefore, the set of 4-tensors in (7) can also be used to construct the amplitudes of $1^+ + 1^+ \to 1^+ + 1^+$, $1^+ + 1^+ \to 1^- + 1^-$, and $1^+ + 1^- \to 1^+ + 1^-$ reactions.

The set of 4-tensors in (7) is not the only possible one. By way of example, we consider the invariant spin combination $R^{25}(p_2, p_1; P) = (u'^* \cdot u)(v'^* \cdot v)$, which corresponds to the 4-tensor $R^{25}_{\mu\nu\alpha\beta} = g_{\mu\alpha} g_{\nu\beta}$. There arises the question of why there are no spin combinations $(u'^* \cdot v'^*)(u \cdot v)$ or $(u'^* \cdot v)(v'^* \cdot u)$ similar to $R^{25}(p_2, p_1; P)$ among the invariant spin combinations $R^i(p_2, p_1; P) = u'^{*\mu} v'^{*\nu} R^i_{\mu\nu\alpha\beta} u^\alpha v^\beta$ corresponding to the 4-tensors in (7). The answer is that these spin combinations are not independent, which can be proven by using the respective Gram determinants. It is well known that, in four-dimensional space, any five 4-vectors are linearly dependent. In our case, this means the vanishing of the Gram determinant

$$G\begin{pmatrix} u, & u'^*, & P, & p_1, & p_2 \\ v, & v'^*, & P, & p_1, & p_2 \end{pmatrix} = 0,$$

which contains the polarization vectors of all particles involved in the reaction and all 4-momenta appearing in the expressions for the 4-tensors $R^i_{\mu\nu\alpha\beta}$. It is necessary to determine the number of independent constraints imposed by the Gram determinants. Owing to the symmetry properties of Gram determinants [17], any permutations of the vectors in the rows and the permutation of the upper and lower rows are possible since this can lead only to the inversion of the determinant sign. Only the permutation of the vectors from the upper and the lower row of a Gram determinant can lead to essentially new constraints. However, the permutation of the vectors $P$, $p_1$, and $p_2$ from the upper and lower rows cannot yield new constraints either, since, upon any such permutation, there would appear two identical 4-vectors in the upper and the lower row, with the result that the respective Gram determinant would vanish. There remain only permutations in the group $\begin{matrix} u, & u'^* \\ v, & v'^* \end{matrix}$. With allowance for the symmetry properties of the Gram determinant, there exist the following independent permutations:

$$\begin{matrix} v, & u'^* \\ u, & v'^* \end{matrix}, \qquad \begin{matrix} u, & v \\ u'^*, & v'^* \end{matrix}. \tag{8}$$

Thus, three Gram determinants vanish:

$$G\begin{pmatrix} u, & u'^*, & P, & p_1, & p_2 \\ v, & v'^*, & P, & p_1, & p_2 \end{pmatrix} = 0, \tag{9}$$

$$G\begin{pmatrix} v, & u'^*, & P, & p_1, & p_2 \\ u, & v'^*, & P, & p_1, & p_2 \end{pmatrix} = 0,$$

$$G\begin{pmatrix} u, & v, & P, & p_1, & p_2 \\ u'^*, & v'^*, & P, & p_1, & p_2 \end{pmatrix} = 0.$$

Upon directly evaluating these determinants, we obtain a homogeneous set of three linear equations. However, the rank of this set of equations is two since the third linear equation is equal to the difference of the first and the second equation. It follows that, among the invariant spin combinations, there are two linearly independent relations, which make it possible to express $(u'^* \cdot v'^*)(u \cdot v)$ and $(u'^* \cdot v)(v'^* \cdot u)$ in terms of $R^1(p_2, p_1; P)$–$R^{25}(p_2, p_1; P)$; that is,

$$\begin{aligned}
(u'^* \cdot v'^*)(u \cdot v) &= \frac{4R^1}{t(-4m^2 + s + t)} \\
&+ \frac{R^4(4m^2 - s)}{st(-4m^2 + s + t)} - \frac{R^5(-4m^2 + s + 2t)}{st(-4m^2 + s + t)} \\
&+ \frac{R^6}{t(-4m^2 + s + t)} + \frac{R^7}{-4m^2 s + s^2 + st} \\
&- \frac{R^8(-4m^2 + s + 2t)}{st(-4m^2 + s + t)} - \frac{R^9}{s(-4m^2 + s + t)} \\
&+ \frac{R^{10}(s - 4t)}{4st(-4m^2 + s + t)} - \frac{R^{11}(4m^2 - s)}{t(-4m^2 + s + t)} \\
&- \frac{R^{12}(-4m^2 + s + 2t)}{2t(-4m^2 + s + t)} + \frac{R^{13}(-4m^2 + s + 2t)}{2t(-4m^2 + s + t)} \\
&+ \frac{R^{14}(-s^2 + 4m^2(s - 4t) + 4st + 4t^2)}{4st(-4m^2 + s + t)} \\
&+ \frac{R^{15}(-4m^2 + s + 2t)}{t(-4m^2 + s + t)} - \frac{R^{16}(4m^2 - s)}{2t(-4m^2 + s + t)} \\
&+ \frac{R^{17}(s^2 - 4m^2(s - 4t) - 2st - 4t^2)}{4st(-4m^2 + s + t)} \\
&+ \frac{R^{22}(-4m^2 + s + 2t)}{t(-4m^2 + s + t)} - \frac{R^{23}(-4m^2 + s)}{2t(-4m^2 + s + t)} \\
&+ \frac{R^{24}(s^2 - 4m^2(s - 4t) - 2st - 4t^2)}{4st(-4m^2 + s + t)} + R^{25};
\end{aligned} \tag{10}$$

$$\begin{aligned}
(u'^* \cdot v)(v'^* \cdot u) &= -\frac{2R^5(-2m^2 + t)}{st(-4m^2 + s + t)} \\
&+ \frac{2R^6(-2m^2 + s + t)}{st(-4m^2 + s + t)} + \frac{R^7(4m^2 - s)}{st(-4m^2 + s + t)} \\
&- \frac{2R^8(-2m^2 + t)}{st(-4m^2 + s + t)} - \frac{R^9(4m^2 - s)}{st(-4m^2 + s + t)} \\
&- \frac{R^{10}(-4m^2 + s + 2t)}{st(-4m^2 + s + t)} + \frac{R^{15}(-4m^2 + s + 2t)}{t(-4m^2 + s + t)}
\end{aligned} \tag{11}$$

$$
\begin{aligned}
&-\frac{R^{16}(4m^2-s)}{2t(-4m^2+s+t)}
+\frac{R^{17}(s^2-4m^2(s-4t)-2st-4t^2)}{4st(-4m^2+s+t)} \\
&-\frac{R^{18}(-4m^2+s+2t)}{t(-4m^2+s+t)}-\frac{R^{19}(4m^2-s)}{2t(-4m^2+s+t)} \\
&-\frac{R^{20}(-4m^2+s)}{2t(-4m^2+s+t)}
+\frac{R^{21}(s^2+6st+4t^2-4m^2(s+4t))}{4st(-4m^2+s+t)} \\
&+\frac{R^{22}(-4m^2+s+2t)}{t(-4m^2+s+t)}-\frac{R^{23}(-4m^2+s)}{2t(-4m^2+s+t)} \\
&+\frac{R^{24}(s^2-4m^2(s-4t)-2st-4t^2)}{4st(-4m^2+s+t)}+R^{25}.
\end{aligned}
$$

For the sake of brevity, we suppressed, in expressions (10) and (11), the arguments of the invariant spin combinations $R^i(p_2, p_1; P)$. In constructing the amplitude in (3), we can use the invariant spin combinations $(u'^* \cdot v'^*)(u \cdot v)$ and $(u'^* \cdot v)(v'^* \cdot u)$ instead of any two spin combinations $R^i$ from expressions (10) and (11).

Let us write the expression for the $P$- and $T$-invariant helicity amplitude of $1^- + 1^- \to 1^- + 1^-$ reactions. We have

$$
\begin{aligned}
&T_{\lambda_3\lambda_4,\lambda_1\lambda_2}(p_2,p_1;P) \\
&= (u'^*_{\lambda_3}\cdot p_1)(v'^*_{\lambda_4}\cdot p_1)(u_{\lambda_1}\cdot p_2)(v_{\lambda_2}\cdot p_2)f_1 \\
&+ ((u'^*_{\lambda_3}\cdot p_1)(v'^*_{\lambda_4}\cdot p_1)(u_{\lambda_1}\cdot p_2)(v_{\lambda_2}\cdot P) \\
&+ (u'^*_{\lambda_3}\cdot p_1)(v'^*_{\lambda_4}\cdot P)(u_{\lambda_1}\cdot p_2)(v_{\lambda_2}\cdot p_2))f_2 \\
&+ ((u'^*_{\lambda_3}\cdot p_1)(v'^*_{\lambda_4}\cdot p_1)(u_{\lambda_1}\cdot P)(v_{\lambda_2}\cdot p_2) \\
&+ (u'^*_{\lambda_3}\cdot P)(v'^*_{\lambda_4}\cdot p_1)(u_{\lambda_1}\cdot p_2)(v_{\lambda_2}\cdot p_2))f_3 \\
&+ ((u'^*_{\lambda_3}\cdot p_1)(v'^*_{\lambda_4}\cdot p_1)(u_{\lambda_1}\cdot P)(v_{\lambda_2}\cdot P) \\
&+ (u'^*_{\lambda_3}\cdot P)(v'^*_{\lambda_4}\cdot P)(u_{\lambda_1}\cdot p_2)(v_{\lambda_2}\cdot p_2))f_4 \\
&+ (u'^*_{\lambda_3}\cdot p_1)(v'^*_{\lambda_4}\cdot P)(u_{\lambda_1}\cdot p_2)(v_{\lambda_2}\cdot P)f_5 \\
&+ ((u'^*_{\lambda_3}\cdot P)(v'^*_{\lambda_4}\cdot p_1)(u_{\lambda_1}\cdot p_2)(v_{\lambda_2}\cdot P) \\
&+ (u'^*_{\lambda_3}\cdot p_1)(v'^*_{\lambda_4}\cdot P)(u_{\lambda_1}\cdot P)(v_{\lambda_2}\cdot p_2))f_6 \\
&+ ((u'^*_{\lambda_3}\cdot p_1)(v'^*_{\lambda_4}\cdot P)(u_{\lambda_1}\cdot P)(v_{\lambda_2}\cdot P) \\
&+ (u'^*_{\lambda_3}\cdot P)(v'^*_{\lambda_4}\cdot P)(u_{\lambda_1}\cdot p_2)(v_{\lambda_2}\cdot P))f_7 \\
&+ (u'^*_{\lambda_3}\cdot P)(v'^*_{\lambda_4}\cdot p_1)(u_{\lambda_1}\cdot P)(v_{\lambda_2}\cdot p_2)f_8 \\
&+ ((u'^*_{\lambda_3}\cdot P)(v'^*_{\lambda_4}\cdot p_1)(u_{\lambda_1}\cdot P)(v_{\lambda_2}\cdot P) \\
&+ (u'^*_{\lambda_3}\cdot P)(v'^*_{\lambda_4}\cdot P)(u_{\lambda_1}\cdot P)(v_{\lambda_2}\cdot p_2))f_9 \\
&+ (u'^*_{\lambda_3}\cdot P)(v'^*_{\lambda_4}\cdot P)(u_{\lambda_1}\cdot P)(v_{\lambda_2}\cdot P)f_{10} \\
&+ ((u'^*_{\lambda_3}\cdot p_1)(v'^*_{\lambda_4}\cdot p_1)(u_{\lambda_1}\cdot v_{\lambda_2}) \\
&+ (u'^*_{\lambda_3}\cdot v'^*_{\lambda_4})(u_{\lambda_1}\cdot p_2)(v_{\lambda_2}\cdot p_2))f_{11} \\
&+ ((u'^*_{\lambda_3}\cdot p_1)(v'^*_{\lambda_4}\cdot P)(u_{\lambda_1}\cdot v_{\lambda_2}) \\
&+ (u'^*_{\lambda_3}\cdot v'^*_{\lambda_4})(u_{\lambda_1}\cdot p_2)(v_{\lambda_2}\cdot P))f_{12} \\
&+ ((u'^*_{\lambda_3}\cdot P)(v'^*_{\lambda_4}\cdot p_1)(u_{\lambda_1}\cdot v_{\lambda_2}) \\
&+ (u'^*_{\lambda_3}\cdot v'^*_{\lambda_4})(u_{\lambda_1}\cdot P)(v_{\lambda_2}\cdot p_2))f_{13} \\
&+ ((u'^*_{\lambda_3}\cdot P)(v'^*_{\lambda_4}\cdot P)(u_{\lambda_1}\cdot v_{\lambda_2}) \\
&+ (u'^*_{\lambda_3}\cdot v'^*_{\lambda_4})(u_{\lambda_1}\cdot P)(v_{\lambda_2}\cdot P))f_{14} \\
&+ (u'^*_{\lambda_3}\cdot p_1)(v'^*_{\lambda_4}\cdot v_{\lambda_2})(u_{\lambda_1}\cdot p_2)f_{15} \\
&+ ((u'^*_{\lambda_3}\cdot p_1)(v'^*_{\lambda_4}\cdot v_{\lambda_2})(u_{\lambda_1}\cdot P) \\
&+ (u'^*_{\lambda_3}\cdot P)(v'^*_{\lambda_4}\cdot v_{\lambda_2})(u_{\lambda_1}\cdot p_2))f_{16} \\
&+ (u'^*_{\lambda_3}\cdot P)(v'^*_{\lambda_4}\cdot v_{\lambda_2})(u_{\lambda_1}\cdot P)f_{17} \\
&+ ((u'^*_{\lambda_3}\cdot v_{\lambda_2})(v'^*_{\lambda_4}\cdot p_1)(u_{\lambda_1}\cdot p_2) \\
&+ (u'^*_{\lambda_3}\cdot p_1)(v'^*_{\lambda_4}\cdot u_{\lambda_1})(v_{\lambda_2}\cdot p_2))f_{18} \\
&+ ((u'^*_{\lambda_3}\cdot v_{\lambda_2})(v'^*_{\lambda_4}\cdot P)(u_{\lambda_1}\cdot p_2) \\
&+ (u'^*_{\lambda_3}\cdot p_1)(v'^*_{\lambda_4}\cdot u_{\lambda_1})(v_{\lambda_2}\cdot P))f_{19} \\
&+ ((u'^*_{\lambda_3}\cdot v_{\lambda_2})(v'^*_{\lambda_4}\cdot p_1)(u_{\lambda_1}\cdot P) \\
&+ (u'^*_{\lambda_3}\cdot P)(v'^*_{\lambda_4}\cdot u_{\lambda_1})(v_{\lambda_2}\cdot p_2))f_{20} \\
&+ ((u'^*_{\lambda_3}\cdot v_{\lambda_2})(v'^*_{\lambda_4}\cdot P)(u_{\lambda_1}\cdot P) \\
&+ (u'^*_{\lambda_3}\cdot P)(v'^*_{\lambda_4}\cdot u_{\lambda_1})(v_{\lambda_2}\cdot P))f_{21} \\
&+ (u'^*_{\lambda_3}\cdot u_{\lambda_1})(v'^*_{\lambda_4}\cdot p_1)(v_{\lambda_2}\cdot p_2)f_{22} \\
&+ ((u'^*_{\lambda_3}\cdot u_{\lambda_1})(v'^*_{\lambda_4}\cdot p_1)(v_{\lambda_2}\cdot P) \\
&+ (u'^*_{\lambda_3}\cdot u_{\lambda_1})(v'^*_{\lambda_4}\cdot P)(v_{\lambda_2}\cdot p_2))f_{23} \\
&+ (u'^*_{\lambda_3}\cdot u_{\lambda_1})(v'^*_{\lambda_4}\cdot P)(v_{\lambda_2}\cdot P)f_{24} \\
&+ (u'^*_{\lambda_3}\cdot u_{\lambda_1})(v'^*_{\lambda_4}\cdot v_{\lambda_2})f_{25},
\end{aligned}
\tag{12}
$$

where $u'_{\lambda_3}$ and $v'_{\lambda_4}$ are the helicity polarization 4-vectors of the respective spin-1 particles in the final state, while $u_{\lambda_1}$ and $v_{\lambda_2}$ are their counterparts in the initial state.

**3.** The Bethe–Salpeter equation is a relativistic relation for the two-particle Green's function $G(x'_1, x'_2; x_1, x_2)$. Specifically, we have

$$
\begin{aligned}
G(x'_1,x'_2;x_1,x_2) &= I(x'_1,x'_2;x_1,x_2) \\
&+ \int K(x'_1,x'_2;x_3,x_4)G(x_3,x_4;x_1,x_2)d^4x_3d^4x_4,
\end{aligned}
\tag{13}
$$

where $x_1$, $x_2$ and $x'_1$, $x'_2$ are, respectively, the initial and the final four-dimensional coordinates of the particles involved. Thus, the Bethe–Salpeter equation relates the total two-particle Green's function $G(x'_1, x'_2; x_1, x_2)$, which is the sum of all respective Feynman diagrams (figure, left-hand side), to a topologically specified part of this sum, $I(x'_1, x'_2; x_1, x_2)$ (figure, the first term on the right-hand side), this part being the sum of all two-particle-irreducible diagrams in the $s$ channel (that is, diagrams that cannot

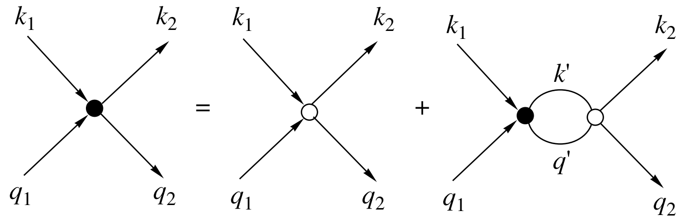

Diagrammatic representation of the Bethe–Salpeter equation.

be broken down, by cutting two lines going in the direction of the $s$ channel, into two parts such that one contains the points $x_1$ and $x_2$, while the other contains the points $x'_1$ and $x'_2$). The kernel $K$ of the Bethe–Salpeter equation is explicitly expressed in terms of the sum of two-particle-irreducible diagrams, $I$, and the single-particle Green's functions for the scattered particles. The second term on the right-hand side of the figure corresponds to the integral term in Eq. (13). The kernel of the Bethe–Salpeter equation is constructed on the basis of the particle-interaction Lagrangian. Thus, Eq. (13) enables one to express the total sum of Feynman diagrams in terms of their two-particle-irreducible part. Since the kernel and the nonhomogeneous term of the equation are constructed by perturbation-theory methods, they can be calculated only approximately. By the Bethe–Salpeter equation, one therefore frequently means an approximate equation that is obtained if the sum of two-particle-irreducible diagrams is taken in the lowest order of perturbation theory, where a single exchange of a field quantum occurs between two interacting particles. This approximation is referred to as the ladder approximation.

In the momentum representation, the Bethe–Salpeter Eq. (13) has the form of an integral equation for the two-particle scattering amplitude $T(p_2, p_1; P)$; that is,

$$T(p_2, p_1; P) = I(p_2, p_1; P) \tag{14}$$
$$+ \int K(p_2, p'; P) T(p', p_1; P) \frac{d^4p'}{(2\pi)^4},$$

where $I$ and $K$ are, respectively, the nonhomogeneous term and the kernel of the equation. In the case of vector-particle scattering, the amplitude $T(p_2, p_1; P)$ and the nonhomogeneous term $I(p_2, p_1; P)$ can be represented as $T(p_2, p_1; P) = u'^{*\mu} v'^{*\nu} T_{\mu\nu\alpha\beta}(p_2, p_1; P) u^\alpha v^\beta$ and $I(p_2, p_1; P) = u'^{*\mu} v'^{*\nu} I_{\mu\nu\alpha\beta}(p_2, p_1; P) u^\alpha v^\beta$, respectively. In this case, Eq. (14) can be written as an integral equation for the tensor $T_{\mu\nu\alpha\beta}(p_2, p_1; P)$ describing the scattering of vector particles. Specifically, we have

$$T_{\mu\nu\alpha\beta}(p_2, p_1; P) = I_{\mu\nu\alpha\beta}(p_2, p_1; P) \tag{15}$$
$$+ \int I_{\mu\nu\epsilon\eta}(p_2, p'; P) G^{\epsilon\gamma}\left(\frac{P}{2} + p'\right) G^{\eta\delta}\left(\frac{P}{2} - p'\right)$$
$$\times T_{\gamma\delta\alpha\beta}(p', p_1; P) \frac{d^4p'}{(2\pi)^4},$$

where $G$ are the propagators for vector particles. In expression (15), the order of 4-indices corresponds to motion against the direction of the particle lines in the figure.

Let us represent $T_{\mu\nu\alpha\beta}$ and $I_{\mu\nu\alpha\beta}$ in the form of expansions in the tensors $R^i_{\mu\nu\alpha\beta}$:

$$T_{\mu\nu\alpha\beta}(p_2, p_1; P) \tag{16}$$
$$= \sum_{i=1}^{25} f_i(p_2, p_1; P) R^i_{\mu\nu\alpha\beta}(p_2, p_1; P),$$

$$I_{\mu\nu\alpha\beta}(p_2, p_1; P) \tag{17}$$
$$= \sum_{i=1}^{25} g_i(p_2, p_1; P) R^i_{\mu\nu\alpha\beta}(p_2, p_1; P).$$

Further, we go over from the tensors $T_{\mu\nu\alpha\beta}$ to the helicity amplitudes

$$T_{\lambda_3\lambda_4, \lambda_1\lambda_2}(p_2, p_1; P) = v^{\mu\nu *}_{\lambda_3\lambda_4}(p_2; P) \tag{18}$$
$$\times T_{\mu\nu\alpha\beta}(p_2, p_1; P) v^{\alpha\beta}_{\lambda_1\lambda_2}(p_1; P),$$

where the tensors $v^{\mu\nu}_{\lambda_3\lambda_4}(p_2; P)$ and $v^{\alpha\beta}_{\lambda_1\lambda_2}(p_1; P)$ are the products of the helicity polarization 4-vectors of the initial and final particles:

$$v^{\mu\nu}_{\lambda_3\lambda_4}(p_2; P) = u'^{\mu}_{\lambda_3}\left(\frac{P}{2} + p_2\right) v'^{\nu}_{\lambda_4}\left(\frac{P}{2} - p_2\right), \tag{19}$$
$$v^{\alpha\beta}_{\lambda_1\lambda_2}(p_1; P) = u^{\alpha}_{\lambda_1}\left(\frac{P}{2} + p_1\right) v^{\beta}_{\lambda_2}\left(\frac{P}{2} - p_1\right).$$

We choose the amplitudes in (6) for independent helicity amplitudes and go over to the c.m. frame. By evaluating the scalar products in (18) explicitly, we obtain a set of 25 linear equations for 25 invariant functions $f_i(p_2, p_1; P)$. This set of linear equations was solved by the Gaussian reduction method with the aid of the Mathematica package. As a result, the invariant functions can be expressed in terms of linear combinations of the helicity amplitudes:

$$f_i(p_2, p_1; P) \tag{20}$$
$$= \sum_{\{\lambda_3\lambda_4, \lambda_1\lambda_2\}} u_{i,\{\lambda_3\lambda_4,\lambda_1\lambda_2\}}(p_2, p_1; P)$$
$$\times T_{\{\lambda_3\lambda_4,\lambda_1\lambda_2\}}(p_2, p_1; P).$$

The transformation coefficients $u_{i,\{\lambda_3\lambda_4,\lambda_1\lambda_2\}}(p_2, p_1; P)$ are given in the Appendix. In expression (20), the symbol $\{\lambda_3\lambda_4, \lambda_1\lambda_2\}$ denotes that summation is performed only over the 25 independent helicity amplitudes listed in (6) rather than over all helicity amplitudes. In the same way, the invariant functions $g_i(p_2, p_1; P)$ appearing in expression (17) can be represented as

$$g_i(p_2, p_1; P) \tag{21}$$
$$= \sum_{\{\lambda_3\lambda_4, \lambda_1\lambda_2\}} u_{i,\{\lambda_3\lambda_4,\lambda_1\lambda_2\}}(p_2, p_1; P)$$
$$\times I_{\{\lambda_3\lambda_4,\lambda_1\lambda_2\}}(p_2, p_1; P).$$

Having derived the matrix specifying the transformation of the helicity amplitudes into the invariant functions, we can represent the Bethe–Salpeter Eq. (15) in the form of a set of integral equations for the invariant functions $f_i$. Specifically, we have

$$f_i(p_2, p_1; P) = g_i(p_2, p_1; P) \tag{22}$$
$$+ \sum_{j=1}^{25} \sum_{\{\lambda_3\lambda_4, \lambda_1\lambda_2\}} \sum_{k=1}^{25} u_{i,\{\lambda_3\lambda_4,\lambda_1\lambda_2\}}(p_2, p_1; P)$$
$$\times v^{\mu\nu *}_{\lambda_3\lambda_4}(p_2; P) \int g_k(p_2, p'; P) R^k_{\mu\nu\epsilon\eta}(p_2, p'; P)$$
$$\times G^{\epsilon\gamma}\left(\frac{P}{2} + p'\right) G^{\eta\delta}\left(\frac{P}{2} - p'\right) R^j_{\gamma\delta\alpha\beta}(p', p_1; P)$$
$$\times f_j(p', p_1; P) \frac{d^4p'}{(2\pi)^4} v^{\alpha\beta}_{\lambda_1\lambda_2}(p_1; P),$$

where the invariant functions $g_i$ and the vector-particle propagators are calculated by perturbation theory on the basis of the interaction Lagrangian—that is, they can be obtained only in some approximation. The set of Eqs. (22) can be represented in the more compact form

$$f_i(p_2, p_1; P) = g_i(p_2, p_1; P) \tag{23}$$
$$+ \sum_{j=1}^{25} \int K_{ij}(p_2, p', p_1; P) f_j(p', p_1; P) \frac{d^4p'}{(2\pi)^4},$$

where the kernel $K_{ij}(p_2, p', p_1; P)$ is a 4-scalar of the form

$$K_{ij}(p_2, p', p_1; P) \tag{24}$$
$$= \sum_{\{\lambda_3\lambda_4, \lambda_1\lambda_2\}} \sum_{k=1}^{25} u_{i,\{\lambda_3\lambda_4,\lambda_1\lambda_2\}}(p_2, p_1; P)$$
$$\times v^{\mu\nu *}_{\lambda_3\lambda_4}(p_2; P) g_k(p_2, p'; P) R^k_{\mu\nu\epsilon\eta}(p_2, p'; P)$$
$$\times G^{\epsilon\gamma}\left(\frac{P}{2} + p'\right) G^{\eta\delta}\left(\frac{P}{2} - p'\right) R^j_{\gamma\delta\alpha\beta}(p', p_1; P)$$
$$\times v^{\alpha\beta}_{\lambda_1\lambda_2}(p_1; P).$$

Thus, the Bethe–Salpeter equation for the amplitude describing the scattering of vector particles has been reduced to a set of integral equations for the invariant functions $f_i(p_2, p_1; P)$.

**4.** In the set of Eqs. (23), integration is performed with respect to four independent variables, $d^4p' = dp'_0 dp'_1 dp'_2 dp'_3 = dp'_0 p'^2 dp' d\Omega'$. By using the partial-wave expansion of the invariant functions $f_i$, we can perform integration over the solid angle $\Omega'$ and reduce the set of four-dimensional integral Eqs. (23) to a set of two-dimensional integral equations for the coefficients in the expansion of the invariant functions in terms of spherical harmonics. We direct the $z$ axis of the c.m. frame along the initial vector $\mathbf{p}_1 = (\mathbf{k}_1 - \mathbf{q}_1)/2$ and assume that the final vector $\mathbf{p}_2 = (\mathbf{k}_2 - \mathbf{q}_2)/2$ corresponds to scattering at an angle $\theta$ in the plane specified by zero azimuthal angle $\phi$. The invariant functions $f_i(p_2, p_1; P)$ depend on the 4-vectors $p_1$, $p_2$, and $P$ only through the invariant variables $s$ and $t$, which are independent of the azimuthal scattering angle $\phi$. Therefore, the expansion of the invariant functions $f_i(p_2, p_1; P)$ and $g_i(p_2, p_1; P)$ in terms of spherical harmonics has the form

$$f_i(p_2, p_1; P) = \sum_l \frac{1}{|\mathbf{p}_2|} \tag{25}$$
$$\times f^l_i(p_{20}, |\mathbf{p}_2|, p_{10}, |\mathbf{p}_1|; P) Y^{0*}_l(\theta, 0),$$
$$g_i(p_2, p_1; P) = \sum_l \frac{1}{|\mathbf{p}_2|}$$
$$\times g^l_i(p_{20}, |\mathbf{p}_2|, p_{10}, |\mathbf{p}_1|; P) Y^{0*}_l(\theta, 0).$$

Although the quantities $p_{10}$, $|\mathbf{p}_1|$, $p_{20}$, and $|\mathbf{p}_2|$ are not independent for free particles, they are written explicitly in the arguments of $f^l_i$ and $g^l_i$ for the case where the particle 4-momenta are off the mass shell. The expansion of the kernel $K_{ij}(p_2, p', p_1; P)$ in terms of spherical harmonics has the form

$$K_{ij}(p_2, p', p_1; P) = \sum_{ll'm'} \frac{1}{|\mathbf{p}_2||\mathbf{p}'|} \tag{26}$$
$$\times K^{l0,l'm'}_{ij}(p_{20}, |\mathbf{p}_2|, p'_0, |\mathbf{p}'|, p_{10}, |\mathbf{p}_1|; P)$$
$$\times Y^{0*}_l(\theta, 0) Y^{m'}_{l'}(\theta', \phi').$$

For the arguments of the kernel $K_{ij}^{l0,l'm'}$, we use here (as was done above) the time components of the 4-momenta $p_2$ and $p_1$—these are independent variables if the corresponding 4-momenta are off the mass shell. Substituting the expansions in terms of spherical harmonics for the quantities $f_i$, $g_i$, and $K_{ij}$ into the set of Eqs. (23) and considering that the invariant functions $f_j(p', p_1; P)$ are independent of the azimuthal angle $\phi'$ of the intermediate momentum $p'$, we arrive at a set of two-dimensional integral equations for $f_i^l$:

$$f_i^l(p_{20}, |\mathbf{p}_2|, p_{10}, |\mathbf{p}_1|; P) \tag{27}$$
$$= g_i^l(p_{20}, |\mathbf{p}_2|, p_{10}, |\mathbf{p}_1|; P)$$
$$+ \sum_j \sum_{l'} \int K_{ij}^{l0,l'0}(p_{20}, |\mathbf{p}_2|, p'_0, |\mathbf{p}'|, p_{10}, |\mathbf{p}_1|; P)$$
$$\times f_j^{l'}(p'_0, |\mathbf{p}'|, p_{10}, |\mathbf{p}_1|; P) \frac{dp'_0 d|\mathbf{p}'|}{(2\pi)^4}.$$

**5.** There are rather complicated relations between the functions $f_i^l$ appearing in Eq. (27) and the partial-wave reaction amplitudes $T^J_{L',S';L,S}$, where $J$ is the total angular momentum; $L$ and $S$ are, respectively, the orbital angular momentum and the total spin of the initial state; and $L'$ and $S'$ are their counterparts in the final state. Therefore, the helicity formalism [18], which makes it possible to derive a set of two-dimensional integral equations for partial-wave helicity amplitudes of $1^- + 1^- \to 1^- + 1^-$ reactions, appears to be preferable. In contrast to the invariant functions $f_i^l$, the partial-wave helicity amplitudes $T^J_{\lambda_3\lambda_4,\lambda_1\lambda_2}$ have a direct physical meaning.

Let us represent the tensor describing the scattering of spin-1 particles in the form of an expansion in the helicity amplitudes; that is,

$$T_{\mu\nu\alpha\beta}(p_2, p_1; P) \tag{28}$$
$$= \sum_{\lambda_1\lambda_2\lambda_3\lambda_4} T_{\lambda_3\lambda_4,\lambda_1\lambda_2}(p_2, p_1; P) u'_{\lambda_3\mu}\left(\frac{P}{2} + p_2\right)$$
$$\times v'_{\lambda_4\nu}\left(\frac{P}{2} - p_2\right) u^*_{\lambda_1\alpha}\left(\frac{P}{2} + p_1\right) v^*_{\lambda_2\beta}\left(\frac{P}{2} - p_1\right),$$

where summation is performed over 81 helicity amplitudes. A similar representation is valid for the tensor $I_{\mu\nu\alpha\beta}$, which is the sum of two-particle-irreducible diagrams. We have

$$I_{\mu\nu\alpha\beta}(p_2, p_1; P) \tag{29}$$
$$= \sum_{\lambda_1\lambda_2\lambda_3\lambda_4} I_{\lambda_3\lambda_4,\lambda_1\lambda_2}(p_2, p_1; P) u'_{\lambda_3\mu}\left(\frac{P}{2} + p_2\right)$$
$$\times v'_{\lambda_4\nu}\left(\frac{P}{2} - p_2\right) u^*_{\lambda_1\alpha}\left(\frac{P}{2} + p_1\right) v^*_{\lambda_2\beta}\left(\frac{P}{2} - p_1\right).$$

Upon contracting the scattering tensor (28) with the helicity 4-vectors of the initial and final particles, we will automatically obtain, owing to their orthogonality, the required helicity amplitudes. In contrast to the invariant functions $f_i(p_2, p_1; P)$, the helicity amplitudes $T_{\lambda_3\lambda_4,\lambda_1\lambda_2}(p_2, p_1; P)$ depend both on the invariant variables $s$ and $t$ and on the azimuthal scattering angle $\phi$. It was shown above that, of 81 helicity amplitudes, only 25 helicity amplitudes (6) are independent because of $P$ and $T$ invariance. Therefore, expressions (28) and (29) can be represented in the form

$$T_{\mu\nu\alpha\beta}(p_2, p_1; P) \tag{30}$$
$$= \sum_{\{\lambda_1\lambda_2,\lambda_3\lambda_4\}} T_{\{\lambda_3\lambda_4,\lambda_1\lambda_2\}}(p_2, p_1; P)$$
$$\times U_{\{\lambda_3\lambda_4,\lambda_1\lambda_2\}\mu\nu\alpha\beta}(p_2, p_1; P),$$
$$I_{\mu\nu\alpha\beta}(p_2, p_1; P)$$
$$= \sum_{\{\lambda_1\lambda_2,\lambda_3\lambda_4\}} I_{\{\lambda_3\lambda_4,\lambda_1\lambda_2\}}(p_2, p_1; P)$$
$$\times U_{\{\lambda_3\lambda_4,\lambda_1\lambda_2\}\mu\nu\alpha\beta}(p_2, p_1; P),$$

where summation is performed over the 25 helicity amplitudes presented in (6) and the tensors $U_{\{\lambda_3\lambda_4,\lambda_1\lambda_2\}\mu\nu\alpha\beta}$ are the sums of the helicity polarization vectors of the initial and final particles with allowance for the $P$- and $T$-invariance relations (4) and (5). For example, the tensor $U_{\{11,11\}\mu\nu\alpha\beta}$ is given by

$$U_{\{11,11\}\mu\nu\alpha\beta} = u'_{1\,\mu} v'_{1\nu} u^*_{1\,\alpha} v^*_{1\beta} + u'_{-1\mu} v'_{-1\nu} u^*_{-1\alpha} v^*_{-1\beta}. \tag{31}$$

The remaining tensors $U_{\{\lambda_3\lambda_4,\lambda_1\lambda_2\}\mu\nu\alpha\beta}$ in (30) can be represented in a similar way. In this form of presentation, the tensors $T_{\mu\nu\alpha\beta}$ and $I_{\mu\nu\alpha\beta}$ will automatically satisfy the requirements of $P$ and $T$ invariance.

For the helicity polarization 4-vectors, we take the vectors

$$u_1^\mu(k) = \sqrt{\frac{1}{2}} \exp(i\phi)(0, -\cos\theta\cos\phi + i\sin\phi, -\cos\theta\sin\phi - i\cos\phi, \sin\theta), \tag{32}$$

$$u_0^\mu(k) = \left(\frac{|\mathbf{k}|}{m}, \frac{k_0 \sin\theta\cos\phi}{m}, \frac{k_0\sin\theta\sin\phi}{m}, \frac{k_0\cos\theta}{m}\right),$$

$$u_{-1}^\mu(k) = \sqrt{\frac{1}{2}}\exp(-i\phi)(0, \cos\theta\cos\phi + i\sin\phi, \cos\theta\sin\phi - i\cos\phi, -\sin\theta),$$

where $\theta$ and $\phi$ are the polar and azimuthal angles of the vector-particle 4-momentum. For arbitrary 4-momenta, which may be off the mass shell, these polarization 4-vectors satisfy the relations

$$k \cdot u_\lambda(k) = 0, \tag{33}$$
$$u_\lambda(k)\cdot u^*_{\lambda'}(k) = ((1+N(k))\delta_{\lambda 0} - 1)\delta_{\lambda\lambda'},$$

where $N(k) = (|\mathbf{k}|^2 - k_0^2)/m^2$. It is obvious from these formulas that the polarization 4-vectors (32) are orthogonal and are normalized to $-1$ for $\lambda = \pm 1$. Only in the case of longitudinal polarization ($\lambda = 0$) are the polarization 4-vectors normalized to the quantity $N(k)$, which is equal to $-1$ if the particle 4-momentum is on the mass shell.

For this choice of the helicity polarization 4-vectors, the scattering tensor $T_{\mu\nu\alpha\beta}$ satisfies the relations

$$T_{\mu\nu\alpha\beta}k_1^\alpha = 0, \quad T_{\mu\nu\alpha\beta}q_1^\beta = 0, \quad T_{\mu\nu\alpha\beta}k_2^\mu = 0, \tag{34}$$
$$T_{\mu\nu\alpha\beta}q_2^\nu = 0,$$

where $k_1, q_1$ and $k_2, q_2$ are the 4-momenta of, respectively, the initial and the final particles. As follows from (34), that part of the vector-particle propagator which is proportional to the product $k^\mu k^\nu$ of the vector-particle 4-momenta will vanish upon contraction with the tensors $T_{\mu\nu\alpha\beta}$ and $I_{\mu\nu\alpha\beta}$. Therefore, only that part of the propagator which is proportional to $g^{\mu\nu}$ will contribute after the contraction of the propagator with $T_{\mu\nu\alpha\beta}$ and $I_{\mu\nu\alpha\beta}$. As a result, the Bethe–Salpeter Eq. (15) takes the form

$$T_{\mu\nu\alpha\beta}(p_2, p_1; P) = I_{\mu\nu\alpha\beta}(p_2, p_1; P) \tag{35}$$
$$+ \int I_{\mu\nu\epsilon\eta}(p_2, p'; P)T^{\epsilon\eta}{}_{\alpha\beta}(p', p_1; P)$$
$$\times \left[D\left(\frac{P}{2}+p'\right)D\left(\frac{P}{2}-p'\right)\right]^{-1}\frac{d^4p'}{(2\pi)^4},$$

where $D(P/2+p')$ and $D(P/2-p')$ are the renormalized denominators of the vector-particle propagators. Using the representations in (28) and (29) for $T_{\mu\nu\alpha\beta}$ and $I_{\mu\nu\alpha\beta}$, respectively, and the orthonormality relations (33) for the polarization 4-vectors, we can recast Eq. (35) into the form

$$T_{\lambda_3\lambda_4,\lambda_1\lambda_2}(p_2, p_1; P) = I_{\lambda_3\lambda_4,\lambda_1\lambda_2}(p_2, p_1; P) + \sum_{\lambda'\lambda''}\int I_{\lambda_3\lambda_4,\lambda'\lambda''}(p_2, p'; P)T_{\lambda'\lambda'',\lambda_1\lambda_2}(p', p_1; P) \tag{36}$$
$$\times \frac{\left(\left(1+N\left(\frac{P}{2}+p'\right)\right)\delta_{\lambda' 0} - 1\right)\left(\left(1+N\left(\frac{P}{2}-p'\right)\right)\delta_{\lambda'' 0} - 1\right)}{D\left(\frac{P}{2}+p'\right)D\left(\frac{P}{2}-p'\right)}\frac{d^4p'}{(2\pi)^4}.$$

In expression (36), there is no summation over the 4-indices; instead, summation is performed over the helicities of intermediate particles. This enables one to go over from the four-dimensional set of integral Eqs. (36) to a two-dimensional set of equations by expanding the helicity amplitudes in terms of partial-wave helicity amplitudes and performing integration with respect to angles.

The expansion of the helicity amplitudes in terms of partial-wave helicity amplitudes has the form [19]

$$T_{\lambda_3\lambda_4,\lambda_1\lambda_2}(p_2, p_1; P) \tag{37}$$
$$= \sum_{JM}\frac{2J+1}{4\pi}D^J_{\lambda_3-\lambda_4,M}(\mathbf{n}_2)D^{J*}_{\lambda_1-\lambda_2,M}(\mathbf{n}_1)$$
$$\times T^J_{\lambda_3\lambda_4,\lambda_1\lambda_2}(p_{20}, |\mathbf{p}_2|, p_{10}, |\mathbf{p}_1|; P),$$

$$I_{\lambda_3\lambda_4,\lambda_1\lambda_2}(p_2, p_1; P) \tag{38}$$
$$= \sum_{JM}\frac{2J+1}{4\pi}D^J_{\lambda_3-\lambda_4,M}(\mathbf{n}_2)D^{J*}_{\lambda_1-\lambda_2,M}(\mathbf{n}_1)$$
$$\times I^J_{\lambda_3\lambda_4,\lambda_1\lambda_2}(p_{20}, |\mathbf{p}_2|, p_{10}, |\mathbf{p}_1|; P),$$

where $\mathbf{n}_1$ and $\mathbf{n}_2$ are the unit vectors along the directions of the 3-momenta $\mathbf{p}_1$ and $\mathbf{p}_2$. In these expressions, the arguments of the $D$ functions are taken to be

$$D^J_{\Lambda M}(\mathbf{n}) = D^J_{\Lambda M}(\phi, \theta, 0) = e^{iM\phi}d^J_{\Lambda M}(\theta), \tag{39}$$

where $\theta$ and $\phi$ are the polar and the azimuthal angle of the unit vector $\mathbf{n}$. By using the orthogonality properties of the $D$ functions, one can perform integration with respect to the angular variables in (36). As a result, the set of 4-dimensional integral Eqs. (36) for the helicity amplitudes reduces to a set of two-dimensional integral equations for partial-wave helicity amplitudes; that is,

$$\begin{aligned} T^J_{\lambda_3\lambda_4,\lambda_1\lambda_2}(p_{20},|\mathbf{p}_2|,p_{10},|\mathbf{p}_1|;P) &= I^J_{\lambda_3\lambda_4,\lambda_1\lambda_2}(p_{20},|\mathbf{p}_2|,p_{10},|\mathbf{p}_1|;P) \\ &+ \sum_{\lambda'\lambda''}\int I^J_{\lambda_3\lambda_4,\lambda'\lambda''}(p_{20},|\mathbf{p}_2|,p'_0,|\mathbf{p}'|;P)T^J_{\lambda'\lambda'',\lambda_1\lambda_2}(p'_0,|\mathbf{p}'|,p_{10},|\mathbf{p}_1|;P) \\ &\times \frac{\left(\left(1+N\left(\frac{P}{2}+p'\right)\right)\delta_{\lambda'0}-1\right)\left(\left(1+N\left(\frac{P}{2}-p'\right)\right)\delta_{\lambda''0}-1\right)}{D\left(\frac{P}{2}+p'\right)D\left(\frac{P}{2}-p'\right)}\frac{|\mathbf{p}'|^2dp'_0d|\mathbf{p}'|}{(2\pi)^4}. \end{aligned} \tag{40}$$

The partial-wave helicity amplitudes satisfy the relations of $P$ and $T$ invariance:

$$\begin{aligned} T^J_{\lambda_3\lambda_4,\lambda_1\lambda_2} &= \eta_1\eta_2\eta_3\eta_4(-1)^{s_3+s_4-s_1-s_2} \\ &\times T^J_{-\lambda_3-\lambda_4,-\lambda_1-\lambda_2}, \\ T^J_{\lambda_3\lambda_4,\lambda_1\lambda_2} &= T^J_{\lambda_1\lambda_2,\lambda_3\lambda_4}. \end{aligned} \tag{41}$$

It follows that, of the 81 partial-wave helicity amplitudes for the $J$ value being considered, only 25 will be independent. For the 25 independent amplitudes, we choose the partial-wave helicity amplitudes having the same helicities as in (6) and number them from 1 to 25. After that, the set of two-dimensional integral Eqs. (40) can be rewritten in terms of the 25 independent partial-wave helicity amplitudes as

$$\begin{aligned} &T^J_i(p_{20},|\mathbf{p}_2|,p_{10},|\mathbf{p}_1|;P) \\ &= I^J_i(p_{20},|\mathbf{p}_2|,p_{10},|\mathbf{p}_1|;P) \\ &+\sum_{j=1}^{25}\int K^J_{i,j}(p_{20},|\mathbf{p}_2|,p'_0,|\mathbf{p}'|;P) \\ &\times T^J_j(p'_0,|\mathbf{p}'|,p_{10},|\mathbf{p}_1|;P)\frac{|\mathbf{p}'|^2}{D\left(\frac{P}{2}+p'\right)D\left(\frac{P}{2}-p'\right)} \\ &\times\frac{dp'_0d|\mathbf{p}'|}{(2\pi)^4}. \end{aligned} \tag{42}$$

The quantities $K^J_{i,j}$ are expressed in terms of $I^J_k$ and the normalization factors $N$. Their explicit form is given in the Appendix.

## ACKNOWLEDGMENTS

This work was supported by the Russian Foundation for Basic Research (project nos. 01-02-17276, 02-02-06866) and by the Ministry of Education of the Russian Federation (project no. E02-3.3-216).

## APPENDIX

In general, the matrix describing the transformation of 25 helicity amplitudes into 25 invariant functions has 625 elements. Some of the matrix elements are given by rather cumbersome expressions. For this reason, the elements of the transformation matrix are quoted in this appendix for the scattering of vector particles having equal masses, $m_1 = m_2 = m$. In this case, 361 of the 625 matrix elements vanish, while the remaining 264 nonzero elements are related by numerous symmetry conditions. The nonzero elements can be broken down into 63 groups within which the elements differ only by constant factors. With the aim of obtaining a more compact presentation, the indices of the helicity amplitudes corresponding to those in (6) are numbered from 1 to 25. Presented immediately below are explicit expressions for the nonvanishing transformation-matrix elements $u_{ij}$ ($i$ is the index of the invariant function $f_i$, while $j$ is the index of the helicity amplitude):

$$u_{1\,1} = \frac{1}{2}u_{1\,3} = \frac{1}{2}u_{1\,7} = u_{1\,9} = -u_{2\,3} = u_{2\,7} = -u_{3\,3} = u_{3\,7} = 2u_{4\,3} = 2u_{4\,7} = 2u_{6\,3} = 2u_{6\,7} = \frac{-8\mathrm{cosec}(\theta)^2}{(-4m^2+s)^2},$$

$$u_{4\,1} = u_{4\,9} = \frac{\mathrm{cosec}\left(\frac{\theta}{2}\right)^2\sec\left(\frac{\theta}{2}\right)^2}{-8m^2s+2s^2},$$

$$u_{5\,1} = u_{8\,1} = -\frac{\left(-4m^2 + s + \left(4m^2 - 2s\right)\cos(\theta)\right)\operatorname{cosec}\left(\frac{\theta}{2}\right)^2 \sec\left(\frac{\theta}{2}\right)^2}{2s(-4m^2+s)^2},$$

$$u_{6\,1} = \frac{\left(-4m^2 + s\cos(\theta)\right)\operatorname{cosec}\left(\frac{\theta}{2}\right)^2 \sec\left(\frac{\theta}{2}\right)^2}{2s(-4m^2+s)^2},$$

$$u_{7\,1} = -u_{9\,1} = \frac{(-1+3\cos(\theta))\operatorname{cosec}\left(\frac{\theta}{2}\right)^2 \sec\left(\frac{\theta}{2}\right)^2}{4\left(4m^2 s - s^2\right)},$$

$$u_{10\,1} = -\frac{\left(-8m^4 - 8m^2 s + 3s^2 + 2(4m^2 - s)s\cos(\theta) + 4(2m^4 - 4m^2 s + s^2)\cos(2\theta)\right)}{8s^2(-4m^2+s)^2}\operatorname{cosec}\left(\frac{\theta}{2}\right)^2 \sec\left(\frac{\theta}{2}\right)^2,$$

$$u_{11\,1} = u_{11\,9} = -u_{11\,17} = -u_{11\,21} = u_{18\,1} = -u_{18\,9} = -u_{18\,17} = u_{18\,21} = \frac{\operatorname{cosec}\left(\frac{\theta}{2}\right)^2 \sec\left(\frac{\theta}{2}\right)^2}{8m^2 - 2s},$$

$$u_{12\,1} = u_{12\,9} = -u_{12\,17} = -u_{12\,21} = -u_{13\,1} = -u_{13\,9} = u_{13\,17} = u_{13\,21} = u_{19\,1} = u_{19\,9} = -u_{19\,17} = u_{19\,21}$$

$$= -u_{20\,1} = u_{20\,9} = u_{20\,17} = -u_{20\,21} = \frac{\cos(\theta)\operatorname{cosec}\left(\frac{\theta}{2}\right)^2 \sec\left(\frac{\theta}{2}\right)^2}{-16m^2 + 4s},$$

$$u_{14\,1} = u_{14\,9} = -u_{14\,17} = -u_{14\,21} = u_{21\,1} = -u_{21\,9} = -u_{21\,17} = u_{21\,21} = \frac{\cos(\theta)^2\operatorname{cosec}\left(\frac{\theta}{2}\right)^2 \sec\left(\frac{\theta}{2}\right)^2}{-32m^2 + 8s},$$

$$u_{15\,1} = \frac{1}{2}u_{15\,3} = u_{15\,17} = -2u_{16\,1} = -u_{16\,3} = -2u_{16\,17} = u_{22\,1} = \frac{1}{2}u_{22\,7} = u_{22\,17} = 2u_{23\,1}$$

$$= u_{23\,7} = 2u_{23\,17} = \frac{\sec\left(\frac{\theta}{2}\right)^2}{-4m^2 + s},$$

$$u_{17\,1} = \frac{1}{2}u_{17\,3} = u_{17\,17} = u_{24\,1} = \frac{1}{2}u_{24\,7} = u_{24\,17} = -\frac{\left(-4m^2 + s + \left(-4m^2 + 2s\right)\cos(\theta)\right)\sec\left(\frac{\theta}{2}\right)^2}{4s\left(-4m^2 + s\right)},$$

$$u_{25\,1} = \frac{1}{2}u_{25\,3} = \frac{1}{2}u_{25\,7} = u_{25\,9} = u_{25\,17} = u_{25\,21} = \frac{1}{2},$$

$$u_{5\,2} = u_{5\,8} = 2u_{6\,2} = 2u_{6\,4} = 2u_{6\,6} = 2u_{6\,8} = 4u_{7\,8} = u_{8\,4} = u_{8\,6} = -4u_{9\,6} = \frac{8\sqrt{2}m\operatorname{cosec}(\theta)}{\sqrt{s}(-4m^2+s)^2},$$

$$u_{7\,2} = -u_{9\,4} = \frac{2\sqrt{2}m\left(8m^2 - 3s\right)\operatorname{cosec}(\theta)}{s^{3/2}(-4m^2+s)^2},$$

$$u_{9\,2} = -u_{7\,4} = -u_{7\,6} = u_{9\,8} = \frac{2\sqrt{2}m\operatorname{cosec}(\theta)}{s^{3/2}\left(-4m^2+s\right)},$$

$$u_{10\,2} = u_{10\,4} = \frac{8\sqrt{2}m\left(3m^2 - s\right)\cot(\theta)}{s^{3/2}(-4m^2+s)^2},$$

$$u_{12\,2} = -u_{12\,8} = -u_{12\,11} = -u_{12\,15} = -u_{13\,4} = u_{13\,6} = -u_{13\,18} = u_{13\,20} = u_{16\,4} = u_{16\,6} = u_{16\,18} = u_{16\,20}$$

$$= u_{19\,2} = u_{19\,8} = -u_{19\,11} = u_{19\,15} = -u_{20\,4} = -u_{20\,6} = u_{20\,18} = u_{20\,20} = -u_{23\,2} = -u_{23\,8}$$

$$= -u_{23\,11} = u_{23\,15} = \frac{2\sqrt{2}m\operatorname{cosec}(\theta)}{\sqrt{s}\left(-4m^2+s\right)},$$

$$u_{14\,2} = u_{14\,4} = -u_{14\,6} = -u_{14\,8} = -u_{14\,11} = -u_{14\,15} = u_{14\,18} = -u_{14\,20} = \frac{1}{2}u_{17\,4} = \frac{1}{2}u_{17\,6} = \frac{1}{2}u_{17\,18}$$

$$= \frac{1}{2}u_{17\,20} = u_{21\,2} = u_{21\,4} = u_{21\,6} = u_{21\,8} = -u_{21\,11} = u_{21\,15} = -u_{21\,18} = -u_{21\,20} = \frac{1}{2}u_{24\,2}$$

$$= \frac{1}{2}u_{24\,8} = \frac{1}{2}u_{24\,11} = -\frac{1}{2}u_{24\,15} = \frac{\sqrt{2}m\cot(\theta)}{\sqrt{s}\,(-4m^2+s)},$$

$$u_{5\,3} = -2u_{7\,3} = u_{8\,7} = 2u_{9\,7} = -\frac{\left(-4m^2+s+4m^2\cos(\theta)\right)\operatorname{cosec}\left(\frac{\theta}{2}\right)^2\sec\left(\frac{\theta}{2}\right)^2}{s(-4m^2+s)^2},$$

$$u_{8\,3} = u_{5\,7} = 2u_{7\,7} = -2u_{9\,3} = \frac{\left(-4m^2+s+\left(-4m^2+2s\right)\cos(\theta)\right)\operatorname{cosec}\left(\frac{\theta}{2}\right)^2\sec\left(\frac{\theta}{2}\right)^2}{s(-4m^2+s)^2},$$

$$u_{10\,3} = u_{10\,7} = \frac{\left(-4m^2+s+4m^2\cos(\theta)\right)\left(-4m^2+s+\left(-4m^2+2s\right)\cos(\theta)\right)\operatorname{cosec}\left(\frac{\theta}{2}\right)^2\sec\left(\frac{\theta}{2}\right)^2}{4s^2(-4m^2+s)^2},$$

$$u_{22\,3} = u_{15\,7} = 2u_{15\,9} = 2u_{15\,21} = 2u_{16\,7} = 4u_{16\,9} = 4u_{16\,21} = 2u_{22\,9} = 2u_{22\,21} = -2u_{23\,3}$$

$$= -4u_{23\,9} = -4u_{23\,21} = \frac{-2\operatorname{cosec}\left(\frac{\theta}{2}\right)^2}{-4m^2+s},$$

$$u_{24\,3} = u_{17\,7} = 2u_{17\,9} = 2u_{17\,21} = 2u_{24\,9} = 2u_{24\,21} = \frac{\left(-4m^2+s+4m^2\cos(\theta)\right)\operatorname{cosec}\left(\frac{\theta}{2}\right)^2}{2\left(4m^2s-s^2\right)},$$

$$u_{10\,5} = \frac{32m^4-16m^2s}{\left(-4m^2s+s^2\right)^2},$$

$$u_{14\,5} = u_{14\,19} = -u_{17\,22} = -u_{17\,24} = -u_{21\,12} = -u_{21\,14} = -u_{24\,10} = -u_{24\,16} = \frac{4m^2}{-4m^2s+s^2},$$

$$u_{10\,6} = u_{10\,8} = -\frac{1}{2}u_{10\,13} = -\frac{1}{2}u_{10\,23} = \frac{8\sqrt{2}m^3\cot(\theta)}{s^{3/2}(-4m^2+s)^2},$$

$$u_{5\,9} = u_{6\,9} = u_{7\,9} = u_{8\,9} = u_{9\,9} = \frac{\left(-4m^2+s-4m^2\cos(\theta)\right)\operatorname{cosec}\left(\frac{\theta}{2}\right)^2\sec\left(\frac{\theta}{2}\right)^2}{2s(-4m^2+s)^2},$$

$$u_{10\,9} = \frac{\left(8m^4-8m^2s+s^2-2\left(4m^2-s\right)s\cos(\theta)-8m^4\cos(2\theta)\right)\operatorname{cosec}\left(\frac{\theta}{2}\right)^2\sec\left(\frac{\theta}{2}\right)^2}{8s^2(-4m^2+s)^2},$$

$$u_{5\,10} = u_{6\,14} = -2u_{7\,10} = 2u_{7\,14} = u_{8\,22} = -2u_{9\,14} = 2u_{9\,22} = \frac{-8m^2\sec\left(\frac{\theta}{2}\right)^2}{s(-4m^2+s)^2},$$

$$u_{10\,10} = u_{10\,22} = \frac{-2m^2\left(4m^2-s+\left(4m^2-2s\right)\cos(\theta)\right)\sec\left(\frac{\theta}{2}\right)^2}{s^2(-4m^2+s)^2},$$

$$u_{2\,11} = -u_{3\,20} = -2u_{4\,11} = -2u_{4\,20} = \frac{16\sqrt{2}m\left(\cot(\theta)-\operatorname{cosec}(\theta)\right)\operatorname{cosec}(\theta)^2}{\sqrt{s}(-4m^2+s)^2},$$

$$u_{5\,11} = -2u_{6\,11} = -2u_{6\,20} = u_{8\,20} = \frac{-4\sqrt{2}m\sec\left(\frac{\theta}{2}\right)^2\tan\left(\frac{\theta}{2}\right)}{\sqrt{s}(-4m^2+s)^2},$$

$$u_{7\,11} = -u_{9\,20} = -\frac{m\left(8m^2-3s+\left(8m^2+s\right)\cos(\theta)\right)\operatorname{cosec}\left(\frac{\theta}{2}\right)\sec\left(\frac{\theta}{2}\right)^3}{\sqrt{2}s^{3/2}(-4m^2+s)^2},$$

$$u_{9\,11} = -u_{7\,20} = -\frac{m\left(4m^2-s+\left(4m^2-3s\right)\cos(\theta)\right)\operatorname{cosec}\left(\frac{\theta}{2}\right)\sec\left(\frac{\theta}{2}\right)^3}{\sqrt{2}s^{3/2}(-4m^2+s)^2},$$

$$u_{10\,11} = u_{10\,20} = -\frac{\sqrt{2}m\cos(\theta)\left(2m^2-s+2m^2\cos(\theta)\right)\operatorname{cosec}\left(\frac{\theta}{2}\right)\sec\left(\frac{\theta}{2}\right)^3}{s^{3/2}(-4m^2+s)^2},$$

$$u_{6\,12} = u_{5\,16} = -2u_{7\,12} = 2u_{7\,16} = u_{8\,24} = 2u_{9\,12} = -2u_{9\,24} = \frac{8m^2\operatorname{cosec}\left(\frac{\theta}{2}\right)^2}{s(-4m^2+s)^2},$$

$$u_{10\,12} = \frac{4m^2\left(-4m^2+s+\left(4m^2-2s\right)\cos(\theta)\right)\operatorname{cosec}\left(\frac{\theta}{2}\right)^2}{(-4m^2s+s^2)^2},$$

$$u_{7\,13} = -u_{9\,13} = \frac{-16\sqrt{2}m^3\operatorname{cosec}(\theta)}{s^{3/2}(-4m^2+s)^2},$$

$$u_{10\,14} = \frac{-4m^2\left(4m^2-s+4m^2\cos(\theta)\right)\sec\left(\frac{\theta}{2}\right)^2}{s^2(-4m^2+s)^2},$$

$$u_{2\,15} = u_{3\,18} = 2u_{4\,15} = -2u_{4\,18} = \frac{-16\sqrt{2}m\operatorname{cosec}(\theta)^2\left(\cot(\theta)+\operatorname{cosec}(\theta)\right)}{\sqrt{s}(-4m^2+s)^2},$$

$$u_{5\,15} = -2u_{6\,15} = 2u_{6\,18} = -u_{8\,18} = \frac{4\sqrt{2}m\cot\left(\frac{\theta}{2}\right)\operatorname{cosec}\left(\frac{\theta}{2}\right)^2}{\sqrt{s}(-4m^2+s)^2},$$

$$u_{7\,15} = u_{9\,18} = \frac{m\left(1+3\cos(\theta)\right)\operatorname{cosec}\left(\frac{\theta}{2}\right)^3\sec\left(\frac{\theta}{2}\right)}{\sqrt{2}\sqrt{s}(-4m^2+s)^2},$$

$$u_{9\,15} = u_{7\,18} = -\frac{m\left(-4m^2+s+\left(4m^2+s\right)\cos(\theta)\right)\operatorname{cosec}\left(\frac{\theta}{2}\right)^3\sec\left(\frac{\theta}{2}\right)}{\sqrt{2}s^{3/2}(-4m^2+s)^2},$$

$$u_{10\,15} = -u_{10\,18} = \frac{\sqrt{2}m\cos(\theta)\left(-2m^2+s+2m^2\cos(\theta)\right)\operatorname{cosec}\left(\frac{\theta}{2}\right)^3\sec\left(\frac{\theta}{2}\right)}{s^{3/2}(-4m^2+s)^2},$$

$$u_{10\,16} = u_{10\,24} = \frac{2m^2\left(-4m^2+s+4m^2\cos(\theta)\right)\operatorname{cosec}\left(\frac{\theta}{2}\right)^2}{(-4m^2s+s^2)^2},$$

$$u_{1\,17} = -\frac{(-3+\cos(\theta))\,\mathrm{cosec}\left(\frac{\theta}{2}\right)^2 \sec\left(\frac{\theta}{2}\right)^4}{\left(-4m^2+s\right)^2},$$

$$u_{2\,17} = -u_{3\,17} = \frac{2\sec\left(\frac{\theta}{2}\right)^4}{\left(-4m^2+s\right)^2},$$

$$u_{4\,17} = \frac{\left(4m^2-3s+\left(4m^2+s\right)\cos(\theta)\right)\mathrm{cosec}\left(\frac{\theta}{2}\right)^2 \sec\left(\frac{\theta}{2}\right)^4}{4s\left(-4m^2+s\right)^2},$$

$$u_{5\,17} = u_{8\,17} = \frac{\left(2m^2-3s\cos(\theta)+\left(-2m^2+s\right)\cos(2\theta)\right)\mathrm{cosec}\left(\frac{\theta}{2}\right)^2 \sec\left(\frac{\theta}{2}\right)^4}{4s\left(-4m^2+s\right)^2},$$

$$u_{6\,17} = \frac{\left(8m^2-5s+2\left(4m^2+s\right)\cos(\theta)-s\cos(2\theta)\right)\mathrm{cosec}\left(\frac{\theta}{2}\right)^2 \sec\left(\frac{\theta}{2}\right)^4}{8s\left(-4m^2+s\right)^2},$$

$$u_{7\,17} = -u_{9\,17} = \frac{\left(-12m^2+s+8\left(-2m^2+s\right)\cos(\theta)-\left(4m^2+s\right)\cos(2\theta)\right)\mathrm{cosec}\left(\frac{\theta}{2}\right)^2 \sec\left(\frac{\theta}{2}\right)^4}{16s\left(-4m^2+s\right)^2},$$

$$u_{10\,17} = \frac{\left(\left(4m^4-16m^2s+3s^2\right)\cos(\theta)+\left(-8m^4-4m^2s+3s^2\right)\cos(2\theta)\right)\mathrm{cosec}\left(\frac{\theta}{2}\right)^2 \sec\left(\frac{\theta}{2}\right)^4}{16s^2\left(-4m^2+s\right)^2}$$

$$+\frac{4\left(2m^4-3m^2s+s^2-m^4\cos(3\theta)\right)\mathrm{cosec}\left(\frac{\theta}{2}\right)^2 \sec\left(\frac{\theta}{2}\right)^4}{16s^2\left(-4m^2+s\right)^2},$$

$$u_{4\,19} = \frac{32m^2\mathrm{cosec}(\theta)^2}{s\left(-4m^2+s\right)^2},$$

$$u_{7\,19} = -u_{9\,19} = \frac{-16m^2\cot(\theta)\,\mathrm{cosec}(\theta)}{s\left(-4m^2+s\right)^2},$$

$$u_{10\,19} = \frac{-16m^2\left(-m^2+s+m^2\cos(2\theta)\right)\mathrm{cosec}(\theta)^2}{s^2\left(-4m^2+s\right)^2},$$

$$u_{1\,21} = \frac{(3+\cos(\theta))\,\mathrm{cosec}\left(\frac{\theta}{2}\right)^4 \sec\left(\frac{\theta}{2}\right)^2}{\left(-4m^2+s\right)^2},$$

$$u_{2\,21} = -u_{3\,21} = \frac{-2\mathrm{cosec}\left(\frac{\theta}{2}\right)^4}{\left(-4m^2+s\right)^2},$$

$$u_{4\,21} = -\frac{\left(-4m^2+3s+\left(4m^2+s\right)\cos(\theta)\right)\mathrm{cosec}\left(\frac{\theta}{2}\right)^4 \sec\left(\frac{\theta}{2}\right)^2}{4s\left(-4m^2+s\right)^2},$$

$$u_{5\,21} = u_{8\,21} = \frac{\left(-2m^2 + s + 3s\cos(\theta) + 2m^2\cos(2\theta)\right)\operatorname{cosec}\left(\frac{\theta}{2}\right)^4 \sec\left(\frac{\theta}{2}\right)^2}{4s(-4m^2+s)^2},$$

$$u_{6\,21} = -\frac{\left(8m^2 + s + \left(-8m^2 + 6s\right)\cos(\theta) + s\cos(2\theta)\right)\operatorname{cosec}\left(\frac{\theta}{2}\right)^4 \sec\left(\frac{\theta}{2}\right)^2}{8s(-4m^2+s)^2},$$

$$u_{7\,21} = -u_{9\,21} = \frac{\left(-4m^2 + s + \left(4m^2 + s\right)\cos(\theta)\right)\operatorname{cosec}\left(\frac{\theta}{2}\right)^4}{4s(-4m^2+s)^2},$$

$$u_{10\,21} = \left(\left(-4m^4 + s^2\right)\cos(\theta) + \left(-8m^4 + 4m^2 s + s^2\right)\cos(2\theta)\right.$$
$$\left. + 2\left(4m^4 - 2m^2 s + s^2 + 2m^4\cos(3\theta)\right)\right)\frac{\operatorname{cosec}\left(\frac{\theta}{2}\right)^4 \sec\left(\frac{\theta}{2}\right)^2}{16s^2(-4m^2+s)^2},$$

$$u_{10\,25} = \frac{16m^4}{(-4m^2 s + s^2)^2}.$$

In these formulas, $\theta$ is the c.m. scattering angle and $s$ is the square of the total energy in the c.m. frame.

Of the 625 elements of the matrix $K^J_{i,j}$, 420 elements vanish. Below, we present the 205 nonzero elements of the matrix $K^J_{i,j}$ [the numbering of the elements corresponds to the order in which the helicity amplitudes are listed in expression (6)]:

$$K^J_{1,1} = I^J_1, \quad K^J_{1,2} = N_2 I^J_2, \quad K^J_{1,3} = I^J_3,$$
$$K^J_{1,4} = N_1 I^J_4, \quad K^J_{1,5} = N_1 N_2 I^J_5, \quad K^J_{1,6} = N_1 I^J_6,$$
$$K^J_{1,7} = I^J_7, \quad K^J_{1,8} = N_2 I^J_8, \quad K^J_{1,9} = I^J_9;$$
$$K^J_{2,2} = I^J_1, \quad K^J_{2,8} = -I^J_9, \quad K^J_{2,10} = -N_2 I^J_2,$$
$$K^J_{2,11} = -I^J_3, \quad K^J_{2,12} = -N_1 I^J_4,$$
$$K^J_{2,13} = -N_1 N_2 I^J_5, \quad K^J_{2,14} = -N_1 I^J_6,$$
$$K^J_{2,15} = -I^J_7, \quad K^J_{2,16} = -N_2 I^J_8;$$
$$K^J_{3,3} = I^J_1, \quad K^J_{3,7} = I^J_9, \quad K^J_{3,11} = -N_2 I^J_2,$$
$$K^J_{3,15} = N_2 I^J_8, \quad K^J_{3,17} = I^J_3, \quad K^J_{3,18} = N_1 I^J_4,$$
$$K^J_{3,19} = N_1 N_2 I^J_5, \quad K^J_{3,20} = N_1 I^J_6, \quad K^J_{3,21} = I^J_7;$$
$$K^J_{4,4} = I^J_1, \quad K^J_{4,6} = -I^J_9, \quad K^J_{4,12} = -N_2 I^J_2,$$
$$K^J_{4,14} = -N_2 I^J_8, \quad K^J_{4,18} = I^J_3, \quad K^J_{4,20} = -I^J_7,$$
$$K^J_{4,22} = -N_1 I^J_4, \quad K^J_{4,23} = -N_1 N_2 I^J_5,$$
$$K^J_{4,24} = -N_1 I^J_6; \quad K^J_{5,5} = I^J_1 + I^J_9,$$
$$K^J_{5,13} = N_2(I^J_8 - I^J_2), \quad K^J_{5,19} = I^J_3 + I^J_7,$$
$$K^J_{5,23} = N_1(I^J_6 - I^J_4), \quad K^J_{5,25} = N_1 N_2 I^J_5;$$

$$K^J_{6,4} = -I^J_9, \quad K^J_{6,6} = I^J_1, \quad K^J_{6,12} = -N_2 I^J_8,$$
$$K^J_{6,14} = -N_2 I^J_2, \quad K^J_{6,18} = -I^J_7, \quad K^J_{6,20} = I^J_3,$$
$$K^J_{6,22} = -N_1 I^J_6, \quad K^J_{6,23} = N_1 N_2 I^J_5,$$
$$K^J_{6,24} = -N_1 I^J_4;$$
$$K^J_{7,3} = I^J_9, \quad K^J_{7,7} = I^J_1, \quad K^J_{7,11} = N_2 I^J_8,$$
$$K^J_{7,15} = -N_2 I^J_2, \quad K^J_{7,17} = I^J_7, \quad K^J_{7,18} = -N_1 I^J_6,$$
$$K^J_{7,19} = N_1 N_2 I^J_5, \quad K^J_{7,20} = -N_1 I^J_4, \quad K^J_{7,21} = I^J_3;$$
$$K^J_{8,2} = -I^J_9, \quad K^J_{8,8} = I^J_1, \quad K^J_{8,10} = -N_2 I^J_8,$$
$$K^J_{8,11} = I^J_7, \quad K^J_{8,12} = -N_1 I^J_6, \quad K^J_{8,13} = N_1 N_2 I^J_5,$$
$$K^J_{8,14} = -N_1 I^J_4, \quad K^J_{8,15} = I^J_3, \quad K^J_{8,16} = -N_2 I^J_2;$$
$$K^J_{9,1} = I^J_9, \quad K^J_{9,2} = -N_2 I^J_8, \quad K^J_{9,3} = I^J_7,$$
$$K^J_{9,4} = -N_1 I^J_6, \quad K^J_{9,5} = N_1 N_2 I^J_5,$$
$$K^J_{9,6} = -N_1 I^J_4, \quad K^J_{9,7} = I^J_3, \quad K^J_{9,8} = -N_2 I^J_2,$$
$$K^J_{9,9} = I^J_1;$$
$$K^J_{10,2} = -I^J_2, \quad K^J_{10,8} = -I^J_8, \quad K^J_{10,10} = -N_2 I^J_{10},$$
$$K^J_{10,11} = -I^J_{11}, \quad K^J_{10,12} = -N_1 I^J_{12},$$
$$K^J_{10,13} = -N_1 N_2 I^J_{13}, \quad K^J_{10,14} = -N_1 I^J_{14},$$
$$K^J_{10,15} = -I^J_{15}, \quad K^J_{10,16} = -N_2 I^J_{16};$$
$$K^J_{11,3} = -I^J_2, \quad K^J_{11,7} = I^J_8, \quad K^J_{11,11} = -N_2 I^J_{10},$$
$$K^J_{11,15} = N_2 I^J_{16}, \quad K^J_{11,17} = I^J_{11}, \quad K^J_{11,18} = N_1 I^J_{12},$$
$$K^J_{11,19} = N_1 N_2 I^J_{13}, \quad K^J_{11,20} = N_1 I^J_{14},$$
$$K^J_{11,21} = I^J_{15};$$

$$K^J_{12,4} = -I^J_2, \quad K^J_{12,6} = -I^J_8, \quad K^J_{12,12} = -N_2 I^J_{10},$$
$$K^J_{12,14} = -N_2 I^J_{16}, \quad K^J_{12,18} = I^J_{11}, \quad K^J_{12,20} = -I^J_{15},$$
$$K^J_{12,22} = -N_1 I^J_{12}, \quad K^J_{12,23} = -N_1 N_2 I^J_{13},$$
$$K^J_{12,24} = -N_1 I^J_{14};$$
$$K^J_{13,5} = I^J_8 - I^J_2, \quad K^J_{13,13} = N_2(I^J_{16} - I^J_{10}),$$
$$K^J_{13,19} = I^J_{11} + I^J_{15}, \quad K^J_{13,23} = N_1(I^J_{14} - I^J_{12}),$$
$$K^J_{13,25} = N_1 N_2 I^J_{13};$$
$$K^J_{14,4} = -I^J_8, \quad K^J_{14,6} = -I^J_2, \quad K^J_{14,12} = -N_2 I^J_{16},$$
$$K^J_{14,14} = -N_2 I^J_{10}, \quad K^J_{14,18} = -I^J_{15}, \quad K^J_{14,20} = I^J_{11},$$
$$K^J_{14,22} = -N_1 I^J_{14}, \quad K^J_{14,23} = N_1 N_2 I^J_{13},$$
$$K^J_{14,24} = -N_1 I^J_{12};$$
$$K^J_{15,3} = I^J_8, \quad K^J_{15,7} = -I^J_2, \quad K^J_{15,11} = N_2 I^J_{16},$$
$$K^J_{15,15} = -N_2 I^J_{10}, \quad K^J_{15,17} = I^J_{15},$$
$$K^J_{15,18} = -N_1 I^J_{14}, \quad K^J_{15,19} = N_1 N_2 I^J_{13},$$
$$K^J_{15,20} = -N_1 I^J_{12}, \quad K^J_{15,21} = I^J_{11};$$
$$K^J_{16,2} = -I^J_8, \quad K^J_{16,8} = -I^J_2, \quad K^J_{16,10} = -N_2 I^J_{16},$$
$$K^J_{16,11} = I^J_{15}, \quad K^J_{16,12} = -N_1 I^J_{14},$$
$$K^J_{16,13} = N_1 N_2 I^J_{13}, \quad K^J_{16,14} = -N_1 I^J_{12},$$
$$K^J_{16,15} = I^J_{11}, \quad K^J_{16,16} = -N_2 I^J_{10};$$
$$K^J_{17,3} = I^J_3, \quad K^J_{17,7} = I^J_7, \quad K^J_{17,11} = N_2 I^J_{11},$$
$$K^J_{17,15} = N_2 I^J_{15}, \quad K^J_{17,17} = I^J_{17}, \quad K^J_{17,18} = N_1 I^J_{18},$$
$$K^J_{17,19} = N_1 N_2 I^J_{19}, \quad K^J_{17,20} = N_1 I^J_{20},$$
$$K^J_{17,21} = I^J_{21};$$
$$K^J_{18,4} = I^J_3, \quad K^J_{18,6} = -I^J_7, \quad K^J_{18,12} = N_2 I^J_{11},$$
$$K^J_{18,14} = -N_2 I^J_{15}, \quad K^J_{18,18} = I^J_{17}, \quad K^J_{18,20} = -I^J_{21},$$
$$K^J_{18,22} = -N_1 I^J_{18}, \quad K^J_{18,23} = -N_1 N_2 I^J_{19},$$
$$K^J_{18,24} = -N_1 I^J_{20};$$
$$K^J_{19,5} = I^J_3 + I^J_7, \quad K^J_{19,13} = N_2(I^J_{11} + I^J_{15}),$$
$$K^J_{19,19} = I^J_{17} + I^J_{21}, \quad K^J_{19,23} = N_1(I^J_{20} - I^J_{18}),$$
$$K^J_{19,25} = N_1 N_2 I^J_{19};$$
$$K^J_{20,4} = -I^J_7, \quad K^J_{20,6} = I^J_3, \quad K^J_{20,12} = -N_2 I^J_{15},$$
$$K^J_{20,14} = N_2 I^J_{11}, \quad K^J_{20,18} = -I^J_{21}, \quad K^J_{20,20} = I^J_{17},$$
$$K^J_{20,22} = -N_1 I^J_{20}, \quad K^J_{20,23} = N_1 N_2 I^J_{19},$$
$$K^J_{20,24} = -N_1 I^J_{18};$$
$$K^J_{21,3} = I^J_7, \quad K^J_{21,7} = I^J_3, \quad K^J_{21,11} = N_2 I^J_{15},$$
$$K^J_{21,15} = N_2 I^J_{11}, \quad K^J_{21,17} = I^J_{21},$$
$$K^J_{21,18} = -N_1 I^J_{20}, \quad K^J_{21,19} = N_1 N_2 I^J_{19},$$
$$K^J_{21,20} = -N_1 I^J_{18}, \quad K^J_{21,21} = I^J_{17};$$
$$K^J_{22,4} = -I^J_4, \quad K^J_{22,6} = -I^J_6, \quad K^J_{22,12} = -N_2 I^J_{12},$$
$$K^J_{22,14} = -N_2 I^J_{14}, \quad K^J_{22,18} = -I^J_{18},$$
$$K^J_{22,20} = -I^J_{20}, \quad K^J_{22,22} = -N_1 I^J_{22},$$
$$K^J_{22,23} = -N_1 N_2 I^J_{23}, \quad K^J_{22,24} = -N_1 I^J_{24};$$
$$K^J_{23,5} = I^J_6 - I^J_4, \quad K^J_{23,13} = N_2(I^J_{14} - I^J_{12}),$$
$$K^J_{23,19} = I^J_{20} - I^J_{18}, \quad K^J_{23,23} = N_1(I^J_{24} - I^J_{22}),$$
$$K^J_{23,25} = N_1 N_2 I^J_{23};$$
$$K^J_{24,4} = -I^J_6, \quad K^J_{24,6} = -I^J_4, \quad K^J_{24,12} = -N_2 I^J_{14},$$
$$K^J_{24,14} = -N_2 I^J_{12}, \quad K^J_{24,18} = -I^J_{20},$$
$$K^J_{24,20} = -I^J_{18}, \quad K^J_{24,22} = -N_1 I^J_{24},$$
$$K^J_{24,23} = N_1 N_2 I^J_{23}, \quad K^J_{24,24} = -N_1 I^J_{22};$$
$$K^J_{25,5} = 2I^J_5, \quad K^J_{25,13} = 2N_2 I^J_{13}, \quad K^J_{25,19} = 2I^J_{19},$$
$$K^J_{25,23} = 2N_1 I^J_{23}, \quad K^J_{25,25} = N_1 N_2 I^J_{25}.$$

In these formulas,

$$N_1 = \frac{|\mathbf{k}'|^2 - k'^2_0}{m^2}, \quad N_2 = \frac{|\mathbf{q}'|^2 - q'^2_0}{m^2}$$

are the normalization factors for vector particles whose 4-momenta are $k' = (k'_0, \mathbf{k}')$ and $q' = (q'_0, \mathbf{q}')$, respectively.

## REFERENCES

1. E. E. Salpeter and H. A. Bethe, Phys. Rev. **84**, 1232 (1951).
2. Y. Nambu, Prog. Theor. Phys. **5**, 614 (1950).
3. C. Itzykson and J.-B. Zuber, *Quantum Field Theory* (McGraw-Hill, New York, 1980; Mir, Moscow, 1984).
4. A. Gerstein, D. A. Owen, *et al.*, Phys. Rev. D **13**, 1140 (1976).
5. K. Schwartz, J. Haidebauer, and J. Frohlich, Phys. Rev. C **33**, 456 (1986).
6. J. Fröhlich, K. Schwartz, L. Streit, and H. Zingl, Phys. Rev. C **25**, 2591 (1982).
7. M. A. Braun and V. B. Senyushkin, Yad. Fiz. **21**, 279 (1975) [Sov. J. Nucl. Phys. **21**, 147 (1975)].
8. M. A. Braun and V. M. Suslov, Nucl. Phys. A **496**, 687 (1989).
9. E. Hummel and J. A. Tjon, Phys. Rev. C **42**, 423 (1990).
10. E. Hummel and J. A. Tjon, Phys. Rev. C **49**, 21 (1994).
11. A. V. Efremov and A. V. Radyushin, Riv. Nuovo Cimento **3**, 1 (1980).
12. P. Jain and H. Munczek, Phys. Rev. D **45**, 438 (1992).
13. P. Jain and H. Munczek, Phys. Rev. D **48**, 5403 (1993).

14. J. R. Henley, Phys. Rev. D **20**, 2532 (1979).
15. J. R. Henley, Phys. Rev. D **22**, 419 (1980).
16. J.-F. Lagae, Phys. Rev. D **45**, 305 (1992).
17. E. Byckling and K. Kajantie, *Particle Kinematics* (Macmillan, London, 1973; Mir, Moscow, 1975).
18. P. D. B. Collins, *An Introduction to Regge Theory and High-Energy Physics* (Cambridge Univ. Press, Cambridge, 1977; Atomizdat, Moscow, 1980).
19. V. B. Berestetskiĭ, E. M. Lifshitz, and L. L. Pitaevskiĭ, *Quantum Electrodynamics* (Nauka, Moscow, 1989, 4th ed.; Pergamon, Oxford, 1982, transl. 2nd ed.).

*Translated by A. Isaakyan*

*Physics of Atomic Nuclei, Vol. 67, No. 4, 2004, pp. 872–873. Translated from Yadernaya Fizika, Vol. 67, No. 4, 2004, pp. 894–895.*
*Original Russian Text Copyright © 2004 by the Editorial Board.*

# FUTURE PUBLICATIONS

## Associated Production of $\phi\Lambda^0$ in the EXCHARM Experiment

**A. N. Aleev, V. P. Balandin, E. A. Gudzovsky, D. K. Gur'ev, D. D. Emel'yanov, A. I. Zinchenko, Z. M. Ivanchenko, I. M. Ivanchenko, M. N. Kapishin, V. D. Kekelidze, Z. I. Kozhenkova, V. V. Koren'kov, I. G. Kosarev, N. A. Kuz'min, A. L. Lyubimov, D. T. Madigozhin, V. G. Maznyi, A. Sh. Mestvirishvili, N. A. Molokanova, A. N. Morozov, R. E. Pis'menny, V. D. Poze, I. A. Polenkevich, Yu. K. Potrebenikov, L. A. Slepets, V. N. Spaskov, O. V. Bulekov, S. V. Eremin, F. M. Sergeev, A. K. Ponosov, N. S. Amaglobeli, I. M. Geshkov, T. S. Grigalashvili, A. A. Loktionov, and T. Ponta**
**The EXCHARM Collaboration**

The features of the associated production of $\phi$ mesons with $\Lambda^0$ hyperons in neutron—carbon interactions were investigated. The experiment was performed with the aid of the EXCHARM spectrometer at the Serpukhov accelerator in a neutron beam of energy in the interval 20—70 GeV. The differential cross section for the inclusive associated production of $\phi\Lambda^0$ was measured.

## Contribution of Excited Nuclei $^{12}$C* to the Channel of the Production of Three $\alpha$ Particles in $^{16}$O$p$ Collisions at 3.25 GeV/$c$ per Nucleon

**E. Kh. Bazarov, V. V. Glagolev, K. G. Gulamov, V. V. Lugovoi, S. L. Lutpullaev, K. Olimov, E. Turumov, A. A. Yuldashev, and B. S. Yuldashev**

A phenomenological analysis of the channel of the production of three $\alpha$ particles in collisions of relativistic oxygen nuclei with protons is performed for the first time. It is shown that one-third of it is saturated by the decay of an excited nucleus $^{12}$C*, while the remaining part is due to direct Fermi breakup or the quasielastic knockout of one $\alpha$ cluster from a loosely bound residual nucleus involving three $\alpha$ particles. The results obtained by simulating the decay of the excited system involving three $\alpha$ particles within the isotropic-phase-space model describe experimental data satisfactorily at moderate values of the excitation energy ($\Delta E^* < 15$ MeV).

## Theoretical Investigation of the Angular-Momentum Dependence of the Mean Time of Fission of Excited Nuclei

**I. I. Gontchar, N. A. Ponomarenko, V. V. Turkin, and L. A. Litnevsky**

Recently, mean nuclear-fission times were measured at the GANIL accelerator by the shadow method at excitation energies between 80 and 400 MeV. These experiments served as a motivation for us to perform systematic calculations of the time distributions of fission events and the mean fission times versus the angular momentum, initial excitation energy, and fissility of a primary excited nucleus. The mean fission times are given as a function of the angular momentum $L$. The calculations were performed within the refined version of the combined dynamical—statistical model. It turned out that, if the height of the fission barrier at $L = 0$ is sizably greater than the neutron binding energy, the $L$ dependence of the mean fission times has a resonance character. Such behavior of the mean fission times $\langle t_{\mathrm{f}}\rangle$ is obtained both from statistical calculations and from a dynamical simulation of the process with allowance for friction. It is shown that the maximum in the $L$ dependence of $\langle t_{\mathrm{f}}\rangle$ is due to the fission of nuclei that lost a considerable part of the initial excitation energy through the emission of neutrons. The majority of the calculations were performed for $^{190}$Pt at an initial excitation energy of 150 MeV. It is shown that the resonance behavior disappears with increasing fissility, but it survives over a broad range of initial excitation energies.

## Dynamics of Effective Gluon Fields in Hadrons within the Method of Vacuum Correlation Functions

**D. S. Kuzmenko**

Within the method of vacuum correlation functions, the mechanism of confinement is studied in terms of effective fields that are defined in a gauge-invariant way with the aid of the Wilson loop. At short distances from sources, gluodynamics in terms of effective fields is described in the leading order of perturbation theory by the

Maxwell equations, the color Coulomb potential for single-gluon exchange being reproduced among other things. The inclusion of three-point correlation functions for gluon fields leads to the pattern of confinement that arises upon the compression of the effective field by effective magnetic currents and the screening of the color Coulomb field owing to vacuum polarization.

## Field-Theory Approach to the Dibaryon Model of Nuclear Forces

**V. I. Kukulin and M. A. Shikhalev**

A covariant field-theory formulation of the recently developed dibaryon model of nuclear forces is given. The model involves an intermediate dibaryon dressed with $\pi$, $\sigma$, $\rho$, and other fields; the corresponding mesons can be in various orbitally excited states with respect to a six-quark bag; and scalar, pseudoscalar, vector, and axial-vector fields are taken into account for the dressed dibaryon. Particular attention is given to $NN$ interaction in even partial waves. A relativistically covariant $NN$ potential is derived. It is shown that a simple generalization of the single-channel model makes it possible to take into account coupling to other baryon channels of the $N\Delta$, $\Delta\Delta$, $NN^*(1535)$, etc., types, this in turn leading to a description of the production of various mesons within this approach. The model also enables one to describe, in a natural way, $2\pi$ production in $NN$ collisions in the isoscalar and in the isovector channel and provides a new formulation of the theory of meson-exchange currents in the physics of electromagnetic interactions. The possible applications of the developed approach in the physics of hadron interactions and in nuclear physics on the whole are discussed.

## Features of the Inverse Current Generated in an Iron Absorber by Protons of Energy above 1 TeV

**D. M. Podorozhny, I. D. Rapoport, and A. N. Turundaevsky**

The generation of the inverse current of particles in dense matter is investigated on the basis of a detailed simulation of cascade processes. The energy dependence of the albedo flux is analyzed along with the spatial and angular distributions of various components of the inverse current.

## Pole Heavy-Quark Masses in the Hamiltonian Approach

**A. M. Badalian, B. L. Bakker, and A. I. Veselov**

Strong restrictions on the pole masses $m_b$ and $m_c$ are obtained from the fact that the nonperturbative self-energy contribution $C_{\mathrm{SE}}$ to the heavy-meson mass is small: $C_{\mathrm{SE}}(b\bar{b}) = 0$ and $C_{\mathrm{SE}}(c\bar{c}) \cong -40$ MeV [Yu.A. Simonov, Phys. Lett. B **515**, 137 (2001)]. An analysis of the $b\bar{b}$ and $c\bar{c}$ spectra with the aid of a relativistic (string) Hamiltonian gives the values of $m_b(\text{2-loop}) = 4.78 \pm 0.05$ GeV and $m_c(\text{2-loop}) = 1.39 \pm 0.06$ GeV, which correspond to the $\overline{MS}$ running masses $\overline{m}_b(\overline{m}_b) = 4.19 \pm 0.04$ GeV and $\overline{m}_c(\overline{m}_c) = 1.10 \pm 0.05$ GeV.

*Physics of Atomic Nuclei, Vol. 67, No. 4, 2004, p. 874. From Yadernaya Fizika, Vol. 67, No. 4, 2004, p. 896.*

## ERRATA

# Erratum: "Correlation Femtoscopy of Multiparticle Processes"

## [*Physics of Atomic Nuclei* 67, 72–82 (2004)]

**R. Lednicky**

On page 78, right column, lines 4–5 from bottom:
Due to the azimuthal symmetry, the angles $\phi_r$ and $\phi_T$ are uniformly distributed and the vector . . .
should read:
Due to the azimuthal symmetry, the vector . . .